BULGARIAN CHEMICAL COMMUNICATIONS

2017 Volume 49 / Number 3

Journal of the Chemical Institutes
of the Bulgarian Academy of Sciences
and of the Union of Chemists in Bulgaria

Bulgarian Chemical Communications, Volume 49, Number 3, (pp. 557 – 561) 2017

Radiation induced formation of poly (*N*-isopropyl acrylamide)-bovine serum albumin covalent conjugates and their immunogenicity

P. Vural[1], M. Karahan[2*], P. Pelit Arayici[3], Z. Mustafaeva[3]

[1]*Yildiz Technical University, Faculty of Arts and Sciences, Department of Chemistry, 34220 Esenler-Istanbul, Turkey*
[2]*Üsküdar University, Faculty of Engineering and Natural Sciences, Department of Bioengineering, 34662 Uskudar-Istanbul, Turkey*
[3]*Yildiz Technical University, Faculty of Chemical and Metallurgical Engineering, Department of Bioengineering, 34220 Esenler-Istanbul, Turkey*

Received May 18, 2014; Accepted October 3, 2016

Poly (N-isopropyl acrylamide) was bioconjugated to bovine serum albumin by ^{60}Co γ-rays at pH 7. The covalent binding mechanism of the radiation induced poly (N-isopropyl acrylamide)-bovine serum albumin conjugate was analyzed by high performance liquid chromatography while the immunization property was analyzed by ELISA tests. High performance liquid chromatography results showed the conjugate formation of polymer with protein and also the increase in the radio stability of the protein as a result of this formation. The immunization results of irradiated conjugates in Balb/c mice were significantly higher than the free BSA immunization results. This system is attractive for application of a novel immunogenic model system in vaccine technology.

Keywords: Immunization, Irradiation, Polyelectrolytes, Proteins, Vaccine.

INTRODUCTION

The bioconjugation of synthetic polymers with biomolecules finds various implementations in many different areas such as biotechnology, medicine, pharmacy and engineering. Furthermore, while the solid state (water insoluble) polymeric systems are used in functional implementations like tissue engineering and cell generation, the water soluble polymer-biomolecule bioconjugates are lately being used in protein purification, enzyme stability, drug delivery systems, biosensor production, intracellular transfer of DNA, and protein modification [1-15].

A new approach is brought about for the resolution of the synthetic vaccine problem. The strong effect of the synthetic polyelectrolytes (PEs) (negatively or positively charged polymers) on the organisms' immune systems qualifies these PEs to be used as carrier matrix (and adjuvant) for microbes and virus antigens (peptides), and a tool for the synthesis of high antigen-specific immunogenic bioconjugates (and biocomplexes). Such synthetic macromolecular bioconjugates (and biocomplexes) display protective immunity against numerous diseases such as tuberculosis, flu, salmonella, working as a synthetic polymeric vaccine system.

Recent *in vivo* studies have shown that the bioconjugates which are synthesized by conjugation of proteins and neutral uncharged synthetic polymers (like polyvinyl alcohol, poly-N-vinylpyrrolidone, polyethylene glycol, dextran, etc. dissolved in water) have relatively poor immunogenic properties in contrast to natural protein antigens. Additionally, it has been proven that the proteins are more stable within longer periods. The conjugation of polyethylene glycol with albumin and liver catalase enzyme decreases the immune reactivity of these proteins. Polymers with such structure do not have adjuvant characteristics. Nevertheless, the high molecular weight synthetic PEs, negatively or positively charged polymers or polymers that are charged at the physiologic conditions of the medium, polybases, polycations, polyacids and their copolymers show similar adjuvant effects independently of the chemical structure of their monomers (auxiliary chemicals which may enter into the organism with the antigens to increase the immunity of the organism). As the complexes or conjugates of different antigens with PEs are immunized to the living organism, the number of formed antigen-specific antibodies increases excessively, and they show protective characteristics on living organisms against viruses acting like a polymeric vaccine [1, 6, 12, 16].

In bioconjugate formation of the antigens with neutral polymers, the surface of the biomolecule is covered with a neutral and flexible hydrophilic lid. Closing the antigen determinants in such a manner makes the antigen molecule inert in the immune procedure [17-19].

Poly (N-isopropyl acrylamide) which carries characteristics of PEs was bioconjugated with bovine serum albumin by ^{60}Co γ-rays at pH 7 in order to develop synthetic polymeric vaccine model

* To whom all correspondence should be sent:
E-mail: mesut.karahan@uskudar.edu.tr

systems. The conjugation of poly (N-isopropyl acrylamide) and bovine serum was analyzed by high performance liquid chromatography, the immunization property was analyzed by ELISA tests.

EXPERIMENTAL

Materials

Poly (NIPAAm) (Mw: 60 kDa) was supplied by Prof. Dr. Yoshihito Osada (Hokkaido University, Sapporo, Japan). Bovine serum albumin (BSA) (Mw: 66 kDa, pI: 4.9) was purchased from Sigma Chemical Company (St. Louis, USA).

Synthesis of Poly (NIPAAm) - BSA Bioconjugates

The mixture of 0.1% poly (NIPAAm) and 0.15% BSA prepared in phosphate buffer solution was exposed to radiation at 100, 300, 500, 700 Gy from a ^{60}Co γ-ray source to form poly (NIPAAm)-BSA conjugate. The same procedure was previously used to prepare 0.1% poly (NIPAAm) and 0.15% BSA solutions each.

Preparation of Phosphate Buffer Solution

In order to prepare 1 l of phosphate buffer solution, each 1.1998 g of NaH_2PO_4 and 2.6807 g of Na_2HPO_4 was dissolved in 500 ml ultra pure water. After mixing these two together, 8.766 g of NaCl was added to the solution. The pH of the prepared solution was adjusted to 7 by adding 0.1 M NaOH solution.

Immunization

Poly (NIPAAm) - BSA bioconjugates were used as immunogens. Free BSA was utilized for controlling purposes. Eight week-old Balb/c mice were immunized with each of the bioconjugates by intravenous injections. The blood was collected into a microfuge tube with sodium citrate and centrifuged at 6000 g to remove red blood cells. A set of dilutions of the serum (1/50 and 1/100) was made in phosphate-buffered saline (PBS). The serum samples were tested by ELISA [20].

ELISA

To assay BSA specific antibodies, ninety-six well polystyrene plates (NUNC-immunoplates) were coated with 200 ng poly (NIPAAm)-BSA bioconjugates in parallel with BSA in 100 μl PBS. Coated plates were incubated at 4^{0}C overnight. The plates were washed two times with wash buffer (0.005% Tween-20 in PBS). Then, 0.2% casein in PBS was added to the wells, and the plates were incubated at 37^{0}C followed by washing as above. The mouse serum in dilution buffer was added to each well and the plates were incubated at 37^{0}C for 1 h. The plates were washed two times with wash buffer. Alkaline-phosphatase conjugation of polyvalent goat-antimouse Ig (Sigma) in 1/750 dilution buffer was then added to each well and incubated for 1 h at 37^{0}C. After repeating the wash step five times with wash buffer as above, the substrate buffer (1mM $ZnCl_2$, 1mM $MgCl_2$, 0.1M glycine, pH 10.4) and 1 mg/ml *p*-nitrophenyl phosphate were added. After 45 min, the absorbances at 405 nm were determined.

Gamma-Radiolysis

Gamma-radiolysis of the aqueous solutions of poly (NIPAAm) - BSA bioconjugates was performed by using a ^{60}Co γ-source (Picker 9 V). 5 ml sample solutions were irradiated at a position of 10 cm away from the source. The dose rate was measured to be 28.61 Gy/h as determined by Fricke dosimetry [21].

Gel Filtration HPLC

Poly (NIPAAm), BSA and the prepared poly (NIPAAm) - BSA were analyzed by HPLC (gel filtration chromatography) before and after irradiation.

The system consisted of a Bio-Sil Sec 250 column (7.8 mm × 300 mm), pump (LC-10Ai) and automatic sample injector (SIL-10Ai HPLC). The eluent was monitored at 214 and 280 nm by using UV detector (SPD-10Ai). A phosphate buffer containing 0.1 mol/l NaCl was used as a mobile phase at a flow rate of 1.0 ml/min at room temperature. The calibration of the column was performed by using a protein kit from Sigma Chemical Co., St. Louis, MO, USA, namely, thyroglobulin (670 kDa), immunoglobulin (155 kDa), ovalbumin (44 kDa), myoglobulin (16.9 kDa), and vitamin B12 (1.35 kDa).

Dynamic Light Scattering Method

Photon correlation spectroscopy with a Zetasizer Nano ZS instrument equipped with 4.0 mV He-Ne laser operating at a wavelength of 633 nm and a temperature of 25°C (Malvern Instruments, UK) was used to examine the average size and the size distribution of polymer and bioconjugate of protein-polymer. Before DLS measurement, each solution was filtered through a 0.2 μm RC-membrane Sartorius filters to remove the impurities in the solutions.

RESULTS AND DISCUSSION

Gel filtration HPLC was used for the poly (NIPAAm), BSA and poly (NIPAAm) - BSA

bioconjugates HPLC chromatograms of poly (NIPAAm) and BSA are given in Figure 1 and Figure 2, respectively.

Figure 1 summarizes the gel filtration HPLC results of the free polymers before and after 700 Gy irradiation. As seen from the figure, while the unirradiated free polymer shows a peak in 7.38 minutes, the polymer solution irradiated with 700 Gy shows no peak at all. It could be said that polymers are forming water insoluble aggregates by forming crosslinks in themselves at this irradiation dose.

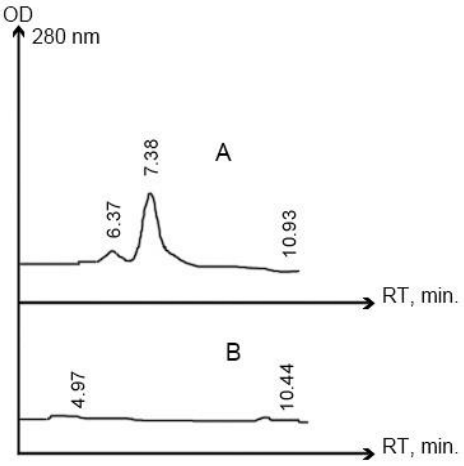

Fig. 1. HPLC results of the unirradiated (A) and irradiated (B) solutions of poly (NIPAAm) at irradiation dose (Gy): 700.

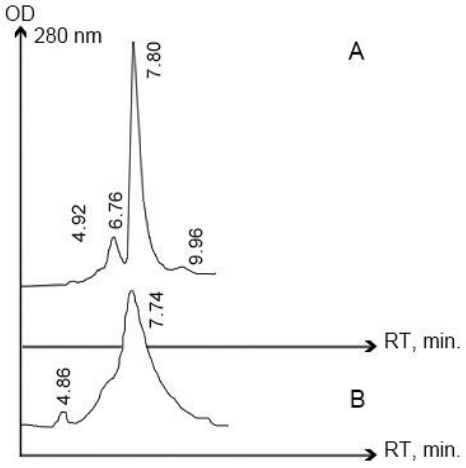

Fig. 2. HPLC results of the unirradiated (A) and irradiated (B) solutions of BSA at irradiation dose (Gy): 700.

The gel filtration results of free BSA before and after irradiation at 700 Gy are shown in Figure 2. As the figure indicates, the retention time (RT) value of the protein irradiated at 700 Gy decreased and the peak generated was significantly deformed. From this, we can suggest that BSA has denatured and its molecular weight has increased due to the 700 Gy irradiation strength.

The gel filtration HPLC results of the poly (NIPAAm) - BSA mixture with and without irradiation at 700 Gy are shown in Figure 3. As it can be understood from the figure, the polymer and the protein formed a bioconjugate by binding after 700 Gy irradiation so there was a shift in peak retention time (B), and the protein molecule in the conjugate structure was protected against irradiation (it is radiostable), which means that it has not denatured.

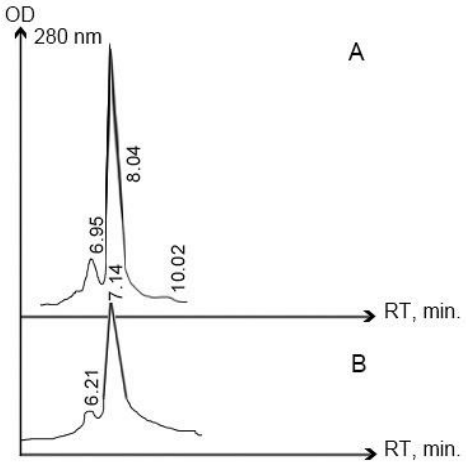

Fig. 3. HPLC results of the unirradiated (A) and irradiated (B) solutions of a poly (NIPAAm) - BSA mixture at irradiation dose (Gy): 700.

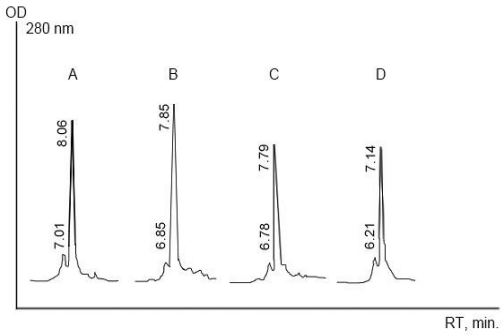

Fig. 4. HPLC results of the irradiated solutions of poly (NIPAAm) - BSA mixture at different irradiation doses (Gy): 100 (A), 300 (B), 500 (C), 700 (D).

HPLC results of the irradiated solutions of the poly (NIPAAm) - BSA mixture at different irradiation doses (Gy): 100 (A), 300 (B), 500 (C), 700 (D) are shown in Figure 4. Homogenous conjugates are formed once radioactive ray between 100-700 Gy was applied to the poly (NIPAAm) - BSA mixture. The figure shows that, as the radiation strength increases, the RT values of the peaks of the generated conjugates decrease, indicating that the generated bioconjugate had a higher molecular weight than the components in the mixture. In addition, it should be mentioned that the best

bioconjugates are obtained at 700 Gy irradiation.

If the irradiation dose increases, the hydrodynamic diameter also increases due to increased interaction between the PE of BSA. (Figure 5).

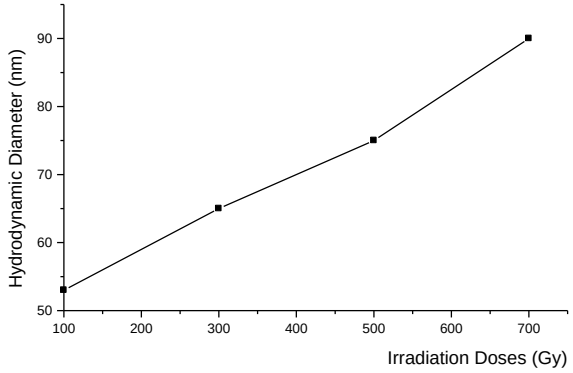

Fig. 5. Hydrodynamic diameter of poly (NIPAAm)-BSA bioconjugate at different irradiation doses (100-700 Gy).

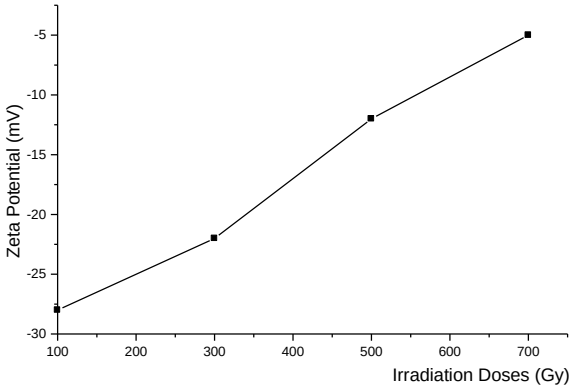

Fig. 6. Zeta potentials of poly (NIPAAm) - BSA bioconjugate at different irradiation doses (100-700 Gy).

The dynamics of formation of BSA specific antibodies (OD $_{405\ nm}$) in the blood serum of mice immunized with poly (NIPAAm) - BSA bioconjugate at different irradiation doses (100-700 Gy), and pure BSA are shown in Figure 7. As seen from the figure, the immunization results of the bioconjugates generated by irradiating at 100, 300, 500 Gy radiation strengths are close to each other, the antibody level obtained against the bioconjugate irradiated with 700 Gy is the highest, and a significantly higher value of the conjugate is observed as compared to the free BSA.

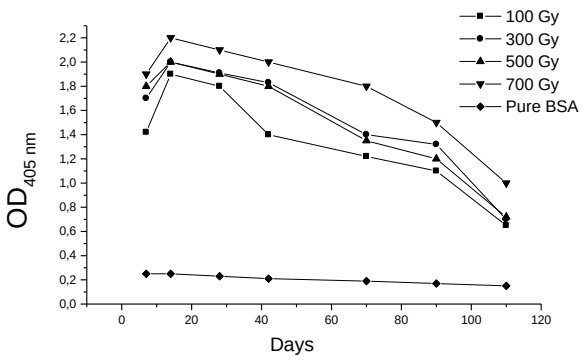

Fig. 7. The dynamics of formation of BSA specific antibodies (OD $_{405\ nm}$) in the blood serum of mice immunized with poly (NIPAAm) - BSA bioconjugate at different irradiation doses (100-700 Gy) and pure BSA.

CONCLUSION

As the results of the HPLC and ELISA tests showed, BSA was successfully conjugated to poly (NIPAAm) at pH 7 under radiation doses of 100-700 Gy without any degradation in its structure. It is seen that the best bioconjugate was generated at a radiation strength of 700 Gy. No denaturation was observed in the structure of BSA protein in this bioconjugate, which indicates an increase in its radio stability. The most important point in the increase of the polymer-protein radio stability is that the polymer macromolecules form a cover on the protein and thus, the protein molecule is protected. This bioconjugate and synthetic vaccine model system was developed by ^{60}Co γ-rays.

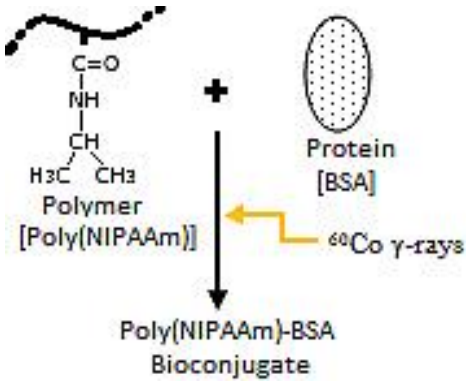

Schema. The hypothetical structure of water soluble bioconjugate irradiated with 700 Gy.

According to this, by binding the suitable synthesized antigenic peptide of a disease with polymer instead of BSA protein in the bioconjugate process, a synthetic vaccine can be developed by using the carrier matrix and adjuvant PEs for the microbes or virus antigens against that disease.

Acknowledgments: *In the loving memory of Founder Head of Yıldız Technical University Bioengineering Department, precious man of science, Prof. Dr. Mamed Mustafaev. Authors would like to thank to Dr. Seval Bayülken for her technical help.*

REFERENCES

1. M.I. Mustafaev, Biopolymers. TUBITAK, Kocaeli, Turkey, 1996.
2. A.S. Hoffman, *Clinical Chem*., **46**(9), 1478 (2000).
3. J. Panyam, V. Labhasetwar, *Advance Drug Delivery Rev.*, **55**, 329 (2003).
4. R. Barbucci, G. Leone, A. Vecchiullo, *J Bio Sci Polym Eng*., **15**, 607 (2004).
5. S. Bayülken, G. Yüce, AY. Erkol, M. Mustafaev, Z. Mustafaeva, *J Radioanal Nuclear Chem*., **259**, 315 (2004).
6. M. Mustafaev, *J Eng Nat Sci*., **4**, 1 (2004).
7. D. Miyamoto, J. Watanabe, K. Ishihara, J Appl Polym *Sci*., **95**, 615 (2005).
8. N. Akkiliç, Z. Mustafaeva, M. Mustafaev, *J Appl Polym Sci*., **105**, 3108 (2007).
9. M. Karahan, Z. Mustafaeva, H. Ozer, *Asian J Chem*., **19**, 1837 (2007).
10. M. Karahan, Z. Mustafaeva, C. Özeroğlu, *Protein J*., **29**, 336 (2010).
11. G. Karakuş, Z.A. Polat, A.S. Yaglıoglu, M. Karahan, A.F. Yenidunya, *J Biomat Sci Polym Ed*., **24**, 1260 (2012).
12. M. Karahan, S. Tuğlu, Z. Mustafaeva, *Artificial Cells Blood Substitutes and Biotech.*, **40**, 363 (2012).
13. Q. Yizhi, C. Ashotosh, *Current Opinion In Chemical Bio*., **28,** 181 (2015).
14. L. Zhongyun, C. Na, D. Chunhong, Acs Applied Materials & Interfaces, **7**, 18997 (2015).
15. P. Chanphai, H. A. Tajmir-Riahi, *J Colloid and Interface Sci*., **461,** 419 (2016).
16. T. Akagi, M. Baba, M. Akashi, *Adv Polym Sci*., **247**, 31 (2012).
17. R.V. Petrov, M.I. Mustafaev, A.Sh. Norimov, Physico-Chemical Criteria for the Construction of Artificial Immunomodulators and Immunogens on the Basis of Polyelectrolyte Complexes, Harwood Acad, GmbH, UK, 1992.
18. C.P. Mallet, T.L. Hale, R.W. Kaminski, T. Larsen, N. Orr, D. Cohen, G.H. Lowell, *Infect Immun*, **63**, 2382 (1995).
19. V.A. Kabanov, *Pure Appl Chem.*, **76**(9), 1659 (2004).
20. A.S. Dilgimen, Z. Mustafaeva, M. Demchenko, T. Kaneko, Y. Osada, M. Mustafaev, *Biomaterials*, **22**, 2383 (2001).
21. A.J. Swallow, Radiation Chemistry, Longmans, London; 1973.

РАДИАЦИОННО ИНДУЦИРАНО ОБРАЗУВАНЕ НА КОВАЛЕНТНО СПРЕГНАТИ ПОЛИ – (*N*-ИЗОПРОПИЛ АКРИЛАМИД)-АЛБУМИНИ ОТ ГОВЕЖДИ СЕРУМ И ТЯХНАТА ИМУНОГЕННОСТ

П. Вурал[1], М. Карахан[2*], П. Пелит Араиджи[3], З. Мустафаева[3]

[1]Технически университет "Йилдиз", Факултет за наука и изкуство, Департамент по химия, 34220 Есенлер-Истанбул, Турция

[2]Университет в Юскюдар, Факултет по инженерство и природни науки, Департамент по биоинженерство, 34662 Юскюдар-Истанбул, Турция

[31]Технически университет "Йилдиз", Факултет по химично инженерство и металургия, Департамент по биоинженерство, 34220 Есенлер-Истанбул, Турция

Постъпила на 18 май, 2016 г.; приета на 3 октомври, 2016 г.

Поли (N-изопропил акриламид) е био-спрегнат към албумин от говежди серум при облъчване с γ-лъчи от източник ^{60}Co при pH 7. Анализиран е механизма на радиационно индуцираното спрягане с помощта на BETX, а имунизационните свойства са анализирани с ELISA-тест. Резултатите от BETX показват образуването на спрегнат полимер с протеина и в резултат – повишена радио-стабилност на протеина. Резултатите за имуногенността на облъчваните конюгати в мишки Balb/c mice са значително по-добри от тези при BSA-имунизационните резултати. Тази система е привлекателна за приложението на нов имуногенен модел в технологията на ваксините

Bulgarian Chemical Communications, Volume 49, Number 3, (pp. 562 – 568) 2017

One-pot three-component synthesis of 1-amidoalkyl-2-naphthols in the presence of phthalimide-*N*-sulfonic acid

H. Kiyani*, H. Darbandi

School of Chemistry, Damghan University, 36715-364 Damghan, Iran

Received April 24, 2015; Revised February17, 2017

A simple one-pot three-component reaction (3CR) was carried out using phthalimide-*N*-sulfonic acid (PISA) as a solid acid organocatalyst for synthesis of a variety of 1-amidoalkyl-2-naphthols. The reaction was conducted in order to preparation of 1-amidoalkyl-2-naphthols under solvent-free reaction conditions at 100 °C within 4-18 minutes and the corresponding products were formed in 75-97 % yields. The catalyst can be recovered and reused several times and is efficient, cost-effective, and eco-friendly. Moreover, the described protocol is easy and cheap to implement.

Keywords: 1-Amidoalkyl-2-naphthol, Phthalimide-*N*-sulfonic acid, Three-component reaction, Solvent-free.

INTRODUCTION

Multicomponent reactions (MCRs) have long been recognized as uniquely powerful tools to synthesis of structurally various chemical libraries of molecules through carbon–carbon and carbon–heteroatom bond formations in a single reaction vessel from readily available starting materials without the isolation of intermediates. MCRs provided considerably higher efficiency and molecular complexity. They are usually associated with a number of advantageous such as green process of bond-forming, shorter reaction times, operational simplicity, avoidance of time-consuming, energy and raw material saving, high bond-forming efficiency, minimal waste generation, reduction in the number of work-up, as well as no need for complicated purification processes [1-6].

Amidoalkyl naphthols can be used in pharmaceutical chemistry [7]. Trough amide hydrolysis reaction on the 1-amidoalkyl-2-naphthol derivatives, they can be converted into biologically useful compounds called 1-aminoalkyl-2-naphthols, which exhibit depressor and bradycardia effects [8]. 1-Amidoalkyl-2-naphthols can be also converted to derivatives of 1,3-oxazines as an exclusive class of bioactive compounds that present in many biologically important natural products and drug candidates [9, 10], which exhibit broad ranges of biological activities such as antihypertensive [11], analgesic [12], antirheumatic [13], antianginal [14], antibacterial, and antiviral [15].

The synthesis of 1-amidoalkyl-2-naphthols using one-pot, three-component reaction (3CR) of various aldehydes, naphthols, and amide derivatives, one of the most effective and efficient reactions in the field of synthetic organic chemistry. In this context, a number of catalysts such as Lewis or Brönsted acids [16, 17], nanomaterials [18-24] and carbohydrates [25] have been used to catalysing this 3CR.

In recent years, catalytic systems containing sulfonic acid groups are used to synthesis of these compounds. Some of these catalysts include sulfanilic acid [26], 1-methyl-3-(2-(sulfooxy)ethyl)-1*H*-imidazol-3-ium chloride [27], poly(4-vinylpyridinium butane sulfonic acid) hydrogen sulfate [28], polyethylene glycol (PEG)-based dicationic acidic ionic liquid (PEG_{1000}-DAIL) [29], polymer supported sulphonic acid NKC-9 [30], 1,3-disulfonic acid imidazolium hydrogen sulfate{[Dsim]HSO_4} [31], heteropolyanion-based SO_3H [32], saccharin sulfonic acid [33], L-pyrrolidine-2-carboxylic acid-4-hydrogen sulfate (supported on silica gel) [34], *β*-cyclodextrin-butane sulfonic acid [35], and ionic liquid [36]. Sonochemically mediated silica chloride catalyst condensation has also been reported for the preparation of amidoalkyl naphthols [37]. However, some of the methods mentioned above, suffer from at least one of the following drawbacks: long reaction times, the use of organic solvents, forcing conditions, create wastes, special instrumentation, relatively expensive as well as toxic the reagents. Due to biological and pharmacological role of substances with amidoalkyl naphthol fragments, major attention has been focused on the development of convenient, efficient, inexpensive, and eco-friendly new methodologies using readily available reagents to synthesis of these types of valuable compounds.

* To whom all correspondence should be sent:
E-mail: hkiyani@du.ac.ir

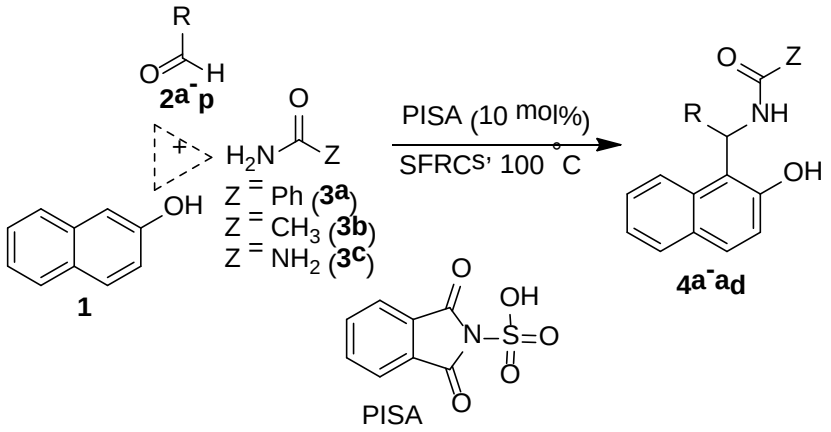

Scheme 1. One-pot three-component reaction (3-CR) of 2-naphthol (**1**), aryl aldehydes (**2a-p**), and amides (**3a-c**) in order to synthesis of 1-midoalkyl-2-naphthols (**4a-ad**) in the presence of PISA under SFRCs

Because many organic solvents are ecologically harmful, strategies for their minimized usage and developments toward benign chemical technologies are highly sought after [38]. From the view point of green chemistry, the exploration of safe methods with the aim to achieve greener, more sustainable, and environmentally friendly conditions is of eminent important. Among the ways to achieve this goal is the development of SFRs. They offer several advantages relative to using organic or other reaction media include: the compounds formed are often sufficiently pure, rapid, no need for specialized equipment, minimizing the energy consumption, avoidance of functional group protection-deprotection, environmentally benign, cost-effective, easy operation, high yields, and avoidance of pollution [39-43].

Phthalimid-*N*-sulfonic acid (PISA) has currently been synthesized and utilized by us as an efficient catalyst in synthesis of the Biginelli compounds [44]. In the present work, we report a rapid, green and easy procedure for the synthesis of 1-amidoalkyl-2-naphthol derivatives (**4a-ad**) using PISA as the solid acidic organic catalyst under SFRCs (Scheme 1).

RESULTS AND DISCUSSION

In continuation of our investigations on synthesis of amidoalkyl naphthols [45], we decided to use the new catalyst for the MCR synthesis of the compounds mentioned above. At the beginning of the present investigation, phthalimid-*N*-sulfonic acid (PISA) was synthesized according to our previous work [44] and applied to preparation of a series of 1-amidoalkyl-2-naphthols (**4a-ad**). In the direction of optimize the reaction conditions (amount of catalysts and reaction temperature) for preparation of 1-amidoalkyl-2-naphthols (**4a-ad**), synthesis of *N*-((2-hydroxynaphthalen-1-yl)(3-nitrophenyl)methyl)benzamide (**4a**) was selected as the model product, and behaviour of its synthesis was explored in the presence of different amounts of PISA under SFRCs. The results are summarized in Table 1.

A test reaction for the synthesis of **4a** at 100 °C deprived of catalyst was implemented with the aim of establishes the efficacy of the catalyst. It was found that no product was observed even after 2 h heating (Table 1, entry 1). The product (**4a**) is formed when neat 2-naphthol (**1**), 3-nitrobenzaldehyde (**2a**), benzamide (**3a**), and 10 mol % of PISA are mixed at 50 °C (Table 1, entry 2). Formation of product upon heating in the presence of a catalytic amount of PISA will further support a PISA for the achievement of products is essential. By increasing the reaction temperature from 50 to 70 and 80 °C, the reaction yield was improved, and the reaction time was shortened (Table 1, entries 3 and 4). The change in the yield from 84 %, to 96 % occurs when the temperature is increased from 80 °C to 100 °C (Table 1, entry 5). Further, at temperatures higher than 100 °C, the reaction did not proceed efficiently (Table 1, entry 6). In addition to the temperature of the reaction, the amount of the catalyst is also an important factor in the product formation. Hence, the effect of catalyst-loading on completion of the reaction at ambient temperature was also studied. The yield of the product was diminished and reaction time was also prolonged, when 5 mol % of catalyst was used (Table 1, entry 7). Higher amounts of the catalyst (i.e., 15 and 20 mol %) neither increased, nor lowered the yield% (Table 1, entries 8 and 9). Screening of the solvents such as EtOH, H_2O, CH_2Cl_2, EtOAc, and CH_3CN as the media reaction lead to low yields of product and prolonged reaction times compared with the SFRCs. Based on

Table 1. Screening the reaction conditions towards synthesis of *N*-((2-hydroxynaphthalen-1-yl)(3-nitrophenyl)methyl)benzamide (**4a**)[a]

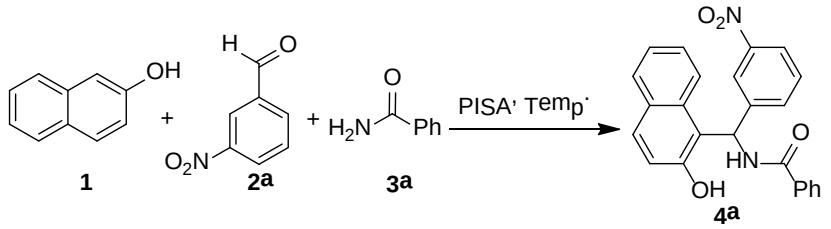

1 **2a** **3a** **4a**

Entry	Amount of catalyst (mol%)	Temp. (°C)	Time (min)[b]	Isolated Yields (%)
1	-	100	120	5
2	10	50	12	50
3	10	70	10	80
4	10	80	7	84
5[c]	10	100	4	96
6	10	120	3	92
7	5	100	6	90
8	15	100	3.5	95
9	20	100	2.5	92

[a] Reaction conditions: a well ground mixture of 1-naphthol **1** (1 mmol), 3-nitrobenzaldehyde **2a** (1 mmol), benzamide **3a** (1 mmol), and the catalyst was magnetically stirred.
[b]Progress of the reaction was monitored by TLC analysis.
[c] Optimized conditions shown in bold.

the above-mentioned studies, 100 °C and 10 mol % PISA was found to be the best optimal quantity and conditions, and satisfactory to push the reaction forward. Hence, these optimal conditions were applied to evaluate the generality of this procedure for the one-pot synthesis of the other amidoalkyl naphthols from 2-naphthol (**1**), a number of benzaldehydes (**2a-m**), heteroaryl aldehydes (**2n-o**), cinnamaldehyde (**2p**), and amides (**3a-c**), under SFRCs at 100 °C (Table 2).

Aromatic aldehydes carrying electron-donating (such as methyl or methoxy) or electron-withdrawing (such as nitro or halide) substituents reacted successfully in the presence of PISA as the catalyst and gave the corresponding products in excellent yields and shorter reaction times. It was also found that substituted benzaldehydes bearing electron-withdrawing groups (Table 2, entries 1-2, 4 and 6) gave higher yields and faster reacted than substituted benzaldehydes containing electron-donating groups (Table 2, entries 7-8, 10-12).When 3-methoxybenzaldehyd is used as substrate, possibly electron-withdrawing inductive effect is applied and most likely, this is one reason for increasing the yield and shortening reaction time (Table 2, entry 9). The reaction of sterically hindered *ortho*-substituted benzaldehydes including 2-chlorobenzaldehyde and 2-nitrobenzaldehyde were studied (Table 2, entries 3 and 5). In these cases, reaction time was longer and the yield of reaction was lower as compared to those of products from other benzaldehydes, which can be attributed to steric factors. The use of acetamide (**3b**), urea (**3c**) instead of benzamide (**3a**) in the synthesis of the titled compounds, also gave similar results, as shown in Table 2 (entries 14-23 and 26-30). This approach was highly operative for the preparation of targeted compounds (**4a-ad**) as well as in all cases, 1-amidoalkyl-2-naphthols were the individual products and no by-product was observed. The reaction of 2-naphthol (**1**), acetamide (**3a**), and an aliphatic aldehyde (i.e., *n*-butyraldehyde) leads to trace amount of corresponding amidoalkyl naphthol product after one day. In addition, a reaction of 2-naphthol (**1**) and acetamide (**3a**) with α,β-unsaturated aldehydes such as cinnamaldehyde was implemented and lead to the formation of the product in good isolated yields (Table 2, entry 26). The reaction of 2-naphthol (**1**), and acetamide (**3a**) with hetero-aromatic aldehydes [for example thiophene-2-carbaldehyde (**2n**) and furan-2-carbaldehyde (**2o**)] leads to corresponding products with 79 and 75 % yields, respectively (Table 2, entries 24-25).

The reusability of the catalyst was also investigated in the model reaction under optimized reaction conditions (Table 3). Upon completion, the catalyst was recovered after each run and reused for the same reaction. It showed nearly the same activity as a catalyst along but with a slight decrease of yields. The procedure was repeated and the results indicated that the catalyst could be recycled five times with only a slight loss of catalytic activity. This indicated that the PISA was an efficient and

recyclable catalyst for the preparation of 1-amidoalkyl-2-naphthol derivatives.

Mechanistically (Scheme 2), formation of 1-amidoalkyl-2-naphthol products (4a-ad) could proceed *via* formation of *ortho*-quinone methides [31-33] between 2-naphthol (1) and the aldehydes (2), assisted by PISA. Then, the Michael addition of amides (3) to the *ortho*-QMs delivers the 1-amidoalkyl-2-naphthols. The SO_3H functional group of PISA could provide acidic site for activating aldehydes efficiently, so facilitating this 3-CR.

In order to display the applicability and comparison the efficacy of the PISA catalyst with other catalysts in the preparation of 1-amidoalkyl-2-naphthols, the obtained results in the synthesis of 4a tabulated in Table 4. Compared with some of those reported in the literature, this method is comparable to the formerly reported methods in terms of reaction times and product yields. It can be seen that, PISA is also an equal or more efficient catalyst for this 3-CR. Contrary to some of the pervious reported methods, this work does not require any ionic liquids, hazardous solvents such as chloroform or special devices such as ultrasound and microwave.

Table 2. The 3C synthesis of 1-amidoalkyl-2-naphthols (**4a-ad**) catalysed by PISA under SFRCs at 100 °C

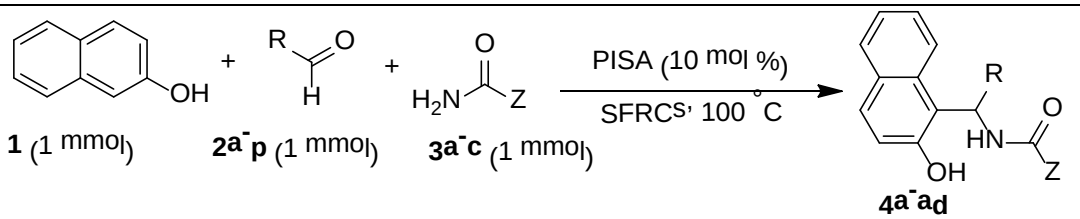

1 (1 mmol) **2a-p** (1 mmol) **3a-c** (1 mmol) **4a-ad**

Entry	R, Aldehyde	Z	Product	Time (min)	Isolated yields (%)	Mp (°C)	
						Obs.	Rep. [ref.]
1	3-NO_2-C_6H_4, **2a**	Ph, **3a**	**4a**	4	96	238-240	234-236 [24]
2	4-NO_2-C_6H_4, **2b**	Ph, **3a**	**4b**	5	92	239-241	238-240 [24]
3	2-NO_2-C_6H_4, **2c**	Ph, **3a**	**4c**	9	88	261-263	262-264 [24]
4	4-Cl-C_6H_4, **2d**	Ph, **3a**	**4d**	6	90	186-187	186-188 [24]
5	2-Cl-C_6H_4, **2e**	Ph, **3a**	**4e**	8	87	198-200	263-265 [24]
6	4-F-C_6H_4, **2f**	Ph, **3a**	**4f**	5	90	194-195	191-193 [16]
7	4-CH_3-C_6H_4, **2g**	Ph, **3a**	**4g**	8	88	216-217	215-216 [24]
8	4-CH_3O-C_6H_4, **2h**	Ph, **3a**	**4h**	8	90	207-209	208-211 [24]
9	3-CH_3O-C_6H_4, **2i**	Ph, **3a**	**4i**	5	94	231-233	232 [20]
10	2,5-$(CH_3)_2O$-C_6H_3, **2j**	Ph, **3a**	**4j**	7	92	237-239	238-240 [46]
11	2,4-$(CH_3)_2O$-C_6H_3, **2k**	Ph, **3a**	**4k**	8	90	228-230	227-229 [9]
12	3-CH_3O-4-OH-C_6H_3, **2l**	Ph, **3a**	**4l**	8	94	218-220	219 [33]
13	C_6H_5, **2m**	Ph, **3a**	**4m**	5	91	237-238	237-239 [16]
14	3-NO_2-C_6H_4, **2a**	CH_3, **3b**	**4n**	5	92	242-243	241-242 [28]
15	4-NO_2-C_6H_4, **2b**	CH_3, **3b**	**4o**	5	92	244-246	243-245 [28]
16	2-NO_2-C_6H_4, **2c**	CH_3, **3b**	**4p**	10	86	181-182	182 [18]
17	4-Cl-C_6H_4, **2d**	CH_3, **3b**	**4q**	7	89	225-227	226-228 [28]
18	2-Cl-C_6H_4, **2e**	CH_3, **3b**	**4r**	8	87	209-211	210-211 [27]
19	4-F-C_6H_4, **2f**	CH_3, **3b**	**4s**	12	84	208-209	206-208 [30]
20	4-CH_3-C_6H_4, **2g**	CH_3, **3b**	**4t**	10	88	220-222	221-223 [28]
21	4-CH_3O-C_6H_4, **2h**	CH_3, **3b**	**4u**	10	87	181-183	181-183 [28]
22	3-CH_3O-C_6H_4, **2i**	CH_3, **3b**	**4v**	6	97	204-206	203-205 [28]
23	C_6H_5, **2m**	CH_3, **3b**	**4w**	5	90	242-243	242-244 [28]
24	2-Thienyl, **2n**	CH_3, **3b**	**4x**	10	79	223-224	222-224 [26]
25	2-Furyl, **2o**	CH_3, **3b**	**4y**	12	75	218-220	218-220 [47]
26	C_6H_5—CH=CH, **2p**	CH_3, **3b**	**4z**	18	88	175-177	174.5-176 [19]
27	3-NO_2-C_6H_4, **2a**	NH_2, **3c**	**4aa**	7	93	193-195	192-194 [24]
28	4-NO_2-C_6H_4, **2b**	NH_2, **3c**	**4ab**	9	94	191-193	192-194 [24]
29	4-Cl-C_6H_4, **2d**	NH_2, **3c**	**4ac**	6	91	165-167	166-168 [24]
30	C_6H_5, **2m**	NH_2, **3c**	**4ad**	12	92	176-177	176-178 [24]

Table 3. Reusability of PISA in the synthesis of **4a**[a]

Catalyst recycle	Time (min)	Isolated yield (%)
Fresh	4	96
1	5	95
2	5	92
3	8	89
4	15	84

[a] The reaction conditions are similar to the optimized conditions described for the template reaction in Table 1.

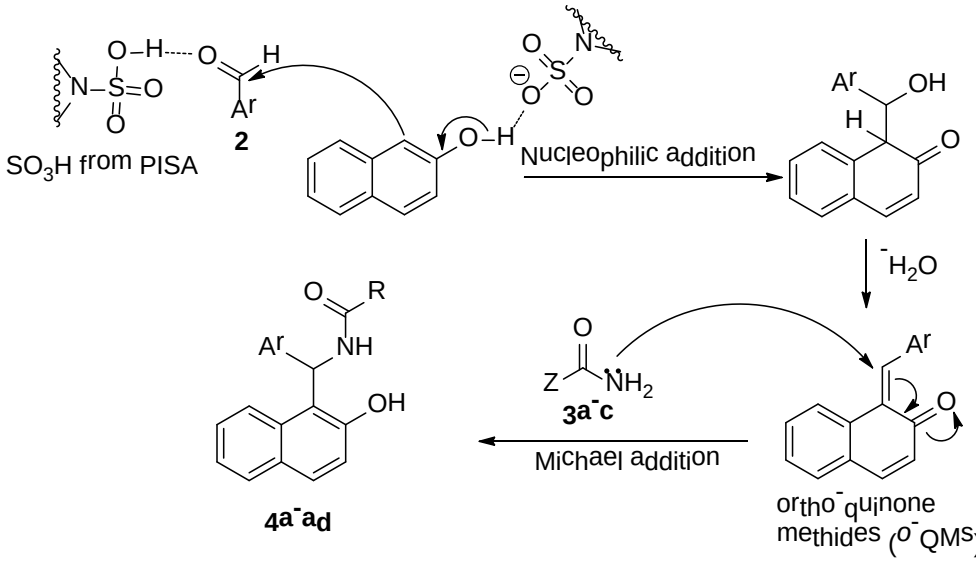

Scheme 2. Proposed mechanism for synthesis of 1-amidoalkyl-2-naphthols (**4a-ad**)

Table 4. Comparison of the catalytic performance of PISA for the one-pot 3C synthesis of **4a** with those obtained by reported catalysts.

Entry	Catalyst (mol %) [g]/conditions [ref.]	Time (min)	Yield (%)
1	[Msim]Cl (10)/SF, 120 °C [16]	5	90
2	Maltose (20)/SF, 100 °C [25]	18	90
3	Sulfanilic acid (20)/SF, MW [26]	8	89
4	Sulfanilic acid (20)/SF, 110-120 °C [26]	14	88
5	MSI (6)/ionic liquid [Bpy]BF_4, 80 °C [27]	25	95
6	PEG_{1000}-DAIL (0.03 mmol)/80 °C [29]	5	94
7	[MIMPS]$H_2PMo_{12}O_{40}$ (10)/SF, 110 °C [32]	5	93
8	Silica chloride [0.1]/US, 28-30 °C [34]	9	98
9	[Dsim]HSO_4 (5)/SF, 80 °C [31]	20	97
10	PSSA-NKC-9 [0.17]/chloroform, reflux [30]	360	88
11	2-HSBA (10)/SF, 100 °C [45]	5	95
12	PISA (10)/SF, 100 °C [Present work]	4	96

[Msim]Cl, 3-methyl-1-sulfonic acid imidazolium chloride; *SF*, solvent-free; *MSI*, 1-methyl-3-(2-(sulfooxy)ethyl)-1*H*-imidazol-3-ium chloride; *[Bpy]BF_4*, *N*-butylpyridinium tetrafluoroborate; *PEG_{1000}-DAIL*, PEG-based dicationic acidic ionic liquid; *MIMPS*, *N*-methyl-imidazolium propane sulphonate; *[Dsim]HSO_4*, 1,3-disulfonic acid imidazolium hydrogen sulfate; *PSSA-NKC-9*, Polymer supported sulphonic acid NKC-9; *US*, ultrasond; *2-HSBA*, 2-hydroxy-5-sulfobenzoic acid.

CONCLUSIONS

In summary, an efficient, simple, and environmentally benign protocol towards synthesis of 1-amidoalkyl-2-naphthols has been developed. Thermal SFRCs were applied to afford the corresponding 1-amidoalkyl-2-naphthol compounds. PISA display excellent catalytic activity toward this 3CR. The use of PISA in this 3CR is included merits such as good to high yields, short reaction times, practical simplicity, recyclable catalyst, clean formation of the target products, no use of solvent, and easy work-up.

EXPERIMENTAL

All chemicals were purchased from Alfa Aesar and Aldrich as well as were used without further purification, with the exception of 4-methylbenzaldehyde, 4-methoxylbenzaldehyde, benzaldehyde, and thiophene-2-carbaldehyde which were distilled before using. All solvents were

distilled before using. The products were characterized by comparison of their physical data with those of known samples or by their spectral data. Melting points were measured on a Buchi 510 melting point apparatus and are uncorrected. NMR spectra were recorded at ambient temperature on a BRUKER AVANCE DRX-400 MHz using $CDCl_3$ or DMSO-d_6 as the solvent. FT-IR spectra were recorded on a Perkin-Elmer RXI spectrometer. The development of reactions was monitored by thin layer chromatography (TLC) analysis on Merck pre-coated silica gel 60 F_{254} aluminum sheets, visualized by UV light.

*General procedure for synthesis of 1-amidoalkyl-2-naphthols (**4a-ad**)*

A mixture of 2-naphthol **1** (1 mmol), aldehyde **2** (1 mmol), amide **3** (benzamide, acetamide, or urea 1 mmol) and PISA (10 mol %) was stirred at 100 °C in an oil bath for 4-18 min. After completion of the reaction (using TLC analysis), the reaction mixture was allowed to cool to room temperature. After that, the products was extracted by hot ethyl acetate (the product is soluble in hot ethyl acetate, but PISA is not soluble in this solvent), and then the catalyst was recovered and washed thoroughly with ethyl acetate and then diethyl ether. After being dried, it was subjected to another reaction with the same substrates. Pure 1-amidoalkyl-2-naphthols were afforded by evaporation of the solvent followed by recrystallization from ethanol. The selected spectral data for representative compounds (**4a** and **4m**) as follows:

*N-((2-Hydroxynaphthalen-1-yl)(3-nitrophenyl)methyl)benzamide (**4a**)* IR (KBr, cm^{-1}): 3374, 3262, 3055, 2974, 1633, 1530, 1504, 1475, 1440, 1345, 1253, 1145, 735; ^{1}H NMR (400 MHz, DMSO-d_6): δ = 10.42 (s, 1H), 9.15 (d, J = 8.0 Hz, 1H), 8.11-8.09 (m, 3H), 7.91-7.84 (m, 4H), 7.72 (d, J = 7.5 Hz, 1H), 7.60-7.49 (m, 5H), 7.41 (d, J = 8.0 Hz, 1H), 7.34 (t, J = 7.5 Hz, 1H), 7.25 (d, J = 8.5 Hz, 1H); ^{13}C NMR (100 MHz, DMSO-d_6): δ = 166.8, 153.9, 148.2, 145.1, 134.4, 133.7, 132.8, 132.1, 130.5, 130.3, 129.3, 128.9, 128.8, 127.9, 127.6, 123.4, 122.9, 122.2, 121.3, 119.2, 117.3, 49.5.

*N-((2-Hydroxynaphthalen-1-yl)(3-nitrophenyl)methyl)acetamide (**4m**)* IR (KBr, cm^{-1}): 3395, 3151, 3090, 2989, 1645, 1530, 1435, 1348, 1295, 1279, 1071, 990, 828, 745, 734; ^{1}H NMR (400 MHz, DMSO-d_6): δ = 10.14 (s, 1H), 8.62 (d, J = 8.0 Hz, 1H), 8.02-7.99 (m, 2H), 7.84 (br, 1H), 7.78 (t, J = 8.6 Hz, 2H), 7.59-7.51 (m, 2H), 7.40 (t, J = 7.6 Hz, 1H), 7.26 (t, J = 7.4 Hz, 1H), 7.18 (d, J = 8.7 Hz, 1H), 7.16 (t, J = 8.0 Hz, 1H), 2.02 (s, 3H); ^{13}C NMR (100 MHz, DMSO-d_6): δ = 170.3, 153.9, 148.2, 145.9, 133.4, 132.7, 130.5, 130.1, 129.2, 128.9, 127.3, 123.2, 123.1, 121.8, 120.9, 118.9, 118.3, 48.2, 23.1.

Acknowledgment: *The authors are thankful to the Damghan University Research Council.*

REFERENCES

1. S. Benetti, R. Romagnoli, C. De Risi, G. Spalluto, V. Zanirato, *Chem. Rev*., **95**, 1065 (1995).
2. A. Dömling, *Chem. Rev*., **106**, 17 (2006).
3. A. Dömling, W. Wang, K. Wang, *Chem. Rev*., **112**, 3083 (2012).
4. B. Jiang, X. Wang, F. Shi, S.J. Tu, G. Li, *Org. Biomol. Chem*., **9**, 4025 (2011).
5. M. S. Singh, S. Chowdhury, *RSC Adv*., **2**, 4547 (2012).
6. C. Graaff, E. Ruijter, R.V.A. Orru, *Chem. Soc. Rev*., **41**, 3969 (2012).
7. I. Mohanram, J. Meshram, *Med. Chem. Res*., **23**, 939 (2014).
8. T. Dingermann, D. Steinhilber, G. Folkes, *Molecular Biology in Medicinal Chemistry*, Wiley-VCH, 2004.
9. J. Safaei Ghomi, S. Zahedi, *Monatsh. Chem*., **144**, 687 (2013).
10. J. Safaei Ghomi, S. Zahedi, M. A. Ghasemzadeh, *Monatsh. Chem*., **145**, 1191 (2014).
11. J. L. Peglion, J. Vian, B. Gourment, N. Despaux, V. Audinot, M. Millan, *Bioorg. Med. Chem. Lett*., **7**, 881 (1997).
12. G.Y. Lesher, A.R. Surrey, *J. Am. Chem. Soc*., **77**, 636 (1955).
13. H. Matsuoka, N. Ohi, M. Mihara, H. Suzuki, K. Miyamoto, N. Maruyama, K. Tsuji, N. Kato, T. Akimoto, Y. Takeda, K. Yano, T. Kuroki, *J. Med. Chem*., **40**, 105 (1997).
14. F. Benedini, G. Bertolini, R. Cereda, G. Donia, G. Gromo, S. Levi, J. Mizrahi, A. Sala, *J. Med. Chem*. **38**, 130 (1995).
15. W.S.I. Abou-Elmagd, A. I. Hashem, *Med. Chem. Res*., **22**, 2005 (2013).
16. M.A. Zolfigol, A. Khazaei, A.R. Moosavi-Zare, A. Zare, V. Khakyzadeh, *Appl. Catal. A: Gen.*, **400**, 70 (2011).
17. S.S. Mansoor, K. Aswin, K. Logaiya, S.P.N. Sudhan, *J. Saudi Chem. Soc*., **20**, 138 (2016).
18. J. Safari, Z. Zarnegar, *J. Indust. Eng. Chem*., **20**, 2292 (2014).
19. V.K. Das, M. Borah, A. Thakur, *J. Org. Chem*., **78**, 3361 (2013).
20. A. Bamoniri, B.F. Mirjalili, S. Nazemian, *J. Iran. Chem. Soc*., **11**, 653 (2014).
21. R. Tayebee, M.M. Amini, H. Rostamian, A. Aliakbari, *Dalton Trans*., **43**, 1550 (2014).
22. R. K. Singh, R. Bala, S. Kumar, *Indian J. Chem*., **55B**, 381 (2016).
23. K. Ghodrati, A. Farrokhi, C. Karami, Z. Hamidi, *Synth. React. Inorg. Metal-Org. Nano-Met. Chem*., **45**, 15 (2015).
24. H. Taghrir, M. Ghashang, M. Najafi Biregan, *Chin. Chem. Lett*., **27**, 119 (2016).

25. B. Adrom, N. Hazeri, M.T. Maghsoodlou, M. Mollamohammadi, *Res. Chem. Intermed*., **41**, 4741 (2015).
26. R.K. Singh, B. Singh, R. Duvedi, S. Kumar, *Res. Chem. Intermed*., **41**, 4083 (2015).
27. C. Wang, Y. Wan, H.-Y. Wang, L.-L. Zhao, J.-J. Shi, X.-X. Zhang, H. Wu, *J. Heterocycl. Chem*., **50**, 496 (2013).
28. A. R. Kiasat, A. Mouradzadegun, S. J. Saghanezhad, *Chin. J. Catal*., **34**, 1861 (2013).
29. J. Luo, Q. Zhang, *Monatsh. Chem*., **142**, 923 (2011).
30. L.T. An, X.H. Lu, F.Q. Ding, W.Q. Jiang, J. P. Zou, *Chin. J. Chem*., **26**, 2117 (2008).
31. A. Zare, T. Yousofi, A.R. Moosavi-Zare, *RSC Adv*., **2**, 7988 (2012).
32. F. Dong, J. Chenning, Z. Ting, Y. Jinming, *J. Chem. Sci*., **125**, 751 (2013).
33. A. Zare, H. Kaveh, M. Merajoddin, A. R. Moosavi-Zare, A. Hasaninejad, M. A. Zolfigol, *Phosphorus Sulfur Silicon Relat. Elem*., **188**, 573 (2013).
34. M. Hajjami, A. Ghorbani-Choghamarani, F. Gholamian, *Bulg. Chem. Commun*., **47**, 119 (2015).
35. K. Gong, H. Wang, X. Ren, Y. Wang, J. Chen, *Green Chem*., **17**, 3141 (2015).
36. A. Chinnappan, A.H. Jadhav, W.-J. Chung, H. Kim, *J. Mol. Liq*., **212**, 413 (2015).
37. B. Datta, M. A. Pasha, *Ultrason. Sonochem*., **18**, 624 (2011).
38. M.S. Yusubov, T. Wirth, *Org. Lett*., **7**, 519 (2005).
39. P.N. Sudhana, M. Ghashang, S. S. Mansoor, *J. Saudi Chem. Soc*., (2015), doi: 10.1016/j.jscs.2015.09.005.
40. M.A.P. Martins, C.P. Frizzo, D.N. Moreira, L. Buriol, P. Machado, *Chem. Rev*., **109**, 4140 (2009).
41. G.W.V. Cave, C.L. Raston, J.L. Scott, *Chem. Commun*., 2159 (2001).
42. A. Trzesowska-Kruszynska, *Crystal Growth & Design*, **13**, 3892 (2013).
43. H. Kiyani, M. Ghiasi, *Res. Chem. Intermed*., **41**, 5177 (2015).
44. H. Kiyani, M. Ghiasi, *Res. Chem. Intermed*., **41**, 6635 (2015).
45. H. Kiyani, H. Darbandi, A. Mosallanezhad, F. Ghorbani, *Res. Chem. Intermed*., **41**, 7561 (2015).
46. A.R. Hajipour, Y. Ghayeb, N. Sheikhanand, A.E. Ruoho, *Tetrahedron Lett*., **50**, 5649 (2009).
47. X.-H. Cai, H. Guo, B. Xie, *Jordan J. Chem*., **6**, 17 (2011).

ЕДНО-СТАДИЙНА ТРИ-КОМПОНЕНТНА СИНТЕЗА НА 1-АМИДОАЛКИЛ-2-НАФТОЛИ В ПРИСЪСТВИЕ НА ФТАЛИМИД-*N*-СУЛФОНОВА КИСЕЛИНА

Х. Кияни*, Х. Дарбанди

Училище по химия, Университет Дамгхан, 36715-364 Дамгхан, Иран

Получена на 24 април 2015 г.; коригирана на 17 февруари 2017 г.

(Резюме)

Изпитана е проста, едно-стадийна три-компонентна реакция (3CR) за синтезата на различни 1-амидоалкил-2-нафтоли при фталимид-*N*-сулфонова киселина като твърд органичен катализатор. Реакцията се провежда без разтворител при 100°C за около 4-18 минути, а съответните продукти са с добиви между 75 и 97%. Катализаторът се възстановява и се използва няколко пъти. Той е ефективен, евтин и екологически съвместим. Освен това описаният протокол е лесен и евтин за изпълнение.

Bulgarian Chemical Communications, Volume 49, Number 3, (pp. 569 – 576) 2017

Kinetic studies on the formation of silver nanoparticles by reduction of silver(I) with glucose in aqueous and micellar media

H.A. Ewais[1*], I.M. Ismail[1,2], K.H. Al-Fahami[1]

[1]Chemistry Department, Faculty of Science, King Abdulaziz University, P.O. Box 80203, Jeddah 21413, Saudi Arabia.
2Center of Excellence in Environmental Studies, King Abdulaziz University, P.O. Box 80216, Jeddah 21589, Saudi Arabia

Received January 7, 2016; Revised April 14, 2017

The kinetics of the formation of silver nanoparticles (AgNPs) by reduction of silver (I) with glucose are studied at different temperatures in aqueous micellar media. The reaction was carried out under pseudo-first-order condition by taking the [glucose] (>10-fold) the [Ag^+]. The effect of [NaOH], [Ag^+], [glucose] and [CTAB] are investigated. Rate of reaction enhance by increasing [OH^-]. CTAB stabilized the rate of growth of nanoparticles and the rate of reaction increases with increasing in temperature. It was observed that nanoparticles are spherical, aggregated and poly dispersed. On the basis of kinetic data, a suitable mechanism is proposed and discussed for the silver sol formation. The particle size of silver sols is characterized by the transmission electron microscopic (TEM) and some physiochemical and spectroscopic tools.

Keywords: Silver nanoparticles; kinetics and mechanism; micelles; reduction; TEM

INTRODUCTION

Metal nanoparticles are attractive due to their easy synthesis, modification as well as their size, shape, distribution which are properties dependent [1, 2]. The preparation of uniform nanosized drug particles with specific size, shape and chemical properties is of great interest in the formulation of new pharmaceutical products [3,4]. Nanoparticles can be used as labels for optical bio-detection, substrate for multiplexed aqueous bioassays, probes for cellular imaging or carriers for therapeutic delivery [5]. The evolution and technological progress of silver nanoparticles in the manufacture are due to their antiviral and antibacterial properties, in addition to numerous industrial applications including microelectronics, cosmetics, an adhesives and catalysis to enhanced solar cells [6-8]. The formation of nanoparticles using biological entities has great important due to their individual shape dependent optical, electrical and chemical properties have potential application in biotechnology [1].

The nanoparticles were formed and stabilized by chemical and physical methods; the chemical method, such as, electrochemical techniques, chemical reduction, and photochemical reduction is most widely used [9] and [10]. The chemical reduction is the most used method for the formation of silver nanoparticles as stable, colloidal dispersions in aqueous or non-aqueous media [11] and [12]. Hydrazine, aniline, ascorbic acid, lactose and sodium borohydride are used as reducing agent in the formation of nanoparticles [13-17]. The stabilizing agent such as cetyltrimethylammoniuom bromide, sodiumdodecyl sulphate, Tritron X-100 and poly(vinyl alcohol) are used as capping agent to control the shape and size of silver nanocrystals [13,16,18]. The reduction of silver ions (Ag^+) in aqueous medium gave a colloidal silver with particle diameters of several nanometers [19]. The oligomeric clusters of nanosilver are formed by reducing of Ag^+ to silver atoms (Ag^o) [20]. The yellow colour of silver sols, which contain smaller particles, gave a peak in the wavelength range 390-450 nm [20].

In this paper, the kinetics of formation of silver nanparticles by reduction method were studied in order to obtain a stable, narrow size, uniform and spherical shape form of silver nanoparticle in aqueous micellar media. Also, the role of [OH^-] in the silver sols formation is investigated.

EXPERIMENTAL

Materials and solutions

Silver nitrate, glucose, cetyltrimethylammonium bromide, sodium hydroxide and potassium permanganate (BDH Ltd Poolle England) were used without further purification. The solutions of silver nitrate and glucose were prepared daily (to arrest the aerial oxidation) in cooled and boiled water. Doubly distilled water was used for the preparation of all solutions.

* To whom all correspondence should be sent:
E-mail: hshalby2002@yahoo.com

Kinetic procedures

UV–visible LABOMED, INC UVD-2960 spectrophotometer and Perkin Elmer EZ-150 recording spectrophotometer were used to monitor the absorbance of the formation of silver sols. TEM images for the determination of the size of silver particle were recorded using transmission electron microscope (JEOL, JEM-1011, Japan) The preparation of samples were carried out by adding a drop of working solution on a carbon-coated standard copper grid (300 mesh) operating at 80 kV. The particles were imaged by LEO 440i Scanning Electron Microscopy (SEM) at an accelerating voltage of 20 kV.

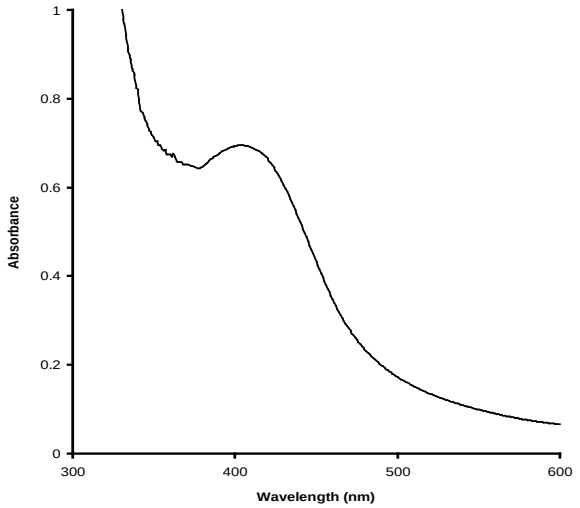

Fig. 1. Absorbance spectra of silver sol. Reaction conditions: $[Ag^+]$ = 5.0 x 10^{-5} mol dm^{-3}, [glucose] = 2.0 x 10^{-3} mol dm^{-3}, [CTAB] = 1.0 x 10^{-3} mol dm^{-3}, $[OH^-]$ = 5.0 x 10^{-3} mol dm^{-3} and T = 50 °C.

The ultraviolet-visible absorption spectra of the products (silver sol) were followed spectrophotometrically for a definite period of time using the LABOMED, INC UVD-2960 spectrophotometer. All reactants were equilibrated at the required temperatures in a thermostated water bath for ca. 15 min before being thoroughly mixed and quickly transferred to an absorption cell. The reaction rates were measured by monitoring the absorbance of product at 405 nm, on a Perkin Elmer EZ-150 spectrophotometer, where the absorption of the products is maximal. The temperature of the reacting solution was adjusted, using automatic circulation thermostat. The thermostat was provided with a special pumping system for circulating water at regulated temperature in the cell holder.

Pseudo-first-order conditions were maintained in all runs by the presence of a large excess (>10-fold) of maltose. Pseudo-first-order rate constants, k_{obs}, were obtained from the slopes of plots of ln $a/(1-a)$ versus time with a fixed-time method where $a = A_t/A_\infty$ and A_t and A_{∞} are the absorbencies at times and infinity, respectively [21].

The preparation of silver nanoparticles by the reduction of silver (I) with glucose in presence of micelles in aqueous medium was investigated. A series of runs were carried out, using a different concentration of glucose, silver nitrate and CTAB to obtain a perfectly clear silver sol. In the similar procedure, 2.0 ml of a 0.001 mol dm^{-3} solution of silver nitrate and 2.0 ml of a 0.1 mol dm^{-3} sodium hydroxide solution was mixed with 4.0 ml of a 0.01 mol dm^{-3} CTAB solution. The pale yellow color of the silver sol is formed, when 4.0 ml of a 0.02 mol dm^{-3} solution of glucose was added to the reaction mixture at the beginning of reaction. The total volume of the reaction mixture was always 40 ml. The presence of pale yellow color, this indicated that the formation of Ag-nanoparticles [22, 23].

RESULTS AND DISCUSSION

Formation and characterization of silver nanoparticles

The synthesis and formation of silver nanoparticles using glucose as reducing agent in presence of active surfactants such as CTAB is very important because the shape and size depend on the nature of stabilizers and reducing agent [24]. For the characterization of silver sol, in a typical experiment, Ag^+ ions (5.0×10^{-5} mol dm^{-3}), [NaOH] (5.0×10^{-3} mol dm^{-3}), glucose (2.0×10^{-3} mol dm^{-3}) with the CTAB (1.0×10^{-3} mol dm^{-3}) were mixed at 50 °C.

UV–visible absorption spectra have been perfectly sensitive to the formation of silver sol because silver nanoparticles show a absorption peak due to the surface plasmon excitation and spectra of the product recorded were at the wavelength ranged from 300 to 600 nm (Fig. 1). The maximum absorption was obtained at wavelength 405 nm showing the formation of Ag-nanoparticles. This indicate that the increase in absorbance at 405 nm with time. The absorption plasmon band with a λ_{max} at 405 nm is the characteristic of spherical or roughly spherical shape Ag-nanoparticles synthesis.

From SEM images it is observed that the particles had a relatively narrow size and a spherical shape. The size of silver nanoparticle is ranging from 10.0 to 45.0 nm and has a various shapes: sphere and irregular with broader size distribution (Fig. 2).

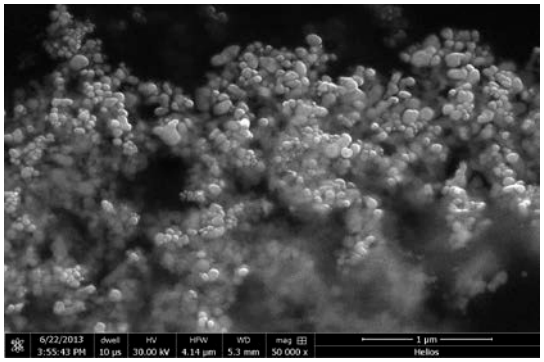

Fig. 2. SEM image of silver nanoparticle.

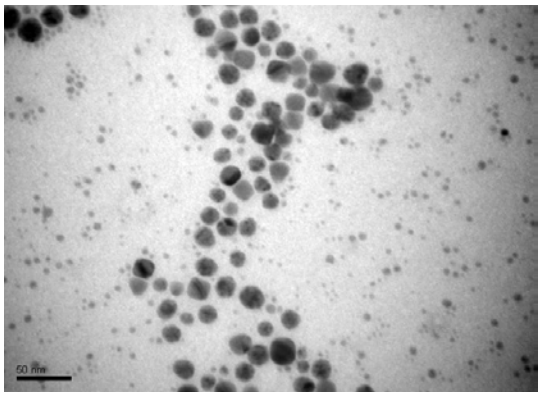

Fig. 3. TEM image of silver nanoparticle.

TEM image of the prepared Ag-nanoparticles is represented as shown in Fig. 3. From Fig. 3, it clear that the size of the nearly spherical nanoparticles ranges between 12.31 and 40.23 nm and their size distribution is relatively wide. The TEM image confirms that the CTAB stabilized particles are spherical rather than hexagonal forms of silver nanocrystals, as was observed for the reduction of Ag^+ ions with hydrazine and ribose, respectively [25, 26].

Kinetics of formation of silver nanoparticles

Preliminary observations showed that the presence of NaOH solution is essential to the reduction of Ag^+ ions by glucose in presence of CTAB. Therefore, the choice of the best conditions for the kinetic experiments is a crucial problem that we address first. In order to examine the effects of variables, experiments were tried at $[Ag^+]$ (1.25 – 6.25) $\times 10^{-5}$ mol dm^{-3}, [glucose] (1.0 – 3.0) $\times$ 10^{-3} mol dm^{-3}, [CTAB] (0.5–3.0) $\times$ 10^{-3} mol dm^{-3} and [NaOH] (2.50–15.0) $\times 10^{-3}$ mol dm^{-3}.

Plotting absorbance versus time (Fig. 4) shows that non-catalytic and autocatalytic reaction path.

Table 1. Dependence of the $[Ag^+]$/[glucose] reaction rate on $[Ag^+]$, [glucose] and [CTAB] = 1.0 x 10^{-3} mol dm^{-3} at T = 50.0 ºC.

$10^3[OH^-]$ mol dm^{-3}	$10^5[Ag^+]$ mol dm^{-3}	10^3[glucose] mol dm^{-3}	10^3[CTAB] mol dm^{-3}	$10^3 k_{obs}$ s^{-1}
2.50	5.00	2.00	1.00	0.85
3.75				1.36
5.00				1.78
7.50				3.46
10.00				3.89
12.50				4.03
15.00				4.12
5.00	5.00	1.00	1.00	0.69
		1.50		1.12
		2.00		1.78
		2.50		2.32
		3.00		2.73
5.00	1.25	2.00	1.00	1.60
	2.50			1.51
	3.75			1.77
	5.00			1.78
	6.25			1.76
5.00	5.00	2.00	0.50	2.51
			0.75	2.03
			1.00	1.78
			1.25	1.37
			1.50	1.04

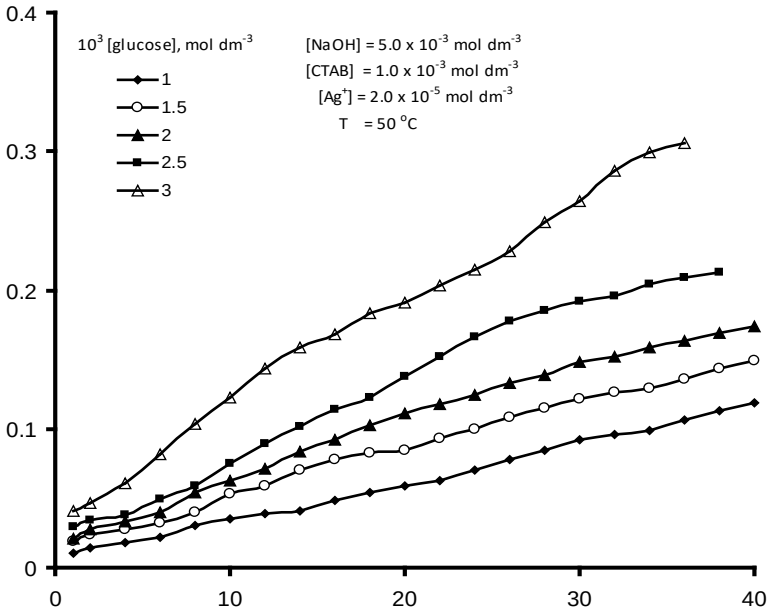

Fig. 4. Absorbance-time curves of silver sol formation at different [glucose]

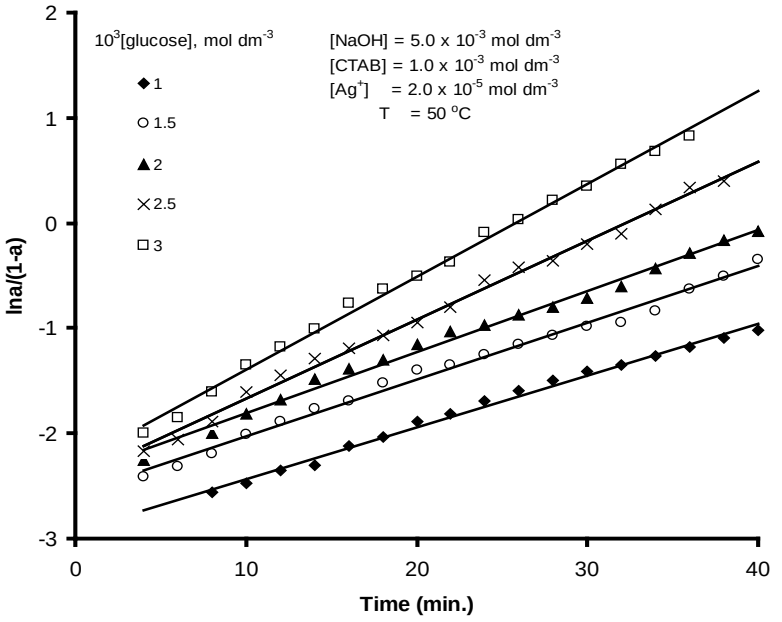

Fig. 5. Plots of ln a/(1-a) versus time at different [glucose] at 50 °C

The observation of autocatalysis in Fig. 4, is due to the formation of metal nucleation center which acts as a catalyst for the reduction of other silver ions present in solution. In the present study it is necessary to point out that the plots of ln $a/(1-a)$ against time are linear up to > 87 % of the reaction (Fig. 5), where $a = A_t/A_\infty$ and A_t and A_∞ are the absorbancies at times t and infinity ∞, respectively [21].

The values of the rate constants were obtained from the slopes of ln $a/(1-a)$ versus time plots (Table 1).

The unaffected of k_{obs} over the $[Ag^+]$ range (1.25–6.25) x 10^{-5} mol dm^{-3} at constant maltose concentration indicating first order dependence on the $[Ag^+]$ as shown in Table 1. The dependence of k_{obs} on glucose was examined over the concentration range (1.0 - 3.0) x 10^{-3} mol dm^{-3} at fixed $[Ag^+]$, $[OH^-]$, CTAB and temperature. The kinetic data are graphically represented in Fig. 5. Table (1), shows that the rate constant, k_{obs}, increases with increasing in glucose concentration.

The kinetics of the formation of silver nanoparticles were carried out over a [NaOH] range

of (2.50 – 15.0) x 10^{-3} mol dm^{-3} at constant [R-CHO] = 2.0 x 10^{-3} mol dm^{-3}, [Ag^+] = 5.0 x 10^{-5} mol dm^{-3}, [CTAB] = 1.0 x 10^{-3} mol dm^{-3} and at T = 50 ^oC. In absence of glucose, the solution become yellow transparent color and the spectra of this color were recorded as a function of time (Fig. 6). Fig. 6 shows that the spectra of Ag^+–OH^- reaction product cover the whole visible region of the spectrum in absence of glucose. No spectral peaks are observed for 40 min. Fig. 7 and Table 1, shows the dependency of k_{obs} on [NaOH]. The reaction is very sensitive to small concentration of NaOH, a concentration of 2.5×10^{-3} mol dm^{-3} being enough to catalyses the reduction of Ag^+ by glucose. On the other hand, no reduction of Ag^+ ions takes place in absence of [OH^-]. The reaction rate increased with increasing [NaOH] up to 7.5x10^{-3} mol dm^{-3} and no significant changes in k_{obs} were observed at [NaOH] $\geq10.0\times10^{-3}$ mol dm^{-3} (Fig. 7). These observations are in good agreement with the results of Huang et al. [27]. Thus we may safely conclude that hydroxide ions play a crucial role in the reaction of Ag^+ ions with paracetamol [27].

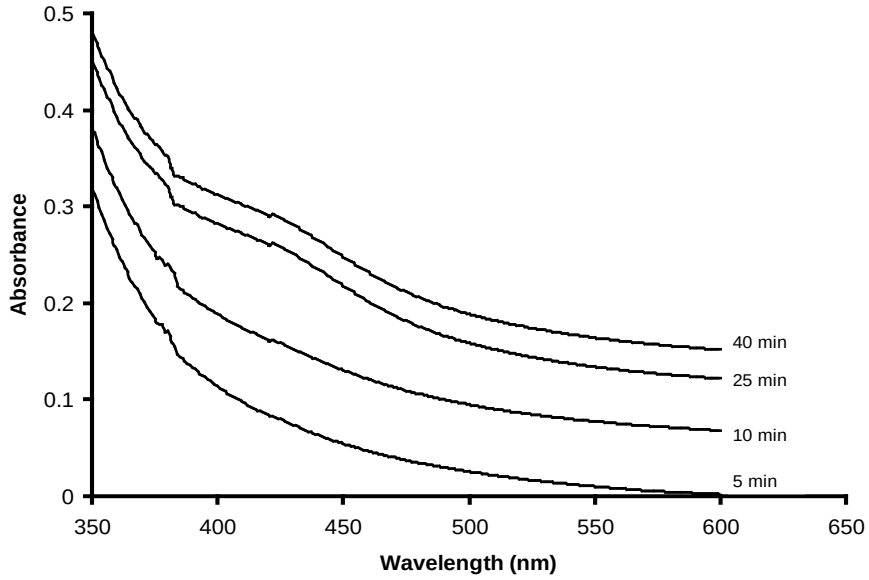

Fig. 6. Absorption spectra of silver sol formation as a function of time. Reaction conditions: [CTAB] =1.0×10^{-3} mol dm^{-3}; [Ag^+] = 5.0×10^{-5} mol dm^{-3}; [NaOH] = 5.0×10^{-3} mol dm^{-3}; T = 50 ^oC

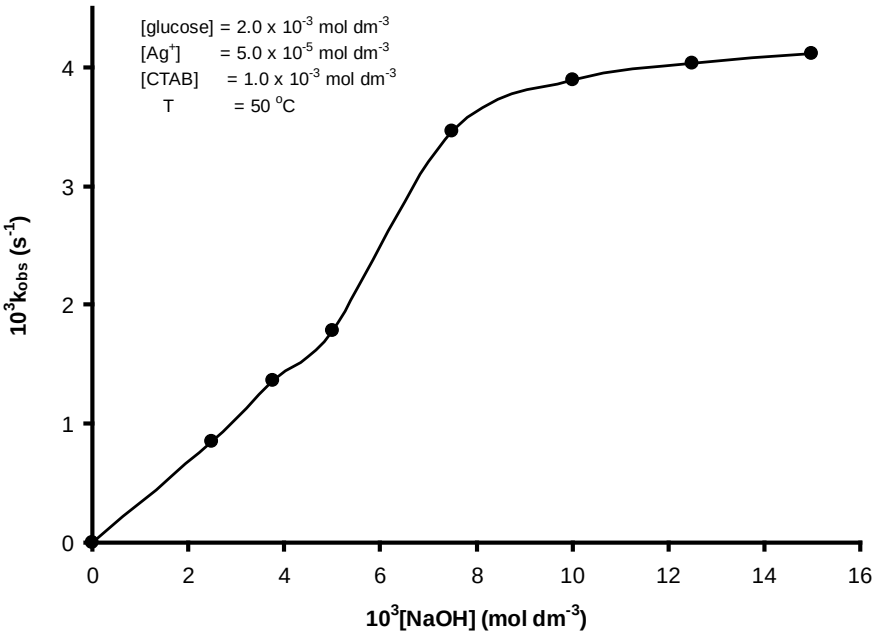

Fig. 7. Variation of k_{obs} with [NaOH]

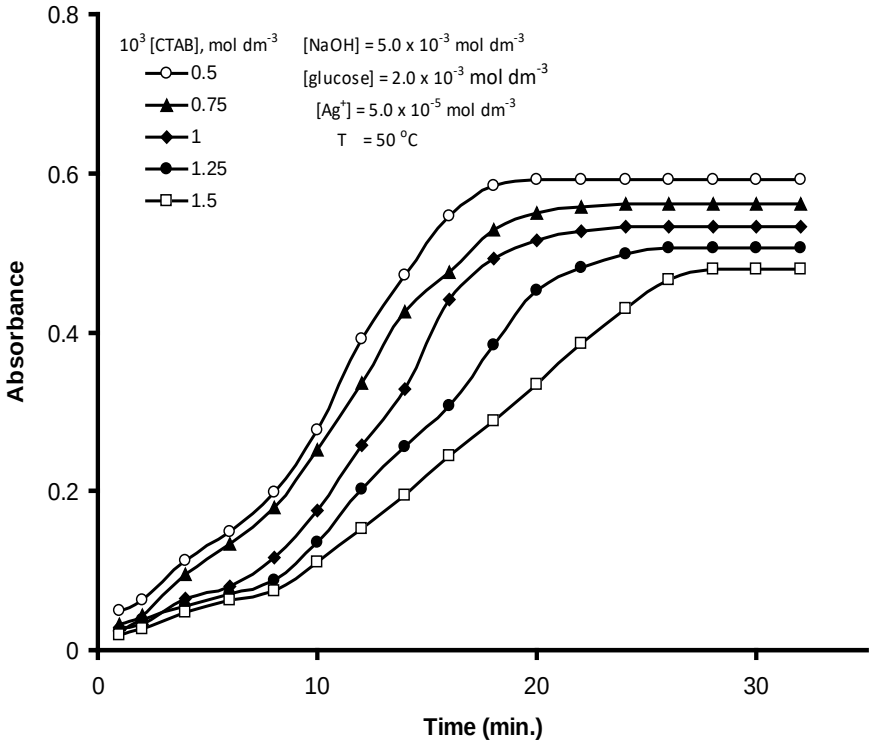

Fig. 8. Variation of absorbance versus time at different [CTAB].

Table 2. Variation of rate constant, k_{obs}, with temperatures.

Temp. (°C)	10^3/T (K^{-1})	$10^3 k_{obs}$ (s^{-1})	-ln k_{obs}/T ($s^{-1}K^{-1}$)
35.0	3.25	0.86	12.79
40.0	3.19	1.23	12.45
45.0	3.14	1.48	12.28
50.0	3.10	1.78	12.11
55.0	3.05	2.03	11.99

The effect of CTAB on the formation of silver nanoparticle by reduction with glucose was carried out at $[Ag^+] = 5.0 \times 10^{-5}$ mol dm^{-3}, [glucose] = 2.0×10^{-3} mol dm^{-3}, $[OH^-] = 5.0 \times 10^{-3}$ mol dm^{-3} for a concentration range of CTAB = $(0.5 – 1.50) \times 10^{-3}$ mol dm^{-3} and T = 50.0 °C. The kinetic data are graphically represented in Fig. 8. Table 1, indicates that the reaction rate decreases gradually with increasing of [CTAB].

The effect of temperature on the rate of reaction of glucose with silver ion was investigated at $[Ag^+] = 5.0 \times 10^{-5}$ mol dm^{-3}, [glucose] = 2.0×10^{-3} mol dm^{-3}, [NaOH] = 5.0×10^{-3} mol dm^{-3} over the temperature range (35.0 – 55.0) °C. Variations of rate constant, k_{obs}, with different temperatures are represented in Table 2. show that the rate of reaction increases with increasing in temperatures (Table 2). From these results thermodynamic activation parameters including enthalpy and entropy associated with k_{obs} are obtained by plotting -lnk_{obs}/T against 1/T, (c.f. Table 2. Enthalpy of activation, ΔH* and entropy of activation ΔS* are equal to 33.1 kJ mol^{-1} and -195.4 $JK^{-1}mol^{-1}$ respectively.

Mechanism

Before attempting to propose a mechanism for the silver sol formation, it is necessary to discuss on the species of Ag^+ existing in the NaOH medium. It is known that formation of silver particles in basic 2-propanol media proceed via formation of Ag_2O species involving the Ag^+ and OH^- [27, 28]. It should be emphasized here that the formation of transparent yellow color was also observed in a mixture of Ag^+, CTAB and OH^- before the addition of glucose (Fig. 6). As the glucose is added, it results in a sudden increase in the absorbance. The Ag_2O is most probably in the colloidal form since no turbidity or precipitation is detected in the solution [27]. In order to identify the role of OH^- concentrations in the reduction Ag^+ ions by glucose, we experimentally tested that at specific

concentration of NaOH ($\geq 7.5\times10^{-3}$ mol dm^{-3}), the reaction mixture ([CTAB] = 1.0×10^{-3} mol dm^{-3} and [Ag^+] = 5.0×10^{-5} mol dm^{-3}), turned turbid in absence of glucose. On the other hand, yellow transparent color appeared at lower [NaOH] ($\leq 7.5\times10^{-3}$ mol dm^{-3}) and the spectra of this color was recorded as a function of time (Fig. 5), indicating the formation of colloidal Ag_2O during the fast reaction of Ag^+ with OH^- [27]. These observations are in good agreement with the results of Huang et al. [27]. Thus we may safely conclude that hydroxide ions play a crucial role in the reaction of Ag^+ ions with glucose. The hydroxide ions is known to have a catalytic effect on the formation of silver sols, provides the significant change in the reactivity of Ag^+ ions that allow the initiation of the electron transfer from glucose to Ag^+ ions, which in turn, preventing a fast corrosion of the very small silver particles at early stages of the reaction [27].

On the basis of these observations, the mechanism is proposed for the reduction of Ag^+ by glucose. Eqs. (1) and (2) represents the fast formation of colloidal Ag_2O and adsorption of Ag^+ from solution onto the surface of Ag_2O particles, respectively. The adsorption of organic reductants on the surface of the colloidal metal particles in quasi-equilibrium reactions prior to the redox rate-determining steps is widely accepted [29, 30]. Thus, the reaction proceeds through the adsorption of glucose onto the surface of colloidal Ag_2O–$(Ag^+)_n$ particles (Eq. (3)). By analogy with previous results, we assume that adsorbed silver ions are then reduced by reaction with glucose (Eq. (4); rate-determining step). In the next step, silver ions adsorbed on the surface of Ag_2O are then reduced via reaction with the delocalized electrons [29] (Eqs. (6) and (7)).

$$2Ag^+ + 2OH^- \rightarrow Ag_2O + H_2O \quad \text{(fast)} \qquad (1)$$

$$Ag_2O + (Ag^+)_n \rightarrow Ag_2O\text{-}(Ag^+)_n \quad \text{(fast)} \qquad (2)$$

$$Ag_2O\text{-}(Ag^+)_n + CH_2OH\text{-}(CHOH)_4\text{-}CHO \rightarrow \rightarrow (Ag_2O\text{-}(Ag^+)_n\text{-}CH_2OH\text{-}(CHOH)_4\text{-}CHO) \qquad (3)$$

$$Ag_2O\text{-}(Ag^+)_n\text{-}CH_2OH\text{-}(CHOH)_4\text{-}CHO \rightarrow \rightarrow CH_2OH\text{-}(CHOH)_4\text{-}COO^- + Ag_2O\text{-}(Ag^{\cdot})_n + H^+ \qquad (4)$$

$$Ag_2O\text{-}(Ag^{\cdot})_n \rightarrow e^-(Ag_2O) \quad \text{(fast)} \qquad (5)$$

$$e^-(Ag_2O) + Ag^+ \rightarrow Ag^o \quad \text{(fast)} \qquad (6)$$

$$2Ag^+ + 2Ag^o \rightarrow Ag_4^{2+} \text{ (silver sol, } \lambda_{max} = 405 \text{ nm)} \quad \text{(fast)} \qquad (7)$$

The role of micelles in catalysis and inhibition of some reactions are due to the solubilization and/or incorporation of reactants into the small volume of micelles through electrostatic, hydrophobic, hydrogen bonding and Van der Walls forces [31, 32]. The role of CTAB in the formation of silver sols can be explained by the positive charge on Ag^+ and its metal particles in the reaction medium. Furthermore, electrostatic repulsion between the positive head group ($-N^+(CH_3)_3$) of CTAB micelles and Ag^+ ions will explain why the rate of reaction decreases with increasing in [CTAB].

In comparison with the formation of silver nanoparticles by reduction with ribose [26] under the same condition, the rate-determining step path *via* one electron oxidation–reduction mechanism in both cases. The rate of formation of silver nanoparticles by the reduction with ribose is more than the rate of formation with glucose.The negative values of the entropies of activation for this reaction may result from the charge concentration of the reactants, which causes substantial mutual ordering of the solvated water molecules [33]. The intermolecular electron transfer steps are endothermic as indicated by the positive ΔH^* values. The support of ΔH^* and ΔS^* to the reaction rate seem to compensate each other. This suggests that the factors affecting ΔH^* should be closely related to those controlling ΔS^*.

CONCLUSIONS

The results from this study show that the reduction of silver (I) by glucose is enhanced in presence of NaOH, leading to the formation of stable and transparent yellow color of silver sol. The kinetics of silver sol formation was monitored by recording the absorbance as a function of time. The reaction proceeds through the adsorption of glucose onto the surface of colloidal Ag_2O–$(Ag^+)_n$ particles. TEM, SEM and UV-SP, show that the formation of spherical, aggregated and poly dispersed nanoparticles.

Acknowledgment: *This project was funded by the Center of Excellence in Environmental Studies under grant number (1/W/1435-P/M). My thanks go the Ministry of Higher Education (MOHE) and Deanship of Scientific Research (DSR), King Abdulaziz University for the financial support.*

REFERENCES

1. C. Burda, X. Chen, R. Narayanan, M.A. El-Sayed, *Chem. Rev*., **105**, 1025 (2005).
2. J. Polte, *Cryst. Eng. Comm*., **17**, 6809 (2015).
3. V.L. Colvin, *Nat. Biotechnol*., **21**, 1166 (2003).

4. G. M. Sulaiman, E. H. Ali, I. I. Jabbar, A. H. Saleem, *Dig. J. Nanomater. Biost*., **9**, 787 (2014).
5. A. Bansal, S.S. Verma, *Phys. Let. A*, **379**, 163 (2015)
6. V.K. Sharma, R.A. Yngard, Y. Lin, *Adv. Colloid Interface Sci.*,**145**, 83 (2009).
7. G.A. Sotiriou, S.E. Pratsinis, *Environ Sci Technol*., **44**, 5649 (2010).
8. N.S. Wigginton, A. de Titta, F. Piccapietra, J. Dobias, V.J. Nesatyy, M.J.F. Suter, R. Bernier-Latmani, *Environ Sci Technol*., **44**, 2163 (2010).
9. S. Iravani, H. Korbekandi, S.V. Mirmohammadi, B. Zolfaghari, *Res Pharm Sci*., **9**, 385 (2014).
10. A. Frattini, N. Pellegri, D. Nicastro, O. de Sanctis, *Mater Chem. Phys*., **94**, 148 (2005)
11. K. M. Abou El-Nour, A. Eftaiha, A. Al-Warthan, R. A. Ammer, *Arab. J. Chem*., **3**, 135 (2010).
12. M. Kiim, J.W. Byun, D.S. Shin, Y.S. Lee, *Mat Res Bull*., **44**, 334 (2009).
13. I. M. Ismail, H. A. Ewais, *Oxid. Coummu*., **39**, 62 (2016).
14. Z. Khan, S.A. Al-Thabati, A.Y. Obaid, A.O. Al-Youbi, *Colloids and Surf B: Biointerface*, **78**, 143 (2010).
15. J.A. Jacob, S. Kapoor, N. Biswas, T. Mukherjee, Colloids Surf. A Physicochem. *Eng. Aspects*, **301**, 329 (2007).
16. I. M. Ismail, H. A. Ewais, *Trans. Met. Chem*., **40**, 371 (2015).
17. J. Polte, X. Tuaev, M. Wuithschick, A. Fischer, A. F. Thuenemann, K. Rademann, R. Kraehnert, F. Emmerling, *ACS Nano*, **6**, 5791 (2012).
18. A. Henglein, *Chem Mater*, **10**, 444 (1998.)
19. B. Wiley, Y. Sun, B. Mayers, *Chem. Eur. J.*, **11**, 454 (2005).
20. W. Qm, L. Ym, L. Kg, *Acc. Chem. Res*., **48**, 1570 (2015).
21. K. Esumi, T. Hosoyo, A. Yamahira and K. Torigoe, *J Colloid Interface Sci.*, **226**, 346 (2000).
22. V.K. Sharma, R.A. Yngard, Y. Lin, *Adv Colloid Interface Sci*., **145**, 83 (2009).
23. A. Henglein, *J. Phys. Chem*., **97**, 5457 (1993).
24. S.W. Heinzman, B. Gamen, *J. Am. Chem. Soc*., **104**, 6801(1982).
25. Y. Tan, Y. Li, D. Zhu, *J. Colloid Interface Sci*., **258**, 244 (2003).
26. H.A. Ewais, I.M. Ismail, K.H. Al-Fahmai, *Res. J. Chem. Environ.*, **91**, 35 (20155).
27. Z.Y. Huang, G. Mills, B. Hajek, *J. Phys. Chem*., **97**, 11542 (1993).
28. S. K Bajpai, M. Y. Murali, M. Bajpai, R. Tankhiwale, V. Thomas, *J. Nanosci. and Nanotechnol.*, **7**, 2994 (2007).
29. Z. H. Dhoondia1, H. Chakraborty, *Nanomater. and Nanotechnol*., **2**, 15 (2012).
30. Z. Khan, P. Kumar, Kabir-ud-Din, *J. Colloid Interface Sci.*, **290**, 184 (2005).
31. C. O. Rangel-Yagui, A. P. Junior, L. C. Tavares, *J. Pharm. Pharmaceut. Sci*., **8**, 147 (2005).
32. C.A. Bunton, *J. Mol. Liq*., **72**, 231 (1997).
33. M.J. Weaver, E.L. Yee, *Inorg. Chem*., **19**, 1936 (1980)

КИНЕТИЧНИ ИЗСЛЕДВАНИЯ ПО ОБРАЗУВАНЕТО НА СРЕБЪРНИ НАНО-ЧАСТИЦИ ЧРЕЗ РЕДУКЦИЯ НА СРЕБРО (I) С ГЛЮКОЗА ВЪВ ВОДНИ И МИЦЕЛАРНИ СРЕДИ

Х.А. Еуаис[1*], И.М. Исмаил[1,2], К.Х. Ал-Фахами[1]

[1]*Химически департамент, Научен факултет, Университет „Крал Абдул Азис“, Джеда 21413, Саудитска Арабия*

[2]*Център за върхови постижения по опазване на околната среда, Университет „Крал Абдул Азис“, Джеда 21413, Саудитска Арабия*

Получена на 7 януари 2016 г.; коригирана на 14 април 2017 г.

(Резюме)

Кинетиката на образуване на сребърни нано-частици (AgNPs) чрез редукция на сребро(I) с глюкоза е изследвана при различни температури във водна мицеларна среда. Реакцията е от псевдо-първи порядък при десетократен излишък на глюкозата. Изследван е ефектът на концентрациите на натриевата основа, Ag^{+}, глюкозата и цетил-триметил-амониев бромид [CTAB]. Реакцията се ускорява при повишаване концентрацията на OH^{-}. CTAB стабилизира растежа на наночастиците, като скоростта на реакцията се повишава с температурата. Наблюдавано е че наночастиците са сферични, агрегирани и полидисперсни. На базата на кинетичните данни е предложен и обсъден подходящ механизъм за формирането на сребърен зол. Размерите на сребърните частици са охарактеризирани чрез трансмисионна електронна микроскопия (TEM) и други физико-химични и спектроскопски средства.

Bulgarian Chemical Communications, Volume 49, Number 3, (pp. 577 – 582) 2017

Modelling of Cs^+ uptake by natural clinoptilolite from water media

N. Lihareva*, O. Petrov, Y. Tzvetanova

Institute of Mineralogy and Crystallography, Bulgarian Academy of Sciences, Acad. G. Bonchev Street, Block 107, 1113 Sofia, Bulgaria

Received September 2, 2016; Revised February 13, 2017

Natural zeolite clinoptilolite from Beli Plast deposit (Bulgaria) was studied and characterized as ion-exchanger for cesium removal from waste water. Batch procedure was applied to investigate the influence of pH, time and Cs concentration on the sorption effectiveness. The studied system was best described by a pseudo-second-order rate model with a rate constant k_2 of 37.03 and 0.103 g meq^{-1} min^{-1} for cesium concentrations of 64.9 and 649 mg L^{-1}, respectively. The equilibrium data were fitted to the Langmuir, Freundlich and Dubinin-Radushkevich (D-R) isotherm models. The best correlation was found with the Langmuir model and the estimated maximum exchange capacity was 1.044 meq/g. The reaction energy, calculated from the D-R model is 13.4 kJ mol^{-1}.

Key words: clinoptilolite, Cs+ ion exchange, kinetics, equilibrium.

INTRODUCTION

Nuclear energetic and other industrial and medical activities lead to generation and deposition of radioactive and other wastes. The most abundant radionuclides in these wastes are the radioactive isotopes of Cs and Sr. Due to their long half lives these elements are hazardous nuclear contaminants. The radioactive forms of cesium Cs^{135} and Cs^{137} have fission yields of 6.54 and 6.18%, respectively [1]. The leaching of cesium isotopes in hydrological cycles, combined with their high solubility and mobility in water media and chemical similarity to potassium make them bioavailable and dangerous for all living systems

The management of radioactive wastes aims to remove the contaminating cations and to make their disposal more efficient and safety. It should be taken into account that the radioactive ions are presented in very low concentrations (ppm and lower) in strong acidic or alkaline solutions with high contents of sodium ions. Different separation techniques and materials are tested for radionuclide removal, which must be chosen to conform to the properties of the liquid phase and the specificity of the solid phase. One appropriate chemical method that achieved this aim is ion exchange and natural zeolites appear to be suitable materials due to their selectivity for Cs isotopes and radiation and mechanical stability. In addition, they are found in nature in high amounts and are relatively cheap.

The ion exchange characteristics of a lot of natural zeolites have been studied with respect to their potential utilization in nuclear wastewater treatment. The research interest is generally centered on clinoptilolite as a member of this group that exhibits good exchange characteristics to metal cations and is widely distributed in nature [2–12].

The published studies describe different aspects of clinoptilolite application as ion exchanger. Cesium removal from aqueous solution by natural clinoptilolite from different localities and countries has been reported by Cortes-Martinez et al. [4] and Rajec and Domianová [5]. Results from investigation of samples containing clinoptilolite and mordenite [6] or clinoptilolite, mordenite and habazite [7] have been reported. Studies of mixtures of zeolites and other alumosilicate materials as bentonites [8] or kaolinite [9] are also presented. Physicochemical characteristics of the uptake, distribution coefficients and maximal capacities are compared and discussed with respect to the mineralogical and chemical composition of ion exchangers. The effect of zeolite modification in different cationic forms on its physicochemical properties for Cs uptake has been discussed as well [10, 11]. The selectivity of natural clinoptilolite towards the main radioactive elements Cs, Sr, and Co in the wastes has been studied by Smičiklas et al. [12].

In the above cited papers the studies aimed to describe different characteristics of the Cs^+ uptake by clinoptilolite applying a variety of techniques. The objective was to find effective and reliable method for removal of cesium from radioactive wastes.

In the present study we continue the characterization of Bulgarian clinoptilolite from Beli Plast deposit as ion exchanger for heavy metals and ions of radinuclides [13, 14, 15]. The aim is to study the Cs^+ behavior as a function of interaction time, pH, temperature and initial concentrations under batch conditions and to apply

* To whom all correspondence should be sent:
E-mail: nlihareva@abv.bg

the obtained data to different kinetics and thermodynamic models in order to receive equations, describing mathematically the run of the processes. The parameters of models give possibility to make conclusions about the uptake mechanism and the rate controlling interactions.

EXPERIMENTAL

The used clinoptilolite rich tuff is from the Beli Plast deposit (East Rhodopes, Bulgaria). After grinding and sieving a portion with a grain size <75 μm was separated for the experiments. The mineralogical composition of the sample was determined by powder XRD analysis and revealed that the zeolitized tuff consists mainly of about 85 wt.% clinoptilolite and minor content of opal-CT ~15 wt.%. The chemical analysis of the adsorbent is described in [15].

The clinoptilolite sample was used in the ion exchange experiments without any pretreatment. All used chemicals were of analytical grade. The cesium stock solution was prepared from CsCl (Merck). The working solutions were prepared by appropriate dilution. Cesium uptake was studied by agitated batch experiments. In general, the procedure for kinetic, equilibrium and pH studies was as follows: to an amount of 0.1 g of material in a screw capped polypropylene bottles there were added 20 ml of cesium solution with pH, adjusted by addition of diluted HCl or NaOH. The bottles were placed on a horizontal shaker, shaken during necessary contact time and the suspensions were separated by centrifugation at 4000 rpm. The recovered supernatant solutions were appropriately diluted if necessary and cesium concentration was determined by atomic absorption spectrometry (Perkin-Elmer 30-30 spectrophotometer). The cesium content in the solid phase was calculated using the equation:

$$q_e = \frac{(C_0 - C_e)V}{m} \quad (1)$$

where, q_e (mg g^{-1}) is the concentration of cesium in the solid phase, C_0 and C_e (mg L^{-1}) are the initial and equilibrium concentrations of the cesium solutions, respectively, V (L) is the volume, and m (g) is the natural clinoptilolite mass. The experiments were carried out in duplicate.

RESULTS AND DISCUSSION

Effect of pH on the Cs uptake

The effect of the initial pH of the solution on the cesium uptake onto clinoptilolite was investigated by the batch procedure as described above using Cs solution with concentration of 664.5 mg L^{-1}, contact time 450 min and pH range from 0.7 to 10.8. As an alkaline element cesium is in the form of monovalent cation in the entire pH interval. The relationships between the initial pH and the final pH and the amount of the retained Cs are presented in Figure 1. It can be seen from the graph that the changes in pH are small for the initial pH <4.0 and pH_{fin} increases in acidic solutions and decreases for pH_{in} in the alkaline range. This fact demonstrates that clinoptilolite has amphoteric properties – it accepts protons at low pH and is deprotonated at high pH. The uptake of Cs is effective even at low pH_{in} = 2 (effectiveness E = 64.48%) and then increases and remains nearly constant (E ~ 69%) at the range of pH_{in} 3 up to 10.8. The corresponding capacities q_e of Cs^+ uptake for these conditions of the pH experiment at equilibrium are q about 0.7 meq g^{-1}.

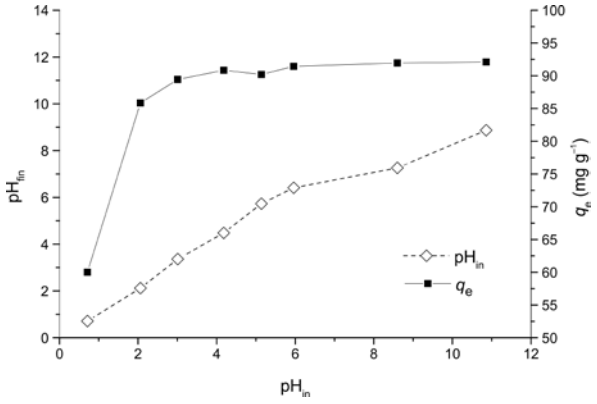

Fig. 1. Effect of pH_{in} on cesium uptake by natural clinoptilolite (0.1 g + 20 ml 664.5 mg L^{-1} Cs, contact time 450 min)

These changes in pH_{fin} and the extent of Cs removal with pH might be explained as follows: at low pH_{in} the H^+ ions are in high concentration and compete with the Cs^+ ions in the interaction with clinoptilolite making ion-exchange with the extra-framework cations This results in low cesium uptake and in increasing of pH. At higher pH more cesium ions can be exchanged and q increases.

Kinetic studies

The kinetic of the Cs^+ uptake by clinoptilolite was studied by bath procedure as described above, using a set of solutions for two concentrations of 649 and 64.9 mg L^{-1} Cs^+ at pH_{init} of 5.4 and contact times of 15, 18. 60, 120, 360, 600, 850 and 1490 min. The rate and extent of removal of Cs^+ are shown on Fig. 2 a.

As seen from the run of the plot of the lower concentration 64.9 mg L^{-1} and the calculated value of q_e, the loaded amount of cesium increases very quickly, reaches equilibrium in the first 25 min and

then remains constant. The removal efficiency (E%) of clinoptilolite for Cs^+ changes from 91.3 to 99.5%, i.e. almost all of the Cs^+ ions were removed within 25 min of reaction. The initial pH of the solutions rose slowly from 5.4 to near neutral value of 6.7 within 120 min and remained at this value to the end of the interaction. For the higher studied concentration the results indicate that q_e increase quickly in the first 25 min then the changes are small until equilibrium is reached after 360–600 min. By this time the removal efficiency increases from 52.1 to 80.8% and pH_{fin} increases to 6.8. These changes of pH are result of exchange of extra framework cations from the clinoptilolite structure for Cs^+ cations from solution.

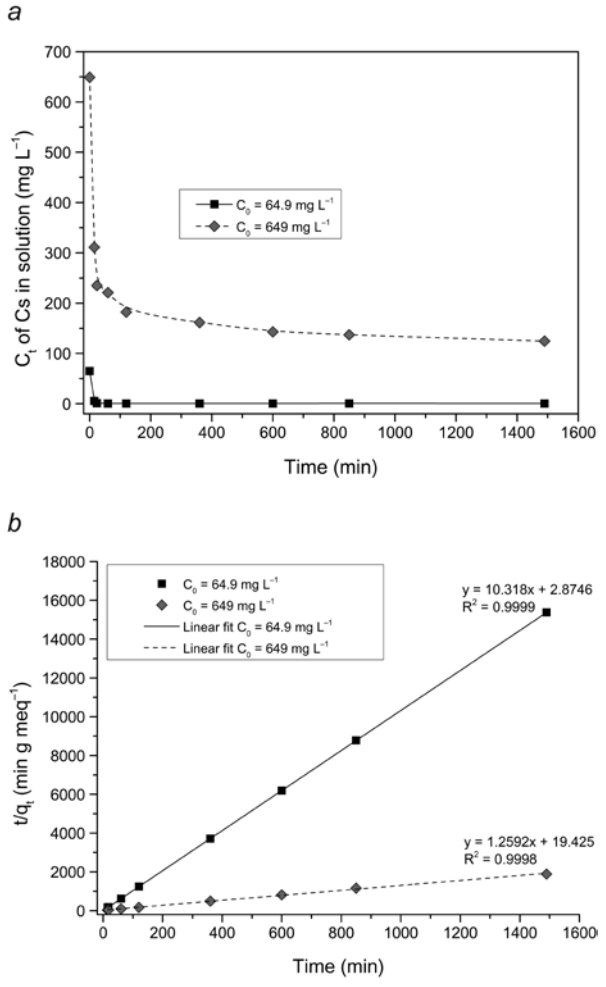

Fig. 2. a) Cesium ion-exchange kinetic for two different concentrations as a function of interaction time (0.1 g material, 20 ml Cs^+ 649 and 64.9 mg L^{-1}, pH_{init} 5.4); b) Pseudo-second-order kinetic model fitted to experimental data for the Cs-uptake by clinoptilolite

To investigate the mechanism and to determine the process that governs the rate of the reaction, three different models describing the kinetics have been applied. They were pseudo-first-order, pseudo-second-order, and intraparticle diffusion models.

The pseudo-first-order rate model was applied in its linear integrated form [16]:

$$\ln (q_e - q_t) = \ln q_e - k_1 t \qquad (2),$$

where q_e and q_t in meq g^{-1} are the concentrations of Cs^+ in the studied natural clinoptilolite sample at equilibrium and at any time t (min), k_1 in min^{-1} is the pseudo-first-order rate constant.

When the relationship between ln ($q_e - q_t$) and t is linear, k_1 is estimated from the gradient of the plot.

The pseudo-second-order kinetics is represented by the linear equation [17]:

$$\frac{t}{q_t} = \frac{1}{k_2 q_e^2} + \frac{1}{q_e} t \qquad (3)$$

where k_2 (in g meq^{-1} min^{-1}) is the apparent pseudo-second-order rate constant. The values of k_2 and q_e may be calculated from the gradient and the intercept of the linear plot, respectively.

The data from the kinetic measurements were interpreted by the method of regression analysis. The relationship between the experimental results and the theoretically fitted lines for the pseudo-second-order model is shown in Fig. 2b. The obtained equations for the two models with the corresponding squares of regression coefficients R^2 and the apparent pseudo-rate constants k_1 and k_2 are listed in Table 1.

The high values of correlation coefficients R^2 (0.9999) for the fitting of pseudo-second-order kinetic model and experimental data are indicative for the validity of this model for both studied concentrations. In addition, the calculated equilibrium values of uptake capacities q_e are very close to the experimentally observed data. The R^2 values obtained by fitting the Cs^+ uptake data to the pseudo-first-order model are also statistically significant (about 0.9) but lower and indicate that this model is less adequate. Moreover, the q_e values obtained from the first–order kinetic model and the experimental q_e values differ from 39.83% to 73.87%. A similar result for kinetics modeling was described previously in [4, 9, 12].

Table 1. Parameters of model kinetics equations for the removal of Cs^+ by natural clinoptilolite.

Cs^+ concentration, mg L^{-1}	First-order-rate model			Second-order-rate model			$q_{e,\,exp}$, (meq g^{-1})
	R^2	k_1 (min^{-1})	$q_{e\,calc}$ (meq g^{-1})	R^2	k_2 (g meq^{-1} min^{-1})	$q_{e\,calc}$ (meq g^{-1})	
64.9	0.9054	0.0014	0.0583	0.9999	37.03	0.097	0.097±0.0001
649	0.8986	0.0039	0.202	0.9999	0.103	0.774	0.773±0.014

As it is known, the simple kinetic models and the calculated equations are mathematical expressions and description of the kinetic process and give only a possibility to predict the results of interaction between the sample and the cations and to compare different systems. The actual chemical reactions and processes that represent the mechanism and determine the rate of uptake include interaction phenomena that are fast and transport phenomena as film diffusion and diffusion of the solute cations into the interior of the pores.

The estimation of the film and the intraparticle diffusion by applying the model equations and a discussion of their role in the uptake is presented in [18]. Our attempt to apply these equations for treating the experimental results gives plots that involve two phases and did not have a zero intercept, i.e. do not correspond to the requirements of the models and do not give exact answer for the rate controlling process. Both mechanisms contribute to the rate of uptake, but no one determines the overall rate.

Isotherms studies

The equilibrium isotherms give a possibility to describe and to design the uptake systems. The equilibrium data for cesium uptake by natural clinoptilolite was collected from agitated batch experiment, varying Cs^+ concentration in the interval 64.9–2596 mg L^{-1}, at pH_{init} ~5.40 and time of interaction of 24 h.

Several isotherm models are known and applied for characterization of uptake equilibrium as relation between the equilibrium concentration of exchanged cation in the liquid and solid phases. Three most often used ones are selected in this study – those of Langmuir [19] and Freundlich [20] and Dubinin–Radushkevich (D-R) [21].

The linear forms of Langmuir and Freundlich isotherm models can be represented by equations (4) and (5), respectively:

$$\frac{C_e}{q_e} = \frac{1}{q_m b} + \frac{C_e}{q_m} \quad (4)$$

$$\log q_e = \log K_F + \frac{1}{n}\log C_e \quad (5)$$

where C_e (meq L^{-1}) and q_e (meq g^{-1}) are respectively the equilibrium cesium concentrations in the aqueous phase and in the solid phase, q_m (meq g^{-1}) represents the maximum uptake capacity, b (L meq^{-1}) is the site energy factor, connecting to the equilibrium constant (affinity term). K_F (meq g^{-1})/(meq $L^{-1})^{1/n}$ and n (dimensionless) are Freundlich parameters.

The nature of the sorption process was investigated by the application of the D-R isotherm model equation (6):

$$\ln q_e = \ln q_m - \beta\varepsilon^2 \quad (6)$$

where, q_e, q_m and C_e (in eq g^{-1}) are as described above, β is a constant related to the sorption energy, R is the gas constant (kJ mol^{-1} K^{-1}), T is the absolute temperature (K), and ε is a Polanyi potential:

$$\varepsilon = RT\ln\left(1+\frac{1}{C_e}\right) \quad (7)$$

The constant β is related to the energy of interaction E by:

$$E = (-2\beta)^{-1/2} \quad (8)$$

The isotherm of Cs uptake by natural clinoptilolite is plotted as a function of concentration of cesium onto clinoptilolite versus the corresponding equilibrium concentration in the solution (Fig. 3a). The initial pH of the solutions increased from the values of 5.4 to between 6.6 and 6.7 units for all concentrations of experiment. The experimental data were fitted by the method of least squares regression analysis to the three models. The corresponding linear fits are presented on Fig. 3b, c, d and the parameters of the three models are presented in Table 2.

Table 2. Langmuir, Freundlich, and D-R isotherm parameters for Cs^+ uptake by natural clinoptilolite

Model	Linear form of equation	R^2	b (L meq^{-1})	$q_{m\,calc}$ (meq g^{-1})	$q_{m\,calc}$ (mg g^{-1})	$q_{m\,exp}$ (meq g^{-1})
Langmuir	$C_e/q_e = 0.957C_e + 0.129$	0.9996	7,384	1.044	138,75	1,031 ±0.006
Model	Linear form of equation	R^2	K_F ($meq^{1-1/n}$ $L^{3/n}$ g^{-1})	$1/n$	n	
Freundlich	$\log q_e = 0.279 \log C_e + 0.172$	0.9410	0,672	0.172	3,57	
Model	Linear form of equation	R^2	$q_{m\,calc}$ (meq g^{-1})	β (eq^2 kJ^{-2})	E (kJ mol^{-1})	
Dubinin – Radushkevich	$\ln q_e = -6.405 + 0.0028\,\varepsilon^2$	0.9850	1.650	0.1726	13.4	

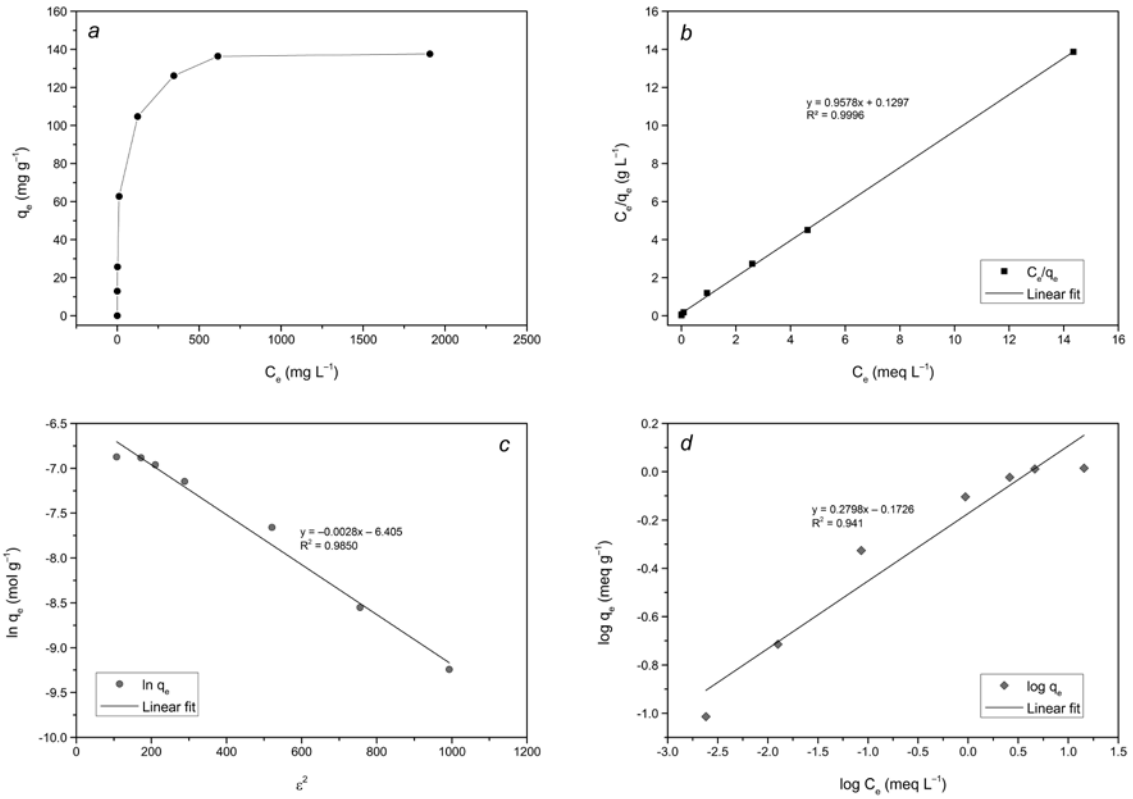

Fig. 3. Isotherm of Cs^+ uptake by natural clinoptilolite (*a*); Isotherm models fitted to experimental data – Langmuir (*b*); Freundlich (*c*); D-R (*d*)

According to the square regression coefficients R^2 the best correlation is obtained with the Langmuir isotherm model. The Freundlich and D-R models were found to correlate a little less although there is a good correlation for the lower initial concentrations in the initial part of the plots. The calculated equilibrium uptake of Cs^+ by the Langmuir isotherm model was 1.044 meq g^{-1} (138.75 mg g^{-1}) and is quite close to the experimentally found value of 1.031 meq g^{-1} − the difference being 1.27%. The results, obtained for equilibrium modeling of Cs^+ uptake by clinoptilolite differ in different studies. Cortés-Martinéz et al [4] observed that the Langmuir-Freundlich model describes the isotherms, Shahwan et al [9] found that isotherm data for Cs^+ uptake by clinoptilolite can be fitted by both Freundlich and D-R models, while in [12] the Langmuir model is in good agreement with the experimental data as are our observations. This result indicates the monolayer uptake and assumes structurally homogeneous material with the energetically identical exchange sites.

The D-R isotherm model gives information about the nature of interaction between clinoptilolite and the cesium cations. The parameter β was applied to calculate the mean energy of interaction, E (eq. 8), related to the mechanism of the uptake reaction [22]. The obtained value of E = 13.4 kJ mol^{-1} is in the range 8–16 kJ mol^{-1} and indicates an ion exchange mechanism.

A lot of papers were found in the literature concerning the study of Cs^+ uptake by clinoptilolite and determination of maximum exchange capacity. In order to make a reasonable comparison, we present only the results obtained using non modified clinoptilolite, the same technique of interaction and similar conditions with those in our investigation. Smičiklas et al. [12] reported for natural clinoptilolite from Serbia a maximal capacity of 45.53 mg g^{-1}. Cortes-Martinez et al [4] have found for two natural clinoptilolite tuffs from Mexico values of q_m 170.35 and 236.31 mg g^{-1}, respectively. Close to them are the results obtained from Boraj et al. [7] for natural clinoptilolite from Japan, Futatsui deposit – 169.8 mg g^{-1}, whereas Schahwan et al. [9] found 7.72 Cs^+ mg g^{-1} for clinoptilolite rich tuffs from Anatolia, Turkey.

An other parameter that characterize the selectivity, capacity and affinity of ion exchange and allows to compare different systems, is the distribution coefficient K_d (in mL g^{-1}), defined by the following equation:

$$K_d = \frac{1000 q_e}{C_e} \qquad (9)$$

K_d is determined using 132.91 mg L^{-1} Cs^+ (1×10^{-3} M) in the above described conditions and

its value is 17 000±1600. This value is very close to distribution coefficient K_d = 15 360 for cesium uptake by sodium titanosilicates [23].

CONCLUSIONS

The natural clinoptilolite from Beli Plast deposit was studied as a potential material for removing Cs^+ from contaminated solutions.

The used clinoptilolite removes Cs^+ with relatively high effectiveness E = 41,3% even from strong acidic solutions with pH = 0.7. At low concentration about 69 mg L^{-1} the cesium retention is about 97–98%. For the studied Cs^+ concentrations >500 mg L^{-1} the effectiveness E reaches 69%.

The exchange kinetics of the process is relatively fast for low cation concentrations. The obtained pseudo-second-order model equations provide a necessary tool for prediction and comparison when such process is carried out.

The modeling of the equilibrium of the process and the respective Langmuir model equations could be used for calculation and estimation of the degree of Cs removal.

On the basis of the obtained results the used natural zeolite material could serve as well-performing and economically effective material for treatment of Cs^+ contaminated wastes.

REFERENCES

1. K. H. Lieser, *Radiochim Acta*, **70/71**, 355 (1995).
2. A. E. Osmanlioglu, *J. Hazard Mater.*, **137**, 332 (2006).
3. N. V. Elizondo, E. Ballesteros, B. I. Kharisov, *Applied Radiation and Isotopes*, **52**, 27 (2000).
4. R. Cortés-Martínez, M. T. Olguín , M. Solache-Ríos, *Desalination*, **258**, 164 (2010).
5. P. Rajec, K. Domianová, *J. Radioan. Nucl. Chem.*, **275**, 503 (2008).
6. P. Rajec, F. Macášek, M. Féder, P. Misaelides, E Šamajová, *J. Radioan. Nucl. Chem.*, **229**, 49 (1998).
7. E. H. Borai, R. Harjula, Leena Malinen, Airi Paajanen, *J. Hazard. Mater.*, **172**, 416 (2009.)
8. G. Atun, N. Bodur, *J. Radioanal. Nucl. Chem.*, **253**, 275 (2002).
9. T. Shahwan, D. Akar, A. E. Eroğlu, *J Colloid Intefac. Sci.*, **285**, 9 (2005).
10. A. Abusafa, H. Yücel, *Sep. Purif. Technol.*, **28**, 103 (2002).
11. H. Faghihian, M. G. Marageh, H. Kazemian, *Appl. Radiation and Isotopes*, **50**, 655 (1999).
12. I. Smičiklas, S. Dimović, I Plećaš, *Appl. Clay Sci.*, **35**, 139 (2007).
13. N. Lihareva, L. Dimova, O. Petrov, Y. Tzvetanova, *Bulg. Chem. Commun.*, **41**, 266 (2009).
14. N. Lihareva, L. Dimova, O. Petrov, Y. Tzvetanova, *Bulg. Chem. Commun.*, **42**, 305 (2010).
15. N. Lihareva, O. Petrov, Y. Tzvetanova, M. Kadiyski, V. Nikashina, *Clay minerals*, **50**, 55 (2015).
16. F. G. Wu, R. L. Tseng, R. S. Juang, *Water Res.*, **35**, 613 (2001).
17. Y. S. Ho, G. McKay, *Process Biochem.*, **34**, 451 (1999).
18. S. S. Gupta, K. G. Bhattacharyya, *J. Colloid and Interface Sci.*, **295**, 21 (2006).
19. Z. Reddal, C. Gerente, Y. Andres, P. le Cloiree, *Environ. Sci. Tech.*, **36**, 2067 (2002).
20. S. Ricordel, S. Taha, I. Cisse, G. Dorange, *Sep. Purif. Technol.*, **24**, 376 (2001).
21. J. Perić, M. Trgo, N. V. Medvidović, *Water Res.*, **38**, 1893 (2004).
22. F. Helferich, Ion Exchange, Mc Graw Hill, New York, 1962.
23. E. A. Behrens, A. Clearfield, *Micropor. Mater.*, **11**, 65 (1997).

МОДЕЛИРАНЕ НА ЙОНЕН ОБМЕН НА Cs^+ С ПРИРОДЕН КЛИНОПТИЛОЛИТ ВЪВ ВОДНИ РАЗТВОРИ

Н. Лихарева, О. Петров, Я. Цветанова

Институт по минералогия и кристалография, Българска академия на науките, ул. „Акад. Георги Бончев“, бл. 107, София 1113, България

Постъпила на 2 септември, 2016 г.; коригирана на 13 февруари, 2017 г.

(Резюме)

В тази статия се представят резултатите от изучаването на природен зеолит клиноптилолит от находище Бели Пласт (България) като йонообменен материал за отстраняване на цезий от замърсени води. Изследването е проведено по метода на сорбция в съд с разбъркване за установяване на влиянието на pH, времето на контакт и концентрацията на Cs върху ефективността на извличането му. Кинетиката на тази система се описва с най-висока степен на корелация на експерименталните данни с уравнението на модела на реакция от втори порядък със скоростна константа k_2 37.03 и 0.103 g meq^{-1} min^{-1} за двете концентрации на Cs – респективно 64.9 и 649 mg L^{-1}.

Експерименталните данни от изследване на равновесието бяха съпоставени с моделите на изотерми на Лангмюир, Фройндлих и Дубинин–Радушкевич. Най-добра корелация беше намерена с модела на Лангмюир като изчисленият максимален обменен капацитет беше 1.044 meq/g. Енергията на реакцията беше изчислена по модела на Дубинин–Радушкевич е E = 13.4 kJ mol^{-1}.

Bulgarian Chemical Communications, Volume 49, Number 3, (pp. 583 – 588) 2017

Development of technology of synthesis of catalysts for neutralization of emissions of the industry and motor transport

L.R. Sassykova[1*], A. Nalibayeva[2], Sh.A. Gil'mundinov[2]

[1]*al-Farabi Kazakh National University, 71, al-Farabi, 050010, Almaty, Kazakhstan*
[2]*D.V. Sokol'sky Institute of Fuel, Catalysis & Electrochemistry*
142 D. Kunaev, 050010, Almaty, Kazakhstan

Received May 19, 2016; Revised November 3, 2016

In the research the technology of preparation of catalysts on block metal carriers was worked out and perfected. As the secondary carrier was used alumina with an additive of zeolite or Ce^{4+}, Ti^{4+}, Zr^{4+}, La^{3+}, Fe^{3+}. The active phase based on compounds Mn, Ni, Co, Fe and the platinum group metals converted into colloidal state was used. The catalysts were tested in the reactions of the complete oxidation of NO_x, CO, C_3H_8 and $NOx+C_3H_6+O_2$ reaction. The activity of Pd-Mo catalyst increases when carrier modifying with cations Ce^{4+}, Zr^{4+}. The activity of a palladium catalyst in oxidation reactions CO - 90-100% and is independent of the concentration of metal, in complete oxidation of C_3H_8 at 473-623 K - 78-90%, for Pt - catalyst - 95-100%. For catalysts based on base metals introducing into the secondary carrier of Ti^{4+} significantly increases the degree of reduction of nitrogen oxides with propylene, at 523 K on a Co-Mn-catalyst - 34%, on Fe-Mn - 29%, at 773 K - 33% and 55%, respectively.

Key words: catalyst, toxic gases, motor transport, industry, block carriers

INTRODUCTION

Carbon monoxide, nitrogen oxides, unburned hydrocarbons, and soot are the major toxic components of exhaust gases of industrial enterprises and released during operation of the engine of internal combustion wastes. Decrease of harmful emissions of motor transport and industry to international standards currently is possible only with catalytic methods, which are the most effective means of cleaning [1-5].

As the catalysts of CO and hydrocarbons oxidation and decomposition of nitrogen oxides are used mainly noble metals on carriers having a high catalytic activity and heat resistance to poisons. Complete removal of toxic gases and poisons in the presence of an effective catalyst is possible at the optimum ratio of oxidizing and reducing agents. For the first time monolithic blocks have been used in the end of '60s as the carriers post-combustion catalysts in non-road means of transport, i.e. in mining equipment in a fork lift truck, etc. Later so-called three-route catalysts (TRC) for reduction of NO_x in exhaust gases have been offered. The greatest distribution was gained by catalysts on metal and ceramic carriers of honey comb and cellular structure with an intermediate layer from γ-Al_2O_3 and an active catalytic covering, as a rule, from noble metals (Pt, Pd, Rh) [6,7]. However, the high cost of these metals and their low resistance to poisons stimulate carrying out of scientific research directed at creation of more optimal from an economic and technological point of view, the compositions and methods of catalytic neutralizers preparation. One of the perspective directions in this area - the partial replacement of noble metal on the oxide components [8-10]. Performance of this subject of researches is caused by need of the solution of questions of ecological safety of Kazakhstan and protection of bioresources. The development of effective catalysts of neutralization of harmful emissions of the transport and industrial enterprises is one of the most important ways to reduce emissions of substances that negatively affect the living organism and flora.

The purpose of the work is development of technology of production of the laboratory and full-size samples of catalysts on the block metal carriers and test their efficiency in the processes of neutralization of toxic emissions of the industry and motor transport.

EXPERIMENTAL

Authors of the present manuscript for many years carry out the researches on synthesis of high-selective stable catalysts of cleaning of exhaust gases of motor transport and harmful emissions of the industry on the basis of monolithic metal block catalysts [11-13]. There is a pilot plant, where all the technological parameters of preparation of neutralizers, as well as technical documentation for the production of neutralizers and drawings on the non-standard equipment have been worked out. The designed monolithic block catalysts with the honey comb structure of channels, developed surface, high thermal and mechanical stability, low pressure

* To whom all correspondence should be sent:
E-mail: larissa.rav@mail.ru

difference maintain high efficiency of cleaning of exhaust gases from CO, hydrocarbons, nitrogen oxides and correspond to the EURO-3 standard. Degree of cleaning of exhaust gases of cars running on gasoline is equal to: CO-CH_x-90-100%, NO_x- 80-100%. Block catalysts have a cylindrical shape and are convenient in placing at the source of toxic emissions. High durability of metal and high workability give the chance to make carrier walls rather thin that as a result provides the general significant increase in the geometrical area of a metal substrate. These factors reduce the total catalyst weight by one third in comparison with the neutralizer on the basis of the ceramic at preservation of catalytic effect. Due to the small thickness of the substrate structure may be configured in such a way that the effective cross-section may be significantly higher than when using a ceramic material: at the same time is achieved and the significant decrease of the hydraulic resistance. For preparation of the block carrier the heat-resistant foil with 50 microns thick of need length and width is cut. Then the foil is subjected to goffering, on a smooth foil the corrugated tape is applied then they are rolled into the cylindrical block. The secondary carrier (washcoat) is applied on the prepared block metal carriers with the honey comb structure of channels. In Figures 1 and 2 are shown the laboratory and full-size samples of neutralizers, respectively.

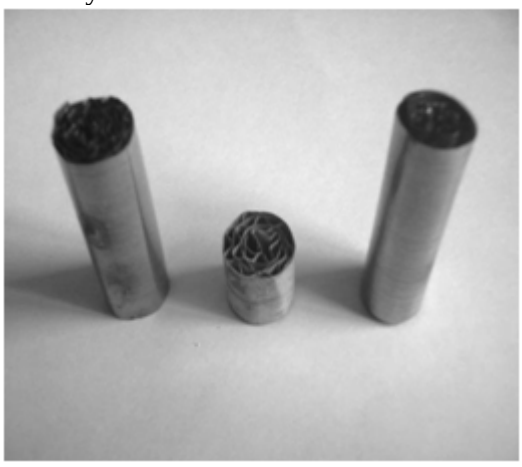

Fig. 1. Laboratory samples of neutralizers on metal blocks

Preparation of full-metal catalysts on the block carriers is carried out on the pilot experimental basis. Equipment for the preparation of full-size catalysts on metal carriers on the basis of experimental development is shown on Figures 3, 4. As a secondary carrier is used alumina with the addition of zeolite and alumina modified by additives Ce^{4+}, Ti^{4+}, Zr^{4+}, La^{3+}, Fe^{3+}. For the preparation of solutions of the active components of the catalysts were applied oxides of Mn, Ni, Co, Fe, prepared from acetates and formates.

Fig.2. Full-size catalytic neutralizers on block metal carriers

Fig. 3. Centrifuge for impregnating metal on the block carrier

Fig.4. The kilns for the full-size metal catalysts

The previously weighed blocks were immersed in a solution of acetate or formate of metal were shaken slightly from the excess solution between the blocks of channels, then were dried at 423 K for 2 hours in a kiln, after which they were calcined in an electric

furnace at 873 K for 2 hours. In this case metal salts are decomposed to form metal oxides on the surface of the carrier the block. The blocks were weighed again and by a difference of masses before and after deposition the concentration of the deposited metal was determined. To increase the activity of platinum catalysts in the reactions of oxidation of CO, hydrocarbons and nitrogen oxides decomposition usually platinum metals were transferred to a colloidal state by impregnation of catalysts by the previously prepared solutions of polymers with inclusion of solutions of the deposited metals with the subsequent thermal decomposition. In the work platinum nano-size particles were prepared by reduction with hydrogen in an aqueous solution containing chloroplatinic acid and citric acid. As the stabilizer of colloid platinum particles is used isopropyl alcohol. The obtained colloidal platinum metal by such methods is coated on carrier block. Block carriers supported on metal sols were dried in the furnace for 4 hours at a temperature of 423 K. The catalysts were calcined in a muffle furnace at 773 K for 2 hours. Also in the synthesis of catalysts based on platinum and palladium as active components of catalysts acetates of Pt and Pd and their π-complexes are used. Solutions of acetate of palladium were prepared by dissolution of Pd in the acetic acid containing 3% of HNO_3. Nitric acid was removed in the course of evaporation before complete cessation of release of nitrogen oxides. π-complexes of Pd and Pt were prepared by reacting of allyl alcohol with the salts of these metals with subsequent drying of the catalysts at 423 K and calcination at T = 773 K for 2 hours. For increase of thermal stability catalysts were modified with additives of the second metal and oxides of refractory metals. For test of catalysts the flowing catalytic installation with the tubular reactor of integrated type was used [14, 15]. The gas mixture was prepared by feeding of hydrocarbons from container and the compressed air from the line into the mixer. The hydrocarbon content of the mixture was about 0.5. %. The oxygen concentration was varied from 2 to 10 vol. %. The gas mixture was analyzed by GLC and OPTOGAZ gas analyzer before and after the reaction. Crystal 2000M and Chrom 3700 chromatographs with the flame ionization detector are used. Time of analysis-20-30 min. For testing was used a sample of the 2 cm^3 colloidal catalyst on the metal carrier. Previously the catalyst was calcinated at 773 K within 4 hours on air in the muffle furnace. The activity of the catalysts was determined at temperatures of 423-773 K. When designing the optimal compositions and methods of preparation of colloid metals were varied its dispersion, the active metals content, their relative proportions and a temperature of the preliminary heat treatment.

RESULTS AND DISCUSSIONS

In Table 1 the data by influence of the concentration of the π- allylic complexes of Pt and Pd to activity of the block catalysts in the reaction of CO, C_3H_8 oxidation and NO_x reduction are shown. Characteristic of activity of the catalyst was the degree of conversion (α) of initial reagent (hydrocarbon, carbon monoxide, nitric oxide). Apparently from Table, activity of Pd-catalyst in reaction of CO oxidation practically didn't depend on concentration of metal and was about 90-100 % in the investigated interval of temperatures. However, efficiency of Pd-catalyst in reaction of complete oxidation of C_3H_8 at low temperatures (623-473 K) was much lower, than that of the Pt-catalyst, and was 78-90 %. The higher activity of the Pt-catalyst in reaction of NO reduction in comparison with Pd the catalyst was observed at contents of Pt equal to 0.1 % and T=773 K.

Research of Pt and Pd catalysts on thermo stability was carried out by maintaining of the catalyst with an interval of 5 hours at T=773 K in a reactionary gas mixture with the contents of 0.5 % of propane-butane with the subsequent analysis of products of reaction. The total time of researches was 100 h. The most stable appeared the catalysts obtained from acetates Pt, less stable - on basis Pd.

Table 1. Influence of concentration of π- allylic complexes of Pt and Pd on a degree of conversion of CO, C_3H_8,NO_x(volumetric speed of a stream of gases- 35000 h^{-1})

Catalyst	The active metal concentration, %	Conversion degree, % at the different temperatures of research of catalysts, K											
		CO				C_3H_8				NO_x			
		773	623	523	473	773	623	523	473	773	623	523	473
Pt π-allyl	0.01	100	100	89	16	95	85	50	0	20	20.7	13.9	0
Pt π-allyl	0.05	100	100	92	50	98	94	73	0	20.7	21.1	14.4	0
Pt π-allyl	0.1	100	100	100	87	100	99	73	17	34.2	36.7	17.1	1.2
Pd π-allyl	0.1	100	100	100	83	53	22	5.0	0	18.4	16.8	8.0	0
Pd π-allyl	0.15	100	100	100	90	59	32	18	0	24	26.6	16	0.5

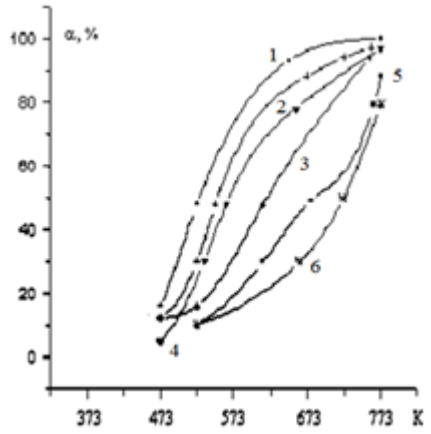

1-0.1% Pt-initial Pt, 2- 0.1% Pt-50 h. of testing, 3-0.1% Pt- 100 h., 4- 0.2% Pd-initial Pd, 5- 0.2% Pd-50 h. of testing , 6- 0.2% Pd-100 h. of testing

Fig.5. Dependence of stability of catalysts in reaction of 0.5 % of propane-butane in air oxidation.

Supporting of the secondary oxidic covering on metal blocks of honey comb structure (oxidic washcoat), as a rule, allows to produce carriers with the developed specific surface and porous structure [16, 17]. High thermal stability of the oxidic washcoat is provided with introduction to it of the modifying additives. For example, into the secondary coating alumina are introduced cations of cerium, zirconium, lanthanum, which do not only stabilize γ-Al_2O_3 phase, but also provide resistance to poisons or sintering of Pt, Pd, Rh- active components of the catalysts [18, 19]. In the work metal block Pd-Mo-catalysts on Al_2O_3 carrier modified by additives of Ce^{4+}, Ti^{4+}, Zr^{4+}, La^{3+}, Fe^{3+} are prepared and investigated in reaction of $NO_x+C_3H_6+O_2$. Activity of Pd-Mo of catalysts increases when modifying the carrier with cations of Ce^{4+}, Zr^{4+}. Activity of Pt-Cu catalysts on the zeolite-containing carriers NaY, ZSM-5 and their hydrogen forms is studied. High activity of the catalyst is noticed when supporting of the active phase on the carrier in H^+-form. A number of oxidic catalysts with the differing structures of the washcoat (γ-Al_2O_3,γ-Al_2O_3+TiO_2) and composition of the active agent (Co+Mn, Fe+Mn) promoted and not promoted by platinum is studied. It is found that introduction into the secondary carrier of titanium dioxide considerably increases extent of reduction of nitrogen oxides by means of propylene on both compositions of oxidic catalysts in all interval of the studied temperatures (423-773 K) and was equal to 34% at 523 K on the Co-Mn-catalyst, to 29% -on Fe-Mn, and at 773 K-33% and 55%, respectively. Promotion with platinum improves the reduction ability of cobalt-manganese catalyst on Al_2O_3 only at temperatures higher than 673 K. On the titanium-containing sample in the presence of platinum degree of NO conversion id decreased.

The samples of catalysts based on platinum group metals were investigated by electron microscope EM-125K with single stage replica method. In a sample with Pt the small congestions of dense particles which don't grow together in units and are dispersed on a carrier surface are observed. The particles size is predominantly 10.0 nm, 5.0 nm and less 9.0 nm (Fig.6, a). In the sample with Pd there are some isolated dense particles in size 12.0 nm-15.0 nm (Fig.6, b). The platinum produced by reduction in solution has the sizes about 15.0-18.0 nm, at the same time, the platinum colloid obtained by reduction with lemon acid had almost monodisperse distribution, the average size of particles was equal to 8.0 nm. It is found that the organometallic complexes of Pd and Pt at magnification of 33,000 times represent translucent areas of the clots of polymer filled with dispersed particles of 3.0 nm. At higher magnification (in the 62,000 times) also small rare congestions of more dense particles of 5.0 nm in size are observed.

Investigation of Pt and Pd-containing catalyst by means of XPA showed X-ray scattering, which confirms the high dispersion of catalysts obtained by thermal decomposition of organometallic complexes. Physical and chemical researches of catalysts on the basis of base metals were carried out by XRD method on x-ray diffractometer DRON-4.0.7 with the copper anode. Samples for research were prepared by mechanical destruction of the catalyst put on a block metal framework. The fallen part of the catalyst was crushed in an agate mortar up to 100 microns and was used for research by method XPA. It was found, that the oxide catalysts represented spinel with cubic lattice $NiMnO_4$ with reflexes 2Å, 52Å, 148Å, 203Å. Also there were small intensive reflexes $_{of}$ CeO_2 (308Å) and alumina (160Å, 256Å). The conducted research of supports and catalysts by means of XPA showed the formation TiO_2- anatase structure, reflexes 3.52; 1.89; 2,38 Å. The carrier based on V_2O_5-WO_3- peaks 4.38, 3.4, 2.8 Å, it has an orthorhombic lattice. In the active phase NiO-crystal lattice is not formed. Catalysts based on base metals had been investigated with an electron microscope EM-on device 125M single by stage replica method. On a nickel-vanadium-tungsten sample the congestions of dense particles which don't grow together in units and are dispersed on a carrier surface are observed. The sizes of particles were mainly 15.0-20.0 nm.

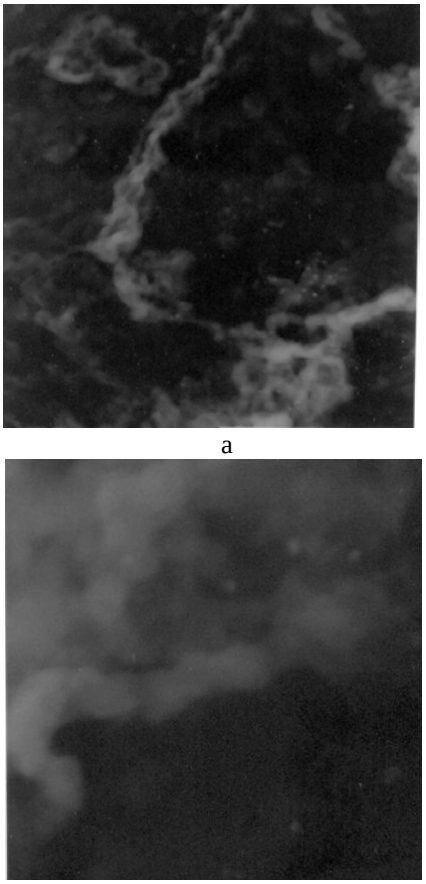

a

b

Fig.6. EM - pictures of distribution of noble metals on the metal carrier: a- Pt on carrier, b-Pd on carrier.

CONCLUSION

Catalysts for neutralization of toxic gases of the industry and motor transport on metal carriers with the honey comb structure of channels are prepared. As the secondary carrier was used alumina with an additive of zeolite or Ce^{4+}, Ti^{4+}, Zr^{4+}, La^{3+}, Fe^{3+}. For preparation of solutions of the active components of catalysts are applied oxides of Mn, Ni, Co, Fe, obtained from acetates and formates. Also were synthesized the samples of catalysts based on metals of the platinum group converted into colloidal state. It was shown that the activity of the palladium catalyst does not depend on the metal concentration in the CO oxidation reaction and is about 90-100%. The effectiveness of the Pd-catalyst in the C_3H_8 complete oxidation reaction at low temperatures (623-473 K) is significantly lower than of Pt-catalyst, and is 78-90%. For catalysts based on base metals introducing into the secondary carrier of Ti^{4+} significantly increases the degree of reduction of nitrogen oxides with propylene, at 523 K on a Co-Mn-catalyst - 34%, on Fe-Mn - 29%, at 773 K - 33% and 55%, respectively.

REFERENCES

1. Yu.A. Alexandrov, K.E. Ivanovskaya, I.A. Vorozheykin, *Journ. of Appl.Chem.*, **8**, 1298 (2003).
2. I.L. Karol, A.A. Kisselev, *Priroda*, **6,** 18 **(**2003).
3. V.L. Inozemtsev, *Priroda*, **1,** 20 (2001).
4. FCCC/CP/1999/7, in: Review of the implementation of commitments and of other provisions of the Convention. UNFCCC guidelines on reporting and review. (Proc. UNFCC Conference of the Parties, Marrakech, Fifth session, Bonn, 25 October-5 November, 1999), 1999.
5. FCCC/CP/2001/20, Guidelines for national systems under Article 5, paragraph 1, of the Kyoto Protocol, (UNFCC Conference of the Parties, Seventh session, 10 November, 2001), 2001.
6. V.Ph. Tretyakov, T.N. Burdeynaya, V.A. Matyshak, L.S. Glebov, in: Proceeding of Environmental catalysis: Achievements and Prospects, (Proc. 17 Mendeleevskii congress on General and Applied Chemistry, Kazan, Russia, 2003), 2003, p. 469.
7. O.V. Krylov, V.Ph. Tretyakov, *Kataliz v promyshlennosti*, **4,** 44**(** 2007)
8. Y.A. Kolbanovskii, *Petrochemistry*, **2,** 154 (2002).
9. S. Sendilvelan, K. Bhaskar, S. Nallusamy, *Rasayan J.Chem.*, **2**, 454(2017)
10. S. Sendilvelan, K.Bhaskar, *Orient J Chem*, **4**, 2111**(**2017)
11. Sh.A. Gilmundinov, L.R. Sassykova, A.M. Nalibayeva, in: Abstracts, (Proc. III-rd Intern.Conference, Catalysis: Fundamentals and Application, Novosibirsk, 2007), 2007, **II**, p. 532.
12. Sh.A. Gilmundinov, L.R. Sassykova, A.M. Nalibayeva, in: Proceeding of International Symposium on Metastable and Nano Materials, (ISMANAM, Corfu, Greece, 2007), 2007, p. 168.
13. L. Sassykova, A. Nalibayeva; Y.Aubakirov et al., *Orient J Chem*, **4**, 1941(2017)
14. L.R. Sassykova, A. Ussenov, A.T. Massenova et al., *Int. J. Chem. Sci*., **1**, 206 (2016**).**
15. L.Sassykova, Sh.Gil'mundinov, A.Nalibayeva, I.Bogdanova, *Revue Roumaine de Chimie*, **2,** 107(2017)
16. J.S. Shuy, W.H. Weber, H.S. Gandhi , *J.Phys.Chem.* **17**, 4964 (1988).
17. M.F. Zwinkels, S.G. Jaras, G. Menon , in: Proc. 6th Int. Symp. on Scientific bases for preparation of heterogeneous catalysis, Lauvain-la-Neuve, Belgium, 1994, p. 85.
18. R. Frety, J. Levy, V. Perrichon et al., in: Proc. 3rd Intern. Cong. on Catalysis and Automotive Pollution Control, CAPOC 3, Brussels, Belgium, 1994, **2**, p. 265.
19. B.Y. Lee, Y. Inoue, I. Yasimori, *Bull. Chem. Soc. Jpn.*, **54**, 3711 (1981).

РАЗРАБОТВАНЕ НА ТЕХНОЛОГИЯ ЗА СИНТЕЗ НА КАТАЛИЗАТОРИ ЗА ОБЕЗВРЕЖДАНЕ НА ЕМИСИИ В ИНДУСТРИЯТА И АВТОТРАНСПОРТА

Л.Р. Сасикова[1, 2*], А. Налибаева[1], Ш. Гильмундинов[1]

[1] *Институт по горива, катализ и електрохимия „Д.В. Сокольский“D.V.Sokol'skii“, 050010 Алмати, Казахстан*
[2] *Казахски национален университет „Ал-Фараби“, 050040 Алмати, Казахстан*

Постъпила на 19 май, 2016 г.; коригирана на 3 ноември, 2016 г.

(Резюме)

Разработена е и е усъвършенствана технология за приготвяне на катализатори върху блокови метални носители. Като вторичен носител е използван алуминиев оксид с добавки на зеолити или йоните Ce^{4+}, Ti^{4+}, Zr^{4+}, La^{3+}, Fe^{3+}. Активната фаза се състои от съединения на Mn, Ni, Co, Fe и метали от платиновата група в колоидно състояние. Катализаторите са изпитани за реакциите на пълно окисление на NO_x, CO, C_3H_8 и $NO_x+C_3H_6+O_2$. Активността на катализатора Pd-Mo нараства, когато носителят е модифициран с Ce^{4+} или Zr^{4+}. Активността на паладиевия катализатор при окислението на CO достига 90-100% и е независима от концентрацията на метала; при пълното окисление на C_3H_8 при 473-623 K превръщането е 78-90%, а за платинов катализатор - 95-100%. При катализатори с вторичен носител Ti^{4+} значително се повишава намаляването на азотните окиси с пропилен при 523 K върху катализатор от Co-Mn (34%); при катализатор върху Fe-Mn - 29% при 773 K - 33% и съответно 55%.

Bulgarian Chemical Communications, Volume 49, Number 3, (pp. 589 – 594) 2017

Characterization of aerodispersed systems with increased concentration according to the kinematic viscosity and mass density of their aerosol phase

K.S. Damov[1,2], I.P. Jordanov[4,5], A.S. Antonov[1], M.T. Iliev[2,3*]

[1]*Neofit Rilski South-West University, 2700 Blagoevgrad, Bulgaria,*
[2]*St. Kliment Ohridski University of Sofia, 1164 Sofia, Bulgaria*
[3]*Georgi Nadjakov Institute of Solid State Physics, Bulgarian Academy of Sciences, Sofia, Bulgaria*
[4]*University of National and World Economy, Sofia, Bulgaria*
[5]*Institute of Mechanics, Bulgarian Academy of Sciences, Sofia, Bulgaria*

Received October 28, 2016; Revised March 22, 2017

Aerodispersed systems, hereinafter referred to as aerosols are an integral part of the natural environment of man. Such are the condensation clouds and fogs, dust clouds in deserts and those caused by volcanic activity. Aerosols are widely used in industry, agriculture, medicine, military science. Therefore, the study of their properties is an essential necessity. If the concentration of their aerosol phase is increased, they possess certain physical properties similar to those of liquids, for example the ability to flow.

The current work offers a laboratory method for the determination of the kinematic viscosity and mass density of concentrated aero dispersed systems formed in a limited volume. This method is based on measuring the time required for a certain amount of aerosol to flow out through a calibrated outlet pipe under the influence of its own hydrostatic pressure. This method uses the Poiseuille's law and the equation of continuity. The time needed for the aerosol to flow out is determined by monitoring its upper borderline "aerosol–air" using a laser system and photoelectric sensors and is based on the scattering of laser light by the aerosol.

Keywords: aerosols, kinematic viscosity, mass density, limited volume, laser beam scan

INTRODUCTION

Dispersion state is the ground state of matter, because most of the substance of the universe is in powder form. We find this thought in the preface to the Russian edition of the Reist monograph [1]. Today, although that statement is disputed, no one can deny the important role of aerosols in human life. Here at terrestrial conditions, we are daily confronted with the wide variety of aerosols – eg. starting from atmospheric aerosols (clouds, fog), on which depends the life of organisms and ending with household aerosols (smoke, dust, steam).

The term "aerosol" is proposed by Donian in the end of World War I [2]. Independently Schmauss used the same term and the first article in which the word "aerosol" was used belongs to him [3].

The aerodispersed systems also called aerosols are mixtures of suspended solid or liquid particles (dispersed phase) in a carrier gas often air [1, 2, 4, 5]. An object of study are aerodispersed systems having a particle diameter of the disperse phase in the range of 1 nm to 1 mm [4]. For the researchers in this area the case when the size of the particles is between 10 nm and 100 μm is of greatest interest [1]. In cases when the particles are smaller, i.e., tent to molecular dimensions their study is the subject of molecular physics. When the size of the particles is significantly larger, the aerosols have a very short life because of the rapid sedimentation and their study is of no interest. Also depending on the dispersibility the nature of the laws describing aerodispersed systems is also changing [4].

It's obvious that investigating the aerodispersed state of matter is essential for human activity. Therefore, in the middle of the twentieth century a new science was established – Nanoparticle Aerosol Science and Technology (NAST) [6]. It evolved on the foundations laid by numerous scientists working in different areas. The aerosol science history edited by Preining and Davis [7], casts a glance at the events, people and organizations which transformed the aerosol science to the internationally acknowledged state it has today in scientific communities.

Today, in the early 21st century the object of study of aerosol science is comprehensive – from the environment in which the humanity lives and works to space (meteorite, interplanetary and galactic dust) [2]. Broadly speaking, the subject of study are the characteristics and laws of the behavior of aerodispersed systems. Their gas medium is characterized by parameters such as temperature, pressure, free path of molecules etc. Most often it is air whose composition and properties are studied to the highest level. Special interest is provoked by the fact that the properties

* To whom all correspondence should be sent:
E-mail: ozo@phys.uni-sofia.bg

of aerosols differ from those of air, where they are formed. The properties of aerosols are largely determined by the dispersed phase – size, shape and composition of particles [1]. In polydispersed aerosols the functions of size distribution and particle mass are also important.

Aerosols are generally characterized by several basic macrophysical parameters. Among them the mostly applied in practice are the viscosity and mass density. They determine the behavior of aerosols in physical reactions taking place in the industry, radiation balance on earth, agriculture, health effects, light scattering, etc. Therefor these two parameters applied to concentrated aerodispersed systems are examined in this study. This type of aero systems is also known as Aerodispersed Systems of Limited Volume (ASLVs).

The concept for ASLVs was introduced for the first time by Fuchs [4] in studying the denotation of aerosol systems formed under laboratory conditions in opened containers, where the volume was limited by the walls of the container and a horizontal aerosol–air border. This condition was described first by Regener [8] and can also be observed in nature too, for example, mist in a valley field [4].

We carried out the ASLVs kinematic viscosity and mass density measurements, that are based on the presence of hydrostatic pressure (in these systems) and take place in the case of the aerosol's flowing out from the container (in which it has been formed) through a calibrated pipe in the bottom of the container. Assuming that the stream flows under the Poiseuille's law, we derived a set of equations for the kinematic viscosity and mass density of ASLV [9–11].

BASIC EQUATIONS AND EXPERIMENTAL SETUP

Figure 1 shows our experimental setup [9, 11, 12]. The aerosol is formed in a chamber for initial aerosol formation 2. Using peristaltic pump (smoking machine) 3 the aerosol is transfered to aerosol chamber 1 (of section S) through tube 4 (about 35s, until full). The calibrated exit tube 5 of length ℓ and diameter $2r$ is closed (not shown). When opened, the aerosol starts to flow out and the upper borderline aerosol–air descends. The laser beam (laser 6, mirror 7) travels by the cylinder's longitudinal axis. Photosensors 8 register only the lights scattered by the aerosol in horizontal direction (90°). The signals are processed by electronic block 9, which consists of DC amplifiers, triggers and a logical unit. A Personal Computer 10 records the moment of crossing the upper aerosol–air border line through each of the photosensors. The final results are processed, visualized and recorded.

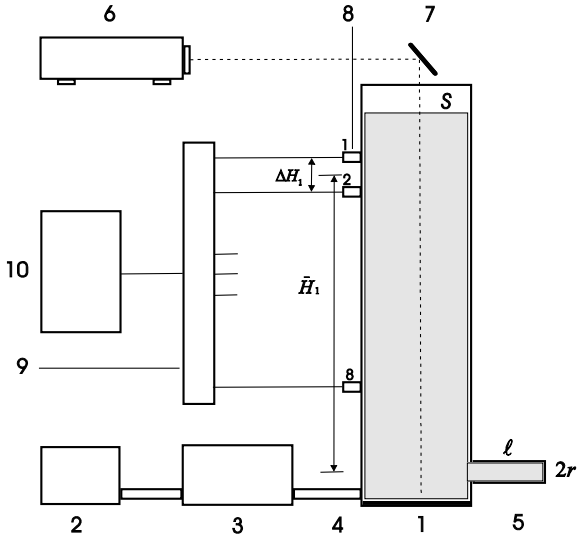

Fig.1. Scheme of the experimental setup: where 1 is an aerosol chamber, 2 container for initial aerosol formation, 3 peristaltic pump, 4 entry to the chamber, 5 calibrated exit tube, 6 laser, 7 mirror, 8 photo sensors, 9 electronic block, 10 PC.

To determine the position of the upper aerosol borderline in the course of time, we used the method of laser light scattering at angle of 90° with respect to the beam followed by detection of the scattered light using photosensors [13]. The methods related to using laser light for scanning have shown their advantages long ago [14]. Therefore in our study we used those methods and further developed them. This led to significant reduction of the setup uncertainty 5% and allowed the use of optoelectronic device [13].

In our setup we used a transperant Polymethyl methacrylate (PMMA) cylinder, 30 mm in diameter as an aerosol chamber. The exit tube's (also made of PMMA) length is ℓ = 30 mm and has a diameter $2r$ = 8 mm. The installation constant is b = 4.65 × 10^{-5} m^2/s^2.

In the presented experimental setup the flow changes direction by 90° when moving from the aerosol chamber to the calibrated exit tube. Therefore determining the Stokes number St in this case is of interest. The Stokes number is the ratio of the stop distance (the product of the characteristic time τ and the fluid velocity u_o) to a characteristic length scale of the flow L. [15]

$$\mathrm{St} = \frac{\tau u_0}{L} = \frac{D_p^2 \rho_p C_c u_0}{18 \mu L} \qquad (1)$$

In (1) D_p is the particle diameter, ρ_p the particle density, C_c the slip correction factor and μ the gas viscosity (air).The Stokes number is ≈10^{-4}–10^{-6} <<

1, therefore the particles are accurately following the change in direction of the flow.

We use 8 sensors (phototransistors), spaced of 30 mm from each other, the first one being 30 cm above the exit tube. After filling the chamber, we let the aerosol stay for 1 min (time retention t_r) before the outflow. We used a He–Ne laser with unpolarized light and power of 5 mW for scanning the aerosol border line.

The aerosol flows in a laminar manner according to Poiseuille's law. The Reinold's number when the aerosol is flowing out through the calibrated exit pipe is Re ≤ 1. The stream inside the aerosol chamber has Re << 1 and these sedimentation of the individual particles Re ≈ 10^{-7}.

If we examine the case in which the upper aerosol–air borderline descends from the level of photosensor 1 to the level of photosensor 2 for a time Δt_1. The volume change V_1 of the aerosol is

$$V_1 = S\,\Delta H_1\,. \qquad (2)$$

For the same ammount of time (Δt_1) the volume V_2 of aerosol that flows out trough the calibrated exit pipe, according to Poiseuille's law is

$$V_2 = \frac{\pi r^4 \nabla p}{8\eta_1 \ell}\nabla t_1\,. \qquad (3)$$

Because of the aerosol's incompressibility and the principle of continuity we can assume that $V_2 = V_1$.

The pressure difference Δp is caused by the aerosol's own hydrostatic pressure. If we assume that during the period in which the aerosol flows between two neighbouring photosensors (in the order of few seconds) the aerosols density will be roughly constant, than the hydrostatic pressure should be

$$\Delta p = \rho_1 g \bar{H}_1\,. \qquad (4)$$

After equalizing equations (1) and (2) and taking in account equation (3), we obtain the kinematic viscosity of ASLV in the form

$$\nu_1 = b\,\frac{H_1}{\Delta H_1}\,\Delta t_1\,, \qquad (5)$$

where $b = \pi r^4 g/8S$.

We obtain the same values for the kinematic viscosity of ASLV in cases when the aerosol–air border line is passing through all the other photosensors. For example, in the case of complete flow out of the examined aerosol through all of the eight photosensors (the time required for the aerosol to travel the distance between photosesors 1 to 8 is 8 to 60 seconds, depending on it's concentration) we will get 7 (roughly equal) values for it's kinematic viscosity. They can be used as an essential physical parameter discribing the aerosol in the moment of measuring.

Unlike liquids, the viscosity and density of aerosols are constantly changeing over time, because of the undergoing processes of sedimentation, coagulation, evaporation through the aerosol–air border, precipitation on the walls of the chamber, etc. Therefore, it is logically to express the aerosols parameters as a function of time. Thereby we obtaing the following summarized equation for determining the kinematic viscosity of aerosols (ASLV) by the fluid flow method

$$\nu(t) = \frac{\eta(t)}{\rho(t)} = b\frac{H}{\Delta H}\,\Delta t\,. \qquad (6)$$

According to the well-known Einstein's equation for the dynamic viscosity of dispersed systems [16]

$$\eta = \eta_0(1+2.5\varphi)\,, \qquad (7)$$

where η is the dynamic viscosity of the dispersed system, η_0 the dispersed medium (air) and φ the volume fraction of the dispersed phase. For the total volume of the aerosol particles (in the case of tabacco smoke) in 1m^3 we get ≈10^{-6} m^3. Therefore $\varphi \approx 10^{-6}$. We can then neglect the second term in equation (7) to obtain $\eta \approx \eta_0 = 1.80 \times 10^{-5}$ Ns/m^2 [17].

We can assume that the last assessment can be applied to other ASLVs systems we examined. If η is replaced by η_0 in equation (6), one obtains the following equation for the mass density of the aerodispersed phase

$$\rho(t) = \frac{\eta_0}{\nu(t)} = \frac{1}{b}\frac{\Delta H}{H}\frac{\eta_0}{\Delta t}\,. \qquad (8)$$

Equation (8) allows us to determine the density of the aerosol phase ρ if we assume that the dynamic viscosity η of the aerosol system is roughly equal to the dynamic viscosity of air η_0 ($\eta \approx \eta_0$) and we measure the time Δt needed for the upper border line to decrease with ΔH.

EXPERIMENTAL RESULTS

We conducted measurements of the kinematic viscosity and mass density of different ASLVs under laboratory conditions – smoke from different types of cigarettes, smoke produced by sublimation and condensation of solid and liquid substances and also screening smokes. The aerosol's phase particles have a very small size and vastly high concentration. Indeed their parameters vary to some extent, depending on the conditions of their formation.

The results of the kinematic viscosity and mass density of several types of aerosols (ASLVs) we have obtained are shown in Table 1. Each of the results listed is an average of 7 experimentally obtained viscosity values (for 7 different volumes of the aerosol) and t_r = 1 min. The experiments

were carried out under standard laboratory conditions and atmospheric pressure of 970–980 hPa. On line 6 we have shown, for comparison, the kinematic viscosity and density of air at 20°C and normal atmospheric pressure [17].

From the results shown, it is clear that the kinematic viscosity of the limited volume aerosols is one or two orders higher than the one of air. Similarly the values of mass density are one or two orders of magnitude smaller.

In Figure 2 are shown the relations of kinematic viscosity (1-a) and the mass density of the aerosol phase (1-b) of ASLVs of the retention time (t_r) from 0 min (when the aerosol is released to flow immediately after filling the aerosol chamber) to 10 min, at 1 min intervals. We used smoke produced by burning cigarettes of different brands (we show only 3) using a peristaltic pump. Moreover, we had the opportunity to fill the aerosol chamber with each cigarette three times. From the 8 photosensors are obtained 7 values. That`s why any point of the graph corresponding to a certain retention time is determined based on 21 values. Relations after results aproximation, give us the reason to consider them as linear, but with fluctuations exceeding the relative error of 5%.

The resulting relationships show that the smoke of cigarettes with lower tar content and better quality filters has a lower density, in analogy with the higher viscosity (in the case Stuyvesant). The reduction of density, similarly the increase in viscosity with the increase of t_r is caused by the loss of mass in the process of evolution. We received similar dependencies with other tested cigarette brands.

We propose to characterize the change of density (also similarly viewed the change of viscosity) of the aerosol system according to the t_r by different volumes (heights from the bottom of the container), using a *density distribution function* (the same concerns the viscosity distribution function) defined by the following equation

$$f_i = \frac{W_i}{\Delta\rho_i} = \frac{N_i}{\sum N_i}\frac{1}{\Delta\rho_i}, \qquad (9)$$

where N_i is the number of the values obtained experimentally in the range $\Delta\rho_i$, ΣN_i is the total number of values. $\Delta\rho_i = \Delta\rho$ = const are the steps in density change (the same for viscosity) that are constant in our experiment. We call this function (f_i) *spectrum of the condition of the aerosol system.* This is a common feature of ASLVs and includes a set of all density values (number 231). They were obtained during its evolution.

Table 1. Values of thekinematic viscosity and mass density of several types of aerosols (ASLVs) obtained by the described method

	Aerosol type	ν, 10^{-4} m^2/s	ρ, 10^{-3} kg/m^3
1	Cigarette smoke – Stuyvesant	14.4 ± 0.8	14.1 ± 0.4
2	Cigarette smoke – Gitanes	10 ± 0.3	19.3 ± 0.5
3	Cigarette smoke – VEGA	8.3 ± 0.3	24 ± 0.8
4	Paraffin vapour	3.9 ± 0.2	46 ± 1.4
5	Screening smoke – white	5.3 ± 0.2	33 ± 1.4
6	Air (at 20°C)	0.15	1200

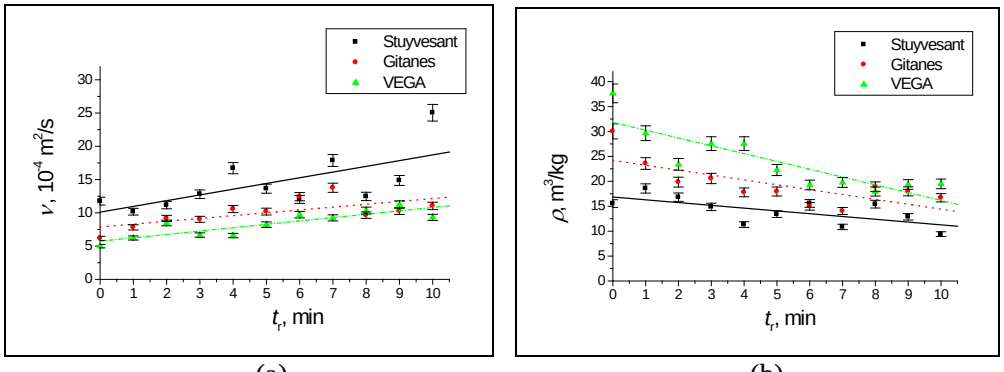

(a) (b)

Fig. 2. Change of viscosity ν (a) and density ρ (b) of ASLVs when the retention time t_r increases.

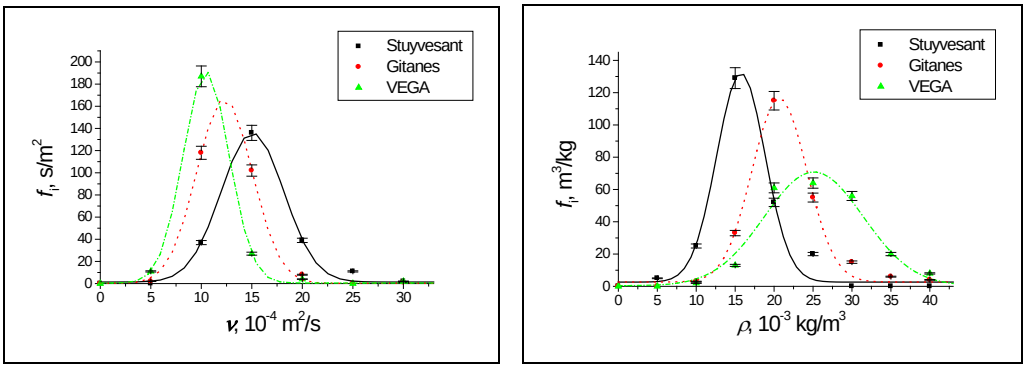

(a) (b)

Fig.3. Spectra of state obtained from the values of the kinematic viscosity (2-a) and the mass density of the aerosol phase (2-b) of ASLVs, obtained from the smoke of three brands of cigarettes.

Table 2. Parameters of the spectrums of the status obtained from the values of the mass density of the aerosol phase, characterizing ASLVs

	Parameters	Cigarettes		
		Stuyvesant	Gitanes	VEGA
1	$\bar{\rho}\,(10^{-3}\ kg/m^3)$	14.1	19.3	24
2	$\sigma_\rho\ (10^{-3}\ kg/m^3)$	0.26	0.34	0.47
3	$\rho_{min}(10^{-3}\ kg/m^3)$	2.8	7.1	6
4	$\rho_{max}\,(10^{-3}\ kg/m^3)$	24.7	38.4	57.7
5	$f_{i-max}\ (m^3/kg)$	130	118	64
6	$\rho_{0.5}\ (10^{-3}\ kg/m^3)$	6	8	17

Figure 3 presents the spectra of condition derived from the values of the kinematic viscosity (2-a) and the mass density of the aerosol phase (2-b) of ASLVs, obtained from the smoke of the three brands. The smoke of a single cigarette can fill the measuring chamber three times and having 8 photosensors we obtain 7 values. We worked with retention times from 0 to 10 min, at 1 min intervals. Therefore, in our case the resulting values are 231. We show for clarity only approximations with the Gauss curve.

The resulting correlations indicate that the spectrum of density of the aerosol phase (2-b), corresponding to the smoke of cigarettes with lower tar content and better filters is shifted to the right, in the direction of the smaller density values. Similarly to the spectrum of the viscosity is obtained shift to the left (2-a), in the direction of larger values of viscosity. Such dependencies we received with other tested cigarette brands.

Parameters of the spectrums of the status obtained from the values of kinematic viscosity and mass density of the aerosol phase, can be used to characterize each ASLV. Table 2 (for example, only the mass density of the aerosol phase of the three brands) shows these basic parameters of the spectra of the state – the average mass density $\bar{\rho}$, corresponding mean square error σ_ρ, minimum $\rho_{\min}$ and corresponding maximum $\rho_{\max}$ value of the entire array (231 values). On the fifth and sixth row are presented the maximum of the density distribution function $f_{\text{i-max}}$ (equation (9)) of the relevant spectrum and its corresponding half-width $\rho_{0.5}$.

DISCUSSION AND CONCLUSION

The current paper, offers a method for determining the kinematic viscosity and mass density of concentrated aerodispersed systems formed in a limited volume (aerosol chamber) ASLVs. This method is based on the measurement of the time needed for a certain amount of aerosol to flow out through a calibrated pipe under the impact of its own hydrostatic pressure. The volume of the flowing aerosol is determined by scanning the upper border aerosol–air. This measurement is performed using a laser beam scan and a photoelectronic circuit, on the basis of light scattering. Poiseuille's law and the continuity equation are applied. Two equations for the determination of kinematic viscosity and mass density of concentrated aero dispersed systems have been obtained, based on the experimentally measured flow out time.

In result of the processes of coagulation and sedimentation within them, the density of the

aerosol phase is constantly decreasing. This leads to reduction of the hydrostatic pressure and after a certain period of time the flow of the aerosol stops. The preliminary results show that this method is applicable to a period of time of the evolution process in relation to the moment of their production in order of 10 to 15 minutes. Most of the experiments we conducted in our experimental setup were using smokes from various types of cigarettes and evolution time of up to 10 minutes. We also investigated the influence of external factors, such as electric and magnetic fields. The data we obtained for the smoke's kinematic viscosity is in the range $(3–65) \times 10^{-4}$ m^2/s and the resolution is $\Delta\nu = 0.15 \times 10^{-4}$ m^2/s. Similarly for the mass density of the aerosol phase we got $(3–60) \times 10^{-3}$ kg/m^3 and the resolution is $\Delta\rho = 0.15 \times 10^{-3}$ kg/m^3. The relative error is 5%.

Results also show that after the examination of the change of two parameters in the process of evolution of the aerodispersed systems and construction of the spectra of the condition, this method can be used to create a new type of ASLVs characterization. The presented experimental data obtained with the use of cigarette smoke proves the potential of the method.

REFERENCES

1. P. Reist, *Introduction to Aerosol Science*, Macmillan Publishing Company, New York, 1984.
2. H. Green, W. Lane, Particulate Clouds: Dust, Smokes and Mists, 2nd ed. D. Van Nostrand, Princeton, NJ, 1964.
3. A. Schmauss, *Umschau*, **24**, 61 (1920)
4. N. Fuchs, Mechanics of Aerosols, Acad. of Sci. USSR, Moscow, 1955.
5. G. Hidy, In: R.A. Meyers (Ed.), Encyclopedia of Physical Science and Technology, 3rd ed, Elsevier Science Ltd., 2003, Chapter: Aerosols, p. 273.
6. W. Chiu-sen, S. Friedlander, L. Mädler, *Chinapart.* **3**, 243 (2005)
7. O. Preining, E. Davis (Eds.), History of aerosol science (Verlag der Osterreichischen Akademie der Wissenschaften, Vienna, Austria, 2000.
8. E. Regener, *Z. Phys. Chem.*, **139**, 416 (1928).
9. K. Damov, In: L. Bumbalov (Ed.), Miscellany of Investigations by Young Researchers 132, SWU Press, Blagoevgrad, Bulgaria, 1991.
10. K. Damov, A. Antonov, *Compt. rend. Acad. bulg. Sci*., **48**, 29 (1995).
11. K. Damov, A. Antonov, (Proc. Intern. Sci. Conf., June 8-11, 2005, Blagoevgrad, Bulgaria) SWU Press, Blagoevgrad, Bulgaria, 2005, p. 346.
12. K. Damov, A. Antonov, *J. Appl. Electromagnetism*, **9**, 57 (2007).
13. K. Damov, M. Iliev, *J. Phys.: Conference Series* 682, 012007 (2016)
14. A. Antonov, A. Petrova, L. Uskeselieva, *Compt. rend. Acad. bulg. Sci*., **30**, 10 (1977).
15. R. C. Flagan, J. H. Seinfeld, Fundamentals of air pollution engineering, Prentice-Hall, New Jersey, 1988.
16. E. Bibik, Reology of Dispersed Systems (St.-Petersburg State University Press, 1981.
17. F. White, Fluid Mechanics, 4th ed., McGraw-Hill, London, 1998.

ОХАРАКТЕРИЗИРАНЕ НА АЕРОДИСПЕРСНИ СИСТЕМИ С ПОВИШЕНА КОНЦЕНТРАЦИЯ ПО КИНЕМАТИЧНИЯ ВИСКОЗИТЕТ И МАСОВАТА ПЛЪТНОСТ НА АЕРОЗОЛНАТА ИМ ФАЗА

К.С. Дамов[1,2], И.П. Йорданов[4,5], А.С. Антонов[1], М.Т. Илиев[2,3*]

[1]Югозападен университет "Неофит Рилски", Благоевград, България
[2] Софийски университет „Св. Климент Охридски", Физически Факултет, София, България
[3]Институт по Физика на Твърдото Тяло „Георги Наджаков" - БАН, София, България
[4]Университет за национално и световно стопанство, София, България
[5]Институт по механика - БАН, София, България

Получена на 28 октомври 2016 г.; коригирана на 22 март 2017 г.

(Резюме)

Настоящата статия предлага метод за определяне на кинематичния вискозитет и масовата плътност на концентрирани аеродисперсни системи, формирани в ограничен обем (аерозолна камера) – ASLVs (Aerodispersed Systems of Limited Volume). Този метод се основава на измерване на времето, необходимо за изтичане на определено количество аерозол през калибрирана изходна тръба под въздействието на собственото му хидростатично налягане. Определянето на обема на аерозола, който изтича, става посредством проследяване на горната граница аерозол–въздух. Проследяването се осъществява с помощта на лазерен лъч и фотоелектронна схема, на базата на разсейването на светлината. Прилагат се законът на Поазьой и уравнението за непрекъснатост. Изведени са две уравнения за определянето на кинематичния вискозитет и масовата плътност на концентрирани аеродисперсни системи на базата на експериментално измерване на времето на изтичане.

Bulgarian Chemical Communications, Volume 49, Number 3, (pp. 595 – 599) 2017

The biological synthesis of anatase titanium dioxide nanoparticles using *Arnicae anthodium* extract

R. Dobrucka

Department of Industrial Products Quality and Ecology, Faculty of Commodity Science, Poznan University of Economics, al. Niepodległości 10, 61-875 Poznan, Poland

Received February 19, 2016; Revised November 25, 2016

The aim of this study was to presentation of the novel ecofriendly method of synthesis of anatase titanium dioxide nanoparticles. In this work, TiO_2 nanoparticles were synthesized using *Arnica montana L*. by reduction method. The prepared titanium dioxide nanoparticles were characterized using Ultraviolet–Visible Spectroscopy (UV-VIS), Total Reflection X-Ray Fluorescence Analysis (TXRF) and Fourier-Transform Infrared Spectroscopy (FTIR). The morphology of the synthesized titanium dioxide nanoparticles was verified by SEM-EDS. X-ray diffraction (XRD) was used to calculate crystallite size. The size of titanium nanoparticles was about 30 nm.

Also, this work presents alterative to chemical methods of synthesis titanium dioxide nanoparticles.

Key words: nanotechnology, nanoparticles, titanium dioxide

INTRODUCTION

Nanotechnology is emerging as a rapidly growing field with its application in science and technology for the purpose of manufacturing new materials at the nanoscale level [1]. In results, nanotechnology has gained massive applications in the fields of biology and pharmacology [2]. Nanoparticles have become significant in recent years and have created an impact in the areas of chemical, energy, electronic, and biological sciences. Although such particles can be synthesized by physical, chemical and biological methods, in the past few years, the last option has gained importance [3]. Preparation of nanoparticles using green technologies is advantageous over chemical agents due to their less environmental consequences. In the biosynthesis method, extracts from plant may act both as reducing and capping agents in synthesis of nanoparticles [4].

TiO_2 is one of the most widely used material owing to its many applications in the field of photocatalysis, gas and humidity sensors, water treatment, selfcleaning, solar cells, photo electrochemical cells, protective coatings on optical elements and bioanalytical chemistry [5]. However, the performances of TiO_2 is strongly influenced by the crystalline structure, the morphology and the size of the particles [6]. Also, among various phases of titania reported, anatase shows a better photocatalytic activity and antibacterial performance [7]. Besides, titanium oxide (TiO_2) is still believed as the most efficient and environmentally [8. TiO_2 nanoparticles have been synthesized using natural products like *Nyctanthes arbortristis* extract, *Catharanthus roseus* aqueous leaf extract, *Eclipta prostrate* aqueous leaf extract and *Aspergillus flavus*. So there is a pressing need to develop clean non-toxic and eco-friendly procedures for the synthesis and assembly of nanoparticles [9].

Arnica montana L. (*Asteraceae family*) is a rhizomatous herbaceous perennial herb originated from the high mountains of the Alps and the Carpathians. Arnica is a medicinal plant widely used as an herbal remedy as well as in cosmetic and liqueur industry [10]. *Arnica montana L.* contains volatile oils, terpenoides, sesquiterpenes lactones, flavonoides [11, 12]. Sesquiterpene lactones are the most active components [13]. In this study TiO_2 nanoparticles were synthesized using *Arnica montana L*. by reduction method.

EXPERIMENTAL

Synthesis of anatase titanium dioxide nanoparticles

5 g powder of *Arnicae anthodium* was boiled for 40 minutes at 80°C with 200 ml of doubly distilled water. 30 ml of the aqueous extract of *A. anthodium* was added in 30 ml of 5mM TiO_2 at room temperature. This solution was stirred at room temperature for 24 h. After this time the solution was heated to 100 °C for the time 30 minutes. The solution was filtered by 0,45 μm Milipore membrane filter and followed by 0,2 μm Millipore membrane filter. TiO_2 nanoparticles solution was stored during 24, 48, and 72 hours.

* To whom all correspondence should be sent:
E-mail: renata.dobrucka@ue.poznan.pl

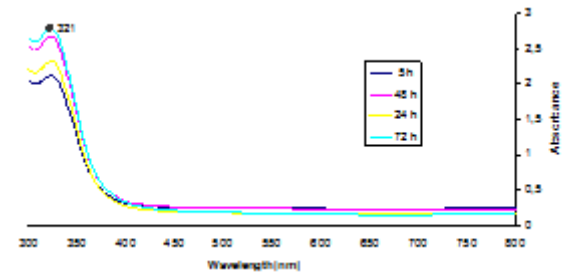

a

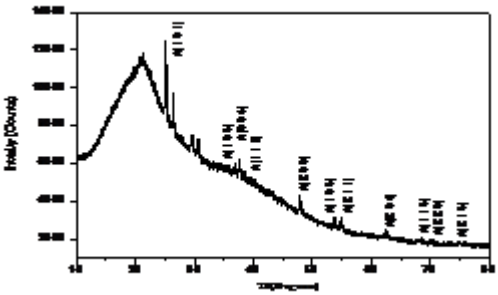

b

Fig. 1. a) UV-Vis absorption spectrum of TiO_2 nanoparticles from water extract of *A.anthodium* b**)** XRD patterns of synthesized TiO_2 nanoparticles

Characterization of anatase titanium dioxide nanoparticles

The optical property of TiO_2 nanoparticles was analyzed UV-VIS absorption spectroscopy (spectrophotometer Cary E 500) in the range 300 nm-800 nm. The morhology of TiO_2 nanopraticles was examined scaning electron microscopy (SU3500, Hitachi with spectral imaging system Thermo Scientific NSS (EDS), the tape of detector (BSE-3D), acceleration voltage (15.0kV), working distance (11,6 mm), the pressure (in the case of a variable vacuum conditions)(40 Pa). The binding properties of TiO_2 nanoparticles were investigated by FTIR analysis. Characterization involved Fourier transform infrared spectroscopy (FTIR) analysis of the dried powder of synthesized TiO_2 nanopraticles by Perkin Elmer Spectrrum 1000 spectrum in attenuated total reflection mode and using spectral range of 4000–400 cm−1 with a resolution of 4 cm−1. To confirm the presence of TiO_2 nanoparticles using X-ray fluorescence spectrometer Bruker S2 TXRF Picofox (50 kV and 600 uA). X-ray diffraction (XRD) studies of the nanoparticles were carried out using a BRUKER D8 ADVANCE brand *-2* configuration (generator-detector) x-ray tube copper S = 1.54 A and LYNXEYE PDS detector. The size of particles estimation was performed by the Scherrer's formula.

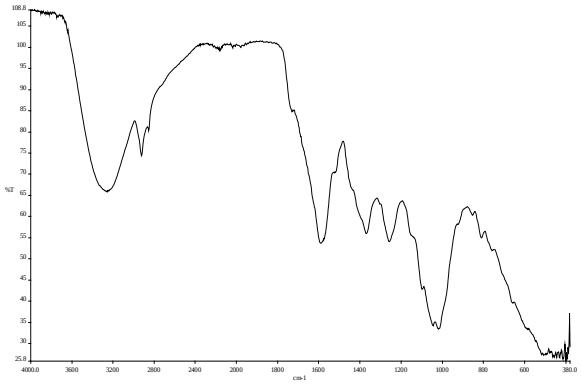

Fig. 2. FTIR spectrum of TiO_2 nanoparticles from water extract of *A. anthodium*

RESULTS AND DISCUSSION

UV VIS and XRD analysis

The absorption spectra were taken at different time intervals. Moreover, 5, 24, 48 and 72 hours after preparation of the solution, absorbance was measured. Figure 1a shows the UV-vis absorption spectrum of TiO_2 nanoparticles between 300 and 800 nm. Figure 1b presents XRD patterns of TiO_2 nanoparticles from water extract of *A. anthodium.*

The peak was observed at 321 nm which is a characteristic band for TiO_2 nanoparticles. According to Silija et al. [14], the intense band with absorption maxima around 300 to 350 nm is associated to the $Ti^{4+}O^{2-}$charge-transfer, corresponding to the electronic excitation from the valence band to the conduction band. The UV–Visible spectra of the resulting solutions were monitored as a function of reaction time. Also, it is observed the increase in absorbance in time. UV-Vis absorption spectrum is compatible with X-ray diffraction profile of titanium nanoparticles. Figure 1b shows the X-ray diffraction profile of titanium nanoparticles. The size of titanium nanoparticles was obtained by Debye-Scherrer's formula given by equation

$D=K\lambda/(\beta\cos\theta)$

where D is the crystal size;

λ is the wavelength of the X-ray radiation (λ=0.15406 nm) for CuKα;

K is usually taken as 0.89;

and β is the line width at half-maximum height [15].

Also, the crystallite sizes were calculated using Scherrer's formula applied to the major intense peaks and found to be the size of 30 nm. TiO_2 nanoparticles synthesized from water extract of *Arnicae anthodium* shows peaks corresponds to the planes at 2θ=25,27° (101), 2θ=36,70° (103), 2θ

=37,80° (004), 2θ = 41, 25° (112), 2θ =47,90° (200), 2θ=53,59° (105), (211), 2θ =62,36° (204), 2θ =54, 39° (211), 2θ =56,64° (220), 2θ = 75,01° (215) indicate anatase form.

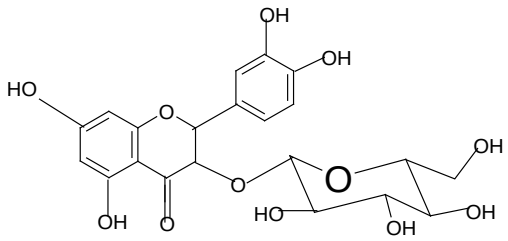

a

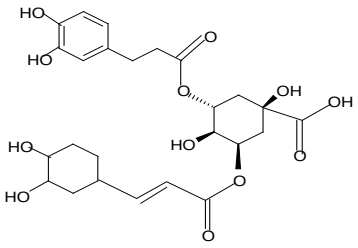

b

Fig. 3. The structure of a) quercetin 3-*O*-glucuronic acid and b) 3,5-dicaffeoylquinic acid

FTIR analysis

FTIR spectrum involves the correlation of the absorption bands (vibrational bands) with the chemical compounds in the sample. In effect, the biomolecules present in plant extracts that are responsible for the reduction and stabilization processes of the green synthesis of nanoparticles can be identified [16]. Also, FTIR spectroscopy was used to determine different groups on *A. anthodium* water extract and predict their role in nanoparticle synthesis (Figure 2). The strong IR bands it is observed at 3269 cm-1, 2924 cm-1, 1591 cm-1, 1369 cm-1, 1258 cm-1, 1020 cm-1 and 416 cm-1. The peaks at 1369, 1258 cm−1 and 1020 cm−1 may be attributed to –C–O and –C–O–C stretching alcohols, carboxylic acids, esters and ethers modes. The band at 1591 cm-11 indicate presence of C=C characteristic of saturated hydrocarbons Strong absorption peaks at 3269 and 2924 cm−1 correspond to -OH stretching and aliphatic methylene group -C-H stretching. The IR band observed at 416 cm-1 indicate presence of TiO_2 nanparticles.

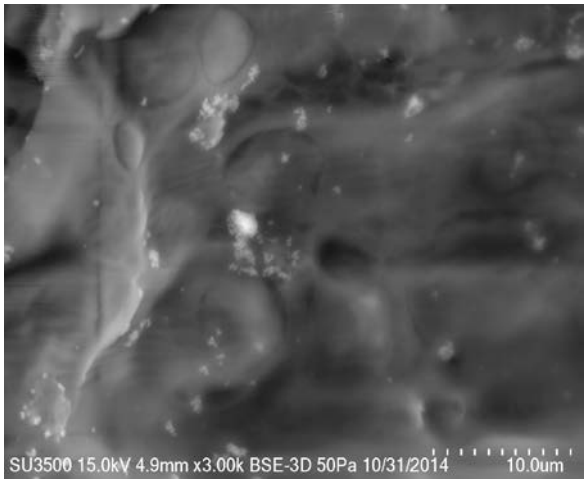

a

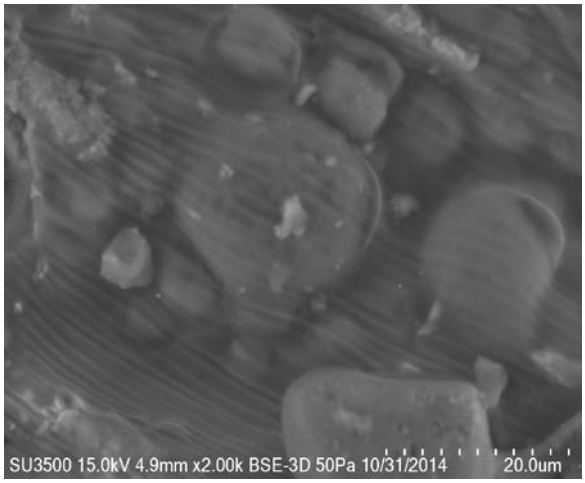

b

Fig. 4. SEM of TiO_2 nanoparticles from water extract of A. anthodium a) the scale bar is 10 μm, b) the scale bar is 20 μm

Also, FTIR analysis confirmed the presence of groups characteristic for flavonoids and phenolic acids. According to Ganzera et al. [17] the most dominant flavonoid was found to be quercetin 3-*O*-glucuronic acid, whereas 3,5-dicaffeoylquinic acid was the major phenolic acid. These compounds show significant antioxidant and antibacterial activities. Figure 3 presents the structure of quercetin 3-*O*-glucuronic acid and 3,5-dicaffeoylquinic acid which are present in extract of *A. anthodium*.

SEM analysis

The morphology of TiO_2 nanoparticles from water extract of *A. anthodium* was verified by SEM-EDS. Figure 4a, 4b and 5a show the SEM images of TiO_2 nanoparticles. The size of TiO_2 nanoparticles was about 100 nm. The larger sizes are results of agglomeration of the particles. In result, agglomeration makes it difficult to study individual nanoparticles. EDS profile of the TiO_2 nanoparticles the presence of elemental metal

signal was confirmed. Figure 5b presents four peaks between 0,5 and 5 kV which are characteristic for anatase for of TiO_2 nanoparticles.

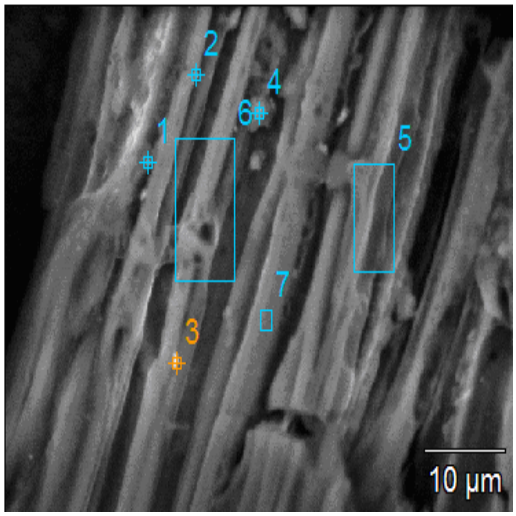

a

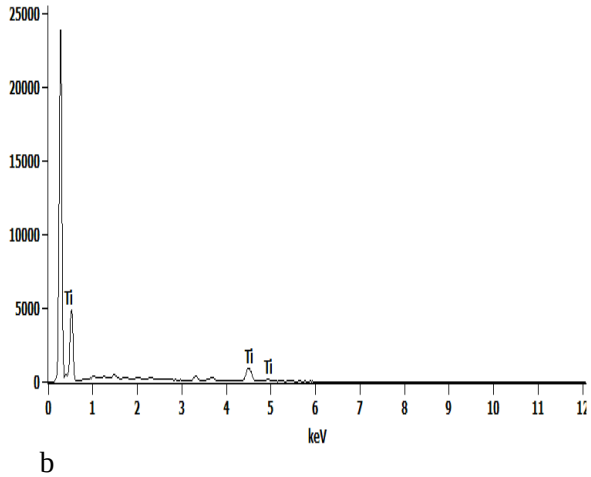

b

Fig. 5. a) SEM and b) EDS profile of TiO_2 nanoparticles from water extract of *A. anthodium*

TXRF analysis

The sample was determined by X-ray fluorescence spectrometer TXRF Bruker S2 Picofox, operated at 50 kV and 600 µA. The strong signal at 4,62 5 keV suggest presence of titanium nanoparticles in water extract of *A. anthodium*. Figure 6 presents TXRF spectrum of TiO_2 nanoparticles from water extract of *A. anthodium*. Also, TXRF analysis confirmed the presence of anatase TiO_2 nanoparticles.

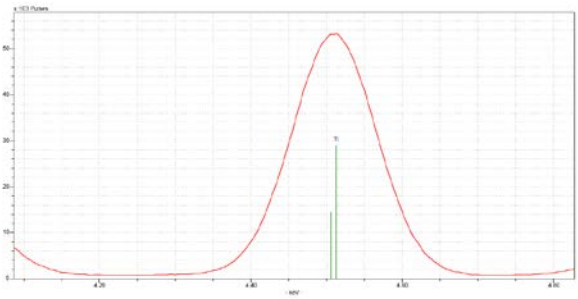

Fig. 6. TXRF spectrum of TiO_2 nanoparticles from water extract of *A. anthodium*

CONCLUSIONS

In the study, ecofriendly synthesis of anatase form of titanium dioxide nanoparticles in low temperature was presented. Titanium dioxide nanoparticles were characterized using UV-VIS, TXRF, FTIR and XRD. The morphology of titanium dioxide nanoparticles was verified by SEM-EDS. Anatase phase exhibits the highest photocatalytic activity. Such properties have led to use of nano-TiO_2 for a wide variety of applications. The water extract of *A. anthodium* could be used instead of chemical solvents. Also, this is eco-friendly and cheap method for the synthesis of photocatalytic form of titanium dioxide nanoparticles.

Acknowledgements:*Research on synthesis of anatase titanium dioxide nanoparticles using A. anthodium extract was carried out thanks to the laboratory of Adam Mickiewicz University Foundation in Poznań, established within the project WND-POIG.05.01.00-00-058/2011 "Waste Cluster – raising the standards of waste management using new technologies". The project is co-financed by the European Union from the European Regional Development Fund.*

REFERENCES

1. M.A. Albrecht, C.W. Evans, C.L. Raston, *Green Chem.*; **8**, 417 (2006)
2. T. Santhoshkumar, A.A. Rahuman, C. Jayaseelan, G. Rajakumar, S. Marimuthu, A.V. Kirthi, K. Velayutham, J. Thomas, J. Venkatesan, S.K. Kim, *Asian Pacific Journal of Tropical Medicin*e, 412 (2013)
3. M. Agnihotri, S. Joshi, A.R. Kumar, S. Zinjarde, S. Kulkarni, M. Agnihotri, *Materials Letter*s; **63**, 1231 (2009)
4. G. Rajakumar, A. Rahuman, B. Priyamvada, V.G. Khanna, D.K. Kumar, P.J. Suzin, *Materials Letters*.; **68**, 115 (2012).

5. A. Maurya, P. Chauhan, A. Mishra, A.K.S. Pandey, *Journal of Research Updates in Polymer Science*, **1**, 43 (2012)
6. M. Koelsch, S. Cassaignon, J.P. Jolivet, *Materials Research Society,* 822 (2004).
7. S. Ragupathyand, K. Raghu, *Int.J.Adv.Res.Biol.Sci.*; **9**, 08 (2014).
8. H. Xu, G. Li, N. Liu, K. Zhu, G. Zhu, S. Jin, *Materials Letters*; **142**, 324 (2015).
9. S.M. Roopan, A. Bharathi, A. Prabhakarn, A.A. Rahuman, K. Velayutham, G. Rajakumar, R.D. Padmaja, M. Leksami, G. Madhumitha, *Spectrochim Acta Part* A ; **98**, 86 (2012).
10. D. Sugier, B. Kołodziej, E. Bielińska, *Journal of Geochemical Exploration*; **129**,76 (2013).
11. M. Ganzera, C.H. Egger, C.H. Zidorn, H. Stuppner *Analytica Chimica Acta*, **614**,196 (2008).
12. D. Sugier, U. Gawlik-Dziki, *Annales UMCS Section E,* **64**, 129 (2009).
13. U. Gawlik-Dziki, M. Świeca, D. Sugier, J. Cichocka, *Acta Scientiarum Polonorum Hortorum Cultus*, **10**, 15 (2011).
14. P. Silija, Z. Yaakob, M.A. Yarmo, S, Sugunan, N.N. Binitha, *Journal of Sol-Gel Science and Technology*; **59**, 252 (2011)
15. R. Vijayalakshmi, V. Rajendran, *Appl.Sci. Res.*; **4**(2), 1183 (2012).
16. S.R. Senthilkumar, T. Sivakumar, *International Journal of Pharmacy and Pharmaceutical Sciences*; 6 (2014).
17. M. Ganzera, Ch. Egger, Ch. Zidorn, H. Stuppner, *Analytica chimica acta*, **614**, 196 (2008).

БИОЛОГИЧНА СИНТЕЗА НА НАНОЧАСТИЦИ ОТ ТИТАНОВ ДИОКСИД (АНАТАЗ) ЧРЕЗ ЕКСТРАКТ ОТ *Arnicae anthodium*

Р. Добруцка

Департамент качество и екология на индустриални продукти, Факултет по стокознание, Познански икономически университет, 61-875 Познан, Полша

Постъпила на 19 февруари, 2016; приета на 25 ноември,, 2016

(Резюме)

Цел на настоящата работа е да се представи нов, екологически съвместим метод за синтез на наночастици от титанов диоксид (анатаз). Наночастиците от TiO_2 са синезирани с помощта на *Arnica montana L.* чрез редукция. Получените частици са охарактеризирани чрез UV-VIS-спектроскопия, рентгеноструктурен флуоресцентен анализ с пълно вътрешно отражение (TXRF) и ИЧ-спектроскопия с Fourier-трансформация (FTIR). Морфологията на наночастиците от синтезирания титанов диоксид е потвърдена чрез сканираща електронна микроскопия (SEM-EDS), рентгеноструктурен анализ (XRD), като са определени и размерите на частиците (около 30 nm). Освен това, работата предлага и други химични методи за синтезата на наночастици от титанов диоксид.

Bulgarian Chemical Communications, Volume 49, Number 3, (pp. 600 – 607) 2017

Catalytic hydrogenation of coal of the kazakhstan fields in presence of polymers

D.A.Baiseitov, M.I. Tulepov*, L.R. Sassykova*, Sh.E. Gabdrashova, A.N. Magazova, O. Dalelkhanuly, Zh.B. Kudyarova, Z.A.Mansurov

al-Farabi Kazakh National University, 71, al-Farabi, 050040, Almaty, Kazakhstan

Received September 9, 2016; Revised March 2, 2017

Objects of investigation are the coals of the central region of Kazakhstan and solid organic wastes in the form of polymers. In this work process of hydrogenation of brown coal of the Kazakhstan fields is studied. The mechanochemical activation of ore catalyst affects not only the degree of carbon conversion but also on the composition of the liquid products. Processing increases activity of the iron-containing catalyst in reactions of conversion of the high-molecular asfaltens into maltens possessing smaller molecular weight i.e. increases cracking properties of the catalyst. The presence of the polymer in the coal leads to release of the volatile and soluble low molecular weight products, which are products of the destructive conversion of coal and polymers. Their yield, composition and structure depend on the condition of the hydrogenation, the stage of coalification of coal, the medium, type and mode of mechanical action. The advantage of the proposed method for producing liquid products from coal is the high yield of hydrocarbon products boiling up to 200°C and the exception of the stages of selection and hydrotreating processes of the pastes, possibility of recycling of industrial and household wastes of polymeric materials.

Key words: coal, catalysts, hydrogenation, polymers, mechanochemical activation.

INTRODUCTION

On the background of the current situation of fuel deficiency in Kazakhstan and reduction of the amount of oil produced, as well as decreasing of oil prices especially actual is the question of finding of alternative fuels, in particular from coal. Complex use of the fossil opens up new perspectives in the area of coal-chemical synthesis. The coal reserves prevail over other types of organic materials, and the problem of disposing of used tires and polyethylene from year to year is increasing worldwide in geometric progression. So the co-processing of solid organic wastes and coal, today - is one of the most promising source for production of liquid, gaseous and solid fuels. In addition, due to such reactions there is a possibility of the synthesis of the most important products for further use in the petrochemical synthesis [1]. Production of liquid fuel and various chemical products by hydrogenation of solid organic materials - the most perspective direction in the fuel and power industry. Scientists of the leading countries of the world carry out the intensive researches of processes of production of synthetic liquid fuels.

Various ways to use catalysts in processes of transformation of coals are so far offered [2-6].

Synthesis of liquid fuel can be carried out by means of direct (destructive) hydrogenation of the initial coal or by hydrogenation of gas, which is previously synthesized in the process of gasification of solid fuels. The best contact is reached at introduction of the catalyst to coal by methods of chemical linkng with reactive groups (for example, -COON, -CH_2OH) on the surface of coal, introduction into the volume of coal substance, and also when using catalysts in the dissolved, melted or volatile states. Implementation of catalytic processes for coal processing by the mechanism of indirect catalysis greatly simplifies their technology. In these cases it is possible to achieve a high efficiency of the process by applying of the mechanical mixture of solid catalyst and carbon which is particulate or suspended in a liquid medium, and a fixed or fluidized bed of catalyst particles. The greatest practical interest is represented by cheap catalysts on the basis of iron (for example, iron salts, iron-containing ores and concentrates). Their use allows to refuse from expensive step of catalyst removal from the solid sludge the process of coal hydrogenation [7, 8]. However the analysis of literary data demonstrates that process of a hydrogenation of coal is carried out at high temperature and pressure in the presence of the active molybdenum-containing catalysts and disposable catalytic additives on the basis of sulfides and sulfates of iron.

It's known [9-12] that mechanochemical processing of solvent and coal is one of the perspective directions in the field of producing of liquid products from coal. As a result of mechanical treatment of coal there is its dispergating leading to increase of a specific surface. This fact gives higher solubility of mechanically activated coal in organic solvents and increase of their reactionary ability in

* To whom all correspondence should be sent:
E-mail: tulepov@rambler.ru, larissa.rav@mail.ru

further chemical reactions. For transformation of the organic mass of coal and solid organic waste in the form of crumb rubber and polyethylene, into liquid products it is necessary to carry out a destruction of coal macromolecules to liquid products and to increase concentration in them of hydrogen that it is usually reached by coal heating under pressure of molecular hydrogen among the pastes-polymers having hydrogen and donor properties. It is known that such polymers as polyethylene contain about 14 wt. % of hydrogen, in worn-out tires the content of hydrogen reaches 9-10%. In the course of the joint thermo-transformation with coal they can act as a potential source of hydrogen necessary for transformation of coal into the easily boiling hydrocarbon fractions. In the course of their joint thermal conversion with coal there is an interaction of radical fragments of thermal destruction of coal with the radicals of polymer that prevents course of secondary reactions of polymerization and polyfunctional condensation of the coal products resulting in the formation of coke.

The aim of the work was to determine the optimal conditions (technological mode of reaction, catalysts) of paste forming to intensify the yield of liquid products from coal and organic wastes. Study of influence of iron-containing catalysts entered into the reactionary mix in the high-disperse form on indicators of process of hydrogenation of brown coal of the Kazakhstan fields.

EXPERIMENTAL

The objects of study were coals of the fields “Karazhira” and “Ekibastuzskii” (Kazakhstan). As the catalysts were used the samples of concentrate of the Balkhash field (BC), Kazakhstan, which are presented the mixture of pyrites and chalcopyrites, in which there are, particularly, Fe-24%, Cu - 30%, Al - 12%, S - 12%. Before carrying out of the experiment the mixtures of solid polymer residues is subjected to heat treatment and then was carried out mechano-processing, joint with coal, to the size of particles more than 200 microns. The resulting mixtures were stored in compliance with the precautions to eliminate the possibility of reaction of oxidation or pollution. As the solvents were used toluene, benzene, alcohols, naphthalene, and acetone.

In the work for the preparation of a necessary additive as a polymer was used a plastic bottle which is warmed and then converted into a powdery state. Polyethylene terephthalate $(C_{10}H_8O_4)_n$ is the most widespread representative of the class of polyesters, condensation product of ethylene glycol with terephthalic acid (fig.1). Polyethylene terephthalate belongs to the group of aliphatic-aromatic polyesters. In the conditions of the mechanoactivation (which is carried out in this work) in which local temperatures reach 1,000°C there is a polymer destruction to producing monomers or oligomers that is easily reached and polymer can be as additinal source of hydrogen, leaving at the same time carbon in a catalyst matrix. In the work described in this manuscript, this substance must be as a source of hydrogen, as it has a low decomposition temperature - 350°C.

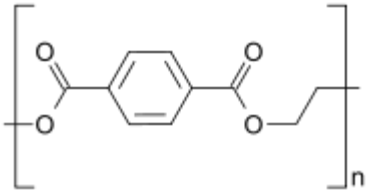

Fig.1. Polyethylene terephthalate $(C_{10}H_8O_4)_n$

IR absorption spectra of the samples were measured with use of the IR spectrometer Perkin Elmer Spectrum 65 in the field 700-3,600 cm^{-1} and UV-750U spectrophotometer in the range of 400-4,000 cm^{-1} in the dismountable cuvettes (liquid samples) and in potassium bromide tablets (solid samples). Definition of micropores, data on textural and structural characteristics of the prepared carbon materials are received with use of the analyzer of a specific surface, and also from calculation of the isotherms of adsorption of nitrogen taken at 350ºC in the range of relative pressures P/P_0 from 0.005 до 0.995 on the device “Sorbtometr-M”. X-ray fluorescent researches and the element analysis of the solid samples were carried out on the FOCUS-M2M microanalyzer with use of Fe-radiation in the range from 2.0 to 37.0 V. The intensity of the diffraction peaks was evaluated by analytical method in the tetragonal system. For samples of initial raw materials (solid polymeric products and coal) the thermogravimetric analysis was carried out. Loss of mass of a sample at the given temperature was determined according to curve of thermogravimetric measurements. The mass loss rate was determined by differential thermogravimetric curve and temperature of maxima of endo - or exo - effects - on the basis of differential thermogravimetric adsorption curve, in accordance to standard procedures. In this work loss of mass is identical to the yield of volatile products, and the rate of loss of mass is equivalent to the rate of allocation of volatile products when heating. Changes of a surface and structure are revealed by means of the scanning electronic microscope NtegraTherma with the lighting modes - "on a gleam" and "on reflection". Aromatics content in the coal hydrogenation products was determined by gas chromatography-

mass spectrometry using Agilent 7890A chromatograph equipped with a mass selective detector Agilent 7000ATripleQuad at registration of the total ion current.

For experiments on coal hydrogenation a rotating 0.5-liter autoclave was used. Reaction was carried out with use of method developed in the laboratory [13-17].

Iron containing catalysts were prepared and introduced into the reaction mixture by following two ways:

1. A powder BC was subjected to mechano-chemical treatment in a mixture with water in the centrifugal planetary mill - activator. The activated catalyst was added to a mixture of coal and water (2:10 wt. parts), at the rate of 10% by weight of organic mass of coal (OMC) and was dispersed for 20 min. The mixture was then dried at 105°C to a moisture of <1 wt. %;

2. The powdery concentrate BC was subjected to mechanochemical processing in mixture with water in a mill-activator, was added to tar accordingly to calculation from 5.0 to 45.0 % to OMC and was dispersed with the subsequent removal of water from mixture at 34°C in a drying box.

RESULTS AND DISCUSSIONS

According to X-ray fluorescence analysis of BC, the main crystalline phase in selected samples of ore after mechanical activation of catalysts are hematite and chalcopyrite transforming into pyrite. At the coal hydrogenation hematite is reduced into magnetite, pyrites is decomposed into pyrrhotine.

The element and phase analysis of the ore catalyst before mechano activation is presented in Table 1. Mechanochemical activation of ore catalysts has impact not only on degree of conversion of coal, but also on the composition of liquid products. Processing increases activity of BC of the catalyst in reactions of transformation of the high-molecular asphaltenes to maltens possessing smaller molecular weight, i.e. increases cracking properties of the catalyst.

IR data of initial coal show the presence of amorphous compounds (fig.2), in particular, the organic component of coals represents mixture of various X-ray amorphous components, presence and quantity of which varies among metamorphism row.

Physico-chemical characteristics of the obtained coal with a polymer, in particular Raman spectrum showed that the main product consists, mainly, of carbon (not less than 90.0%) and to 10.0% of the mineral impurity entering to a basis of polymeric material (fig.3). At the content of polymeric material in mixture less than 10.0 wt. % degree of conversion of mixture into the liquid and gaseous products is low that interferes to the effective implementation of process.

The degree of coal conversion and yield of the low-boiling products grow at increase in amount of synthetic polymeric material in mixture to 70.0% per mixture weight. Data of IR - spectroscopy (fig.4, 5) of initial coal and of coal together with polymer after hydrogenation showed that after mechanical treatment of coals the number of saturated CH-bonds in the form of the methylene and methyl groups is decreased (fig.5) In the liquids extracted from coals after hydrogenation according to IR spectra was observed destruction of carboxyl groups, ketones and esters and decrease in number of the methylene structures. On IR spectra intensity of absorption bands of CH-aromatic groups is increased (in the range of 537-1,017 cm^{-1}); the absorption caused by stretching of vibrations of C-H (the methylene and the methyl) groups in the area of 2,922-3,418 cm^{-1} is decreased. The absorption intensity corresponding to carbonyl groups in aldehydes, lactones, esters (1,720 cm^{-1}) is changed. Data of IR - spectra (fig.5) show that in the reaction products the intensity of absorption bands of aliphatic hydrogen at 2,922 cm^{-1}, of the methyl groups at 1,342 – 1,410 cm^{-1} is increased. Presumably, the growth of the hydroxyl groups associated with the break of ester bonds, an increase of methyl groups is a consequence of the adherence of ethylene from polyethylene and carbonyls growth, is probably the result of acylation of aromatic carbon fragments.

Further increase of the polymeric material in the mixture does not lead to significant changes in these parameters of the process. The proposed process for producing of liquid products from coal can increase the yield of low-boiling hydrocarbon fraction from 12.0 to 60.0 wt.%. An advantage of the proposed method for producing liquid products from coal is the high yield of hydrocarbon products boiling up to 200°C, exception of the processes of allocation and hydrotreating stages of polymers from the technological scheme and possibility of recycling of industrial and household wastes of polymeric materials. In the presence of polymers as a part of mixture coal-polymer the content of high-molecular asphalt and resinous components - asphaltenes and benzene pitches is decreased in the field 360–443ºC. As a result of thermal influence in bitumen the role of components with smaller molecular weight - benzene pitches and oils is

Table 1. The composition of the ore samples before and after mechanical activation

The samples	Composition, %					
Elemental analysis	Fe	Zn	Al	Cu	Cl	S
MC	41.4	-	-	36.5	7.3	-
BC	32.8	6.4	21.11	22.58	-	15.5
The main crystalline phase						
Phase analysis	The initial sample			After mechanical activation		
MC	CuO, $FeCl_3$			Fe_2O_3, CuO, Cu		
BC	$CuFeS_2$, Fe_2O_3, FeS_2,			Fe_3O_4, FeS, CuO, Cu		

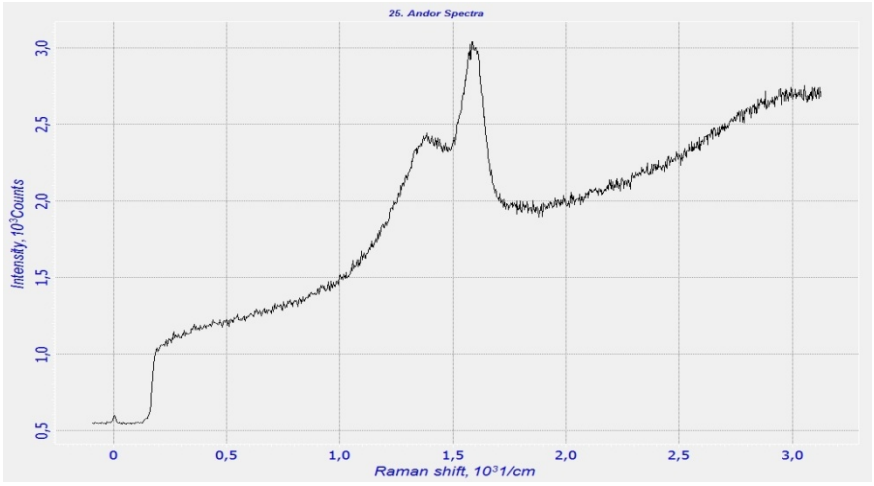

Fig. 2. Raman spectrum of initial carbon materials

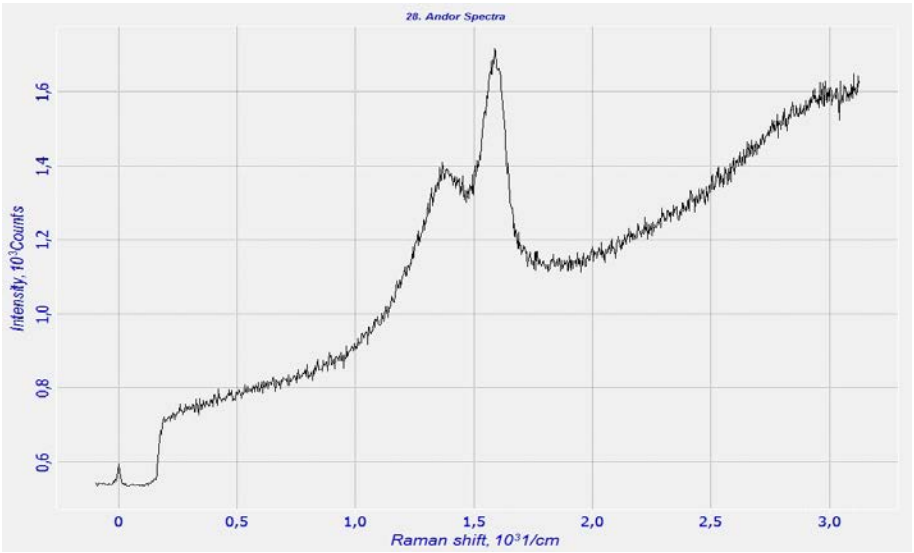

Fig. 3. Raman spectrum of coal with the polymer

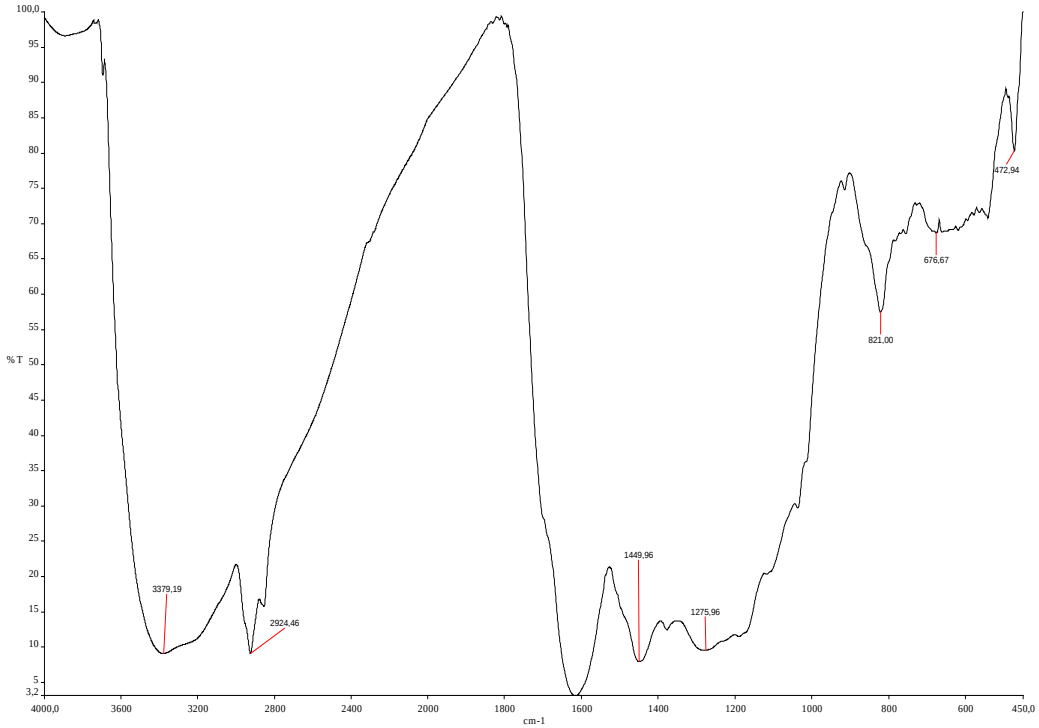

Fig. 4. IR-spectra of the initial coal

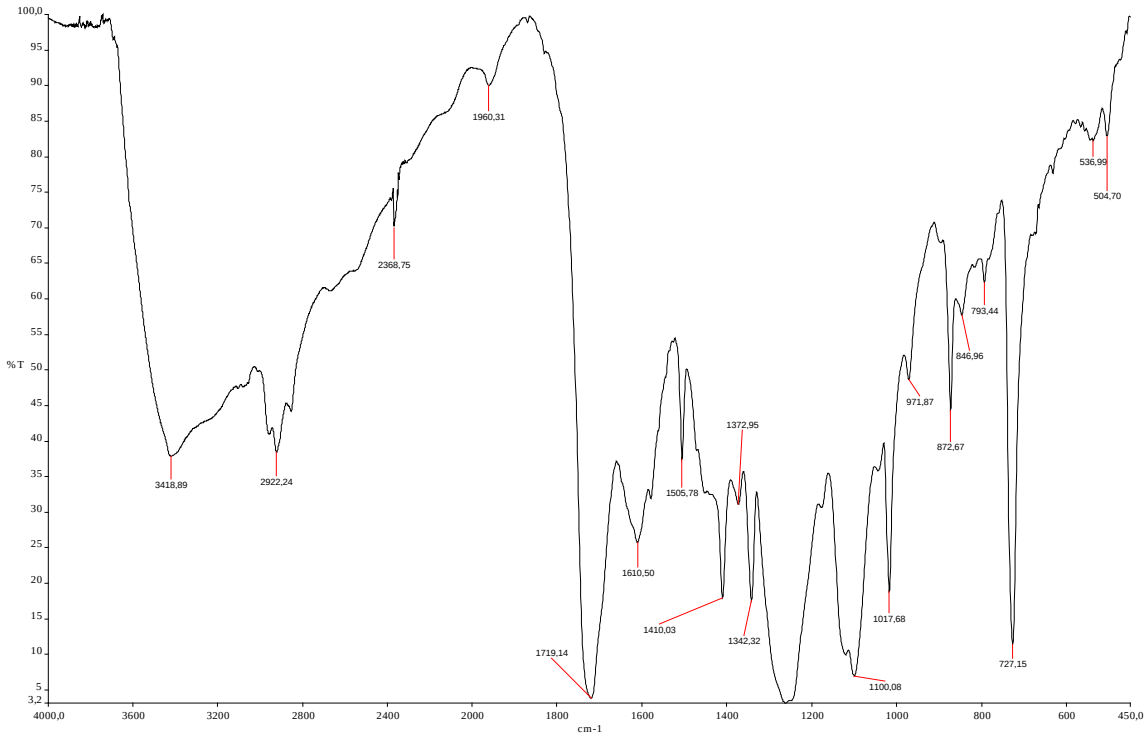

Fig. 5. IR -spectra of coal with a polymer after the hydrogenation reaction

increased. As a part of the oil fraction is increased the content of light petroleum-ether resins and aromatic hydrocarbons in the field 443-527ºC. At hydrogenation of coal in tar possessing the hydrogen-donating properties, the researched catalysts considerably increased OMC.

In the course of a coal hydrogenation in the tar possessing hydrogen-donors properties, the studied catalysts considerably increase degree of conversion of the organic mass of coal (OMC) (Tab.2)

Table 2. Hydrogenation of coal in presence of polymers

Composition (coal, tar, concentrate of Balkhash field), wt.%	Degree of OMC conversion, wt. %	Yield of gaseous products,wt.%	Yield of solid products, wt. %	Hydrogen consumption, vol. %
Coal/tar:50/50	68.1	42.1	5.8	0.5
Coal/tar/concentrate: 45/45/10	65.1	43.5	5.7	1.5
Mechanical activated coal/tar/concentrate: 45/45/10	72.1	50.4	5.4	1.8
Mechanical activated coal/polyethylene/ concentrate: 80/10/10	70.2	44.2	6.8	1.9
Mechanical activated coal/rubber crumb/ concentrate: 80/10/10	69.2	45.2	6.1	2.0

Table 3. Chromatographic analysis of hydrogenation products

Compound	Initial	In the presence of polymer
	The liquid phase,vol.%	
C_2H_5OH	3.3	2.6
C_6H_6	8.4	9.4
$C_6H_5CH_3$	10.4	10.9
p- xylene	7.0	6.4
ethyltoluene	8.1	6.0
ethylbenzene	4.6	6.6
	Gaseous phase, vol.%	
H_2	18.1	24.3
CO	3.6	5.1
CO_2	13.2	19.1
CH_4	7.5	6.7
C_2H_6	2.1	1.8
C_2H_4	-	1.0
C_3H_8	1.2	0.9
C_4H_{10}	1.3	1.0

The highest exponents of coal conversion (72.1 wt.%) and the yield of liquid products (50.4 wt.%) were observed in the composition of mechano-activated coal/tar/concentrate 80/10/10. For catalyst supported in the highly dispersed form on the surface of brown coal in the presence of polyethylene and crumb rubber the relatively low coal conversion rates were obtained. It can be explained by the fact that the activated iron is in the form of the complex aggregates in structure of polymers of polyethylene and a rubber crumb, which can create diffusion limitations for certain coal thermal degradation products, which can create certain diffusion limitations for the products of coal thermal destruction. In the conditions of process of a hydrogenation tar is dehydrogenated, transforming into liquid hydrocarbons. Apparently, dehydrogenation of tar in presence of coal occurs as result of its interaction with OMC or as the products of its thermal destruction. The studied catalysts accelerate coal hydrogenation by molecular hydrogen of tar with formation of liquid products that leads to increase in its content in reactionary mixture. Results of a gas chromatography show that gaseous products of a hydrogenation of coal are presented generally by carbon oxides, the content of hydrocarbonic gases C_1-C_4 doesn't exceed 20 wt.%. In the course of a hydrogenation there is a consumption of molecular hydrogen by coal. It can be concluded (Tab.3), that sufficiently high yield of hydrocarbon gases takes place in the presence of polymers, i.e. in cases where the free hydrogen is abundant. Allocation of CO_2 after hydrogenation is can be explained by processes of decarboxylation of polymers, emergence of hydrocarbonic gases promotes to the deep destructive processes of organic synthesis of a liquid phase and substance of coal with the immediate filling of uncompensated bounds with the allocated hydrogen.

Table 4. Influence of polyethylene and composition of the mixture on yield of liquid products of hydrogenation

Composition	Quantity of polymer in the mix, wt.%	Degree of conversion, wt.%	Yield of the products of liquid fraction, wt. %	
			$T_{boiling}$<200°C	$T_{boiling}$>200°C
Mechanical activated coal/polyethylene /concentrate: 80/10/10	10.0	70.2	5.2	44.2
Mechanical activated coal/polyethylene /concentrate: 70/20/10	20.0	71.6	10.3	45.4
Mechanical activated coal/polyethylene /concentrate: 50/40/10	40.0	75.2	23.7	37.5
Mechanical activated coal/polyethylene /concentrate: 30/60/10	60.0	77.0	32.5	40.5
Mechanical activated coal/polyethylene /concentrate: 15/75/10	75.0	78.0	30.7	48.0
Mechanical activated coal/tar/concentrate/ polyethylene: 10/10/10/70	70.0	73.1	52.4	10.2
Mechanical activated coal/tar/concentrate/ polyethylene: 10/5/10/75	75.0	72.1	60	8.3

Type of added polymers has a significant effect on the degree of conversion of OMC and the yield of products (Tab.4). In medium polyethylene, which has the ability to dissolve the coal hydrogenation products, but does not have a hydrogen-donating properties, the degree of OMC conversion much lower than those of obtained in the tar medium. It was revealed that in the selected conditions polyethylene dehydrogenation does not proceed.

In the course of a coal hydrogenation in tar and polyethylene iron-containing catalysts accelerate as reaction of direct hydrogenation of organic mass of coal and products of its destruction by molecular hydrogen, as hydrogenation (reduction of hydrogen and donor properties) of the dehydrogenated hydrogen and donor solvent – tar in the presence of polyethylene. At the content of polymeric material in mixture less than 10 wt.% conversion degree of mixture into liquid and gaseous products is low that interferes with efficient implementation of process. Conversion degree of coal and the yield of the light-boiling products increase at increase in amount of synthetic polymeric material in mixture to 70% per the weight of mixture. The proposed process for producing of liquid products from coal can increase the yield of low-boiling hydrocarbon fraction from 12 to 60 wt. %.

CONCLUSION

Thus, in the work hydrogenation of brown coal of the Kazakhstan fields was studied. Objects of investigation were the coals of the central region of Kazakhstan and solid organic wastes in the form of polymers. Mechano-chemical activation of the iron-containing catalyst affects not only the degree of carbon conversion but also on the composition of liquid products. Processing increases activity of the iron-containing catalyst in reactions of conversion of the high-molecular asphaltenes into maltens possessing smaller molecular weight i.e. increases the cracking properties of the catalyst. It was shown that addition of polymer leads to allocation of the volatile and soluble low molecular weight products, which are the products of the destructive conversions of coal and polymers. The yield, composition and structure of this type of products depends on the conditions of hydrogenation, the stage of coalification of coal, medium, type and mode of mechanical action.

The difference in indicators of non-catalytic transformation of coal in the environment of tar and polyethylene characterizes contribution of hydrogen-donor properties of the paste forming in the total process. In the presence of polymers as a part of mixture coal-polymer is decreased the content of high-molecular asphalt and resinous components asphaltenes and benzene pitches in field 360 – 443ºC. As a result of thermal influence in

bitumen the role of components with smaller molecular weight - benzene pitches and oils is increased. As a part of the oil fraction is increased the content of light petroleum-ether resins and aromatic hydrocarbons in the field 443-527ºC. At hydrogenation of coal in tar possessing the hydrogen-donating properties, the researched catalysts considerably increased OMC. Conversion degree of coal and the yield of the light-boiling products increase at increase in amount of synthetic polymeric material in mixture to 70% per the weight of mixture. The proposed process for producing of liquid products from coal can increase the yield of low-boiling hydrocarbon fraction from 12 to 60 wt. %. The advantage of the offered method for producing liquid products from coal is the high yield of hydrocarbon products boiling up to 200°C, the exception from the technological scheme of the stages of selection and hydrotreating processes of the pastes, and the possibility of recycling of industrial and household wastes of polymeric materials.

REFERENCES

1. A.A. Krishko, Hydrogenation of coal of USSR, CSRIEI coal, M, 1984, p. 110.
2. L.R. Sassykova. Chemistry and physics of petroleum, gas and coal. Educational manual, Almaty:Qazaq university, 2017, p.11-33, 153-165. ISBN 978-601-04-2663-4.
3. Z.Y. Liu, J.W. Zondlo, A.H. Stiller, D.B. Dadyburjor, *Energy & Fuels*, **9,** 673 (1995)
4. G.M. Abotsi, K.B. Bota, G. Saha, S.Mayes, *Prepr. Pap.-Am. Chem. Soc., Div. Fuel Chem.*, **41**, 984 (1996)
5. Z. Liu, J. Yang, J.W. Zondlo, A.H. Stiller, D.B. Dadyburjor, Fuel, **75**, 51 (1996)
6. J.–J. Kim, S. Weler, *Fuel Process Technol.*, **11**, 205 (1985)
7. S. Sendilvelan, K. Bhaskar, *Rasayan Journal of Chemistry*, **10**, 111(2017).
8. A.S. Maloletnev, D.Yu. Ryabov, O.A. Mazneva, *Solid Fuel Chemistry*, **4,** 231 (2015),
9. K. Murase, W.Jackson, F.P.Larkins, M. Marshall, I.D. Watkins, *Fuel*, **12,** 1694 (1984),
10. M. Prabhahar, R. Muralimanohar, S. Sendilvelan, *European Journal of Scientific Research*, **73(4)**, 504-511 (2012)
11. M. Tulepov, L. Sassykova, M. Atamanov, D. Eshimbetova, Zh. Amir, Z. Mansurov, *Industry of Kazakhstan*, **3**, 82 (2015**)**
12. D.A. Baiseitov, Sh.E. Gabdrashova, A.N. Magazova, O. Dalelkhanuly, Zh.B. Kudyarova, L.R. Sassykova, M.I. Tulepov, Z.A. Mansurov, A.B. Dalton, *International Journal of Biology and Chemistry*, **2,** 66 (2015)
13. D.A. Baiseitov, Sh.E. Gabdrashova, A.K. Akylbai, O. Dalelkhanuly, Zh.B. Kudyarova, L.R. Sassykova, M.I. Tulepov, Z.A. Mansurov, *Int. J. Chem. Sci.*, **1,** 261 (2016)
14. D.A. Baiseitov, Sh.E. Gabdrashova, A.N. Magazova, O. Dalelkhanuly, Zh.B. Kudyarova, M.I. Tulepov, L.R. Sassykova, Z.A.Mansurov, *Int. J. Chem. Sci.*, **1,** 244 (2016)
15. D. A. Baiseitov, M.I. Tulepov, L.R. Sassykova, Sh.E. Gabdrashova, E. Gul'dana, D.A.Zhumabai, K.K.Kudaibergenov, Z. A.Mansurov, *Int.J.Chem.Sci.*, **13(2),** 1027-1033(2015).
16. D.Baiseitov, M. Tulepov, L.Sassykova, Sh.Gabdrashova, K.Kudaibergenov, Z.Mansurov, *Rev. Roum.Chim*, **62(3)**,249-253*(*2017).
17. D.A.Baiseitov, M.I.Tulepov, L.R.Sassykova, Sh.E.Gabdrashova, G.A.Essen, K.K.Kudaibergenov, Z.A.Mansurov, *Bulg. Chem. Commun.*, **49(2)**, 335(2017)

КАТАЛИТИЧНО ХИДРИРАНЕ НА ВЪГЛИЩА ОТ КАЗАХСТАНСКИ НАХОДИЩА В ПРИСЪСТВИЕ НА ПОЛИМЕРИ

Д.А. Байсейтов, М.И. Тулепов*, Л.Р. Сасикова*, Ш.Е. Габдрашова, А.Н. Магазова, О. Далелханули, Ж.Б. Кудярова, З.А. Мансуров

Казахски национален университет „Ал-Фараби", 050040 Алмати, Казахстан

Получена на 9 септември 2016 г.; коригирана на 2 март 2017 г.

(Резюме)

Обект на изследването са въглища от централния район на Казахстан и твърди органични полимерни отпадъци. В тази работа е изследван процесът хидриране на кафяви въглища от казахстански находища. Механо-химичното активиране на катализатора влияе на не само на степента на превръщане, но и състава на течните продукти. Процесът повишава активността на желязо-съдържащия катализатор на реакцията на превръщане на високомолекулните асфалтови вещества в малтени с по-малка молекулна маса, т.е. повишава се крекиращата способност на катализатора. Наличието на полимери води до отделянето на летливи вещества, продукти на деструктивното превръщане на въглищата и полимерите. Техният добив, състав и структура зависят от условията на хидриране, степента на овъгляване на въглищата, средата, типа и способа на механично въздействие. Предимство на предложения метод за получаването на течни продукти от въглища е високия добив на въглеводородни продукти, кипящи до 200°C и изключването на стадиите на селекция и хидро-третиране на твърдия остатък, както и възможността за рециклиране на промишлени и битови отпадъци от полимери.

Bulgarian Chemical Communications, Volume 49, Number 3, (pp. 608 – 610) 2017

Unidirectional growth of $CoNi(SO_4)_2.12H_2O$ single crystal by Sankaranarayanan–Ramasamy (SR) method

S. Karvar, H. Rezagholipour Dizaji*

Crystal Growth Lab., Physics Department, Semnan University, Semnan-35195-363, I. R. Iran

Received July 7, 2016; Revised February14, 2017

Large cylindrical [010] cobalt nickel sulfate twelvehydrate (CNSH) crystal with 18 mm diameter and 150 mm length was grown from an aqueous solution by Sankaranarayanan–Ramasamy (SR) method. The grown crystal was examined by X-ray diffraction, UV-Vis spectroscopy and TGA/DTA analysis methods. The grown crystal was found to possess high transmission efficiency in UV region and high absorption in the other regions introducing it as a good candidate for use as UV band-pass filter. The grown crystal showed dehydration temperature higher than that of commercially available nickel sulfate hexahydrate (NSH) crystal.

Key words: Growth from solution, Transmission, X-ray diffraction, UV filter, Thermogravimetric analysis

INTRODUCTION

Crystalline materials having narrowband transitive in particular wavelength region and strongly absorptive over all others are usually used in band-pass filters. Generally, most optical crystals have continual optical transmission characteristics in the range from UV to near IR wavelengths. There are few exceptional crystals in this sense. Those crystals showing discontinue in the UV to near IR wavelengths region can be used as optical filter in UV region.

Nickel sulfate hexahydrate (NSH) crystal is a well-known UV band pass filter crystal having high transmission efficiency over a narrowband at 250-340 nm, moderate transmission at 450-600 nm, and strong absorption over all other wavelengths [1].

The ultraviolet light filters and UV sensors of NSH crystals are already commercially available [2]. However it has some drawbacks among which the most important one is its low dehydration temperature [73 ºC]. This parameter is very important when considering an optical system employed to detect the UV signal characterizing the jet engine of a missile to operate at various climate conditions, including those associated with elevated temperatures, which might be experienced in the desert. Also, temperature of 85 ºC or higher and low relative humidity conditions can be reached when aboard an aircraft, armored vehicle or a ship, as a combined result of both solar heating and engine-generated heat. Thus, the crystal should have not only proper spectral transmission but thermal stability. Accordingly, it is desirable to provide a crystal having optical properties similar to that of NSH but having greater thermal stability. Therefore, other NSH – based compounds such as cobalt nickel sulfate twelvehydrate (CNSH)[2], iron nickel sulfate twelvehydrate (FNSH)[3], potassium nickel sulfate hexahydrate (KNSH)[4], rubidium nickel sulfate hexahydrate (RNSH)[5], ammonium cobalt nickel sulfate hexahydrate (ACNSH)[6], potassium cobalt nickel sulfate hexahydrate (KCNSH)[7], and potassium manganese nickel sulfate hexahydrate (KMNSH)[8] were grown possessing dehydration temperature higher than that of NSH crystal.

Crystals of cobalt nickel sulfate twelvehydrate $CoNi(SO_4)_2.12H_2O$ (CNSH) belong to the monoclinic system with the space group C2/c and crystal lattice parameters a=9.996(Å), b=7.2265(Å), c=24.218(Å) and β=98.32(3)º [2].

In the present investigation, CNSH crystal has been grown in the [010] direction using a novel technique called Sankaranarayanan-Ramasamy (SR) method [9]. The main advantages of this technique over conventional solution growth method employed by Su et al to grow CNSH crystal [2] are the ability to grow a crystal unidirectionally as well as to convert solution to crystal with 100% efficiency. The grown crystal was subjected to X-ray diffraction, UV-Vis and TGA/DTA analysis.

EXPERIMENTAL

Experimental set-up

The SR set-up for crystal growth shown in Fig. 1 consists of two ring heaters positioned at the top and bottom of the growth ampoule each connected to a temperature controller maintaining constant temperature.

* To whom all correspondence should be sent:

E-mail: hrezhgholipour@semnan.ac.ir

The entire SR set-up is placed in a water bath in order to avoid temperature fluctuations during the growth process. The top heater provides the necessary temperature for solvent evaporation, while the bottom one is used to maintain the solid-liquid interface at the saturation temperature. It is moved upwards depending on the growth rate of the crystal.

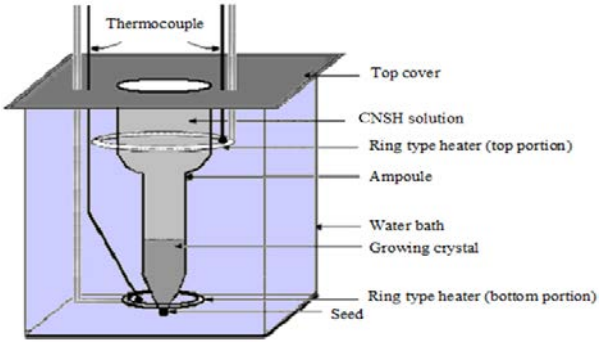

Fig. 1. SR growth set-up

Crystal growth

The equal molar proportion $CoSO_4.7H_2O$ and $NiSO_4.6H_2O$ powders of 98% purity were dissolved in twice distilled water. The saturated CNSH solution was prepared at room temperature (27 °C) and filtered using a membrane filter of 0.45μm porosity at the same temperature.

The vessel containing the prepared solution was placed in a constant temperature bath set at saturation temperature and left for several days in order to obtain seed crystal through solvent evaporation. After 14 days, brown transparent CNSH crystal grew. A disk shape seed with 4 mm thick and 5 mm diameter was cut from the already grown crystal and mounted at the bottom of the ampoule. The plane was so fitted not to allow other faces to grow. The ampoule was filled with saturated solution of CNSH at 27 °C.

The temperature of the bottom and top portions was set as 27 °C and 29 °C respectively. Gradual evaporation of the solvent from the top portion of the solution caused the seed to grow. After 40 days, cylindrical shape CNSH crystal of 150 mm height and 18 mm diameter was grown which is shown in Fig. 2.

Fig. 2. CNSH cylindrical crystal (a) after removing from ampoule and (b) Cut and polished piece.

RESULTS AND DISCUSSION

The physical phase and structure of the product was confirmed by X-ray diffraction (XRD) analysis using an X-ray diffractometer with intensity Cukα radiation (λ=1.5406 Å). The grown crystal was ground and pestle in order to determine the crystal phases by XRD. Figure 3 shows the X-ray diffraction pattern of CNSH grown crystal. According to the results obtained from XRD data, the CNSH crystal belongs to the monoclinic space group C2/c and lattice parameters of a = 9.97 Å, b = 7.24 Å, c = 24.23 Å, β = 98.34°, V = 1729.78 $Å^3$.

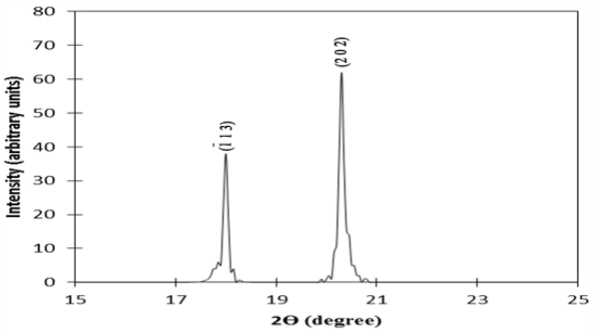

Fig. 3. X-ray diffraction pattern of CNSH crystal.

Figure 4 represents the optical transmission of 2mm thick CNSH crystal obtained in UV-Vis spectrophotometer (Model UV-1650 PC) with performing wavelength ranged from 190 to 1100 nm. The grown crystal has two sharp transmission bands centered at 292.5 and 496.5 nm. Transmission efficiency at 292.5 nm is about 77.44% which is higher than the reported value [2]. It is also observed that the other wavelengths are strongly absorbed. This transmission behavior is the characteristics of a UV band pass filter.

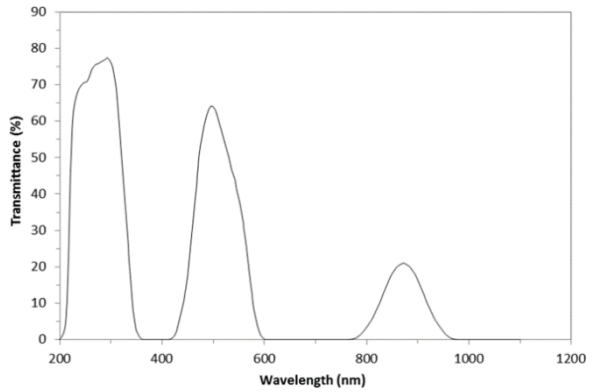

Fig. 4. Transmission spectrum of the CNSH crystal.

The thermo-gravimetric analysis on freshly grown CNSH crystal was performed by using Perkin-Elmer diamond TGA/DTA instrument in air atmosphere. It is observed from TGA/DTA curve shown in Fig. 5 that the dehydration temperature of

CNSH crystal is about 85.25 °C which is higher than that of NSH crystal and nearly the same as reported by Su et al [2].

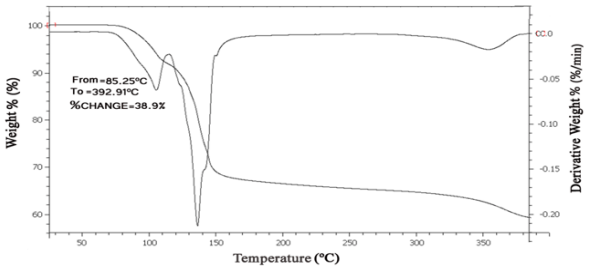

Fig. 5. Thermo-gravimetric and differential thermal analysis curves of CNSH crystal.

CONCLUSIONS

CNSH single crystal in cylindrical shape with 18 mm diameter and 150 mm length was grown by SR method. The XRD analysis proved good crystalinity of the grown crystal. Optical transmission spectrum of this crystal showed its high transmission efficiency at UV region and high absorption in the other regions making it suitable for use as UV band-pass filter. The transmission of the CNSH crystal grown by SR method was found to be slightly higher than that grown by conventional solution technique. Thermal analysis of the grown crystal revealed its dehydration temperature of 85.25 °C, well higher than that of NSH crystal.

REFERENCES

1. M. Hemmati, H. Rezagholipour Dizaji, *Cryst. Res. Technol.*, **47**, 703 (2012).
2. G. Su, X. Zhuang, Y. He, Z. Li , G. Li, J. Wang, G. Ma, Z. Huang, *Cryst. Res. Technol.*, **38**, 1087 (2003).
3. G. Su, X. Zhuang, Y. He, Z. Li, G. Wang, G. Li, Z. Huang, *J. Cryst. Growth*, **243**, 238 (2002).
4. Y. He, J. Chen, G. Su, X. Zhuang, G. Lee, R. Jiang, *J. Cryst. Growth*, **233**, 809 (2001).
5. V.L. Manomenova, E.B. Rudneva, L.F. Malakhova, N.G. Furmanova, A.E. Voloshin, T.N. Smirnova, *J. Crystallog. Rep.*, **52**, 918 (2007).
6. G. Su, X. Zhuang, Y. He, G. Zheng, Opt. Mater., **30**, 916 (2008).
7. X. Zhuang, G. Su, Y. He, G. Zheng, *Cryst. Res. Technol.*, **41**, 1031(2006).
8. V. Duraikkan, S.A. Bahadur, S. Athimoolam, *J. Miner. and Mater. Character. and Eng.*, **11**, 1121 (2012).
9. K. Sankaranarayanan, P. Ramasamy, *J. Cryst. Growth*, **280**, 467 (2005).

ЕДНОПОСОЧЕН РАСТЕЖ НА ЕДИНИЧЕН МОНОКРИСТАЛ ОТ $CoNi(SO_4)_2.12H_2O$ ПО МЕТОДА НА Sankaranarayanan–Ramasamy (SR)

С. Карвар, Х. Резаголипур Дизаджи*

Лаборатория по кристален растеж, Департамент по физика, Университет в Семнан, Семнан -35195-363, И.Р. Иран

Постъпила на 20 септември, 2016 г.; Коригирана на 14 януари, 2017 г.

(Резюме)

Израстван е голям цилиндричен кристал [010] от кобалто-никелов сулфат додекахидрат (CNSH) с диаметър 18 mm и дължина 150 mm length из водна среда по метода на Sankaranarayanan–Ramasamy (SR). Полученият кристал е изследван с рентгено-структурен анализ, UV-Vis спектроскопия и TGA/DTA-анализ. Полученият кристал притежава голяма предавателна ефективност в UV-областта и висока абсорбция за останалите дължини на вълната. Затова тези кристали са добър кандидат за филтри на UV-вълни. Полученият кристал показва по-висока температура на дехидратиране отколкото на комерсиално достъпния никелов сулфат-хексахидрат (NSH).

Bulgarian Chemical Communications, Volume 49, Number 3, (pp. 611 – 616) 2017

Effect of residual gases in the electrodialysis cell on mass transfer

J. Erkmen

Department of Chemical Engineering, Faculty of Engineering and Architecture, Kafkas University, Kars 36300, Turkey

Received August 5, 2016; Revised April 4, 2017

The preset work investigated the problems associated with the gases generated during the production of an acid and an alkali from a sodium salt in a three-chamber electrodialysis cell with bipolar membranes remaining in the cell. The study was conducted at three different flow rates, three different potentials and at two different concentrations. All experiments were conducted repeatedly under both conditions where the gas exhaust ports of the cell were either on or off. The system was observed to underperform particularly under conditions where the gas produced during the process could not be removed and thus formed a surface film on the membrane and the electrodes of the cell. The loss of current efficiency was in the range of 15 – 28%. The study highlighted the significance of maintaining the optimal operating conditions in electrodialysis processes for the prevention of loss of energy and workforce.

Keywords: Electrodialysis, Bipolar Membrane, Mass Transfer, Gas

INTRODUCTION

Membrane processes are among the most environmentally friendly production processes. Electrodialysis is a process where ions are removed from an electrolyte solution or where an electrolyte solution becomes more concentrated through the use of electrical potential as the driving force [1], Electrodialysis was employed in order to obtain potable water from salt- or brackish water, removal of juice acidity, pH control and in the recovery of heavy metals, as well as in the production of caustic soda in chlorine-alkaline production plants [2, 3]. Bipolar membrane electrodialysis was used to generate protons and hydroxyl ions [4]. This process was frequently employed in environmental applications [5-7] such as the recovery of carbon dioxide in the treatment of wastewater containing organic acids [8, 9] from the food industry [10, 11]. Numerous previous studies on bipolar membranes established their economic feasibility for the recovery of inorganic, organic or amino acids [12].

Separation processes are affected by the differences in the charge of the ions in solution. Separation using charged membranes is facilitated by the exclusion of the ions with a similar fixed charge as that of the fixed charge of the ions in the structure of the membrane. Ion-charged membranes were used to separate electrolytic solutions [13-15]. A comparison of the conventional ion exchange method and bipolar electrodialysis in the production of acid and alkali from salt solutions indicated a decrease in energy requirements as low as 1 kWh/kg at a current density of 10-12 mA/cm^2 [16]. One of the most important aspects in a successful electrodialysis application was attributed to the cleanliness of the membrane and electrode surfaces[17]. Earlier studies demonstrated the direct proportionality between the efficient use of membranes and electrodes and efficiency of the cell. The performance of the membrane was determined through selectivity and current parameters [18].

The current study investigated problems in mass transfer associated with the adverse effect of the gases generated during the three-chamber membrane separation process coating the surface of the membrane. The aim of the study was to facilitate the employment of bipolar membrane electrodialysis systems in the broadest possible operating capacity possible. The study highlighted the significance of maintaining the optimal operating conditions in electrodialysis processes for the prevention of loss of energy and workforce.

EXPERIMENTAL METHOD

NaF, HF, NaOH, and all other chemicals were obtained from MERCK. The analyses on sodium were performed using flame photometer and the analyses on fluoride were performed using a Mettler Toledo ion meter.

The temperature, concentration, flow rate and the changes in voltage were investigated separately. The changes in current density were investigated for different experimental trials. The experiments were conducted in a lab-scale, three-chamber bipolar membrane commercial electrodialysis cell. The cell was constructed from polyethylene. The cathode was stainless steel whereas the anode was made from Pt /Ir-MMO coated titanium of dimensions 110 mm x 110 mm. The characteristics of the membranes used in the study are displayed in Table 1. Polyethylene spacers were used to separate membranes from one another. The interspacing between the membranes was 0.5 mm whereas the membrane-electrode interface was 1 mm.

* To whom all correspondence should be sent:
E-mail: jerkmen@hotmail.com

Table 1. Characteristics of the homopolar membranes employed in the study

	PC acid 60	PC SK
Transference number	>0.95	>0.95
KCl (0.1 / 0.5 N) [a]	55	
Acid (0.7/3 N) [b]		
Resistance / Ω.cm^2	~ 2	~ 2.5
Water content (wt%)	~ 17	~ 9
Ion exch. capacity	ca 1.14	n/a
Strong basic (meq.g^{-1}):	ca 0.45	
Weak basic (meq.g^{-1}):		

[a] calculated from potentiometric measurements
[b] observed current efficiencies

The experiments were conducted at concentrations of 0.05 M and 0.025 M, at flow rates of 0.38 L/min, 0.5 L/min and 0.75 L/min, using potential differences of 5V, 7.5V, and 10V. The gas discharge ports of the cell were initially blocked in order to prevent gas exhaust thus the discharge was allowed to facilitate the comparison of the two conditions. The effect of the autochthonous accumulation of gas on the system was investigated under high and low flow rate conditions. The cell efficiency was determined under each condition and the results were compared. All experiments were conducted in repeated trials and the standard deviation was determined to be 0.012 at its maximum.

RESULTS AND DISCUSSION

The desired characteristics of an ideal membrane in electrodialysis are high selectivity or retention and high current density or permeability. H_2 and O_2 gases were always reported to generate during electrodialysis due to the dissociation of water [19]. These gases must be removed from the system to prevent their accumulation. The accumulating gas due to overproduction or failure to remove it will deposit on the surface of the electrode and membrane surfaces. This accumulation is schematically represented in Figures 1 and 2.

The following reactions listed below occur in the electrodialysis cell.

Anode reaction : $2OH^- = 1/2\ O_2 + H_2O + 2\ e^-$ (1)

Cathode reaction: $2H_2O^+ + 2\ e^- \leftrightarrow H_2 + 2OH^-$ (2)

Acid reaction: $H^+ + F^- \rightarrow HF$ (3)

Base reaction: $Na^+ + OH^- \rightarrow NaOH$ (4)

Overall reaction: $NaF + H2O \rightarrow NaOH + HF$ (5)

The ion exchanges within the cell are displayed in Figure 3. Mass transfer during electrodialysis occurs either through diffusion or migration:

$$J_i = J_i^{migration} + J_i^{diffusion} = D_i \frac{\mathrm{dCi}}{\mathrm{dx}} - D_i \frac{z_i C_i F}{RT} \frac{dV}{dx} \quad (6)$$

where J is the ion flux across the membrane (mol/m^2 s), Di is the coefficient of ion diffusion, R is the gas constant (8.314 J/ mol K), T is temperature (K) ,V is the potential (V), and x is the perpendicular distance from the membrane (m). The mean coefficient of dialysis (D_{dif}) is calculated as shown in Equation 7. Here M represented the amount of

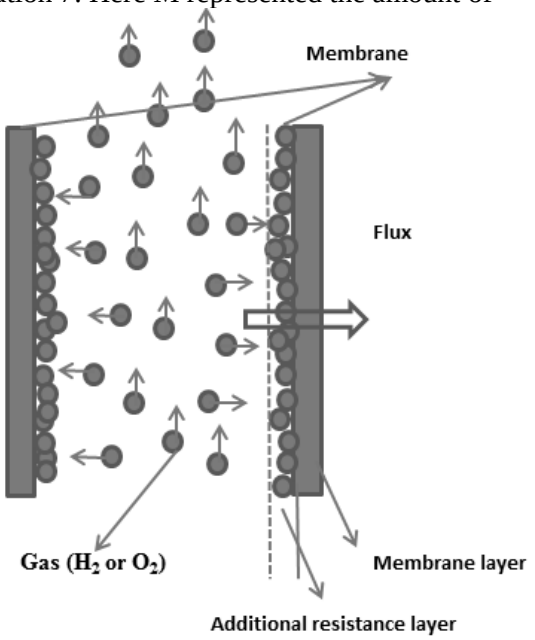

Fig. 1. Gas deposit on membrane surfaces

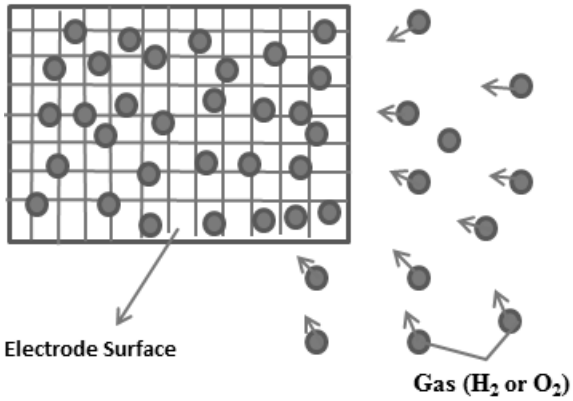

Fig. 2. Gas deposit on electrode surfaces

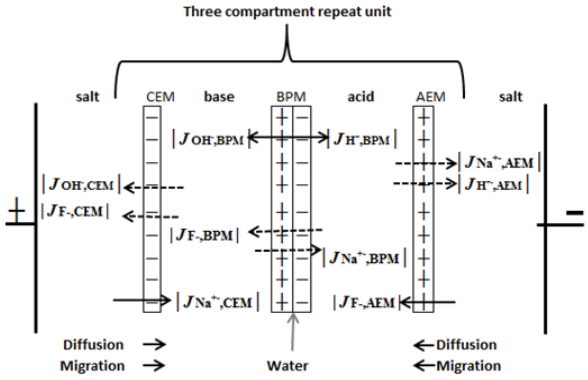

Fig. 3. Ion exchange within the three-chamber cell.

material (mol), A stood for the active surface area of the membrane, t represented time (in hours), and ΔC represented the logarithmic mean concentration between the two compartments [20]. Mass transfer reduced with dx increase, it can be seen from Equation 6.

$$D_{dif} = \frac{\mathrm{M}}{\mathrm{A.t.\Delta C}} \quad (7)$$

The selective coefficient of dialysis (D_{dif}) was observed to be affected by the membrane surface area for each different membrane as given in Equation 7. Electrodialysis displays the characteristic features of both dialysis and electrolysis thus setting the surface area of the active membrane, which is one of the most important parameters. Although the bipolar membrane electrodialysis process was reported to generate less gas than polar electrodialysis [21], the system performance was reduced by the insufficient removal of the generated gas.

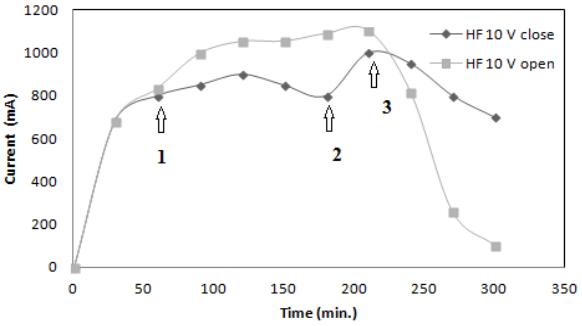

Fig. 4. Plot of current against time for gas exhaust ports of the system remaining on or off (experimental conditions: concentration of 0.05M, flow rate of 0.38L/min, potential of 10 V)

Different amounts of gas accumulation on different membranes was reported to result in concentration polarization [22]. The accumulation reduces the performance of the electrodes and interferes with mass transfer. The additional gas surface film forming on the membrane surfaces causes additional resistance. This film layer also slows down mass transfer by increasing the distance for the molecules to travel since mass transfer across the membrane is directly proportional to the resistance encountered during the transfer and the thickness of the membrane.

The region identified as 1 in Figure 4 represents the drop in current density due to the surface being covered in film layer as the concentration of the gas increased. The region identified as 2 represents the maximum gas compression within the cell. The stoppers were automatically released after this point with incremental increase in pressure as the system was adjusted to release the internal pressure at any value beyond this point. A major fraction of the gas accumulation within the cell was thus released, leading to a rapid increase in current density.

Figures 5 and 6 represent the effect of the accumulation of gas on mass transfer in the cell. The flow of both the anion and the cation was observed to be reduced during the period when gas discharge was blocked.

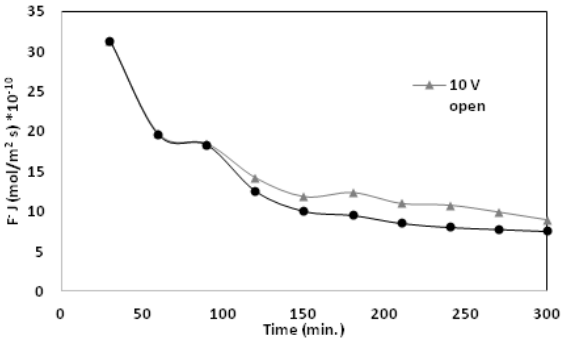

Figure 5. Plot of molar flow of F^- ion for gas exhaust ports of the system remaining on or off (experimental conditions: concentration of 0.05M, flow rate of 0.38L/min, potential of 10 V)

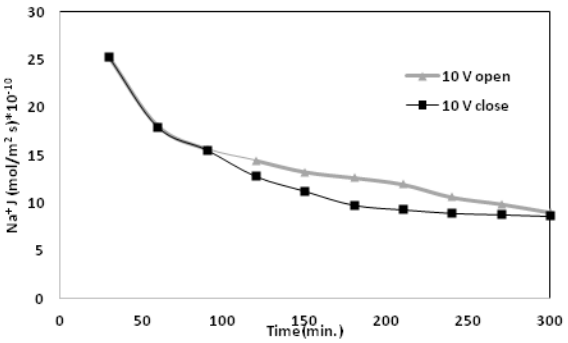

Fig. 6. Plot of molar flow of Na^+ ion for gas exhaust ports of the system remaining on or off (experimental conditions: concentration of 0.05M, flow rate of 0.38L/min, potential of 10 V)

Mixing is a method that is frequently employed to overcome the accumulation of gas on the surface of the membrane. However, the only method to allow mixing in electrodialysis is to adjust the flow rate of materials since the membrane-membrane and membrane-electrode interfaces are small. The idea behind this is to drag the newly formed gas along with the flow to prevent its adherence on the surface of the membrane.

A reduction in or the cessation of mass transfer in electrodialysis can be monitored via the reduction of current density. If the necessary conditions for the discharge of the accumulating gas are not fulfilled, mass transfer will be reduced, as the accumulated gas will coat the membrane surface. Mass transfer will further be reduced since this situation will continue to narrow down the membrane-membrane

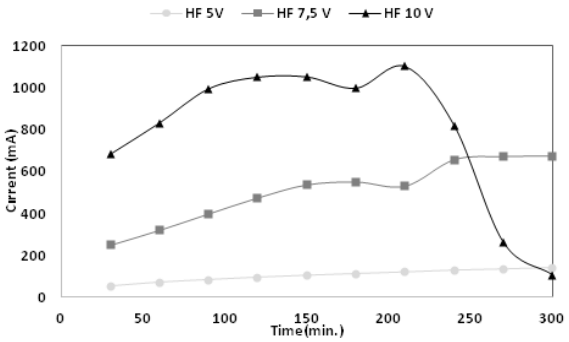

Fig. 7. Plot of current against time for the formation of HF at different potentials **(**experimental conditions: concentration of 0.05M, flow rate of 0.38L/min)

or membrane-electrode interspace and reducing the total amount of material fed into the system. Additionally in Figure 7, a reduction in the concentration of the ions required for mass transfer below a given limit will sharply reduce the current flow and remain constant at a very low value as observed in the curve for the 10 V potential during the period of 180- 240 minutes virtually ceasing current flow. The 10 V curve in Figure 8 is an example for this phenomenon.

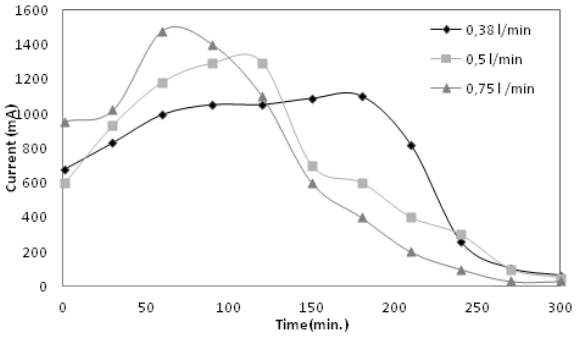

Fig. 8. Plot of current against time for the formation of HF at different flow rates **(**experimental conditions: concentration of 0.05M, flow rate of 0.38L/min)

Figure 8 displays the direct proportionality between the flow rate and the rate of electrodialysis. An increase in flow rate also increases circulation of the solution, thus dragging the gas away from the environment. Consequently, the accumulation of any matter including that of gas on the surface of the membrane is considerable reduced.

The short membrane-membrane and membrane-electrode interspatial distances do not allow the necessary extent of mixing required for mass transfer operations. The problem of mixing can only be attacked by the determination of an optimum rate of material flow in such systems. A fast circulation of solution simultaneously allows for interspatial mixing in the membrane-membrane and electrode-membrane regions. A concentration gradient forms on both sides of the membrane under conditions of insufficient mixing, which can be rectified by increasing the flow rate. In commercial electrodialysis systems concentration polarization is controlled by delivering the solution at a high flow rate.

Flow pumps consume approximately $1/4^{th}$ of the total power of contemporary electrodialysis systems. Concentration polarization occurring under these conditions cannot be fully controlled since the actual energy consumption greatly exceeds the theoretical value. Many adversities in electrodialysis systems are caused by the challenges of controlling concentration polarization. This dysfunction can be summarized as a reduction in the flow across the membrane. Factors affecting this reduction were reported as concentration polarization, adsorption, and the formation of a gel film and the congestion of pores [23].

Ideally, the only resistance observed during the operation of membrane processes is the membrane resistance (Rm). Materials rejected by the membrane were reported to increase in the feed concentration causing concentration polarization resistance (Rcp) [23]. An additional film layer forms over the membrane surface as a result of the concentration polarization reducing current flow. This layer of membrane was observed to increase the additional resistance.

The amount of ions carried towards the membrane is directly proportional to the electrical current I (A) or to the current intensity (A/cm^2). Ohm's law states that electrical current is related to the electrical potential as:

$$E=I.R \quad (8)$$

The total resistance of the membrane pack could be represented as R. The value of R was determined by multiplying the number of cell pairs in the membrane pack (N) by the resistance Rcp of each cell pair.

$$Rtot= Rcp.N$$

$$Rcp = Ram+ Rpc+ Rcm+ Rfc \quad (9)$$

Where Rcp is the resistance of a cell pair in unit area, Ram is the resistance of the anion exchange membrane, Rpc is the resistance of the leakage compartment, Rcm is the resistance of the cation exchange membrane, and Rfc is the resistance of the feed compartment. The resistance of the cell pair is equivalent to the sum of the four resistances in series. The gas film forming on the surface of the membrane increases Rcp, thus increasing energy consumption and resulting in unnecessary energy losses.

The key element in describing the total efficiency in electrodialysis processes is the energy consumed

Table 2. Current efficiency under the investigated experimental conditions

Potential Volt	İnitial salt concentration M	Flow rate L/min	Current efficiency Gas output is open	Current efficiency Gas output is close
5	0.5	0.38	0.961791	0.838902
7.5	0.5	0.38	0.969363	0.817584
10	0.5	0.38	0.995128	0.706543
5	0.25	0.38	0.938402	0.757572
7.5	0.25	0.38	0.962072	0.826782
10	0.25	0.38	0.967055	0.802345
5	0.5	0.5	0.981025	0.922792
7.5	0.5	0.5	0.988750	0.915694
10	0.5	0.5	0,991523	0.995981
5	0.25	0.5	0.947786	0.878783
7.5	0.25	0.5	0.981313	0.934263
10	0.25	0.5	0.980593	0.914671

in the separation process. Energy consumption E (kilowatt) is related to the current flowing through the pack I and to the resistance of the pack R in the following relationship;

$$E = I^2R = V.I \quad (10)$$

Gas accumulation on the surface of the electrode and membrane results in additional resistance, causing an increase in energy consumption and time to achieve the same level of productivity. This means additional energy and time-associated costs for the production process.

Average current density was calculated using the following equation:

$$\text{Average current density} = \frac{\int i.dt}{t.A} \quad (11)$$

where A: membrane area (9×64 cm^2), t: time (min), $\int$ i. dt: amount of current passing during time t (amp.min). m $_{(theoretical)}$ was calculated as given by the Faraday's law:

$$m = \int_a^b \frac{M.i.dt}{n.F} \quad (12)$$

where $M_{(theoretical)}$: theoretical amount of substance released from the electrode (g), M: molecular weight (g), n: valency, i: current intensity (A), t: time (min), F: Faraday constant (96485 As/mol).

Current efficiency was calculated using the relation provided below:

$$Current\ efficiency = \frac{\text{m (used)}}{\text{m (theoretical)}} \quad (13)$$

Here, $m_{(used)}$ represented the amount of material actually used in the experiments that were conducted and $m_{(theoretical)}$ represented the theoretical amount of salt, which should have been consumed, as calculated from the relationship representing Faraday's Law.

The decrease in current efficiency displayed in Table 2 was lower than expected. The bulk flow of the solution removed a large fraction of the gas away from the cell although the gas exhaust ports were off. The fraction, which could not be removed by bulk flow, remained in the cell, reducing the activity of the membrane. A decrease of minimum 15% and maximum 28% was observed in current efficiency for the experiments conducted by limiting gas exhaust except through bulk flow of materials Table 2. This indicated the undesirable situation of achieving less production by consuming equal amounts of energy. This situation bears the inevitable increase in process time and in workforce requirements.

CONCLUSIONS

This study investigated several situations where selection of incorrect operating conditions caused the accumulation of gas during acid and alkali production employing electrodialysis and suggested alternative modes of operation for the prevention of such problems. Very high current densities were obtained under optimal operating conditions in the present study. The maximum current efficiency achieved was determined as 0.995128. The current efficiency decreased to 0.838902 under similar conditions with the exception of confining the generated gas within the cell. Although a current efficiency value of 0.838902 would appear as very high for the electrodialysis processes, much higher values could be obtained outperforming this trial. Current efficiency was also a measure for conversion of salt into its acid and alkali counterparts, indicating the extent of mass transfer within the system. A decrease in current efficiency also indicated a reduction in mass transfer. A minimum of 15% and a maximum of 28% reduction were observed in current efficiency in the present study. A major disadvantage of the electrodialysis (ED) processes is the excessive consumption of energy. The accumulation of gas created an additional resistance in the system thus increasing energy requirements even further.

REFERENCES

1. J.J. Krol, Monopolar and Bipolar İon Exchange Membranes. University Of Twente, Enschede, Netherlands, 1997.
2. R.W. Baker, Membrane Technology and Applications. Second Edition. John Wiley& Sons. Ltd. England, 2004.
3. D. Paul, S.K. Sikdar, *Clean Products and Processes,* **1**, 39 (1998)
4. B.Bauer, F.J. Gerner, H. Strathman, *Desalination,* **68**, 279 (1998).
5. M.A.B. Ali, M. Rakib, S. Laborie,P. Viers ,G. Durand, *J. Membrane Science,* **244**, 89 (2004).
6. M.L. Lameloise, R. Lewandowski, *J. Membrane Science,* **403-404**,196 (2012).
7. A. Iizuka, K. Hashimoto, H. Nagasawa, K. Kumagai, Y. Yanagisawa, A.Yamasaki , *Sep. Purif .Technol.* **101**, 49 (2012).
8. M. Bailly, *Desalination,* **144**, 157 (2002).
9. X.Li, C. Zhang, Y. Wang, J. Luo, T. Xu, *J. Membrane Science,* **379**,184 (2011).
10. E. Vera, J. Sandeaux, F. Persin,G. Pourcelly, M. Dornier, J. Ruales, *J. Food. Eng*., **90**, 67 (2009)
11. A.L. Quoc, M. Mondor, F. Lamarche, J. Makhlouf, *Innov. Food. Sci. Emerg. Technol*., **12**, 45 (2011).
12. H. Strathmann, B. Bauer, H.J. Rapp, *Chemtech.*, **23**, 17 (1993)
13. P.T. Cardew, M.S. Le, Membrane Processes: A Technology Guide. Athenacum Press Ltd., England, 1998, p. 1.
14. R.W. Baker, Membrane Technology and Applications. Second Edition, John Wiley& Sons. Ltd., England, 2004.
15. X. Tongwen, *Resources, Conservation and Recycling*, **37**, 1, (2002)
16. C.G. Pinto, M.E.F. Laespada, J.L.P. Pavon, B.M. Cordero, *Laboratory Automation and Information Management.* **34**, 115 (1999)
17. A.P. Brown, F.C Andson, *Anal. Chem*., **49**, 1589 (1977).
18. R. Singh, *Industrial Membrane Separation Processes. Chemtech*., **4**, 33 (1998)
19. F.L.T. Shee, J. Arul, S. Brunet, L. Bazinet, *Journal of Membrane Science,* **290**, 29 (2007)
20. T.W. Xu, W.H. Yang, *J. Membrane Science,* **183**, 193 (2001).
21. K. Scott, The Royal Society of Chemistry. Chambridge, UK, 1995.
22. T. Aritomi, Th. van den Boomgaard, H. Strathmann, *Desalination*, **104**, 13 (1996)
23. J.J. Krol, M. Wessling, H. Strathmann, *Journal of Membrane Science.*, **162**, 145 (1999).

ЕФЕКТ НА ОСТАТЪЧНИТЕ ГАЗОВЕ ВЪРХУ МАСОПРЕНАСЯНЕТО В КЛЕТКА ЗА ЕЛЕКТРОДИАЛИЗА

Дж. Еркмен

Департамент по химично инженерство, Факултет по инженерство и архитектура, Университет Кафкас, Карс 36300, Турция

Получена на 5 август, 2016 г.; коригирана на 4 април, 2017 г.

(Резюме)

В настоящата работа се изследва проблема, свързан с газовете, генерирани при производството на киселини и алкали от натриеви соли в три-камерна електродиализна клетка с би-полярни мембрани. Изследването е проведено при три дебита, три различни потенциала и две различни концентрации. Експериментите са проведени двукратно при включени и изключени изходи на газовете. Наблюдава се влошена работа на клетката, когато газовете не се отделят напълно от нея. Така се формират повърхностни филми върху мембраната и върху електродите. Загубата на добив по ток е между 15 и 28%. Изследването изяснява значението за поддържане на оптимални условия при електродиализата за да се избегнат загубите на енергия.

Bulgarian Chemical Communications, Volume 49, Number 3, (pp. 617 – 620) 2017

Gas-liquid flows in porous media and coupling effects

Bu Yahui

Exploration and Development Research Institute, Shengli Oilfield, Sinopec, Dongying 257000, China

Received May 19, 2017; Revised August 25, 2017

Gas flood (N_2/CO_2) are promising EOR methods, meanwhile CO_2 trapping and sequestration are important for environmental protection. How to inspect and control gas-liquid flows are the core technology. Based on fundamental principle, established the numerical model to simulate coupling effects of gas-liquid flows in reservoir. Result shows that CO_2 swept area would form a low electrical potential enclosure, and gas-liquid front is the place where potential begin to decrease while production, this area would enlarge till injected gas break thought at production well, then potential begin to recover to zero, spatial variance would disappear. The result is instructive to the monitor gas-liquid flow process.

Key words: Gas-liquid Flows; Coupling Effect; Dynamic Monitoring; Gas Flood

INTRODUCTION

Gas-liquid flows phenomena are of significance for enviorment protection and reservior stimulation. CO_2 trapping and sequestration techniques are important methods to deal with global climate change and slow down greenhouse gas emissions currently. The main buried sites include oil and gas reservoirs, deep salt water layers and non-exploitable coal beds [1]. Meanwhile, gas stimulation methods, including gas flood, huff-puff, foam flooding are promising EOR method not only for unconvienial reservoir, also for the hight permeability reservor development. There are many challenges behind the considerable economic and social benefits.How to inspect and control gas-liquid flows are the core technology. Its process level directly related to the injection of gas into the target layers, play the desired role and not leak to the outside. Current engineering measures include [2-3]: gravity, sonic logging, time-lapse seismic, 3D/4D seismic, resistivity tomography, and micro seismic monitoring. However, these methods are restricted by factors such as resolution, efficiency, price and so on. Each has its limitations. Cheap, continuous and efficient monitoring methods are the direction of future. In this paper , we simulated coupling electrical potential field changes caused by artifical gas source.

EQUATIONS AND MODELS

Streaming potential is a coupling effect between fluid flow and electrical flow in porous media. The measurement target is the signal in formation environment produced naturally. The basic equations can be described by (1) and (2) formulas [2].

$$\mathbf{q} = -L_{11}\nabla p - L_{12}\nabla \varphi \qquad (1)$$

$$\mathbf{j} = -L_{21}\nabla p - L_{22}\nabla \varphi \qquad (2)$$

q is flow velocity, j is current density,p is fluid pressure, φ is electrical potential, σ_r electrical conductivity of saturated fluid. $L_{11} = k/\mu$ $L_{12} = L_{21} = C_v\sigma_r$, $L_{22} = \sigma_r$. C_v is called flow potential coupling coefficient,which is an important parameter describing flow potential effect, and its definition is as follows (3).

$$C_v = \frac{\Delta\varphi}{\Delta p} = -\frac{L_{12}}{L_{22}} \qquad (3)$$

The second item on the right of formula (1) can be regarded as the feedback effect of the electrokinetic effect on the liquid flow. Under deep reservoir condition, this feedback effect is very small and can be neglected. Thus, (1) can be simplified as Darcy's law, and the coupling process becomes a one-way process of producing current.
The simulation is based on the injection of carbon dioxide. The critical temperature and pressure of CO_2 are 31 ^oC and 7.38MPa When the temperature and pressure are greater than the condition, they would enter into critical supercritical state [4-5].

The relative permeability of supercritical CO_2 and formation water is calculated by Van Genuchten-Mualem (VGM) method. The formula is as follows.

* To whom all correspondence should be sent:
E-mail: b.bradley@163.com

$$K_{rw}=\begin{cases}\sqrt{S^*}(1-(1-(S^*)^{1/\lambda})^{\lambda})^2 & S_w<1\\ 1 & S_w=1\end{cases} \quad (4)$$

$$K_{rg}=\begin{cases}1-K_{rw} & S_{gr}=0\\ (1-\hat{S})^2 \quad (1-\hat{S}^2) & S_{gr}\neq 0\end{cases} \quad (5)$$

$$S_w^*=(S_w-S_{wc})/(1-S_{wc}) \quad (6)$$

$$\hat{S}=(S_w-S_{wc})/(1-S_{wc}-S_{gr}) \quad (7)$$

K_{rw} is the relative permeability of water phase, K_{rg} is the relative permeability of gas phase, S_w is water saturation, S_{wc} is irreducible water saturation, S_{gr} is residual gas saturation. In this run, parameter value are $S_{wc}=0.25, S_{gr}=0.05, \lambda=0.75$.

The potential coupling coefficient and conductivity are important parameters affecting amplitude and distribution of potential data. Measurement target of multiphase flow conditions is mainly affected by water saturation, although at present about the multiphase flow coupling coefficient changes have no unified quantitative model, but the main trend is that coupling coefficient has positive correlation growth with water saturation. According to core test results [6], relationship between relative coupling coefficient and water saturation can be deseribed by the linear formula (8).

$$C_r=\hat{S} \quad (8)$$

The calculation of electrical conductivity adopts Archie's law, such as (9), neglecting the conduction of rock surface

$$\sigma_r=\phi^{1.8}S_w^{\ 2}\sigma_w \quad (9)$$

σ_r is the conductivity of rock saturated by fluid, ϕ is the porosity of rock, S_w is saturation of formation water, σ_w is the conductivity of formation water .

RESULTS AND DISSCUSSIONS

As shown in Figure 1, reservoir size is 300×150 ×10m, the complete study area size is 3000×3000× 2000m, reservoir depth is 1500m, initial pressure is 15MPa, CO_2 density is 780kg/m^3, viscosity of supercritical CO_2 is 0.05 $mPa\cdot s$, the density of water is 1000kg/m^3, water viscosity is 0.65. Homogeneous reservoir with porosity 25% and permeability 0.65D, one injection well (I1) with steady pressure 17MPa, one production well (P1) with steady flow rate 20m^3/d, run for 6 years.

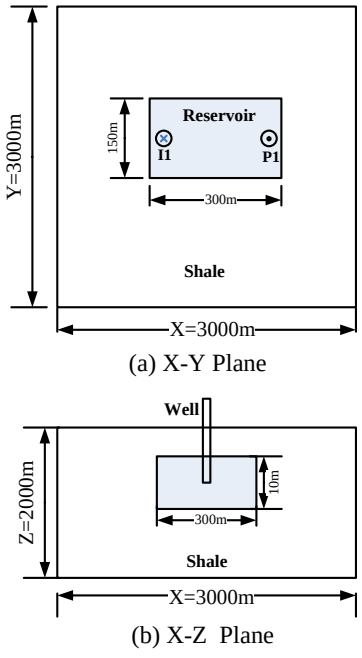

Fig. 1. Schematic diagram of model

According to Berea sandstone core test [6], under saturated water conditions, core conductivity is 0.003S/m, coupling coefficent is about -30mV/0.1MPa; under steady-state conditions, CO_2 flow through the core is about -3mV/0.1MPa, conductivity is 0.0026 S/m. This result shows that the difference between the two conditions is of one order magnitude, but conductivity variations are quite limited.

If liquid CO_2 passes through air dried core, it will change to -0.02mV/0.1MPa. The whole area is wrapped by shale, shale's conductivity is 0.01S/m. The calculation process is, firstly the flow of CO_2 and formation water is solved, and then finite difference method is used to solve the electrical problem.

As shown in Figure 2, electrical potential (U) and gas saturation (Sc) saturation distribution in X-Y plane. The left column is the potential distribution of middle depth at different time, the right column is correspond CO_2 saturation distribution. The saturation map shows that, along with CO_2 injected into the formation, it would promote stable gas-liquid front. After 900 days of production, the front has swept half areas of reservoir .After 1350 days, injected CO_2 breakthrough at production well.

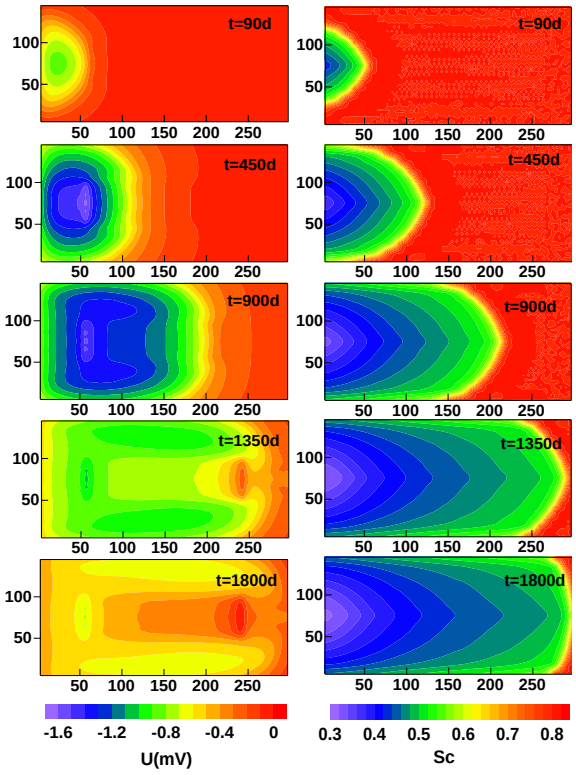

Fig. 2. Electrical potential (U) and gas saturation (Sc) in X-Y plane

Compare with potential map, after 90 days injection well bottom would form a low potential area, the low potential would expand and form an enclosed area. Potential at injection well began to increase at 450 days. Along with production, low potential region would move on to the production well continuously. So position of the potential drop is basically same as saturation front. When CO_2 arrived at production well, potential drop reached maximum, then gradually recovered from negative to zero, so the red part of 1350 ~1800 days would gradually increase to initial state. If multi-position electrical potential can be obtained at surface or underground condition, these data would be a visual representation of CO_2 migration process.

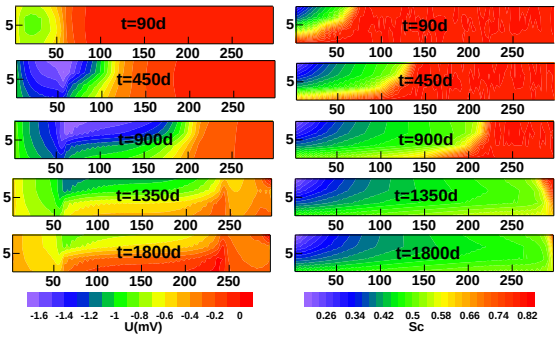

Fig. 3. Electrical potential (U) and gas saturation (Sc) in X-Z plane

As shown in Figure 3, electrical potential (U) and gas saturation (Sc) in X-Y plane, due to density difference, injected gas would form an arc front. At 450 days, injected CO_2 contact the bottom of the reservoir. Potential distribution shows a closed low potential area with narrow width, which is related to the geometry of the model.

When gas move along X-axis direction, after 450~900 days affected areas gradually increased, potential value began to decline .After 900 ~1350 days, zero potential areas began to recover ,after 1800 days, potential at bottom of the reservoir has restored to the initial state. If the geological structure is polygon, and CO_2 emitted at the top or bottom layers, abnormal potential changes would happen.

The above results show that injection of CO_2 may cause marked difference of electrical potential, and the main trend is the decrease of potential, especially at the leading edge position [7-8]. However, calculated magnitude of the potential difference is no more than 2mV, interpretation quality depend on the interference of environment conditions. Refer to electrical logging experience [9-10], it is difficult to obtain abundant and sufficient observation value; however, the vertical direction with fixed electrodes and continuous measuring, thus potential signals are quite useful, and is the development direction of future.

CONCLUSION

The CO_2 swept area would form a electrical potential drop zone, which will continue move to the production well. When CO_2 breaks through extraction well, electrical potential would gradually returns. The injected CO_2 moves along the top of the reservoir, whose changes are more obvious than other place in reservoir. The reasonable measuring position should be selected at the bottom of the injection well, or at bottom of producing well and observation well. By placing a plurality of measuring electrodes, electrical potential can be obtained continuously. The plane and vertical difference of potential can characterize the migration liquid-gas contact front. The coupling coefficient and low salinity of formation water in liquid CO_2 only differ by an order of magnitude, the conductivity properties similar to the calculated potential difference was smaller, whether has the potential interference intensity may depend on interpretation of the measured formation environment, according to the needs of strata and fluid terms and conditions.

Acknowledgements*: *The first author acknowledges the financial grant from National Science and Technology Major Project, EOR technology for complex fault block reservoirs (2016ZX05011-002).

REFERENCES

1. B.Q. Tian, P.F. Xu, Z.H. Pang, S.Q. Ling, H.L. Guo, J. Hou, *Progress in Geophysics* (in Chinese), **3**, 1431 (2014).
2. X.A. Zhu, Y.D. Wang, *China Coalbed Methane*, **5**, 3 (2011).
3. G.M. Hoversten, E. Gasperikova, Investigation of novel geophysical techniques for monitoring CO_2 movement during sequestration, Lawrence Berkeley National Laboratory, Final Report, (2003) http://escholarship.org/uc/item/0ch1f5xt.
4. L. Jouniaux, A. Maineult, V. Naudet, M. Pessel, P. Sailhac, *Comptes Rendus Geoscience*, **341**, 928 (2009).
5. X.B. Han, Supercritical fluid science and technology, Sinopec press, Beijing, 2005.
6. J.R. Moore, S.D. Glaser, H.F. Morrison, G.M. Hoversten, *Geophys Res Lett*, **31**, Paper L17610, doi:10.1029/2004GL020774 (2004).
7. Z.H. Duan, R. Sun, *Chemicaleology*, **193**, 257 (2003).
8. S.R. Ren, L.Z. Hang, *Journal of China University of Petroleum* (Edition of Natural Science), **34**, 93 (2010).
9. M.Y. Chen, B. Raghuraman, I.D. Bryant, Paper SPE 102106 presented at the SPE Annual Technology Conference and Exhibition, San Antonio, Texas, 24-27 September. http://dx.doi.org/10.2118/102106-MS (2006).
10. S. Bachu, *Canadian Petroleum technology*, **41**, 51 (2002).

ТЕЧЕНИЕ ГАЗ-ТЕЧНОСТ В ПОРЬОЗНА СРЕДА И СВЪРЗАНИ ЕФЕКТИ

Бу Яхуи

Изследователски и развоен институт, Петролно находище „Шенгли“, Синопек, Донгинг 257000, Китай

Постъпила на 19 май, 2017 г.; коригирана на 25 август, 2017 г.

(Резюме)

Продухването с газова смес (N_2/CO_2) е обещаваш метод за ускорен добив на нефт, като улавянето и отстраняването на CO_2 е много важно за опазването на околната среда. Наблюдението и контролът върху на течението газ-течност в този случай са ключови за тази технология. За тази цел е съставен математичен модел, чрез който се симулират свързаните ефекти в резервоара. Резултатите показват, че зоната на изчистване на CO_2 формира включение с нисък електричен потенциал. Фронтът на фазовата граница газ-течност е мястото, където потенциалът започва да намалява. Тази зона се увеличава до пробива на инжектирания газ в кладенеца, като потенциалът спада до нула. Резултатите са полезни за наблюдението на газо-течния процес.

Bulgarian Chemical Communications, Volume 49, Number 3, (pp. 621 – 628) 2017

Coordination behavior of Coenzyme A towards gold ions: Spectroscopic, mass spectrometric and microbiological studies

C. Andries[1], M. Manea[2], C.L. Pocanschi[3], A. Pui[1], G. Drochioiu[1],V.R. Gradinaru[1]*

[1] *Department of Chemistry, Faculty of Chemistry,Alexandru Ioan CuzaUniversity of Iasi, Romania*
[2] *Department of Chemistry and Zukunftskolleg, University of Konstanz, Konstanz, Germany*
[3] *Tanz Centre for Research in Neurodegenerative Diseases, University of Toronto, Toronto,Ontario,Canada*

Received July 22, 2015; Revised October 20, 2016

The interaction of Coenzyme A (CoA) with gold ions was investigated at various pH values by means of UV-*Vis*, FT-IR spectroscopy, as well as electrospray ionization-mass spectrometry. Furthermore, the protective role of CoA against gold induced toxicity in *Pichia pastoris* was studied. For the first time, we clearly showed that weak CoA-Au(I) complexes with 1:1 stoichiometry were formed at physiological pH. The complexation process was accompanied by gold reduction and it was strongly influenced by the reaction milieu. Moreover, a reaction byproduct, thiocoenzyme A, was identified by mass spectrometry.

Keywords: Coenzyme A; Au complexes; Spectroscopy; Mass spectrometry; *Pichia Pastoris*.

INTRODUCTION

Gold has been used since ancient times to treat smallpox, skin ulcers and measles and recently, the attention has been turned to possible therapeutic applications of gold-based materials [1,2]. A series of gold complexes capable of catalyzing chemical transformations in living organisms has been investigated in previous studies [3].The first gold complex was introduced by Robert Koch for the treatment of tuberculosis. Gold(III) chloride has been employed since 19th century in the treatment of syphilis. Moreover, gold(I) thiolate complexes were considered the drug of choice in the case of rheumatoid arthritis [4]. Auranofin, a Au(I) complex, and its analogs were found to exert a potent cytotoxic activity against certain types of cancer cells [5]. Furthermore, the proteasome is a target for Au(III) complexes [6]. It has been shown that Au(I) ions have a better affinity for thiolate S instead of O- or N-ligands. The aminoacid L-cysteine reduces Au(III) to Au(I) and forms a stable Au(I) complex in aqueous solutions [7]. This complex has recently been investigatedby UV-Vis and CD spectroscopy [8].A Au(I) complex with N-acetyl-L-cysteine ligand has also been reported [9]. Electrospray ionization-mass spectrometric analysis (negative ion mode)showed the presence of a glutathionato-S-Gold(III) during the reduction of auricyanide by L-glutathione [10]. Furthermore, methionine-gold interaction under acid conditions indicated that this amino acid plays the role of a bidentate ligand [11]. Thiol affinity for gold (I) was indirectly demonstrated since gold(I)-based catalysts were easily deactivated by these compounds [12]. Gold-protein complexes were intensively investigated, proteins containing cysteine residues being able to easily bind Au(I). Auoxo1, an Au(III) complex, has been shown to interact with cytochrome c, the resulting gold (I) being tightly attached to the protein [13]. In the bloodstream, gold is transported by albumin, in which Cys34 acts as a binding site [14]. Under acidic conditions, gold (III) has the ability to deprotonate the amide peptide group of GGH tripeptide [15]. Gold (III) complexes with Glycyl-Histidine and Alanyl-Histidine dipeptides have recently been reported [16]. Au(III) is tightly bound to xanthine derivatives, nucleosides or nucleotides [17,18]. In particular, the phosphate moiety could be involved in complexation [19]. Studies on microorganisms-gold interaction have been reported indicating that some microorganisms have the capacity to reduce Au(III) to Au(I) or gold nanoparticles [20 - 23].

In bacteria, many enzymes require Coenzyme A (CoA, Fig. 1) as a cofactor [24].

This biomolecule is involved in fatty acids oxidation pathway and/or in calmodulin-dependent protein kinase (CaMKII) activation [25]. The concentration of CoA in mitochondria is relatively high, in the range of 2.2–5 mM [26, 27]. CoA could be essential for proper cellular detoxification. In this respect, moderate CoA levels in *E. coli* impair the bacteria growth [28]. However, in certain bacterial species, CoA and its derivatives seem to play a significant role in maintaining the reducing environment of the cell, acting in a similar fashion as glutathione, which is missing in these microorganisms [29].

* To whom all correspondence should be sent:
E-mail: robert.gradinaru@uaic.ro

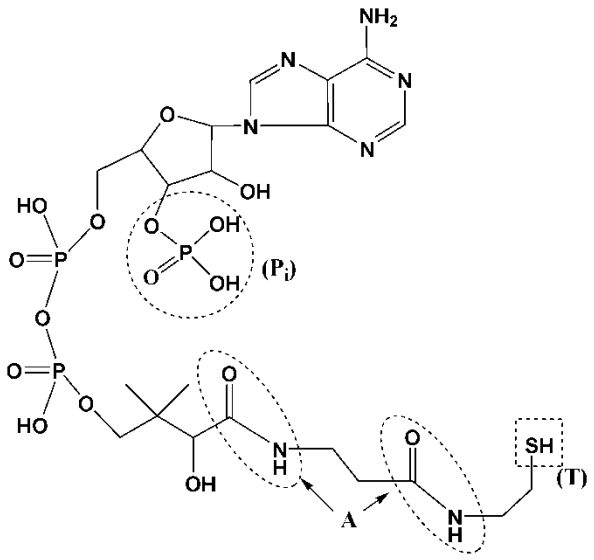

Fig. 1. Chemical structure of Coenzyme A (CoA). Phosphate (P_i), peptide bonds (A) and thiol (T) moieties were labeled.

An NMR study has drawn attention to the La-CoA complexes in aqueous solution [30]. CoA is a versatile ligand, forming stable complexes with both soft and borderline metal ions. Soft metal ions such as Hg^{2+} coordinate through the thiol sulfur and amide groups of CoA [31]. Based on this, a versatile sensor for biomolecules such as cysteine, Glutathion (GSH) or CoA was reported [32]. No preliminary study has reported the existence of Au-CoA complexes yet. Nevertheless, little is known about the relationship between CoA and gold ions in microorganisms. For this reason, in the present study Au-CoA complex was investigated by spectroscopic, mass spectrometric and/or toxicity methods (using *P. Pastoris* as a model microorganism). The complex was investigated at various pH values and in different buffer systems and the stoichiometry was also estimated.

EXPERIMENTAL

Materials

Sodium phosphate dibasic dihydrate was purchased from Sigma-Aldrich (Germany), disodium tetraborate decahydrate from Carl Roth (Karlsruhe, Germany), Glycine and Tris (base) from Carl Roth, ammonium acetate from Riedel-de Haen (Seelze, Germany), Gold (III) chloride from Titolchimica (Potecchio Polesine, Italy) and Coenzyme A (lithium salt) was a Walldorf (Germany) product. Potassium bromide was purchased from Fluka (Steinheim, Germany). All buffers were prepared using ultrapure water (Milli-Q, Millipore, 18.2 MΩ resistivity).

Methods

UV-Vis absorption spectra of free CoA and its complex were recorded on a Libra UV-Vis single beam spectrophotometer (Biochrom, Cambridge, UK) equipped with a Peltier thermostated to ensure a constant temperature (25 °C). The UV-*Vis* spectra were acquired in the wavelength range from 200 to 400 nm using a quartz cuvette (Helma/Müllheim) with a 1 cm path length.

The complex stoichiometry was estimated using the Yoe-Jones method [33]. The concentration of CoA was kept constant (0.25 mM) and the gold ion concentrations were varied (0.05-2.5 mM), depending on the buffer (borate, glycine, or Tris). The minimum of the curves corresponded to the maximum formation of the complex. The complex stoichiometry was estimated from the point where this curve changes its slope.

The IR spectra of CoA and its gold complex were acquired using a Jasco FT/IR660 Plus Fourier spectrometer in the range 4000 – 200 cm^{-1}. In order to prepare pellets, the reaction mixture was evaporated at room temperature or by heating the mixture at 70 ^{0}C and later mixed with 100 mg of dried KBr.

Electrospray ionization-mass spectrometric (ESI-MS) analyses were carried out on an Esquire 3000+ ion trap mass spectrometer (Bruker Daltonics, Bremen, Germany). Spectra were acquired in positive ion mode, in the 50 - 2500 m/z range. A mixture of CoA and metal salt at various molar ratios was prepared in 5 mM NH_4HCO_3, pH 7.4.

Similarly, *Pichia* (SMD1168H *P. Pastoris*, Invitrogen, USA) growth tests were performed in YEPD medium (10 g yeast extract, 20 g peptone and 20 g glucose in 1 L; pH 6.0). A 100 mL preculture was obtained in a 500 mL Erlenmeyer flask at 30 °C under continuous stirring (100 rpm). After one day of incubation, an optical density (580 nm) of 4.1 was reached. Both CoA (0.5 mM) and $AuCl_3$ (0.5; 1 or 1.5 mM) solutions were prepared in YEPD medium. A set of sterile 10 mL glass tubes containing 1 mL of YEPD medium and appropriate concentration of CoA and gold ions was used. After treatment, each sample was inoculated with 50 μL preculture and incubated at 30 ºC with stirring. The cells' densities were quantified by absorbance measurements of diluted samples at 580 nm after 8.0 h.

RESULTS AND DISCUSSION

Steady-state absoption study

CoA and its thioesters display two main characteristic absorption peaks at 200 and 260 nm. Initially, the formation of the complex, CoA-Au(III),

was investigated at lower pH (Glycine buffer, pH 6.8) or mitochondrial pH (Tris buffer, pH 8.5). The characteristic band of the complex in the region 280-300 nm could not be observed at a CoA concentration of 10-20 μM. This result intrigued us, since the complex of CoA with mercury was easily assessed at pH 8 [31]. Considering that CoA contains a thiol group, with potential affinity for gold, we expected that the complexation would mainly be dictated by its ionization. The pKa value of the mercapto group of coenzyme A was estimated to be 10.4 [34]. This value is at least one unit higher than the pK values of common biological thiols (cysteine and glutathione). Moreover, the formation of CoA dimers, at pH higher than 8, should be taken into account. Therefore, these parameters should be considered for the complex formation and its stability.

After several trials, we found that the interaction of CoA with Au(III) ions could easily be assessed using an alkaline borate solution (pH 10). The contribution of free Au(III) ions (a peak with a maximum at 210 nm) was subtracted, since its absorbtion band superposed the one of the complex at higher concentration. Surprisingly, at a lower CoA concentration (57 μM, Fig. 2, solid line spectrum), the CoA-Au(III) complex was not observed. The shape of the spectra did not exhibit any major changes at 260 nm; however, the intensity decreased by 15% (Fig. 2, dotted-line spectrum). This behavior suggested an electrostatic interaction between the positively charged gold ions and their counterpart, CoA's phosphate moiety. However, a drastic decrease around 50% of the peak intensity at 200 nm was noticed. In addition, a bathochromic shift was observed and more individual peaks could be distinguished in this area. At a higher CoA concentration (171 μM), a low intensity band was observed around 300 nm, when a stoichiometric amount of Au(III) was used. The complex was quite difficult to assess, since at higher Au(III) concentration (higher than 750 μM $AuCl_3$) a very high intensity band was detected in the same region. However, at elevated CoA (250 μM) and Au(III) concentrations (2-3 equivalents), the intensity at 300 nm considerably increased (more than 50-60%). The spectral differences revealed two new absorption peaks at 280 and 300 nm, respectively. All the results presented above support the idea that higher ligand and CoA concentrations are a prerequisite for complex formation. The investigated complex is characterized by an apparent dissociation constant in millimolar range (around 2 mM) and a relatively higher molar extinction coefficient (2.58 ± 0.5 $mM^{-1}cm^{-1}$) than the corresponding value of uncomplexed Au(III) ions, 0.4 $mM^{-1}cm^{-1}$ at 300 nm. Thus, the complex is characterized by a moderate stability.

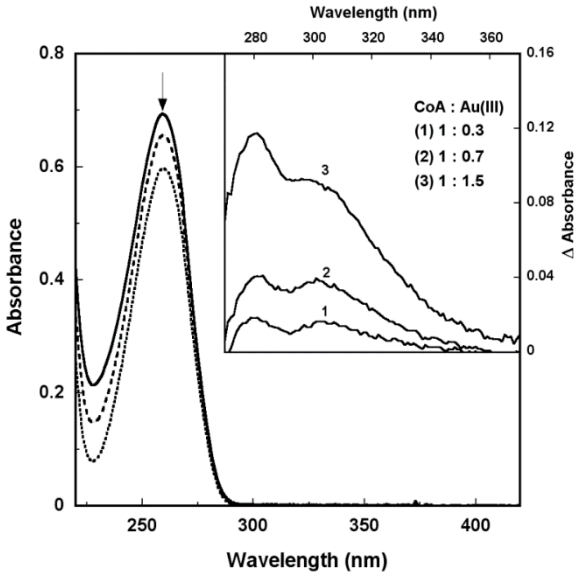

Fig. 2. UV-*Vis* spectra of CoA alone (57 μM) and in the presence of 1.8 or 4.6 equivalents of Au(III) recorded in borate buffer, pH 10. *Inset*: Difference spectra at various CoA:Au ratios (CoA concentration 220 μM).

The stoichiometry of the complex formed in 50 mM borate buffer at pH 10 was CoA: Au (I or III) = 0.9:1. Probably, the presence of borate ions in the complex outer shell could be attributed to this ratio. However, a similar stoichiometry for gold thiolate drugs with a molar excess of thiol over gold (I) has previously been reported [35].

Previous studies on CoA-Au(III) complexes under physiological conditions have been unsuccessful since gold ions could be sequestered by various buffer components. The most suitable buffers at pH 7 are for instance phosphate, HEPES, MES, Glycine, Tris. The drawback of phosphate buffer usage is that gold phosphate tends to precipitate in solution and cannot be used in spectral titration assays. HEPES and MES (Good's buffers) have the tendency to form blue nanoparticles [36]. At slightly acidic pH, glycine reduces Au(III) to Au(I) [37]. On the basis of these considerations, we decided to use Tris buffer instead of all systems mentioned above, although its optimal buffering capacity is situated up to one pH unit.

At an elevated CoA concentration (180 μM), the spectral differences at 300 nm were reasonable and the apparent dissociation constant was estimated to be 0.49±0.16 mM. Thus, we noticed that the complex was more stable at pH 7 than at pH 10. At neutral pH, the complex was characterized by a lower dissociation constant (3-4 fold) than that of the well-studied CoA-Hg(II) system [31, 32]. Beside coenzyme A, another important thiol compound for

organisms is glutathione, a tripeptide that displays a similar behavior towards metal ions (Fig. 3 inset). The spectral differences were more evident at 270 nm using a tripeptide concentration higher than 360 μM. In this particular case, the apparent dissociation constant was estimated to be 0.124±0.050 mM. For this reason, a competition between these two thiols, CoA and GSH, for gold ions is expected in the cells.

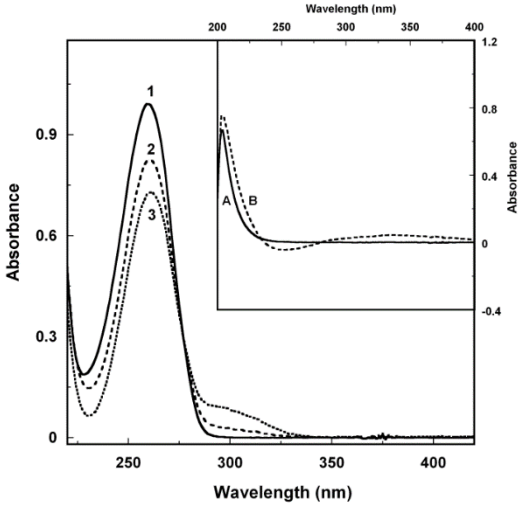

Fig. 3. Difference spectra at two different CoA:Au ratios (1:0.9 and 1:2, dotted) and their comparison with uncomplexed CoA (90 μM). *Inset*: Difference spectrum at GSH:Au molar ratios of 1:0.9 (dotted) in comparison with uncomplexed GSH (90 μM). Conditions: 50 mM Tris buffer, pH 7.

FT-IR studies

The FT-IR spectra of free CoA and its gold complex are shown in Fig. 4. Significant spectral changes were observed after adding gold ions. A couple of bands were detected in the region 400-500 cm^{-1} in the second derivate spectrum of complex. The most evident change in the parent spectrum of uncomplexed CoA was observed at 426 cm^{-1} (Fig. 4A, inset). This band could easily be attributed to a C-N out of plane bending. Furthermore, the signals at 476 and 485 cm^{-1} were assigned to the Au-N tetrahedral distortion. In this context it should be mentioned that the band at 515 cm^{-1}, which could be attributed to adenosine moiety, disappeared and a new band arose at 427 cm^{-1} after complexation. Other sensitive changes due to the CoA-gold complexation were noticed in the second derivative spectra. The complex possessed a small broad band centered at around 618 cm^{-1} that could be assigned to the C-S stretching vibration mode. The signals from 650-810 cm^{-1} region were characterized by lower intensity and most of them were slightly shifted (1-3 cm^{-1}) to higher wavenumbers. Only the signal from 680 cm^{-1} was shifted down (678 cm^{-1}). These are prominent features for a gold-nitrogen stretching vibration. Far FT-IR assignments attributed above are in agreement with data reported by Creutz's group [38]. Moreover, shifting from 790 to 798 cm^{-1} (Fig. 4A) can be assigned to adenine coordination through its N5 atom (Au-N stretching vibration).

Some stretching vibration bands corresponding to CoA's diphosphate moiety and its ether linkages were highlighted in the 900-1200 cm^{-1} region (Fig. 4B). The bands at 918, 989 and 1073 cm^{-1} were more pronounced in the complex and could be assigned to the P-O-P and P-O-H asymmetric stretching or to O-H deformation band (Fig. 4B. inset). Moreover, distinct bands were observed for the complex at 2142, 2151 and 2237 cm^{-1}. All those signals could be assigned to the symmetric stretching vibration of O-H groups of pyrophosphate moiety. Furthermore, the broad band observed in the second derivate spectra at 2464 cm^{-1} and two resolved bands noticed at 2641 and 2653 cm^{-1} corresponded to the asymmetric stretching vibration of O-H groups of pyrophosphate moiety. It should be taken into account that at pH 8, the phosphate groups are partly ionized. All the above data support the hypothesis that the diphosphate moiety undergoes significant conformational changes after gold coordination.

The bands observed in the spectrum of Coenzyme A, attributed to the S-H group, at 2560 and 2609 cm^{-1} were shifted to 2570 respectively 2612 cm^{-1} and were well defined in the complex [39].

Some spectral shifts were also determined in the 3100-3300 cm^{-1} region. Thus, a set of signals assigned to CoA were distinguished at 3120, 3130, 3139 and 3174 cm^{-1}. These peaks were slightly shifted to 3118, 3127, 3138 and 3173 cm^{-1} in the complex. More defined bands at 3224, 3232, 3266, 3277 and 3290 cm^{-1} were observed in the complex. These signals correspond to symmetric and antisymmetric N-H stretching vibration characteristic for associated amides. However, the amide I band (C=O stretching vibration) distinguished in free CoA declined slightly (1654 and 1669 cm^{-1}) in the complex. Simultaneously, a new band arose at 1225 cm^{-1} and signal intensity at 1252 cm^{-1} diminished (amide III band; N-H bending and C-N stretching along with deformation vibrations) [40]. All above data indicate that a number of small structural changes occur at the level of CoA's amide group(s) in the presence of gold ion.

Mass spectrometric analysis

In all mass spectra, CoA was denoted as H_3CoA for easy assignment of signals; the singly charged molecular ion at m/z 768.15 was assigned to

Coenzyme A molecular ion ($[H_3CoA+H]^+$. Furthermore, in the mass spectra, peaks corresponding to singly charged lithium or potassium adducts of Coenzyme A ($[H_3CoA+Li]^+$ and $[H_3CoA+K]^+$ at m/z 774.14 and 806.05), respectively were also observed.

In order to determine the stoichiometry of the complex formed between the CoA and gold ions, a solution of CoA:$AuCl_3$ (molar ratio 1:1) in ammonium acetate buffer was analysed by mass spectrometry. Surprisingly, in addition to the signal corresponding to the gold containing complex, three different signals were detected that were attributed to singly charged protonated species of free thiocoenzyme A ($[H_3CoASSH+H]^+$, m/z 800.27) and its corresponding adducts with Na^+ and K^+ $[H_3CoASSH+Na]^+$, m/z = 822.25 and ($[H_3CoASSH+K]^+$, m/z = 838.16 (Fig. 5, Panel A). A similar result was earlier reported by Murray et al. [41]. In the recorded mass spectrum, characteristic peaks for both free CoA and CoA-gold complex with the stoichiometry 1:1 ($[H_3CoA+Au(I)]^+$ at m/z 964.09) were identified. Thus, singly charged gold-attached coenzyme A $[H_3CoA+Au(I)]^+$ ions were unambiguously detected by mass spectrometry. Furthermore, a weak signal at m/z 999.96 suggests that an intermediate compound $[H_2CoA+Au(I)+Cl+H]^+$ is formed. The reduction of Au(III) to Au(I) is not surprising. In a recent study, it has been shown that human angiotensin I peptide may form various complexes in the presence of Au (III), where gold ions are in a single or both oxidation states. However, in that report, singly, doubly and triply charged species were detected [42]. It is important to mention that this decapeptide has more peptidic moieties, a higher molecular weight and no cysteine residue to facilitate a complete gold reduction. The thiol group of CoA may confer an advantage in this process. Thus, we can not exclude the formation of a mixed gold (I) bisulfide (a brown colour was observed) during reaction. Furthermore, another weak signal at m/z 962.07 ($[HCoA+Au(III)]^+$ (Fig. 5, Panel B) was noticed. In this situation, two protons were expelled from the ligand (from thiol, respectively adenine) and most probably two new bonds (Au-S and Au-N) were formed. While Au(III) was found in tetra- or hexa-coordinated complexes, Au(I) complexes are linear or tetrahedral. In this respect, ionized phosphate and pyrophosphate groups and amides moieties of CoA could be essential to complete the gold coordination sphere.

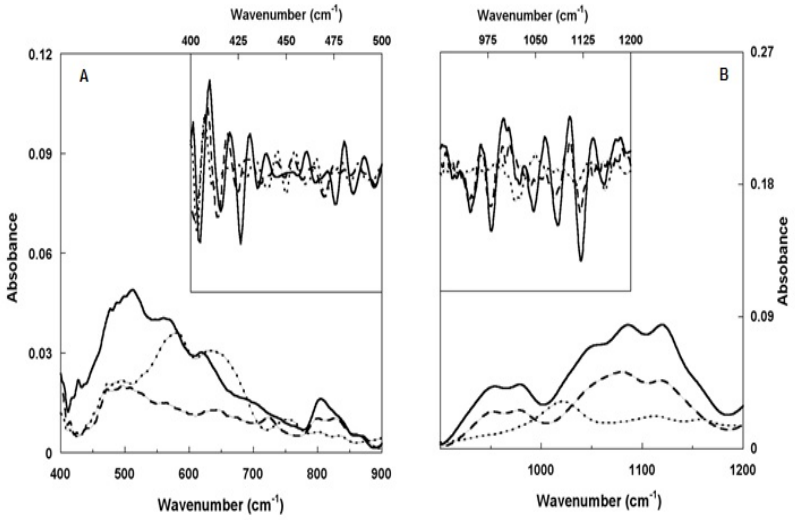

Fig.4. FT-IR spectra of free ligand (0.75µmol, dashed line), free Au(III)(10 equivalents, dotted line) and their complex (solid line). All reactions were performed in Tris 9 mM, pH 8. (A) 400-900 cm^{-1}; (B) 900-1200 cm^{-1}; Insets: second derivate spectra

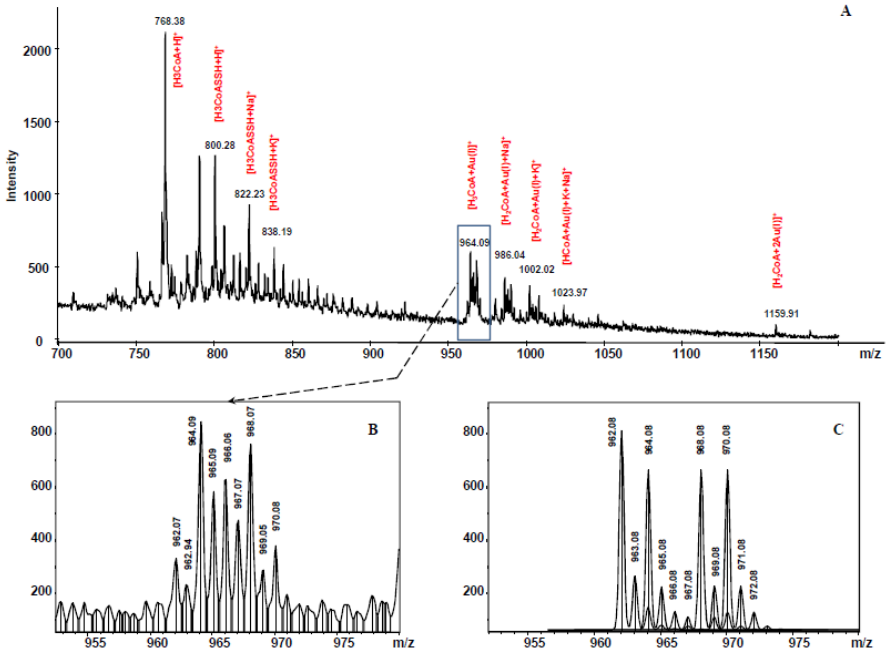

Fig.5.ESI-mass spectrum (positive ion mode) of CoA complexes with Au(III). (A) Full ESI-MS spectrum; (B) Au-CoA complex (m/z 964.09) experimental data; (C) Au-CoA complex (m/z 964.08) - simulated data.

In addition to this signal, two peaks corresponding to Na^+ and K^+ adducts of the gold (I) complex were observed (m/z 986.04 and 1002.02). Moreover, a singly charged gold-double-attached ion $[H_2CoA+2Au(I)]^+$ (m/z 1159.9) was detected by ESI-MS. On the basis of these data, we can conclude that Au(III) reduction accompanies the complexation process. The results reported here are in line with our assumptions, since Au(I) is a soft metal ion, possessing an electron configuration ($[Xe]4f^{14}5d^{10}$), and a remarkable thiophilicity.

Effect of CoA on Au(III) cytotoxicity

Yeast cells have the ability to immobilize Au(III) ions and reduce them to Au(0) in the peptidoglycan layer [43].The lethal doses of Au(III) on yeast cells are in millimolar range (0.2-1.5 mM) [44, 45].Our study on *Pichia pastoris* system demonstrated that even at 0.5 mM Au(III) concentration, the survival was moderate (about 20%) and slightly lowered at 1.5 and 2.5 mM. However, in the presence of CoA (stoichiometric amount), the toxicity was drastically impaired (Fig.6). An excess of Au(III) ions (3:1 or 5:1) increased the amount of the complex and decreased the free CoA concentration inside the *Pichia* cells. Since CoA is an important hybrid molecule for cell metabolism and division, its concentration can be well correlated by following microorganisms growing profile or their optical densities at various incubation times. These results are in agreement with our spectroscopic studies suggesting a moderate affinity of CoA for gold ions.

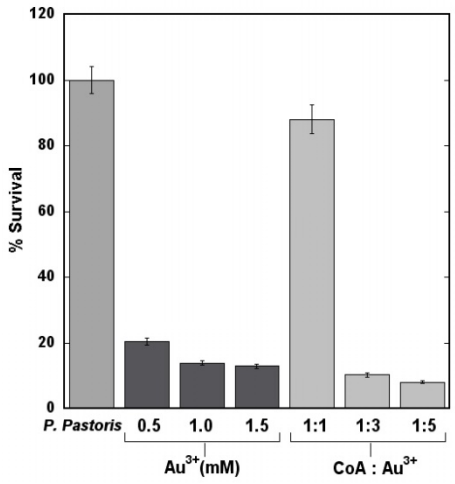

Fig.6. Effect of Au(III) on *P.Pastoris* cells (SMD1168H) in the absence (dark bars) and presence of CoA (lighter bars; the CoA (0.5 mM) and 1, 3 and 5 equivalents Au(III) were used).

Acknowledgements: *This work was supported by the strategic grant POSDRU/159/1.5/S/133652, co-financed by the European Social Fund within the Sectorial Operational Program Human Resources Development 2007-2013and R.G. thanks to DAAD fellowship awarded to carry out a short-term research stay at the University of Konstanz, Germany (September 2013).*

REFERENCES

1. D.A. Giljohann, S.S. Dwight, L.D. Weston, D.M. Matthew, C.P. Pinal, A.M. Chad, *Angew. Chem., Int. Ed.*, **49**, 3280 (2010).
2. S.P. Pricker, *Gold Bull.*, **9**, 53 (1996).
3. P.K. Sasmal, N.S. Craig, E. Meggers, *Chem. Commun. (Camb)*, **49**, 1581 (2013).
4. G.D. Champion, G.G. Graham,J.B. Ziegler, *Baillieres Clin. Rheumatol*, **4**, 491 (1990).
5. S.P. Fricker, R. Skerjl, B.R. Cameron, R. Mosi, Y. Zhu, In: Gold 2003 conference: new industrial applications for gold.
6. V. Milacic,Q.P. Dou, *Coord. Chem. Rev.*, **253**, 1649 (2009).
7. D.H. Brown,W.E. Smith, *Proc. R. Soc. Med.*,**70**, 41 (1977).
8. T. Mortier, PhD thesis, Chemistry Department, Catholic University of Leuven, Belgium, 2006.
9. P.P. Corbi, F.A. Quintão, D.K.D. Ferraresi, W.R. Lustri, A.C. Amaral, A.C. Massabni, *J. Coord. Chem.*,**63**, 1390 (2010).
10. P.M.Yangyuoru, J.W.Webb, C.F. Shaw, *J. Inorg. Biochem.*,**102**, 584 (2008).
11. A.V. Vujačić, J.Z. Savić, S.P. Sovilj, K.M. Szécsényi, N.Todorović, M.Ž. Petković,V.M.Vasić, *Polyhedron*, **28**, 593 (2009).
12. P.C. Young, S.L.J. Green, G.M. Rosair,A.L. Lee, *Dalton Trans.*, **42**, 9645 (2013).
13. A. Casini, C. Hartinger, C. Gabbiani, E. Mini, P. J. Dyson, B. K. Keppler, L. Messori, *J. Inorg. Biochem.*, **102**, 564 (2008).
14. J. Christodoulou, P.J. Sadler, A.Tucker, *Eur. J. Biochem.*, **225**, 363 (1994).
15. S.L. Best, T.K. Chattopadhyay, M.I. Djuran, R.A. Palmer, P.J. Sadler, I. Sovago, K.Varnagy, *J. Chem. Soc. Dalton Trans.*, **72**, 46 (2009).
16. U. Rychlewska, B. Warzajtis, B. D.Glisić, M. D. Zivković, S. Rajković and M. I. Djuran, *Dalt. Trans.*, **39**, 8906 (2010).
17. E. Colacio-Rodriguez, J. M. Salas-Peregrin and M. N. Moreno Carretero, *Monatshefte fur Chemie*,**117**, 941 (1986).
18. D.W.Gibson, M. Beer, R.J. Barrnett, *Biochemistry*, **10**, 3669 (1971).
19. D.Chatterji, U.S. Nandi,S.K. Podder, *Biopolymers*, **16**, 1863 (1977).
20. I. Savvaidis,V.I. Karamushka, H. Lee,J.T. Trevors, *BioMetals*, **11**, 69 (1998).
21. L. Du, H. Jiang, X. Liu, E.Wang, *Electrochem. Commun.*, **9**, 1165 (2007).
22. M.R. Sapkal,A.M. Deshmukh, *Res. J. Biotechnol.*, **3**, 36 (2008).
23. M.F. Lengke, B. Ravel, M.E. Fleet, G.Wanger, R.A. Gordon, G. Southam, *Environ. Sci. Technol.*, **40**, 6304 (2006).
24. T.P. Begley, C. Kinsland, E. Strauss, S.Taylor, M. Tandon, R. Nicewonger, M. Wu, H.-J. Chiu, N. Kelleher, N. Campobasso, Y. Zhang In: Biosynthesis: Polyketides and Vitamins, F. J. Leeper, J. C. Vederas (ed.), Springer, Berlin, Heidelberg 1998, p 93-142.
25. F. McCoy, R. Darbandi, H.C. Lee, K. Bharatham, T. Moldoveanu, C.R. Grace, K. Dodd, L. Wenwei, S.-I. Chen, R.P. Tangallapally, M. Kurokawa, R.E. Lee, A.A. Shelat, T.Chen, D.R. Green, R.A. Harris, S.-H. Lin, R.A. Fissore, R.J. Colbran, L. K. Nutt, *Mol. Cell.*, **52**, 325 (2013).
26. J.A. Idell-Wenger, L.W. Grotyohann, J.R. Neely, *J. Biol. Chem.*, **253**, 4310 (1978).
27. J.R.Williamson, B.E. Corkey, *Methods Enzymol.*, **55**, 200 (1979).
28. S. Jackowski,C.O. Rock, *J. Bacteriol.*, **166**, 866 (1986).
29. R. Leonardi, S. Chohan,Y.-M. Zhang, K.G. Virga, R.E. Lee, C.O. Rock, S. Jackowski, *J. Biol. Chem.*, **280**, 3314 (2005).
30. G.V. Fazakerley, P.W. Linder,D.G. Reid, *Eur. J. Biochem.*, **81**, 507 (1977).
31. R. Gradinaru, A. Ionas, A. Pui, G. Zbancioc, G. Drochioiu, *BioMetals*, **24**, 1115 (2011).
32. S.Vallejos, P. Estévez, S. Ibeas, F.C. García, F. Serna, J.M. García, *Sensors (Basel)*, **12**, 2969 (2012).
33. J. Yoe, A.L. Jones, *Ind. Eng. Chem. Anal. Ed.*, **16**, 111 (1944).
34. I.H. Pitman,I.J. Morris, *Aust. J. Chem.*, **33**, 1625 (1980).
35. A.A. Isab,P.J. Sadler, *J. Chem. Soc. Chem. Commun.*, **24**, 1051 (1976).
36. A. Habib, M. Tabata,Y.G.Wu, *Bull. Chem. Soc. Jpn.*, **78**, 262 (2005).
37. P.K. Sen, N. Gani, J.K. Midya, B. Pal, *Transit. Met. Chem.*, **33**, 229 (2007).
38. J. Petroski, M. Chou, C. Creutz, *J. Organomet. Chem.*, **694**, 1138 (2009).
39. W. Qian, S. Krimm, *Biopolymers*, **32**, 1503 (1992).
40. S.E. Glassford, B. Byrne,S.G. Kazarian, *Biochim. Biophys. Acta*, **1834**, 2849 (2013).
41. C.I. Murray, J. E.Van Eyk, *Circ. Cardiovasc. Genet.*, **5**, 591 (2012).
42. J. Lee, L.P. Jayathilaka, S. Gupta, J.-S. Huang and B.-S. Lee, *J. Am. Soc. Mass Spectrom.*, **23**, 942 (2012).
43. Z. Lin, J. Wu, R. Xue, Y. Yang, *Spectrochim. Acta. A. Mol. Biomol. Spectrosc.*, **61**, 761 (2005).
44. V.I. Karamushka, G. M. Gadd, *Biometals*, **12**, 289 (1999).
45. D.N. Mitchel, H. A. Godwin, E. Claudio, *Nanoscape*, **1**, 59 (2004).

КООРДИНАЦИОННИ ОТНАСЯНИЯ НА КОЕНЗИМ А СПРЯМО ЗЛАТНИ ЙОНИ: СПЕКТРОСКОПСКИ, МАС-СПЕКТРОМЕТРИЧНИ И МИКРОБИОЛОГИЧНИ ИЗСЛЕДВАНИЯ

К. Андрис[1], М. Маня[2], К.Л. Поканчи[3], А. Пуи[1], Г. Дрокиою[1], В.Р. Градинару[1]*

[1] *Департамент по химия, Химически факултет, Университет „Александру Йоан Куза“, Яш, Румъния*

[2] *Департамент по химия, Университет в Констанц, Констанц, Германия*

[3] *Център за изследвания на невро-дегенеративни болести, Университет в Торонто, Онтарио, Канада*

Получена на 22 юли, 2015 г.; коригирана на 20 октомври, 2017 г.

(Резюме)

Взаимодействието на коензим А (CoA) със златни йони е изследвано при различни pH-стойности с помощта на UV-*Vis и* FT-IR-спектроскопии, както и с електро спрей-йонизационна мас-спектрометрия. Освен това е изследвана защитната роля на CoA срещу индуцираната токсичност на златните йони спрямо *Pichia pastoris.* За пръв път са показани слаботе комплекси CoA-Au(I) при стехиометрично отношение 1:1 при физиологични стойности на pH. Процесът на комплексообразуване е придружен от редукция на златото и силно зависи от реакционната среда. Тио-коензимът А е идентифициран чрез мас-спектрометрия като страничен продукт на реакцията.

Bulgarian Chemical Communications, Volume 49, Number 3, (pp. 629 – 634) 2017

Investigation of sugar irradiated with He, Ne and C ions for dosimetric purposes

Y.G. Karakirova[1*], K. Nakagawa[2], N. D. Yordanov[1]

[1]*Institute of Catalysis, Bulgarian Academy of Sciences, 1113 Sofia, Bulgaria*
[2]*Department of Radiological Life Sciences, Graduate School of Health Sciences, Hirosaki University, 66-1 Hon-cyo, Hirosaki, 036-8564 Japan*

Received November 3, 2016; Revised February 17, 2017

Electron paramagnetic resonance (EPR) study on solid sugar irradiated by He, Ne and C ions and UV spectrometric study of its water solutions are presented. The samples are treated with different doses of radiation in the region of 50 - 300 Gy and several values of linear energy transfer (LET). All samples exhibit identical EPR spectra, due to radiation induced stable sugar radicals, and UV absorption at 267 nm of their water solutions. The EPR signal amplitude (peak-to-peak of the first derivative) and the UV absorption at 267 nm are used as dosimetric indexes. The dependence of these parameters as a function of LET and absorbed dose radiation is studied. The present results show that the EPR response with increase of LET of a given particle decreases, while the UV absorption at 267 nm increases. In addition, the new relation between LET of irradiating particles and UV absorbance is obtained.

Keywords*:* Sugar; irradiation; heavy ion; EPR dosimetry; UV spectrometry

INTRODUCTION

In the last decades, the extensive use of ionizing radiation in various fields of human activities requires effective radiation protection and reliable dosimetric systems to estimate the received radiation doses. On the other hand, it is well known that treatment of sugar with various types of radiation generates stable long-lived free radicals [1, 2, 3, 4, 5, 6, 7, 8, 9]. The application of heavy particles in medicine leads to the investigation of sugar in the last two decades as a dosimetric material for heavy particles irradiation [6, 10, 11, 12, 13, 14, 15, 16, 17, 18]. It is found that identical EPR spectra of radiation induced stable free radicals are obtained both with photons and heavy particles.

On the other hand, the irradiation of sugar creates products of radical recombination besides paramagnetic species. These recombination products are used in solid state/UV dosimetric system [19] and aqueous solutions/UV dosimetric system [4, 5, 20, 21, 22, 23]. A characteristic band at 267 nm is appears in aqueous solutions of irradiated sugar [4, 5, 21] or at 263 nm as reported by other authors [7].

This new application of UV spectrophotometry is very important because it is a calibrated method. Thus, before EPR dose estimations each spectrometer has to be calibrated by a separate calibration graph for each batch of samples, which is only valid for the appropriate EPR spectrometer and laboratory. In order to overcome the above disadvantage, an attempt was recently made to calibrate EPR using UV spectrophotometry [22]. By this approach it is possible to calibrate not only sugar, but also other, for example alanine dosimeters, if they are simultaneously irradiated.

In the present paper, are reported the first results on the effect of LET of the He, Ne and C ions on the UV response. The relation between UV absorption and LET of the irradiating particles is reported.

EXPERIMENTAL

Materials and sample preparation

Sucrose (sugar) of the highest grade is purchased from Nacalai Tesque Inc., Japan and used as received. Sugar sample weight of 0.50 g is used in order to fill the EPR cavity. The same sample is then used for preparation of 5% water solution for UV spectrophotometry.

Each sugar sample is placed before irradiation on an acrylic plate (40 mm x 40 mm) and wrapped with a thin plastic sheet. The thickness of the sample is approximately 1.0 mm. The wrapped samples are mounted on a sample holder for irradiation.

Heavy-ion irradiation

Heavy-ions sample irradiation is performed in a biology experiment room of a heavy ion medical accelerator in Chiba (HIMAC) at the National Institute of Radiological Sciences (NIRS). The biology room was equipped with an irradiation system similar to that found in a treatment room, including dose monitors, a binary filter, and a wobbler system. A target in the atmosphere was placed at a distance of 50 cm from a thin aluminum window that sealed the vacuum in the beam ducts. The wobbler system realized a 10 cm diameter uniform field with a uniformity of 2% or less. The beam intensity was measured using dose monitors

* To whom all correspondence should be sent:
E-mail: daniepr@ic.bas.bg

installed in the beam course. A binary filter composed of poly (methyl methacrylate) plates with thicknesses ranging from 0.5 to 128 mm was used to adjust the LET. Residual ranges of the beams, when plates of various thicknesses were inserted, were measured precisely before the irradiation. LET values at the target position were estimated by a simulation code using the data of residual ranges [24]. The sugar samples were irradiated from 5 to 300 Gy with follow ions and LET: 1) with helium (150 MeV/u with LET 3, 4, 5, 7.9 and 10 keV/μm); 2) with neon (400 MeV/u with LET 30.9, 50, 60, 80, 100.9, 119.7, 120 and 139 keV/μm) and 3) with carbon (290 MeV/u with LET 10.9, 20.5, 30.2 and 49). All processes of irradiation and measurements are carried out at ambient temperature. A schematic illustration of the experimental setup for sample irradiation is presented in Figure 1.

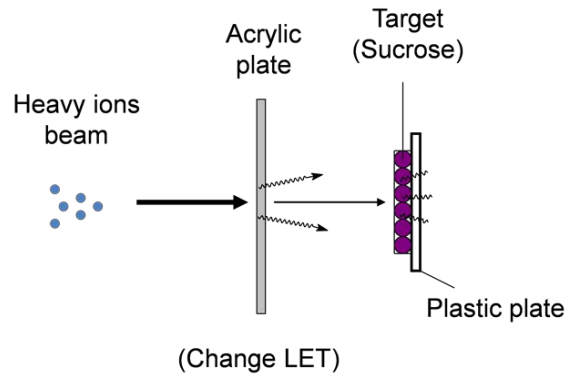

Fig. 1. Schematic illustration of the experimental setup for irradiation with heavy ions.

Instrumentation and procedures of measurements

The EPR spectra are recorded on a JEOL JES-FA 100 EPR spectrometer operating in the X–band with standard TE_{011} cylindrical resonator at room temperature. After irradiation the crystal sugar is directly transferred to EPR quartz sample tube with 5 mm o.d. and 4 mm i.d. and fixed in the cavity center. The EPR signal intensity i.e. peak-to-peak of the first derivative in the EPR spectrum is used as a measure for the quantity of radiation generated free radicals. Eight to twelve EPR measurements are performed for each irradiation dose and the results are averaged.

UV measurements are performed on a Specord UV-VIS (Carl Zeiss, Jena) spectrophotometer at room temperature. All UV spectra of water solutions of irradiated sugar are recorded versus distilled water. At the same conditions non-irradiated sugar has no absorption in the studied UV region (240-360 nm). All water solutions after preparation are heated up to 70°C for 1 h to reach stable with the time UV absorption [21]. Quartz sample cells with a path length of 5 cm are used. Five measurements were made for every sample.

RESULTS AND DISCUSSION

EPR investigation of crystal sugar irradiated with He, Ne and C ions.

All sugar samples are EPR silent before irradiation. A typical signal due to radiation induced free radicals is recorded in the EPR spectrum after sample irradiation. The signal is complex and is a superposition of the spectra of different paramagnetic species [25].

The influence of the instrumental parameters (microwave power and modulation amplitude) on the EPR response is examined in order to record undistorted and maximal intense signal. For this purpose, the EPR spectra of irradiated sugar with Ne ions of 50 Gy dose and LET 50 keV/μm is performed in the region of 0.1 to 20 mW microwave power and 0.05 to 1 mT modulation amplitude. The experiments show that the influence of the above parameters on the intensity and the shape of the EPR signal are avoided when all EPR spectra are recorded at 1 mW microwave power and modulation amplitude of 0.4 mT. The EPR spectra of sugar irradiated with He, Ne and C ions are identical with those described in the literature [14, 17]. There is no difference in the shape of the spectra of irradiated with these ions samples except their intensities (number of radiation induced free radicals). The intensity of the observed EPR spectrum depends on the concentration of the radiation induced radicals. As the dose response is of paramount importance for any dosimetry method, are providing raw results of the measurements (Table 1) to enable an interested reader to see the statistical significance of the results. Ten measurements for every sample were used for statistical study. The relative standard deviation of replicate signals was 2.4, 5.5 and 4.7% for lowest dose helium, carbon and neon ions, respectively. For highest dose it is 1.35, 1.52 and 2.09%, respectively. These data also characterize the reproducibility of measurements at various radiation doses and irradiating ions.

Table 1. The experimentally obtained values from the EPR measurements and standard deviation.

irradiation	He		Ne		C	
Dose, Gy	5	50	5	300	5	300
I_1	73.42	450	18.25	1323	20.74	1779
I_2	71.25	452	19.03	1358	21.56	1765
I_3	75.32	455	21.55	1369	19.88	1788
I_4	74.05	460	20.19	1322	23.54	1757
I_5	73.23	442	21.66	1378	20.11	1778
I_6	70.21	458	18.47	1351	22.36	1745
I_7	73.23	446	17.55	1364	20.85	1784
I_8	74.25	452	20.18	1353	18.78	1698
I_9	70.15	446	21.06	1388	24.53	1752
I_{10}	73.21	459	22.18	1297	19.77	1744
Mean I_{pp}	72.832	452	20.012	1350.3	21.212	1759
Std. deviation	1.73399	6.09189	1.6141	28.24516	1.80136	26.78723

The scatter of doses determined with replicate samples is due to variation of the density of the samples and usually very small of the geometry and the position of the sample. Although the uncertainty of around 4-5% in the low doses is not sufficiently low for primary calibration, sugar can be successfully used in dosimetry. Linear increase in the EPR signal intensity with increasing absorbed dose of C, He and Ne ions in the investigated dose range is found. This statement is already known [12] and will not be discuss here.

The relation between the EPR response and the atomic weight of the irradiating ions is confirmed [16], the heavier ions in the order He < C < Ne giving lower EPR response. The irradiation of sugar samples with He, Ne and C of different LET shows in the present study that EPR signal intensity increases with decreasing LET of every ion. This tendency is in a good agreement with previous observations [6, 10, 11, 12, 13, 26]. Therefore, EPR spectrum of sugar is sensitive both to the weight of the particles and their LET.

UV investigation of He, Ne and C ions irradiated crystal sugar

As was mentioned above, water solutions of non-irradiated crystal sugar do not exhibit UV absorbance, whereas water solutions of irradiated crystal sugar show an absorption band at 267 nm [4, 5, 21, 17]. Figure 2 shows UV spectra of Ne and C ions irradiated crystal sugar. Samples of sugar irradiated with He ions do not exhibit UV absorbance.

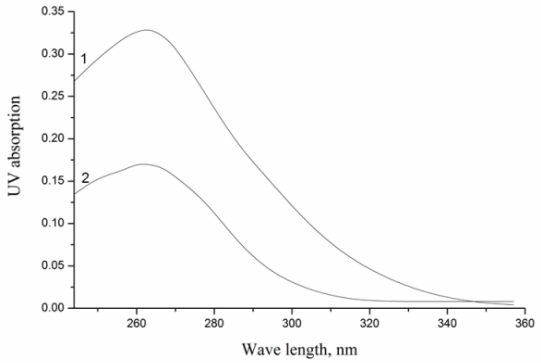

Fig. 2. UV spectra of 5% aqueous solutions of sugar samples irradiated with: 1) Ne (300 Gy, LET 50 keV/μm) and 2) C (300 Gy, LET 49 keV/μm) ions.

Previous UV spectrophotometric study of gamma irradiated sugar [21] shows that detection limit of c.a. 55 Gy may be obtained by using 5 cm sample cell and 20% solution. Having in mind that the highest He ion dose in the present study is 50 Gy with LET 10 keV/μm and in view of its relatively low atomic weight, the effect of He ion could be expected to be closely below that of gamma irradiation. Therefore, this explains absence of UV absorption in case of He ion irradiation. The appearance of 267 nm peak is due to recombination products of radiation induced free radicals in sugar. According to literature data [27, 28] absorption band in this spectral region is typically associated with carbonyl groups in organic compounds. It is assumed that glycoside bond breaks and the formation of carbonyl group may be common mechanism in the radiation chemistry of disaccharides [29].

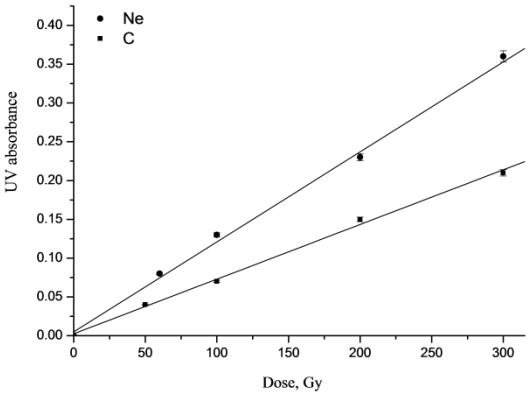

Fig. 3. The dependence of UV absorption of water solution of solid sucrose irradiated with Ne (LET 30.9 keV/μm) and C (LET 30.2 keV/μm) ions as a function of absorbed dose ionizing radiation.

The UV absorbance at 267 nm is used as a dosimetric index for the absorbed dose of photons and heavy particles [21, 14]. The dependence of the UV absorbance at 267 nm on the absorbed dose of C and Ne ions is shown in Fig. 3. As seen from Fig. 3, the UV absorbance intensity linearly increases, but with different slope for samples irradiated with Ne and C ions. In comparison with EPR UV results have better reproducibility and the standard deviation for low doses is 1%, whereas for high doses it is under 1%. The error bars represent a standard uncertainty in percent of five measurements for every sample.

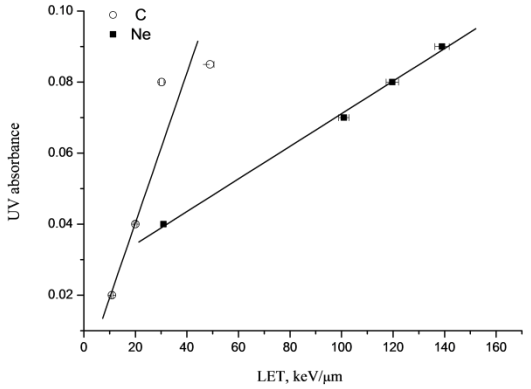

Fig. 4. Dependence of UV absorption maximum of aqueous solutions of solid sugar irradiated with dose of 50 Gy as a function of LET of Ne and C particles.

In addition, it is found that UV absorption intensity increases with increasing weight of the ions. In order to determine more deeply the effect of various LET of the particle on the UV absorption, the relation between UV absorption and LET was studied. The obtained results on Fig. 4 show that the UV absorption increases with increasing LET of the particle. This statement is contrary to the EPR result where EPR signal intensity decreased when LET of the particle increased. Since the absorption band depends on the particle species, their LET and the applied dose, to find the UV dose response of irradiated with heavy particles sugar have to take in account and LET.

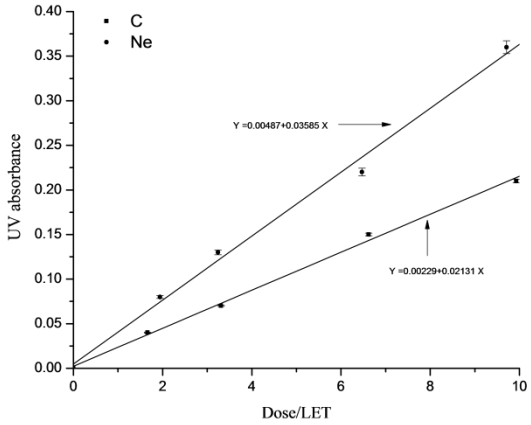

Fig. 5. UV absorbance at 267 nm as a function of the ratio of the absorbed dose and LET of the particles.

Figure 5 shows dependence of UV absorbance from the attitude of the dose and LET. As can see the linearity of the dose response is retained. Therefore in both cases with and without accounting LET the UV spectrometry may be used as a method for dosimetry of irradiated with heavy ions sugar because of the linear dose response.

Comparison between EPR and UV response of He, Ne and C ions irradiated sugar.

The relation between EPR and UV response for different heavy particles was discussed before [14, 16, 17]. However, the EPR and UV response of sugar irradiated with heavy particles with different LET is not discussed up to now. During irradiation, the effects that are measured with EPR and UV spectrometry are different. EPR measures free radicals whereas UV spectrometry measures some kinds of recombination products formed because of dissolving in water. Fact is that these effects are created from the irradiation with ionizing radiation. So this gives opportunity to compare both effects and methods. The dependence of EPR and UV response of sugar irradiated with Ne and C ions with LET 30 and 50 keV/μm shows a perfect linearity (Fig. 6).

Therefore, the linearity remains independently from LET and the particle species. Thus UV spectrometry could be used for calibration of EPR results when it is necessary.

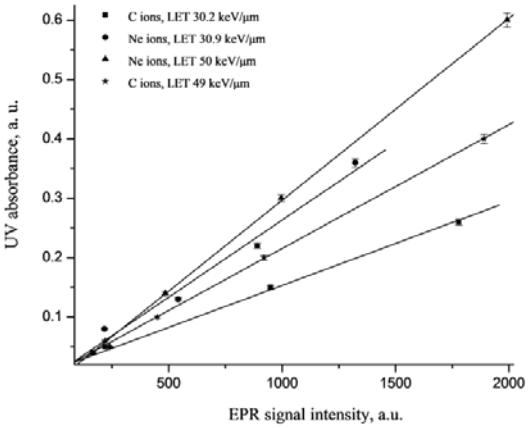

Fig. 6. Comparison between the results obtained by UV and EPR spectroscopy of sugar irradiated with Ne and C ions.

CONCLUSIONS

The UV spectra of water solution of irradiated with Ne and C ions solid sugar shows an absorption band at 267 nm. The intensity of this band linearly increases with increasing of the absorbed dose high energy radiation for samples irradiated with Ne and C. The samples irradiated with He ions do not exhibit UV spectrum due to the lower dose and LET of irradiation than the detection minimum. The relation between UV absorbance and LET of irradiating particles, studied for the first time in this paper, shows that the UV absorption increased with increasing LET of every particle. Taking in account the LET of the irradiating ions, the linear dependence of dose response do not change. Therefore, the effect of LET of the particle could be neglect.

Acknowledgements: *Part of this research was supported by Research Project Heavy Ions at NIRS-HIMAC, a Grant-in-Aid for Challenging Exploratory Research (24650247, 15K12499) and for Scientific Research (B) (25282124) from the Japan Society for the Promotion of Science (JSPS) (K.N.), and A-step (AS262Z00876P) from the Japan Science and Technology (JST) (K.N.).*

REFERENCES

1. T. Nakajima, *Health Phys.* **55** (6), 951 (1988).
2. T. Nakajima, *Br. J. Radiol.* **62**, 148 (1989).
3. P. Fattibene, T.L. Duckworth, M.F. Desrosiers, *Appl. Radiat. Isot.* **47**(11-12), 1375 (1996).
4. N. Yordanov, V. Gancheva, E. Georgieva, *Radiat. Phys. Chem.* **65**, 269 (2002).
5. N. Yordanov, V. Gancheva, E. Georgieva, In Kawamori, A. (Ed.), Adv. EPR App. Biosciences, Kwansei Gaikun University, Japan, 2002, p. 128.
6. K. Nakagawa, Y. Sato, *Spectrochim. Acta Part A* **60**, 1315 (2004).
7. Z. Peimel-Stuglik, and S. Fabisiak, *Radiat. Phys. Chem.*, **78**(7-8), 449 (2009).
8. Y. Karakirova, N.D. Yordanov, H. De Cooman, H. Vrielinck, F. Callens, *Radiat. Phys. Chem.* **79**, 654 (2010).
9. M. Mikou, N. Ghosne, R. El Baydaoui, Z. Zirari, F. Kuntz, *Appl. Radiat. Isot.* **99**, 1 (2015).
10. K. Nakagawa, and T. Nishio, *Radiat. Res.* **153**, 835 (2000).
11. K. Nakagawa and Y. Sato, *Adv. ESR Appl.* **18**, 253 (2002).
12. K. Nakagawa and Y. Sato, *Radiat. Res.* **164**, 336 (2005).
13. K. Nakagawa, and Y. Sato, *Spectrchim. Acta Part A* **63**, 851 (2006).
14. Y. Karakirova, E. Lund, and N. D. Yordanov. *Radiat. Meas.* **43**, 1337 (2008).
15. M. Mikou, S. Benzina, P. Bischoff, J.M. Denis and Gueulette, Appl. Radiat. Isot. **67**, 1738 (2009).
16. Y. Karakirova, and N. D. Yordanov. *Radiat. Meas.* **45**, 831 (2010).
17. Y. Karakirova, K. Nakagawa, N. D. Yordanov, *Radiat. Meas.* **45**, 10 (2010).
18. K. Nakagawa, Y. Karakirova and N. D. Yordanov, *J. Radiat. Res.* **56** (3), 405 (2015).
19. C. Flores, E. Cabrera, T. Calderon, E. Munoz, E. Adem, J. Hernandez, J. Boldu, P. Ovalle, H. Murrieta. *Appl. Radiat. Isot.* **52**, 1229 (2000).
20. N. Yordanov, and E. Georgieva, *Spectrochim. Acta Part A* **60**, 1307 (2004).
21. N. D. Yordanov, and Y. Karakirova, *Radiat. Meas.* **42**, 121 (2007).
22. N. D. Yordanov, and Y. Karakirova, *Radiat. Meas.* **42**, 347 (2007).
23. R. Amraei, M. Kheirkhah, G. Raisali. *Radiat. Prot. Dosim.* **149** (4), 357 (2012).
24. T. Kanai, E. Masahiro, S. Minohara, N. Miyahara, H. Koyama-Ito, H. Tomura, N. Matsufuji, Y. Futami, A. Fukumura, T. Hiraoka, Y. Furusawa, K. Ando, M. Suzuki, F. Soga, K. Kawachi. *J. Radiat. Oncol. Biol. Phys.* **44** (1), 201 (1999).
25. E. R. Georgieva, L. Pardi, G. Jeschke, D. Gatteschi, L. Sorace, and N. Yordanov. *Free Radical Res.* **40** (6) 553 (2006).
26. K. Nakagawa, N. Ikota, K. Anzai, *Spectrochim. Acta Part A* **69**, 1384 (2008).
27. A.S. Wingrove and R.L. Caret, Organic Chemistry. Harper & Row, New York, 1981, p. 502.
28. A. Supe, and Yu. Tiliks, *High Energy Chem.* **28**, 193 (1994).
29. H. De Cooman, E. Pauwels, H. Vrielinck, E. Sagstuen, S. Van Doorslaer, F. Callens, and M. Waroquier. *Phys. Chem. Chem. Phys.* **11**, 1105 (2009).

ИЗСЛЕДВАНЕ НА ЗАХАР ОБЛЪЧЕНА С He, Ne И С ЙОНИ ЗА ДОЗИМЕТРИЧНИ ЦЕЛИ

Й. Г. Каракирова[1*], К. Накагава[2], Н. Д. Йорданов[1]

[1] *Институт по катализ, Българска академия на науките, София 1113, България*
[2]*Университета на Хиросаки, Хиросаки, Япония*

Получена на 3 ноември, 2016 г.; коригирана на 17 февруари, 2017 г.

(Резюме)

Представено е Електрон парамагнитен резонанс (ЕПР) изследване на захар облъчена с He, Ne и C йони и УВ изследване на водните и разтвори. Пробите са третирани с различни дози йонизиращо лъчение (50-300 Gy) и няколко стойности на линейно енергийния трансфер (ЛЕТ). Всички твърди проби показват идентични ЕПР спектри, дължащи се на радиационно индуцирани стабилни радикали в захар, а водните им разтвори - УВ абсорбционна ивица при 267 nm. Като дозиметричен индекс са използвани амплитудата на ЕПР сигнала (разстоянието от пик до пик в първата производна на ЕПР спектъра) и УВ абсорбцията при 267 nm. Изследвани са зависимостите на тези параметри като функция от ЛЕТ и абсорбираната доза радиационно лъчение. Представените резултати показват, че с нарастване на ЛЕТ на частицата, ЕПР отклика намалява, докато УВ абсорбцията при 267 nm нараства.

Bulgarian Chemical Communications, Volume 49, Number 3, (pp. 635 – 642) 2017

Adsorption properties of 4-Phenylphenol in aqueous solution with adsorption resins chemically modified

C.Z. Ke[1, 2], N. Wang[1, 2], W.X. Li[2], W.Z Shi[2], Z. H. Fei[*, 2]

[1]*Nanjing University & Yancheng Academy of Environmental Protection Technology and Engineering, Yancheng, China*

[2]*College of Chemistry and Chemical Engineering, Yancheng Teachers University, Yancheng, China*

Received May 23, 2017; Revised August 21, 2017

The hypercrosslinked adsorption resins modified with atrazine (named KCZ-1), o-Phthalic anhydride(named KCZ-2), trimellitic anhydride(named FJ-1) and 2-Imidazolidone hemihydrate(named FJ-2) respectively were successfully prepared by the crosslinking and chemical modification reaction and characterized by IR and BET. The structural characterization results indicated that the resins possessed predominant micropores/mesopores, moderate specific surface area. The adsorption capacity of 4-Phenylphenol onto the four resins was very large due to hydrogen bond interaction between 4-Phenylphenol and modified group on the resins. Adsorption behaviors of 4-Phenylphenol onto the KCZ-1, KCZ-2, FJ-1 and FJ-2 resins were studied by isotherm adsorption and adsorption kinetics experiments. Moreover, the adsorption thermodynamics and adsorption kinetics are also calculated to study adsorption mechanism of the adsorption of 4-Phenylphenol on adsorption resins. The isotherms were correlated by the Langmuir and Freundlich equations and the Langmuir equation was shown to be the most suitable. The enthalpy change ΔH is positive, and Gibb's free energy change ΔG and entropy change ΔS were calculated to be negative. The efficiency of dynamic adsorption on FJ-1 resin is better than that on other resins. When temperature was 333K, nearly 75% regeneration efficiency for the adsorbent was achieved at the flow rate of 0.5BV/h.

Key words: Resin, 4-Phenylphenol, Adsorption, Adsorption isotherms, Dynamic adsorption, Desorption.

INTRODUCTION

4-Phenylphenol($C_{12}H_{10}O$), also known as 4-Hydroxybiphenyl, an important phenol chemical and widely used as fungicide and preservative agent in agriculture and industry, slightly soluble in water, soluble in methanol, acetone, benzene and other organic solvents. 4-Phenylphenol has bactericidal and is widely used in households, industry, and hospitals to disinfect surfaces, in addition to being utilized as a preservative in cosmetics, plastics, lame retardants antisepsis and sterilizing of fruit and vegetable, etc.[1-3]. However, 4-Phenylphenol is a toxic organic pollutant in the industrial waste water, which will be harmful to human being and animals even at low concentrations [4,5]. Therefore, remediation of aromatic compounds containing waste water is an imminent and important issue for environmental protection.

In recent years, a wide range of physical and chemical technologies including photocatalytic oxidation, membrane separation, electrochemical oxidation, solvent extraction, ion exchange and adsorption are employed for aromatic compounds removal from aqueous solution [6-8], among which the adsorption-based process is probably the most favorable treatment option due to its efficacy, practicality and economic feasibility [9]. Several of materials have been used as adsorbents, including polymeric resins [10], activated carbon and so on [11]. Although activated carbons exhibit an excellent adsorption capacity for 4-Hydroxybiphenyl removal from waste water, the used activated carbon adsorbents are difficult to regenerate and quite expensive to dispose. Therefore, it is necessary to look for alternative adsorbents that are equally effective and easier to regenerate and dispose. Recently, a new kind of hypercrosslinked polymeric adsorbent was found to be very effective for removing aromatic compounds from aqueous solution [12,13]. Since the 1970s, hypercrosslinked resins are recognized as one kind of efficient polymeric adsorbents for adsorptive removal of aromatic compounds from aqueous solution [14,15]. The hypercrosslinked resins owe their high adsorption potential due to their unique synthesis method. In general, they are synthesized from linear polystyrene–divinylbenzene polymer (PS) or low crosslinked PS by adding bi-functional cross-linking reagants such as monochloromethylether, 1,4-bis(chloromethyl) benzene, and FriedelCrafts catalysts including anhydrous zinc chloride, iron (III) chloride, aluminum (III) chloride and stannic (IV) chloride are employed in the synthesis procedure. They can also be prepared from macroporous low cross-linked chloromethylated PS via its self-fielder–Crafts reaction [16]. After the

* To whom all correspondence should be sent:
E-mail: feizhenghao@163.com

corresponding reactions, the obtained hypercrosslinked PS networks consist of an intensive bridging of strongly solvated PS chains with conformationally rigid links, leading to a major shift of their pore diameter distribution from predominately mesopores to mesopores–micropores bimodal distribution, and hence results in a sharp increase of the Brunauer–Emmet–Teller (BET) surface area and pore volume [17, 18]. Because of these significant changes, the hypercrosslinked resin displays very large adsorption capacities towards non-polar and weakly polar aromatic compounds in aqueous solution. In order to increase their adsorption capacities towards polar aromatic compounds, the resins are often modified by introducing polar units into the copolymers, using polar compounds as the crosslinking reagent and addition of polar compounds in the Friedel–Crafts reaction [19, 20]. The previous studies indicated that the chemically modified hypercrosslinked resins exhibited improved adsorption properties toward polar aromatic compounds by introducing certain specific functional groups on their surface [21].

In this paper, the hypercrosslinked adsorption resins modified with atrazine (named KCZ-1), o-Phthalic anhydride(named KCZ-2), trimellitic anhydride(named FJ-1) and 2-Imidazolidone hemihydrate(named FJ-2)respectively, were successfully prepared by the cross-linking and chemical modification reaction. The adsorption properties and adsorption mechanism of 4-Hydroxybiphenyl onto the KCZ-1, KCZ-2 and FJ-1, FJ-2 resins were studied by isotherm adsorption, dynamic adsorption and desorption.

EXPERIMENTAL

Materials

Analytical methods

Styrene-divinylbenzene copolymer was purchased from Nanjing Maike Fei Co. LTD. Amino sulfonic acid and Trimellitic anhydride was purchased from Element Mall. Ethanol, nitrobenzene, anhydrous aluminum chloride and hydrochloric acid were analytical grade, which were purchased from Shanghai Chemical Reagent. Ethanol, nitrobenzene, anhydrous aluminum chloride and hydrochloric acid were analytical grade, which were purchased from Shanghai Chemical Reagent.

DF-101S collector-type thermostat heating magnetic stirrer(Zhengzhou Great Wall Branch Co,Henan,China.); Pore surface area analyzer Micromeritics,ASAP2010,USA);High Performance Liquid Chromatography (HPLC,ULTIMATE 3000, Thermo-Fisher, USA); Infrared spectrometer (IR, Bruker company Vertex 80 Switzerland).

The synthesis of adsorption resins

Fifteen grams of chloromethylcated styrenedivinylbenzene copolymer (CLPs) were dried at 333K in vacuum for 12 h, and then fully swollen in nitrobenzene at room temperature for 12h. After that, the mixture of the CLPs and nitrobenzene is heated to 353K while stirring, six grams atrazine and seven point five grams aluminum chloride were added to respectively the reaction system above and then the reaction was kept at this temperature for 8 h under a moderate mechanical stirring. The atrazine modified hypercrosslinked resin was obtained accordingly. After the reaction, the solid particles from the reaction mixture were filtrated. the atrazine modified hypercrosslinked resin was firstly rinsed by 1% hydrochloric acid (in ethanol) to remove unreacted nitrobenzene, followed by 10% sodium hydroxide solution, 5% hydrochloric acid and deionized water until neutral pH. Finally, the resin was extracted by ethanol for 8 h and dried under vacuum at 323 K for 8 h. Atrazine is replaced by o-Phthalic anhydride, trimellitic anhydride and 2-Imidazolidone hemihydrate respectively under the same conditions in order to obtain a series of hypercrosslinked adsorption resins (named KCZ-1, KCZ-2, FJ-1 and FJ-2) respectively. Synthetic process was shown in fig.1.

Characterization of adsorption resins

The pore structure of the resins such as specific surface area, microporous area, micropore volume and average pore radius were measured by BET(Bruaaures. S-Emmett H-Teller) method. The concentration of 4-Phenylphenol in aqueous solution was analyzed by HPLC. The IR spectra of the resin were determined by FT-IR spectrometer.

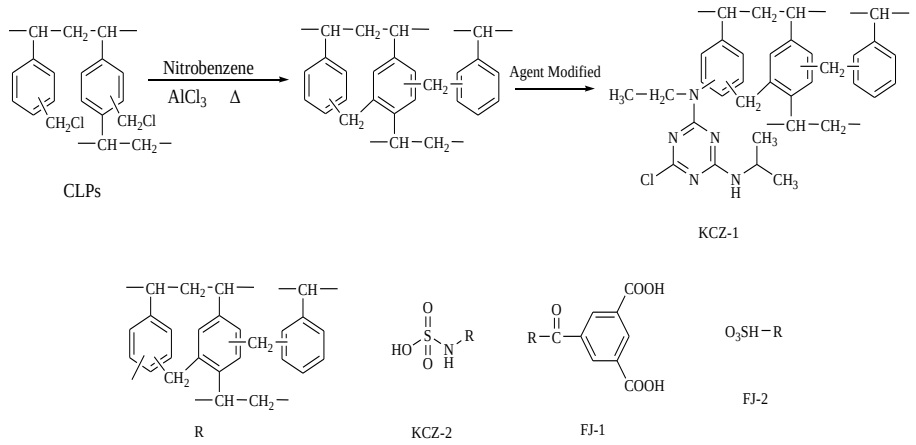

Fig.1. The synthetic procedure of modified resin

The Fourier transforms infrared spectroscopy (FT-IR) of adsorption resins were collected with a pellet of powdered potassium bromide and resin on a Vertex 80 infrared spectroscopy (FT-IR) of adsorption resins were collected with a pellet of powdered potassium bromide and resin on a Vertex 80 infrared spectrometer. Results were shown in Fig.2: The results show that the functional groups have been successfully modified. Surface property of resins was shown in Table 1.

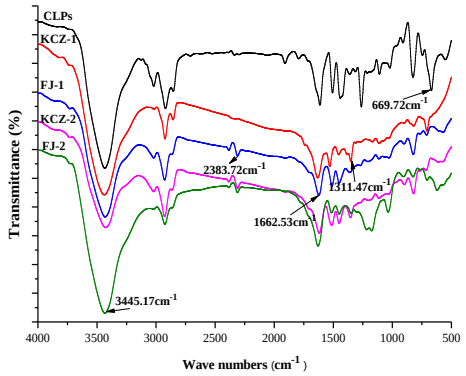

Fig. 2. IR spectra of resins and CLPS

Table. 1. Surface property of resins

Propertie	KCZ-1	KCZ-2	FJ-1	FJ-2
Specific surface area (m^2/ g)	743.9	761.0	804.7	768.5
Average pore radius (nm)	2.58	1.10	3.69	1.33
Microporous area (m^2/ g)	455.2	393.8	689.5	581
Microporous volume (mL/ g)	61.02	40.42	24.96	2.60

Adsorption isothermal experiment

Adsorption equilibrium data were determined by contacting about 0.1000 g of resin with 100 ml of 4-Phenylphenol aqueous solution. The nitial concentration of 4-Phenylphenol, C_0(mg/l), was set to be about 100, 200, 300, 400, 500 mg/l. Then the conical flasks having a series of different concentrations were shaken in a constant temperature oscillator for twenty four hours to reach equilibrium at speed of 110 rpm and temperature (288, 303, 313 and 288K*). After the adsorption equilibrium, 1.5ml adsorption equilibrium solution was withdrawn with the injector and the equilibrium concentration of 4-Phenylphenol, Ce(mg/l), was determined by HPLC. The equilibrium adsorption capacity of 4-Phenylphenol on the resin, Qe (mg/g), was calculated according to the following formula:

$$Qe = (C_0 - Ce)V/W \quad (1)$$

Where Ce is the equilibrium concentration of the adsorbate (mg/L), Qe is the equilibrium adsorption capacity (mg/g). C_0 is the initial concentration (mg/L), V is the solution volume (L), W is resins weight (g).

Dynamic adsorption and desorption

1BV(1BV=10mL, BV is the volume of resin bed) wet resins were packed in the glass column(16mm of diameter) to assembly a resin column at 288K. The initial concentration of 4-Phenylphenol was 400mg/L and passed through the resin column at a flow rate. The residual concentration of 4-Phenylphenol in the effluent from the resin column, C_1 (mg/L), was recorded until it almost reached the initial concentration. The effluents from the column were analyzed quantitatively. The concentrations of 4-Phenylphenol compounds were determined by

using HPLC. After the dynamic adsorption, ethanol (v/v) passed through the resin column for the desorption process, the effects of desorption temperature and desorption velocity on the desorption properties of the resin were investigated.

RESULTS AND DISCUSSION

Static equilibrium adsorption isotherm

The relationship curve of equilibrium adsorption capacity of the adsorbate on the adsorbent (Qe) and solution equilibrium concentration of the adsorbate (Ce) is called the adsorption isotherm at constant temperature. As shown in Fig.3, the equilibrium adsorption capacity of 4-Pheylphenol on the KCZ-1, KCZ-2, FJ-1, FJ-2 increases with the increment of equilibrium adsorption concentration. The overall adsorption capacity of 4-Phenylphenol on the KCZ-1, KCZ-2 and FJ-1 resins were better than that on FJ-2 resin at the same temperature and concentration, this was mainly because that the specific surface area of the FJ-2 resins was less than the other resins. The adsorption capacity of 4-Phenylphenol on the KCZ-1, KCZ-2, FJ-1 and FJ-2 resins increased with increasing temperature from 288K to 303K, which shows that the adsorption process is mainly chemical adsorption. Compared with those in 303K, the adsorption capacity of 4-Phenylphenol decreased when the temperature increased to 318K, which is mainly due to the increment of temperature continuously. Although it is beneficial to the chemical adsorption, the physical adsorption force decreased obviously. The adsorption increased capacity of the irreversible chemical action less than decreased adsorption capacity of physical adsorption. Therefore, the adsorption capacity of 4-Phenylphenol on the resins decreased. When the temperature dropped from 318K to 288K*, the adsorption capacity of 4-Phenylphenol was significantly higher than that of the adsorption capacity of 4-Phenylphenol on the resins at 288K.This also shows that the adsorption process does have a strong irreversible chemical adsorption.

The Langmuir equations for the equilibrium adsorption can be written as:

$$Ce/Qe = 1/(K_L \times Qm) + Ce/Qm \quad (3)$$

Where Qe is the equilibrium adsorption capacity (mg/g) with the equilibrium concentration Ce , Qm is the maximum monolayer adsorption capacity (mg/g) and K_L is a Langmuir constant related to adsorption energy (l/mg).

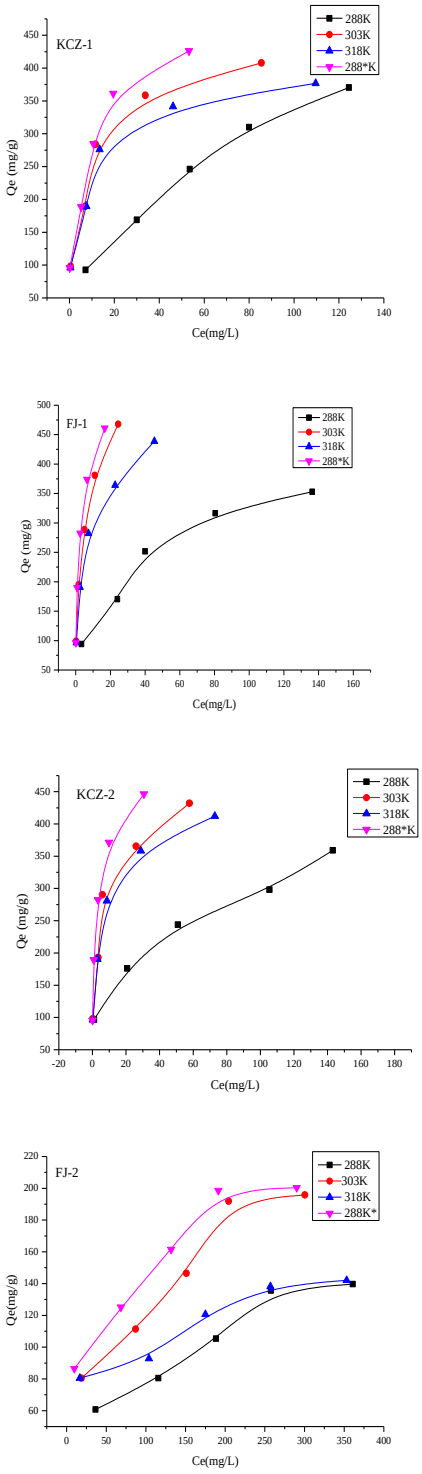

Fig.3. Equilibrium adsorption isotherms of 4-Phenylphenol on resins at different temperatures.

The Freundlich equations for the equilibrium adsorption can be written as:

$$\ln Qe = 1/n \ln Ce + \ln K_F \quad (4)$$

Where K_F [(mg/g)(l/mg)1/n] and n are the characteristic constants and they are temperature dependent. The parameter n is usually greater than

unity. As this value becomes larger, the adsorption isotherm becomes more nonlinear as its behavior deviates further away. When the n value is less than 1, it is non preferential adsorption; when the n value is more than 1, it is preferential adsorption; when the n value is 1, it is linear adsorption.

According to the research of Zhang Y *et al*, the adsorption data can be fitted by Langmuir and Freundlich equation, and the results were shown in Table.2 and Table.3.

Table.2. Fitting result of the Langmuir isotherm equation

Resins	T（K）	Ce/Qe= Ce/ Qm +1/(K_L•Qm)	R^2	Qm	KL*
	288	Ce/Qe=0.0022 Ce +0.0699	0.9952	454.5	0.0290
	303	Ce/Qe=0.0021 Ce +0.0283	0.9988	476.1	0.0811
KCZ-1	318	Ce/Qe=0.0026 Ce +0.0165	0.9991	384.6	0.247
	288*	Ce/Qe=0.0023 Ce +0.0045	0.9934	434.8	0.526
	288	Ce/Qe=0.0032 Ce +0.0304	0.9827	312.5	0.101
	303	Ce/Qe=0.0021 Ce +0.0181	0.9826	476.2	0.163
KCZ-2	318	Ce/Qe=0.0023 Ce +0.0104	0.9987	434.8	0.217
	288*	Ce/Qe=0.0022 Ce +0.0062	0.9966	454.5	0.530
	288	Ce/Qe=0.0031 Ce +0.0501	0.9826	322.6	0.0680
	303	Ce/Qe=0.0021 Ce +0.0204	0.9858	476.2	0.0922
FJ-1	318	Ce/Qe=0.0022 Ce +0.0103	0.9933	454.5	0.235
	288*	Ce/Qe=0.0021 Ce +0.0025	0.9910	479.2	0.834
	288	Ce/Qe=0.0054 Ce +0.3079	0.9921	185.2	0.0360
	303	Ce/Qe=0.0044 Ce +0.4017	0.9822	227.3	0.0100
FJ-2	318	Ce/Qe=0.0066 Ce +0.1807	0.9943	151.5	0.0360
	288*	Ce/Qe=0.0051Ce +0.1003	0.9726	196.1	0.0490

As shown in Table 2 and Table 3, the value of the correlation coefficient (R^2) in the Langmuir isotherm model is more than 0.98 for KCZ-1, KCZ-2, FJ-1, FJ-2 resins, which suggested that the Langmuir isotherm model was more suitable to fit the adsorption equilibrium data. The Langmuir is thermal adsorption equation is based on the homogeneous solid adsorbent surface, it is the single molecular layer adsorption. Moreover, for the FJ-1 resins, the R^2 in the Freundlich isotherm model and in the Langmuir isotherm model were all greater than 0.99, which suggested that the Langmuir isotherm model and Freundlich isotherm model can fit the experimental data well. In addition, for the KCZ-1, KCZ-2, FJ-1 and FJ-2 resins, the parameters n in Freundlich isotherm model at different temperatures were all greater than 1, which found the four kinds of resins are preferential adsorption for 4-Phenylphenol.

Table. 3. Fitting result of the Freundlich isotherm equation

Resins	T（K）	lnQe=1/nlnCe +lnK_F	R^2	n	KF*
	288	lnQe=04902lnCe +3.4962	0.9771	2.03	32.9
	303	lnQe=0.307lnCe +4.8028	0.9601	3.25	122
KCZ-1	318	lnQe=0.262lnCe +4.8033	0.9559	3.82	122
	288*	lnQe=0.2441lnCe +5.0610	0.9401	4.09	158
	288	lnQe=0.1592lnCe +4.5401	0.9293	6.28	93.7
	303	lnQe=0.2704lnCe +5.0172	0.9905	3.69	151
KCZ-2	318	lnQe=0.2903lnCe +5.0058	0.9779	3.44	149
	288*	lnQe=0.2792lnCe +5.3017	0.9902	3.58	200
	288	lnQe=0.3099lnCe +4.0972	0.9870	3.23	60.0
	303	lnQe=0.3399lnCe +5.1027	0.9982	2.94	164
FJ-1	318	lnQe=0.3148lnCe +5.0160	0.9906	3.18	157
	288*	lnQe=0.2939lnCe +5.3027	0.9970	3.40	201
	288	lnQe=0.4803lnCe +2.2901	0.9090	2.08	9.87
	303	lnQe=0.4002lnCe +3.2038	0.9027	2.49	24.6
FJ-2	318	lnQe=0.2008lnCe +3.7999	0.9750	4.98	44.7
	288*	lnQe=0.2592lnCe +4.0710	0.9017	3.85	58.6

Because the n value is larger, the adsorption performance is better. Moreover, the n value for KCZ-1, KCZ-2, FJ-1 is larger than that for FJ-2, indicating that the adsorption performance for 4-Phenylphenol on the KCZ-1, KCZ-2 and FJ-1 resins is better than that on the FJ-2 resins.

Adsorption thermodynamics

The enthalpy change of adsorption and the adsorption capacity are closely related, when the adsorption capacity is fixed at a constant value, the adsorption enthalpy change is known as the equivalent enthalpy change. The adsorption enthalpy change can be calculated by Clausius-Clapeyron equation:

$$\ln Ce = \Delta H/RT - \ln K \quad (5)$$

Where Ce is the equilibrium concentration of the adsorbate (mg/L). Here Ce was obtained from the fitted isotherms by the Langmuir equation at a defined qe. T is the absolute temperature (K), ΔH is the isosteric enthalpy change of adsorption (kJ/mol), R is the ideal gas constant (8.314 J/mol) and K is a constant. ΔH was determined by plotting lnCe versus 1/T and could be calculated from the slope of the fitting line.

Adsorption free energy can be calculated as:

$$\Delta G = -nRT \quad (6)$$

Where ΔG is the adsorption free energy (kJ/mol), n represents the Freundlich exponent and R is the ideal gas constant (8.314 J/mol K).

The adsorptive entropy change, ΔS(J/mol•k) were calculated using the Gibbs–Helmholtz equation:

$$\Delta S = (\Delta H - \Delta)G/T \quad (7)$$

As shown in Table.4, The value of ΔH were all positive indicating an endothermic process and 4-Phenylphenol is more easily adsorbed with temperature rising. The negative values of ΔG also indicated the adsorbate tends to adsorb from the solution to the surface of the adsorbent, suggesting the adsorption of 4-Phenylphenol on the KCZ-1, KCZ-2, FJ-1 and FJ-2 resin were spontaneous. Moreover, the absolute value of the free energy of adsorption increased with the rising of temperature, indicating that the trend of adsorption is much easier and rising of temperature was beneficial to adsorption. Positive values of ΔS showed the increasing randomness of the solid-solution interface during the adsorption of 4-Phenylphenol onto four kinds of resins. These positive values of ΔS might be due to the presence of the adsorbent surface chemisorption though degrees of freedom of adsorbate drop during the adsorption of 4-Phenylphenol. These results further show that exist irreversible chemical adsorption during the adsorption of 4-Phenylphenol on four kinds of resins.

Table.4. Thermodynamic parameters of 4-Phenylphenol adsorption based on resins at different temperatures

Resins	ΔH (KJ/mol)	ΔG(KJ/mol)			ΔS(J/mol·k)		
		288K	303K	318K	288K	303K	318K
KCZ-1	51.3	-4.272	-8.35	-10.2	189	200	199
KCZ-2	32.7	-15.1	-9.51	-9.27	169	138	136
FJ-1	53.6	-7.71	-7.38	-8.50	215	202	196
FJ-2	12.8	-5.04	-6.32	-12.9	63.4	63.7	85.0

Dynamic adsorption

Due to the satisfactory adsorption capacity for the 4-Phenylphenol compounds on resins in our research, it is hopeful for resins to be developed as a polymeric adsorbent for the removal of organic pollutants from drinking water or the recovery of organics from waste water. It is necessary to test the dynamic adsorption and desorption. 3 kinds of resins were selected for dynamic adsorption, which had been used in the above static adsorption. The concentration of each 5 BV effluent was determined respectively. Fig.4 shows the dynamic curve for the adsorption of 4-Phenylphenol on 3 kinds of resins. From the beginning of 25 BV, the concentrations of effluent liquid for 4-Phenylphenol onto three kinds of resins was increased rapidly and the slope of adsorption breakthrough curve is larger, indicating the adsorption rate in wastewater was faster. The concentrations of effluent liquid for 4-Phenylphenol on FJ-1 resin was lowest. Therefore, the efficiency of dynamic adsorption on FJ-1 resin is better than that on other resins.

Effect of desorption temperature on dynamic desorption

After the dynamic adsorption, the ethanol were used to desorb 4-Phenylphenol from FJ-1 resin column.at the flow rate of 0.5BV/h, Fig.5 shows dynamic desorption curves of 4-Phenylphenol onto FJ-1 at different temperature. The higher the temperature is, the greater the desorption efficiency is. When desorption temperature was 333K, nearly 75% regeneration efficiency for the adsorbent was

achieved. This is mainly due to the possibility of increasing the electrostatic force between the adsorbate and the FJ-1 resin at higher temperatures. Therefore, 333K is the best desorption temperature.

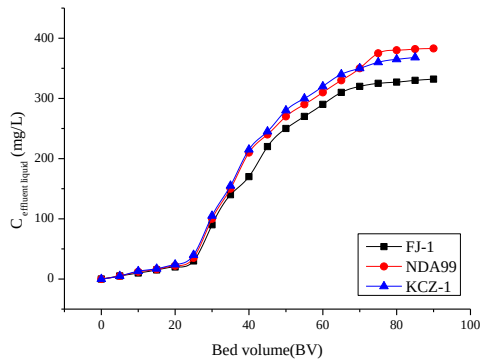

Fig. 4. Dynamic Adsorption Curves of 4-Phenylphenol in Water onto different Resins at 288K.

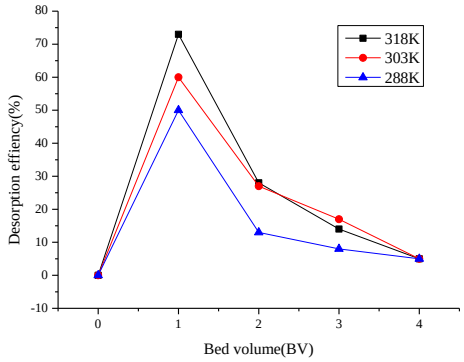

Fig.5. Dynamic Desorption Curves of methyl anthranilate onto FJ-1 at different temperature

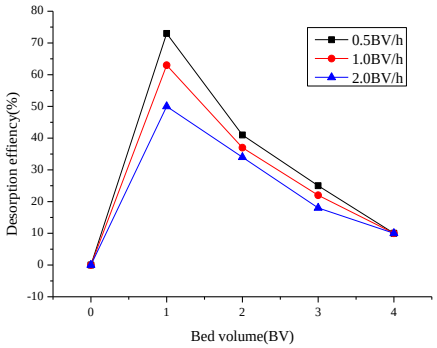

Fig.6. Dynamic Desorption Curves of methyl anthranilate onto FJ-1 at Different Flow Rate at 333K

Effect of desorption velocity on dynamic desorption

The ethanol were used to desorb 4-Phenylphenol from FJ-1 resin column.at 333k, Fig.6 shows dynamic desorption curves of 4-Phenylphenol onto FJ-1 from 0.5 BV/h to 2 BV/h.. When velocity desorption is 0.5BV/h, regeneration efficiency for the adsorbent is the largest. Therefore, 0.5BV/h is the best desorption velocity.

CONCLUSION

IR spectra of KCZ-1, KCZ-2, FJ-1and FJ-2 resins show that four kinds of hypercrosslinked adsorption resins were successfully prepared. The four resins have better adsorption properties. However, as shown in fig.3, at the same temperature and concentration, the adsorption capacity of 4-Phenylphenol on the KCZ-1, KCZ-2 and FJ-1 resins is better than FJ-2 resins, mainly due to modified functional groups and its specific surface area. As shown in Table.4, The value of ΔH was all positive indicating an endothermic process. 4-Phenylphenol is more easily adsorbed with temperature rising, ΔG shown that the adsorption of phenol on four kinds of resins was a feasible spontaneous endothermic process. ΔS showed the increasing randomness of the solid-solution interface during the adsorption of 4-Phenylphenol on resins. The Langmuir isotherm model can fit the adsorption process for the four resins well. However, Freundlich isotherm model also can fit the adsorption for the FJ-1 resins well. The efficiency of dynamic adsorption on FJ-1 resin is better than that on other resins. When temperature was 333K, nearly 75% regeneration efficiency for the adsorbent was achieved at the flow rate of 0.5BV/h.

Acknowledgment: *Zheng-hao Fei gratefully acknowledges Yancheng Teachers University and Analysis and Test Center because of their help to this work. This work was funded by the National Science Foundation (No. 21307103), Jiangsu Province Education Department Major Project (*17KJA610006*) and Jiangsu Provincial Technology Department (Grant Code BY2015058-03).*

REFERENCES

1. N. Kolbe, J.T. Andersson, *J. Agric. Food Chem*, **54**, 5736 (2006).
2. Y. Higashi*, Y. Fujii, *Journal of Analytical Chemistry*, **70**, 346 (2015).
3. M. De Boeck, B.van der Leede, K. De Vlieger, *Mutation Research*, **786–788**, 151 (2015).
4. M. Khalid, G. Joly, A. Renaud, P. Magnoux, *Industrial & Engineering Chemistry Research*, **43**, 5275 (2004).
5. G. Busca, S. Berardinelli, C. Resini, L. Arrighi, *Journal of Hazardous Materials*, **160**, 265 (2008).
6. B. Pourabbas, B. Jamshidi, *Chem. Eng. J*, **138**, 55 (2008).
7. J. Huang, X. Jin, J. Mao, *Journal of Hazardous Materials*, **217–218**, 406 (2012).

8. H.T. Li, M.C. Xu, Z.Q. Shi, B.L. He, *J. Colloid Interface Sci*, **271**, 47 (2004).
9. K. László, P. Podko´scielny, *Appl. Surf. Sci*, **252**, 5752 (2006).
10. A. Li, Q. Zhang, G. Zhang, J. Chen, Z. Fei, F. Liu, *Chemosphere*, **47**, 981 (2002).
11. A. Da˛browski, P. Podkos´cielny, Z. Hubicki, M.Barczak, *Chemosphere*, **58**, 1049 (2005).
12. A.L. He, J.H. Huang, C. Yan, J.B. Liu, L.B. Deng, K.L. Huang, *J. Hazard. Mate*r, **180**, 634 (2010).
13. A.C. Pan, W. Du, W.M. Zhang, X. Zhang, Q.R. Zhang, B.J. Pan, L. Lv, Q.X. Zhang,J.L. Chen, *Environ. Sci. Technol*, **41**, 5057 (2007).
14. M.P. Tsyurupa, V.A. Davankov, *React. Funct. Polym*, **66**, 768 (2006).
15. X. Wang, R. Deng, X. Jin, *Chemical Engineering Journal*, **191**, 195 (2012).
16. A.M. Li, Q.X. Zhang, G.C. Zhang, J.L. Chen, Z.H. Fei, F.Q. Liu, *Chemosphere*, **47**, 981 (2002).
17. V.A. Davankov, M.P. Tsyurupa, *React. Polym*, **13**, 27 (1990).
18. M.P. Tsyurupa, V.A. Davankov, *React. Funct. Polym*, **53**, 193 (2002).
19. X.H. Yuan, X.H. Li, E.B. Zhu, J. Hu, W.C. Sheng, S.S. Cao, *Carbohydr. Polym*, **74**, 468 (2008).
20. C.L. He, J.H. Huang, C. Yan, J.B. Liu, L.B. Deng, K.L. Huang, *J. Hazard. Mater*, **180**, 634 (2010).
21. C.G. Oh, J.H. Ahn, S.K. Ihm, *Funct. Polym*, **57**, 103 (2003).

АДСОРБЦИОННИ СВОЙСТВА НА 4-ФЕНИЛФЕНОЛ ВЪВ ВОДЕН РАЗТВОР С ХИМИЧЕСКИ МОДИФИЦИРАНА АДСОРБЦИОННА СМОЛА

Ц. Ке[1,2], Н. Уанг[1,2], В. Ли[2], У. Ши[2], З. Фей[*,2]

[1]Колеж по химия и химично инженерство, Технически университет в Нанджинг, Нанджинг, Китай
[2]Колеж по химия и химично инженерство, Университет за учители Янчен, Янчен, Китай

Постъпила на 23 май, 2016 г.; коригирана на 21 август, 2017 г.

(Резюме)

Приготвена е адсорбираща смола от атразин (KCZ-1), о-фталов анхидрид (KCZ-2), тримелитов анхидрид (FJ-1) и 2-имодазолидон (FJ-2) чрез успешно кръстосано свързване и химическа модификация. Смолата е охарактеризирана чрез IR-спектроскопия и BET-анализ. Структурното охарактеризиране показва, че смолата има предимно микропори/мезопори и умерена специфична повърхност. Адсорбционният капацитет на 4-фенилфенол върху четирите смоли е много голям поради взаимодействието чрез водородни връзки между 4-фенилфенола и модифицираните функционални групи на смолата. Адсорбционните отнасяния на 4-фенилфенола върху KCZ-1, KCZ-2, FJ-1 and FJ-2 са изследвани чрез адсорбционните изотерми и кинетиката на адсорбция. Освен това, адсорбционната термодинамика и кинетика са използвани за изучаването на механизъма на адсорбцията. Изотермите се корелират с уравненията на Лангмюир и Фройндлих, като изотермата на Лангмюир е по-подходяща. Изменението на енталпията ΔH е положително, а изменението на свободната енергия по Гибс ΔG и на ентропията ΔS са отрицателни. Ефективността на динамичната адсорбция върху смолата FJ-1 е по-добра, отколкото на останалите. При температура 333K почти 75% от адсорбента се възстановява при дебит 0.5BV/h.

Bulgarian Chemical Communications, Volume 49, Number 3, (pp. 643 – 651) 2017

Synthesis, *in vitro* antiproliferative and antimycobacterial activity of thiazolidine-2,4-dione and hydantoin derivatives

V.T. Angelova[1*], V. Valcheva[2], N. Vassilev[3], R. Buyukliev[1], R. Mihaylova[1], G. Momekov[1]

[1]*Faculty of Pharmacy, Medical University of Sofia, 2 Dunav Str., 1000 Sofia, Bulgaria;*
[2]*"Stefan Angelov" Institute of Microbiology, Bulgarian Academy of Sciences, 26 Acad. Bonchev Str., 1113 Sofia, Bulgaria;*
[3]*Institute of Organic Chemistry with Centre of Phytochemistry, Bulgarian Academy of Sciences, 9 Acad. Bonchev Str., 1113 Sofia, Bulgaria*

Received February 23, 2017; Revised April 27, 2017

New 2*H*-chromene derivatives bearing thiazolidine-2,4-dione or hydantoin moieties were synthesized and the structures were confirmed by ^{1}H NMR and ^{13}C NMR as well as 2D NMR, FTIR and HR-ESI-MS spectra. The compounds were evaluated for their *in vitro* cytotoxicity against four human cancer cell lines, namely HL-60 (acute promyelocyte leukemia), REH (lymphoid leukemia), K-562 (chronic myeloid leukemia) and EJ **(**urinary bladder carcinoma**)**. The 2*H*-chromene derivative containing thiazolidine-2,4-dione ring **5** was potent against a panel of three cancer cell lines, with an IC_{50} in the range of 13.1-39.6 μM and exhibited pronounced antiproliferative activity against lymphoid leukemia (REH cell line) with an IC_{50} value of 13.1 μM. The hydantoin containing 2*H*-chromene derivative **7** having an IC_{50} value of 83.7 μM was highly effective against chronic myeloid leukemia K-562. Compounds **5** and **7** also demonstrated significant antimycobacterial activity against *Mycobacterium tuberculosis* H37Rv strain with minimum inhibitory concentration (MIC) ranging from 0.29 and 0.36 μM, respectively.

Keywords: Antiproliferative/cytotoxic effects, Antimycobacterial activity, 2*H*-Chromene, Hydantoin, Thiazolidine-2,4-dione.

INTRODUCTION

The hydantoin (1,3-imidazolidinedione) derivatives [1] and thiazolidinediones (thiazolidine-2,4-diones) [2, 3] exhibit a plethora of biochemical and pharmacological activities. The thiazolidinediones (TZDs) have been characterized as a new dawn in cancer chemotherapy with a broad spectrum of cytotoxicity towards different human cancer cells [4, 5]. It is well known that TZDs exert their anti-diabetic effects through a mechanism that involves activation of PPARγ receptor. The wide spectrum of PPARγ activation effects may also be beneficial in the treatment of different types of cancer [6]. Thus, several new drugs such as efatutazone, netoglitazone, rosiglitazone and troglitazone (Fig. 1), exhibit their anticancer activity via PPARγ -dependent or -independent signaling pathways [7]. In the meantime, the antitumor effect of hydantoin derivatives has been reported by a number of authors (Fig. 1). Some of hydantoin derivatives, characterized by a 1-phenethyl and a 5-(*E*)-benzylidene substituent, inhibit EGFR autophosphorylation and polyGAT phosphorylation, as well as inhibit the growth and proliferation of human A431 cells, which overexpress EGFR [8] (Fig. 1). The hydantoin derivatives tested by Rajic *et al*., showed rather marked inhibitory activity against HeLa and MCF-7 cell lines, and no cytotoxic effects on normal cells [9]. The anti-cancer potential of 5-benzylidene-hydantoins demonstrating its relation to SIRT inhibition was proved by Lionel *et al*. [10]. Mudit *et al*., [11] described phenylmethylene hydantoins, as a novel antimetastatic lead class with the potential to control metastatic prostate cancer. The compounds synthesized by Reddy *et al.*, [12] contain an *N*-benzylindole nucleus linked to a hydantoin moiety *via* a double bond with Z-geometry were described as potential anticancer agents for the treatment of breast cancer. 5-(1*H*-indol-3-ylmethyl)-2-thiohydantoins and 5-(1*H*-indol-3-ylmethyl)hydantoins were found to be potent necrostatins [13]. In addition, (Z)-5-(4-hydroxybenzylidene)-imidazolidine-2,4-dione display moderate antiproliferative activity against the human cervical carcinoma (HeLa) cell line [14].

On the other hand, many studies have shown that azole heterocycles such as thiazolidine-2,4-dione and imidazolidine-2,4-dione are useful pharmacophores possessing antimycobacterial activity [15]. There have been reports on some thiazolidine-2,4-dione derivatives [16] and various imidazolidine-2,4-dione derivatives [17, 18], evaluated in the primary assay for antimycobacterial activity which exhibit

* To whom all correspondence should be sent:
E-mail:violina_stoyanova@abv.bg;
violina@pharmfac.net

remarkable growth inhibitory activity towards *M. Tubrculosis*. Also, 2-substituted 2*H*-chromenes have wide range of applications [19] as antimycobacterial [20] and antitumor agents [21], inclusive. Therefore, our hypothesis is that chromenyl thiazolidines and hydantoin derivatives might have a broad spectrum of pharmacological activities as well as selective cytotoxicity against cancer cell lines. Continuing the research on the biological activity of 2*H*-chromene derivatives, now we present the synthesis of compounds that comprise a 2*H*-chromene scaffold and thiazolidine-2,4-dione or imidazolidine-2,4-dione heterocyclic rings. Herein we also report on the *in vitro* screening against *M. Tuberculosis* H37Rv as well as antiproliferative/cytotoxic effects of the newly synthesized compounds in a panel of human tumor cell lines.

EXPERIMENTAL

General

The IR spectra were recorded on a Nicolet iS10 FT-IR Spectrometer from Thermo Scientific (USA) using an ATR technique. The NMR experiments on a Bruker Avance II+ 600 MHz NMR spectrometer in DMSO-d_6 allowed the assignment of the structures. The precise assignment of the ^{1}H and ^{13}C NMR spectra (resolved signals) was accomplished by measurements of 2D homonuclear correlation (COSY), DEPT-135 and 2D inverse detected heteronuclear (C–H) correlations (HMQC and HMBC) and NOESY. HR-ESI-MS spectra were recorded on an LTQ Orbitrap Discovery® spectrometer (ThermoFisher, Germany) equipped with electrospray ionization module Ion Max® (ThermoScientific, USA) operating in positive mode. The melting points were determined using a Buchi 535 apparatus. For TLC was used silica gel 60 GF254 Merck pre-coated aluminum sheets, eluted by hexane-chloroform-acetone 5:3:2 (vol. parts). All reagents were purchased from E. Merck (Darmstadt, Germany) and Aldrich (Milwaukee, MI, USA).

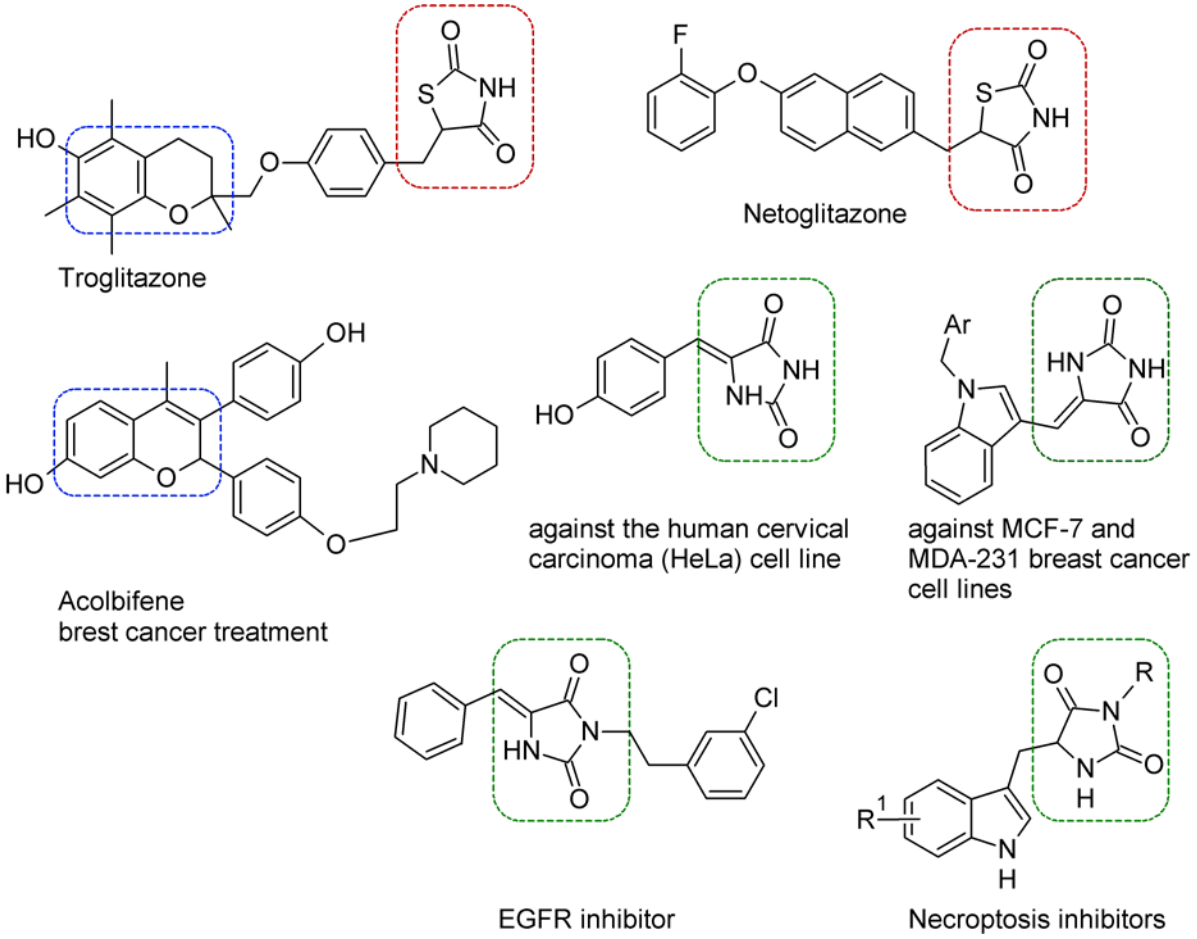

Fig. 1. Representative examples of 2*H*-chromene, thiazolidinedione and hydantoin derivatives with anticancer activity and rationale for the designed target compounds.

SYNTHESIS

2-Methyl-2H-chromene-3-carbaldehyde 3a was obtained according to the literature [20]. Yield 0.70 g (57 %), yellow oil. HRMS (ESI) *m/z*: Calcd. $[M+H]^+$ 175.0753; Found $[M+H]^+$ 175.07527.

2-Phenyl-2H-chromene-3-carbaldehyde 3b was synthesized according to the literature [23] with modifications. In a typical example, 3.19 ml (3.3 g, 25 mmol) cinnamaldehyde, 3.05 ml (3.05 g, 25 mmol) salicylaldehyde, benzoic acid (0.61 g, 5 mmol) and pyrrolidine (0.41 ml, 5 mmol) were dissolved in 100 ml toluene. The mixture was stirred vigorously at 25 oC for 20 hours. The reaction was monitored by thin layer chromatography. The solution was filtered and toluene evaporated on a rotary evaporator at elevated temperature. The residue was dissolved in 5 ml of $CHCl_3$ and 5 ml hexane, and filtered over 15 g silicagel with eluent hexane–EtOAc mixture 10:1. After eluent evaporation, yellow crystals of the final compound **3b** were obtained. Yield 60%, 3.36 g; yellow crystals; m.p. 75-77 °C; lit. m.p. (23) 75-76 °C. ^{1}HNMR (600 MHz, DMSO-d_6, ppm) δ: 6.257 (s, 1H, H-2), 6.86 (d, J = 8.2 Hz, 1H, H-9), 6.996 (dt, J = 1.1, 7.5 Hz, 1H, H-7), 7.28-7.31 (m, 5H, Ph), 7.324 (ddd, J = 1.6, 7.4, 8.2 Hz, 1H, H-8), 7.457 (dd, J = 1.6, 7.5 Hz, 1H, H-6), 7.879 (s, 1H, H-4), 9.673 (s, 1H, CHO). ^{13}CNMR (150 MHz, DMSO-d_6, ppm): δ 73.63 (C-2), 117.21 (C-9), 120.65 (C-5), 122.44 (C-7), 127.30 (o-Ph), 129.05 (m-Ph), 129.15 (p-Ph), 130.27 (C-6), 133.51 (C-3), 134.12 (C-8), 139.12 (i-Ph), 141.78 (C-4), 154.30 (C-10), 191.56 (CHO). HRMS(ESI) *m/z* found: 237.09076 $[M+H]^+$; calcd. for $C_{16}H_{13}O_2$: 237.091006 $[M+H]^+$.

(Z,s-cis)-5-[(2-Methyl-2H-chromen-3-yl)methylidene]-1,3-thiazolidine-2,4-dione 5. 1,3-Thiazolidine-2,4-dione **4** (3 mmol, 0.35 g) and 2-methyl-2H-chromene-3-carbaldehyde **3** (3 mmol, 0.52 g) were dissolved in abs. ethanol (15 ml). The solution was refluxed for 8 h in the presence of a small amount (0.2 ml) of piperidine as a catalyst. After completion of the reaction (monitored by TLC), the mixture was cooled, the precipitate was filtered and crystallized from ethanol to give the corresponding product as orange-red solid. Yield 0.330 g, (44 %); m.p. 214-215 °C. FTIR cm^{-1}: 3350, 1734, 1673, 1607, 1573**.** ^{1}H NMR (600 MHz, DMSO-d_6): δ (ppm) = 1.304 (d, J = 6.5 Hz, 3H, CH_3), 5.257 (q, J = 6.5 Hz, 1H, H-2), 6.858 (d, J = 8.0 Hz, 1H, H-5), 6.948 (dt, J = 1.0, 7.5 Hz, 1H, H-7), 7.037 (s, 1H, H-4), 7.23-7.26 (m, 1H, H-8), 7.270 (dd, J = 1.4, 7.6 Hz, 1H, H-6), 7.291 (s, 1H, CH H-vinylic), 12.599 (s, 1H, NH). ^{13}C NMR (150 MHz, DMSO-d_6): δ (ppm) = 19.93 (CH_3), 71.30 (C-2), 116.45 (C-9), 121.32 (C-S), 121.85 (C-7), 122.61 (C-5), 128.37 (C-8), 128.77 (CH), 130.41 (C-4), 131.59 (C-8), 131.93 (C-3), 151.68 (C-10), 167.22 (C=O), 167.49 (C=O). HRMS (ESI) *m/z*: Calcd. $[M+H]^+$ 274.05324; Found $[M+H]^+$: 274.05334.

5-[Hydroxy(2-phenyl-2H-1-benzopyran-3-yl)methyl]imidazolidine-2,4-dione 7. 2-Phenyl-*2H*-chromene-3-carbaldehyde **3b** (3 mmol, 0.71 g) and imidazolidine-2,4-dione **6** (3 mmol, 0.30 g) were dissolved in abs. ethanol (15 ml). The solution was refluxed for 48 h in the presence of a small amount of piperidine (0.2 ml) as a catalyst. The precipitate thus obtained was collected by filtration and washed with ethanol. Crystallization from methanol and ethyl acetate (1:1) afforded a yellow crystalline product. Yield 0.551 g (54 %); yellow solid; m.p.: 250-251 °C. FTIR cm^{-1}: 3227, 1731, 1653, 1603. ^{1}H NMR (600 MHz, DMSO-d_6): δ (ppm) = 4.200 (dd, J = 1.0, 2.3 Hz, 1H, CH-NH), 4.490 (d, J = 5.2 Hz, 1H, CHOH), 5.670 (d, J = 5.2 Hz, 1H, OH), 6.006 (s, 1H, H-2), 6.630-6.650 (m, 2H, H-9 + H-4), 6.800-6.830 (m, 1H, H-7), 7.020 (dt, J = 1.4, 7.7 Hz, 1H, H-8), 7.113 (dd, J = 1.4, 7.5 Hz, 1H, H-6), 7.220-7.280 (m, 3H, m-Ph + p-Ph), 7.372 (d, J = 6.8 Hz, 1H, o-Ph), 8.035 (s, 1H, CHN*H*), 10.539 (s, 1H, CONHCO). ^{13}C NMR (150 MHz, DMSO-d_6): δ (ppm) = 64.21 (CHNH), 71.67 (CHOH), 75.75 (C-2), 116.52 (C-9), 121.22 (C-4), 121.53 (C-7), 122.73 (C-5), 127.18 (C-6), 128.36 (o-Ph), 128.63(m-Ph + p-Ph), 129.60 (C-8), 134.45 (C-3), 139.58 (i-Ph), 151.95 (C-10), 158.10 (NHCONH), 173.61 (CONH). HRMS (ESI) *m/z*: Calcd. $[M+H]^+$ 337.118283; Found $[M+H]^+$ 337.11804.

PHARMACOLOGY

Antiproliferative activity. The study was conducted using a panel of cell lines, namely HL-60 (acute myeloid leukemia, established from the peripheral blood of a patient with acute promyelocyte leukemia), K-562 (chronic myeloid leukemia), REH (lymphoid leukemia) and EJ (human urinary bladder carcinoma). EJ cells (also designated MGH-U1) were originally isolated from a high grade (G3) invasive bladder carcinoma. These cell lines had been well validated in our laboratory as a proper test system for platinum agents. The EJ cell line was obtained from the unit of Toxicology and Chemotherapy at the Deutsches Krebsforschungszentrum. The other cell lines were obtained from DSMZ German Collection of Microorganisms and Cell Cultures.

The cell culture flasks and the 96-well microplates were obtained from NUNCLON (Denmark). The stock solutions of the tested compounds (10 mM) were freshly prepared in DMSO. The serial dilutions of the tested compounds were prepared immediately before use. After the final dilutions, the obtained concentrations of DMSO never exceeded 1%. Cytotoxicity of the compounds was assessed using the MTT [3-(4,5-dimethylthiazol-2-yl)-2,5-diphenyltetrazolium bromide] dye reduction assay as described by Mossman [24] with some modifications [25]. Exponentially growing cells were seeded in 96-well microplates (100 lL/well at a density of 3.5/105 cells/mL for the adherent and 1/105 cells/mL for the suspension cell lines) and allowed to grow for 24 h prior the exposure to the studied compounds. The cells were exposed to the tested agents for 72 h, whereby a set of 8 separate wells was used for each concentration. Every test was run in triplicate. After incubation with the tested compounds MTT solution (10 mg/mL in PBS) aliquots were added to each well. The plates were further incubated for 4 h at 37 C and the formazan crystals formed were dissolved by adding 110 lL of 5% HCOOH in 2-propanol. The MTT-formazan absorption was measured using a multimode microplate reader (Beckman Coulter DTX880) and the results were normalized as a percentage of the untreated control (set as 100% viable). The MTT-bioassay data were normalized as a percentage of the untreated control (set as 100 % viability), were fitted to sigmoidal dose response curves and the corresponding IC50 values (concentrations causing 50 % suppression of cellular viability) were calculated using non-linear regression analysis (Curve-fir; GraphPad Prism software for PC).

The cell lines were purchased from the DSMZ GmbH, (Braunschweig, Germany). They were cultured under standard conditions - RPMI-1640 medium supplemented with 10% fetal bovine serum (FBS) and 2 mM L-glutamine - in cell culture flasks housed at 37 °C in an incubator, BB16-Function Line‘ Heraeus (Kendro, Germany) with humidified atmosphere and 5 % of CO_2. The cell cultures were maintained in log phase by supplementation with fresh medium two or three times weekly.

Antimycobacterial activity. The antimycobacterial activity was determined towards reference strain *M. Tuberculosis* H37Rv through the proportional method of Canetti [26]. This method, recommended by WHO, is the one most used worldwide for exploration of sensitivity/resistance of tuberculosis strains towards chemotherapeutics. It allows precise determination of the proportion of mutants resistant to a certain drug. A sterile suspension/solution of the tested compound was added to Löwenstein-Jensen based medium before its coagulation (30 min at 85 °C). The compound was tested at four concentrations – 2 μg/ml, 0.2 μg/ml, 0.1 μg/ml and 0.05 μg/ml, (in DMSO). Tubes with Löwenstein-Jensen medium (5 ml) containing the tested compounds and those without them (controls) were inoculated with a suspension of *M. tuberculosis* H37Rv (105 cells/ml) and incubated for 45 days at 37 °C. The ratio between the number of colonies of *M. tuberculosis* grown in medium containing the compounds and the number of colonies in the control medium were calculated and expressed as a percentage of inhibition. The cell culture flasks and the 96-well microplates were obtained from NUNCLON (Denmark). The stock solutions of the tested compounds (10 mM) were freshly prepared in DMSO. The serial dilutions of the tested compounds were prepared immediately before use. After the final dilutions the obtained concentrations of DMSO never exceeded 1%. Cytotoxicity of the compounds was assessed using the MTT [3-(4,5-dimethylthiazol-2-yl)-2,5-diphenyltetrazolium bromide] dye reduction assay as described by Mossman [24] with some modifications [25]. Exponentially growing cells were seeded in 96-well microplates (100 lL/well at a density of 3.5/105 cells/ mL for the adherent and 1/105 cells/mL for the suspension cell lines) and allowed to grow for 24 h prior the exposure to the studied compounds. Cells were exposed to the tested agents for 72 h, whereby a set of 8 separate wells was used for each concentration. Every test was run in triplicate. After incubation with the tested compounds MTT solution (10 mg/mL in PBS) aliquots were added to each well. The plates were further incubated for 4 h at 37 C and the formazan crystals formed were dissolved by adding 110 μl solvent (5% HCOOH in 2-propanol). The MTT-formazan absorption was measured using a multimode microplate reader (Beckman Coulter DTX880) and the results were normalized as a percentage of the untreated control (set as 100% viable). The MTT-bioassay data were normalized as a percentage of the untreated control (set as 100 % viability), were fitted to sigmoidal dose response curves and the corresponding IC_{50} values (concentrations causing 50 % suppression of cellular viability) were calculated using non-linear regression analysis (Curve-fir; GraphPad Prism software for PC).

The MIC was defined as the minimum concentration of the compound required to inhibit bacterial growth completely (0% growth). The MIC values were calculated and given as μM. Ethambutol and isoniazid were used as controls.

RESULTS AND DISCUSSION

Synthesis. The synthetic route for preparing the compounds was illustrated in Schemes 1 and 2. 2*H*-Chromene derivatives **3a,b** were selected as starting compounds and were synthesized *via* Michael-aldol reaction, according to the known procedure [27] (Scheme 1). The reaction of 2-hydroxybenzaldehyde with α,β-unsaturated aldehydes under basic conditions afforded appropriate 2-substituted 2*H*-chromene-3-carbaldehyde **3a,b.** The preparation of 2-methyl-2*H*-chromene-3-carbaldehyde **3a** is conducted in 1,4-dioxane under reflux. For the synthesis 2-phenyl-2*H*-chromene-3-carbaldehyde **5** we used piperidine as a catalyst [23].

The new compound 5-[(2-methyl-2*H*-chromen-3-yl)methylidene]-1,3-thiazolidine-2,4-dione **5** was synthesized by Knoevenagel condensation of 2-methyl-2*H*-chromene-3-carbaldehyde **2a** and 1,3-thiazolidine-2,4-dione **3** (Scheme 2).

Several conditions were tested (sodium acetate in acetic acid, sodium acetate in DMF and piperidine in ethanol/methanol under thermal conditions) for the preparation of 2-methylchromene - derivative **5**, but the best result (a moderate yield of 44 %) was obtained by refluxing ethanol and in the presence of a catalytic amount of piperidine. As outlined in Scheme 2, when 2-phenyl-2*H*-chromene-3-carbaldehyde **5** reacted with hydantoin **6** under the selected

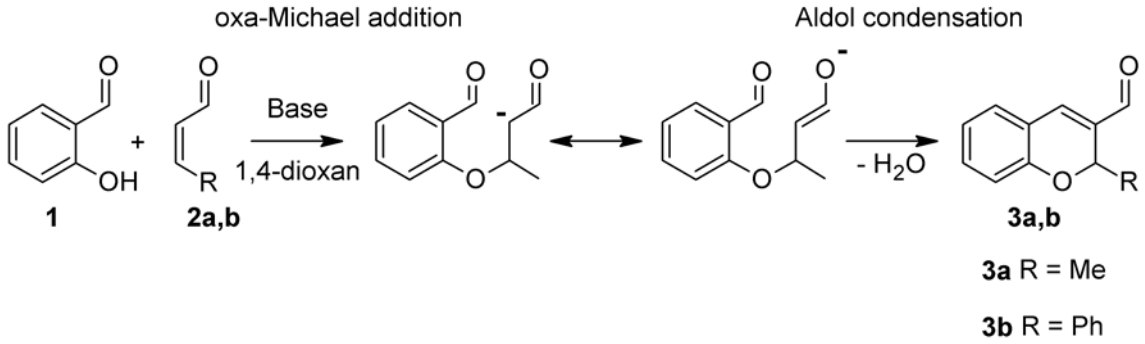

Scheme 1. Synthesis of 2-methyl-2*H*-chromene-3-carbaldehyde **3a** and 2-phenyl-2*H*-chromene-3-carbaldehyde **3b** through the domino oxa-Michael/aldol condensation reactions.

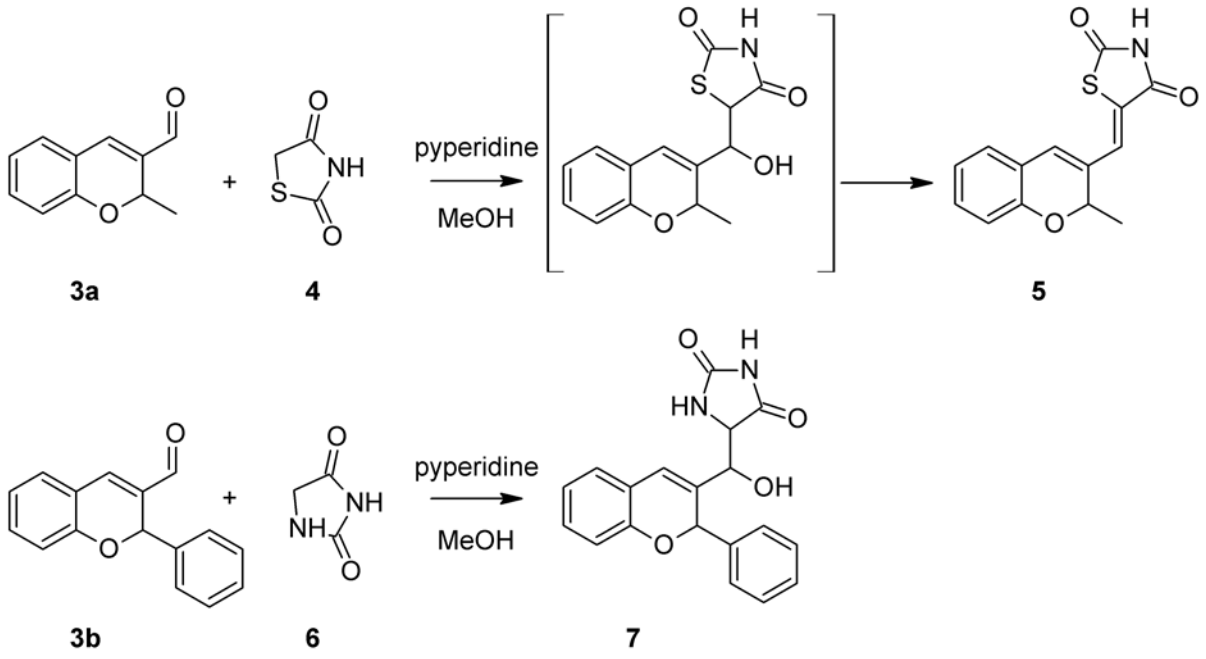

Scheme 2. Synthesis of 2-methylchromene derivative **5** and 2-phenylchromene derivative **7**.

conditions, dehydration did not occur and the final product is intermediate alcohol 5-[hydroxy(2-phenyl-2*H*-chromen-3-yl)methyl]imidazolidine-2,4-dione **7**. Our efforts to obtain a Knoevenagel product after the condensation reaction under the conditions described above failed and suggested that other factors might influence the reaction.

The structures of novel compounds **5** and **7** were proven by means of FTIR, ^{1}H, ^{13}C NMR and HR-ESI-MS spectral methods and were confirmed additionally by extensive two-dimensional (2D) NMR (COSY, multiplicity-edited HSQC, HMBC) and NOESY spectra. In the ^{1}H NMR in DMSO-d6 spectrum of product **5** the signal for CH_2 protons in thiazolidinedione ring is absent and in addition to the aromatic protons of chromene ring (6.858-7.291 ppm), a sharp singlet due to vinyl proton is observed at 7.291 ppm. The ^{13}C NMR spectrum of 2-methylchromene derivative **4** shows 13 signals. The signal for C-2 of chromene ring appears at 71.30 ppm, the vinyl proton resonates at 151.68 ppm and the signals for the carbonyl are observed at 167.22 and 167.49, respectively. Meanwhile, in the ^{1}H NMR spectra of 2-methylchromene derivative **5** only a set of signals occurs what confirms that only one stereoisomer *Z* has been obtained during the condensation. That is in agreement with the literature [27] and isomer *Z* appears to be more thermodynamically stable than isomers *E*. The NOESY spectrum (Fig. 2) shows a NOE effect and proximity between the vinyl proton and H-2; and between the vinyl proton and CH_3 protons. That proves the (*s*-*cis*)-conformation of the two conjugated double bonds. The described 2-methylchromene derivative **5** possessing a chiral center at C-2 position is a racemate.

In the ^{1}H NMR spectrum of product **7** in DMSO-d_6, there is no signal for CH_2 protons in the hydantoin ring. In addition to the aromatic protons of chromene ring (6.630-7.372 ppm), a doublet of doublets at 4.200 for CH-NH and a broad doublet at 4.490 (*J*=5.2 Hz) for CHOH are observed. A doublet at 5.670 for the hydroxyl group with the same coupling constant of 5.2 Hz is registered. The lack of a cross peak for this signal in HSQC spectrum for OH proton, indicates that there is not a carbon atom connected directly to it. Having localized the position of OH proton it is easy to assign the remaining protons from COSY spectrum. All carbon signals are assigned using HSQC and HMBC. The signal at 4.200 ppm is coupled by two small *J* constants (1.0 and 2.3 Hz). One of these constant is a *J* constant to the NH proton, the other is a gauche constant in the 4-substituted ethane structure. The infrared spectrum of 2-methylchromene derivative **5** shows a strong absorption at 1733 cm^{-1} and 1678 cm^{-1} corresponding to C=O functional groups, a band at 1607 cm^{-1} (C=C stretching in chromene ring) and 1573 cm^{-1}corresponding to C=C bond. The IR spectrum of compound **7** shows bands at 3227 cm^{-1} (NH stretching), 1731 and 1698 cm^{-1} (C=O functional groups) and 1603 cm^{-1} (C=C stretching in chromene ring). In addition, the novel structures are supported by a positive HR-ESI-MS spectrum which reveals a molecular ion peak at *m/z* 274.05334 $[M+H]^+$, (calcd. $[M+H]^+$ 274.05324) and 337.11804 $[M+H]^+$ (calcd. $[M+H]^+$ 337.118283) and allows confirming the molecular formulas, $C_{14}H_{11}NO_3S$ and $C_{19}H_{16}N_2O_4$, of compounds **5** and **7**, respectively.

Antiproliferative/cytotoxic effects. Table 1 summarizes the antiproliferative effects of 5-[(2-Methyl-2*H*-chromen-3-yl)methylidene]-1,3-thiazolidine-2,4-dione **5** and 5-[Hydroxy(2-phenyl-2H-1-benzopyran-3-yl)methyl]imidazolidine-2,4-dione **7** against a panel of four human tumor cell lines, namely HL-60 (acute promyelocyte leukemia), REH (lymphoid leukemia), K-562 (chronic myeloid leukemia) and EJ **(**urinary bladder carcinoma), using the alkylating agent melphalan as a reference anticancer drug.

The results of the *in vitro* cytotoxicity bioassay indicated that the compounds **5** and **7** exerted moderate to potent growth inhibition against the tested cancer cells with IC_{50} values of 13.1- 98 μM Compound **5** showed higher activity than compound **7** against HL-60, REH and EJ with the IC_{50} values of 39.6, 13.1 and 26.2 μM, respectively. As for the activity against chronic myeloid leukemia K-562, the highest cytotoxic activity was displayed by compound **7** with IC_{50} a value of 83.7 μM. Additionally, compound **5** was found to be more potent against REH tumor cell lines (IC_{50} = 13.1 μM) than Melphalan. REH cells were the most sensitive to the studied compounds and the potency of the most active compounds is similar to that of Melphalan. EJ cells seem to be the most resistant to compound **7**. However, compound **5** showed a relatively high antiproliferative potency toward EJ cells.

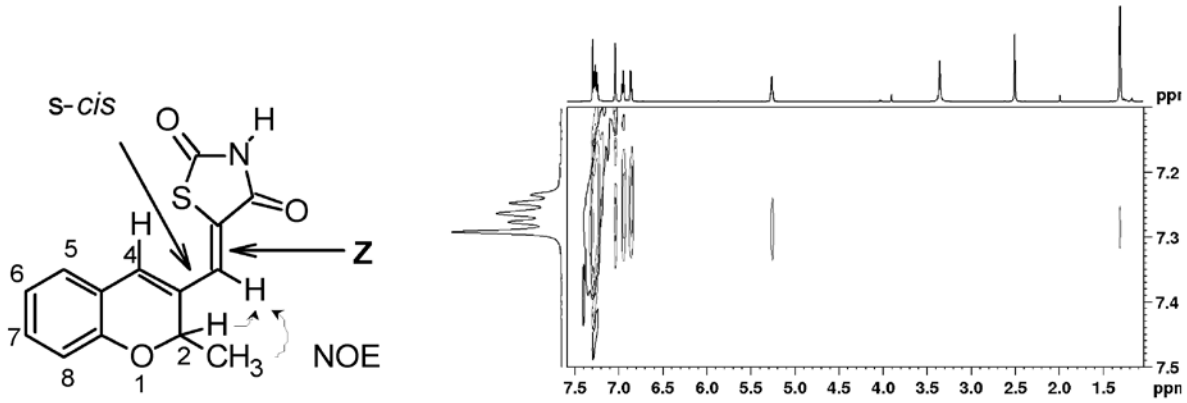

Fig. 2. Part of NOESY spectrum of 2-methylchromene derivative **5** showing the NOE effects between vinyl proton at 7.291 and 5.257 (H-2) ppm, and between 7.291 and 1.304 (CH_3) ppm, which confirms the (s-*cis*)-conformation.

Table 1. Cytotoxicity (IC_{50}) of the compounds **5** and **7** against different cell lines and antimycobacterial activity against reference strain *Mycobacterium tuberculosis* H37Rv.

Compd	Structure	IC_{50} (μM)[1]				MIC[6] (μM)
		HL-60[2]	K-562[3]	REH[4]	EJ[5]	
5	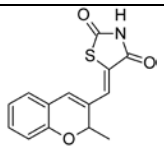	39.6 ± 2.7	98.0 ± 3.9	13.1 ± 2.4	26.2 ± 2.5	0.360
7	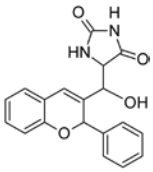	73.2 ± 4.8	83.7 ± 3.6	26.3 ± 2.8	117.5 ± 4.0	0.297
Melphalan[7]		11.2 ± 1.9	28.3 ± 3.2	14.6 ± 3.1	13.7 ± 1.9	-
EMB_2HCl[8]		-	-	-	-	1.45
INH[9]		-	-	-	-	0.64

[1]Means±sd from eight independent experiments. Cell line: [2]HL-60 (acute promyelocyte leukemia), [3]K-562 (chronic myeloid leukemia), [4]REH (lymphoid leukemia) and [5]EJ **(**urinary bladder carcinoma); [6]reference strain of *Mycobacterium tuberculosis* H37Rv, MIC (μM) was defined as the lowest concentration resulting in a complete inhibition of the bacterial growth and reproduction; [7]Melphalan - reference compound; [8]Isoniazid - reference compound and [9]EMB-2HCl (ethambutol dihydrochloride) - reference compound.

Antimycobacterial activity. The *in vitro* antimycobacterial activity of all compounds against *Mycobacterium tuberculosis* H37Rv reference strain was evaluated using the proportional method of Canetti and the resazurin microtiter assay. Ethambutol - EMB-2HCl (ethambutol dihydrochloride) and isoniazid were used as controls. The MIC is defined as the lowest concentration effecting the 100 % reduction in fluorescence, relative to controls. The data for the compounds **5** and **7** are shown in Table 1. The tested compounds exhibited significant antimycobacterial activity against the chosen strain, whereby the MIC values were within the nanomolar range, lower than those of ethambutol and INH.

CONCLUSION

New thiazolidine-2,4-dione and hydantoin derivatives were synthesized and their structures were elucidated on the basis of FTIR, ^{1}H NMR, ^{13}C NMR, 2D spectra (COSY, HMQC, HMBC) and HRMS data. The aldol product **5** was exclusively obtained in (Z)-configuration. The compounds **5** and **7**, were tested for cytotoxic activity with MTT-dye reduction assay against leukemia-derived HL-60 cells, REH, K-562, and urinary bladder

carcinoma cells (EJ). The tested compounds displayed promising micromolar antiproliferative activity. The most potent compound was 2*H*-chromene derivative **5** with IC_{50} values ranging from 13.1 - 0.98 μM. Also, the tested compounds **5** and **7** were found highly potent against the *M. tuberculosis* H37Rv, demonstrating a nanomolar activity (MICs ranging from 0.27 to 0.71 μM). The obtained results could be useful for the design and synthesis of new substituted 2,4-thiazolidindione with superior antiproliferative potency as potential anticancer agents. Taken together our data give the reason to consider 2,4-imidazolinone derivative **5** and hydantoin derivative **7** promising new leads for further exploration as potential antimycobacterial agents.

REFERENCES

1. A. Smarandache, V. Nastasa, M. Boni, A. Staicu, J. Handzlik, K. Kiec-Kononowicz, L. Amaral, M.-L. Pascu, *Physicochemical and Engineering Aspects*, **505**, 37 (2016).
2. A.A. Napoleon, *International Journal of PharmTech Research*, **9**(3), 429 (2016).
3. V.S. Jain, D.K. Vora, C.Ramaa, *Bioorganic & medicinal chemistry*, **21**(7), 1599 (2013).
4. H.L.T. Anh, N.T. Cuc, B.H. Tai, P.H. Yen, N.X. Nhiem, D.T. Thao, N.H.Nam, C.V. Minh, P.V. Kiem, Y.H. Kim, *Molecules*, **20**(1):1151 (2015).
5. R. Romagnoli, P.G. Baraldi, M.K. Salvador, M.E. Camacho, J. Balzarini, J. Bermejo, J. bermejo, F. Estevez, *European journal of medicinal chemistry*, **63**, 544 (2013).
6. K.A. Szychowski, M.L. Leja, D.V. Kaminskyy, U.E. Binduga, R. Pinyazhko, R.B. Lesyk, J. Gminski, *Chemico-Biological Interactions*, **262**, 46 (2017).
7. H. Joshi, T. Pal, C. Ramaa, *Expert opinion on investigational drugs*, **23**(4), 501 (2014).
8. C. Carmi, A. Cavazzoni, V. Zuliani, A. Lodola, F. Bordi, P.V. Plazzi, R.R. Alfieri, P.G. Petronini, M. Mor, *Bioorganic & medicinal chemistry letters*, **16**(15), 4021 (2006).
9. Z. Rajic, B. Zorc, S. Raic-Malic, K. Ester, M. Kralj, K. Pavelic, et al., *Molecules*, **11**(11), 837 (2006).
10. L. Sacconnay, L. Ryckewaert, G.M. Randazzo, C. Petit, C.D.S. Passos, J. Jachno, V. Michailoviene, A. Zubriene, D. Matulis, P.-A. Carrupt, C.A. Simoes-Pires, A. Nurisso, *European Journal of Pharmaceutical Sciences*, **85**, 59 (2016).
11. M. Mudit, M. Khanfar, A. Muralidharan, S. Thomas, G.V. Shah, R.W. van Soest, K.A. El Sayed, *Bioorganic & medicinal chemistry*, **17**(4), 1731 (2009).
12. Y.T. Reddy, P.N. Reddy, S. Koduru, C. Damodaran, P.A. Crooks, *Bioorganic & medicinal chemistry*, **18**(10), 3570 (2010).
13. 13. X. Teng, A. Degterev, P. Jagtap, X. Xing, S. Choi, R. Denu, J. Yuan, G.D. Cuny, *Bioorganic & medicinal chemistry letters*, **15**(22), 5039 (2005).
14. D.T. Youssef, L.A. Shaala, K.Z. Alshali, *Marine drugs*, **13**(11), 6609 (2015).
15. K. Ozadali, O.U. Tan, P. Yogeeswari, S. Dharmarajan, A. Balkan, *Bioorganic & medicinal chemistry letters*, **24**(7), 1695 (2014).
16. 16. F.M. Shaikh, N.B. Patel, G. Sanna, B. Busonera, P. La Colla, D.P. Rajani, *Medicinal Chemistry Research*, **24**(8), 3129 (2015).
17. D. Łażewska, P. Maludziński, E. Szymańska, K. Kieć-Kononowicz, *Biomedical Chromatography*, **21**(3), 291 (2007).
18. Y. Liu, W. Zhong, S. Li, *Chinese Chemical Letters*, **23**(2),133 (2012).
19. N. Thomas, S.M. Zachariah, *Asian J Pharm Clin Res.*, **6**(2), 11 (2013).
20. V.T. Angelova, V. Valcheva, N.G. Vassilev, R. Buyukliev, G. Momekov, I. Dimitrov, et al., *Bioorganic & Medicinal Chemistry Letters*, **27**(2), 223 (2017).
21. S. Rahmani-Nezhad, M. Safavi, M. Pordeli, S.K. Ardestani, L. Khosravani, Y. Pourshojaei, et al., *European journal of medicinal chemistry*, **86**, 562 (2014).
22. V.T.Angelova, N.G. Vassilev, B. Nikolova-Mladenova, J. Vitas, R.Malbaša, G. Momekov, L. Saso, *Medicinal Chemistry Research*, **25**(9), 2082 (2016).
23. I. Ibrahem, H. Sundén, R. Rios, G-L. Zhao, A. Córdova, *CHIMIA International Journal for Chemistry*, **61**(5), 219 (2007).
24. T. Mosmann, *Journal of immunological methods*, **65**(1-2), 55 (1983).
25. S.M. Konstantinov, H. Eibl, M.R. Berger, *British Journal of Haematology*, **107**(2), 365 (1999).
26. G. Canetti, W. Fox, A. Khomenko, H. Mahler, N. Menon, D. Mitchison, et al., *Bulletin of the World Health Organization*, **41**(1), 21 (1969).
27. M. Azizmohammadi, M. Khoobi, A. Ramazani, S. Emami, A. Zarrin, O. Firuzi, et al., *European journal of medicinal chemistry*, **59**, 15 (2013).

СИНТЕЗ, *in vitro* АНТИПРОЛИФЕРАТИВНА И АНТИМИКОБАКТЕРИАЛНА АКТИВНОСТ НА ТИАЗОЛИДИН-2,4-ДИОН И ХИДАНТОИНОВИ ПРОИЗВОДНИ

В. Т. Ангелова[1,*], В. Вълчева [2], Н. Василев[3], Р. Буюклиев[1], Р. Михайлова[1], Г. Момеков[1]

[1]Фармацевтичен факултет, Медицински университет София, ул. Дунав 2, 1000 София, България;
[2]Институт по микробиология "Стефан Ангелов", Българска академия на науките, ул. Акад. Бончев 26, 1113 София, България;
[3]Институт по органична химия с Център по фитохимия, Българска академия на науките, ул. Акад. Бончев 9, 1113 София, България

Получена на 23 февруари 2017 г.; приета на 27 април 2017 г.

(Резюме)

Синтезирани са нови 2*H*-хроменови производни, съдържащи тиазолидин-2,4-дионов и хидантоинов фрагменти и структурата им е потвърдена чрез ^{1}H NMR, ^{13}C NMR, 2D NMR, FTIR спектрални методи и HR-ESI-MS. Съединенията са изследвани *ин витро* за цитотоксичната им активност срещу четири човешки туморни клетъчни линии - HL-60 (остра промиелоцитна левкемия), REH (лимфоидна левкемия), K-562 (хронична миелоидна левкемия) и EJ (карцином на пикочния мехур). 2*H*-Хромен съдържащият тиазолидин-2,4-дион **5** е мого активен срещу три ракови клетъчни линии, с IC_{50} от порядъка на 13.1-39.6 μM и показва най-изразена антипролиферативна активност срещу лимфоидна левкемия (клетъчна линия REH) със стойност на IC_{50} = 13.1 μM. Хидантоин съдържащото 2*H*-хроменово производно **7** е високо най-ефективно срещу хронична миелоидна левкемия K-562 със стойност на IC_{50} = 83.7 μM. Съединенията **5** и **7** демонстрират също и значителна антимикобактериална активност срещу *Mycobacterium tuberculosis* H37Rv с минимална инхибираща концентрация (MIC) в диапазона от 0.29 и 0.36 μM, съответно.

Bulgarian Chemical Communications, Volume 49, Number 3, (pp. 652 – 657) 2017

Photocatalytic ability of abiotic and biotic materials for discoloration of Malachite Green and Reactive Black 5 dyes

K.L. Zaharieva[1]*, K.I. Milenova[1], M.G. Shopska[1], M.P. Tsvetkov[2], A.E. Eliyas[1], G.B. Kadinov[1]

[1]*Institute of Catalysis, Bulgarian Academy of Sciences, Acad. G. Bonchev St., bl. 11, 1113 Sofia, Bulgaria*
[2]*Institute of Physical Chemistry, Bulgarian Academy of Sciences, Acad. G. Bonchev St., Bl. 11, 1113 Sofia, Bulgaria*

Received April 14, 2016; Revised December 20, 2016

The photocatalytic properties of nanodimensional abiotic (AR) and biotic iron-containing materials produced, respectively, in sterile and infected by *Leptothrix* genus of bacteria medium of Lieske and goethite (AS), synthesized by precipitation and sonication were tested in the reaction of discoloration of Malachite Green (MG) and Reactive Black 5 (RB5) dyes as model pollutants in aqueous solutions under UV-light illumination. IR spectroscopy and powder X-ray diffraction analysis confirmed the presence of α-FeOOH and γ-FeOOH phases in the biotic material. Only goethite was registered in the abiotic materials (AS and AR). The synthesized goethite demonstrated the highest photocatalytic activity for discoloration of Malachite Green (MG) and Reactive Black 5 (RB5). The biotic material was more efficient as photocatalyst for discoloration of MG than RB5.

Keywords: photocatalysts, goethite, lepidocrocite, biogenic material, Malachite Green, Reactive Black 5.

INTRODUCTION

Lot of microorganisms possesses the ability to change the oxidation state of metals and the process can be used for various applications. For example some microorganisms like *Leptothrix sp*. and *Galionella sp*. have been established to participate in Fe oxidation [1] giving rise to various iron oxides and hydroxides. The latter are widespread in the nature and as solid catalysts they affect the environment, including the biosphere, atmosphere, lithosphere, and hydrosphere. For this reason, the application of iron transforming organisms has been studied in a number of scientific disciplines, ranging from medicine, biology, and environmental chemistry to industrial chemical technology [2]. The water pollution by industrial hazardous waste is important problem related to environment protection [3]. Photocatalytic technology is environmentally friendly since it utilizes irradiation energy for the catalytic reactions and is widely investigated for elimination of pollutants [4]. The photocatalytic properties of iron oxide materials [5-7] and hydrolytic Fe (III) species [8] are discussed in the literature. S. Rahim Pouran *et al.* concluded in a review paper that heterogeneous catalysts (iron oxides) showed significant improvements in Fenton reactions for elimination of pollutants from contaminated medium due to their higher activity in a wide range of pH values in contrast to soluble iron salts [9]. Iron nanoparticles containing mainly iron oxide and iron oxyhydroxide have been prepared using extracts of green tea leaves and showed as Fenton-like catalyst high ability for degradation of Methylene Blue and Methyl Orange [10]. B. Ahmmad *et al*. have investigated the photocatalytic activity of mesoporous α-Fe_2O_3 nanoparticles synthesized by an extract of green tea leaves [11]. *Amaranthus dubius* and sodium borohydride mediated iron nanoparticles were tested about discoloration efficiency for Methyl Orange and as antioxidant for 1,1-diphenyl-2-picrylhydrazyl [12]. The biogenic jarosite is found to be an efficient catalyst for decolorization of Reactive Blue 19 (98%) in Fenton-like reaction [13]. The photocatalytic activity of goethite (α-FeOOH) in degradation of different organic pollutants as Methyl Orange [14], Methylene Blue [4], C.I. Acid Orange 7 [15], Rhodamine B [16], Rhodamine 6G [17], salicylate and oxalate [18], benzo[a]pyrene [19] has been investigated. The photo-Fenton degradation of Orange-II and 2,4-dichlorophenol [20], Mordant Yellow 10 [21,22], Methyl Orange [23] using α-FeOOH as photo-catalyst was studied by a number researchers. The photocatalytic properties of the α-FeOOH/oxalate system for degradation of Rhodamine B under irradiation using high-pressure Hg-lamp (wave-length range from 200 to 700 nm, the main - 365 nm) with different light intensity were investigated by Chen *et al*. [24]. Li *et al*. have used a heterogeneous Fenton-like system α-FeOOH/H_2O_2 for the degradation of *p*-chloronitrobenzene in water [25]. Zhang *et al*. have determined that α-FeOOH nanorods possess excellent adsorption properties for Congo Red dye [26]. The photo-decolorization of Crystal Violet with visible light

* To whom all correspondence should be sent:
E-mail: zaharieva@ic.bas.bg

was studied in a system consisting of lepidocrocite and H_2O_2 [27]. Chen *et al*. have determined that the synthesized low-crystalline lepidocrocite samples possess large specific surface areas and demonstrated high photocatalytic and adsorption activity in the photodegradation of Orange II [28]. Porous network-like FeOOH/carbonized bacterial cellulose has been found to be an effective adsorbent for the removal of Methyl Orange from aqueous solution [29]. Various precipitation procedures using different iron containing compounds - $Fe(NO_3)_3$•$9H_2O$, $FeCl_3$•$6H_2O$ and precipitating agents - NaOH, KOH or tetramethylammonium hydroxide are presented in the literature for the preparation of goethite [30-34]. The such modified precipitation procedure was used for obtaining of abiotic α-FeOOH in this study.

The goal of the present work was to study the photocatalytic properties of abiotic and biotic iron-containing materials (prepared in sterile and infected by *Leptothrix* genus of bacteria medium of Lieske, respectively), and synthesized goethite for the photocatalytic discoloration under UV-irradiation of two dyes as model contaminant - Malachite Green (MG) and Reactive Black 5 (RB5). The physicochemical properties of abiotic and biotic samples were studied by powder X-ray diffraction analysis (PXRD), infrared (IR) spectroscopy and adsorption using single point BET method.

EXPERIMENTAL

Preparation and physicochemical characterization

The biotic iron-containing material was obtained by cultivation of *Leptothrix* genus bacteria in Lieske medium. The abiotic material (AR) was prepared in a sterile Lieske medium (containing $FeSO_4$, iron grits, $MgSO_4.7H_2O$ traces, $Mg(HCO_3)_2$ saturated solution 1:10, K_2HPO_4 traces, distilled water) not infected by bacteria as a reference product for a pure chemical reaction. Both materials were supplied by Prof. V. Groudeva, Dr. M. Iliev and coworkers from the Faculty of Biology at St. Kliment Ohridski University. The preparation procedure is described in [35]. Another abiotic compound (AS) was synthesized by precipitation using 0.35M aqueous solution of $Fe(NO_3)_3$•$9H_2O$ (Alfa Aesar) and 3.6M NaOH (Valerus Co.). The precipitating agent (NaOH) was dropwise added under continuous stirring until pH = 14 was reached. After precipitation the suspension was stirred for one hour. The precipitate was left to age, centrifuged and washed with distilled water until neutral reaction (pH = 7). The obtained material was sonicated in distilled water for 4 minutes.

The phase composition, structure and specific surface area of the samples were investigated by powder X-ray analysis, infrared spectroscopy and Brunauer-Emmet-Teller (BET) method. The powder X-ray diffraction analysis was performed on a PANalytical Empyrean apparatus equipped with a multichannel detector (Pixel 3D) within the range of 2θ values between 7º and 110º using Cu K_α radiation (λ = 0.154056 nm) at 40 kV, 40 mA. The present phases were identified by using of JCPDS database (Powder Diffraction Files, Joint Committee on Powder Diffraction Standards, Philadelphia PA, USA, 1997). Infrared spectra (IR) of the samples were recorded on a Nicolet 6700 FTIR spectrometer (Thermo Electron Corporation, USA) using the method of dilution of studied material in KBr pellet (0.5% of the studied substance). The spectra were collected in the middle IR region using 50 scans at a resolution of 4 (data spacing 1.928 cm^{-1}). The specific surface area of the materials was studied in a conventional volumetric apparatus Micromeritics FlowSorb II 2300 (USA) applying single point BET method and using nitrogen adsorption from a mixture 30% N_2+70% He at the boiling temperature of liquid nitrogen (77.4 K). Before measuring the specific surface area the samples were degassed at 423 K for 30 min to liberate the entire surface from adsorbed impurities until the residual pressure became lower than 1.333×10^{-2} Pa. The nitrogen (N_2) monolayer formed was used to evaluate the specific surface area (A_{BET}) using the BET equation, whereupon He was the carrier-gas.

Photocatalytic tests

The photocatalytic efficiency of abiotic, biotic and synthetic iron-containing materials was tested in the reactions of discoloring of Malachite Green (MG) and Reactive Black 5 (RB5) dyes in aqueous solution under UV-A polychromatic illumination (18 W with maximal emission at 365 nm) and illumination intensity 0.66 mW/cm^2. The change of absorbance during the photocatalytic reaction was monitored by UV-1600PC Spectrophotometer in the wavelength range from 200 to 800 nm, observing especially the wavelength maximum of absorbance at λ_{max} = 615 nm for MG and λ_{max} = 599 nm for RB5. The absorbance signal was calibrated by a series of solutions of known concentration. The initial concentration of RB5 and MG dyes in the used 150 ml aqueous solutions was 20 ppm and 10 ppm, respectively, falling within the linear range of absorbance dependence up to 100 ppm. The

fixed amount of the tested photocatalysts, charged in the photocatalytic reactor, was 0.12 g. A semi-batch slurry photocatalytic reactor was used continuously feeding air flow creating large excess of O_2 compared to stoichiometry. All photocatalytic measurements were carried out at a constant stirring rate (400 rpm) under ambient conditions. The tested systems were left to reach equilibrium state (established spectrophotometrically) in the dark for about 30 min before switching on the UV irradiation. The measurement of the photocatalytic conversion degree over abiotic and biotic samples was carried out by taking aliquot samples of the suspension out of the reaction vessel after regular time intervals. The powder was then separated from the aliquot solution by centrifugation before the UV–Vis spectrophotometrical measurements. After that, the aliquot solution, together with the photocatalyst powder, were returned back quantitatively into the reaction vessel, which ensured the operation under constant volume and constant catalyst amount.

RESULTS AND DISCUSSION

The powder X-ray diffraction analysis registered the presence of goethite phase (PDF-81-0464) both in recorded patterns of abiotic AR and AS samples. The biotic material contained goethite (α-FeOOH) (PDF-81-0464) and lepidocrocite (γ-FeOOH) (PDF-74-1877) phases (Figure 1).

The determined mean crystallite sizes, lattice microstrain parameters and unit cell parameters of investigated abiotic and biotic materials using PowderCell 2.4 program [36] are presented in Table 1. The results established that the nanosized goethite phase had average crystallite size of about 10-12 nm for the abiotic and biotic samples. The mean crystallite size of lepidocrocite phase in the biotic material was calculated to be about 25 nm.

Figure 2 shows infrared spectra of the studied samples. A set of α-FeOOH characteristic bands (619, 667, 796, 877, and about 3200 cm^{-1}) is present in all samples [23, 37-39]. The bands at 459, 1024 and 1115 cm^{-1} in the biogenic material spectrum show, also, presence of biogenic lepidocrocite (γ-FeOOH) [40,41]. The increased absorbance level in the interval 980–1200 cm^{-1} is assigned to the presence of phosphate residual from the feeding medium (phosphates are characterized by three bands of middle intensity in this region) [42]. In all spectra the occurrence of carbonates is registered by the bands positioned at around 1500, 1440, 1460 cm^{-1} [42,43], which are either result of the preparation procedures or carbonization during contact with air. Common features of the spectra are the bands characteristic of physically adsorbed water (1639 cm^{-1}), hydroxyl coverage of the surface (3415 cm^{-1}) and hydrocarbons (2850, 2923 and 2958 cm^{-1}) [33,40].

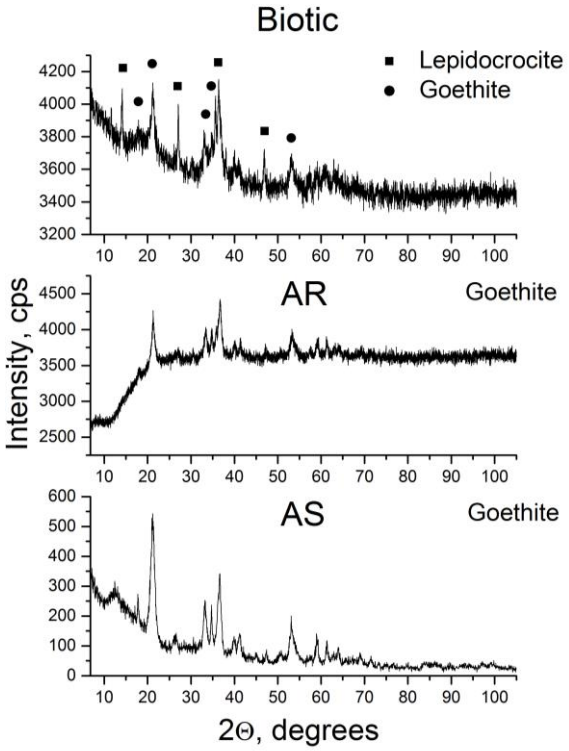

Fig. 1. PXRD patterns of biotic and abiotic Fe-containing materials.

The specific surface area measurements, listed in Table 2, determined that the biogenic material possessed the highest specific surface area (S_{BET} = 123 m^2/g). The abiotic sample (AR) formed in Lieske medium possessed the lowest dispersion (lowest S_{BET} = 68 m^2/g, respectively).

Table 1. Average crystallite size (D), lattice strain (ε) and unite cell parameter (a) of abiotic and biotic Fe-containing materials.

Material	Phase	Content, %	D, nm	ε, a.u	a, Å
Abiotic (AS)	goethite	100	10	2×10^{-3}	4.637
Abiotic (AR)	goethite	100	12	2.4×10^{-3}	4.634
Biotic	goethite	48.1	12	2.2×10^{-3}	4.613
	lepidocrocite	51.9	25	1.9×10^{-3}	3.867

Table 2. Specific surface area of biotic and abiotic Fe-containing materials.

Material	S_{BET} (m^2/g)
Biotic	123
Abiotic (AS)	109
Abiotic (AR)	68

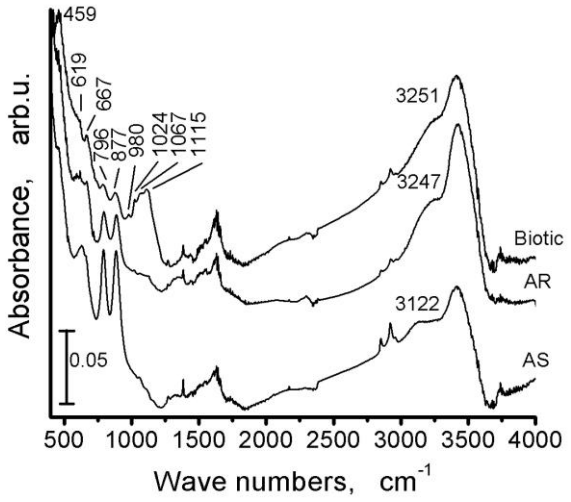

Fig. 2. IR spectra of biotic and abiotic Fe-containing materials.

The photocatalytic activity was evaluated based on the changes in dye concentration (according to the callibrated values of the absorbance peak maximum at 599 nm for RB5 dye and at 615 nm for MG dye) with the time interval of UV irradiation and correlated with the surface area of the catalyst. The results are displayed as change of the relative efficiency ($(C/C_0)/(S_{BET}.m)$, $1/m^2$) in Figure 3.

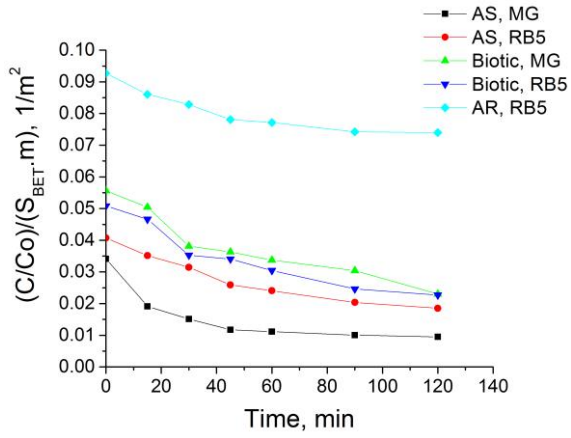

Fig. 3. Photocatalytic efficiency of biotic and abiotic Fe-containing materials in Malachite Green and Reactive Black 5 dyes discoloration under UV-irradiation (concentration changes of dyes related to the surface area of the catalysts).

The different starting points for the catalytic curves in Figure 3 are due to the different adsorption capacities since at the same initial concentrations (C_0) of the RB5 and MG dyes (20 ppm and 10 ppm), respectively, the photocatalytic reactor was charged with the same amount of the catalysts with different specific surface area. The adsorption capacities by mass (mg-dye/g-catalyst) were calculated after 30 min adsorption time in the dark performed to allow establishing the adsorption-desorption equilibrium (see Table 3) by the equation:

$$Q = \frac{(C_0 - C).V}{m} \quad (1)$$

where C_0 and C are the initial and after 30 minutes in the dark concentrations of the dye, V is the solution volume and m is the mass of the catalyst.

The synthesized abiotic goethite demonstrated the highest adsorption capacity (by mass) compared to the other investigated materials (about 0.291 mg/g for MG and 0.241 mg/g for RB5) (Table 3).

Table 3. Adsorptions capacities of abiotic and biotic samples.

Material	Used dye	Adsorption capacity (mg/g)
Abiotic (AS)	MG	0.291
Abiotic (AS)	RB 5	0.241
Biotic	RB 5	0.129
Abiotic (AR)	RB 5	0.126
Biotic	MG	0.102

The biotic sample showed almost the same adsorption capacity (by mass) for RB5 dye (0.129 mg/g) compared to the abiotic (AR) one (0.126 mg/g) despite almost twice higher specific surface area. This unexpected tendency is also seen comparing the adsorption capacity (by mass) to the dyes of abiotic (AS) and biotic materials. At the present state of research we suppose that the procedure of preparation both of biotic and abiotic (AR) materials could result in strongly adsorbed on the surface one or more components of the medium including substances resulting from the life activity of the bacteria. No specific operations to clear the surface have been applied except washing the material with distilled water and drying at room temperature.

Highest degree of photocatalytic discoloration of both MG and RB 5 dyes was achieved in the presence of abiotic synthesized goethite (AS). However, complete discoloration was not obtained with any of the studied materials. All of them did not demonstrate photocatalytic activity after about 100 min of UV-irradiation. In the course of the photocatalytic reaction of oxidative discoloration of RB5 dye the abiotic material demonstrated very low photocatalytic efficiency. As it can be seen the biotic sample has lower photocatalytic efficiency compared with the synthesized goethite in the

discoloration of MG and RB5. These results are in accordance with the proposed above explanation that significant part of the surface of biogenic material have been blocked by compounds formed during the bacterial life cycle and/or some components of Lieske medium. In addition, it is reasonably to suppose that in the blocking of active sites on the surface take part the molecules of dyes so as the rests of them after destruction of the respective chromophore groups (intermediates of the dye oxidation). Comparing the photocatalytic activity of biotic and abiotic materials formed in Lieske medium (Fig. 3, curves Biotic RB5 and AR RB5) a conclusion could be derived that the adsorption of some Lieske medium components has, evidently, significant effect on the decrease of catalytic activity.

CONCLUSIONS

The studied photocatalytic properties of nanosized abiotic and biogenic materials during the reaction of discoloration of MG and RB5 dyes as model contaminants in aqueous solutions under UV-light revealed strong adsorption of both dyes on the surface of the catalysts. The dominant photocatalytic ability of synthesized goethite for removing of the two tested dyes was established. The biogenic material is more efficient as photocatalyst for discoloration of RB5 dye compared with abiotic sample formed in the same Lieske medium. The existence of goethite (α-FeOOH) with average crystallite size about 10-12 nm in investigated materials and also lepidocrocite (γ-FeOOH) phase in the biotic sample with average crystallite size about 25 nm is proved by powder XRD and IR spectroscopy. Deactivation effect is observed after 100 min of illumination whose explanation is complicated and this aspect will be illuminated in future research work.

Acknowledgements: *The authors thank to the National Science Fund for the financial support through project DFNI-T02-17/2014. The supply of biotic and abiotic materials by Prof. V. Groudeva and Dr. M. Iliev from Faculty of Biology, St. Kliment Ohridski University is greatly appreciated.*

REFERENCES

1. T. Hennebel, B. De Gusseme, N. Boon, W. Verstraete, *Trends Biotechnol*., **27**(2), 90 (2009).
2. H. Jung, H. Park, J. Kim, J.-H. Lee, H.-G. Hur, N. V. Myung, H. Choi, *Environ. Sci. Technol*., **41**(13), 4741 (2007).
3. M. Mishra, D.-M. Chun, *Appl. Catal. A: General*, **498**, 126 (2015).
4. Y.-H. Chen, F.-A. Li, *J. Coll. Interface Sci*., **347**, 277 (2010).
5. P. Xu, G. M. Zeng, D.L. Huang, C.L. Feng, S. Hu, M.H. Zhao, C. Lai, Z. Wei, C. Huang, G.X. Xie, Z. F. Liu, *Sci. Total Environ.*, **424**, 1 (2012).
6. Y.L. Pang, S. Lim, H.C. Ong, W.T. Chong, *Ceram. Int.*, **42**, 9 (2016).
7. A. Di Paola, E. García-López, G. Marcì, L. Palmisano, *J. Hazard. Mater*., **211– 212**, 3 (2012).
8. W. Feng, D. Nansheng, *Chemosphere*, **41**, 1137 (2000).
9. S. Rahim Pouran, A.A. Abdul Raman, W.M.A. Wan Daud, *J. Clean. Prod*., **64**, 24 (2014).
10. T. Shahwan, S. A. Sirriah, M. Nairat, E. Boyacı, A. E. Eroğlu, T. B. Scott, K. R. Hallam, *Chem. Eng. J*., **172**, 258 (2011).
11. B. Ahmmad, K. Leonard, Md.S. Islam, J. Kurawaki, M. Muruganandham, T. Ohkubo, Y. Kuroda, *Adv. Powder Technol*., **24**, 160 (2013).
12. M. Harshiny, C.N. Iswarya, M. Matheswaran, *Powder Technol*., **286**, 744 (2015).
13. Z. Wang, D. Xiao, R. Liu, Y. Guo, X. Lou, J. Liu, *J. Adv. Oxid. Technol*., **17**(1), 104 (2014).
14. S. Li, Gaowu W. Qin, Y. Zhang, W. Pei, L. Zuo, C. Esling, *Adv. Eng. Mater*., **12**(10), 1082 (2010).
15. A. R. Amani-Ghadim, S. Alizadeh, F. Khodam, Z. Rezvani, *J. Mol. Catal. A: Chemical*, **408**, 60 (2015).
16. J. Cao, G. Li, Y. Wang, G. Sun, H. Bala, X. Wang, Z. Zhang, *Int. J. Photoenergy*, **2014**, 1 (2014).
17. S. Kang, G. Wang, M. Fang, H. Wang, X. Wang, W. Cai, *J. Mater. Res*., **30**(10), 1629 (2015).
18. J. Krýsa, J. Jirkovský, O. Bajt, G. Mailhot, *Catal. Today*, **161**, 221 (2011).
19. H. Gupta, B. Gupta, *Chemosphere*, **138**, 924 (2015).
20. Y. Zhang, M. Zheng, A-P. Deng, Y. Gu, Y.-P Huang, K.-jian Deng, A.-Q. Zhang, *Environ. Sci. Technol*., **10**, 24 (2011).
21. J. He, X. Tao, W. Ma, J. Zhao, *Chem. Lett*., **31**(1), 86 (2002).
22. J. He, W. Ma, J. He, J. Zhao, J. C. Yu, *Appl. Catal. B: Environmental*, **39**, 211 (2002).
23. Y. Wang, Y. Gao, L. Chen, H. Zhang, *Catal. Today*, **252**, 107 (2015).
24. R. Chen, X. Zhang, H. Liu, X. Song, Y. Wei, *RSC Adv*., **5**, 76548 (2015).
25. X. Li, Y. Huang, C. Li, J. Shen, Y. Deng, *Chem. Eng. J*., **260**, 28 (2015).
26. E.L. Zhang, X. J. Sun, X.T. Liu, Q.D. Wang, *Mater. Res. Innov*., **19**(5), 385 (2015).
27. Y. Lin, Y. Wei, Y. Sun, *J. Mol. Catal. A: Chemical*, **353– 354**, 67 (2012).
28. R. Chen, S. Zhao, X. Meng, H. Liu, Y. Wei, *RSC Adv*., **4**, 47521 (2014).
29. Z. Wang, Y. Ma, H. He, C. Pei, P. He, *Appl. Surf. Sci*., **332**, 456 (2015).
30. A. N. Christensen, T. R. Jensen, C. R.H. Bahl, E. DiMasi, *J. Solid State Chem*., **180**, 1431 (2007).
31. S. Mustafa, S. Khan, M. I. Zaman, *Water Res*., **44**, 918 (2010).
32. H. Fu, X. Quan, *Chemosphere*, **63**, 403 (2006).

33. S. Krehula, S. Popović, S. Musić, *Mater. Lett.*, **54**, 108 (2002).
34. R.J. Atkinson, A.M. Posner, J.P. Qurk, *Clays Clay Miner*., **25**, 49 (1977).
35. M. Shopska, Z. Cherkezova-Zheleva, D. Paneva, M. Iliev, G. Kadinov, I. Mitov, V. Groudeva, *Cent. Eur. J. Chem*., **11**, 215 (2013).
36. W. Kraus, G. Nolze, Powder Cell for Windows, Federal Institute for Materials Research and Testing, Berlin, Germany, 2000.
37. M. Katoh, M. Orihara, T. Moriga, I. Nakabayashi, S. Sugiyama, S. Tanaka, *J. Solid State Chem*., **156**, 225 (2001).
38. H. Fan, B. Song, Q. Li, *Mater. Chem. Phys*., **98**, 148 (2006).
39. G.N. Kustova, E.B. Burgina, V.A. Sadykov, S.G. Poryvaev, *Phys. Chem. Miner*., **18**, 379 (1992).
40. S. Rahimi, R.M. Moattari, L. Rajabi, A.A. Derakhshan, M. Keyhani, *J. Ind. Eng. Chem*., **23**, 33 (2015).
41. H. Liu, P. Li, M. Zhu, Y. Wei, Y. Sun, *J. Solid State Chem*., **180**, 2121 (2007).
42. G. Lefèvre, *Adv. Colloid Interface Sci*., **107**, 109 (2004).
43. T. Hiemstra, R. Rahnemaie, W.H. van Riemsdijk, *J. Colloid Interface Sci*., **278**, 282 (2004).

ФОТОКАТАЛИТИЧНА СПОСОБНОСТ НА АБИОТИЧНИ И БИОТИЧНИ МАТЕРИАЛИ ЗА ОБЕЗЦВЕТЯВАНЕ НА МАЛАХИТОВО ЗЕЛЕНО И РЕАКТИВНО ЧЕРНО 5 БАГРИЛА

К.Л. Захариева[1], К.И. Миленова[1], М.Г. Шопска[1], М.П. Цветков[2], Ал.Ел. Елияс[1], Г.Б. Кадинов[1]

[1]Институт по катализ, Българска академия на науките, ул. „Акад. Г. Бончев“, бл. 11, 1113 София, България

[2]Институт по физикохимия, Българска академия на науките, ул. „Акад. Г. Бончев“, бл. 11, 1113 София, България

Постъпила на 14 април, 2016 г.; приета на 20 декември, 2016 г.

Изследвани са фотокаталитичните свойства на наноразмерни абиотичен (АР) и биогенен желязосъдържащи материали, получени в стерилна и заразена с *Leptothrix* бактерия среда на Лиске, и гьотит (АС) синтезиран чрез утаяване и обработка с ултразвук, в реакцията на обезцветяване на багрила Малахитово Зелено (МЗ) и Реактивно Черно 5 (РЧ5) като моделни замърсители във водни разтвори чрез облъчване с УВ светлина. Инфрачервената спектроскопия и рентгенофазовия анализ потвърдиха присъствието на α-FeOOH и γ-FeOOH в биогенния материал. Единствено гьотит е регистриран в абиотичните материали (АС и АР). Синтезираният гьотит показа най-висока фотокаталитична активност за обезцветяването на Малахитово Зелено и Реактивно Черно 5. Биогенният материал е по ефективен като фотокатализатор за обезцветяването на МЗ в сравнение с РЧ5.

Bulgarian Chemical Communications, Volume 49, Number 3, (pp. 658 – 663) 2017

Chromatography of separation and qualitative, quantitative analysis biflavonoids from crude extract of *Selaginella tamariscina*

H.L. Bai, J. Wang, C.M. Liu*

Department of Chemistry, Changchun Normal University, Changchun, China, 130032

Received June 7, 2015; Revised February 27, 2017

Previous investigations reported that the class of biflavonoids represents a great pharmacological activity, which remained to be fully exploited, since most of them have not yet been found in nature or else have not been synthesized. Owing to its significant bioactivities and the quality control of medicine herb, effective methods for the extraction, isolation and purification of biflavonoids from *S. tamariscina* become necessary. In order to evaluate the performances of the optimal extract method, four extraction solvent and five extraction methods (Accelerated solvent extraction, SFE-CO_2 extraction, reflux extraction, Soaking extraction and Ultrasonic extraction)were used to extract the bioactive compounds from *Selaginella tamariscina* (Beauv) Spring. HPLC method was attempted for quantitative analysis and comparison with different extract by determining the content of amentoflavone. The result indicates that extraction temperature has significant impact on the extraction efficiency, and reflux extraction is proved to be the effective technique for extracting biflavonoid of *S. tamariscina*. Reverse-phase medium-pressure liquid chromatography(RP-MPLC) was first applied to separate and isolate biflavonoid from extract of *S. tamariscina*. High-purity biflavonoid was obtained and at over 98% purity as determined by HPLC. Furthermore, electrospray ion source mass spectroscopy (ESI-MS) was employed for rapid identification of the obtained compound from extract of *S. tamariscina*. Amentoflavone were identified based on the detection of the molecular ions, and the fragment ions of the molecular ion obtained in the CID experiments with those of the data reported in the literature. The chromatography technologies we employed were effective and feasible for the extraction, separation, qualitative and quantitative analysis of biflavonoids from *S. tamariscian*.

Keywords: *Selaginella tamariscina* (Beauv) Spring; amentoflavone; RP-MPLC; ESI-MS; extraction

INTRODUCTION

Selaginella tamariscina(Beauv) Spring belongs to the family Selaginellaceae, the genus of *Selaginellace* contains about 80 species in the world, of which about 50 species are distributed in China. *S. tamariscina* is a traditional medicine, which was first recorded by "ShenNong Ben Cao Jing" around 1700 years ago. It has been used in oriental medicine to treat amenorrhea, dysmenorrheal, metrorrhagia, hematuria, prolapse of the anus, chronic hepatitis and hyperglycaemia.

Data from preliminary research has shown that different classes of natural products have been isolated from these species, including flavonoids, lignans, anthraquinone, alkaloids [1-2]. Investigation of the phytochemical constituents of *S. tamariscina* revealed that the major constituents in *Selaginella tamariscina*are flavonoids, especially a rich source of biflavonoids. Biflavonoids are flavonoid dimmers connected with a C–C or a C–O–C bond, which exhibited several biological activities, including cytotoxic [3], antiallergenic, anti-inflammatory [4-5], antiviral, antioxidant [6-7], inhibition of nuclear factor-k B activation [8], hypoglycemic and hypolipidemic [9], antiplasmodial and leishmanicidal activity [10]. In addition, sometimes the bioactivity of a biflavonoid is greater than that of the corresponding monomers. Amentoflavone is the main biflavonoid of *S. tamariscina*, with higher content in crude extract, and represents a great pharmacological activity.

Owing to bioflavonoids' significant bioactivities and the quality control of medicine herb, effective methods for the extraction, isolation and purification biflavonoids of *S. tamariscina* become necessary. However, extract and separate analysis of chemical components from *S. tamariscina* has been reported less. Traditionally, the extraction method of biflavonoids almost applied the conventional method, such as organic solvent extraction and reflux extraction; in recent years, a series of modern technology has been widely used to extract, contained accelerated solvent extraction (ASE), SFE-CO_2 extraction, microwave and Ultrasonic extraction, etc. But the technology is more suitable for the extraction of active substances need to be experimental investigation. The conventional preparative separation and purification of flavonoids employed column chromatograph, such as silica gel, Sephadex LH-20 and macroporous adsorptive resin, which are often involve repeated chromatographic

* To whom all correspondence should be sent:
E-mail: baihelong2000@126.com

steps on different columns. Comparing preparative HPLC separation, the MPLC has high flow rate and low pressure, the analytical grade solvents were used as elution solvent, so it is time consuming and lower costs. MPLC has enabled a significantly improved efficiency in separation and purification of the compounds of interest in short time.

In this work, five different extraction technologies, containing ASE, SFE-CO2 extraction, reflux extraction, soaking extraction and ultrasonic extraction were applied to extract the biflavonoids from *S. tamariscian*. The extraction technologies were optimized with the extraction quantity of amentoflavone as investigated by HPLC-DAD. Then, RP-MPLC was selected to separate the crude extract of *S. tamariscina* and enrich the interested fraction containing amentoflavone,whicn was further determined by HPLC-DAD. Finally, ESI-MS was employed for rapid identification of main bioactive compounds from extract of *S. tamariscina*. Fig.1 shows the structure of amentoflavone.

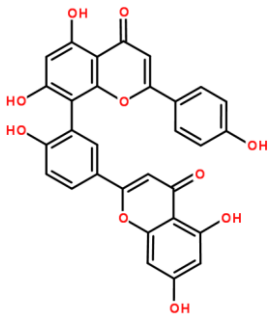

Fig.1. The strcture of the amentoflavone

EXPERIMENTAL

Chemicals and reagents

S. tamariscian was purchased from HebeiKanghui Medicinal Company (Hebei, China); all organic solvents used for extraction and RP-MPLC separation were of analytical grade and purchased from Beijing Chemicals (Beijing, China); Methanol and acetic acid were HPLC grade and purchased from Fisher chemical Ltd. (USA). Water was purified on a Milli-Q water purification system (Millipore, France).

Sample preparation

In order to compare the extraction effects of different methods, four different extract solvent and five extraction methods were carried out to extract the biflavonoids from *S. tamariscian*.

Different solvent extraction

Four *S. tamariscina* powder (5.001, 5.002, 5.006, 5.007 g) was accurately weighed and place in 100 mL erlenmeyer flask, respectively, then extracted with 50 mL of 70% aqueous ethanol, hexane, n-butanol, ethyl acetate by sonication for 2 h at room temperature. Four extraction mixtures were filtered, concentrated to dryness in vacuo at 55 ℃, dissolved in 10 mL volumetric flask with methanol and filtered through a 0.45 μm filter prior to use for following analysis.

Supercritical fluid extraction

In this work, the SFE apparatus used was performed on a Speed™ SFE Prime device (Applied Separations Inc). Carbon dioxide (99.99% purity) obtained from an oxygen factory (Changchun, China) was used as the extraction solvent. The operating methodology was as follows: Accurate weighing 5.006 g of *S. tamariscina* power was placed inside the 24 mL extractor equipped with filter film, filter wool on both ends to prevent the particles being flushed out. The loaded extractor was then introduced into the extraction vessel and CO_2 was let in. The device was cooled for 1 h before being set the desired pressure and temperature. Experimental conditions: extractor temperature at 60 ℃, pressure 200 bar, static extraction time for 0.5 h and dynamic extraction time for 1 h, outlet temperature at 90 ℃, entrainment agents was 70% ethanol 40mL. The crude extract was collected after the desired time and concentrated to dryness in vacuo at 55℃. The sample obtained was dissolved in 10 mL volumetric flask with methanol and filtered through a 0.45 μm filter prior to use for following HPLC analysis.

Accelerated solvent extraction（ASE）

Accelerated Solvent Extraction 150 System (Dionex, Sunnyvale, CA, USA) with 100 mL stainless steel ASE vessels was used for the pressurized liquid extraction. Accurate weighing 5.005 g of *S. tamariscina* powder was placed into the extraction cell (34 mL). The extraction cells were placed into the ASE system and the extraction conditions and process were as follows: 70% ethanol was used as the extract solvent, firstly, static time of 4 min, followed by a flush elution with 60% volume, and followed by the nitrogen purge of 60 s, and extracted three time. The extraction temperature was 80 ℃, and pressure was below 1500 psi. The ethanol extract was concentrated to dryness in vacuo at 55℃. The sample obtained was dissolved in 10 mL volumetric flask with methanol and filtered through a 0.45 μm filter prior to use for following analysis.

Reflux extraction

S. tamariscina powder (5.009 g) was accurately weighed and place in 100 mL round-bottomed flask, then extracted with 50 mL of 70% aqueous ethanol for 1 h at 90 ℃. The extraction mixture was filtered, concentrated to dryness in vacuo at 55℃, dissolved in 10 mL volumetric flask with methanol and filtered through a 0.45 μm filter prior to use for following analysis.

Soaking extraction

S. tamariscina powder (5.007 g) was accurately weighed and place in 100 mL erlenmeyer flask, then extracted with 50 mL of 70% aqueous ethanol for 2 h at 40 ℃. The extraction mixture was filtered, concentrated to dryness in vacuo at 55 ℃, dissolved in 10 mL volumetric flask with methanol and filtered through a 0.45 μm filter prior to use for following analysis.

Ultrasonic extraction

S. tamariscina powder (5.005 g) was accurately weighed and placed in 100 mL erlenmeyer flask, then extracted with 50 mL of 70% aqueous ethanol by sonication for 1 h at room temperature. The extraction mixture was filtered, concentrated to dryness in vacuo at 55 ℃, dissolved in 10 mL volumetric flask with methanol and filtered through a 0.45 μm filter prior to use for following analysis.

RP-MPLC Separation

RP-MPLC Separation was carried out in an Isolera one MPLC system (Biotage Switzerland). The separation was carried out with a Biotage® SNAP Cartridge KP- C18-HS column (12 g). The binary mobile phase consisted of methanol (solvent A) and water containing 0.2% acetic acid (solvent B). A binary gradient elution program with the flow-rate of 4 mL/min was used for the separation. The system was run with a gradient program: 20 mL 80% B; 50 mL 80-70 % B; 10 mL 70-40% B; 30 mL 40-15% B; 10 mL 15% B. The column was first equilibrated with 20 mL 80% B, the 1.024 g *S. tamariscian* extracted by ultrasonic dissolved in 2 mL methanol was then injected into the column. Peaks of interest were monitored at 337 nm by a DAD detector. The fractions were collected into test tubes per 10 mL with a fraction collector, and further analyzed by HPLC-DAD. The fractions were determined at over 98% purity by HPLC were combined, which was prepared for further ESI-MS analyses, then freeze-dried. The purified compounds were stored at -20 ºC before HPLC quantitative analysis.

HPLC Analysis

HPLC equipped with DAD detector was used for the analysis of biflavonoids of *S. tamariscina*. The separation was carried out in an Agilent Extend-C_{18} column (250×4.6 mm, 5μm) with a C_{18} guard column. The binary mobile phase consisted of methanol (solvent A) and water containing 0.2% acetic acid (solvent B). All the solvents were filtered through a 0.45 μm filter prior to use. The sample injection volume was 10 μL. The flow-rate was constantly kept at 1.0 mLmin-1 with a total run time of 20 min. Column temperature: 30 ℃. The system was run with a gradient program: 0–5 min: 70% B to 40% B; 5–10 min: 40% B to 20% B; 10–18 min: 20% B to 10% B; 18–20 min: 10% B to 70% B; detection wavelength: 337 nm.

Seven amentoflavone methanol samples of different concentrations (0.1 mg/mL~2.5 mg/mL) were loaded into HPLC system for construction of the calibration curve by plotting the peak areas (Y) versus the quality (X). Each extract sample was loaded into HPLC system for identification and quantification of amentoflavone in *S. tamariscina*, respectively.

ESI-MS experiments

The mass spectrometry experiments were performed on a Thermo Scientific LCQ Fleet mass spectrometer with an electrospray ionization (ESI) interface (ThermoFisher, USA). The flow-rate was constantly kept at 10 μL/min. The sheath gas and auxiliary flow rates were set at 40 and 10 (arbitrary unit), respectively. The capillary voltage was set at 4.5 V and its temperature was controlled at 350 °C. The isolation width for ESI-MSn was 2.0 Da, and the collision energy (%) was 20-25%. Full scan of ions ranged from 100 to 1500 molecular weights in the negative ion mode.

RESULTS AND DISCUSSION

HPLC quantification of amentoflavone content of different extract

In this study, we prepared seven amentoflavone methanol samples of different concentrations to construct the calibration curve and quantified the *S. tamariscina* extracts with different extraction method by HPLC. The linear regression equation was calculated as Y= 254190X - 52.189, (r=0.9998), which showed good linear regression within the test ranges (1~25 μg). The amentoflavone content in different *S. tamariscina* extracts was calculated as shown in Table 1 and Table 2.

Comparison of different extraction solvent

It is known that biflavonoid are flavonoid dimmers connected with a C–C or a C–O–C bond, most of them have lower polarity than flavonoid containing many hydroxyl groups. Hence, 70% aqueous ethanol, hexane, n-butanol, ethyl acetate had been tested. As shown from the result of Table 1, amentoflavone content of 70% aqueous ethanol extract was higher (14.051 mg/g) than others, and that of hexane extract was the lowest (0.404 mg/g). It is not significantly different from those obtained by n-butanol (1.718 mg/g) and ethyl acetate extracts (1.707 mg/g). The reason may be the polarity of 70% aqueous ethanol is similar with the amentoflavone. So 70% ethanol was proved to be most efficient to extract the biflavonoids from the *S. tamariscina.*

Comparison of different extraction methods

In order to evaluate the performances of the optimal method, five extraction methods were also applied. The chromatogram of the extract obtained by the ultrasonic extraction method was shown in Fig. 2A.

The amentoflavone content of different crude extract (Table 2) obtained by five methods mentioned above were significantly different; the extraction yields obtained by the reflux method are higher than those obtained by the other four methods. As shown from the result, we should know that extraction temperature has significant impact on the extraction efficiency. Increasing the temperature could improve the yield of amentoflavone, the reflux extraction with 90 ℃ obtained the highest extraction amount (33.006 mg/g). If the extraction temperature was lower, the content of amentoflavone would be reduced obviously. Followed by accelerated solvent extraction（ASE） with 80 ℃ (27.880 mg/g) , SFE-CO_2 extraction with 60 ℃ (20.181 mg/g), respectively. From the result, it is not significantly different from those obtained by soaking extraction and ultrasonic extraction, the reason may be the extraction temperature was similar (40 ℃ and room temperature), the both methods obtained the lower content (Table 2).

Compared with temperature, the extraction pressure probably influenced less on the extraction yield, reflux extraction with atmospheric pressure got the highest content of amentoflavone, ASE and SFE with higher pressure but lower content than reflux extraction. The extraction time of reflux method is longer than that of ASE (12 min). ASE extraction process included injecting extract solvent, elevating pressure, static time of 4 min, flushing elution with 60% volume, and purging the nitrogen of 60 s, extracting three times, relieving pressure. It would take more time to complete the extraction, not much shorter than that of reflux extraction. The results indicated that the reflux method was suitable for extracting amentoflavone from *S. tamariscina*.

Separation amentoflavone by RP-MPLC

MPLC has enabled a significantly improved efficiency in separation and purification of the compounds of interest, and enriched some lower content compounds in the herb in short time. The theory of MPLC separation is much similar with HPLC， so we selected the separation condition depended on the condition of HPLC. In RP-MPLC Separation, a Biotage® SNAP Cartridge KP-C18-HS column (10 g) was used to separate biflavonoids in the extract of *S. tamariscina* and the RP-MPLC chromatogram is given in Fig.2. As shown in Fig.2,

Table 1. Amentoflavone content of different extraction solvent

Extraction solvent	Crude drug (g)	Amentoflavone (mg/g)
70% aqueous ethanol	5.001	14.051
n-butanol	5.002	1.718
Ethyl acetate	5.006	1.707
Hexane	5.007	0.404

Table 2. Amentoflavonecontent of different extraction methods

Extraction methods	Crude drug(g)	Extraction time	Temperature	Amentoflavone (mg/g)
Accelerated solvent extraction（ASE）	5.005	12 min	80 ℃	27.880
SFE-CO2 extraction	5.006	1.5 h	60 ℃	20.181
Reflux extraction	5.009	1 h	90 ℃	33.006
Soaking extraction	5.007	2 h	40 ℃	14.727
Ultrasonic extraction	5.005	1 h	Room temperature	14.051

one major fraction was observed, and the fractions were collected into test tubes per 10 mL with a fraction collector, and further analyzed by HPLC. All fractions of the same compound at high purity determined by HPLC were combined, and freeze-dried. The present RP-MPLC Separation produced a total of 0.44 mg of fraction Ⅰfrom1.024 g of crude extract in one run.

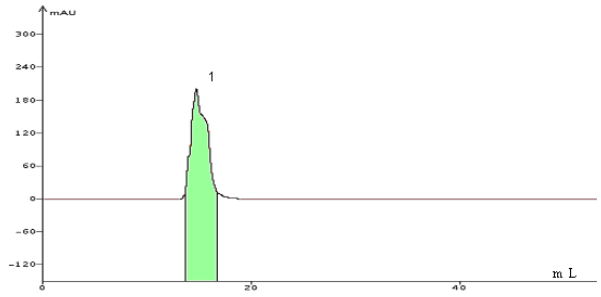

Fig. 2.RP-MPLC chromatogram of *S. tamariscina* extract

The crude extract of *S. tamariscina* and the fractions corresponding to each peak isolated by RP-MPLC were further analyzed by HPLC, and the results are given in Fig. 3 (A-B). Tentative identification of the compound in RP-MPLC separation was achieved by the comparison of congruent retention time with that of the crude extract of *S. tamariscina* (Fig. 3). HPLC analyses of the MPLC fraction revealed that the biflavonoid was over 98% purity.

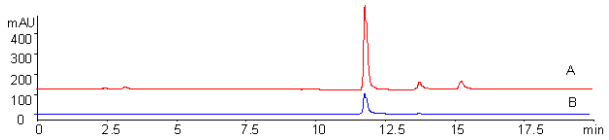

Fig.3. HPLC profiles of the compounds in S. tamariscina (A. The crude extract; B. Compound 1 in RP-MPLC separation)

Identification by ESI-MSn

To further investigate the structure of the compound in RP-MPLC separation, ESI-MS^n experiment was attempted. Compound related to the peak 1 exhibited intense molecular ions $[M-H]^-$ at m/z 537 in the negative mode, and low intensity dimer $[2M-H]^-$ ions at m/z 1075, from which the molecular weights of peak 1 was confirmed to be 538. In ESI-MS^n experiment, the deprotonated molecular ion $[M-H]^-$ at m/z 537, and four main fragment ions at m/z 443, 417, 375 and 331 were observed in NI-MS.

The proposed fragmentation route is, main daughter ion at m/z 433 produced directly from m/z 537 by two γ-H of the A-ring in flavonoid part Ioccurred McLafferty rearrangement, losses of C_3O_2, followed by the cleavage of the C-ring in flavonoid part Ⅰ at positions 0/4 （0,4A）, losses of C_2H_2. The MS^2 spectra of the $[M-H]^-$ ions also showed one daughter ion of m/z 417, which indicated the loss of $C_7H_5O_2$ via the cleavage of the C-ring in flavonoid part II at positions 0/2 （0,2A）. In the MS^3 spectra, low abundance fragment ion at m/z 331 also be found, which could be obtained by two γ-H of the Ⅰ-A-ring in m/z 417 undergone McLafferty rearrangement, losses of C_3O_2, and lose a H_2O molecule via intramolecular dehydration between –OH on the IB4' and IIA7''. The fragment ion at m/z 375, which corresponded to the loss of a $C_9H_6O_3$ unit from the cleavage of the C-ring in flavonoid part II at positions 0/4 in the parent ion m/z 537, it is similar with biflavonoids mass spectra of previous report studied [11-12]. Generally, fragmentation routes involving the cleavage of the C-ring in flavonoid part II at positions 0/2 and 0/4 are the primary pathways of amentoflavone-type biflavonoids in our experiment. By comparing the retention time, peak order and molecular weights information of ESI-MS data with above LC-ESI-MS experiment, the compound 1 was confirmed as amentoflavone. Based on the LC peak cases, detection of the molecular ions and the fragment ions of the molecular ion obtained in the CID experiments with those of the data reported in the literature, the compound corresponding to peak 1 was therefore identified as amentoflavone [13-15]. The structure of the amentoflavone (peak 1) is showed in Fig. 1. Amentoflavone is a biflavonoids consist of two flavonoids connected by IC3'-IIC8''.

CONCLUSION

The present paper describes several chromatography methods were joint applied to analyze and separate the bioactive compounds of *S.tamariscina*.To establish the quantitative analysis HPLC method to compare with different extract by determining the content of amentoflavone. The result indicates that extraction temperature has significant impact on the extraction efficiency, and reflux extraction is proved to the more effective technique for extracting biflavonoid than ASE, SFE-CO_2 extraction, soaking extraction and ultrasonic extration. RP-MPLC was successfully applied to separate biflavonoid from extract of *S. tamariscina*. High-purity amentoflavone was obtained and at over 98% purity as determined by HPLC. ESI-MS^n method could also be applied to rapid identification of obtained compound based on the detection of the molecular ions, and the fragment ions of the molecular ion with those of the data reported in the

literature. The research demonstrates that chromatography technologies we employed were effective and feasible for the extraction, separation, qualitative and quantitative analysis of biflavonoids from *S. tamariscian*or other medicinal plants.

Acknowledgements: *Project was supported by the National Natural Science Foundation of China (No. 31400453, 31370374, 81373899) and the Educational Commission of Jilin Province (No. [2013]254).*

REFERENCES

1. Y.F. Bi, X.K. Zheng, W.S. Feng, S.P. Shi,*ActaPharmaceuticaSinica*, **39**, 41 (2004).
2. X.K. Zheng, K.K. Li, Y.Z. Wang, W.S. Feng,*Chinese ChemLett*, **19**, 79 (2008).
3.
4. J.J. Chen, C.Y. Duh, J.F. Chen, *Planta. Med*., **71**, 659 (2005).
5. H.P. Kim, H. Park, K.H. Son, H.W. Chang, S.S. Kang, *Arch. Pharm. Res*., **31**, 265 (2008).
6. M.A. Mahjoub, S. Ammar, H. Edziri, N. Mighri, A. Bouraoui, Z. Mighri, *Med. Chem. Res*., **19**, 271 (2010).
7. O.A. Adaramoye, I.A.J. Medeiros, *Smooth Muscle Res.*, **45**, 39 (2009).
8. S. Liang, J. Tang, Y.H. Shen, H.Z. Jin, J.M. Tian, Z.J. Wu, W.D. Zhang, S.K. Yan, *Chem. Pharm. Bull.*, **56**, 1729 (2008).
9. E.R. Woo, Y.R. Pokharel, J.W. Yang, S.Y. Lee, *Biol. Pharm. Bull*., **29**, 976 (2006).
10. X.K. Zheng, Y.J. Li, L. Zhang, W.S. Feng, X. Zhang, *Spring, J. Ethnopharmacol.*, **133**, 531 (2011).
11. O. Kunert, R.C. Swamy, M. Kaiser, A. Presser, S. Buzzi, A.V.N.A. Rao, *Phyto. Lett*., **41**, 1 (2008).
12. S.Y. Shi, H.H. Zhou, K.L. Huang, *Chromatographia*, **68**, 173 (2008).
13. A. Romani, C. Galardi, P. Pinelli, *Chromatographia*, **56**, 469 (2002).
14. Y. Yuan, B.Q. Wang, L.J. Chen, H.D. Luo, D. Fisher, I.A. Sutherland, Y.Q. Wei, *J. Chromatogr. A*, **1194**, 192 (2008).
15. Y.X. Zhang, Q.Y. Li, L.L. Yan, Y. Shi, *Rapid Commun. Mass Spectrom*., **25**, 2173 (2011).
16. J.W. Yang, Y.R. Pokharel, M.R. Kim, E.R. Woo, H.K. Choi, K.W. Kang, *J. Ethnopharmacol*, **105**, 107 (2006)

ХРОМАТОГРАФИЯ НА РАЗДЕЛЯНЕТО, КАЧЕСТВЕНИЯ И КОЛИЧЕСТВЕНИЯ АНАЛИЗ НА БИФЛАВОНОИДИ В СУРОВИ ЕКСТРАКТИ ОТ *Selaginella tamariscina*

Х.Л. Бай, Дж. Ванг, Ц.М. Лю*

Департамент по химия, Университет в Чангун, Чангун130032, Китай

Постъпила на 7 юни, 2016 г.; приета на 27 февруари, 2017 г.

(Резюме)

Известно е от предишни изследвания, че класът бифлавоноиди има голяма фармакологична активност, която трябва да се използва по-пълно, тъй като много от тях не се срещат в природата. Поради тяхната голяма биологична активност и качествения контрол на медицинските растения е необходимо създаването на ефективни методи за екстракция, изолиране и пречистване на бифлавоноидите от растението *S. tamariscina*. За оценяването на оптимален метод за екстракция са изпитани четири разтворителя, пет метода за екстракция (ускорена течна екстракция, свръх-критична екстракция SFE-CO_2, екстракция с рецикъл, с промиване и ултразвукова екстракция) за извличане на биологично-активни вещества от *Selaginella tamariscina*. Изпитан е BETX-метод за количествен анализ и е направено сравнение с определянето на амантофлавон в различните екстракти. Резултатите показват, че температурата на екстракция има значително влияние върху ефективността на екстракция, а екстракцията с рецикъл предлага най-ефективен способ за извличане на бифлавоноиди от *S. tamariscina*. Течната хроматография с обратна фаза и умерено налягане (RP-MPLC) е приложена на-напред за разделянето и изолирането на бифлавомоиди от екстракти от *S. tamariscina*. Получени са бифлавоноиди с висока чистота (над 98%), както е определеноч чрез BETX. Освен това, електроспрей-йонна мас-спектрометрия (ESI-MS) е приложена за бързата идентификация на съединенията получени от екстрактите от *S. tamariscina*. Аменофлавонът е идентифициран чрез детекция на молекулни йони, а фрагментните йони, получени при CID-експериментите са сравнени с данни от литературата.

Приложените хроматографски технологии са ефективни и подходящи за екстракция, разделяне, количествен и качествен анализ на бифлаоноидите от растението *S. tamariscina*.

Bulgarian Chemical Communications, Volume 49, Number 3, (pp. 664 – 668) 2017

Investigation on the effect of nano-TiO_2 synthesized by the hydrothermal method on LNCaP cancer cells

F.B. Emre[*,1,2], F. Okuşluk[1,2], S. Tekin[3], S. Sandal[3]

[1] *Prof. Dr. Hikmet Sayılkan Advanced Materials Research an Application Laboratory, Scientific and Technological Research Center, İnönü University, Malatya, 44280, Turkey*
[2]*Department of Elementary Education, Faculty of Education, İnönü University, Malatya, 44280, Turkey*
[3]*Department of Physiology, Faculty of Medicine, İnönü University, Malatya, 44280, Turkey*

Received November 15, 2016; Revised March 11, 2017

The nanosized TiO_2 synthesis was performed through the hydrothermal method by using titanium alkoxides. The structural, physical and chemical characteristics of the nanosized TiO_2 were determined via XRD, SEM and particle size analyzer. The synthesized nano-TiO_2 particles were obtained in a completely anatase form. Different concentrations of nano-TiO_2's turned into sol were applied into the LNCaP cells in the cell culture media, and their anti-tumour/proliferation activities were tried to be determined photocatalytically with and without the UV-ray. For this, the numbers of living and dead cells were detected by means of MTT method, and thus, the anticancer characteristic was determined.

Keywords: Nano-TiO_2, hydrothermal method, MTT assay method, LNCaP

INTRODUCTION

TiO_2 nanoparticles are used in a number of fields, such as photocatalyst [1-3], solar cell [4, 5] and gas sensors [6]. Separately, TiO_2 is also used efficiently in the degradation of organic compounds and coloring agents as well as neutralizing/warding off microorganisms. TiO_2 is a semi-conductor with a band-gap energy of 3.2 eV, and it has a far more quantum effect compared to normal substances [7]. In an aqueous medium, reactive oxygen species (ROS) like hydroxyl radicals, superoxide anions and hydrogen peroxide occur thanks to e^-/h^+ gap pairs that occur on TiO_2 nanoparticles under the UV ray [8-10]. These active oxygen species play an efficient role in several chemical reactions as well as annihilating microorganisms due to their high redox activities. It has been reported in the studies conducted recently that TiO_2 could also be applied in the treatment of cancer [11-15]. Within the cancer cells and in the cell membrane [15] have the active oxygen species (ROS) been effective, as well. In such oxidation reactions, the cell toxicity is dependent on the cell stability and the chemical combination (order) on the surface structure of the cell [16].

In this study, the nano-sized TiO_2 was synthesized through the hydrothermal method, and its effect on the LNCaP cells was examined under the effect of the UV-ray, without the presence of the UV-ray.

EXPERIMENTAL

Chemicals and Reagents

Titanyum (IV) isopropoksit (TTIP) (97%, Alfa-Aesar), isopropyl alcohol (99.5%, LabKim), Hydrochloric acid (%37, Merck), Acetic acid (99.5%, J.T.Baker), Newborncalf serum (FCS) and pensilin-streptomycin (Biological Industries), Sodium chloride, Sodium hydroxide, Dimetyl sulfoxide (DMSO) (Merck) were purchased. The water used in the experiment was doubly distilled and deionized.

Berghoff BTR-2000A Model hydrothermal unit interfaced with a temperature controller and timer unit was used for synthesizing nano-sized TiO_2. Malvern Nanoseries Zetasizer was used for particle size analyzer. The crystalline phase of the nano-TiO_2 particles was analyzed by X-ray powder diffraction (XRD) pattern obtained from Rigaku Geigerflex D Max/B diffractometer with Cu Kα radiation (λ = 0.15418 nm) in the region 2θ = 10–90° with a step size of 0.04°. The crystallite size of the anatase particle was calculated from the X-ray diffraction peak, according to the Scherrer's equation. SEM (LEO EVO 40) was used to examine the surface morphology.

Preparation of nano-TiO_2

Titanium (IV) isopropoxide, [$Ti(OPr^i)_4$], was added into i-propanol in the way that it would reach 10% in mass, and thus, a homogeneous mixture was obtained. As the catalyst, the mixture of HCl/HAc was added into the reaction medium in the way that the Acid/$Ti(OPr^i)_4$ rate would reach

* To whom all correspondence should be sent:
E-mail: fatma.emre@inonu.edu.tr

0.05 and 0.07, respectively. In order for the hydrolysis-condensation reaction to start, the prepared water was instilled in the way that the $H_2O/Ti(OPr^i)_4$ rate would be (mol/mol) 3, and then, a homogenous and transparent/ crystalline solution was obtained after the reaction had lasted for approximately 10 minutes more. The sol-solution was first placed into a Teflon cup of 250 mL and then onto the hydrothermal unit. After having been kept at 200 °C for 4 hours, it was taken out of the hydrothermal unit and was cooled at room temperature. The obtained solid TiO_2 particles, after having been separated from the solution medium through a centrifuge, were dried up/dehydrated at 40 °C in the vacuum incubator. Hence, the nano-sized TiO_2 particles were obtained.

Preparation of the sols in the RPMI-1640 medium

The sol of the pure nano-TiO_2 particles which was synthesized through the hydrothermal method was prepared within RPMI-1640 medium. In this process, RPMI-1640 medium was added onto 1 gram of TiO_2 particles in the way that it would make up 1% sol by weight and then was placed into the ultrasonic bath. In order to prepare a solution in 4 different concentrations, a 1% main stock sol was used. The nano-TiO_2 to be tested was dissolved in the medium, and their 1-100 mM concentrations were prepared to be used during the experiment. The stock solutions were kept at the +4 °C throughout the experiment.

Cell Cultures

LNCaP cells were obtained from The Middle East Technical University (METU), the Department of Biology (Ankara). All the cells were fed by f (that which is prepared by adding into it 10% FCS, 100 U/mL penicillin and 0.1mg/mL streptomycin) within the culture flasks of 25 cm^2. The mediums of the cells kept in the carbon dioxide (5% CO_2) incubator, within a humid environment at 37 °C were changed twice a week. When the cells were confluent, they were removed from the flasks by using a trypsin-EDTA solution and were then poured into the plaques with 96 wells to be used in 3-(4,5-dimethylthiazol–2-yl)-2,5-diphenyltetrazolium bromide (MTT) analyses.

Statistical Analyze

Statistical analysis of the data was performed with SPSS program (16.0). Non-parametric method of analysis was used because of the number of repetitions in the groups are n<20. Due to the number of groups are more than 2, Kruskal-Wallis analysis of variance was used for multiple comparisons. Statistically significant $p<0.05$ was considered significant.

RESULTS AND DISCUSSION

Characterization of the nanocomposite

Whether or not the nano-sized pure particles synthesized through the hydrothermal method were of a crystalline structure was determined by using X-ray dust diffractometry. Throughout the analysis, CuK_α ray was applied, and 2θ values were selected as 0-80°, and the scanning rate as 0.04 cm/s. It was determined that the peaks seen in the XRD spectrums (Fig. 1) of the particles had corresponded to the crystalline reflections determined for TiO_2 in the form of anatase crystal (1 0 1), (0 0 4), (2 0 0) and (2 1 1). No reflections of rutile and brookite, which are the other crystalline modifications of TiO_2, were found.

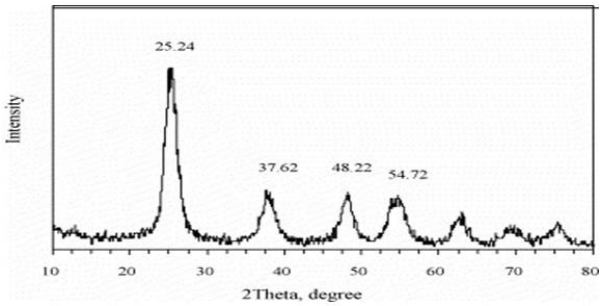

Fig. 1. XRD results for the nano-TiO_2

SEM analysis of anatase TiO_2 particles with nano-size was performed on the surface of the particles, which was covered by carbon. It can be seen from SEM analysis results (Fig. 2) that the particles resemble one another quite a great deal in terms of their structure and that they had a spheric form in general; yet, a total spheric structure failed to take shape among the particles in some areas. The reason for this is that the particles are likely to be exposed to agglomeration due to a thermal treatment, with the result that the sizes of some of the particles may grow, whereas those of some others could become smaller.

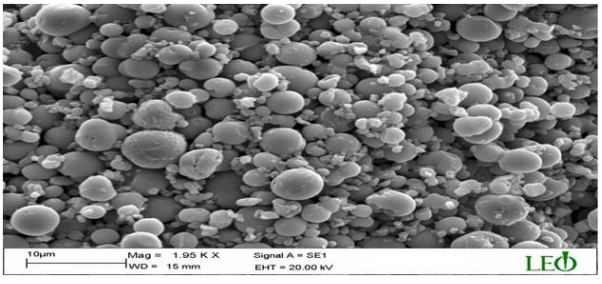

Fig. 2. SEM images for the nano-TiO_2

The volumetric particle-size distributions of the nano-sized TiO_2 particles were determined via Zeta-

sizer. The sol of the synthesized nano-TiO_2 particles, which were prepared in the water, was used for measurements. As the result of the measurements performed for determining the particle-size distribution, the TiO_2 particles were found to be 4.78 nm at a rate of 95.9% (Fig. 3).

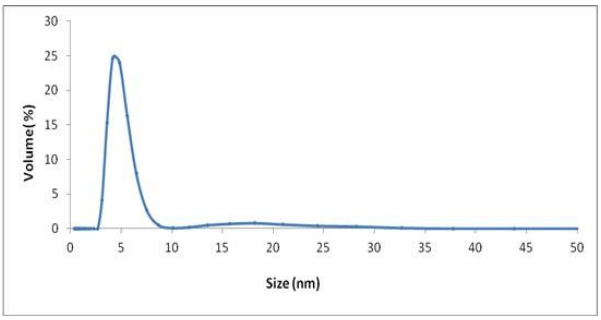

Fig. 3. Particle size distribition results for the nano-TiO_2

Cytotoxicity tests

The synthesized nano-particles were screened for their cytotoxicity against prostate cancers (LNCaP) by using MTT assay method. The pale-yellow tetrazolium salt [3-(4,5-dimethyl-2-thiazolyl)-2,5-diphenyl-2H-tetrazolium bromide] (MTT), was cleaved by active mitochondria to form a dark blue formazan product, that can be completely solubilized in acidified isopropanol and detected by a microtiter plate reader [17]. The assay provides a simple way to detect living and growing cells without using radioactivity. Briefly, $15x10^3$ prostate cancer cells were plated in triplicate in 96-well flat bottom tissue culture plates, and treated with different concentrations (0.01 mM, 0.1 mM, 1 mM and 10 mM) of agents. The culture plates were exposed to UV light at four different time points (0, 5, 15 and 30 minutes) and then cells were incubated for 24 h at 37°C in 5% CO_2 humidified incubator. MTT (0.005 g/mL in phosphate buffer saline) was added to the cell culture and incubated for 4 h. The formazan crystals formed during the reaction of active mitochondria with MTT, were dissolved in 0.04 N (100 mL) in isopropanol and readings were taken by a microtiter plate reader (Biotek Synergy) using a 570 nm filter. Each data represented an average of 10 measurements.

It was seen as the result of the measurements that there was no mortality in LNCaP cells without the UV-ray; on the contrary, it was observed that this situation brought about proliferation. On the other hand, mortality in LNCaP cells was observed when the UV-ray was applied. As the period of exposure to the UV-ray extended, so did the cell death increase. The best results were observed in the 0.01 mM nano-TiO_2 concentration exposed to the UV-ray for 30 minutes, and almost 65% mortality occurred in the cells (Fig. 4).

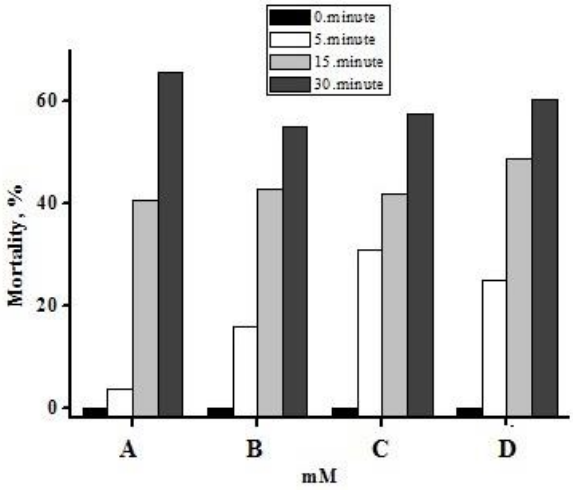

Fig. 4. Results of the mortality (%) for LNCaP cells. (A, B, C and D symbols was represented concentrations respectively 0.01, 0.1, 1 and 10 mM.) Statistically significant $p<0.05$ was considered significant.

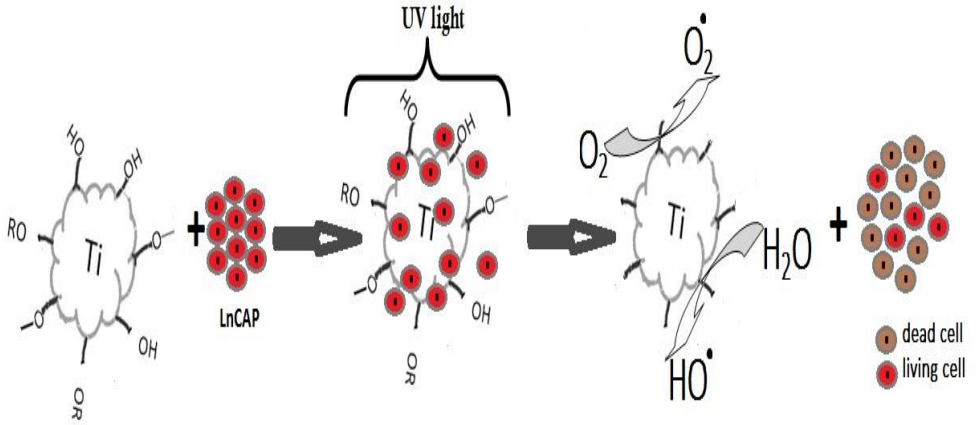

Fig. 5. The formation of active oxygen species at the surface of TiO_2.

The fact that there is a proliferation without the UV-ray, but a decrease in the vitality of the cancer cells with the effect of the UV-ray indicates the fact that active regions are generated at the surface of TiO_2 with the effect of the UV-ray, allowing for the emergence of active oxygen species (ROS) in the medium [18]. The active oxygen species form non-duplicated electron pairs. Hydroxyl radical ($OH^{\cdot}$), along with superoxide radical ($^{\cdot}O_2$) and non-radical H_2O_2 and singlet oxygen ($_1O_2$) constitute an oxidation-reduction reaction [19]. Active oxygen species are also used in cancer drugs, such as procarbazine, doxorubicin, buthionine sulfoximine, motexafin gadolinium and rituximab [20-23]. Active oxygen species (Fig. 5) are also formed at the surface of TiO_2, which lead to the death of cancer cells.

CONCLUSION

In conclusion, in this study, the nano-sized TiO_2 particles were successfully synthesized, and their effect on the LNCaP cell was analyzed. The nano-sized TiO_2 particles synthesized through the hydrothermal method showed a photocatalytic and anti-cancer characteristic on the LNCaP cell. The death of cancer cells was accomplished by means of the active oxygen species that occurred on the surface of TiO_2 via the applied UV-ray. Approximately 65% of mortality took place in 30 minutes. The use of the synthesized nano-TiO_2 could be possible in the treatment of cancer. If the nano -TiO_2's are applied to the cancerous area exposed to the UV-ray, they may cause the cancer cells to diminish or to get destroyed. The X-rays can even be used for starting photocatalytic reactions on the nano-TiO_2 [24]. In order to be able to pull the applied wavelength to the visible area, different studies can be performed by attaching transition metal dopants into the nano-TiO_2 [25].

Acknowledgement: *Financial support supplied from I.U-BAP with grant 2012/36 is gratefully acknowledged.*

REFERENCES

1. M. Asiltürk, F. Sayılkan, S. Erdemoğlu, M. Akarsu, H. Sayılkan, M. Erdemoğlu, E. Arpaç, *J. Hazard. Mater.*, **129**, 164 (2006).
2. K. Nakata, A. Fujishima, *Photochem. Photobiol. C: Photochem. Rev.*, **13(3)**, 16 (2012).
3. T. Fotiou, T. M. Triantis, T. Kaloudis, A. Hiskia, *Chem. Eng. J.*, **261,** 17 (2015).
4. [4] S. J. Kwon, H. B. Im, J. E. Nam, J. K. Kang, T. S. Hwang, K. B. Yi, *Appl.Surf. Sci.*, **320**, 487 (2014).
5. S. J. Lue, Y.L. Wu, Y.L. Tung, C.M. Shih, Y. C. Wang, J. R. Li, *J. Power Sources*, **274**, 1283 (2015).
6. B. Lyson-Sypien, A. Czapla, M. Lubecka, P. Gwizdz, K. Schneider, K. Zakrzewska, K. Michalow, T. Graule, A. Reszka, M. Rekas, A. Lacz, M. Radecka, *Sens. Actuators, B: Chemical*, **175**, 163 (2012).
7. X. Chen, S. S. Mao, *Chem. Rev.*, **107**, 2891 (2007).
8. Y. Kubota, T. Shuin, C. Kawasaki, M. Hosaka, H. Kitamura, R. Cai, H. Sakai, K. Hashimoto, A. Fujishima, *Br. J. Cancer*, **70**, 1107 (1994).
9. A. Mills, S. L. Hunte, *J. Photochem. Photobiol. A*, **108,** 1 (1997).
10. G.F. Fu, P.S. Vary, C.T. Lin, *J. Phys. Chem. B*, **109,** 8889 (2005).
11. N.P. Huang, M.H. Xu, C.W. Yuan, R.R. Yu, *J Photochem Photobiol A: Chem.*, **108**, 229 (1997).
12. A.P. Zhang, Y.P. Sun, *World J Gastroenterol.*, **10,** 3191 (2004).
13. J. W. Seo, H. Chung, M.Y. Kim, J. Lee, I.H. Choi, J. Cheon, *Small*, **3**, 850 (2007).
14. P. Thevenot, J. Cho, D. Wavhal, R. B. Timmons, L. Tang, *Nanomed Nanotech Biol Med.*, **4**, 226 (2008).
15. L. Liu, P. Miao, Y. Xu, Z. Tian, Z. Zou, G. Li, *J. Photochem. Photobiol. B: Biol.*, **98,** 207 (2010).
16. D. M. Blake, P. C. Maness, Z. Huang, E. J. Wolfrum, J. Huang, *Sep Purif Methods*, **28**, 1 (1999).
17. Z.K. Genc, S. Tekin, S. Sandal, M. Sekerci, M. Genc, *Res. Chem. Intermed* **41**, 4477 (2015).
18. R. Cai, Y. Kubota, T. Shuin, H. Sakai, K. Hashimoto, A. Fujishima, *Cancer Res.*, **52**, 2346 (1992).
19. K.A. Conklin, *Integr. Cancer Ther.*, **3**, 294 (2004).
20. J.M. MateÂs, M. Francisca, J.Â SaÂnchez, *Int J Biochem Cell B*, **32**, 157 (2000).
21. M.F. Renschler, *Eur. J. Cancer*, **40**, 1934 (2004).
22. T. Ozben, *J. Pharm. Sci.*, **96**, 2181 (2007).
23. J. Wang, J. Yi, *Cancer Biol. Ther.*, **7**, 1875 (2008).
24. T. Kazuhisa, O. Yoshihisa, K. Hiroyuki, Y. Hideki, T. Tetsu, F. Akira, M. Jun'ichiro, *Electrochim Acta*, **52**, 6938 (2007).
25. N. Siva, I. Reddy, B. Thirupathi, S. Makram, G. S. Panagiotis, *Appl Catal B-Environ.*, **144**, 333 (2014).

ИЗСЛЕДВАНЕ НА ЕФЕКТА НА НАНОЧАСТИЦИ ОТ TiO_2, СИНТЕЗИРАНИ ПО ХИДРОТЕРМАЛНИЯ МЕТОД ВЪРХУ LnCap-РАКОВИ КЛЕТКИ

Ф.Б. Емре [*1,2], Ф. Окушлук[1,2], С. Текин[3], С. Сандал[3]

[1]*Лаборатория по изследване и приложения на нови материали, Научно-технологичен изследователски център, Университет „Иньоню“, Малатия 44280, Турция*

[2]*Департамент по основно образование, Образователен факултет, Университет „Иньоню“, Малатия 44280, Турция*

[3]*Департамент по физиология, Медицински факултет, Университет „Иньоню“, Малатия 44280, Турция*

Получена на 15 ноември, 2016 г.; коригирана на 11 март, 2017 г.

(Резюме)

Извършена е синтеза на наноразмерен TiO_2 по хидротермалния метод от титанови алкоксиди. Структурните, физичните и химичните свойства на наночастиците са определени чрез рентгеноструктурен анализ, сканираща електронна микроскопия и анализ на размера на частиците. Синтезираните TiO_2 – наночастици са изцяло в анатаз – полиморфна модификация. Наночастиците в различни концентрации и приведени в зол-състояние са приложени спрямо LNCaP-ракови клетки в културална среда, а техната анти-туморна и забавяща пролиферацията активност е изпитана фотокаталитично с и без ултравиолетово лъчение. Броят на живите и мъртвите клетки беше установен по MTT-метода, като с това са определени противо-раковите свойства на наночастиците.

Bulgarian Chemical Communications, Volume 49, Number 3, (pp. 669 – 677) 2017

The degradation and corrosion characteristics of blended amine solution in the coal bed methane decarburization process

Jinhua Chen[1*], Juan Wen[2]

[1] *Correspondence author at Chongqing Research Institute of China Coal Technology & Engineering Group Corporation, 55 ShangqiaoSancun, Shapingba District, Chongqing, P.R.CHINA.*
[2] *Chongqing Real Estate College, 3 Mingde Road, Shapingba District, Chongqing, P.R.CHINA*

Received February 20, 2017, Revised August 31, 2017

For years, the degradation and corrosion of amine solutions has become an essential issue for the coal bed methane (CBM) decarburization process. And the degradation and corrosion characteristics of amine solutions are not clearly yet. Aimed to solve the sebarriersin this study, the degradation characteristics of blended amine solutions with or without antioxidants were studied in a rich oxygen environment. Results show without antioxidants here was a high oxidative degradation of amine solutions without antioxidants. While after adding certain antioxidants, such as sodium metavanadate (NaVO3), sodium sulfite or sodium potassium tartrate, the oxidative degradation ratio of blended amine solutions showed an obvious decrease. The amine solutions which added sodium metavanadate had the best antioxidant ability, followed by which added potassium sodium tartrate and then sodium sulfite. When added 1% sodium metavanadate, the oxidative degradation ratio of methyldiethanolamine (MDEA) +piperazine (PZ) (8:2) solution reduced 32%. And the corrosion characteristics of fresh amine solutions and rich amine solutions were investigated by the corrosion experiments at 90°C for 72 hours. Both the results of corrosion ratio test and the SEM show the corrosion ratio of rich amine solutions was much larger than that of fresh amine solutions. After adding 0.5% NaVO3 and 0.5% V2O5 as inhibitor, the corrosion of rich amine solutions were declined. According to the results of the degradation and corrosion characteristics, the decarburization agent for CBM process was recommended as MDEA+PZ(8:2) with 0.5% NaVO3 and 0.5%V2O5 .

Key words: blended amine, decarburization, antioxidant, oxidative degradation, corrosion.

INTRODUCTION

In the coal bed methane (CBM) utilization industry, it is essential to remove CO_2 before CBM liquefaction. And currently, amine-based absorption method is the most widely used to remove CO_2 from the natural gas and which is a well-proven commercial technology [1-4]. With the continuous studying on CO_2 absorbent by amine such as steric amine and enamine, the absorption characteristics of CO_2 absorbent is clearly known, and their different reactivity or rate for CO_2 absorption were investigated and reported [5]. Now, the research trend is shown to find a new blended solution which concludes all advantages of single CO_2 absorbents by studying the absorption of mixture absorbents.

MDEA is one of the most famous CO_2 absorbents and wildly applied in nature gas decarburization process. Although the corrosion that the MDEA single amine solution brought to piping equipment is much smaller than that of the other amine solutions [6,7], the influence of the degradation products of MDEA-based blended amine on the equipment system should not be underestimated[8,9]. During the decarburization process, accompany with the amine solution degradation the amine is gradually losing, as a result the absorption capacity of amine solution is decreasing. On the other hand, with the decomposition of amine the equipment corrosion caused by amine solution is raising, which will not only reduce the stability of absorption system, but also increase the construction costs and operating costs of the system, and result in direct economic losses. Furthermore, the degradation of amine solutions may lead to the erosion of the vessel wall, which result greater losses and more serious security risks. So in order to obtain a good strategy for the prevention of degradation of MDEA-based blended amines, a good understanding of the degradation process is necessary.

In the decarburization process, the two degradation types of organic amines are mainly oxidative degradation and thermal degradation [10]. The thermal degradation refers to the amine degradation that occurs in desorption tower, reboiler, heat exchanger and other high temperature regions, and does not require O_2 participation. While oxidative degradation refers to a redox reaction between organic amine and O_2 in the role of active groups [10]. The reaction balance of MDEA in aqueous solution is as follow [12-18].

To whom all correspondence should be sent:
E-mail: cqchenjinhua@163.com

$CH_3\text{-}N(CH_2CH_2OH)_2 + H_2O \leftrightarrow CH_3\text{-}NHCH_2CH_2OH + HOCH_2CH_2OH$ (1)

When oxygen is present, the hydrolysis equilibrium products ethylene glycol will be further oxidized in the role of Fe^{2+} as catalyst, and oxalic acid and formic acid will be produced.

$HOCH_2CH_2OH \rightarrow HOCH_2CHO \rightarrow OHCHO \rightarrow HOOCCHO \rightarrow HOOCCOOH \rightarrow HCOOH + CO_2$ (2)

The oxidative degradation products are acidic and have a strong corrosive effect on devices. And the smaller the molecular weight of organic acid, the greater the corrosive effect [9].

At present, the knowledge of the corrosion and oxidative degradation of the blended amine solutions for CO2 absorption was limited. There are a few reports on the degradation of organic amines from University of Regina [5, 19-22], University of Texas at Austin, French Petroleum Institute, Norwegian Technology University and Dow Chemical Company [11]. While in China, reports on the degradation problems of organic amine solution in CO_2 absorption process are rare, only Chen Changhe [11], Lu Jiangang [23], Zhang Chengfang [24], Zhang Yongchun [25] and several other scholars did researches on that. So there is no enough date to optimizing industrial design and calculating CO_2 fraction. Thus, it is particularly necessary to conduct investigations to reduce the oxidative degradation of MDEA amine solutions effectively by strict controlling the operating conditions and adding corrosion inhibitors or antioxidants.

This study aimed to understand the degradation characteristics and corrosion characteristics of amine solutions in the decarburization process, and realized by testing the degradation ratio of amine solutions and the corrosion ratio of steel sample sheets immersing in the amine solutions. Finally improved the CO_2 absorption ability of amine solution for, and certain antioxidants and inhibitors were added into the solutions to reduce the degradation and corrosion ratio.

METHODS AND MATERIALS

The materials and equipment used in the degradation and corrosion experiments are listed in Table 1 and Table 2 as below.

Table 1. The materials for degradation experiments and corrosion experiments

Name	Specification	Resource
CO_2	99.999%	Chengdu Hong Jin chemical (gas) Co., Ltd.
MDEA	99%AR	Chengdu Kelong Chemical Reagent Factory
DETA	99%AR	Chengdu Kelong Chemical Reagent Factory
MEA	99%AR	Chengdu Kelong Chemical Reagent Factory
PZ	99%AR	Chengdu Kelong Chemical Reagent Factory
sodium sulfite	AR	Chongqing Chuandong Chemical (Group) Co., Ltd
Sodium aluminate	AR	Chengdu Kelong Chemical Reagent Factory
sodium potassium tartrate	AR	Chengdu Kelong Chemical Reagent Factory
V_2O_5	99%	Chengdu Jinshan Chemical Reagent CO,.LTD
Steel sheet	Q235	Cutting by subcontractor into the size of 40*40*2 （mm ）
abrasive paper	GRIT No.CW800	NAMKYUNG ABRASIVE IND.CO,.LTD
H_2SO_4	AR	Chongqing Chuandong Chemical (Group) Co., Ltd
acetone	AR	Chongqing Chuandong Chemical (Group) Co., Ltd
HNO_3	AR	Chongqing Chuandong Chemical (Group) Co., Ltd

Table 2. The apparatus for degradation experiments and corrosion experiments

Name	Model	Resource
Electronic balance	FA-2004N	Shanghai Minqiao Precision Scientific Instruments Co., Ltd.
Automatic titration analyzer	ZD-2	Shanghai Dapu Instrument Co., Ltd.
Precision pH meter	PHS-3C	Shanghai Dechuan Precision Instruments Co., Ltd.
Constant temperature convection oven	101	Shanghai Dongxing Test Equipment Co., Ltd.
Constant temperature water bath	HH-S11-NI6	Beijing Scientific Instruments & Materials Corp
Vernier caliper	0-150MM	Guilin Guanglu Measuring Instrument Co., Ltd
SEM	Tescan Vega	FEI Nova400, China

Degradation experiments

In the coal bed methane decarburization process, the temperature in the absorption tower usually is 45°C and the pressure is 0.4MPa, while in the desorption tower, the temperature usually is 115°C and the pressure is 0.06MPa. The degradation of amine solutions caused by thermal or chemical is very slight that it is not necessary to consider them separately. So in this study, the thermal degradation and chemical degradation were tested together in the thermal degradation experiments, while the oxidation degradation of amine solutions was tested alone. And according to the results of Idem R. O.'s research [5] ,that there was no significant degradation of MEA and MDEA which induced by CO_2 at both lower and higher total amine concentrations at a temperature range of 328-393 K.

We assumed that the thermal degradation of CO_2 loaded amine solution was similar with the thermal degradation of fresh amine solution. Thus we did not investigate the thermal degradation of CO_2 loaded amine solution here, and it will be investigated in our next work.

Thermal degradation experiments

In the thermal degradation experiments, reactors containing a certain amount of fresh amine solutions were sealed and put in a constant temperature convection oven, and were heated at 95 °C constantly for a period of time. And during the heating, for every designed time interval1 mL sample were taken out from the reactors, and the total amine concentration of the samples were determined by an automatic titration analyzer. After the measured total amine concentration in the solutions reduced to a constant value and changed slightly, the thermal degradation experiments would be stopped. The thermal degradation of the fresh amine solutions and the rich amine solutions were tested respectively. By the analysis of the total amine concentration in the solutions at different time periods under high temperature heating conditions, the thermal degradation characteristics of amine solutions were obtained.

Oxidation degradation experiments

In this study, different kinds of fresh amine solutions with or without adding antioxidants were prepared for oxidation degradation experiments. A certain amount of amine solutions were taken into the reactor, and the reactor was fed in oxygen for a while, then the reactor was sealed and placed in a heated convection oven to keep a constant temperature. Samples were taken at different time periods. By using an autoburette, the total amine concentration in the sample can be analyzed, and then the oxidative degradation characteristics of amine solutions would be obtained. By comparing the oxidative degradation characteristics of different amine solutions with different antioxidants, the amine formulations with excellent stability will be selected out.

Corrosion experiments

Q235 steel sheets with a size of 40×40×2(mm) were selected as the specimens for corrosion experiments. And the steel sheets were immersed in different amine solutions in different 250mL beakers. These beakers were sealed and placed in a constant temperature water bath for heating at 90 °C for 72 hours. The mass of each specimen before and after the corrosion experiments were measured. The corrosion characteristics of the decarburization amine solutions were quantitative and qualitative analyzed by using the gravimetric method and scanning electron microscopy (SEM). The corrosion rate of specimens can be calculated by Equation(1).

$$\overline{\mu} = \frac{m_0 - m_i}{t \times s} \quad (3)$$

Where,

$\overline{\mu}$ is the metal corrosion rate, g/(m^{2}h);

m_0 is the first mass of specimen before corrosion test, g;

m_i is the final mass of specimen after corrosion test for a certain period and the corrosion products on the surface of specimen was removed , g;

S is the surface area of specimen exposed to the corrosive environment, m^2;

And *t* is the corrosion time, h.

RESULTS AND DISCUSSION

Thermal degradation

Six different kinds of fresh amine solutions of 30% mass fraction were prepared. 100 mL amine solutions were put into different beakers. Then sealed the beakers and placed them at a constant temperature of 95 °C for 44 hours. During this period, every 12 hours 1mL amine solution sample was taken out for analyzing. 0.5 mol/L hydrochloric acid solution was used for titration analyzing, the consumption volume of hydrochloric acid were measured when the pH value of the amine solutions reached 7. Then the total amine concentration in the amine solution can be calculated, and the amine thermal degradation ratio were obtained.

Table 3. The hydrochloric acid consumption amount of each 1 L amine solutions (mol/L)

Time	MDEA	MEA	DETA	MDEA+MEA 7 : 3	MDEA+DETA 8 : 2	MDEA+PZ 8 : 2
0h	2.565	5.005	5.935	2.968	3.194	2.616
12h	2.540	4.929	5.703	2.917	3.169	2.616
24h	2.490	4.829	5.734	2.917	3.169	2.590
44h	2.490	4.653	5.659	2.842	3.144	2.565

The results are shown in Table 3 and Fig. 1.

It can be seen in Table 3, the hydrochloric acid consumption amount of each 1L amine solutions decreased slightly with time. This is because that under the constant heating environment at 95 °C, the amine degraded, and the total amine concentration of the amine solutions decreased with time, which resulted in the decrease of hydrochloric acid consumption amount.

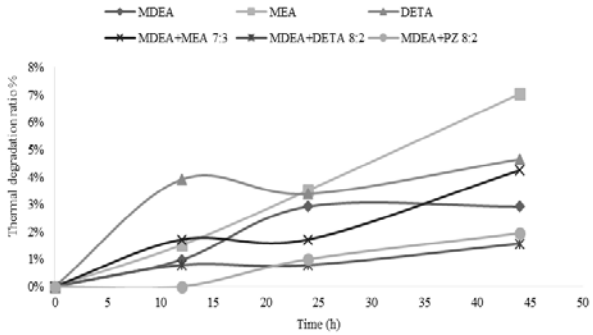

Fig.1. The change of thermal degradation ratio of amine solutions with time

In Fig.1, the thermal degradation ratio of MEA solution had the fastest increasing rate with heating time, and after 44 hours heating the ratio is 7.03%. Then the thermal degradation increasing rate turned to slower for others amine solutions with an order as: DETA> MDEA+MEA (7:3)> MDEA+ DETA (8:2)> MDRA+PZ (8:2). And it can be found that the thermal degradation ratio of MDEA+PZ(8:2) blended amine solution was just 1.6% after 44 hours, which indicated that the thermal degradation of this blended amine solution is so slightly that can be ignored.

Oxidative degradation

The oxidative degradation characteristics of single amine solutions and blended amine solutions without anti-oxidants

Prepared different kinds of fresh amine solutions of 30wt%. 150mL amine solutions were put into a volumetric flask and then fed pure oxygen for 2 minutes. Then sealed the volumetric flask and placed it at room temperature for a design time. During this period, every 96 hours took 1mL of amine solution sample for analyzing. 5mol/L hydrochloric acid solution was offered for titration analyzing, the consumption volume of hydrochloric acid were measured when the pH value of the amine solutions reached 7.Then the total amine concentration in the amine solution could be calculated, and the amine degradation ratio were obtained. The results are shown in Table 4 and Fig. 2.

Table 4 shows that the total amine concentration declined before held for 303 hours. This was due to the amine in solutions was oxidized in oxygen-rich condition. The oxidative degradation of single MEA amine solution and MDEA+MEA blended amine solution is larger than that of single MDEA amine solution and MDEA+PZ blended amine solution. And all amine concentrations declined slightly with time.

In Fig. 2, it can be seen that, the oxidative degradation ratio of MDEA+MEA blended amine solution raising fastest with holding time, and also had the highest ratio after held for 399 hours compare with other amine solutions. Then is that of MEA single amine solution. Then the single MEA amine had a lower oxidative degradation ratio than MDEA+MEA (7:3) blended amine. Lowest oxidative degradation ratio was found for single MDEA after 399 hours oxidization, and MEDA+ PZ (8:2) has a little higher ratio than MDEA which was found as 24.63%.

According Table 4 and Fig. 2, a conclusion can be obtained that the in these four amine solutions, MDEA +PZ blended amine solutions was affected by oxygen a little, whose oxidative degradation ratio is only 3.8% at the first 44 hours, but still

Table 4. The hydrochloric acid consumption amount of each 1 L amine solutions（mol/L）

Time	MDEA	MEA	MDEA+MEA	MDEA+PZ
0h	2.565	5.030	3.471	3.93
96h	2.515	4.829	2.842	3.8052
192h	2.389	4.552	2.766	3.7204
303h	2.414	4.389	2.641	3.6156
399h	2.414	4.276	2.616	3.607

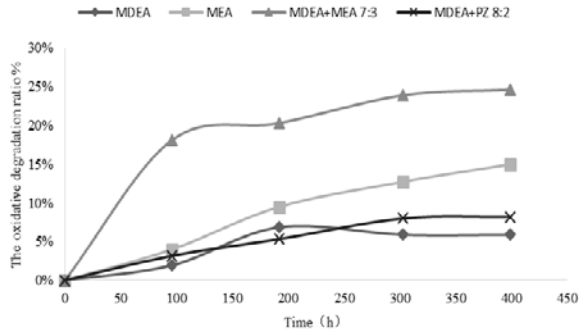

Fig. 2. The change of oxidative degradation ratio of amine solutions with time

more larger than its thermal degradation ratio of 1.6% at the first 44 hours. As the effect of oxygen on amine solutions exists almost in the whole decarburization process, while the effect of heat exists only in the amine solution recovery process, the influence of oxygen on amine degradation is much larger than that of thermal.

The oxidative degradation characteristics of blended amine solutions with anti-oxidants

The 30% amine concentration solution which contained by MDEA+PZ (8:2) blended amine was reported had a good CO2 absorption ability with a high CO2 absorption rate and regeneration ratio[15]. Moreover, the above thermal degradation experiments and oxidative degradation experiments proved that the MDEA+PZ (8:2) had a reliable stability even in high temperature and high oxygen content atmosphere.

Therefore, the blended amine solution MDEA+PZ (8:2) was selected as an optimization CO2 absorption compound of the investigation for studying the effect of anti-oxidants. 1wt% of three kinds of antioxidants, namely potassium sodium tartrate tetrahydrate, sodium sulphite and sodium metavanadate was added in the blended amine solution. The oxidative degradation characteristics study results are shown in Table 5 and Fig. 3.

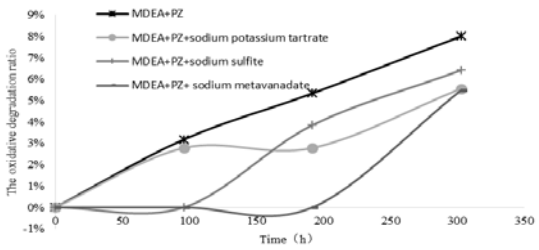

Fig.3. The change of oxidative degradation rate of blended amine solutions with time

Table 5 shows that the hydrochloride consumption amount of each 1 L amine solutions reduced with increasing of held time, which means the total amine concentration decreased gradually with time, and indicates that the oxidative degradation occurred in the amine solution. But the total amine concentration of MDEA+PZ (8:2) blended amine solutions with anti-oxidants did not change significantly.

From Fig.3, it can be seen that, after adding three different anti-oxidants, the oxidative degradation ratio of MDEA+PZ (8:2) solutions was decreased. This indicated that the anti-oxidants did effort on protecting the amine solutions from degradation caused by oxygen. Results show sodium metavanadatehad the best ability to reduce the degradation caused by oxygen in these three anti-oxidations, and the degradation ratio reduced 32% after 303 hours reaction compare with the blended amine solution without any anti-oxidations. And it was found that t sodium potassium tartrate had a better ability to reduce the degradation than sodium sulfite.

Corrosion results

Corrosion characteristics of fresh amine soliotions

The corrosion characteristics of six different fresh amine solutions of 30wt% total amine concentration were investigated by the corrosion experiments at the same temperature of 90°C for 72 hours. The results are shown in Table 6.

.

Table 5. The hydrochloric acid consumption amount of each 1 L amine solutions (mol/L)

Time	MDEA+PZ + sodium potassium tartrate	MDEA+PZ + sodium sulfite	MDEA+PZ + sodium metavanadate	MDEA+PZ
0h	3.7728	4.0872	3.8252	3.93
96h	3.668	4.0872	3.8252	3.8052
192h	3.668	3.93	3.8252	3.7204
303h	3.5632	3.8252	3.6156	3.6156

Table 6. Corrosion characteristics of fresh amine solutions

Fresh amine solutions	Amine Concentration wt%	Surface area 10^{-6} m^2	Specimen mass before erosion g	Specimen mass after erosion g	Corrosion rate g/(hm^2)
MDEA	30%	3568	32.5308	32.5269	0.01518
MEA	30%	3446	31.3111	31.3071	0.01612
DETA	30%	3616	32.7790	32.3841	1.51668
MDEA+PZ	30%(8：2)	3524	31.8979	31.8921	0.02286
MDEA+DETA	30%(8：2)	3585	31.7671	31.7603	0.02634
MDEA+MEA	30%(8：2)	3450	31.3799	31.3734	0.02617

Among these three single amine solutions, the lowest corrosion rate was found on the specimen immersing in the MDEA single amine solution, while that in DETA single amine solution had a highest corrosion rate, which indicated that the corrosion rate of specimen in amine solutions has a positive correlation with the alkalinity of amine solutions. That means the better CO_2 absorption characteristics, the stronger corrosion characteristics. After adding different activators (PZ, DETA and MEA) in the MDEA solutions, the specimens in these three blended amine solutions had a larger corrosion rate than that in the MDEA single amine solutions, but still much lower than that in the DETA single amine solutions. And the specimen in the MDEA+PZ blended amine solutions had the lowest corrosion rate among these three blended amine solutions.

Corrosion characteristics of rich amine solutions

The rich amine solutions were prepared by piping CO2 into the fresh amine solutions for enough time. Then the corrosion characteristics of rich amine solutions were studied by the corrosion experiments at the same temperature of 90°C for 72 hours. The results were as shown in Table 7. From Table 7 it can be seen that, the largest corrosion rate of specimen immersing was found in the MEA rich amine solitions, while that in MDEA rich amine solitions is the lowest. The corrosion rate of specimen in MDEA+PZ rich amine solutions is 0.0999 gm-2/h, which is slightly higher than that in MDEA rich amine solitions. Compared with Table 6, it is obviously that the corrosion rate of specimen in rich amine solutions is much higher than that in the relative fresh amine solutions, which indicated that the corrosion characteristics of rich amine solutions is much stronger than that of fresh amine solutions. And in these blended rich amine solutions, the specimen in the MDEA+PZ rich amine solutions still had the lowest corrosion rate.

Corrosion characteristics of rich amine solutions with inhibitors

According to the corrosion experimental results above, whether among the fresh amine solutions or the rich amine solutions, specimen in the MDEA+PZ(8:2) blended amine solutions had a relatively small corrosion rate. So the MDEA+PZ(8:2) blended rich amine solution was taken for investigation in this part of experiments. 0.5% -1% of sodium vanadate and vanadium pentoxide as corrosion inhibitors was added into the MDEA+PZ(8:2) blended rich amine solutions, the corrosion experiments were carried out at 90 ℃ for 72hours. The corrosion rate of specimens in the MDEA+PZ(8:2) blended rich amine solutions with different inhibitors were measured, and the results were shown in Table 8. Compared Table 7 and Table 8, it can be seen that, afteradding inhibitors, the corrosion rate of specimens in the MDEA+PZ(8:2) blended rich amine solutions had a significant decrease, the corrosion rate decreased from 0.0999 g/(hm^2) for the amine without inhibitors to 0.0026 g/(hm^2) which was the largest corrosion rate after adding inhibitors. The anti-corrosion ratios of these six solutions with different inhibitors were larger than 97%. The anti-corrosion effect of inhibitor V_2O_5 was slightly better than that of inhibitor $NaVO_3$when same amount of inhibitors was added. And it was found the influence of inhibitor amount on the

Table 7. Corrosion characteristics of rich amine solutions

Rich amine solutions	Concentration wt%	Surface area 10^{-6}m^2	Specimen mass before erosion g	Specimen mass after erosion g	Corrosion rate g/(hm^2)
MDEA	30%	3514	32.2393	32.2160	0.0896
MEA	30%	3429	31.2417	30.8665	1.4786
MDEA+PZ	30%(8：2)	3408	31.2460	31.2208	0.0999
MDEA+MEA	30%(8：2)	3566	32.4742	32.4338	0.1531

anti-corrosion effect is similar in the range from 0.5% to1%. And the he highestanti-corrosion ratio, 99.2%, was found in the solution which added 1% inhibitors of $NaVO_3$+V_2O_5(0.5%:0.5%)is t up to. The specimen surface corrosion characteristics were observed by using SEM at different scale, 5um,10um, 20um, 50umand 100um respectively. The SEM results of specimen before and after immersed in MDEA+PZ(8:2) blended rich amine solutions are shown in Fig 4-1a and Fig 4-1b respectively. Compared these two groups of images, it can be seen that, without adding any inhibitors, after immersing in the MDEA+PZ (8:2) blended rich amine solutions for 288h, that pitting appeared on the specimen surface was observed at 5um,10um and 20um scale, while at the 50umand 100um scale, that cracks increased on the specimen surface was observed. The results indicated that the rich amine solutions has a strong corrosion effect on the steel sample sheets, which is consistent with the results of corrosion ratio tests above. Fig 4-2a and Fig 4-2b show the SEM results of specimen before and after immersed in MDEA+PZ(8:2) blended rich amine solutions with inhibitors of $NaVO_3$+V_2O_5(0.5%:0.5%),respectively. Compared these two groups of micrographs, it can be seen that, with adding inhibitors of $NaVO_3$+V_2O_5(0.5%:0.5%),no significant difference can be observed on the specimen surface. This results indicated that the inhibitors of $NaVO_3$+V_2O_5(0.5%:0.5%) had an obviously anti-corrosion effect and protected the steel sample sheets from corrosion by rich amine solutions.

Table 8. Corrosion characteristics of MDEA+PZ (8:2) blended rich amine solutions with inhibitors

Inhibitor	Surface area $10^{-6}m^2$	Specimen mass before erosion g	Specimen mass after erosion g	Corrosion rate $g/(h*m^2)$	Anti-corrosion ratio %
$NaVO_3$(0.5%)	3654	34.2612	34.2605	0.0026	97.40
$NaVO_3$(1%）	3434	32.4299	32.4293	0.0024	97.60
V_2O_5(0.5%）	3623	34.1066	34.1069	0.0011	98.90
V_2O_5(1%)）	3534	33.1796	33.1790	0.0023	97.70
$NaVO_3$ + V_2O_5(0.25%:0.25%）	3506	32.6926	32.6920	0.0023	97.70
$NaVO_3$+ V_2O_5（0.5%:0.5%）	3441	32.1723	32.1721	0.0008	99.20

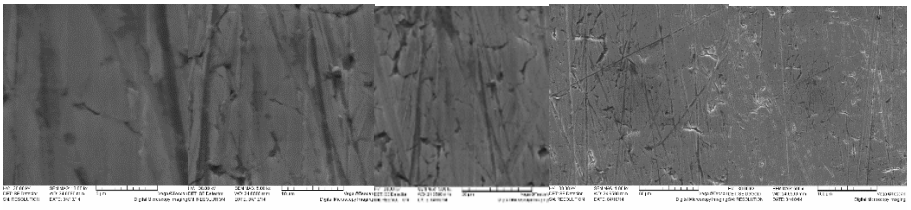

Fig 4-1a. SEM results of specimen before immersed in MDEA+PZ (8:2) blended rich amine solutions

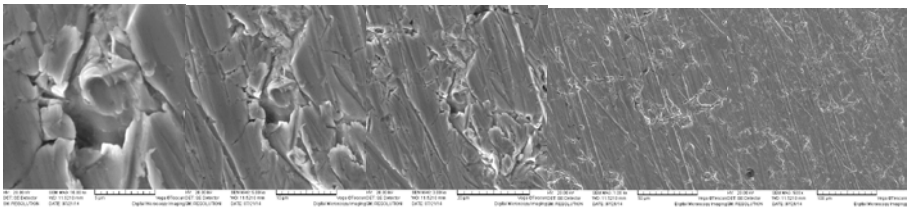

Fig 4-1b. SEM results of specimen immersed in MDEA+PZ (8:2) blended rich amine solutions after 288h

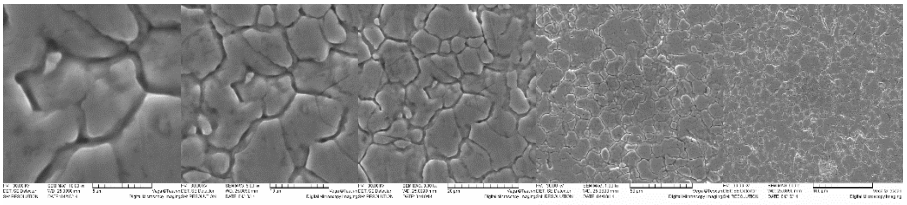

Fig 4-2a. SEM results of specimen before immersed in MDEA+PZ (8:2) blended rich amine solutions with inhibitor

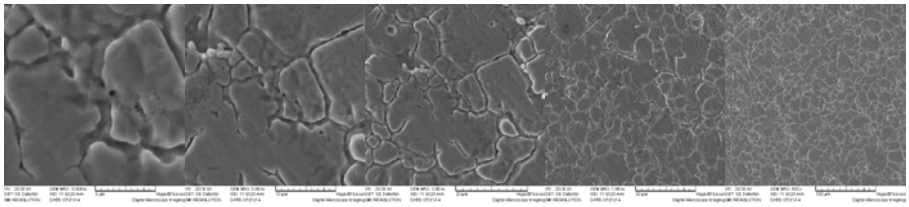

Fig 4-2b. SEM results of specimen immersed in MDEA+PZ(8:2) blended rich amine solutions with inhibitor after 288h

CONCLUSIONS

In the CBM decarburization process, amine degradation is mainly caused by oxygen, which result in low decarburization efficient and bring serious corrosion problems at the same time. Experiments were carried out to investigate the degradation and corrosion characteristics of amine solutions in the decarburization process. The results show that by adding certain antioxidants, the oxidative degradation ratio of blended amine solutions decreased obviously. The amine solutions with sodium metavanadate $NaVO_3$ has the most conspicuous antioxidant effects, followed by that with potassium sodium tartrate, and the last is with sodium sulfite. By adding 1% sodium metavanadate $NaVO_3$, the oxidative degradation ratio of MDEA+PZ (8:2) solution can be reduced by 32%. And the results of corrosion experiments show that the corrosion characteristics of rich amine solutions was much stronger than that of fresh amine solutions. The influence of inhibitor amount on the anti-corrosion effect is very small in the range of 0.5% to1%, and the anti-corrosion ratio of the solutions with 1% inhibitors of $NaVO_3$+V_2O_5(0.5%:0.5%)is the highest, up to 99.2%. The SEM results also show that with adding 1% inhibitors of $NaVO_3$+V_2O_5(0.5%:0.5%） the surface of specimen immersed in the MDEA+PZ blended rich amine solutions changed merely. The recommended decarburization agent formula is MDEA+PZ(8:2) with 0.5% $NaVO_3$ and 0.5% V_2O_5 as inhibitor.

REFERENCES

1. J. H. St. Clair, W. F. Simister, *Oil Gas J*.; (United States), **81**, 7 (1983).
2. J. Wen, C. X. Huo, B. Zhang, **864-867**, 194 (2014)
3. M. T. Sander, C. L. Mariz, *Energy ConVers Manage*., **33**, 341 (1992)
4. F. A. Tobiesen, H. F. Svendsen, *Industrial & Engineering Chemistry Research*, **45**(8), 2489 (2006)
5. A. O. Lawal, R. O. Idem, *Industrial and Engineering Chemistry Research*, **45**(8), 2601 (2006)
6. P. C. Rooney, M. S. Dupart, T. R. Bacon, *Hydrocarbon Process*, **77**, 109, (1998).
7. J. H. Chen, Ju. Wen. *Guangdong Chemical Industry*, **42**(12), 45 (2015).
8. X. W. Feng, X. P. Guo, *Journal of Chinese Society for Corrosion and Protection*, **23**(2),79 (2003).
9. Q.G. Ye, F.Q. Lu. *Corrosion science and protection technology*, **12**(3), 173 (2000).
10. S. Chi, G. Rochelle, *Industrial & Engineering Chemistry Research*, **41**(17), 4178 (2002).
11. Sh. Zhou, Sh.J. Wang，G.T. Rochelle, C.G. Chen, *J. Tsinghua University* (Sci&Tech), **56**(1), 81 (2012).
12. M.X. Yang, C.C, Xu, X.R. Fang. *Corrosion & Protecion*, **28**(10), 519 (2007)
13. X.Q. Yan, *Chemical Engineering of Oil & Gas*, **38**(4), 308 (2000).
14. A. Chakma, A. Meisen, *Can. J. Chem. Eng*., **75**(5), 861 (1997).
15. P.C. Rooney, M.S. Dupart, T.R. Bacon, *Hydro Proc*., **77**(7), 109 (1998).
16. T. Supap, R. Idem, P.Tontiwachwuthikul, C. Saiwan, *International Journal of Greenhouse Gas Control*, **3**(2), 133 (2009).
17. T. Supap, R. Idem, P. Tontiwachwuthikul, C. Saiwan, *Industrial and Engineering Chemistry Research*, **45**(8), 2437 (2006).
18. M. Howart, A. Sargent, *Oil&Gas Journal*, **99**, 52, (2001).
19. A. O. Lawal, R. O. Idem, *Ind. Eng. Chem. Res.* **44**(4), 986 (2005).
20. O. Lawal, A. Bello, R. Idem, *Ind. Eng. Chem. Res.* **44**(4), 1874 (2005).
21. A. Bello, R. O. Idem, *Industrial and Engineering Chemistry Research*, **45**(8), 2569 (2006).
22. W. Tanthapanichakoon, A. Veawab, B. McGarvey *Industrial and Engineering Chemistry Research* , **45**(8), 2586 (2006),
23. C.F. Zhang, L.J. Chen, CN1367170, 2002.
24. J.G. Lu, Y.F. Zheng, M.D. Chen, H.C. Zhou, Z.B. Guo, CN101063207,2007.
25. Y.C. Zhang, G.M. Li, X.F. Wang, C. Guo, S. Chen CN102284229A, 2011.

ХАРАКТЕРИСТИКИ НА ДЕГРАДАЦИЯ И КОРОЗИЯ ЗА РАЗТВОР НА СМЕС ОТ АМИНИ ПРИ ОТНЕМАНЕТО НА ВЪГЛЕРОДА ОТ МЕТАН В СЛОЙ ВЪГЛИЩА

Джинхуа Чен[1*], Джуан Вен[2]

[1] *Чонгсин изследователски институт при Китайския инженерна корпорационна група по технология на въглищата, 55 Шангкиао Санкун, район Шапингба, Чонгсин, Китайска НР*
[2] *Колеж по недвижима собственост Чонгсин, 3 Мингде, район Шапингба, Чонгсин, Китайска НР*

Постъпила на 20 февруари, 2017; коригирана на 31 август, 2017 г.

(Резюме)

През годините деградацията и корозията от разтворите на амини са станали основен проблем за отнемането на метан от въглища (CBM). Тези характеристики на разтворите от амини досега не са изяснени. В настоящата работа са изследвани деградационните характеристики на смеси от разтвори на амини в среда, богата на кислород с и без антиоксиданти. Резултатите показват, че отсъствието на антиоксидани е налице висока окисилителна деградация. След добавянето на антиоксидант, т.е. натриев метаванадат (NaVO3), натриев сулфид или натриево-калиев тартарат се забелязва очевидно понижение на деградацията на разтворите. Най-добри антиксидантни свойства има натриевият метаванадат, след него натриево-калиевият тартарат и накрая – натревият сулфид. При добавянето на 1% натриев метаванадат степента на окислителна деградация на метил-диетаноламин (MDEA) + пиперазин (PZ) (в начално отношение 8:2) намалява до 32%.

Изследвани са корозионните характеристики на пресни разтвори от амини в експерименти при 90°C за 72 часа. Резултатите от тестовете за корозия и от сканираща електронна микроскопия (SEM) показват, че степента на корозия в богати на амини разтвори еп о-висока, отколкото в пресни разтвори. След добавянето на 0.5% $NaVO_3$ и 0.5% V_2O_5 като инхибитор корозията на разтворите, богати на амини намалява. Според получените резултати за деградацията и корозията за декарбинизиращ агент при for CBM-процеса се препоръчва разтвор на MDEA+PZ(8:2) с добавка от 0.5% $NaVO_3$ и 0.5%V_2O_5 .

Bulgarian Chemical Communications, Volume 49, Number 3, (pp. 678 – 684) 2017

Study on removing impurity from magnesite ore by two step reverse flotation. Study on removing impurity by two step reverse flotation

W.H. Sun[1], S.J. Dai[2]*, W.G. Liu[3], L.T.Yu[2]

[1]*College of Resources and Metallurgy, Guangxi University, Nanning, Guangxi, 543002,China*
[2]*School of Mining Engineering Liaoning University of Science and Technology, Anshan, Liaoning, 114.51, China*
[3]*School of Resources and Civil Engineering, Northeastern University, Shenyang，Liaoning, 110004, China*

Received May 13, 2017; Revised June 7, 2017

The main impurity elements in magnesite ore are silicon, calcium and iron etc. The index of concentrate grade for 97.16%, content of SiO_2, CaO, Fe_2O_3 for 0.18%, 0.65% and 0.49% in concentrate, and recovery for 74.43% were got on the condition of grinding fineness for -0.075mm70%, pH of the pulp for about 5.5, the dosage of sodium metaphosphate for 150g/t, the dosage of water glass for 1500g/t, the dosage of collector LKD for 175g/t (roughing for 75g/t, first cleaning for 50g/t, and second cleaning for 25g/t) at the grade of crude for 92.94%, contents SiO_2, CaO, Fe_2O_3 for 1.71%, 0.89% and 0.66% in the crude ore by reverse flotation of one time roughing and two times cleaning. The index of concentrate grade for 97.52%, content of SiO_2, CaO, Fe_2O_3 for 0.18%, 0.51% and 0.39% in concentrate, and a recovery of 74.35% were received by one time cleaning again by using sodium oleate for collector and pH for 2.5. Zeta-Potential analysis and infrared spectrum analysis showed that physical adsorption was the main adsorption form between the collector LKD to magnesite and dolomite. The physical adsorption and chemical adsorption existed between the sodium hexametaphosphate, water glass and sodium oleate to surface of magnesite and dolomite.

Key words: magnesite ore, reverse flotation, removing impurity by two step

AIMS AND BACKGROUND

The reserves of magnesite ore in China are rich, taking about 1/4 of the world total. The main impurities in magnesite ore. The angue mineral in magnesite ore can be divided into two categories which are mineral containing silicon such as talc quartz, chlorite etc, minerals containing calcium such as dolomite, and minerals containing iron et al according to the kinds of minerals. It is general using water glass and sodium hexametaphosphate as adjustor, the cation collectors of amine as collectors under acidic conditions by reverse flotation to removing gangue minerals containing silicon from magnesite ore, and positive flotation is general used to remove dolomite from magnesite ore and at alkaline conditions by anion collectors. The flowsheet of reverse flotation and positive flotation should be used to for most magnesite ore which is containing silicon and calcium minerals at the same time [1,2].

The fatty acid collectors which is used in the positive flotation in general and it need to be heated in order to obtain good separation results. The dosage of collectors is big, effect of separation is poor, and the cost was high because magnesite is been inhibited at first ,and floated at next in the flowsheet of reverse flotation and positive flotation[3].flowsheet of reverse flotation and positive flotation was replaced by flowsheet of single reverse flotation in 1990s.Study on the removing silicon and calcium by a single reverse flotation process become the industry hot and difficult. Li Xiaoan, Chen Gonglun et al. studied the feasibility by using twelve alkyl phosphate to separate of magnesite and dolomite [4-6].The results show that the existence of PO_4^{3-} made the adsorption effect of dolomite is obviously better than the adsorption effect of magnesite. Zhang Zhijing studied the adsorption of sodium oleate on magnesite and dolomite mineral surface mechanism [7].Research shows that sodium oleate in the pulp mainly ionic and molecular clathrate, and the chemical adsorption is main adsorption form of minerals with sodium oleate. Yuan Shiquan think that the concentration of Ca^{2+} / Mg^{2+} in pulp was related closely to surface electric of magnesite and dolomite[8].

The study used cationic collector by reverse flotation to remove impurities silicon, and the anionic collector was be used to remove calcium and iron by reverse flotation. The sillcon was removed effective, and calcium and iron were removed at same time by the flowsheet of removing impurity by two step from magnesite ore by reverse flotation.

EXPERIMENT

Experimental samples

Mineral composition and content: The samples of magnesite ore for experimental is from Haicheng magnesium refractory factory, which was crushed

* To whom all correspondence should be sent:
E-mail: shujuandai@163.com

sieved, mixed and divided. The mineral composition of Haicheng magnesium ore is relatively complex, and there are many kinds of minerals in it. The main mineral is magnesite, talc, brucite, dolomite, quartz and clinochlore (Opal), and a little of iron minerals. The talc and clinochlore may impact on processing because they are easy sliming.

Composition and content of elements in ore: The main aim elements and impurities such as iron, calcium, silicon aluminum in the ore are analyzed, and the results are shown in Table 1.

From table 1 we can see that grade of crude ore (MgO content when IL=0, %) is lower, content of impurities for silicon, calcium and iron are higher.

Experimental methods

Flotation experiment: Flotation experiment is carried out by adding sample for 400g with water for 600mL to 1L XFD type flotation machine, controlling speed for 1800r/min, adjusting the pH value of the pulp, adding adjustor and stirring for 5min, adding collector and stirring for 3min,adding foaming agent and stirring for 1min, scraping bubble flotation for 5min.The products are then filtered, dried, weighed, analyzed, and the recovery and removal rate of impurity can be calculated

Zeta potential measurement: The JS94H zeta potential apparatus is used to measure the dynamic electrokinetic point. The pure mineral was grinded by ZXM-1 vibration mill to -5 μm. Taking samples for 250mg into volumetric flask of 250mL and making it into slurry. Taking the slurry for 30mL into a beaker, adjusting the dosage of agent. The liquid forv0.5mL is placed in the electrophoresis tank a time, the zeta potential is measured with a micro electrophoresis apparatus, and the 4-6 numbers is measured at each observation point. average value is the measuring value after removing interference number.

Fourier transform infrared spectroscopy: Infrared absorption spectra are recorded on a Perkin Elmer Spectrum One FT-IR Spectrophotometer. The KBr pellet technique is used to record the spectra.

X ray diffraction: The sample to be studied is grinded to -37μm, and is placed in the X ray diffractometer at room temperature after being pressed into slice. The diffraction pattern is analyzed according to the powder diffraction data standard joint committee international diffraction data center (JCPDS-ICDD) version of the PDF2-2004 card.

RESULTS AND DISCUSSION

The amine and fatty acid collector are commonly used as collectors of magnesite ores. The effects of grinding fineness, pulp pH value and kind and dosage of adjustor on flotation indexes are investigated by amine collector LKD which was developed by University of Science and Technology Liaoning[3,9].

Grinding fineness experimental

The grinding fineness is an important factor affecting the flotation index. Increasing grinding fineness can improve the liberation degree of mineral,but also increase the slime formation. The experimental of effects of grinding fineness on flotation indexes is done on the conditions of pH for about 5.5, the dosage of sodium metaphosphate for 150g/t, the dosage of water glass for 1500g/t, dosage of LKD for 75g/t by one roughing process, the results are shown in Fig.1.

It can be seen from Fig.1.,that the grinding fineness has a great influence on the recovery of the concentrate and the effect of removing the silicon. The comprehensive grade, recovery and impurity removal effect, the appropriate grinding fineness is -0.075mm70%.This result is consistent with the previous research conclusion[10,11].

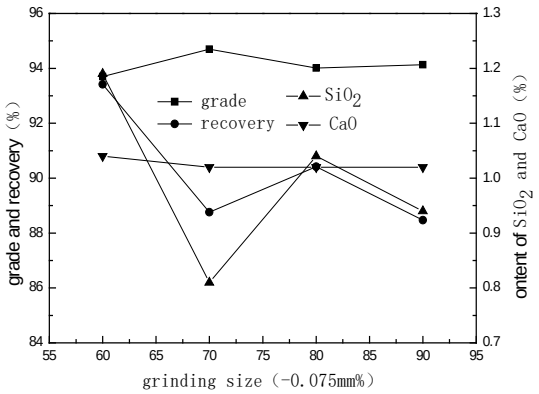

Fig.1. The experimental results of grind size

The pH value experiment

The pH value is an important factor affecting the flotation index because pH value will affect the dissolution characteristics of mineral and electricity in mineral surface which H^+ and OH^- are locating ion. pH value experimental is done on the conditions of the grinding fineness for -0.075mm 70%, the dosage of sodium metaphosphate for 150g/t, the dosage of water glass for 1500g/t, dosage of LKD for 75,50,25g/t by one time roughing and two times cleaning process, the results are shown in Fig.2.

As can be seen from Fig.2 with the increase of the pH value, the concentrate yield decreased, while the concentrate grade and the content of SiO_2 and CaO in the concentrate increased at some time and decreased at some time, and the appropriate pH value is 5.5.

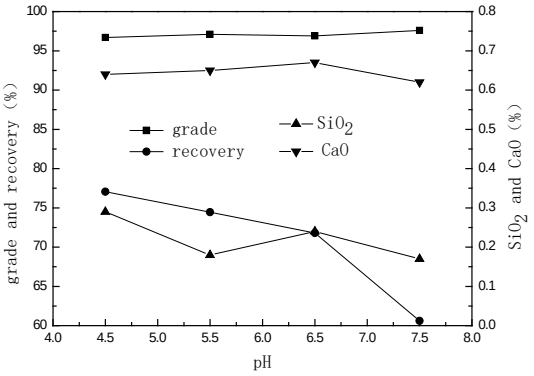

Fig. 2. The experimental results of pH

Water glass experiment

Fine minerals in ore is more, and distribution rate of silicon, calcium in fine particle is larger, selectivity of flotation process is reduced for more fine minerals. The dosage of water glass experimental is done for its good dispersant. The experimental results are shown in Fig.3.

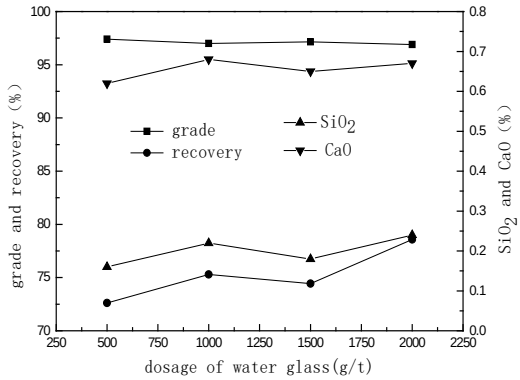

Fig. 3. Test results of dosage of water glass.

It can be seen from Fig.3,the concentrate yield increase gradually, the concentrate grade drop at first , then increase, and then drop and content of SiO_2, CaO increase firstly and then decrease with the increasing of the dosage of water glass in the dosage of water glass for 500-2000g/t. The dosage of water glass for 1500g/t is suitable.

The experimental of dosage of sodium hexametaphosphate

Sodium hexametaphosphate can significantly enhance the collecting angue minerals as selective activator of gangue mineral. On the other hand, sodium hexametaphosphate is an inorganic ionic dispersant, it can been adsorbed on the surface of carbonate minerals after ionization in the slurry. Particles are more dispersed because increasing negative charge in surface of particles. electrostatic repulsion may enhance between particles. The removal rate of gangue minerals improve for increasing action opportunity of collectors with gangue minerals[12].Experimental results of dosage of sodium hexametaphosphate are shown in Fig.4.

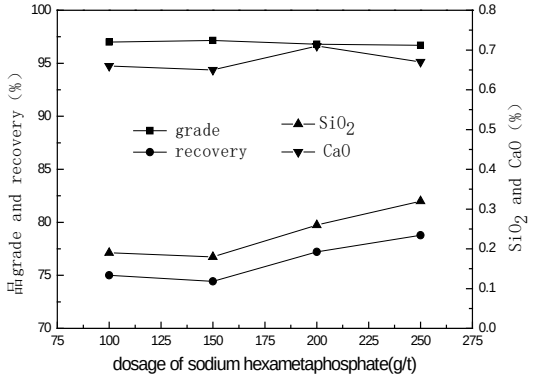

Fig. 4. Test results of dosage of sodium hexametaphosphate

It can be seen from Fig.4,concentrate yield increase and concentrate grade first rise and then drop with the increase of the dosage of sodium hexametaphosphate. The concentrate yield decrease slightly, the grade increase gradually when dosage of sodium metaphosphate is 0-150g/t. Tt indicates that sodium hexametaphosphate is activation of gangue minerals. When dosage of sodium hexametaphosphate is more than 150g/t, the yield of concentrate began to rise, the concentrate grade decrease because sodium hexametaphosphate is inhibitor when it is excess. The dosage sodium hexametaphosphate for 150g/t is suitable.

Experiment of dosage of collector

The content of calcium (CaO) in experimental samples is high to 0.89%. We need to consider removing calcium in addition to considering the effect of Sillon in the experiment to ensure the quality of concentrate. The experimental of the effects of dosage of collector on the flotation index is done by using LKD as collector, the experimental results are shown in Fig.5.

Table 1. The chemical analysis results of samples

elements	IL	CaO	Fe_2O_3	Al_2O_3	SiO_2	MgO	MgO(IL=0)
Content（%）	50.14	0.89	0.66	0.26	1.71	46.34	92.94

Table 2. The experimental results of kind of acid

Kind of acid	yield (%)	Content(%)							Recovery (%)
		CaO	Fe_2O_3	Al_2O_3	SiO_2	IL	MgO	MgO(IL=0)	
HCL	71.22	0.65	0.49	0.16	0.18	51.48	47.14	97.16	74.43
HNO_3	72.12	0.59	0.48	0.13	0.14	51.69	46.97	97.2	75.45
H_2SO_4	70.19	0.78	0.48	0.13	0.21	51.69	46.71	96.69	72.92

Table 3. The experimental results of pH of second step reverse flotation

pH	yield (%)	content (%)							recovery (%)
		CaO	Fe_2O_3	Al_2O_3	SiO_2	IL	MgO	MgO(IL=0)	
2.5	70.88	0.51	0.39	0.13	0.18	51.10	47.68	97.52	74.35
3.5	70.96	0.64	0.49	0.13	0.19	51.50	47.02	97.1	74.23
4.5	70.94	0.64	0.46	0.11	0.2	51.26	47.33	97.1	73.90
5.5	70.86	0.55	0.47	0.11	0.17	51.47	47.23	97.32	74.03

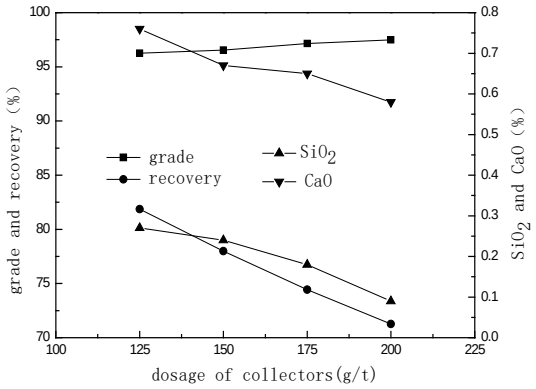

Fig. 5. The test results of dosage of collectors

It can be seen from Fig.5,the concentrate yield decrease, the content of CaO and SiO_2 in the concentrate constantly reduce with the increase of the dosage of collector. The better index of concentrate yield for 71.22%, the content of CaO and SiO_2 in the concentrate for 0.65% and 0.18%,and the concentrate grade for 97.16% are got when the dosage of collector is 175g/t.

Kind of pH value regulator (acid) experimental

The pH value is an important factor affecting the flotation index. The kinds of acid experimental is carried out by using hydrochloric acid, nitric acid and sulfuric acid as pH value adjusting agent for suitable pH value for 5.5.The results are shown in Table.2.

Table 2.shows the kind of acid has a great influence on the experimental indexes in contrast, when the nitrate is used as the pH regulator, the experimental index was the best, and the index of hydrochloric acid is slightly lower than that of hydrochloric acid. When the sulfuric acid is used the pH value adjustor, the experimental index is the worst, and the pH value is extremely unstable. The order of dosage of acid is sulfuric acid< hydrochloric acid<nitric acid. Hydrochloric acid is selected as pH value adjustor for its cheap price and less using amount.

The pH experiment of second step reverse flotation

The second step reverse flotation by using sodium oleate for 50 g/t as collector is carried out to remove calcium for the content of CaO in concentrate is still more than 0.6% by a time roughing two times cleaning process of cationic collector in reverse flotation. pH experimental results of reverse flotation with sodium oleate are shown in Table 3.

It can be seen from table 3., the content of CaO in concentrate can be reduced from 0.65% to 0.51% by the reverse flotation process removing calcium and using sodium oleate as collector. The technology which use sodium oleate as collector by a time reverse flotation again after 1 time rough and 2 times cleaning have some disadvantage for the low pH value,big using amount of acid, serious corrosion to equipment, and so on.

THE INTERACTION MECHANISM BETWEEN AGENT AND MINERALS

Floatability of magnesite and dolomite is smaller because they both belong to carbonate minerals and their lattice structure is similar. The key of effective separation of minerals in magnesite ore is expanding the floatability difference between objective magnesite mineral and gangue minerals by adding flotation agent to change the physical and chemical properties of mineral surfaces, increase or decrease the floatability of the minerals[13].The influence of different agents on surface of minerals are studied by using two kinds of pure minerals for magnesite and dolomite as the research object.

Effect of agent on electrical properties of mineral surface

Taking 3g pure mineral magnesite and dolomite respectively to 30 mL suspension in cone, adding water glass for 300 mg/L, sodium hexametaphosphate for 30mg/L LKD for 60mg/L to suspension. The results of ζ-potential of magnesite and dolomite before and after they acting with agent are shown in Fig.6.

Fig.6 shows that the electric potential of the two minerals are similar on the conditions of different pH. The isoelectric point of magnesite and dolomite are pH=5.0 and pH=5.6.The mineral surface is negatively charged when pH is higher than the isoelectric point, and mineral surface is positively charged when pH is lower than the isoelectric. The electrical properties of magnesite is different from dolomite in pH=5.0-5.6.

The addition of water glass can significantly change the zeta potential of the magnesite [12], magnesite zeta potential under alkaline conditions significantly decrease, and the zeta potential of the acidic environment of magnesite improve slightly. The isoelectric point of magnesite rise from pH=5.0 to about pH=6.0. The addition of water glass has little effect on the surface potential of dolomite, the isoelectric point is stable at about pH=5.6. This shows that in the pH=5.0-6.0 , adding water glass is benefit for separation of dolomite from magnesite ore.

The sodium hexametaphosphate can change magnesite and dolomite surface electric, It makes isoelectric point of magnesite down to pH=5.3 and can significantly reduce the zeta potential of magnesite after pH>6.The sodium hexametaphosphate can significantly reduce the zeta potential of dolomite to pH=5.

The addition of LKD can significantly increase the zeta potential of the magnesite and dolomite. The isoelectric point of magnesite and dolomite both shift to big pH, that are pH=7 and pH=6.2 repectively.

Infrared spectroscopy analysis

Taking 3g sample in the agent solution in different concentration. The concentration of water glass, sodium hexametaphosphate and collector (LKD, sodium oleate) is 300, 100 and 100 mg/L respectively. Adjusting pH to 5-6 with 5% hydrochloric acid and 5% sodium hydroxide. Mixing fully by stiring for 15min, cleaning the sample which acting with agent already for 3 times with distilled water, and samples is Filtered by vacuum filter and dried at room temperature[14,15].The results of infrared spectrum measurement are shown in Fig.7.

Water glass is used as the adjustor of mineral flotation, and its cost is low. It not only has a selective inhibiting function for minerals, but also can disperse the slurry to prevent mud effectively. After action of magnesite with water glass, The peak at 2536.89cm^{-1} changed and shifted obviously, and the characteristic peaks of CO_3^{2-} changed obviously too. After action of dolomite with water glass, wo stretching vibration peak of Si—OH and S—O—Si at 3449.17cm^{-1} and 683.15cm^{-1} appear, the absorption peak of dolomite itself CO_3^{2-} at 1440.45cm^{-1} change to sharp. The above results show that the function formation between water glass and two minerals was chemical adsorption, adsorption of water glass on the dolomite was stronger than it is on magnesite.

After action of magnesite with sodium hexametaphosphate, a small new peak appeare at 710cm^{-1} and peak in 2538.03cm^{-1} increase. After action of dolomite with sodium hexametaphosphate, the new peak appeare at 681.61cm^{-1} and 1102.58cm^{-1}, the peat at 1102.58cm^{-1} is the stretching vibration peak of P—O, peak at 2531.12cm^{-1} strench obviously. The stretching vibration peak of P=O at 1277cm^{-1} is not obvious for near the antisymmetric stretching vibration frequency of CO_3^{2-} at 1453.79cm^{-1}.Chemical adsorption is main action formation between mineral for magnesite, dolomite with LKD,and adsorption of dolomite with sodium hexametaphos-
phate is stronger than its on magnesite.

The spectra of before and after action of magnesite, dolomite with LKD is almost no change, combining to Zeta potential experimental, electrostatic adsorption is main function formation between mineral for magnesite, dolomite with LKD.

After function of magnesite with sodium oleate, the absorption peak at 1581.04cm^{-1} and peak at 1535.98cm^{-1} is asymmetric and symmetric stretching vibrations of COO^- and the characteristic peak of oleate magnesite. The absorption peak of —COO— .exists at 1660.32cm^{-1} and 1719.96 cm^{-1} and 1821.81cm^{-1}.After function of dolomite with sodium oleate, a new asymmetric stretching vibration absorption peaks of COO- appear at 1580.77cm-1, it is possible that oleate magnesite or calcium oleate formate at mineral

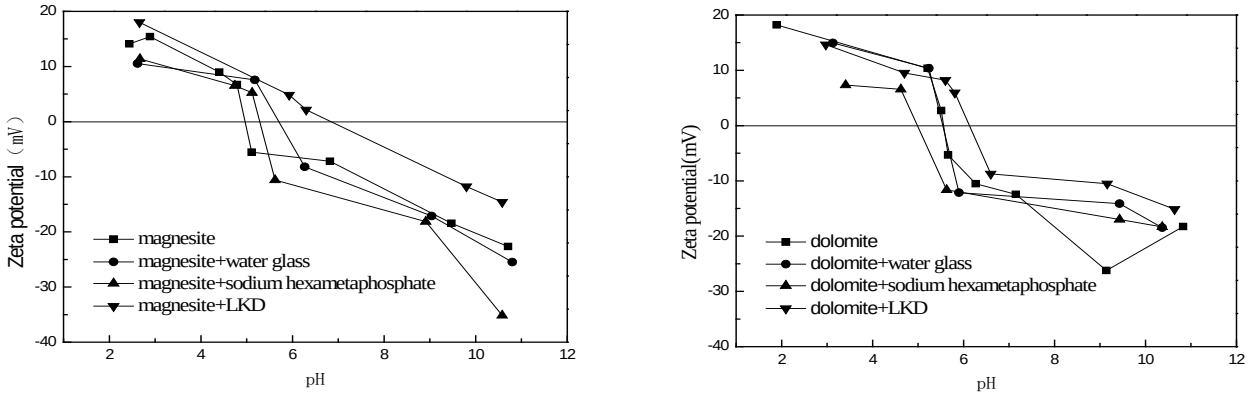

Fig. 6. The effect of different agent on zeta potential of magnesite and dolomite

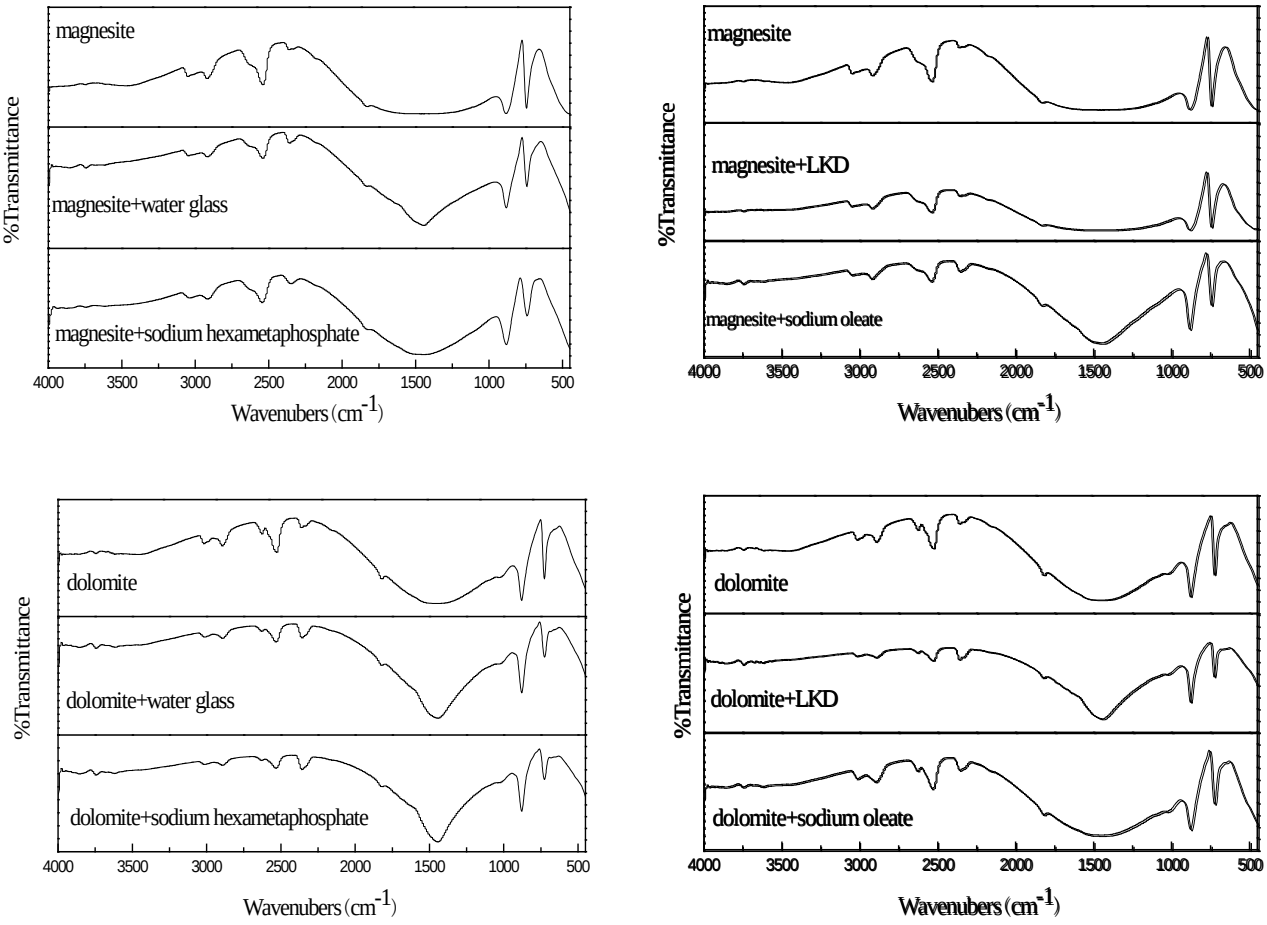

Fig. 7. Infrared spectra analysis

surface. Characteristic absorption peak of -COO- in R-COOH appear at 1821.38cm^{-1}, 1719.12cm^{-1} and 1659.86cm^{-1} too. Chemical adsorption and physical adsorption are both presenting in two kinds of minerals with sodium oleate

CONCLUSIONS

Magnesite ore flotation experimental results show that the effect of removing silicon and calcium from magnesite ore by LKD is good, the removing rate of silicon is above 90%, the removing rate of calcium is about 45%.The effect of removing calcium is poorer than silicon comparely. The second step experimental is carried out to remove calcium again at dosage of sodium oleate for 50g/t by reverse flotation base on the reverse flotation flowsheet of one time roughing and two times cleaning. The method can improve the effect of removing calcium and iron, and its shortcoming is low pH, and serious corrodes to equipment. The better index of concentrate grade for 97.52%,content of SiO_2,CaO and Fe_2O_3 for 0.18%,0.51% and 0.39%,the recovery

for 74.35% are achieved at grinding fineness for -0.075mm70%, pH of the pulp for about 5.5, the dosage of six sodium metaphosphate for 150g/t, the dosage of water glass for 1500g/t, the dosage of collector LKD for 175g/t, (roughing for 75g/t, first cleaning for 50g/t, and second cleaning for 25g/t) by first step reverse flotation and at pH of the pulp for about 2.5,dosage of sodium oleate for 50g/t by second step reverse flotation.

Zeta potential and infrared spectrum analysis of minerals before and after function with agents show that physical adsorption is main form in magnesite or dolomite with collector of LKD (amine collector).Physical adsorption and chemical adsorption are both exsiting between magnesite or dolomite with sodium hexametaphosphate or water glass.

Acknowledgment:*The study was supported by Liaoning Province Natural Science Foundation (201602387)*

REFERENCES

1. Z.M. Wang, *CN Non Metallic Ind. guide Pub.*, **5**, 6 (2006).
2. Z.Y. Chen, H.X. Li, *Nai huo Cailiao*, **39**(1), 6 (2005).
3. J.L. Wang, T.C. Sun, Y.N. Liu, *CN mining magazine*, **17**(10), 60 (2008).
4. X.A. Ii, G.L. Chen, *Metals Mine*, **5**,136 (2000).
5. 5.X.A. Ii, G.L. Chen, S.Y. Wang, Z.Q. Zhang, *CN Mining Magazine*,**6**(3),78 (1997).
6. G.L. Chen, X.A. Ii, *CN Mining Magazine*, **9**(1), 78 (2000).
7. J.F. Mao, Z.J. Zhang, *CN mining magazine*, **9**(1), 2 (2000).
8. S.Q. Yuan, H.E. Zhang, *Minging and Metallurgical Engineering*, **10**(4), 19 (1990).
9. L.P. Ma, P. Ning, S.C. Zheng, *Ind. and Eng. Chem. Research*, 49(8), 3597 (2010).
10. X.A. Li, S.J. Dai, L.J. Zhou, Y. Li, *Non-Metallic Mines*, **35**(1), 18 (2012).
11. X.A. Li, S.J. Dai, L.J. Zhou, Y. Li, *CN mining magazine*, **21**(2), 63 (2012).
12. X.A. Li, *Journal of Anshan Institute of Iron and Steel Technology*, **11**(4), 13 (1988).
12. Y.S. Zhu, J.G. Zhu, The chemical principle of flotation Reagents, Centre South University Press, Changsha, 2005.
13. H.Q. Zhong, Introduction to infrared spectrometry Chemical industry press, Beijing, 1984.
14. V.C. Farmer. Infrared spectrum of minerals. Science press, Beijing,1982.

ИЗСЛЕДВАНЕ ВЪРХУ ОТСТРАНЯВАНЕТО НА ЗАМЪРСЯВАНИЯ ОТ МАГНЕЗИТОВА РУДА ЧРЕЗ ДВУСТЕПЕННА ОБРАТНА ФЛОТАЦИЯ

У.Х. Сун[1], С.Дж. Дай[2]*, У.Г. Лю[3], Л.Т. Ю[2]

[1]Колеж по ресурси и металургия, Университет Гуангси, Нанинг, Гуангси, 543002, Китай
[2]Училище по минно инженерство, Научно-технологичен университет Ляонинг, Аншан, Ляонинг, 11451, Китай
[3]Училище по ресурси и строително инженерство, Северозападен университет, Шенянг, Ляонинг, 110004, Китай

Постъпила на 13 май, 2017 г.; Коригирана на 7 юни, 2017 г.

(Резюме)

Главните онечиствания при магнезитовата руда са силиция, калция, желязото и др. Индексът на магнезитовия концентрат за 97.16%, предвижда за SiO_2, CaO, Fe_2O_3 съответно 0.18%, 0.65% и 0.49% в него. Достига се добив от 74.43% при фино смилане до 70% с размери 0.075mm, pH около 5.5; съдържание на натриев метафосфат 150g/; на водно стъкло 1500 g/t; на LKD от 175g/t (грубо 75g/t, след първо пречистване 50 g/t и след второ пречистване 25 g/t). Сурова руда с чистота 92.94% и съдържаща SiO_2, CaO, Fe_2O_3 съответно 1.71%, 0.89% и 0.66%, се подлага на еднократна обратна флотация с двукратно пречистване. При индекс на концентрата 97.52% (съдържание на SiO_2, CaO, Fe_2O_3 съответно 0.18%, 0.51% and 0.39%) се постига добив от 74.35% при еднократно пречистване с натриев олеат и pH 2.5. Анализът на č-потенциала и на инфрачервения спектър показва, че физичната адсорбция е основната причина за свързването на LKD с магнезита и доломита. Физичната адсорбция и хемо-сорбцията съществуват между натриевия хексаметафосфат, водното стъкло и натриевия олеат с повърхността на магнезита и доломита.

Bulgarian Chemical Communications, Volume 49, Number 3, (pp. 685 – 689) 2017

Adsorption of copper ions by montmorillonite/sodium humate/N-isopropyl acrylamide composite

Y.-l. Feng*, L.-j. Yu, R.-w. Cao

School of Resources and Environment, Henan Polytechnic University, Jiaozuo, 454003, China

Received May 23, 2017; Revised August 21, 2017

The montmorillonite-based composites can be used to adsorb copper ions to relieve contamination. The montmorillonite/sodium humate/copper ion complex, which can be obtained by mixing montmorillonite, sodium humate (surface modification of montmorillonite), and N-isopropyl acrylamide, is ideal candidate for adsorption of copper ions. First, the modified montmorillonite-based adsorbents were characterized by infrared spectroscopy and scanning electron microscopy. Then, effects of incubation time and initial concentration of copper ions on adsorption of copper ion by modified montmorillonite were investigated. The results revealed that modification by (3-acrylamidopropyl) trimethylammonium chloride, N-isopropyl acrylamide, or sodium humate can significantly improve the adsorption capability of montmorillonite. The adsorption rates at initial concentration of 1000 mg/L can be up to 96.98% and 95.02%. In summary, the montmorillonite/sodium humate/N-isopropyl acrylamide composite shows great adsorption capability towards copper ions.

Keywords: montmorillonite modification; humatic acid sodium; Acrylamide; copper ion; waste water treatment

INTRODUCTION

Owing to its severe toxicity, concentration along the food chain upwards, and absence of effective separation approaches, heavy metals in natural water bodies has been a global environment issue. Over the past decades, contamination of water bodies in domestic cities caused by long-term, considerable discharge of municipal and industrial waste water has been a significant issue [1]. To make it worse, contamination of water bodies may lead to significant soil contamination due to sewage flow and sewage irrigation. Therefore, a cost-effective and efficient sewage treatment approach has been urgently needed [2].

Montmorillonite ($A1_2(OH)_2Si_4O_{10}$) is a lamellar aluminosilicate with considerable reserve. This substance is characterized by large inner surface area and inter-layer domain adjustability. Hence, montmorillonite-based materials for effective, low-cost, and facile water treatment have gain increasing popularity. Consisting of Al_2O_3, SiO_2, and several ions (e.g., Ca^{2+}, K^+, Mg^{2+}, Fe^{2+}, Na^+), montmorillonite has a octahedron crystal structure (SiO_2:Al_2O_3 = 2:1). As is known, aluminum ions and silicon ions can substitute each other. As a result, the montmorillonite crystal cell is negatively charged and can adsorb certain cations, although the interaction is so weak that the cations are readily exposed to substitution by other low-valence ions. As the ion substitutions take place in the inter-layer space, the structure of montmorillonite is relatively stable. However, the ion substitutions have a significant effect on the physical and chemical properties of montmorillonite.

Montmorillonite swells significantly in water as the inter-layer space can adsorb considerable amount of water molecules. The fine crystal grains of montmorillonite lead to large specific surface area, while the weak inter-layer interactions result in easy expansions and separations of montmorillonite crystal layers in solvent [3]. As a result, montmorillonite has relatively large inner surface area. Nevertheless, the adsorption capability of montmorillonite is not outstanding. For instance, the Langmuir adsorption capacities of untreated and acid activated bentonite for copper have been demonstrated to be 42.41 mg/g and 32.17 mg/g [4], respectively. Hence, the adsorption capability of montmorillonite needs to be further improved. Owing to loose aromatic ring structure and the pores with varying sizes, humics can interact with heavy metals via complexation. Additionally, high contents of carboxyl, hydroxyl, and carbonyl functional groups were observed in humic acid. Therefore, humic acid can easily adsorb on soil minerals in natural environment. The humic acid in sodium humate can interact with active surface of clay via complexation [5]. Also, sodium humate can increase the density of complexation sites and generate ligands on the surface of montmorillonite [6]. In this article, montmorillonite/sodium humate/n-isopropyl acrylamide complex was prepared and used for adsorption of copper ions.

* To whom all correspondence should be sent:

E-mail:fengyouli66@163.com

This study provides references for treatment of copper ion containing wastewater.

SAMPLE PREPARATION

Equipment and materials

Equipment: 50 mL beaker, 2000 mL beaker, balance (graduated value = 0.1 mg), glass rod, 2000 mLm measuring flask, filter paper, oven, three-neck bottle, nitrogen bottle, water bath container, polyethylene tube, and shaking incubator.

Materials: distilled water, 0.1 mol/L HCl and NaOH solution, 2-acrylamido-2-methylpropane sulfonic acid (purchased from Shanghai Macklin Biochemical Co., Ltd.), ammonia sulfate, N-isopropyl acrylamide (purchased from Shanghai Saen Chemical Co., Ltd.), (3-acrylamidopropyl) trimethylammonium chloride (purchased from Shanghai Saen Chemical Co., Ltd.), Ca-based montmorillonite (Ca-MMT, purchased from Linyi Luse Chemical Co., Ltd.), sodium humate (SH, purchased from Linyi Luse Chemical Co., Ltd.). All chemicals used were analytical grade.

Preparation of composite adsorbent

a) 11.39 g 2-acrylamido-2-methylpropane sulfonic acid was added into a three-neck flask equipped with thermometer and condenser and stirred at room temperature, followed by addition of 3.3 g Ca-MMT and 5 g SH. Then, nitrogen was injected and kept for 30 min, followed by heating to 40~50 ºC in water bath.

b) 96 mg ammonia sulfate was added into 2.5 mL of water and kept for 10 min. Then, the solution was heated up to 80 ºC and kept for 3 h. Herein, w(Ca-MMT) = 20% and w(SH) = 30%.

c) The product was collected and dried at 70 ºC until no weight loss was observed; the product was then sieved using a 200-mesh sieve.

d) 2-acrylamido-2-methylpropane sulfonic acid was replaced by 6.22 g of N-isopropyl acrylamide and 15.2 g of (3-acrylamidopropyl) trimethylammonium chloride. Adsorbents were prepared by following the steps mentioned above and labelled appropriately.

Sample characterization

Characterization by scanning electron microscopy

The scanning electron microscope used was Quanta 250 FEG-SEM field emission scanning electron microscope (FESEM) purchased from FEI Corp., USA. The scanning was conducted under low vacuum mode and 10 kV voltage and the resolution was 2.5 nm.

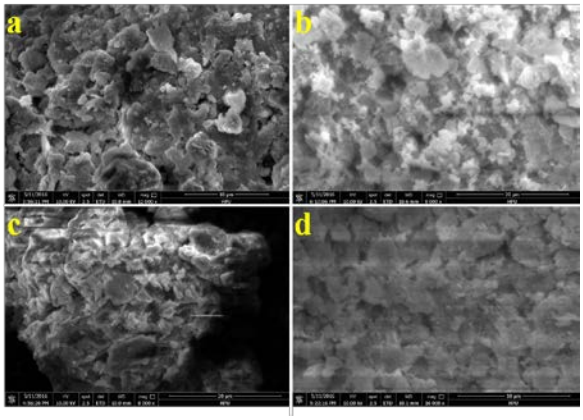

Fig. 1. The SEM photos of sample a, b, c and d represent sample 1, 2, 3 and MMT

Fig. 1 a, b, c, and d shows FESEM images of (3-acrylamidopropyl) trimethylammonium chloride/sodium humate/montmorillonite (Sample A), N-isopropyl acrylamide/sodium humate/ montmorillonite (Sample B), 2-acrylamido-2-methylpropane sulfonic acid/sodium humate/montmorillonite (Sample C), and montmorillonite (Sample D), respectively. Herein, Sample D shows typical properties of montmorillonite: the particles were coarse, clusters with varying sizes, large thicknesses, and irregular shapes [7]. As observed, modified and unmodified samples exhibited similar structures, while Sample A and B showed relatively loose structures (original size of montmorillonite particles varies from 3 μm ~ 4 μm). Sample A showed in homogeneous particle size with average size of 1 μm, while Sample B showed clustered surface particles, indicating that the presence of adsorbents increased the specific surface area of montmorillonite and exposure of increasing metal ions. As a result, the adsorbing capability was enhanced. In Fig. 1 c, agglomeration was observed and the internal channels were blocked, resulting in reduced adsorbing capability.

3.2 Characterization by Fourier Transform infrared spectroscopy

The FTS-40 Fourier Transform infrared spectroscopy (FTIR) was purchased from BIO-RAD Co. Ltd., USA. Samples were prepared accordingly and characterized using FTIR. The resolution is 16 cm^{-1}, the scanning wave number ranges from 4000 cm^{-1} to 300 cm^{-1}, and the scanning lasts for 16 cycles for each sample.

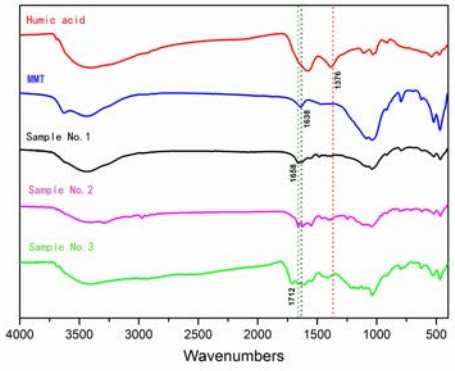

Fig. 2. FTIR curves of samples

Fig. 2 a, b, c, and d show FTIR curves of Sample A, B, C, and D, respectively. As shown in Fig. 2a, the strong and relatively broad peak at 3440 cm^{-1} corresponds to the stretching vibration absorption of aliphatic and aromatic -OH groups or -NH groups [8] and the peak at 1658 cm^{-1} corresponds to the (-CONH-)II band in secondary amide. As shown in Fig. 2a, the peak at 3000~2800 cm^{-1} corresponds to the stretching vibration absorption of aliphatic C-H, and the adsorption peaks at 1612 cm^{-1} and 1545 cm^{-1} correspond to the pyridine in the aromatic ring, which can be regarded a compound that is generated by replacing a -CH group in benzene molecule using -N group or the product of reaction between sodium humate and isopropyl acrylamide. As shown in Fig. 2d, the double peak at 1033 cm^{-1} corresponds to stretching vibration of Si-O-Si, while the peak at 500(±50) cm^{-1} is shoulder-shaped, which may be a result of flexural vibration of Si-O-Mg. This was observed in Fig. 2 a, b, and c, especially in Fig. 2 a and b. Therefore, it is deduced that the adsorption valleys were caused by the presence of humic acid [9]. As shown in Fig. 2c, the intensity of the adsorption peak at 3500~1850 cm^{-1} degraded significantly, indicating decomposition of organic components in the composites.

ADSORPTION OF COPPER IONS BY COMPLEX ADDITIVE

Effects of initial concentration on adsorption capability

0.1g of each composite adsorbent was add in a separate centrifuge tube (50 ml) containing 20 ml of copper ions with different concentrations (50 mg/L, 100 mg/L, 200 mg/L, 500 mg/L, and 1000 mg/L), followed by 10 min vibration at room temperature and 20 min centrifugation (4000 rpm). 10 ml of supernatant was collected and the concentration of residual copper ions was determined using the spectrophotometry. The adsorption capability and the removal ratio of heavy metal can be calculated using the following equation:

$$Q=V(C_0-C)/m \qquad RE=C_0-C/C_0*100\%$$

where Q is the adsorption capability of montmorillonite towards copper ions at equilibrium, V is the volume of adsorbed solution, C_0 is the initial concentration of copper ions, C is the concentration of copper ions at equilibrium, m is the quantity of complex additive used, and RE is the removal ratio of copper ions at equilibrium [10].

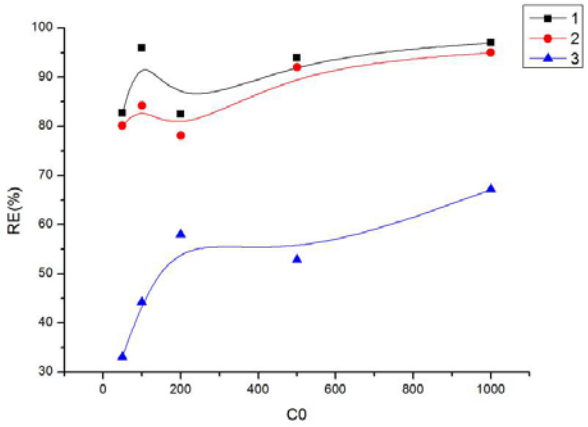

Fig. 3. The removal curve of ratio of copper.

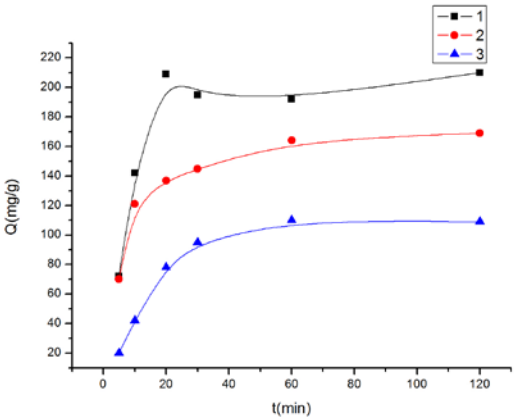

Fig. 4. The relationship between adsorption ability and time.

Fig.4 shows adsorption curves of Sample 1, 2, and 3 under different initial concentrations of copper ions. As observed in Fig. 3, all composite samples exhibited improved adsorption capability (193.95 mg/g, 190.01 mg/g, and 136.33 mg/g for Sample 1, 2, and 3, respectively), as compared with 42.41 mg/g for montmorillonite [11]. The results are consistent with those of structural characterization mentioned above. With initial concentration of 1000 mg/L, the adsorption rate of Sample 1 and 2 reached 96.98% and 95.02%, respectively. This can be attributed to the 3D

networked structures of Sample 1 and 2 [12]. Specifically, the 3D networked structures allow presence of a significant quantity of anion functional groups from N-isopropyl acrylamide and sodium humate and these anions can attract and retain Cu^{2+} by electrostatic interaction and complexation. Hence, the adsorption capability of Sample C was limited by its relatively small inner surface area. Additionally, the adsorption capabilities of these samples increased with the initial concentration of Cu^{2+}. The optimized quantity of adsorbent bentonite varies with the initial concentration of Cu^{2+} and the adsorbent used and the adsorption capability degrades once the bentonite quantity exceeds the critical value. For Sample 1 and 2, 0.1 g/L composite adsorbent is ideal for initial concentrations below 1000 mg/L.

Effects of incubation time on adsorption capability

0.1g of each composite adsorbent was add in a separate centrifuge tube (50 ml) containing 20 mL of 500 mg/L copper ions and kept for 5 min, 10 min, 20 min, 30 min, 1 h, and 2 h, respectively. Fig. 4 summarizes the concentration of copper ions in solution samples collected at different time. As observed, Sample 1 reached equilibrium at 30 min, Sample 2 and 3 reached equilibrium at 1 h, Sample C reached equilibrium at 4 h [13]. Additionally, Sample 1 and 2 follow the secondary adsorption dynamic model ($dp/dt=k(q_e-q)^2$). In other words, adsorptions of copper ions by these adsorbents were related to the concentration of copper ions and the density of surface active sites.

CONCLUSIONS

The adsorption capabilities of (3-acrylamidopropyl) trimethylammonium chloride/sodium humate/montmorillonite and N-isopropyl acrylamide/sodium humate/montmorillonite adsorbents towards copper ions were significantly higher than that of 2-acrylamido-2-methylpropane sulfonic acid/sodium humate/montmorillonite adsorbent. The saturated adsorption rates of (3-acrylamidopropyl) trimethylammonium chloride/sodium humate/montmorillonite and N-isopropyl acrylamide/sodium humate/montmorillonite adsorbents reached 193.95 mg/L and 190.01 mg/L, respectively; the saturated removal rates of (3-acrylamidopropyl) trimethylammonium chloride/sodium humate/montmorillonite and N-isopropyl acrylamide/sodium humate/montmorillonite adsorbents reached 96.98% and 95.02%, respectively. The saturated adsorption rate and removal rate of 2-acrylamido-2-methylpropane sulfonic acid/sodium humate/montmorillonite adsorbent were 136.33 mg/L and 68.17%, respectively. Nevertheless, the adsorption capabilities of all montmorillonite-based composites were significantly improved compared with that of montmorillonite. This can be attributed to the presence of anion functional groups in the composites.

The adsorption efficiencies of composite adsorbents were relatively high. (3-acryl-amidopropyl) trimethylammonium chloride/sodium humate/montmorillonite adsorbent reached maximum adsorption capability after 30 min, while 2-acrylamido-2-methylpropane sulfonic acid/ sodium humate/montmorillonite and N-isopropyl acrylamide/sodium humate/montmorillonite adsorbents reached maximum adsorption capability after 1 h.

Owing to the gelation nature of 2-acrylamido-2-methylpropane sulfonic acid, the adsorption capability of 2-acryl-amido-2-methylpropane sulfonic acid/sodium humate/montmorillonite adsorbent was significantly limited as some channels were blocked.

REFERENCES

1. K. G. Bhattacharyya, Susmita Sen Gupta. Advances in Colloid and Interface Science, 140,114(2008).
2. J. Liu. Chem. *Real Issue*, 3,30(2010).
3. W. J. Chen, G. H. Wang, L. F. Ai. China Surf. *Deter.t & Cosm.*, 3, 220(2012).
4. E. Eren, E. Afsin, Hazard. Mater., 151,682(2008).
5. X.H. Li. , *Soil chemical*. Higher Education Press, 2001.
6. P. F. Liao, P. X. Wu, W.M. Wu, Q. F. Chen, Y. F. Xu. *Bulletin of Mine. Petro. and Geochem.*, 3,272(2009).
7. P. X. Wu, H.F Zhang, F. Y. Wang, J. G. Guo, W. X. Zhao. 1:19-23. *Mineral and Rocks*, 1,19(1999).
8. O. K. Borggaard，B. Raben Lange，A. L. *Gimsing. Geoderma*，127 ,270(2005).
9. J. L. Liu, T. P. Cao, L.H. Wang, *Industrial Safety and Environ. Protection*, 11,3(2016).
10. Y. Y. Wang, Research and Exploration in Laboratory, 2,41(2016)
11. H. S. Shi, y. H. Liu, Journal of Building Materials, 9,507 (2006)
12. H. X. Zhou, J. He, H.F. Zhang, C.Xiang, Y. Qin, B.C. Li, *Jour. Kunming Univ. Tech.(Sci.s Edit.)*, 5,15(2012).
13. Y. A.Zheng, X. H. Yang, A.Q. Wang, Fine *Chem. Eng.*, 25,1045 (2008).

АДСОРБЦИЯ НА МЕДНИ ЙОНИ ОТ КОМПОЗИТ ОТ МОНТМОРИЛОНИТ/НАТРИЕВ ХУМАТ/N-ИЗОПРОПИЛ-АКРИЛАМИД

И.И. Фенг*, Л.Дж. Ю, Р.У. Цао

Училище по природни ресурси и околна среда, Политехнически университет в Хенан, Джиаозуо, 454003, Китай

Постъпила май, 2017 г.; коригирана на 21 август, 2017 г.

(Резюме)

Композитите на основа монтморилонит може да се използват за адрорбцията на медни йони за намаляване на замърсяванията. Комплексът от монтморилонит/натриев хумат/меден йон, който може да бъде получен при смесване на монтморилонит с натриев хумат (повърхностна модификация на монтморилонита и n-изопропил-акриламид е отлична възможност за адсорбция на медни йони.

Bulgarian Chemical Communications, Volume 49, Number 3, (pp. 690 – 696) 2017

DFT study of nitrogenated heterocycles of six and seven links

H. Merouani[1,3], A. Ounissi[2,3], N. Ouddai[3]*

[1]*Department of Chemistry, Faculty of Science, University Mohamed Boudiaf M'sila, 28000 M'sila, Algeria.*
[2]*Laboratoire de Génie des procédés chimiques, Université Setif-1, Algeria*
[3]*Laboratoire de chimie des matériaux et des vivants: Activité, Réactivité, University EL-Hadj Lakhdar Batna, 05000 Batna, Algeria*

Received October 30, 2016; Revised December 14, 2016

The 1,3-dipolar cycloadditions (13DC) of the azides were carried out at the B3LYP / 6-31G (d) level. The results obtained show that the aziridinemorpholine formation from the triazoline by removing the di-azote molecule is thermally spontaneous starting from 463,15 K. However, that of seven chains undergoes a cycloreversion at 533.15 K with the R7 reagent (2,4-hexadienyloxypropyl azide), this reaction requires irradiation with ultraviolet light.

Keywords: nitrogenated heterocycles, DFT calculation, molecules reactivity, descriptor dual

INTRODUCTION

The 1,3-dipolar cycloaddition (CD13) reactions are a widespread category of reactions on which numerous studies have been carried out in particular by Huisgen, who has made an exhaustive study of the possible reactions between dipoles and dipolarophiles [1]. Houk et al. Have also contributed to understanding and predicting the reactivity and regioselectivity of(CD13) reactions [2]. These reactions are also used for the synthesis of natural products such as sugar derivatives [3], β-lactams [4], amino acids [5], alkaloids [6] and products of pharmacological interest such as pyrazolines having several biological activities (anti-inflammatory, analgesic, herbicides, etc.) [7]. The 1,3-dipolar cycloadditions are an excellent method for forming 5-membered heterocycles. Thus the use of azide constitutes a good way to synthetise the nitrogenous heterocycles.

The aziridines are three-membered heterocycles comprising nitrogen and two carbons, two methylenes linked to a secondary amine, which is isolatable and even possible to distill [8]. On account of the intrinsic instability of aziridines, these are not abundant in nature, but chemists have nevertheless synthesized some analogues with interesting properties, for example, we can mention the proteins comprising an aziridine in place of a methylene on a glycine [9]. The best example of biologically active molecules comprising an aziridine is certainly the mitomycin family [10], the expulsion of two nitrogen atoms from the triazoline ring in form of molecular nitrogen "N2" allows the formation of an aziridine [11,12].This process can be carried out by irradiation with ultraviolet light or by thermolysis using high temperature heating(scheme 1).

Morpholine skeleton compounds are of great biological interest because of their fungicides, analgesics and antidepressant properties.

Our aim in this research activity is to carry out a theoretical study on the synthesis of six-chain (aziridinomorpholine) and seven-chain nitrogen heterocycles, we will focus on the stereochemical analysis of the 1,3-dipolar cycloaddition and then determine whether the conversion of the cycloadduittriazoline to the corresponding aziridine allows a stereochemical control.The synthesis of aziridinomorpholine from azide (R6) where the presence of a dipolarophilic double bond and the "N3" group as dipolar species provides adequate conditions for the 1,3-dipolar intramolecular cycloaddition reaction. Heating of the azide (R6) in the refluxing toluene for five days conducted stereospecifically to a single cycloadduit via the intermediate triazoline, The latter having decomposed thermally to give, after removal of N2, aziridinomorpholine (scheme 2).

The azide (R7) is heated to reflux with toluene in order to obtain the corresponding aziridine, the thermolysis is not complete insofar as there was no complete disappearance of the starting material, even at the end Of the twentieth day.

* To whom all correspondence should be sent:
E-mail: Ouddai_nadia@yahoo.fr

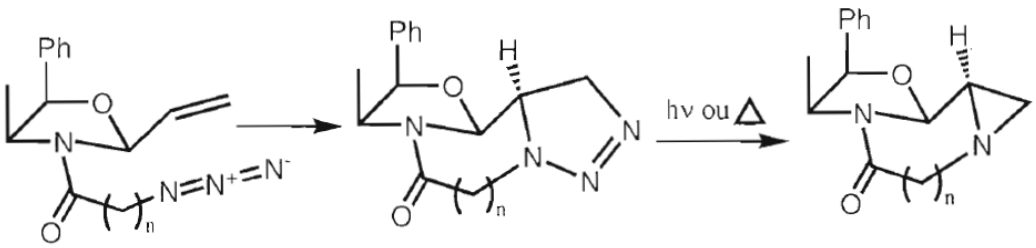

Scheme 1.Cycloaddition to chiral triazoline and transformation to aziridine

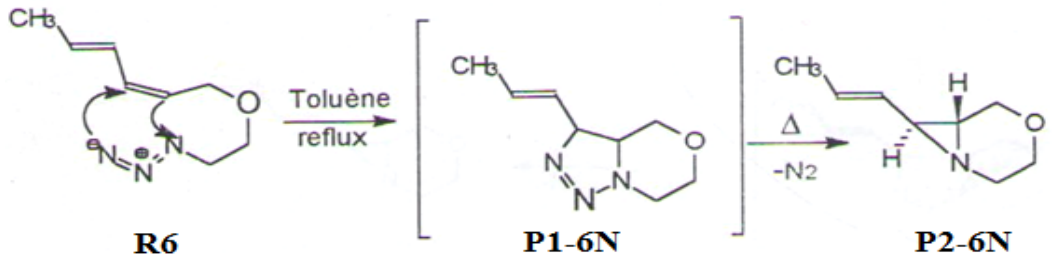

Schéma 2.Synthesis of aziridinomorpholine

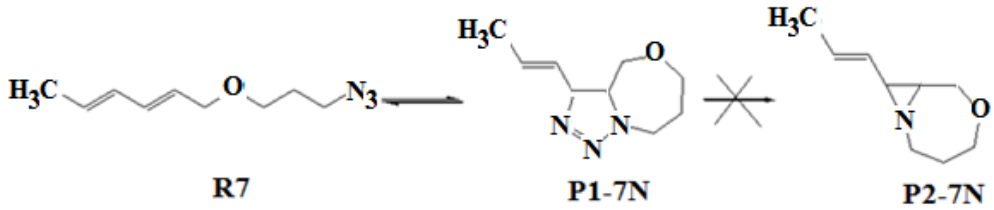

Scheme 3. 1,3-dipolar cycloaddition of R7 and cycloreversion

Thermolysis gave the azide as reaction product, the corresponding triazoline underwent a known cycloreversion (variant of a retro Diels-Alder reaction) regenerating the starting product. The non-disappearance of the starting azide would certainly be due to an equilibrium established with the corresponding triazoline (Scheme 3).

CALCULATION METHODOLOGY

The equilibrium geometries were optimized at the B3LYP 6-31G (d) level, using the Gaussian09W program[13]. The corresponding transition states have been located at B3LYP / 6-31G (d) [14,15,16], their existence was confirmed by the presence of one and only one imaginary frequency in the Hessian matrix. The enthalpy and free enthalpy of each stationary point were evaluated at T = 298.15K and P = 1atm, in the approximation of a rigid rotator and a harmonic oscillator for the first step of the reactions (Preparation of triazolin). For the second part" N2 removal", the free enthalpy was evaluated at different temperatures (from T = 463.15K to T = 533.15K) and P = 1atm. Finally, in order to reproduce as best as possible the solvent in which the intramolecular dipolar cycloaddition reaction takes place, l SCRF PCM (polarizable continuum Model) Mode of Tomasi[17] was chosen to model the solvent by a continuum of dielectric constant equal to that of the toluene ε = 2.38.

RESULTS AND DISCUSSION

Analysis of geometric structures

The control of stereochemistry in 1,3-dipolar cycloadditions depends on the approach of dipole and dipolarophile orbitals in space. The overlapping is done suprafacially for both species and summarized by the denomination [2 + 4] [18,19].Concretely, the suprafacial approach indicates that the two groups must overlap with parallel planes. Thus the intramolecular 1,3-dipolar cycloaddition reaction begins with the folding of the azides so that the dipolarophilic and the dipole part are held in proximity, this relation allows a good control of the stereochemistry as for all the suprafacial approaches, which makes it possible to know, in advance, that E di-substituted alkenes will give cycloadduits having a trans orientation. Indeed, the dipolarophiles have a π-bond which makes them linear or plane and the same is true for dipoles. The "R6" and "R7" folded azides are shown in (FIG 1).

In this study, the alkenes used are planar, characterized by the dihedral angle C5-C6-C7-C8 equal to 180 ° and they should orient themselves appropriately with azides which are mainly linear. Thus, without other effects, spatial orientation of a group related to the other is random, since the N3-C6 distance is about (3.6A) for the two reactants and about (3.4 - 3.7Å) For the N1-C7 distance for R6 and R7, respectively. Analysis of the intramolecular geometric parameters such as the σ: N1-C7 and N3-C6 bonds, formed in the transition state, shows that they have different values, This is quite normal because of the dissymmetry of the dipolarophile.The asynchronicity of the cycloaddition process can be estimated using the difference: $\Delta r = \left| d(N1\text{-}C7) - d(N3\text{-}C6) \right|$. The results obtained for the first step of the reaction are 0.12 Å and 0.24 Å for TS1-P6N and TS1-P7N respectively, this allows us to conclude that the cycloaddition of R7 is more asynchronous.

The bonding order concept can be used to obtain a deeper analysis of the extent of formation/breakdown for the bonds along a reaction path, this theoretical tool is used to study the molecular mechanism of chemical reactions. In order To find the nature of the formation process of "N3-C6", "N1-C7" bonds for the transition states TS1-6N, TS1-7N and the "N3-C6", "N3-C7" bonds for the transition states TS2-6N, TS2-7N, the Wiberg[20] binding index was calculated using the NBO analysis implemented in the Gaussian09 program. The results are illustrated in (Table 1).

The general analysis of the obtained values for bond's orders, relative to all the transition structures, indicates that the TS1-7N is more asynchronous in the bonds formation process, these values [0.0155-0.2684] are in good agreement with asynchronicity analysis, previously discussed for these azide cyclization reactions. On the other hand TS2-7N is more asynchronous in the second part "N2 removal" of triazoline in the process of formation of N3-C6 and N3-C7 bonds. In contrast, in the "N2 removal" reaction, the" N1-N2" Bonding order is close to 3 which implies the formation of a triple bond N1≡N2 and the bonding index "N1-C7" tends towards zero, which means breaking of this bond.

Transition states TS1-P6, TS2-P6, TS1-P7 and TS2-P7 were located at the B3LYP / 6-31G * level. The transition states were confirmed by the presence of one and only one negative eigen value in the matrix of force constants, in other words a single imaginary frequency in the Hessian matrix. The transition states are shown in (Fig. 2)

Table 1. Wiberg binding order at the transition structures corresponding to TS1-6N, TS2-6N, TS1-7N and TS2-7N.

	TS1-6N	TS1-7N	TS2-6N	TS2-7N
N2-N3	1.0913	1.1207	0.1449	0.4427
N1-N2	1.6022	1.5038	2.9790	3.2435
N3-C6	0.1868	0.2684	1.2624	0.5785
N1-C7	0.0155	0.1902	0.0003	0.0006
N3-C7			0.9062	0.1695

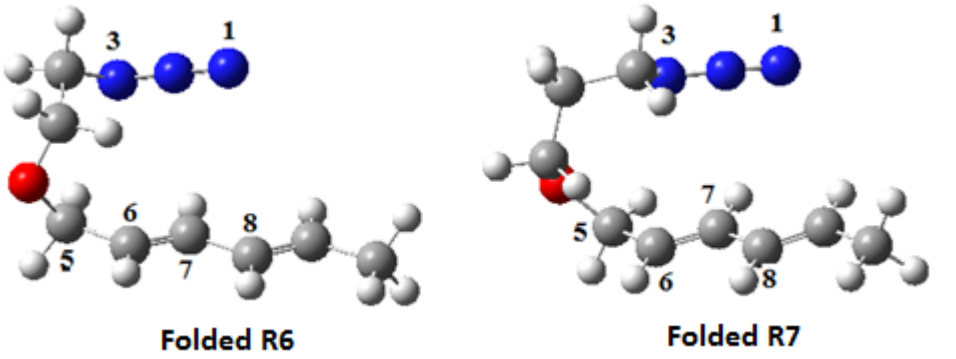

Fig. 1. Optimized geometries (B3LYP / 6-31G (d)) of folded reagents.

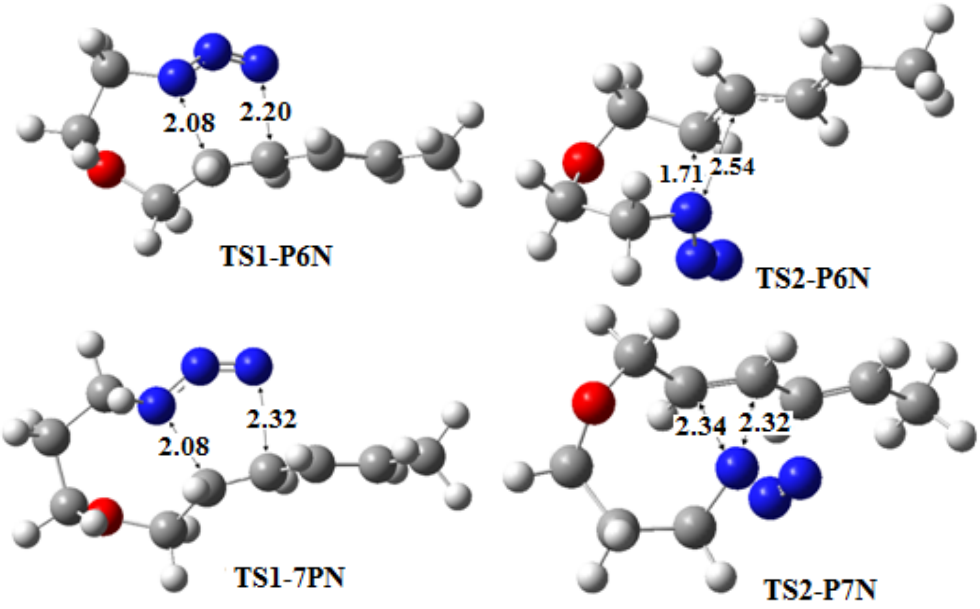

Fig. 2. Optimized geometries (B3LYP / 6-31G (d)) of the transition structures (distance in Å)

Analysis of reactivity by the dual descriptor.

The studies on the molecules reactivity and reaction mechanisms began to be carried out through the analysis of the wave function which defines the quantum state of a molecular system, for example, the Frontier Orbitals[21,22] theory has been very effective in understanding the regioselectivity of organic reactions, through the study of the phase or opposition phase recovery between the highest occupied orbital of the nucleophile and the most vacant base orbital of the electrophile. It was shown that the spin densities of the N + 1 / N-1 systems were good approximations for the Fukui functions, thus the dual descriptor was calculated by the difference between spin densities of the N + 1 / N-1 systems.

In all the representations of the dual descriptor isodensity maps, zones where the values of the descriptors are negative (Δf (r) <0) will be colored yellow, while the zones where the descriptor values are positive (Δf (r) >0) will be colored red.

The use of the dual descriptor Δf (r) allows an unambiguous prediction of the most reactive site with respect to an electrophilic or nucleophilic attack.

(Fig.3) shows the isodensity map of the dual descriptor for the azides "R 6" and "R 7" , on which it can be observed that the nitrogens possess nucleophilic characters (Δf (r) < 0, colored in yellow), and will thus react preferentially with the electrophiles, such as the C6 and C7 carbons of the alkene.The discrimination between the electrophilic and nucleophilic properties of the nitrogen and carbon of the double bond is thus clearly established by the use of the dual descriptor. Same meanings, when studying the "N2 removal" reactions of the triazoline, the dual descriptors of the transition states which lead to the product P2-6N and P2-7N are presented in (Fig.3).

Finally, we conclude that the formation of the two six- and seven-membered heterocycles is under orbital control.

On the other hand, the stability of the products can be studied by the LUMO-HOMO energy gap, (Fig. 4) illustrates this energy gap for the products P1-6N, P1-7N, P2-6N and P2-7N.

Analysis of the potential energy surface and prediction of the reaction mechanism

An exhaustive exploration of the potential energy surface allowed us to determine the different transition structures. The values of the relative enthalpies of the stationary points, entropies, and free energies associated with these intramolecular 1,3-dipolar cycloadditions of the azide and the "N2 removal" of the triazoline were also calculated. The energy results are presented in Table 2. The inclusion of zero-point energy (ZPE) and thermal contributions to barriers does not significantly modify the activation enthalpies for TSs. Indeed, the free enthalpy is inaccessible in solvent because the PCM model includes entropy effects of solvation in the determination of the energy of the system. The evolution of the free enthalpy can be followed in a medium of dielectric constant $\varepsilon = 1$ and in a medium of dielectric constant $\varepsilon = 2.38$, which makes it possible to analyze, in part, the influence of the solvent.

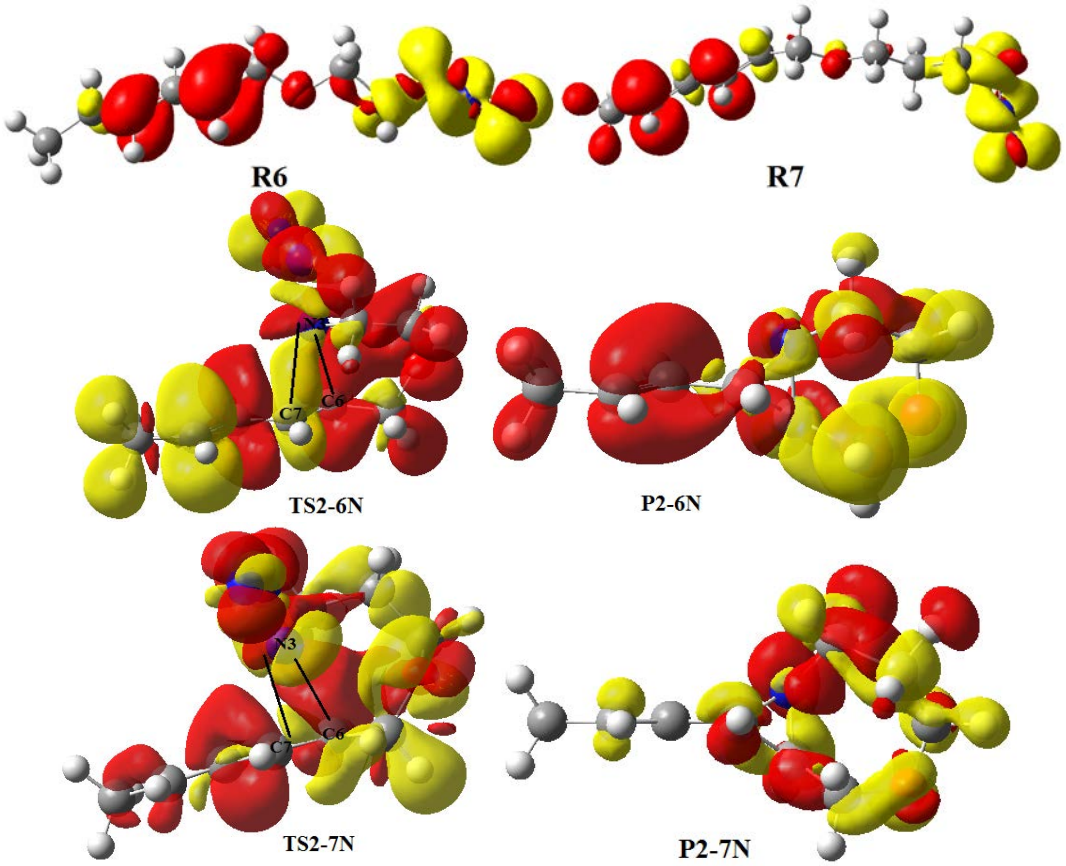

Fig. 3. Isodensity map of the dual descriptor of the azides R6, R7, TS2-6N, P2-6N, TS2-7N and P2-7N

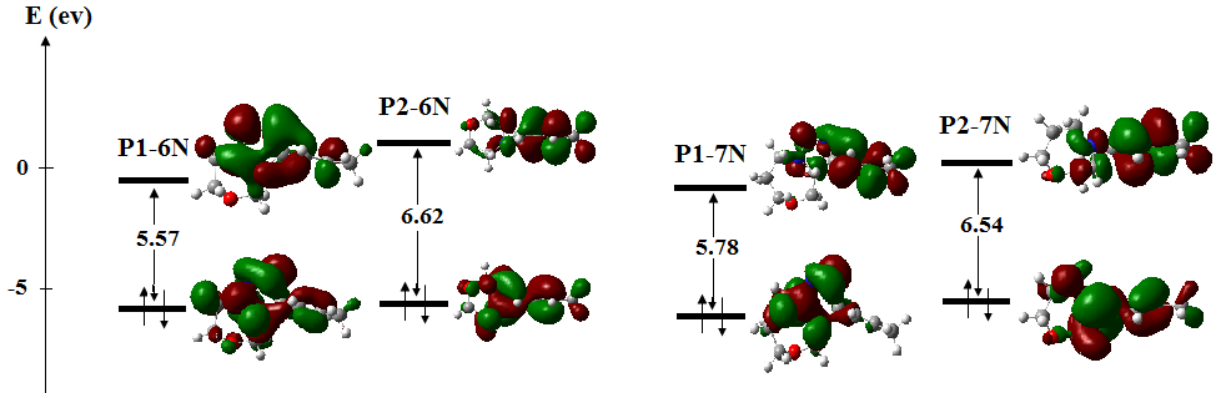

Fig. 4. The energy differences in (ev) for the products P1-6N, P1-7N, P2-6N and P2-7N

Table 2. Relative enthalpy in vacuum (ΔHε = 1, kJ / mol), free relative enthalpy in vacuum (ΔGε = 1, kJ / mol), entropies (ΔSε = 1, J / mol), free relative enthalpy in Toluene (ΔGε = 2.38, kJ / mol), for the stationary points of the reaction mechanism studied, calculated at 298.15K and 1atm.

	$\Delta H_{\varepsilon=1}$	$\Delta G_{\varepsilon=1}$	$\Delta S_{\varepsilon=1}$	$\Delta G_{\varepsilon=2.38}$
P1-6N	-29.69	-7.23	-75.31	-13.53
TS1-P6N	107.72	128.89	-71.01	128.15
P2-6N+N_2	204.67	170.80	113.60	
TS2-P6N	156.14	176.08	-66.85	
P1-7N	-48.70	-23.94	-83.05	-27.17
TS1-P7N	113.44	135.19	-72.94	135.05
P2-7N+N_2	229.69	195.14	100.58	
TS2-P7N	215.34	224.76	-31.59	

Relative to reagents R6 and R7

Table 2 shows that in the intramolecular 1,3 dipolar cycloaddition of the azides R6 and R7, the thermodynamic step is decisive, with an enthalpy ($\Delta H\varepsilon = 1 = -29.69$ kJ / mol) for "P1-6N" and ($\Delta H\varepsilon = 1 = -48.70$ kJ / mol) for "P1-7N", while the free enthalpy ($\Delta G\varepsilon = 1 = -7.23$kJ / mol) for "P1-6N" and ($\Delta G\varepsilon = 1 = -23.94$kJ / mol) for "P1-7N". The solvation does not have a great influence on the energy barrier to cross to achieve this stage.

The calculations show that the step of removing a nitrogen molecule from P1-6N and P1-7N is thermodynamically non-spontaneous at 298.15K. The formation of the aziridine P2-6N and P2-7N can be carried out by irradiation with ultraviolet light or by thermolysis by means of heating at elevated temperature, it is for this reason that we have recalculated the energies for the geometries of the second stage of the reaction at different temperatures of 463.15K up to 533.15K, the corresponding free enthalpies are summarized in (Table 3)

Table 3. Free relative enthalpy ΔG (kJ / mol) to aziridine formation.

	P2-6N ΔG	P2-7N ΔG	R7 ΔG_R
463.15K	-215.89	185.78	6.88
473.15K	-217.87	183.74	5.95
483.15K	-219.84	181.71	5.01
493.15K	-221.82	179.67	4.07
503.15K	-223.80	177.64	3.12
513.15K	-225.78	173.09	2.18
523.15K	-227.76	173.56	1.23
533.15K	-229.74	171.52	0.28

Relative to reagents P1-6N and P1-7N.

The theoretical study of the triazoline P1-6N thermolysis for the nitrogen molecule removal is spontaneous from 463.15K. For P1-7N, the reaction is impossible whatever the temperature, the reaction is directed towards photolysis. However, the free enthalpy $\Delta GR = 0.28$kJ / mol at temperature T = 533.15K when the thermolysis gave the azide R7 as the reaction product (Scheme 3), We find that an equilibrium between triazoline P1-7N and azide R7 has been established, The corresponding triazoline thus underwent a known cycloreversion (variant of a retro-Diels-Alder reaction). These results are in good agreement with the experimental part.

CONCLUSION

The intramolecular 1,3-dipolar cycloaddition reaction mechanism of the azides for the six- and seven-membered heterocycles were studied using the DFT method at the B3LYP / 6-31G (d) level. The analysis of the results proposed by the dual descriptor implies that the nitrogen possess nucleophilic characteristics. The activation energies calculation, the potential energy surface analysis (SEP) and the calculation IRC show that these cycloadditions follow asynchronous concerted mechanisms and that the solvation does not have a great influence on the energy barrier. The formation of aziridinemorpholine from the removal of a dinitrogen molecule from the triazoline cycle is spontaneous at 463.15K, while that of seven links is impossible under the same conditions, Nevertheless an equilibrium is obtained at 533.15 K between the triazoline and the azide R7. We conclude that it is probably a photolysis that can be carried out by irradiation with ultraviolet light.

REFERENCES

1. R. Huisgen, *AngewandteChemie International Edition in english*, **2**,565 (1963).
2. K.N. Houk, J. Sims, R.E. Duke, R.W. Strozier, J.K. George, *Journal of the American Chemical Society*, **95**,7287 (1973).
3. P. De Shong, J.M. Leginus, S.W. Lander, J. Org. Chem., **51**,574 (1986).
4. T. Kametani, S.D. Chu, T. Honda, J. Chem. Soc. Perkin Trans, 1,1598 (1988).
5. R. Annuziata, M.Chinquini, F. Cozzi, L. Raimondi, Tetrahedron, **43**,4051 (1987).
6. (a) J. Tufariello, *J. Acc. Chem. Res.*, **11**,369 (1979).
   (b) S.A. Ali, J.H. Khan, M.I.M. Wazeer, *Tetrahedron*, **44**,5911 (1988).
   (c) A. Hall, K. P. Meldrum, P. R. Therond, R. H. Wightman, *Synlett*, 123 (1997).
   (d) A. Goti, V. Fedi, L. Nanneli, F. De Sarlo, A. Brandi, **Synlett**, (1997) 577.
7. (a) A.R. Katritzky, In: Comprehensive Heterocyclic Chemistry», C.W. Rees, Eds.;Pergamon Press, Oxford,1984.
   (b) N. Araino, J. Miura, Y. Oda, H. Nishioka, *ChemAbstr*, **125,**300995 (1996).
   (c) C.R. Harrison, R.M. Lett, S.F.Mccann, R. Shapiro, T.M. Stevenson, *Chem Abstr*,124, 202246 (1996).
   (d) N.I. Gusar, L.I.Gulko, N.R.Gorodetskova, B.M. Klebanov, *ChemAbstr.*,**122**,290766(1995).
   (e) P. Pankaj, K. Sushil, S. Manish, P. Hansa, IL FARMACO, 1995.
8. J. Sweeney, *Chem. soc. rev.*, **31**, 247 (2002)**.**
9. M. Mladenovic, T. Schirmeister, S. Thiel, W. Thiel, B. Engels, *Chem. med. chem.*, **2**,120 (2007).
10. M. Kasai, M. Kono, *Synlett*, 778(1992).
11. P. Garner, W.B. Ho, S.K. Grandhee, W.J. Youngset V.O. Kennedy, *Journal of organic chemiSIJy*, **56**, 5893 (1991).
12. R. Ducray, M.A. Ciufolini, *Angew. Chem. Inl. Ed. Engl.*, **41,** 4688 (2002).
13. M.J.Frisch, G.W. Trucks, H.B.Schlegel, G.E.Scuseria, M.A.Robb, J.R.Cheeseman, G.Scalmani, V.Barone, B.Mennucci, G.A. Petersson, H.Nakatsuji, M.Caricato, X.Li, H.P.Hratchian, A.F. Izmaylov, J.Bloino, G.Zheng, J.L.Sonnenberg, M.Hada, M.Ehara, K.

Toyota, R.Fukuda, J.Hasegawa, M.Ishida, T.Nakajima, Y. Honda, O.Kitao, H.Nakai, T.Vreven, J.A.Jr. Montgomery, J.E.Peralta, F. Ogliaro, M. Bearpark, J.J.Heyd, E.Brothers,K.N. Kudin, V.N.Staroverov, R.Kobayashi, J.Normand, K.Raghavachari, A.Rendell, J.C.Burant, S.S.Iyengar, J.Tomasi, M.Cossi, N.Rega, J.M.Millam, M.J.Klene, E.Knox, J.B.Cross, V.Bakken, C.Adamo, J.Jaramillo, R.Gomperts, R.E.Stratmann, O.Yazyev, A.J.Austin, R.Cammi, C.Pomelli, J.W.Ochterski, R.L.Martin, K.Morokuma, V.G.Zakrzewski, G.A.Voth, P.Salvador, J.J.Dannenberg, S.Dapprich, A.D.Daniels, O.Farkas, J.B.Foresman, J.V.Ortiz, J. Cioslowski, D.J. Fox, Gaussian 09, Revision A.1; Gaussian, Inc.: Wallingford, CT, 2009.

14. A.D Becke, Density-functional thermochemistry. III. The role of exact exchange. *J. Chem. Phys*, **98**, 5648 (1993).
15. C.W. Lee, Yang, RG. Parr, *Phys. Rev. B*, **37**, 785 (1988).
16. M.S. Gordon, *Chem. Phys. Lett*, **76**, 163 (1980).
17. (a) J. Tomasi, M. Persico, *Chem. Rev*., **94**,2027 (1994);
    (b) B.Y. Simkin, I. Sheikhet, Quantum Chemical and Statistical Theory of Solutions-AComputational Approach; Ellis Horwood: London, 1995;
    (c) E. Cances, B. Mennucci, J. Tomasi, *J. Chem. Phys.*, **107**,3032 (1997);
    (d) M. Cossi, V. Barone, R. Cammi, J. TomasiChem. *Phys. Lett*., **255**,327 (1996);
    (e) V. Barone, M. Cossi, J. Tomasi, *J. Comput. Chem*., **19**,404 (1998).
18. I. Fleming, Frontier orbitais and organic chemical reactions, Avon, John Wiley & sons, 1976.
19. [1]C.J. Eston, C. M. M. Hughes, G. P. Savage, G.W. Simpson., *Advances in heterocycle chemistry*,**60**, 269 (1994).
20. B.K.Wiberg,*Tetrahedron*, **24,**1083(1968).
21. K. Fukui, T. Yonezawa, H. Nagata,*J. Chem. Phys*., **22**, 1433(1954).
22. K. Fukui,Théory of Orientation and Stereoselection, Springer, Berlin, 1970.

DFT-ИЗСЛЕДВАНЕ НА НИТРИРАНИ ХЕТЕРОЦИКЛЕНИ СЪЕДИНЕНИЯ С ШЕСТ И СЕДЕМ ВРЪЗКИ

Х. Меруани[1,3], А. Униси[2,3], Н. Уддаи[3*]

[1]Департамент по химия, Научен факултет, Университет „Мохамед Будиаф М'сила", 28000 М'сила, Алжир.
[2]Лаборатория по химично инженерство, Университет « Сетиф-1", Алжир
[3]Лаборатория по химия на материалите и живата материя: активност, реактивоспособност, Университет „Ел-Хаджс Лахдар Батна", ,05000 Батна, Алжир

Получена на 30 октомври, 2016 г.; коригирана на 14 декември 2016 г.

(Резюме)

1,3-диполярното циклично присъединяване (13DC) на азиди е извършено на ниво B3LYP / 6-31G (d).Получените резултати показват, че образуването на азидин-морфолин от триазолин чрез отстраняването на азотна молекула става спонтанно при нагряване до 463,15 K. Обаче правите вериги от седем атома претърпяват обратно циклизиране при 533.15 K с реагента R7 (2,4-хексадиенил-оксипропил азид). Тази реакция изисква облъчване с ултравиолетова светлина.

Bulgarian Chemical Communications, Volume 49, Number 3, (pp. 697 – 705) 2017

Differences of Cd uptake and expression of Cd-tolerance related genes in two varieties of ryegrasses

T. Li[1], W. H. Xu[1]*, Y. R. Chai[2]*, Z. Y. Wang[1], D. T. Xie[1]

[1]*College of Resources and Environmental Sciences, Southwest University, Chongqing 400715, P. R. China*
[2]*College of Agronomy and Biotechnology, Southwest University, Chongqing 400715, P. R. China*

Received March 24, 2016; Revised May 23, 2017

Effects of different Cd levels (0, 75, 150, 300 and 600 mg·kg^{-1}) on biomass, Cd content and accumulation and cadmium tolerance related gene expression levels of two cultivars of ryegrasses (Bond and Aberd) were studied in soil culture experiment. The results showed that dry weights of shoot and the plant of Bond and Aberd increased by 10.06% and 4.04%, 25.84% and 16.89%, respectively compared with the control when exposed to 75 mg·kg^{-1} and 150 mg·kg^{-1} Cd, respectively. Cadmium concentration and Cd accumulation of shoot and root were significantly increased with the increase of soil Cd level (P <0.05). When exposed to 150 mg·kg^{-1} Cd, Cd concentrations of shoot and root in Bond and Aberd were 171.83 mg·kg^{-1}, 374.49 mg·kg^{-1}and 169.12 mg·kg^{-1}, 229.68 mg·kg^{-1}, respectively. Cadmium accumulation in Abed was greater than that in Bond at the same Cd level. The trend of the expression of OAS and IRT gene was consistent with the bimodal curve by increasing of cadmium levels. 75-150 mg·kg^{-1} Cd stress promoted the expression of OAS and IRT genes in ryegrasses. Considering two cultivars of ryegrasses, Abed has more suitable as a phytoremediation materials to repair soil Cd pollution due to higher biomass and cadmium accumulation.

Keywords: cadmium; ryegrasses; cadmium uptake; OAS gene; IRT gene

AIMS AND BACKGROUND

Cadmium (Cd) is the first heavy metal contaminant due to strong mobility in the soil and high toxic to the crop [1] of soil. According to statistics, the world releases about 30,000 tons of Cd to the environment each year, of which, about 82% -94% Cd penetrate into the soil [2]. China's annual discharge of cadmium to the environment by industrial waste totals 680 t, Cd pollution area of farmland reaches 280,000 hm^2, and annual production of agricultural products with exceeded cadmium approaches1.5 million t [3-4]. Cadmium content of approximately 24.1% vegetable garden soil exceeds the national soil environmental quality secondary standard [5]. Studies have shown that Cd will be enriched in the human body through the food chain and damage human health when crops exposed to Cd-contaminated soils [6]. Therefore, Soil Cd pollution control and remediation have been widely concerned by scholars at home and abroad in the field of environmental science.

Phytoremediation technology, as a green biotechnology, has the advantages of simple operation, economy and technical possibility of large area implementation [7]. Ryegrasses (*Lolium multiflorum* L.) is an ideal heavy metal restoration plant due to high growth rate, strong tillering ability and high yield, and strong enrichment effect on soil heavy metals [8]. There are significant differences in uptake and accumulation of Cd between different species and different cultivars, which is mainly related to genotype [9]. So far, there have been many metal ion transporter genes isolated and cloned from plants. Their transporters are closely related to absorption, transport, accumulation and fixation of metal ions, and play an important role in plant tolerance to Cd or Cd accumulation. ZIP gene, i.e. zinc-iron regulating protein gene, includes two types of genes of ZRTP (Zinc Regulated Transporter) and IRT (Iron Regulated Transporter), which are respectively responsible for the transport of Zn and Fe. Iron deficiency-induced increased expression of IRT1 in the root is beneficial to the uptake of Fe by root, and also causes more Zn^{2+} and Cd^{2+} accumulation in the root, indicating that IRT1 is related to absorption of Cd by root [10]. The report by He [11] has shown that RsIRT1 gene in radish is induced by exogenous Cd stress. RsIRT1 is involved in absorption and transport of cadmium under Cd stress. Phytochelatins (PCs) are a class of sulfhydryl-containing polypeptides of varying lengths consisting of cysteine (Cys), glutamic acid (Glu), glycine (Gly), etc.[12]. PCs can decrease Cd activity by chelating with the heavy metal ion Cd^{2+} in plant cells via sulfhydryl group, and alleviate Cd toxicity to plant [13]. Dominguez-Solis et al. [14] found that Cd stress strongly induced the expression of OASTL in *Arabidopsis thaliana*, whereas overexpression of OASTL also increased the tolerance of *Arabidopsis thaliana* to Cd. Unfortunately, there are few studies

* To whom all correspondence should be sent:
E-mail: xuwei_hong@163.com; chaiyourong1@163.com

on the differences in the expression levels of Cd tolerance related genes among different cultivars of ryegrasses Therefore, pot experiment was conducted to study the difference in biomass, Cd content and accumulation, the expression level of Cd tolerance related gene among different Cd levels and between two cultivars of ryegrasses (Bond and Aberd).

EXPERIMENTAL

Plant material, soil and Cd treatments

The soil pH was 5.23, organic matter content was 8.87 $g \cdot kg^{-1}$, total nitrogen content was 1.54 $g \cdot kg^{-1}$, available nitrogen content was 74.60 $mg \cdot kg^{-1}$, available potassium content was 65.07 $mg \cdot kg^{-1}$, available phosphorous content 38.59 $mg \cdot kg^{-1}$, cation exchange capacity (CEC) was 0.178 $mol \cdot kg^{-1}$. The total cadmium 0.11 $mg \cdot kg^{-1}$, and available cadmium was not detected. Seeds of two cultivars of ryegrasses (Bond and Aberd) were purchased from Jiangxi Scarecrow Agricultural Garden.

Five levels s of Se (0, 75, 150, 300 and 600 $mg \cdot kg^{-1}$) prepared from $CdCl_2 \cdot 2.5H_2O$ were set up for the pot experiment. Moreover, air-dried soil (5 kg) was sieved using a 40-mesh sieve, and treated with the $CdCl_2 \cdot 2.5H_2O$ solution and mixed to be homogeneously put in a plastic pot (diameter, 25 cm; height, 17 cm) and kept balance for two weeks. The seedlings of ryegrasses (*Lolium multiflorum* L.) with 10 cm high were then transplanted 30 plant for each pot. The moisture content in soil was kept 60% of the maximum moisture in the fields with deionized water. Fast- measurement of Soil Moisture (TZS-IW, Zhejiang Tuopu Instrument Co., Ltd., China) was used to determine the moisture content in soil. In the basic fertilizer the used amount of P ($NH_4H_2PO_4$) and K (KCl) were 100 and 150 $mg \cdot L^{-1}$ respectively and Nitrogen content ($NH_4\ H_2\ PO_4$ and urea) was 180 $mg \cdot L^{-1}$. N fertilizer was applied in three installments: 40% for basal and 60% each for seedling stages which applied with 15 days' interval after transplanting, each time 30%. All experiments were performed in triplicate and arranged at random. The harvested plants were oven-dried at 105 ˚C for 15min, and oven drying to constant weight in 60˚C.

ANALYSIS OF SOIL CD CONCENTRATIONS

Soil total Cd was digested with HNO_3-$HClO_4$ (5: 1 by volume) and determined by atomic absorption spectrophotometry (Perkin Elmer SIMMA 6000, Norwalk, USA). Soil available Cd content was determined by DTPA extraction (GBT 23739-2009) and atomic absorption spectrophotometry (Perkin Elmer SIMMA 6000, Norwalk, USA). Soil reference materials (GBW # 08303) provided by National Institute of Standards and Technology were used for quality monitoring of the determined results. The Cd recovery of all soil samples was higher than 95% and accuracy of relative standard deviation (RSD) was within 10%.

ANALYSIS OF CD CONCENTRATIONS IN THE PLANTS

Plant Cd concentration was digested with HNO_3:$HClO_4$ (4: 1), and Cd^{2+} solution after digestion was determined by atomic absorption spectrophotometry (Perkin Elmer SIMMA 6000, Norwalk, USA). The detection limit was 0.005 $mg \cdot kg^{-1}$. Plant reference materials (GBW # 08513) provided by National Institute of Standards and Technology were used for quality monitoring of the determined results. The Cd recovery of all plant samples was higher than 95% and accuracy of relative standard deviation (RSD) was within 10%.

DETECTION OF GENE EXPRESSION

Total RNA extraction

RNA was extracted from each leaf tissue sample. The specific procedure was performed with reference to the Biomed RNA Extraction Kit operation manual.

Purification of total rna and detection

Reverse transcription of RNA used TaKaRa's PrimeScript™ RT reagent Kit with gDNA Eraser (Perfect Real Time). First, use DNase I to treat the remaining DNA in RNA, and the treatment time was extended from 2 min in manual to 20 min, for sufficient removal of heavily contaminated total genome DNA from RNA and reverse transcription into cDNA. The specific operation is: (1) RNA purification: take 200μl RNase-free centrifuge tube configuration reaction system mixture, 5×gDNA Eraser Buffer 2.0 μl, gDNA Eraser 1.0 μl, Total RNA 1.0 μg, RNase Free dH_2O Up to 10 μl. After configuration of mixture, PCR instrument was heated at 42°C for 20 min, and then cooled to 4°C for1~2 min. (2) RNA reverse transcription into cDNA. 20 μl reaction system: 5× PrimeScrip Buffer 4 μl, PrimeScrip RT EnzymeMix I 1 μl, RT Primer MIX 1 μl, purified RNA 10 μl, RNase Free dH2O supplemented to 20 μl. Reverse transcription was performed on a PCR instrument at 37°C for 15 min → 85°C for 5 sec → 4°C for1 min. The resulting cDNA was stored at -20°C refrigerator for standby use.

Primer design and synthesis

Seven Cd-resistant genes (OAS, IRT, HAM, NRAMP, MT, PCS and CAM) were studied in this study (Table 1). Based on BLAST and multiplex alignment (Vector NTI Advance 11.51) of sequence of Cd-resistant gene family members in ryegrasses, RT-PCR specific primers of seven genes and 25S rRNA primers of reference genes were designed (Table 2), which were synthesized by Nanjing Kingsley Biotech Co., Ltd.

PCR amplification of CDNA

The obtained cDNA was specifically amplified with an ABI-9700 PCR instrument. The total volume of the reaction system was 25 μl, including 2.5 μl 10 × PCR Buffer (containing Mg^{2+}), 0.5 μl dNTPs (10 mM), 0.5 μl forward and reverse primers (10 μM), 0.25 μl Easy-Taq DNA polymerase (5 $U \cdot \mu l^{-1}$), 0.5μl cDNA template, and the rest was ddH_2O. PCR reaction procedure: pre-degeneration at 94˚C for 2 min, degeneration at 94˚C for 30 s, annealing (at 61.5˚C) for 45 s, extension at72˚C for30 s, to be repeated 35 cycles, with last extension at 72˚C for 3 min, at 16˚C for 5 min. PCR products were subject to 1.0% agarose electrophoresis detection. If clear band of predicted target size (about 250 bp) is obtained, then the reverse transcription is successful.

Real-time quantitative PCR

The cDNA after reverse transcription was diluted 30 times with ddH_2O, and the transcriptional expression level of the target gene was detected by qRT-PCR using FastStart Essential DNA Green Master kit of F.Hoffmann-La Roche AG. The data was analyzed on Bio-Rad CFX Manager 3.0 software via CFX96TM Real-Time System of real-time quantitative PCR. The operation was carried out with reference to the instruction manual. The reaction system is as follows: FastStart Essential DNA Green Master (2X) 5μl, F-primer (10 μM) 0.5 μl, R-primer (10 μM) 0.5 μl, cDNA template 3 μl, ddH_2O 1μl. Reaction conditions: pre-degeneration at 95˚C for 10 min, degeneration at 95˚C for 10s, annealing at 61.5˚C for 30 s, to be repeated 40 cycles. The product melting curve was tested from 65˚C to 95˚C, and repeat 3 times with 25 s as internal reference gene.

THE STATISTICAL ANALYSIS

Three-way analysis of univariate ANOVA and correlation analysis were performed using SPSS version 21.0 package (SPSS, 2009). The variables analyzed separately were Cd concentration and Cd uptake in ryegrass. The level of significant was 0.05.

Table 1. Selection of Cd-tolerance related genes

Gene name	Gene symbol	Encoded protein	Literature resources
Calmoduline gene	*TcCaM2*	Calmoduline	Han et al. [15]
Plant synthase gene	*AtPCS1* *BjPCS*1	Plant synthase	Clemens et al. [16]
Metallothionein gene	*BjMT2*	Metallothionein	Zhang et al. [17] An et al. [18] (2006)
OASTL gene	*OAS*	O-acetyl-ser(thi0l)-lyase	Dominguez-Solis et al. [14]
HMA family	*HMA2* *HMA3* *HMA4*	Related ATP enzyme	Mills et al. [19] Hussain et al. [20] Gravot et al. [21] Bernard et al. [22]
Nramp family	*AtNramp3* *AtNramp4*	Encoded metal ion transport protein	Thomine et al. [23]
ZIP family	*IRT1*	Encoded plasma membrane transporter	Eide et al. [24](1996) Clemens et al. [25] (2006)

Table 2. Primers for qRT-PCR of Cd-tolerance related genes in ryegrass

Gene	Primer	Sequence (5'→ 3')	Tm˚C
OAS1	FLmOAS1q（Forward primer）	5'-GCTGGTTGGAATATCTTCTGGC-3'	61.5
	RLmOAS1q（Reverse primer）	5'-CCATGCTCTCAGCCTCCTTCT-3'	
OAS2	FLmOAS2q	5'-GCTGGTTGGAATATCTTCCGGT-3'	61.5
	RLmOAS2q	5'-CATGTTCTCGGCCTTCCTCC-3'	
OAS3	FLmOAS3q	5'-GCAAAGCAGTTGGCTCTTCAG-3'	61.5
	RLmOAS3q	5'-CTGCTCGCACTCTTCTCTGATG-3'	
OAS4	FLmOAS4q	5'-GTTACCACGGGAGAGGCAGT-3'	61.5
	RLmOAS4q	5'-CGGAACAGGATGCTAGAGATGT-3'	
OAS5	FLmOAS5q	5'-AGGTGAAAGGTGAGGATGCTG-3'	61.5
	RLmOAS5q	5'-CAGCTTCCTTCCTCAAACCCT-3'	
OAS6	FLmOAS6q	5'-CACTGAGGATGCAATGACGAAC-3	61.5
	RLmOAS6q	5'-CAGTGGCAAAGAGGTCCGAGTT-3'	
OAS7	FLmOAS7q	5'-AGTCATCGACGAAGTGGTCACT-3'	61.5
	RLmOAS7q	5'-TGCTGCAAAGAGGTGTGAGTC-3'	
OAS8	FLmOAS8q	5'-GGTGATTGACGAGATCCTTGCA-3'	61.5
	RLmOAS8q	5'-TTCCACGAAGAGGTCAGAGGAA-3'	
OAS9	FLmOAS9q	5'-GGTCACACAAGATTCAGGGTACA-3'	61.5
	RLmOAS9q	5'-GTCACATTCCTCCCTAACAAGTG-3'	
IRT4	FLmIRT4q	5'-CCGAAACGATCCGTCACAGA-3'	61.5
	RLmIRT4q	5'-AAGAAGGTCGCCATGAGCAC-3'	
ITR6	FLmIRT6q	5'-GAAGCAGAAGATGGTCTCCAAG-3'	61.5
	RLmIRT6q	5'-CACATGTAACCCACTGTTGCCA-3'	
ITR7	FLmIRT7q	5'-GCTCCGTCGTGGTGTCACAG-3'	61.5
	RLmIRT7q	5'-GCTCCGTCGTGGTGTCACAG-3'	
ITR8	FLmIRT8q	5'-TCCGAGGACGAAAAGGACAC-3'	61.5
	RLmIRT8q	5'-CAGAAGAAGAGGATCATGGTCAC-3'	
ITR10	FLmIRT10q	5'-CCATGGGAGCGAGGAGAGAC-3'	61.5
	RLmIRT10q	5'-AGCCATGAGGAGTGCAGAGA-3'	
HMA2	FLmHMA2q	5'-CTGCCGCCCATCATCCTCA-3'	61.5
	RLmHMA2q	5'-CTTCACATCCTGGCAAGCAAC-3'	
HMA3	FLmHMA3q	5'-TCGAGACCCTGGCTTGCAC-3'	61.5
	RLmHMA3q	5'-CTGCTTGGGCACCGGATAA-3'	
NRAMP2	FLmNRAMP2q	5'-GTGGTTACGAGCAATGATCACAC-3'	61.5
	RLmNRAMP2q	5'-CGGACTTCGTCGGTATAGAAGGA-3'	
NRAMP6	FLmNRAMP3q	5'-CTGAGGGCGCTGATAACCAGA-3'	61.5
	RLmNRAMP3q	5'-CAGCCACTGTCCAGGTTACAG-3'	
NRAMP6L	FLmNRAMP6Lq	5'-AGCTGTCGCTCTGTACTTCAAC-3'	61.5
	RLmNRAMP6Lq	5'-TTGATCACGATTGGCAGAGACG-3'	
MT1	FLmMT1q	5'-GGATGTCTTGCAGCTGTGGAT-3'	61.5
	RLmMT1q	5'-CCGGAGGCCATCTCAAACT-3	
MT2A	FLmMT2Aq	5'-CATCATGTCGTGCTGCGGT-3'	61.5
	RLmMT2Aq	5'-CACTTGCAGCCTCCGTTCT-3'	
MT2B	FLmMT2Bq	5'-GGAAGGAGAATGTCTTGCTGCA-3'	61.5
	RLmMT2Bq	5'-ACTTGCAGGTGGTGCAGTC-3'	
MT2C	FLmMT2Cq	5'-GAAGATGTCTTGCTGCTCAGGA-3'	61.5
	RLmMT2Cq	5'-TGGTGCCGCAGTTGCACTT-3'	
PCS	FLmPCSq	5'-CGCTCTCCGTCGTCCTCAAC-3'	61.5
	RLmPCSq	5'-TGGATGGTGGTCTGGTCTGC-3'	
CAM	FLmCAMq	5'-GAGCAGATCGCCGAGTTCAAGGA-3'	61.5

RESULTS

Biomass

As shown in Fig. 1, significantly different of dry weight in shoots, roots and the plant in Bond and Aberd were found between cultivars and among different Cd levels (P <0.05). The dry weight of shoots in Bond and Aberd increased first and then decreased with the increase of soil Cd level. The highest dry weight of shoots and the plant were observed at 75mg·kg^{-1} Cd, increased by10.06% and 4.04% compared with the control respectively. The dry weight of shoots and the plant of Aberd reached highest value at 150mg·kg^{-1} Cd, increased by

25.84% and 16.89% respectively compared with the control.

Concentration of CD in shoot and root

The concentrations of Cd in shoot and root of cultivars increased significantly with the increase of soil Cd (P <0.05) (Fig. 2). At different Cd levels, Cd concentrations of roots were higher than that of shoots. When soil Cd level was at 150 mg·kg^{-1}, Cd concentrations of shoots and roots of Bond and Aberd were 171.83 mg·kg^{-1}, 374.49 mg·kg^{-1} and 169.12 mg·kg^{-1}, 229.68 mg·kg^{-1} respectively, with Cd concentrations exceeding the critical value of cadmium hyper-accumulator (100 mg·kg^{-1}).

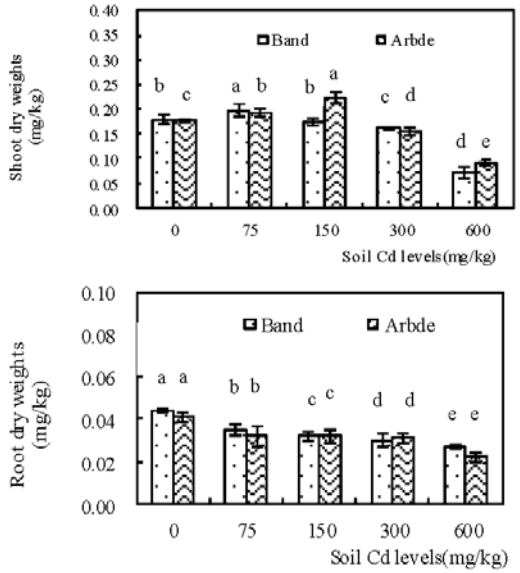

Fig.1. Effects of different Cd levels on dry weights of shoot and root in ryegrass. Different letters (a, b, c) indicate significant difference at P≤0.05 among different Cd levels in the same variety.

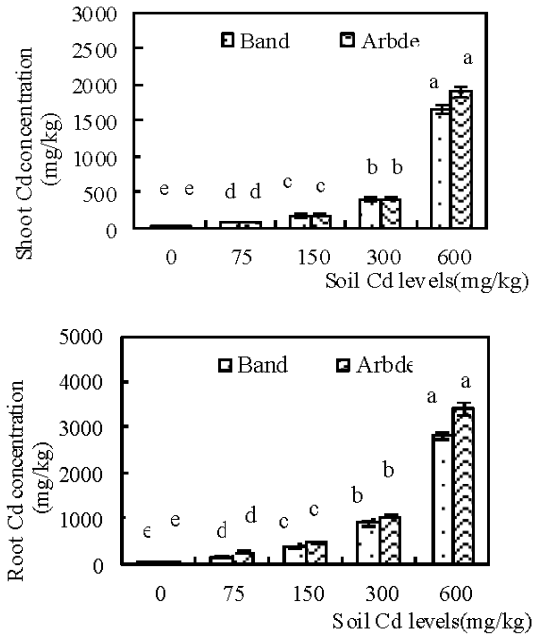

Fig. 2. Cadmium concentration in shoot and root of ryegrass. Different letters (a, b, c) indicate significant difference at P≤0.05 among different Cd levels in the same variety

CD accumulation in shoot and root

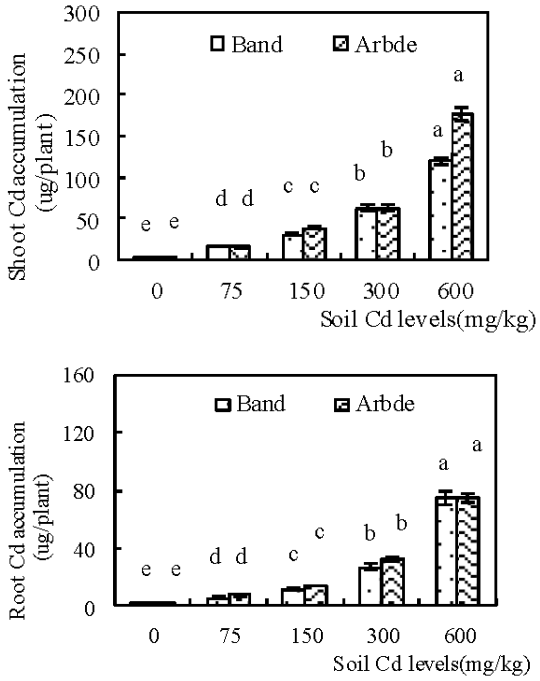

Fig. 3. Effect of different Cd levels on Cd accumulation of shoot and root in ryegrass. Different letters (a, b, c) indicate significant difference at P≤0.05 among different Cd levels in the same variety

As shown in Fig. 3, Cd accumulation in each part of plant increased with the increase of soil Cd level, and significant difference was found between cultivars and among soil Cd levels(P <0.05). The accumulations of cadmium in the shoots and roots of Bond were 53.84-422.93 times and 8.10- 116.56 times higher than that of the control respectively at 75, 150, 300 and 600 mg·kg^{-1} Cd.; while the accumulations of cadmium in shoots and roots of Aberd were 25.72- 304.23 and 6.94-70.04 times higher than that of the control respectively. At different Cd levels, the total of Cd accumulation in Aberd was greater than that in Bond.

Detection of cd-resistance related gene expression

The results of testing of OAS gene family of two cultivars of ryegrass were seen from Fig. 4. The trends of the expression of OAS5, OAS6 and OAS7 at different Cd levels were basically consistent with bimodal curve. The expression levels of OAS5, OAS6 and OAS7 of Bond cultivar were significantly increased by 13.63, 15.42 and 41.31 times higher than that of the control at 75 mg·kg^{-1} Cd, respectively. Expression levels of OAS5, OAS6 and OAS7 in Bond cultivar decreased at the level of

150-300 mg·kg^{-1}Cd, but increased at 600 mg·kg^{-1} Cd; Expression levels of OAS5, OAS6 and OAS7 in Aberd increased at the level of 75-150 mg·kg^{-1}Cd, decreased at 300 mg·kg^{-1}Cd, but increased at 600 mg·kg^{-1} Cd.

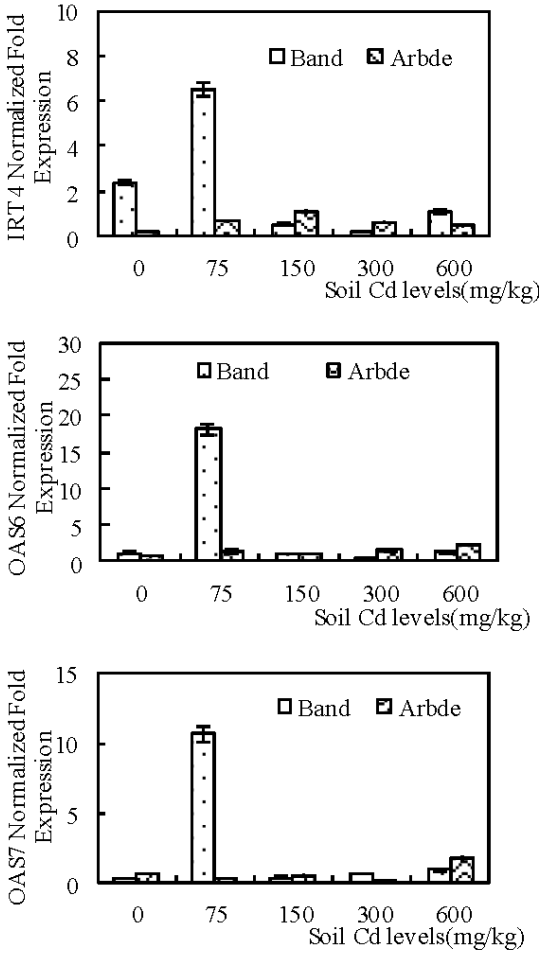

Fig. 4. Real-time PCR analysis of OAS in leaf of Ryegrass

As shown in Fig. 5, the expression trends of IRT gene family of two ryegrass cultivars at different cadmium levels were different. The expression trend of IRT gene family of Bond was basically consistent with bimodal curve. Expression level of IRT gene family in Bond significantly increased by 2.77, 3.60, 9.84, 4.40 and 1.80 times higher than that of the control at the level of 75 mg·kg^{-1} Cd respectively; while the expression level of IRT gene family in Bond decreased at the level of 150-300 mg·kg^{-1} Cd, then increased at the level of 600 mg·kg^{-1} Cd. The expression level of IRT gene family in Aberd increased first and then decreased, showing unimodal curve at 75-300 mg·kg^{-1} cadmium. The highest of expression level of IRT4 and IRT6 was observed at the level of 150 mg·kg^{-1} Cd, and then decreased when Cd level ≥ 300 mg·kg^{-1}. The expression level of IRT4 was significantly increased at 300 mg·kg^{-1} Cd. The highest of expression level of IRT8 and IRT10 was found at the level of 75 mg·kg^{-1} Cd, but significantly decreased when Cd level ≥ 150 mg·kg^{-1}. Significantly differences of expression level of IRT4, IRT6, IRT7, IRT8 and IRT10 genes were observed between cultivars of ryegrass and among soil Cd levels (P <0.05).

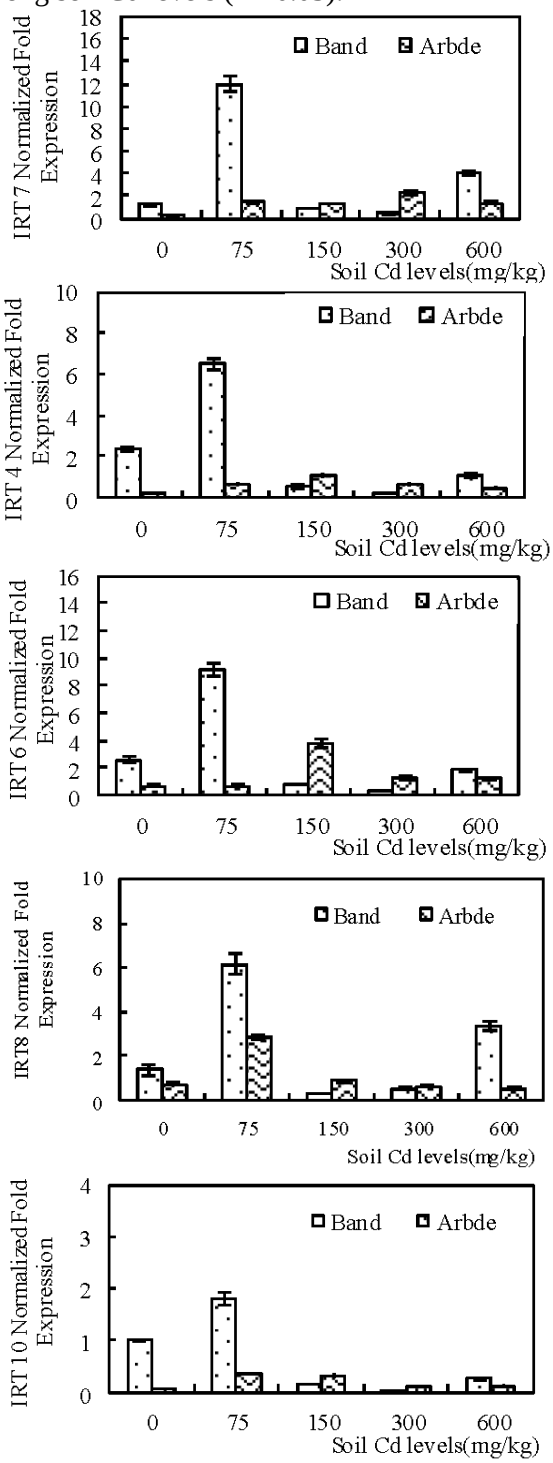

Fig. 5. Real-Time PCR analysis of IRT in leaf of ryegrass

DISCUSSION

Under Cd stress, the growth of plants are often inhibited and the toxic effect increases with the

increase of Cd stress level [26]. However, a few studies also have shown that Cd has no significant effect on plant growth under low Cd concentration [27], and even stimulates plant growth [28]. In our study, with the increase of soil Cd level, the dry weights of shoots of Bond and Aberd increased first and then decreased. Low Cd (≤75mg·kg^{-1} or 150mg·kg^{-1}Cd) stimulates the growth of Bond and Aberd, but high Cd (>75mg·kg^{-1} or 150mg·kg^{-1}Cd) inhibits the growth of shoots and roots of the two cultivars. The result is similar to the report by Shi et al. [28]. Significant differences in tolerance to Cd were found among different plant varieties or cultivars due to genotypic difference [29]. The recent experiment also supported this view, which Cd tolerance of Aberd was greater than that of Bond.

Cadmium hyper-accumulators should have three characteristics: First, under the same growth condition, shoot Cd concentration of plant is 100 times higher than that of ordinary plants, with cadmium critical content at 100 mg·kg^{-1}; second, Cd concentration in root is less than that in shoot; third, plant growth does not show obvious toxic symptoms, and has a strong tolerance to cadmium [30]. Shoot Cd concentrations of the two ryegrass cultivars (Bond and Aberd) exceeded the critical value of hyper-accumulator (100mg·kg^{-1}) when exposed to 150 mg·kg^{-1} Cd. It indicated that ryegrass was one of cadmium hyper-accumulators. The results were similar to those reported by Fang et al. [31]. Cadmium is highly mobile and readily absorbed by plants, and most plants can transfer cadmium from root to shoot [32]. However, the recent experiment showed that Cd concentrations of roots in Bond and Aberd were higher than that of shoot at the same Cd level in soil. It replied that roots of ryegrass had strong ability to enrich soil Cd, while its ability of transferring Cd to shoots from roots was weaker. These results were similar to the report of Sun et al. [33]. Significant differences in uptake and accumulation of cadmium between cultivars due to genotypic difference [34]. At the same level of cadmium, Cd concentrations and Cd accumulations of shoots and roots in Aberd were higher than that in Bond. This result supported to the report of Nesler et al. [34]. Comparing with two cultivars of ryegrass, Aberd has greater repairing ability in Cd pollution soil.

The study of glutathione metabolism is one of the important research contents in resistance / tolerance mechanism of plant under environmental stress [35]. There are two key enzymes, O-acetyl-serine (thiol) ligase (OAS-TL) and glutamylcysteine synthetase (γ-GCS), in the process of biochemical synthesis of glutathione [36]. These two enzymes impacts detoxification of cells and heavy metal enrichment due to limit the amount of glutathione synthesis, and affect synthesis and activity of polypeptide in the plant that can integrate heavy metal ions, i.e. phytochelatins (PCs) [37]. Harada et al. [13] introduced some of the genes into model plant tobacco using transgenic techniques. The results showed that tolerability of stress was much greater than that of the control group, and synthesis ability of cysteine in the plant was significantly improved. In this study, the highest expression level of OAS genes for Bond was found at 75mg·kg^{-1}Cd, while the highest expression level of OAS genes for Aberd was found at 75-150mg·kg^{-1}. It showed that Cd stress level at 75-150 mg·kg^{-1} promoted the expression of OAS genes in ryegrass. However, with the increase of soil Cd level, the expression level of OAS genes in ryegrass decreased gradually. These results were different to Wang‘s report, which the transcription expression of OAS-TL6 gene in collard increased when exposed to Cd-contaminated soil. The expression level of two Cd related genes (family) in ryegrass by Cd induced were significantly different between cultivars and among different cadmium treatments. These results are consistent with the report by Takahashi et al. [38].

IRT was first discovered as an iron transporter in *Arabidopsis thaliana*, which regulates cadmium absorption and transport [39]. The expression product of IRT1 and IRT2 is iron ion transport regulating protein located on the plasma membrane, and it is responsible for absorption of Fe^{2+} in the root and outer cortex. It is also related to Cd^{2+} absorption, and OSIRT1, AtIRT1 and AtIRT2 overexpression can increase accumulation of cadmium [38, 40]. In recent experiment, 75-150 mg·kg^{-1} cadmium stress increased the expression level of IRT genes in ryegrass, while high cadmium stress (≥600 mg·kg^{-1}) decreased the expression level of IRT genes in ryegrass, which was lower than that of the control. It may be the toxicity of Cd on growth and metabolic levels of ryegrass when exposed to high Cd stress. However, these results are inconsistent with the report by Uraguchi and Fujiwara [41].

CONCLUSION

The dry weight of shoot and the plant of the two ryegrass cultivars (Bond and Aberd) increased first and then decreased with the increase of soil cadmium pollution, and reached the peak at 75 mg·kg^{-1} and 150mg·kg^{-1} Cd respectively. Shoot Cd

concentrations of the two cultivars (Bond and Aberd) were higher than the critical value of hyper-accumulator (100mg·kg^{-1}) at 150 mg·kg^{-1} Cd. At the same soil Cd level, Cd concentrations of shoot and root in Aberd were higher than that in Bond. Cadmium stress (75-150 mg·kg^{-1}) promoted the expression levels of OAS and IRT genes in ryegrass. The expression levels of the two cadmium metabolism related genes (family) were significantly different between cultivars and among soil Cd levels (P <0.05).

Acknowledgments: *This work was supported by Fund of China Agriculture Research System (Nycytx-23), the National Science and Technology Pillar Program of China (No. 2007BAD87B10), and the Specialized Research Fund for the Doctoral Program of Higher Education (20130182110006).*

REFERENCES

1. X.Y. Lin, R.X. Mou, Z.Y. Cao, P. Xu, X.L. WU, Z.W. Zhu, M.X. Chen, *Science of the Total Environment*, **569**, 97 (2016)
2. Y. N. Hu, H. F. Cheng, S. Tao, *Environment international*, **92**, 515 (2016)
3. C. L. Wang, W. H. Xu, H. Li, K. Zhou, J. Liu, M. Z. Zhang, *Wuhan University Journal of Natural Sciences*, **18**, 541 (2013)
4. W. Y. Hu, B.Huang, K.Tian, P. E. Holm, Y. X. Zhang, *Chemosphere*, **167**, 82 (2017)
5. X. B. Zeng, L. F. Li, X. R. Mei, *Scientia Agricultura Sinica*, **40**, 2507 (2007)
6. Y. Z, Liu, T. F. Xiao, P. C. Baveye., J. M. Zhu, Z. P. Ning, H. J. Li, *Ecotoxicology and environmental safety*, **112**, 122 (2015)
7. M. Xue, Y. H. Zhou, Z. Y. Yang, B. Y. Lin, J. G. Yuan, S. S. Wu, *Frontiers of Environmental Science & Engineering*, 226 (2014)
8. W. H. Xu, H. Liu, Q. F. Ma, *Pedosphere*, **17**, 389 (2007)
9. Y. Zhi, K. X. He, T. Sun, Y. Q. Zhu, Q. X. Zhou, *Journal of Environmental Sciences*, **35**, 108 (2015)
10. E. L. Connolly, J. P. Fett, M. L. Guerinot, *Plant Cell*, **14**, 1347 (2002)
11. X. Y. He, Y Q. Gong, L. Xu, D. Q. Nai, T. C. Wen, L. Q. Liu, *Molecular characterization of iron-regulated transporter gene RsIRT1 in radish*, *Journal of Nanjing Agricultural University*, **36**, 13 (2013)
12. J. Ramos, L. Naya, M. Gay, J. Abián, M. Becana, *Plant Physiology*, **148**, 536 (2008)
13. E. Harada, Y. Choi, A. Tsuchisaka, O. Hitoshi, S. Hiroshi, *J. Plant Physiol*., **158**, 655 (2001)
14. J. R. Dominguez-SOLIS, G. Gutierrez-ALCALA, J. M. Vega, G. Cecilia, *J Biol Chem*, **276**, 9297 (2001)
15. L. Han, W. Wei, Z. Q. Guan, J. Xu, T. Y. Chaio, *Journal of the Graduate School of the Chinese Academy of Sciences*, **24**, 465(2007)
16. S. Clemens, E. J. Kim, D. Neumann, J. I. Schroeder, *EMBO J*, **18**, 3325 (1999)
17. Y. Zhang, C. P. Yang, Y. C. Wang, *Plant Physiology Communications*, **43**, 693 (2007)
18. Z. G. An, C. J. Li, Y. G. Zu, Y. J. Du, A. wachter, R. Gromes, T. Rausch, *Journal of Experimental Botany*, , **57**, 3575 (2006)
19. R. F. Mills, G. C. Krijger, P. J. Baccarini, J. L. Hall, L. E. Williams, *Plant Journal*, **35**, 164 (2001)
20. D. Hussain, M. J. Haydon, Y. W. Wang, E. Wong, S. M. Sherson, J. Young, J. Camakaris, J. F. Harper, .C. S. Cobbett, *Plant Cell*, **16**, 1327 (2004)
21. A. Gravot, L. A. Ieutaud, F.Verret, P. Auroy, A. Vavasseur, P. Richaud, *FEBS Letters*, **561**, 22 (2004)
22. C. Bernard, N. Roosens, P. Czernic, M, Lebrun, N, Verbruggen, *FEBS Letters*, **569**, 140 (2004)
23. S. Thomine, R. Wang, J. M. Ward, N. M. Crawford, J. I. Schroeder, *Proc Natl Acad Sci, USA*, **97**, 4991(2000)
24. D. Eide, B. M. Roderius, J. Fett, M. L. Guerinot, *Proc Natl Acad Sci, USA*, **93**, 5624 (1996)
25. S. Clemens, *Biochimie*, **88**, 1707 (2006)
26. V. Antoniadis, S. M. Shaheen, J. Boersch, G. D. Laing, J. Rinklebe, *Journal of Environmental Management*, **186**, 192 (2017)
27. S. H. Liu, X. S. Shi, Y. Z. Pan, j. J. Ding, Y. He, l. Wang, *Acta Prataculturae Sinica*, **22**, 154 (2013)
28. C. Shi, C. L. Wang, C. F. Huang, S. Z. An, *Acta Agrestia Sinica*, **23**, 526 (2015)
29. Y. Chen, T. Q. Li, X. Han, Y. J. Du, W. Andreas, R. Thomas, *Journal of Zhejiang University Science B*, **13**, 494 (2012)
30. P. Li, X. J. Peng, Z. K. Luan, T. K. Zhao, C. J. Zhang, B. C. Liu, *Journal of Soils and Sediments*, **16**, 2097 (2016)
31. Z. G. Fang, Z. Y. Hu, H. H. Zhao, L. Yang, C. L. Ding, L. Q. Lou, Q. S. Cai, *Grassland Science*, **63**, 36 (2017)
32. N. Ghazanfarirad, K. Dehghan, M. Fakhernia, F. Rahmanpour, M. Bolouki, F. Zeynali, J. Asadzadeh, M. Bahmani, *JNAS*, **3**, 452 (2014)
33. Y. Y. Sun, P. Guan, S. He, J. M. Shi, *Acta Agrestia Sinica*, **8**, 1589 (2016)
34. A. Nesler, G. Dalcorso, E. Fasani, A. Manara, G. P. D. Sansebastiano, E. Argese, A. Furini, *New Biotechnology*, **35**, 54 (2017)
35. S. Kopriva, *Annals of botany*, **97**, 479 (2006)
36. S. M. Wang, Y. K. Chen,S. L. Wang,J. G. Lei, S. F. Cai, Analysis of Effects and Enrichment of Cd Stress on Thiol Peptide Protein Content of 15 Wild Vegetables, *Fujian Fruits*, **26**, 1 (2016)
37. I. Matityahu, L. Kachan, I. I. Bar, R. Amir, *Amino Acids*, **30**, 185 (2006)
38. R. Takahashi, Y. Ishimaru, T. Senoura, H. Shimo, S. Ishikawa, T. Arao, H. Nakanishi, N. K. Nishizawa, *Journal of Experimental Botany*, **62**, 4843 (2011)
39. T. S. Chou, Y. Y. Chao, W. D. Huang, C.Y. Hong, H. K. Ching, *Journal of Plant Physiology*, **168**, 1021 (2011)
40. S. Lee, G. An, *Plant Cell Environ*, **32**, 408 (2009)
41. S. Uraguchi, T. Fujiwara, *Current Opinion in Plant Biology*, **16**, 328 (2013)

РАЗЛИКИ В УСВОЯВАНЕТО НА Cd И ЕКСПРЕСИЯТА НА Cd-ТОЛЕРАНТНИ ГЕНИ В ДВЕ РАЗНОВИДНОСТИ НА РАЙГРАС

Т. Ли[1], У.Х. Су[1]*, И.Р. Чай[2]*, З.И. Уанг[1], Д. Сие[1]

[1] *Колеж по ресурси и екологични науки, Югозападен университет, Чунцин 400715, Н. Р. Китай*
[2] *Колеж по агрономия и биотехнология, Югозападен университет, Чунцин 400715, Н. Р. Китай*

Постъпила на 24 март 2016 г.; Коригирана на 23 май, 2017 г.

(Резюме)

Изследван е ефекта на различни нива на кадмий в почвата (0, 75, 150, 300 и 600 mg·kg^{-1}) и биомасата, съдържанието на Cd, натрупването му и експресията на Cd-толерантни гени в две култури на райграс (Bond и Aberd) при експерименти с почвени култури. Резултатите показват, че сухото тегло на издънки и растения от Bond и Aberd се повишават с 10.06% и 4.04% и съответно 25.84% и 16.89%, спрямо контролните експерименти с данни от съответно 75 mg·kg^{-1} и 150 mg·kg^{-1} Cd. Концентрациите и натрупването на Cd в издънките и корените значително нарастват с нарастването на нивата на кадмий в почвата (P <0.05). При въздействие от 150 mg·kg^{-1} Cd концентрацията на последния в издънките и корените на културите Bond и Aberd са съответно 171.83 171.83 mg·kg^{-1}, 374.49 mg·kg^{-1} и 169.12 mg·kg^{-1}, 229.68 mg·kg^{-1}. Натрупването наCd в Aberd е по-високо отколкото в Bond при еднакви нива на кадмий. Тенденцията за експресия OAS- и IRT-гените последователна с би-модална крива с повишаването на нивата на кадмия. Стрес от кадмий от 75-150 mg·kg^{-1} промотира експресията на OAS- и IRT-гените в райграса. Културата Aberd е по-подходяща за ремедиация на почвата спрямо кадмия, поради по-голямото количество на биомаса и натрупването на кадмия.

Bulgarian Chemical Communications, Volume 49, Number 3, (pp. 706 – 710) 2017

New models of industrial column chemical reactors

B. Boyadjiev, Chr. Boyadjiev*

Institute of Chemical Engineering, Bulgarian Academy of Sciences, Acad. G. Bonchev str., Bl. 103, 1113 Sofia, Bulgaria

Received July 13, 2017; Accepted July 21, 2017

A new approach to modeling the industrial column chemical reactors is presented. A theoretical analysis of the effect of the radial non-uniformity of the axial velocity component in the industrial column chemical reactors is presented. A numerical analysis shows, that average concentration model, where the radial velocity component is equal to zero (in the cases of a constant velocity radial non-uniformity along the column height), is possible to be used in the cases of an axial modification of the radial non-uniformity of the axial velocity component. The use of experimental data, for the average concentration at the column end, for a concrete process and column, permits to be obtained the model parameters, related with the radial non-uniformity of the velocity. These parameter values permit to be used the average concentration model for modeling of different processes.

Keywords: Column apparatus, chemical reaction, convection-diffusion model, average concentration model, velocity radial non-uniformity.

INTRODUCTION

The fundamental problem in the column apparatuses modeling is result of the complicated hydrodynamic behavior of the flows in the columns and as a result the velocity distributions in the columns are unknown.

The industrial column chemical reactors is possible to be modeled, using a new approach [1-4] on the base of the physical approximations of the mechanics of continua, where the mathematical point is equivalent to a small (elementary) physical volume, which is sufficiently small with respect to the apparatus volume, but at the same time sufficiently large with respect to the intermolecular volumes in the medium. As a result, a convection-diffusion type model (for qualitative analysis) and an average concentration type model (for quantitative analysis) are possible to be used in the cases of isothermal chemical reactions [1-4].

CONVECTION-DIFFUSION MODEL

The physical elementary volumes will be presented as mathematical points in a cylindrical coordinate system (r,z), where r and z [m] are radial and axial coordinates. The concentrations [kg-mol.m^{-3}] of the reagents are $c_i(r,z)$, $i=1,2,...,i_0$, i.e. the quantities of the reagents (kg-mol) in 1 m^3 of the column volume.

In the cases of a stationary fluids motion in cylindrical column apparatus, when the radial non-uniformity of the axial velocity component $u(r)$ [m.s^{-1}] is permanent along the column height, the radial velocity component is equal to zero.

The homogeneous chemical reaction, as a volume source or sink in the column volume is $Q_i(c_i)$ [kg-mol.m^{-3}.s^{-1}], $i=1,2,...,i_0$ (i_0 - reagent number). They lead to different values of the reagent (substance) concentrations in the elementary volumes $c_i(r,z)$, $i=1,2,...,i_0$ and as a result, two mass transfer effects exist – convective transfer (caused by the fluid motion) and diffusion transfer (caused by the concentration gradient).

The mathematical model of the processes in the column apparatuses, in the physical approximations of the mechanics of continua, is mass balances in the elementary volumes between the convective transfer, the diffusive transfer and the volume mass sources (sinks) (as a result of the chemical reaction). In the stationary case, the convection-diffusion equations (as a mathematical structures of the mass transfer process models in the industrial column chemical reactors) [1-4] are:

$$\begin{aligned} & u\frac{\partial c_i}{\partial z}=D_i\left(\frac{\partial^2 c_i}{\partial z^2}+\frac{1}{r}\frac{\partial c_i}{\partial r}+\frac{\partial^2 c_i}{\partial r^2}\right)+Q_i(c_i); \\ & r=0, \quad \frac{\partial c_i}{\partial r}\equiv 0; \quad r=r_0, \quad \frac{\partial c_i}{\partial r}\equiv 0; \\ & z=0, \quad c_i\equiv c_i^0, \quad u^0c_i^0\equiv u\,c_i^0-D_i\left(\frac{\partial c_i}{\partial z}\right)_{z=0}; \\ & i=1,2,\ldots,i_0, \end{aligned} \tag{1}$$

* To whom all correspondence should be sent:
E-mail: chr.boyadjiev@gmail.com

where u^0, c_i^0 are the inlet velocity and concentrations, D_i [m^2.s^{-1}] - diffusivities, r_0 [m] - column radius.

In the cases of a two components complex chemical reactions $i=1,2$, $Q_i=-kc_1^m c_2^n$, where m, n are the reaction orders. For big difference between inlet concentrations of the reagents $\left(c_1^0 \gg c_2^0\right)$ and $m=1$, from (1) follows the pseudo-first-order reactions case $\left(i_0=1,\ c_1=c,\ c_2\equiv c_2^0\right)$:

$$
\begin{aligned}
&u\frac{\partial c}{\partial z}=D\left(\frac{\partial^2 c}{\partial z^2}+\frac{1}{r}\frac{\partial c}{\partial r}+\frac{\partial^2 c}{\partial r^2}\right)-k\,c;\\
&r=0,\quad \frac{\partial c}{\partial r}\equiv 0;\quad r=r_0,\quad \frac{\partial c}{\partial r}\equiv 0;\\
&z=0,\quad c\equiv c^0,\quad u^0c^0\equiv u\,c^0-D\left(\frac{\partial c}{\partial z}\right)_{z=0}.
\end{aligned}
\tag{2}
$$

AVERAGE CONCENTRATION MODEL

The average values of the velocity and concentration, at the column cross-sectional area is possible to be presented [1-4] as:

$$
\bar{u}=u^0=\frac{2}{r_0^{\,2}}\int_0^{r_0} r u(r)\,dr,\quad \bar{c}(z)=\frac{2}{r_0^{\,2}}\int_0^{r_0} r c(r,z)\,dr. \tag{3}
$$

The functions $u(r)$, $c(r,z)$ in (2) can be presented by the help of the average functions (3):

$$
u(r)=\bar{u}\,\tilde{u}(r),\quad c(r,z)=\bar{c}(z)\,\tilde{c}(r,z), \tag{4}
$$

where $\tilde{u}(r),\tilde{c}(r,z)$ present the radial non-uniformity of the velocity and concentration and satisfy the next conditions:

$$
\frac{2}{r_0^{\,2}}\int_0^{r_0} r\,\tilde{u}(r)\,dr=1,\quad \frac{2}{r_0^{\,2}}\int_0^{r_0} r\,\tilde{c}(r,z)\,dr=1. \tag{5}
$$

The average concentration model may be obtained if put (4) into (2), multiply by r and integrate over r in the interval $[0,r_0]$. As a result, the following is obtained:

$$
\begin{aligned}
&\alpha\bar{u}\frac{d\bar{c}}{dz}+\frac{d\alpha}{dz}\bar{u}\,\bar{c}=D\frac{d^2\bar{c}}{dz^2}-k\bar{c};\\
&z=0,\quad \bar{c}(0)=c^0,\quad \frac{d\bar{c}}{dz}=0,
\end{aligned}
\tag{6}
$$

where

$$
\alpha(z)=\frac{2}{r_0^{\,2}}\int_0^{r_0} r\tilde{u}\tilde{c}\,dr. \tag{7}
$$

GENERALIZED VARIABLES

In (2) and (6) is possible to be introduced the generalized variables [2]:

$$
\begin{aligned}
&r=r_0R,\quad z=lZ,\quad u(r)=\bar{u}U(R),\\
&\tilde{u}(r)=\frac{u(r)}{\bar{u}}=U(R),\quad c(r,z)=c^0C(R,Z),\\
&\bar{c}(z)=c^0\bar{C}(Z),\quad \bar{C}(Z)=2\int_0^1 RC(R,Z)\,dR,\\
&\tilde{c}(r,z)=\frac{c(r,z)}{\bar{c}(z)}=\frac{C(R,Z)}{\bar{C}(Z)},\\
&\alpha(z)=\alpha(lZ)=A(Z)=2\int_0^1 RU(R)\frac{C(R,Z)}{\bar{C}(Z)}\,dR
\end{aligned}
\tag{8}
$$

and as a result is obtained:

$$
\begin{aligned}
&U\frac{\partial C}{\partial Z}=\mathrm{Fo}\left(\varepsilon\frac{\partial^2 C}{\partial Z^2}+\frac{1}{R}\frac{\partial C}{\partial R}+\frac{\partial^2 C}{\partial R^2}\right)-\mathrm{Da}\,C;\\
&\varepsilon=\mathrm{Fo}^{-1}\,\mathrm{Pe}^{-1};\\
&R=0,\quad \frac{\partial C}{\partial R}\equiv 0;\quad R=1,\quad \frac{\partial C}{\partial R}\equiv 0;\\
&Z=0,\quad \mathrm{C}\equiv 1,\quad 1\equiv U-\mathrm{Pe}^{-1}\frac{\partial C}{\partial Z}.
\end{aligned}
\tag{9}
$$

$$
\begin{aligned}
&A(Z)\frac{d\bar{C}}{dZ}+\frac{dA}{dZ}\bar{C}=\mathrm{Pe}^{-1}\frac{d^2\bar{C}}{dZ^2}-\mathrm{Da}\,\bar{C};\\
&Z=0,\quad \bar{C}=1,\quad \frac{d\bar{C}}{dZ}=0,
\end{aligned}
\tag{10}
$$

where Fo, Da and Pe are the Fourier, Damkohler and Peclet numbers, respectively:

$$
\mathrm{Fo}=\frac{Dl}{\bar{u}r_0^2},\quad \mathrm{Pe}=\frac{\bar{u}l}{D},\quad \mathrm{Da}=\frac{kl}{\bar{u}}. \tag{11}
$$

The convection-diffusion model (9) permits to be made [1-4] a qualitative analysis of the process (model) for to be obtained the main, small and slight physical effects (mathematical operators), and to be rejected the slight effect (operators). As a result the process mechanism identification is possible to be made. On this base are possible different approximations for high column $\left(0=\varepsilon\le 10^{-2}\right)$, big average velocity $\left(0=\mathrm{Fo}\le 10^{-2}\right)$, small $\left(0=\mathrm{Da}\le 10^{-2}\right)$ or big $\left(0=\mathrm{Da}^{-1}\le 10^{-2}\right)$ chemical reaction rate.

In an industrial column ($l>1$ [m]), the average velocity is $\bar{u}>1$ [m.s^{-1}] and the diffusivity is $D_1<10^{-4}$ [m^2.s^{-1}]. In these conditions is possible to

be obtained the order of magnitude of the parameters values:

$$\mathrm{Pe}^{-1} < 10^{-4}, \quad \frac{h_0}{l} > 10^{-1}, \quad \mathrm{Fo} < 10^{-2}, \qquad (12)$$

and the models (9), (10) have convective forms:

$$U\frac{\partial C}{\partial Z} = -\mathrm{Da}\, C; \quad Z = 0, \quad \mathrm{C} \equiv 1. \qquad (13)$$

$$A(Z)\frac{d\bar{C}}{dZ} + \frac{dA}{dZ}\bar{C} = -\mathrm{Da}\,\bar{C}; \quad Z = 0, \quad \bar{C} = 1. \qquad (14)$$

The average concentration models allow a quantitative analysis of the processes in column apparatuses. The theoretical analysis of the models (13), (14) shows [1-4], that the function $A(Z)$ is possible to be presented as a linear approximation:

$$A = a_0 + a_1 Z, \qquad (15)$$

where the model parameters a_0, a_1 is possible to be obtained, using experimental data for a short column ($Z = 0.1$).

The presented theoretical analysis shows that the basic approximation of the convection-diffusion model (13) and average concentration model (14) is $\frac{\partial \tilde{u}}{\partial z} \equiv 0$.

MODELING OF THE INDUSTRIAL COLUMN CHEMICAL REACTORS

Very often in industrial conditions, an axial modification of the radial non-uniformity of the velocity, is realized. The radial non-uniformity of the axial velocity component in the column apparatuses is caused by the fluid hydrodynamics at the column inlet, where it has as maximum and decreases along the column height as a result of the fluid viscosity. The theoretical determination of the change in the radial non-uniformity of the axial velocity component in a column is difficult in one-phase processes and practical impossible in two-phase and three-phase processes. For a theoretical analysis of the effect of the axial modification of the radial non-uniformity of the velocity, this difficulty can be circumvented by appropriate hydrodynamic model, where the average velocity at the cross section of the column is a constant, while the maximal velocity (and as a result the radial non-uniformity of the axial velocity component too) decreases along the column height.

Let's considers the velocity distribution

$$u_n(r, z_n) = \bar{u}\ \tilde{u}_n(r, z_n) \qquad (16)$$

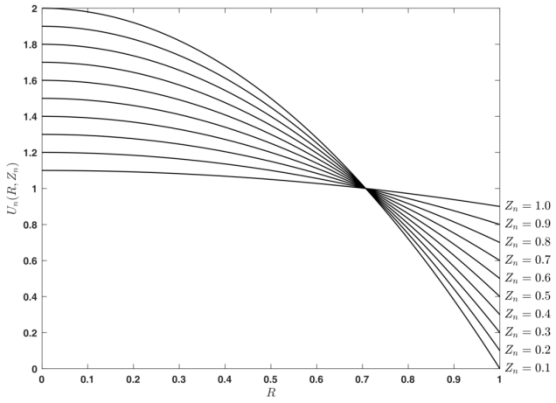

Fig.1. Velocity distributions $U_n(R, Z_n)$, $Z_n = 0.1(n+1),\ n = 0,1,...,9.$

and an axial step change of the radial non-uniformity of the axial velocity component in a column (Fig. 1):

$$\begin{aligned} &\tilde{u}_n(r, z_n) = \tilde{u}_n(r_0 R, lZ_n) = \\ &= U_n(R, Z_n) = a_n - b_n R^2, \\ &a_n = 2 - 0.1n, \quad b_n = 2(1 - 0.1n), \\ &0.1n \le Z_n \le 0.1(n+1) \quad n = 0,1,...,9, \end{aligned} \qquad (17)$$

where $\tilde{u}_n(r, z_n)$ satisfy the equation:

$$\frac{2}{r_0^2}\int_0^{r_0} r\ \tilde{u}_n(r, z_n)\ dr = 1, \qquad (18)$$

i.e. $\bar{u} = const$.

If put (16), (17) in (13), the convection-diffusion model has the form:

$$\begin{aligned} &U_n \frac{\partial C_n}{\partial Z_n} = -\mathrm{Da}\, C_n; \quad 0.1n \le Z_n \le 0.1(n+1); \\ &Z_n = 0.1n, \quad \mathrm{C}_n(R, Z_n) = C_{n-1}(R, Z_n); \\ &n = 0,1,...,9; \\ &Z_0 = 0, \quad \mathrm{C}_0(R, Z_0) \equiv 1. \end{aligned} \qquad (19)$$

MODEL EQUATIONS SOLUTION

The solution of (19) $C(R, Z) = C_n(R, Z_n),\ Z_n = 0.1(n+1),\ n = 0,1,...,9$ in the case $\mathrm{Da} = 1$ is presented on the Fig. 2. This solution $C(R, Z)$ permits to be obtained in (8) the average ("theoretical") concentration distribution $\bar{C}(Z) = \bar{C}_n(Z_n),\ Z_n = 0.1(n+1), \quad n = 0,1,...,9$ in the column (the points on the Fig. 3) and function $A(Z)$ (the points on the Fig. 4) on every step:

$$\bar{C}(Z)=\bar{C}_n(Z_n)=2\int_0^1 RC_n(R,Z_n)\,dR,$$

$$A(Z)=A_n(Z_n)=2\int_0^1 RU_n(R)\frac{C_n(R,Z_n)}{\bar{C}_n(Z_n)}\,dR, \qquad (20)$$

$$Z_n=0.1(n+1),\quad n=0,1,...,9,$$

which are presented on the Figs. 3, 4. From Fig. 4 is seen, that the function $A(Z)$ is possible to be presented as a quadratic approximation:

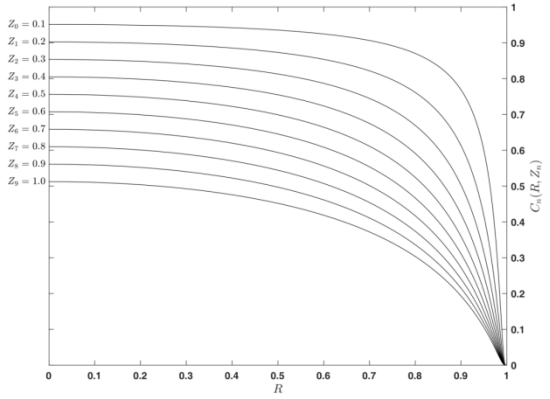

Fig. 2. Concentration distributions $C_n(R,Z_n)$, $Z_n=0.1(n+1)$, $n=0,1,...,9$.

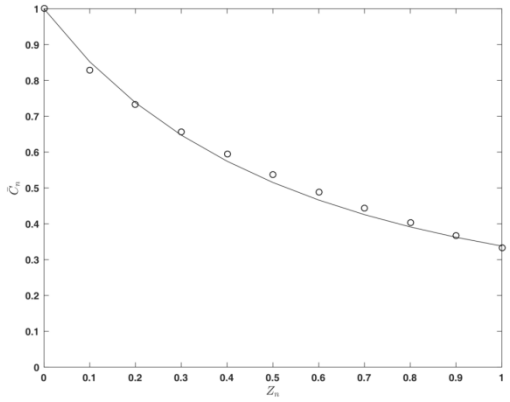

Fig. 3. Average concentration distribution: "theoretical" values (as solution of (19) and (20) $\bar{C}_n(Z_n)$, $Z_n=0.1(n+1)$, $n=0,1,...,9$ (points); $\bar{C}(Z)$ as a solution of (22)(22) for "experimental" values of a_0, a_1, a_2 (line).

$$A(Z)=a_0+a_1Z+a_2Z^2, \qquad (21)$$

where the ("theoretical") values of a_0, a_1, a_2 are presented in the Table 1. As a result, in the case of axial modification of the radial non-uniformity of the velocity, the model (14) has the form:

$$\left(a_0+a_1Z+a_2Z^2\right)\frac{d\bar{C}}{dZ}+\left(a_1+2a_2Z\right)\bar{C}= \qquad (22)$$
$$=-\mathrm{Da}\,\bar{C};\quad Z=0,\quad \bar{C}=1,$$

where the parameters a_0, a_1, a_2 must be obtained, using experimental data.

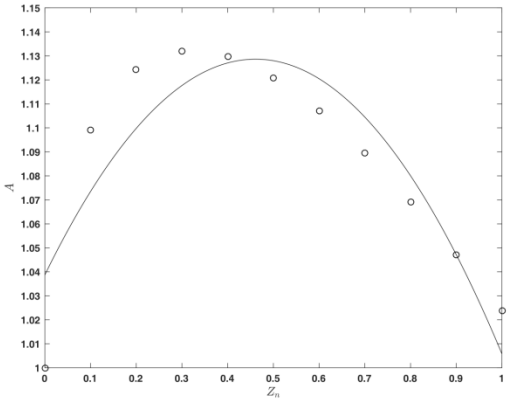

Fig. 4. Function $A(Z)$: $A(Z_n)$, $Z_n=0.1(n+1)$, $n=0,1,...,9$;as a quadratic approximation (21) (line).

PARAMETERS IDENTIFICATION

The obtained value of the function $\bar{C}_9(1)$ (Fig. 3) permit to be obtained the artificial experimental data $\bar{C}^m_{\exp}(1)$ for the column end ($Z_9=1$):

$$\bar{C}^m_{\exp}(1)=(0.95+0.1B_m)\bar{C}_9(1), \qquad (23)$$
$$m=1,...,10,$$

where $0\le B_m\le 1$, $m=0,1,...,10$ are obtained by a generator of random numbers.

The obtained artificial experimental data (23) are used for the illustration of the parameters (a_0, a_1, a_2) identification in the average concentrations model (22) by the minimization of the least-squares function:

$$Q(a_0,a_1,a_2)= \qquad (24)$$
$$=\sum_{m=1}^{10}\left[\bar{C}(1,a_0,a_1,a_2)-\bar{C}^m_{\exp}(1)\right]^2,$$

where the value of $\bar{C}(1,a_0,a_1,a_2)$ is obtained after the solution of (22) for $Z=1$. The obtained "experimental" parameter values are presented on the Table 1.

The obtained ("experimental") parameter values are used for the solution of (22) and the result (the line) is compared with the average ("theoretical") concentration values $\bar{C}(Z)=\bar{C}_n(Z_n)$, $Z_n=0.1(n+1)$, $n=0,1,...,9$. (points) (as solution of (19) and (20)) on the Fig. 3.

INFLUENCE OF THE MODEL PARAMETER

The model (22), with "experimental" parameters values of a_0, a_1, a_2 in the Table 1, is used for the calculation the average concentrations in the case $\mathrm{Da} = 2$ and the result (line) is compared (Fig. 5) with the average ("theoretical") concentration

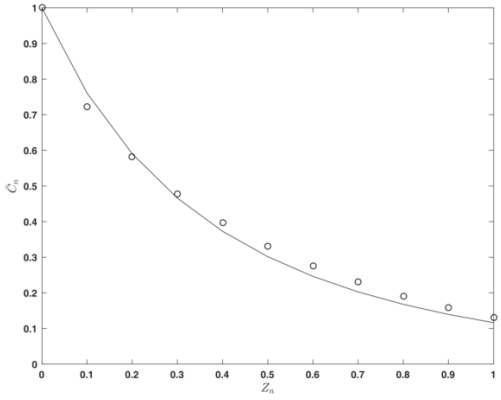

Fig. 5. Effect of the chemical reaction rate $(\mathrm{Da} = 2)$: average ("theoretical") concentration values $\bar{C}_n(Z_n), Z_n = 0.1(n+1), n = 0,1,...,9.$ (as solutions of (19) and (20) (points)); solution of (22) (line) values $\bar{C}_n(Z_n), Z_n = 0.1(n+1), n = 0,1,...,9.$ (as solutions of (19) and (20) (points)) for this case.

Table 1. Parameters a_0, a_1, a_2.

Parameters	"Theoretical" values	"Experimental" values
a_0	1.0387	0.8582
a_1	0.3901	0.4505
a_2	−0.4230	−0.4343

CONCLUSIONS

The presented numerical analysis of the industrial column chemical reactors shows, that average concentration model, where the radial velocity component is equal to zero (in the cases of a constant velocity radial non-uniformity along the column height), is possible to be used in the cases of an axial modification of the radial non-uniformity of the axial velocity component. The use of experimental data, for the average concentration at the column end, for a concrete process, permits to be obtained the model parameters (a_0, a_1, a_2), related with the radial non-uniformity of the velocity. These parameter values permit to be used the average concentration model for modeling of different processes (different values of the parameter Da, i.e. different values of the column height, average velocity, reagent diffusivity and chemical reaction rate constant).

REFERENCES

1. Chr. Boyadjiev, M. Doichinova B. Boyadjiev, P. Popova-Krumova, Modeling of Column Apparatus Processes, Springer-Verlag, Berlin Heidelberg, 2016.
2. Chr. Boyadjiev, Theoretical Chemical Engineering. Modeling and simulation, Springer-Verlag, Berlin Heidelberg, 2010.
3. M. Doichinova, Chr. Boyadjiev, *Int. J. Heat Mass Transfer*, **55**, 6705 (2012).
4. Chr. Boyadjiev, *J. of Pure Appl. Math.: Advances and Applications*, **10**(2), 131 (2013).

НОВИ МОДЕЛИ НА ИНДУСТРИАЛНИ КОЛОННИ ХИМИЧНИ РЕАКТОРИ

Б. Бояджиев, Хр. Бояджиев

Институт по инженерна химия, Българска академия на науките, ул. „Акад. Г. Бончев", бл. 103, 1113, София България

Получена на 13 юли, 2017 г.; приета на 21 юли, 2017 г.

(Резюме)

Представен е нов подход за моделиране на промишлени колонни химични реактори. Предложен е теоретичен анализ на ефекта на радиалната неравномерност на аксиалната компонента на скоростта в промишлени колонни химични реактори. Численият анализ показва, че моделът на средните концентрации, когато радиалната компонента на скоростта е равна на нула (в случаите на постоянна радиална неравномерност на скоростта по височината на колоната), е възможно да бъде използвана в случаите на аксиално изменение на радиалната неравномерност на аксиалната компонента на скоростта. Използването на експериментални данни за средната концентрация на изхода на колоната, за конкретен процес и колона, позволява да бъдат намерени моделните параметри, свързани с радиалната неравномерност на скоростта. Тези стойности на параметрите позволяват използването на модела на средните цонцентрации за моделиране на различни процеси.

Bulgarian Chemical Communications, Volume 49, Number 3, (pp. 711 – 719) 2017

New models of industrial column absorbers. 1. Co-current absorption processes

B. Boyadjiev, Chr. Boyadjiev*

Institute of Chemical Engineering, Bulgarian Academy of Sciences, Acad. St. Angelov str., Bl. 103, 1113 Sofia, Bulgaria

Received July 20, 2016; Revised February 2, 2017

A new approach to modeling the industrial column absorbers is presented. A theoretical analysis of the effect of the velocity radial non-uniformity on the co-current absorption processes in the column apparatuses is presented. The average concentration model, where the radial velocity component is equal to zero (in the cases of a constant velocity radial non-uniformity along the column height), is used in the cases of an axial modification of the radial non-uniformity of the axial velocity components in the gas and liquid phases. The use of experimental data, for the average concentrations in the gas and liquid phases at the column end, for a concrete process (absorption of an average soluble gas), permits to be obtained the gas and liquid phase model parameters, related with the radial non-uniformity of the velocities. These parameter values permit to be used the average concentration models for different absorption processes modeling in co-current columns.

Keywords: Column apparatus, gas absorption, co-current flows, convection-diffusion model, average concentration model, velocity radial non-uniformity.

INTRODUCTION

In the first paper [1] was shown, that average concentration model, where the radial velocity component is equal to zero (in the cases of a constant velocity radial non-uniformity along the column height), is possible to be used in the cases of an axial modification of the radial non-uniformity of the axial velocity component. The use of experimental data, for the average concentration at the column end, for a concrete process and column, permits to be obtained the model parameters, related with the radial non-uniformity of the velocity. These parameter values permit to be used the average concentration model for modeling of different processes in the cases of different values of the column height, average velocity, reagent diffusivity and chemical reaction rate constant. This possibility will be used for modeling of the gas absorption processes in a co-current column.

CO-CURRENT ABSORPTION PROCESSES

The new approach of the processes modeling in the column apparatuses [2-5] permits to be created the convection-diffusion and average concentration models of the gas absorption process. In the cases of a constant radial non-uniformity of the velocities along the column height $\left(u_j = u_j(r),\ j=1,2\right)$, the convection-diffusion and average concentration models of a chemical absorption (with a pseudo-first-order chemical reaction in the liquid phase) in a co-current column [6] have the forms:

$$
\begin{aligned}
&u_1\frac{\partial c_1}{\partial z} = D_1\left(\frac{\partial^2 c_1}{\partial z^2}+\frac{1}{r}\frac{\partial c_1}{\partial r}+\frac{\partial^2 c_1}{\partial r^2}\right)-\\
&-k\left(c_1-\chi c_2\right);\\
&u_2\frac{\partial c_2}{\partial z} = D_2\left(\frac{\partial^2 c_2}{\partial z^2}+\frac{1}{r}\frac{\partial c_2}{\partial r}+\frac{\partial^2 c_2}{\partial r^2}\right)+\\
&+k\left(c_1-\chi c_2\right)-k_0 c_2;\\
&r=0,\quad \frac{\partial c_j}{\partial r}\equiv 0;\quad r=r_0,\quad \frac{\partial c_j}{\partial r}\equiv 0;\quad j=1,2;\\
&z=0,\quad c_1\equiv c_1^0,\quad c_2\equiv 0,\\
&u_1^0 c_1^0 \equiv u_1 c_1^0 - D_1\left(\frac{\partial c_1}{\partial z}\right)_{z=0},\quad \left(\frac{\partial c_2}{\partial z}\right)_{z=0}=0.
\end{aligned}
\tag{1}
$$

$$
\begin{aligned}
&\alpha_1(z)\bar{u}_1\frac{d\bar{c}_1}{dz}+\frac{d\alpha_1}{dz}\bar{u}_1\bar{c}_1 = D_1\frac{d^2\bar{c}_1}{dz^2}-\\
&-k\left(\bar{c}_1-\chi\bar{c}_2\right);\\
&\alpha_2(z)\bar{u}_2\frac{d\bar{c}_2}{dz}+\frac{d\alpha_2}{dz}\bar{u}_2\bar{c}_2 = D_2\frac{d^2\bar{c}_2}{dz^2}+\\
&+k\left(\bar{c}_1-\chi\bar{c}_2\right)-k_0\bar{c}_2;\\
&z=0,\quad \bar{c}_1(0)\equiv c_1^0,\quad \bar{c}_2(0)\equiv 0,\\
&\frac{d\bar{c}_1}{dz}\equiv 0,\quad \frac{d\bar{c}_2}{dz}\equiv 0;\\
&\alpha_j(z)=\frac{2}{r_0^2}\int_0^{r_0} r\tilde{u}_j\tilde{c}_j\,dr,\quad \tilde{u}_j(r)=\frac{u_j(r)}{\bar{u}_j},\\
&\tilde{c}_j(r,z)=\frac{c_j(r,z)}{\bar{c}_j(z)},\quad j=1,2.
\end{aligned}
\tag{2}
$$

* To whom all correspondence should be sent:
E-mail: chr.boyadjiev@gmail.com

In (1, 2) $u_j(r), c_j(r,z), D_j,\ j=1,2$ are the velocities, concentrations and diffusivities in the gas and liquid phases, $\bar{u}_j, \bar{c}_j(z),\ j=1,2$ - the average velocities and concentrations at the column cross-sectional area, $\tilde{u}_j(r), \tilde{c}_j(r,z),\ j=1,2$ - the radial non-uniformities of the velocities and concentrations.

GENERALIZED VARIABLES

In (1), (2) is possible to be introduced the generalized variables:

$$r = r_0 R, \quad z = lZ, \quad u_j(r) = \bar{u}_j U_j(R),$$
$$c_1(r,z) = c_1^0 C_1(R,Z),$$
$$c_2(r,z) = \frac{c_1^0}{\chi} C_2(R,Z), \quad \bar{c}_1(z) = c_1^0 \bar{C}_1(Z), \qquad (3)$$
$$\bar{c}_2(z) = \frac{c_1^0}{\chi} \bar{C}_2(Z),$$

and as a result is obtained:

$$U_1 \frac{\partial C_1}{\partial Z} = \mathrm{Fo}_1 \left(\varepsilon \frac{\partial^2 C_1}{\partial Z^2} + \frac{1}{R} \frac{\partial C_1}{\partial R} + \frac{\partial^2 C_1}{\partial R^2} \right) -$$
$$-K_1 (C_1 - C_2);$$
$$U_2 \frac{\partial C_2}{\partial Z} = \mathrm{Fo}_2 \left(\varepsilon \frac{\partial^2 C_2}{\partial Z^2} + \frac{1}{R} \frac{\partial C_2}{\partial R} + \frac{\partial^2 C_2}{\partial R^2} \right) +$$
$$+K_2 (C_1 - C_2) - \mathrm{Da}\, C_2; \qquad (4)$$
$$R = 0, \quad \frac{\partial C_j}{\partial R} \equiv 0;$$
$$R = 1, \quad \frac{\partial C_j}{\partial R} \equiv 0; \quad j = 1,2;$$
$$Z = 0, \quad C_1 \equiv 1, \quad C_2 = 0,$$
$$1 \equiv U_1 - \mathrm{Pe}_1^{-1} \frac{\partial C_1}{\partial Z}, \quad \frac{\partial C_2}{\partial Z} \equiv 0.$$

$$A_1(Z) \frac{d\bar{C}_1}{dZ} + \frac{dA_1}{dZ} \bar{C}_1 = \mathrm{Pe}_1^{-1} \frac{d^2 \bar{C}_1}{dZ^2} -$$
$$-K_1 (\bar{C}_1 - \bar{C}_2);$$
$$A_2(Z) \frac{d\bar{C}_2}{dZ} + \frac{dA_2}{dZ} \bar{C}_2 = \mathrm{Pe}_2^{-1} \frac{d^2 \bar{C}_2}{dZ^2} + \qquad (5)$$
$$+K_2 (\bar{C}_1 - \bar{C}_2) - \mathrm{Da}\, \bar{C}_2;$$
$$Z = 0, \quad \bar{C}_1 = 1, \quad \bar{C}_2 = 0,$$
$$\frac{d\bar{C}_1}{dZ} = 0, \quad \frac{d\bar{C}_2}{dZ} = 0,$$

where Fo, Da and Pe are the Fourier, Damkohler and Peclet numbers, respectively:

$$\mathrm{Fo}_j = \frac{D_j l}{\bar{u}_j r_0^2}, \quad \mathrm{Pe}_j = \frac{\bar{u}_j l}{D_j}, \quad \mathrm{Da} = \frac{k_0 l}{\bar{u}_2},$$
$$\varepsilon = \mathrm{Fo}_j^{-1} \mathrm{Pe}_j^{-1}, \qquad (6)$$
$$K_1 = \frac{kl}{\bar{u}_1}, \quad K_2 = \omega K_1, \quad \omega = \frac{\bar{u}_1 \chi}{\bar{u}_2}, \quad j = 1,2.$$

In the cases of a physical absorption $\mathrm{Da} = 0$.

In (5) are used the expressions:

$$\bar{C}_j(Z) = 2 \int_0^1 R C_j(R,\mathrm{Z})\, dR,$$
$$\tilde{c}_j(r,z) = \frac{c_j(r,z)}{\bar{c}_j(z)} = \frac{C_j(R,Z)}{\bar{C}_j(Z)}, \qquad (7)$$
$$\alpha_j(z) = \alpha_j(lZ) = A_j(Z) =$$
$$= 2 \int_0^1 R U_j(R) \frac{C_j(R,Z)}{\bar{C}_j(Z)} dR, \quad j = 1,2$$

The convection-diffusion model (4) permits to be made [2-6] a qualitative analysis of the process (model) for to be obtained the main, small and slight physical effects (mathematical operators), and to be rejected the slight effect (operators). As a result the process mechanism identification is possible to be made. On this base are possible to be obtained different approximations for high column ($0 = \varepsilon \le 10^{-2}$), big average velocities ($0 = \mathrm{Fo}_j \le 10^{-2},\ j = 1,2$), small ($0 = \mathrm{Da} \le 10^{-2}$) or big ($0 = \mathrm{Da}^{-1} \le 10^{-2}$) chemical reaction rate, highly soluble ($0 = \omega \le 10^{-2}$) or lightly soluble ($0 = \omega^{-1} \le 10^{-2}$) gas.

PHYSICAL ABSORPTION OF AVERAGE SOLUBLE GAS

Let's consider the physical absorption ($\mathrm{Da} = 0$) of an average soluble gas ($\omega \square 1$)? in an industrial absorption column ($l > 1$ [m]), in the cases of down co-current gas-liquid drops flow. The average gas velocity and the average liquid drops velocity are $\bar{u}_1 > 1, \bar{u}_2 > 1$ [m.s^{-1}], the diffusivities in the gas (air) and the liquid (water) are $D_1 < 10^{-4}, D_2 < 10^{-9}$ [m^2.s^{-1}] . In these conditions is possible to be obtained the order of magnitude of the parameters values:

$$\mathrm{Pe}_1^{-1} < 10^{-4}, \quad \frac{r_0}{l} > 10^{-1}, \quad \mathrm{Fo}_1 < 10^{-2},$$
$$\mathrm{Pe}_2^{-1} < 10^{-9}, \quad \mathrm{Fo}_2 < 10^{-7}, \qquad (8)$$

and the model (4) has a convective form:

$$U_1 \frac{dC_1}{dZ} = -K_1\left(C_1 - C_2\right);$$
$$U_2 \frac{dC_2}{dZ} = \omega K_1\left(C_1 - C_2\right); \quad (9)$$
$$Z = 0, \quad C_1 \equiv 1, \quad C_2 = 0.$$

In the conditions (8) the average concentration model (5) has the form:

$$A_1(Z)\frac{d\bar{C}_1}{dZ} + \frac{dA_1}{dZ}\bar{C}_1 = -K_1\left(\bar{C}_1 - \bar{C}_2\right);$$
$$A_2(Z)\frac{d\bar{C}_2}{dZ} + \frac{dA_2}{dZ}\bar{C}_2 = \omega K_1\left(\bar{C}_1 - \bar{C}_2\right); \quad (10)$$
$$Z = 0, \quad \bar{C}_1 = 1, \quad \bar{C}_2 = 0.$$

The theoretical analysis of the model (9) shows [2-6], that the functions $A_j(Z)$, $j = 1,2$ is possible to be presented as linear approximations:

$$A_j = \alpha_{j0} + \alpha_{j1} Z, \quad j = 1,2, \quad (11)$$

where the model parameters α_{j0}, α_{j1}, $j = 1,2$ is possible to be obtained, using experimental data for a short column ($Z = 0.1$).

The theoretical analysis [6] shows, that the basic approximations of the convection-diffusion models (1) and average concentration models (2) are $\partial\tilde{u}_j / \partial z \equiv 0$, $j = 1,2..$

EFFECT OF THE AXIAL MODIFICATION OF THE RADIAL NON-UNIFORMITY OF THE VELOCITY

The radial non-uniformity of the axial velocity components in a co-current column apparatus is the result of the fluid hydrodynamics at the column inlet, where it is a maximum and decreases along the column height as a result of the fluid viscosity. For a theoretical analysis of the effect of the axial modification of the radial non-uniformities of the velocities in a two phases co-current column, this difficulty can be circumvented by appropriate hydrodynamic model, where the average velocities in the phases at the cross section of the column are constants, while the maximal velocities (and as a result the radial non-uniformity of the axial velocities components too) decrease along the column height.

Let's considers [1, 7] the velocity distributions

$$u_{jn}(r, z_n) = \bar{u}_j \tilde{u}_{jn}(r, z_n), \quad j = 1,2 \quad (12)$$

and an axial step change of the radial non-uniformity of the axial velocity component in a column:

$$\tilde{u}_{jn}(r, z_n) = \tilde{u}_{jn}(r_0 R, lZ_n) =$$
$$= U_{jn}(R, Z_n) = a_{jn} - b_{jn} R^2,$$
$$a_{jn} = 2 - 0.1n, \quad b_{jn} = 2(1 - 0.1n), \quad (13)$$
$$0.1n \le Z_n \le 0.1(n+1),$$
$$n = 0,1,...,9, \quad j = 1,2,$$

where $\tilde{u}_{jn}(r, z_n)$, $j = 1,2$ satisfy the equations:

$$\frac{2}{r_0^2}\int_0^{r_0} r\tilde{u}_{jn}(r, z_n)\,dr = 1, \quad j = 1,2, \quad (14)$$

i.e. $\bar{u}_j = const$, $j = 1.2$.

If put (13) in (9), the convection-diffusion model has the form:

$$U_{1n}\frac{dC_{1n}}{dZ_n} = -K_1\left(C_{1n} - C_{2n}\right);$$
$$U_{2n}\frac{dC_{2n}}{dZ_n} = \omega K_1\left(C_{1n} - C_{2n}\right);$$
$$0.1n \le Z_n \le 0.1(n+1); \quad (15)$$
$$Z_n = 0.1n, \quad C_{jn}(R, Z_n) = C_{j(n-1)}(R, Z_n);$$
$$n = 0,1,...,9; \quad j = 1,2;$$
$$Z_0 = 0, \quad C_{10}(R, Z_0) \equiv 1, \quad C_{20}(R, Z_0) = 0.$$

The parameter ω in (15) is known beforehand. The solution of (15), for concrete process $(\omega = 1)$ and "theoretical" value of $K_1 = 1$, permits to be obtained the concentration distributions $C_{jn}(R, Z_n)$, $j = 1,2$ for different $Z_n = 0.1(n+1)$, $n = 0,1,...,9$ (Fig. 1).

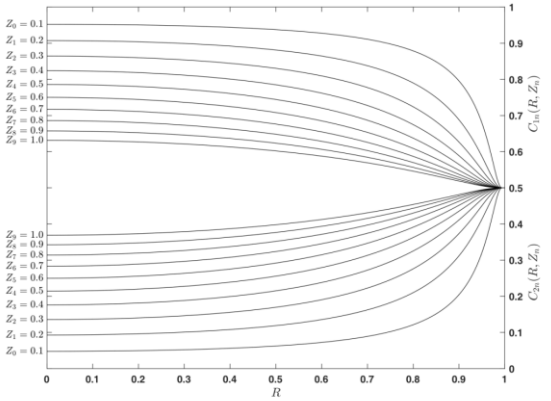

Fig. 1. Concentration distributions $C_{jn}(R, Z_n)$, $j = 1,2$ in the case $\omega = K_1 = 1$ for different $Z_n = 0.1(n+1)$, $n = 0,1,...,9$.

The solution of (15) (Fig. 1) and (7) permit to be obtained the "theoretical" average concentration distributions $\bar{C}_{jn}(Z_n)$, $j = 1,2$ (the points in the Fig. 2) and the functions $A_{jn}(Z_n)$, $j = 1,2$ (the

points in the Fig. 3) for different $Z_n = 0.1(n+1),\ n = 0,1,...,9.$

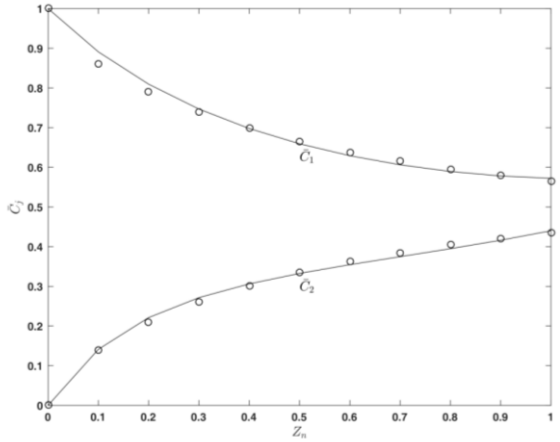

Fig. 2. Average concentration $\bar{C}_j(Z),\ j=1,2$ in the case $\omega = K_1 = 1$: "theoretical" values $\bar{C}_j(Z) = \bar{C}_{jn}(Z_n),\ j=1,2$ as solutions of (15) and (7) for different $Z_n = 0.1(n+1),\ n = 0,1,...,9$ (points); $\bar{C}_j(Z),\ j=1,2$ as a solution of (17), using the "experimental" parameter values $a_{j0}, a_{j1}, a_{j2},\ j=1,2, K_1$ (lines).

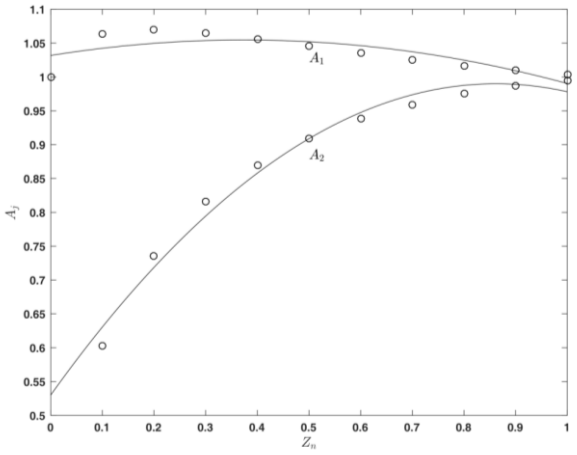

Fig. 3. Function $A_{jn}(Z_n),\ j=1,2$ in the case $\omega = K_1 = 1$: as a solution of (15) and (7) for different $Z_n = 0.1(n+1),\ n = 0,1,...,9$ (points); $A_j(Z),\ j=1,2$ as a quadratic approximation (16) (lines).

From Fig. 3 is seen, that the functions $A_{jn}(Z_n), n = 0,1,...,4,\ j=1,2$ are possible to be presented as quadratic approximations:

$$\begin{aligned} A_1(Z) &= a_{10} + a_{11}Z + a_{12}Z^2, \\ A_2(Z) &= a_{20} + a_{21}Z + a_{22}Z^2, \end{aligned} \tag{16}$$

where the ("theoretical") values of $a_{j0}, a_{j1}, a_{j2},\ j=1,2$ are presented in the Table 1.

As a result, in the case of axial modification of the radial non-uniformity of the velocity, the model (10) has the form:

$$\begin{aligned} &\left(a_{10} + a_{11}Z + a_{12}Z^2\right)\frac{d\bar{C}_1}{dZ} + \\ &+\left(a_{11} + 2a_{12}Z\right)\bar{C}_1 = -K_1\left(\bar{C}_1 - \bar{C}_2\right); \\ &\left(a_{20} + a_{21}Z + a_{22}Z^2\right)\frac{d\bar{C}_2}{dZ} + \\ &+\left(a_{21} + 2a_{22}Z\right)\bar{C}_2 = \omega K_1\left(\bar{C}_1 - \bar{C}_2\right); \\ &Z = 0, \quad \bar{C}_1 = 1, \quad \bar{C}_2 = 0. \end{aligned} \tag{17}$$

where, at an unknown velocity distribution in the two phases, ω is known beforehand for a concrete process, while the parameters $K_1, a_{j0}, a_{j1}, a_{j2},\ j=1,2$ must be obtained, using experimental data.

PARAMETERS IDENTIFICATION

The obtained the values of the functions $\bar{C}_{jn}(Z_n),\ j=1,2,$ for a concrete process $(\omega = 1)$, "theoretical" value of $K_1 = 1$ and different $Z_n = 0.1(n+1),\ n = 0,1,...,9$ (Fig. 2), permit to be obtained the values of $\bar{C}_j(1) = \bar{C}_{j9}(Z_9), Z_9 = 1,\ j=1,2$ and the artificial experimental data:

$$\begin{aligned} &\bar{C}^m_{j\exp}(1) = (0.95 + 0.1B_m)\bar{C}_j(1), \\ &j = 1,2, \quad m = 1,...,10, \end{aligned} \tag{18}$$

where $0 \le B_m \le 1, m = 1,...,10$ are obtained by a generator of random numbers.

The obtained artificial experimental data (18) are used for the illustration of the parameters ($K_1, a_{j0}, a_{j1}, a_{j2},\ j=1,2$ $a_{j0}, a_{j1}, a_{j2},\ j=1,2, K_1$) identification in the average concentrations model (17) by the minimization of the least-squares function with respect to $K_1, a_{j0}, a_{j1}, a_{j2},\ j=1,2$:

$$\begin{aligned} &Q\left(1, K_1, a_{j0}, a_{j1}, a_{j2}, j=1,2\right) = \\ &= \sum_{m=1}^{10}\left[\begin{matrix}\bar{C}_1\left(1, K_1, a_{j0}, a_{j1}, a_{j2}, j=1,2\right) - \\ -\bar{C}^m_{1\exp}(1)\end{matrix}\right]^2 + \\ &+ \sum_{m=1}^{10}\left[\begin{matrix}\bar{C}_2\left(1, K_1, a_{j0}, a_{j1}, a_{j2}, j=1,2\right) - \\ -\bar{C}^m_{2\exp}(1)\end{matrix}\right]^2, \end{aligned} \tag{19}$$

where the values of $\bar{C}_i\left(1, K_1, a_{j0}, a_{j1}, a_{j2}, j=1,2\right),\ i=1,2$ are obtained

as solutions of (17). The obtained (after the minimization) "experimental" parameter values $K_1, a_{j0}, a_{j1}, a_{j2},\ j=1,2$ are compared with the "theoretical" values on the Table 1.

Table 1. Parameters $K_1, a_{j0}, a_{j1}, a_{j2},\ j=1,2$ (physical absorption).

Parameters	"Theoretical" values	"Experimental" values
a_{10}	1.0318	0.9348
a_{11}	0.1226	0.1286
a_{12}	−0.1640	−0.1616
a_{20}	0.5301	0.5547
a_{21}	1.0671	1.0267
a_{22}	−0.6190	−0.6300
K_1	1	1.0637

The obtained ("experimental") parameter values $K_1, a_{j0}, a_{j1}, a_{j2},\ j=1,2$ are used for the solution of (17) and the results (the lines) are compared with the "theoretical" average concentration values on the Fig. 2.

The obtained "experimental" value of K_1 permits to be obtained the "experimental" value of the interphase mass transfer coefficient $k = K_1 \bar{u}_1 / l$.

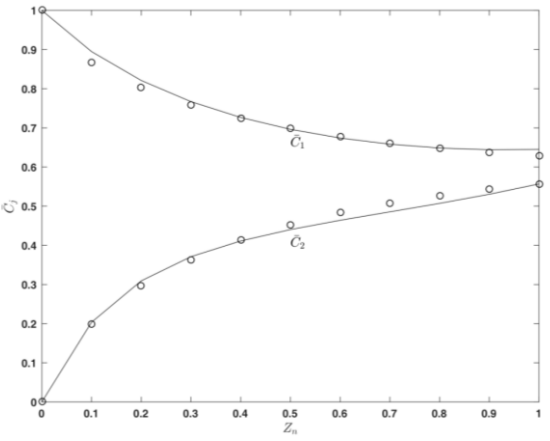

Fig. 4. Average concentration distribution $\bar{C}_j(Z),\ j=1,2$ in the case $\omega = 1.5$: "theoretical" values as solutions of (15) and (7) for different $Z_n = 0.1(n+1),\ n = 0,1,...,9$ (points); as a solution of (17), using the "experimental" parameter values $K_1, a_{j0}, a_{j1}, a_{j2},\ j=1,2$ (lines).

In the same velocities distribution in the phases (the same "experimental" values of $K_1, a_{j0}, a_{j1}, a_{j2},\ j=1,2$ in the Table 1), for other concrete process ($\omega = 1.5$), the solution of (15) and (7) permit to be obtained the "theoretical" average concentrations $\bar{C}_j(Z),\ j=1,2$, which are compared (Fig. 4), with the solution of (17), using the "experimental" values of $K_1, a_{j0}, a_{j1}, a_{j2},\ j=1,2$ in the Table 1.

CHEMICAL ABSORPTION

In the case of chemical absorption, from (4, 5, 8, 16) follow the models:

$$
\begin{aligned}
&U_{1n}\frac{dC_{1n}}{dZ_n} = -K_1\left(C_{1n} - C_{2n}\right);\\
&U_{2n}\frac{dC_{2n}}{dZ_n} = \omega K_1\left(C_{1n} - C_{2n}\right) - \mathrm{Da}\, C_{2n};\\
&0.1n \le Z_n \le 0.1(n+1);\\
&Z_n = 0.1n,\quad \mathrm{C}_{jn}\left(R, Z_n\right) = C_{j(n-1)}\left(R, Z_n\right);\\
&n = 0,1,...,4;\quad j = 1,2;\\
&Z_0 = 0,\quad \mathrm{C}_{10}\left(R, Z_0\right) \equiv 1,\quad C_{20}\left(R, Z_0\right) = 0.
\end{aligned}
\tag{20}
$$

$$
\begin{aligned}
&\left(a_{10} + a_{11}Z + a_{12}Z^2\right)\frac{d\bar{C}_1}{dZ} +\\
&+\left(a_{11} + 2a_{12}Z\right)\bar{C}_1 = -K_1\left(\bar{C}_1 - \bar{C}_2\right);\\
&\left(a_{10} + a_{21}Z + a_{22}Z^2\right)\frac{d\bar{C}_2}{dZ} +\\
&+\left(a_{21} + 2a_{22}Z\right)\bar{C}_2 = \omega K_1\left(\bar{C}_1 - \bar{C}_2\right) - \mathrm{Da}\,\bar{C}_2;\\
&Z = 0,\quad \bar{C}_1 = 1,\quad \bar{C}_2 = 0.
\end{aligned}
\tag{21}
$$

The parameters ω, Da in (20), (21) are known beforehand. The solution of (20) for a concrete process ($\omega = 1, \mathrm{Da} = 1$) and a "theoretical" value of $K_1 = 1$ permits to be obtained the concentration distributions $C_{jn}\left(R, Z_n\right),\ j=1,2$ for different $Z_n = 0.1(n+1),\ n = 0,1,...,9$ (Fig. 5).

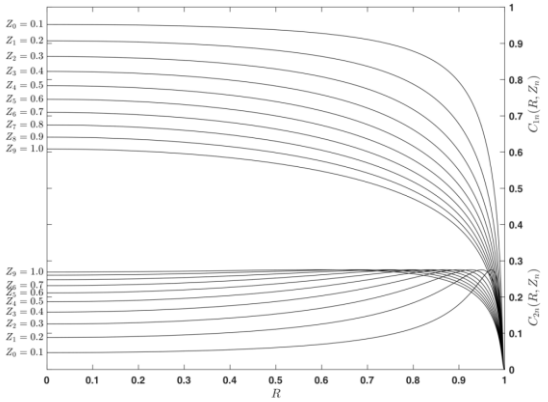

Fig. 5. Concentration distributions $C_{jn}\left(R, Z_n\right),\ j=1,2$ in the case $\omega = \mathrm{Da} = K_1 = 1$ for different $Z_n = 0.1(n+1),\ n = 0,1,...,9$ (chemical absorption).

The solution of (20) (Fig. 5) and (7) permit to be obtained the "theoretical" average concentration $\bar{C}_{jn}(Z_n)$, $j=1,2$ (the points in the Fig. 6) and the functions $A_{jn}(Z_n)$, $j=1,2$ (the points in the Fig. 7) for different $Z_n=0.1(n+1)$, $n=0,1,...,9$.

From Fig. 7 is seen, that the functions $A_{jn}(Z_n)$, $Z_n=0.1(n+1)$, $n=0,1,...,9$ are possible to be presented as quadratic approximations (16) and the "theoretical" values of a_{j0}, a_{j1}, a_{j2}, $j=1,2$, are presented in the Table 2.

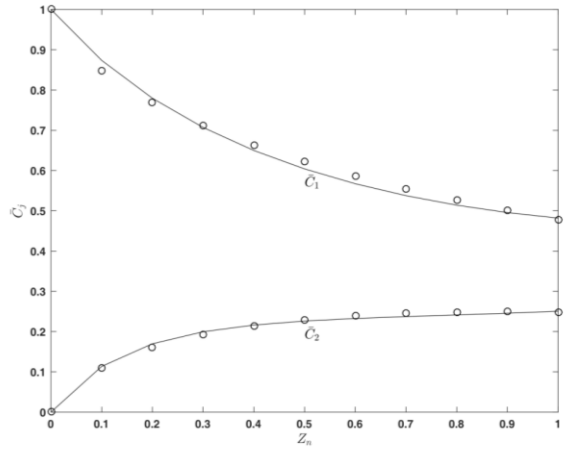

Fig. 6. Average concentration distributions $\bar{C}_{jn}(Z_n)$, $j=1,2$ in the case $\omega=\mathrm{Da}=K_1=1$: "theoretical" values as solutions of (20) and (7) for different $Z_n=0.1(n+1)$, $n=0,1,...,9$ (points); as a solution of (21), using the "experimental" parameter values $K_1, a_{j0}, a_{j1}, a_{j2}$, $j=1,2$ (lines).

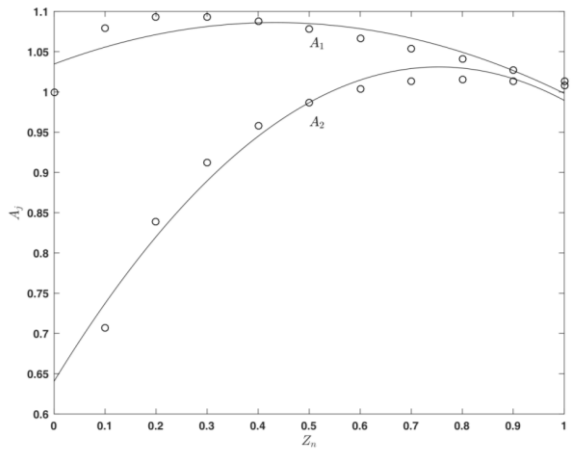

Fig. 7. Function $A_{jn}(Z_n)$, $j=1,2$ in the case $\omega=\mathrm{Da}=K_1=1$: as a solution of (20) and (7) for different $Z_n=0.1(n+1)$, $n=0,1,...,9$ (points); $A_j(Z)$, $j=1,2$ as a quadratic approximation (16) (line).

The "theoretical" average concentration values $\bar{C}_j(1)=\bar{C}_{j9}(Z_9)$, $Z_9=1$, $j=1,2$ (Fig. 6) are used for to be obtained and the artificial experimental data (18). As a result, the minimization of the least-squares function (19) with respect to $K_1, a_{j0}, a_{j1}, a_{j2}$, $j=1,2$ permits to be obtained the "experimental" values of the parameters $K_1, a_{j0}, a_{j1}, a_{j2}$, $j=1,2$, presented in the Table 2.

The "theoretical" average concentration as solutions of (20) and (7) for different $Z_n=0.1(n+1)$, $n=0,1,...,9$ (points) are compared (Fig. 5) with the solution of (21) for the same case ($\omega=1$, $\mathrm{Da}=1$) (the line), where the "experimental" values of the parameters $K_1, a_{j0}, a_{j1}, a_{j2}$, $j=1,2$ in the Table 2 are used.

Table 2. Parameters $K_1, a_{j0}, a_{j1}, a_{j2}$, $j=1,2$ (chemical absorption).

Parameters	"Theoretical" values	"Experimental" values
a_{10}	1.0346	0.8825
a_{11}	0.2378	0.2423
a_{12}	−0.2742	−0.2771
a_{20}	0.6405	0.6586
a_{21}	1.0359	1.1074
a_{22}	−0.6869	−0.6794
K_1	1	1.0684

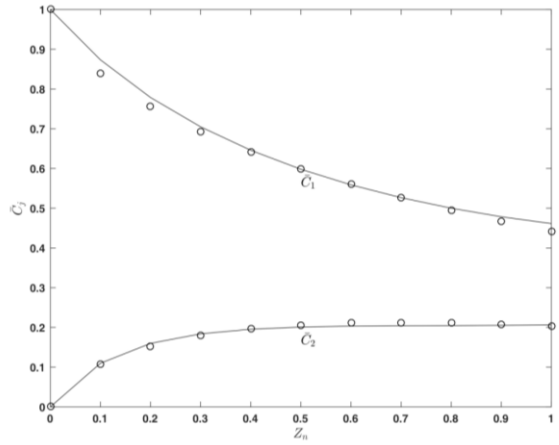

Fig. 8. Average concentration distribution $\bar{C}_j(Z)$, $j=1,2$ in the case $\omega=1$, $\mathrm{Da}=1.5$: "theoretical" values as solutions of (20) and (7) for different $Z_n=0.1(n+1)$, $n=0,1,...,9$ (points); as a solution of (21) (lines), using the "experimental" parameter values $K_1, a_{j0}, a_{j1}, a_{j2}$, $j=1,2$ in the Table 2.

In the same velocities distribution in the phases (the same "experimental" values of $K_1, a_{j0}, a_{j1}, a_{j2}$, $j=1,2$ in the Table 2), for other

concrete process ($\omega = 1, \mathrm{Da} = 1.5$), the solution of (20) and (7) permit to be obtained the "theoretical" average concentrations $\bar{C}_j(Z)$, $j = 1,2$, which are compared (Fig. 8), with the solution of (17), using the "experimental" values of $K_1, a_{j0}, a_{j1}, a_{j2}$, $j = 1,2$ in the Table 2.

PHYSICAL ABSORPTION OF HIGHLY SOLUBLE GAS (ω = Da = 0)

In the cases of physical absorption of highly soluble gas ($\omega = \mathrm{Da} = 0$), from (15), (17) follows $C_{2n} = \bar{C}_{2n} \equiv 0, n = 0,1,...,9$, and as a result the models (15), (17) have the forms:

$$U_{1n}\frac{dC_{1n}}{dZ_n} = -K_1 C_{1n}; \quad 0.1n \le Z_n \le 0.1(n+1);$$
$$Z_n = 0.1n, \quad \mathrm{C}_{1n}(R, Z_n) = C_{1(n-1)}(R, Z_n); \qquad (22)$$
$$n = 0,1,...,4; \quad Z_0 = 0, \quad \mathrm{C}_{10}(R, Z_0) \equiv 1.$$

$$\left(a_{10} + a_{11}Z + a_{12}Z^2\right)\frac{d\bar{C}_1}{dZ} + \\ +\left(a_{11} + 2a_{12}Z\right)\bar{C}_1 = -K_1\bar{C}_1; \quad Z = 0, \quad \bar{C}_1 = 1. \qquad (23)$$

The solution of (22) for "theoretical" value of $K_1 = 1$ (dimensionless interphase mass transfer coefficient in the gas phase) permits to be obtained the "theoretical" concentration distributions $C_{1n}(R, Z_n)$ for different $Z_n = 0.1(n+1), n = 0,1,...,9$. This solution of (22) and (7) permit to be obtained the "theoretical" average concentrations $\bar{C}_{1n}(Z_n)$ for different $Z_n = 0.1(n+1)$, $n = 0,1,...,9$ (the points on the Fig. 9), which are compared with the solution of (23) (the line on the Fig. 9), where the "experimental" values of the parameters $a_{10}, a_{11}, a_{12}, K_1$ in the Table 1 are used.

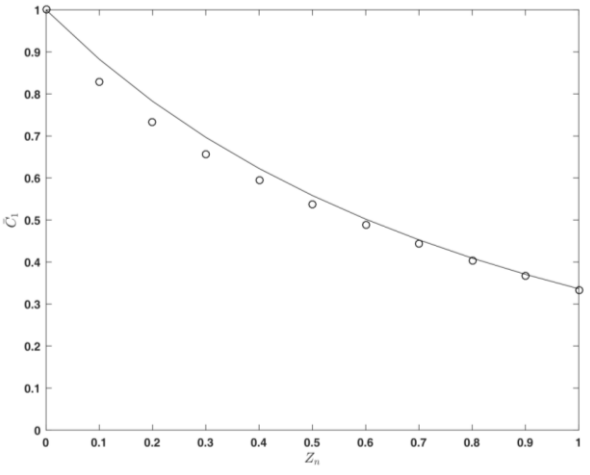

Fig. 9. Average concentration distribution $\bar{C}_1(Z)$ in the case $\omega = \mathrm{Da} = 0$: "theoretical" values of $\bar{C}_{1n}(Z_n)$ for different $Z_n = 0.1(n+1)$, $n = 0,1,...,9$ (points); $\bar{C}_1(Z)$ as solutions of (23) for "experimental" values of $a_{10}, a_{11}, a_{12}, K_1$ (line).

PHYSICAL ABSORPTION OF LIGHTLY SOLUBLE GAS (ω^{-1} = 0)

The model (15), (17) is possible to be presented as

$$U_{1n}\frac{dC_{1n}}{dZ_n} = -\omega^{-1}K_2\left(C_{1n} - C_{2n}\right);$$
$$U_{2n}\frac{dC_{2n}}{dZ_n} = K_2\left(C_{1n} - C_{2n}\right);$$
$$0.1n \le Z_n \le 0.1(n+1); \qquad (24)$$
$$Z_n = 0.1n, \quad \mathrm{C}_{jn}(R, Z_n) = C_{j(n-1)}(R, Z_n);$$
$$n = 0,1,...,9; \quad j = 1,2;$$
$$Z_0 = 0, \quad \mathrm{C}_{10}(R, Z_0) \equiv 1, \quad C_{20}(R, Z_0) = 0.$$

$$\left(a_{10} + a_{11}Z + a_{12}Z^2\right)\frac{d\bar{C}_1}{dZ} + \\ +\left(a_{11} + 2a_{12}Z\right)\bar{C}_1 = -\omega^{-1}K_2\left(\bar{C}_1 - \bar{C}_2\right);$$

$$\left(a_{20} + a_{21}Z + a_{22}Z^2\right)\frac{d\bar{C}_2}{dZ} + \qquad (25)$$
$$+\left(a_{21} + 2a_{22}Z\right)\bar{C}_2 = K_2\left(\bar{C}_1 - \bar{C}_2\right);$$
$$Z = 0, \quad \bar{C}_1 = 1, \quad \bar{C}_2 = 0.$$

In (24), (25) $K_2 = \omega K_1 = 1$ in the case $\omega = K_1 = 1$.

In the case of physical absorption of lightly soluble gas ($\omega^{-1} = 0$), from (24), (25) follows $C_{1n} \equiv 1, n = 0,1,...,9$ and as a result from (24) and (25) is possible to be obtained

$$U_{2n}\frac{dC_{2n}}{dZ_n} = K_2\left(1 - C_{2n}\right);$$
$$0.1n \le Z_n \le 0.1(n+1);$$
$$Z_n = 0.1n, \quad \mathrm{C}_{2n}(R, Z_n) = C_{2(n-1)}(R, Z_n); \qquad (26)$$
$$n = 0,1,...,9;$$
$$Z_0 = 0, \quad C_{20}(R, Z_0) = 0.$$

$$\left(a_{20} + a_{21}Z + a_{22}Z^2\right)\frac{d\bar{C}_2}{dZ} + \\ +\left(a_{21} + 2a_{22}Z\right)\bar{C}_2 = K_2\left(1 - \bar{C}_2\right); \qquad (27)$$
$$Z = 0, \quad \bar{C}_2 = 0.$$

The solution of (26) for "theoretical" value of $K_2 = 1$ (dimensionless interphase mass transfer coefficient in the liquid phase) permits to be obtained the "theoretical" concentration distributions $C_{2n}(R, Z_n)$ for different $Z_n = 0.1(n+1), n = 0,1,...,9$. This solution of (26) and (7) permit to be obtained the "theoretical" average concentration values $\bar{C}_{2n}(Z_n)$ for different $Z_n = 0.1(n+1), \quad n = 0,1,...,9$ (the points on the Fig. 10), where are compared with the solution of (27) (the line), where the "experimental" values of the parameters $a_{20}, a_{21}, a_{22}, K_2 = K_1$ in the Table 1 are used.

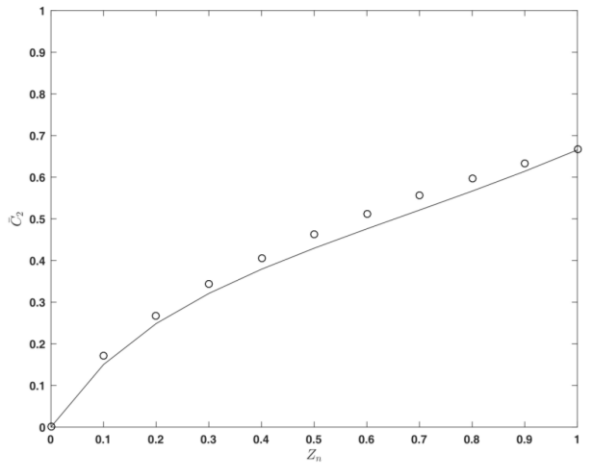

Fig. 10. Average concentration distribution $\bar{C}_2(Z)$ in the case $\omega^{-1} = 0$: "theoretical" values $\bar{C}_{2n}(Z_n)$ for different $Z_n = 0.1(n+1), \quad n = 0,1,...,9$ (points); $\bar{C}_2(Z)$ as solutions of (27) for "experimental" values of $a_{20}, a_{21}, a_{22}, K_2 = K_1$ in the Table 1 (line).

The comparison of the Figs. 2, 9, 10 shows that the obtained parameters in the cases of highly and lightly soluble gases can be used at average soluble gases, where is necessary an experimental determination of the interphase mass transfer coefficient, only.

CONCLUSIONS

The presented numerical analysis of a co-current absorption process in column apparatus shows, that the average concentration model, where the radial velocity components in the phases are equal to zero (in the cases of constant velocity radial non-uniformities along the column height), is possible to be used in the cases of an axial modification of the radial non-uniformities of the axial velocity components. The use of experimental data, for the average concentrations at column end, for a concrete process, permits to be obtained the model parameters ($K_1, a_{j0}, a_{j1}, a_{j2}, j = 1,2$), related with the radial non-uniformities of the velocities in the gas and liquid phases. These parameter values permit to be used the average concentration model for modeling of physical and chemical absorption, absorption of highly and lightly soluble gases (different values of the parameters ω, Da, i.e. different values of the column height, average velocities, chemical reaction rate constant and gas solubility).

REFERENCES

1. B. Boyadjiev, Chr. Boyadjiev, Chr., New Models of Industrial Column Chemical Reactors, *Bulg. Chem. Communications*, **49**(3), 2017 (in press).
2. Chr. Boyadjiev, *Int. J. Heat Mass Transfer*, **49**, 796 (2006).
3. Chr. Boyadjiev, Theoretical Chemical Engineering. Modeling and Simulation, Springer-Verlag, Berlin Heidelberg, 2010.
4. M. Doichinova, Chr. Boyadjiev, *Int. J. Heat Mass Transfer*, **55**, 6705 (2012).
5. Chr. Boyadjiev, *J. Pure Appl. Mathematics: Advances and Applications*, **10**(2), 131 (2013).
6. Chr. Boyadjiev, M. Doichinova, B. Boyadjiev, P. Popova-Krumova, Modeling of Column Apparatus Processes, Springer-Verlag, Berlin Heidelberg, 2016.

НОВИ МОДЕЛИ НА ИНДУСТРИАЛНИ КОЛОННИ АБСОРБЕРИ. 1. ПРАВОТОЧНИ АБСОРБЦИОННИ ПРОЦЕСИ

Б. Бояджиев, Хр. Бояджиев

Институт по инженерна химия, Българска академия на науките, ул. „Акад. Г. Бончев“, бл. 103, 1113, София България

Получена на 20 юли, 2016 г.; приета на 2 февруари, 2017 г.

(Резюме)

Представен е нов подход за моделиране на индустриални колонни абсорбери. Предложен е теоретичен анализ на ефекта на радиалната неравномерност на скоростта при правоточни абсорбционни процеси в колонни апарати. Моделът на средните концентрации, където радиалната компонента на скоростта е нула (в случаите на постоянна радиална неравномерност на скоростта по височината на колоната), е използван в случаите на аксиално изменение на радиалната неравномерност на аксиалните компоненти на скоростите в газовата и течната фази. Използването на експериментални данни за средните концентрации в газовата и течната фази на изхода им от колоната за конкретен процес (абсорбция на средно разтворим газ), позволява намирането на моделните параметри в газовата и течната фази, свързани с радиалната неравномерност на скоростите. Тези стойности на параметрите позволяват използването на моделите на средните концентрации за моделиране на различни абсорбционни процеси в правоточни колони.

Bulgarian Chemical Communications, Volume 49, Number 3, (pp. 720 – 728) 2017

New Models of Industrial Column Absorbers. 2. Counter-current absorption process

B. Boyadjiev, Ch. Boyadjiev*

Institute of Chemical Engineering, Bulgarian Academy of Sciences, Acad. G. Bonchev str., Bl. 103, 1113 Sofia, Bulgaria

Received July 13, 2017; Accepted July 21, 2017

A theoretical analysis of the effect of the velocity radial non-uniformity on the counter-current absorption processes in the column apparatuses is presented. The average concentration model, where the radial velocity component is equal to zero (in the cases of a constant velocity radial non-uniformity along the column height), is used in the cases of an axial modification of the radial non-uniformity of the axial velocity components in the gas and liquid phases. The modeling problem in the counter-current flows is complicated, because the model equations has to be presented in two-coordinate systems (in a one-coordinate system one of the equations has no solution due to the negative Laplacian value).

The use of experimental data, for the average concentrations in the gas and liquid phases at the column end in the cases of highly and lightly soluble gases, permits to be obtained the gas and liquid phases model parameters, related with the radial non-uniformity of the velocities. These parameter values permit to be used the average concentration models for different absorption processes modeling in counter-current columns.

Keywords: Column apparatus, gas absorption, counter-current flows, convection-diffusion model, average concentration model, velocity radial non-uniformity.

INTRODUCTION

In two papers [1, 2] was shown, that average concentration model, where the radial velocity component is equal to zero (in the cases of a constant velocity radial non-uniformity along the column height), is possible to be used in the cases of an axial modification of the radial non-uniformity of the axial velocity component. The use of experimental data, for the average concentration at the column end, for a concrete process and column, permits to be obtained the model parameters, related with the radial non-uniformity of the velocity. These parameter values permit to be used the average concentration model for modeling of different processes in the cases of different values of the column height, average velocity, reagent diffusivity and chemical reaction rate constant. This possibility will be used for modeling of the gas absorption processes in the counter-current columns, where the problem is complicated [3], because the mass transfer process models has to be presented in two-coordinate systems (in a one-coordinate system one of the equations has no s

Counter-current absorption processes

The modeling of the counter-current absorption processes uses two cylindrical coordinate systems $\left(r, z_j\right)$, $j=1,2$ in the gas $\left(j=1\right)$ and liquid $\left(j=2\right)$ phases, i.e. the axial coordinates in the co-current models [2] must be replaced by $z=z_1$, $z=z_2$ in the gas and liquid phases, respectively. As a result, the convection-diffusion and average concentration models of the counter-current chemical absorption processes have the forms:

$$
\begin{aligned}
&u_1\frac{\partial c_1}{\partial z_1}=D_1\left(\frac{\partial^2 c_1}{\partial z_1^2}+\frac{1}{r}\frac{\partial c_1}{\partial r}+\frac{\partial^2 c_1}{\partial r^2}\right)-\\
&-k\left(c_1-\chi c_2\right);\\
&u_2\frac{\partial c_2}{\partial z_2}=D_2\left(\frac{\partial^2 c_2}{\partial z_2^2}+\frac{1}{r}\frac{\partial c_2}{\partial r}+\frac{\partial^2 c_2}{\partial r^2}\right)+\\
&+k\left(c_1-\chi c_2\right)-k_0 c_2;\\
&r=0,\quad \frac{\partial c_j}{\partial r}\equiv 0;\\
&r=r_0,\quad \frac{\partial c_j}{\partial r}\equiv 0;\quad j=1,2;\\
&z_1=0,\quad c_1\equiv c_1^0,\\
&u_1^0c_1^0\equiv u_1c_1^0-D_1\left(\frac{\partial c_1}{\partial z}\right)_{z=0};\\
&z_2=0,\quad c_2\equiv 0,\quad \left(\frac{\partial c_2}{\partial z}\right)_{z=0}=0.
\end{aligned}
\tag{1}
$$

* To whom all correspondence should be sent:
E-mail: chr.boyadjiev@gmail.com

$$\alpha_1(z)\bar{u}_1\frac{d\bar{c}_1}{dz_1}+\frac{d\alpha_1}{dz_1}\bar{u}_1\bar{c}_1=D_1\frac{d^2\bar{c}_1}{dz_1^2}-k\left(\bar{c}_1-\chi\bar{c}_2\right);$$

$$\alpha_2(z)\bar{u}_2\frac{d\bar{c}_2}{dz_2}+\frac{d\alpha_2}{dz_2}\bar{u}_2\bar{c}_2=D_2\frac{d^2\bar{c}_2}{dz_2^2}+$$

$$+k\left(\bar{c}_1-\chi\bar{c}_2\right)-k_0\bar{c}_2;$$

$$z_1=0,\quad \bar{c}_1(0)\equiv c_1^0,\quad \frac{d\bar{c}_1}{dz}\equiv 0; \tag{2}$$

$$z_2=0,\quad \bar{c}_2(0)\equiv 0,\quad \frac{d\bar{c}_2}{dz}\equiv 0;$$

$$\alpha_j\left(z_j\right)=\frac{2}{r_0^2}\int_0^{r_0} r\tilde{u}_j\tilde{c}_j\,dr,\quad \tilde{u}_j(r)=\frac{u_j(r)}{\bar{u}_j},$$

$$\tilde{c}_j\left(r,z_j\right)=\frac{c_j\left(r,z_j\right)}{\bar{c}_j(z)},\quad j=1,2.$$

In (1, 2) $u_j(r), c_j\left(r,z_j\right), D_j,\ j=1,2$ are the velocities, concentrations and diffusivities in the gas and liquid phases, $\bar{u}_j,\bar{c}_j\left(z_j\right),\ j=1,2$ - the average velocities and concentrations at the column cross-sectional area, $\tilde{u}_j(r),\tilde{c}_j\left(r,z_j\right),\ j=1,2$ - the radial non-uniformities of the velocities and concentrations.

Generalized variables

In (1, 2) is possible to be introduced the generalized variables [4-7]:

$$r=r_0R,\quad z_1=lZ_1,\ z_2=lZ_2,\quad u_j(r)=\bar{u}_jU_j(R),$$

$$\tilde{u}_j(r)=\frac{u_j(r)}{\bar{u}_j}=U_j(R),\quad j=1,2;$$

$$c_1\left(r,z_1\right)=c_1^0C_1\left(R,Z_1\right),\quad \bar{c}_1\left(z_1\right)=c_1^0\bar{C}_1\left(Z_1\right), \tag{3}$$

$$c_2\left(r,z_2\right)=\frac{c_1^0}{\chi}C_2\left(R,Z_2\right),\quad \bar{c}_2\left(z_2\right)=\frac{c_1^0}{\chi}\bar{C}_2\left(Z_2\right)$$

and as a result is obtained:

$$U_1\frac{\partial C_1}{\partial Z_1}=\mathrm{Fo}_1\left(\varepsilon\frac{\partial^2C_1}{\partial Z_1^2}+\frac{1}{R}\frac{\partial C_1}{\partial R}+\frac{\partial^2C_1}{\partial R^2}\right)-$$

$$-K_1\left(C_1-C_2\right);$$

$$U_2\frac{\partial C_2}{\partial Z_2}=\mathrm{Fo}_2\left(\varepsilon\frac{\partial^2C_2}{\partial Z_2^2}+\frac{1}{R}\frac{\partial C_2}{\partial R}+\frac{\partial^2C_2}{\partial R^2}\right)+$$

$$+\omega K_1\left(C_1-C_2\right)-\mathrm{Da}\,C_2; \tag{4}$$

$$R=0,\quad \frac{\partial C_j}{\partial R}\equiv 0;\quad R=1,\quad \frac{\partial C_j}{\partial R}\equiv 0;\quad j=1,2;$$

$$Z_1=0,\quad C_1\equiv 1,\quad 1\equiv U_1-\mathrm{Pe}_1^{-1}\frac{\partial C_1}{\partial Z_1};$$

$$Z_2=0,\quad C_2=0,\quad \frac{\partial C_2}{\partial Z_2}\equiv 0.$$

$$A_1\left(Z_1\right)\frac{d\bar{C}_1}{dZ_1}+\frac{dA_1}{dZ_1}\bar{C}_1=\mathrm{Pe}_1^{-1}\frac{d^2\bar{C}_1}{dZ_1^2}-K_1\left(\bar{C}_1-\bar{C}_2\right);$$

$$A_2\left(Z_2\right)\frac{d\bar{C}_2}{dZ_2}+\frac{dA_2}{dZ_2}\bar{C}_2=\mathrm{Pe}_2^{-1}\frac{d^2\bar{C}_2}{dZ_2^2}+$$

$$+\omega K_1\left(\bar{C}_1-\bar{C}_2\right)-\mathrm{Da}\,\bar{C}_2; \tag{5}$$

$$Z_1=0,\quad \bar{C}_1=1,\quad \frac{d\bar{C}_1}{dZ}=0;$$

$$Z_2=0,\quad \bar{C}_2=0,\quad \frac{d\bar{C}_2}{dZ}=0.$$

In (4, 5) Fo, Da and Pe are the Fourier, Damkohler and Peclet numbers, respectively:

$$\mathrm{Fo}_j=\frac{D_jl}{\bar{u}_jr_0^2},\quad \mathrm{Pe}_j=\frac{\bar{u}_jl}{D_j},\quad \mathrm{Da}=\frac{k_0l}{\bar{u}_2},$$

$$\varepsilon=\mathrm{Fo}_j^{-1}\mathrm{Pe}_j^{-1},\quad K_1=\frac{kl}{\bar{u}_1},\quad \omega=\frac{\bar{u}_1\chi}{\bar{u}_2},\quad j=1,2. \tag{6}$$

In the cases of a physical absorption $\mathrm{Da}=0$.

In (5) are used the functions:

$$\bar{C}_j\left(Z_j\right)=2\int_0^1 RC_j\left(R,\mathrm{Z}_j\right)dR,$$

$$\tilde{c}_j\left(r,z_j\right)=\frac{c_j\left(r,z_j\right)}{\bar{c}_j\left(z_j\right)}=\frac{C_j\left(R,Z_j\right)}{\bar{C}_j\left(Z_j\right)},$$

$$\alpha_j\left(z_j\right)=\alpha_j\left(lZ_j\right)=A_j\left(Z_j\right)= \tag{7}$$

$$=2\int_0^1 RU_j(R)\frac{C_j\left(R,Z_j\right)}{\bar{C}_j\left(Z_j\right)}dR,\quad j=1,2.$$

The convection-diffusion model (4) permits to be made [1-4] a qualitative analysis of the process (model) for to be obtained the main, small and slight physical effects (mathematical operators), and to be rejected the slight effect (operators). As a result the process mechanism identification is possible to be made. On this base are possible to be

obtained different approximations for high column ($0 = \varepsilon \le 10^{-2}$), big average velocities ($0 = \mathrm{Fo}_j \le 10^{-2}$, $j = 1,2$), small ($0 = \mathrm{Da} \le 10^{-2}$) or big ($0 = \mathrm{Da}^{-1} \le 10^{-2}$) chemical reaction rate, highly soluble ($0 = \omega \le 10^{-2}$) or lightly soluble ($0 = \omega^{-1} \le 10^{-2}$) gas. In the industrial absorption column [2], the model parameters have very small values:

$$\begin{aligned} &\mathrm{Fo}_1 \approx 10^{-6}, \quad \mathrm{Fo}_2 \approx 10^{-10}, \\ &\mathrm{Pe}_1^{-1} \approx 10^{-6}, \quad \mathrm{Pe}_2^{-1} \approx 10^{-10} \end{aligned} \tag{8}$$

and the models (4, 5) have the convective forms:

$$\begin{aligned} &U_1 \frac{dC_1}{dZ_1} = -K_1 (C_1 - C_2); \\ &U_2 \frac{dC_2}{dZ_2} = \omega K_1 (C_1 - C_2) - \mathrm{Da}\, C_2; \\ &Z_1 = 0, \quad C_1 \equiv 1; \quad Z_2 = 0, \quad C_2 = 0. \end{aligned} \tag{9}$$

$$\begin{aligned} &A_1(Z_1) \frac{d\bar{C}_1}{dZ_1} + \frac{dA_1}{dZ_1} \bar{C}_1 = -K_1 (\bar{C}_1 - \bar{C}_2); \\ &A_2(Z_2) \frac{d\bar{C}_2}{dZ_2} + \frac{dA_2}{dZ_2} \bar{C}_2 = \omega K_1 (\bar{C}_1 - \bar{C}_2) - \mathrm{Da}\, \bar{C}_2; \\ &Z_1 = 0, \quad \bar{C}_1 = 1; \quad Z_2 = 0, \quad \bar{C}_2 = 0. \end{aligned} \tag{10}$$

Physical absorption of the average soluble gases

In the case of physical absorption ($\mathrm{Da} = 0$) of an average soluble gas ($\omega \approx 1$) from (9, 10) follows

$$\begin{aligned} &U_1 \frac{dC_1}{dZ_1} = -K_1 (C_1 - C_2); \\ &U_2 \frac{dC_2}{dZ_2} = \omega K_1 (C_1 - C_2); \\ &Z_1 = 0, \quad C_1 \equiv 1; \quad Z_2 = 0, \quad C_2 = 0. \end{aligned} \tag{11}$$

$$\begin{aligned} &A_1(Z_1) \frac{d\bar{C}_1}{dZ_1} + \frac{dA_1}{dZ_1} \bar{C}_1 = -K_1 (\bar{C}_1 - \bar{C}_2); \\ &A_2(Z_2) \frac{d\bar{C}_2}{dZ_2} + \frac{dA_2}{dZ_2} \bar{C}_2 = \omega K_1 (\bar{C}_1 - \bar{C}_2); \\ &Z_1 = 0, \quad \bar{C}_1 = 1; \quad Z_2 = 0, \quad \bar{C}_2 = 0. \end{aligned} \tag{12}$$

The theoretical analysis of the model (12) shows [3-7], that the functions $A_j(Z_j)$, $j = 1,2$ is possible to be presented as linear approximations:

$$A_j = \alpha_{j0} + \alpha_{j1} Z_j, \quad j = 1,2, \tag{13}$$

where the model parameters α_{j0}, α_{j1}, $j = 1,2$ is possible to be obtained, using experimental data for a short column ($Z_j = 0.1$, $j = 1,2$).

The presented theoretical analysis shows, that the basic approximations of the convection-diffusion models (4, 9) and average concentration model (5, 10) are $\frac{\partial \tilde{u}_j}{\partial z_j} \equiv 0$, $j = 1,2$.

Effect of the axial modification of the radial non-uniformity of the velocity

Let's considers the velocity distributions [2]:

$$u_{jn}(r, z_{jn}) = \bar{u}_j \tilde{u}_{jn}(r, z_{jn}), \quad j = 1,2 \tag{14}$$

and axial step changes of the radial non-uniformity of the axial velocity components in the column:

$$\begin{aligned} &\tilde{u}_{jn}(r, z_{jn}) = \tilde{u}_{jn}(r_0 R, lZ_{jn}) = \\ &\qquad = U_{jn}(R, Z_{jn}) = a_{jn} - b_{jn} R^2, \\ &a_{jn} = 2 - 0.1n, \quad b_{jn} = 2(1 - 0.1n), \\ &0.1n \le Z_{jn} \le 0.1(n+1), \quad n = 0,1,...,9, \quad j = 1,2, \end{aligned} \tag{15}$$

where the average velocities at the cross section of the column are constants, while the maximal velocities (and as a result the radial non-uniformity of the axial velocity components too) decrease along the column height.

If put (15) in (11), the model has the form:

$$\begin{aligned} &U_{1n} \frac{dC_{1n}}{dZ_{1n}} = -K_1 (C_{1n} - C_{2n}), \\ &0.1n \le Z_{1n} \le 0.1(n+1); \\ &U_{2n} \frac{dC_{2n}}{dZ_{2n}} = \omega K_1 (C_{1n} - C_{2n}), \\ &0.1n \le Z_{2n} \le 0.1(n+1); \\ &Z_{jn} = 0.1n, \quad C_{jn}(R, Z_{jn}) = C_{j(n-1)}(R, Z_{jn}); \\ &n = 0,1,...,9; \quad j = 1,2; \\ &Z_{10} = 0, \quad C_{10}(R, Z_{10}) \equiv 1; \\ &Z_{20} = 0, \quad C_{20}(R, Z_{20}) \equiv 0. \end{aligned} \tag{16}$$

The solution of (16), using the method in [2, 8], for concrete process ($\omega = 1$) and "theoretical" value of $K_1 = 1$, permits to be obtained the concentration distributions $C_{jn}(R, Z_{jn})$, $j = 1,2$ for different $Z_{jn} = 0.1(n+1)$, $j = 1,2$, $n = 0,1,...,9$. These results and (7) permit to be obtained the "theoretical" average concentration values $\bar{C}_{jn}(Z_{jn})$, $Z_{jn} = 0.1(n+1)$, $j = 1,2$, $n = 0,1,...,9$ (the points on Fig. 1) and the function values $A_{jn}(Z_{jn})$, $j = 1,2$ (the points on Fig. 2) for different $Z_{jn} = 0.1(n+1)$, $j = 1,2$, $n = 0,1,...,9$.

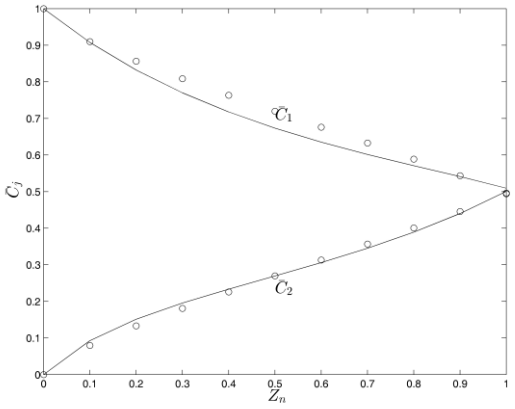

Fig. 1. Average concentration $\bar{C}_j\left(Z_j\right),\ j=1,2$ in the case $\omega=K_1=1$: "theoretical" values $\bar{C}_j\left(Z_j\right)=\bar{C}_{jn}\left(Z_{jn}\right),\ j=1,2$ as solutions of (16) and (7) for different $Z_{jn}=0.1(n+1),\ j=1,2,\ n=0,1,...,9$ (points); $\bar{C}_j\left(Z_j\right),\ j=1,2$ as a solution of (18), using the "experimental" parameter values $a_{j0}, a_{j1}, a_{j2},\ j=1,2,\ K_1=K_2=\dfrac{K_1+K_2}{2}=1.05$ in the Table 1 (lines).

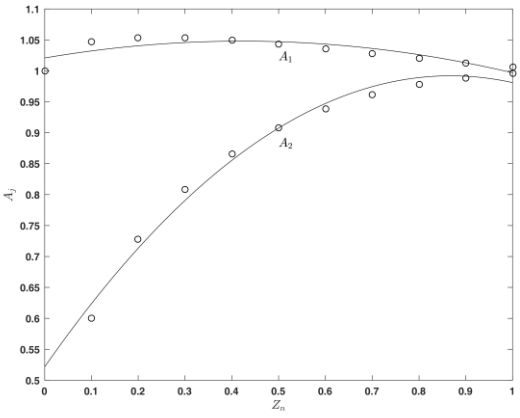

Fig. 2. Function $A_{jn}\left(Z_{jn}\right)$ for different $Z_{jn}=0.1(n+1),\ j=1,2,\ n=0,1,...,9$ (points); $A_j\left(Z_j\right),\ j=1,2$ as a quadratic approximation (17) (line).

From Fig. 2 is seen, that the functions $A_{jn}\left(Z_{jn}\right), n=0,1,...,4,\ j=1,2$ are possible to be presented as quadratic approximations:

$$A_j\left(Z_j\right)=a_{j0}+a_{j1}Z_j+a_{j2}Z_j^2,\quad j=1,2, \tag{17}$$

where the ("theoretical") values of $a_{j0}, a_{j1}, a_{j2},\ j=1,2$ are presented in the Table 1.

As a result (in the case of axial modification of the radial non-uniformity of the velocity) the model (10) has the form:

$$\begin{aligned}
&\left(a_{10}+a_{11}Z_1+a_{12}Z_1^2\right)\frac{d\bar{C}_1}{dZ_1}+\\
&\quad+\left(a_{11}+2a_{12}Z_1\right)\bar{C}_1=-K_1\left(\bar{C}_1-\bar{C}_2\right);\\
&\left(a_{20}+a_{21}Z_2+a_{22}Z_2^2\right)\frac{d\bar{C}_2}{dZ_2}+\\
&\quad+\left(a_{21}+2a_{22}Z_2\right)\bar{C}_2=\omega K_1\left(\bar{C}_1-\bar{C}_2\right);\\
&Z_1=0,\quad \bar{C}_1=1;\quad Z_2=0,\quad \bar{C}_2=0.
\end{aligned} \tag{18}$$

Physical absorption of highly soluble gas ($\omega=\mathrm{Da}=0$)

In the cases of physical absorption of highly soluble gas ($\omega=\mathrm{Da}=0$), from (16, 18) follows $C_{2n}=\bar{C}_{2n}\equiv 0$, and as a result the models (16, 18) have the forms:

$$\begin{aligned}
&U_{1n}\frac{dC_{1n}}{dZ_{1n}}=-K_1C_{1n};\quad 0.1n\le Z_{1n}\le 0.1(n+1);\\
&Z_{1n}=0.1n,\quad \mathrm{C}_{1n}\left(R,Z_{1n}\right)=C_{1(n-1)}\left(R,Z_{1n}\right);\\
&n=0,1,...,9;\quad Z_{10}=0,\quad \mathrm{C}_{10}\left(R,Z_{10}\right)\equiv 1.
\end{aligned} \tag{19}$$

$$\begin{aligned}
&\left(a_{10}+a_{11}Z_1+a_{12}Z_1^2\right)\frac{d\bar{C}_1}{dZ_1}+\left(a_{11}+2a_{12}Z_1\right)\bar{C}_1=\\
&\qquad=-K_1\bar{C}_1;\\
&Z_1=0,\quad \bar{C}_1=1.
\end{aligned} \tag{20}$$

The solution of (19) for "theoretical" value of $K_1=1$ permits to be obtained the "theoretical" concentration distributions $C_{1n}\left(R,Z_{1n}\right)$ for different $Z_{1n}=0.1(n+1), n=0,1,...,9$. This solution of (19) and (7) permit to be obtained the "theoretical" average concentrations $\bar{C}_{1n}\left(Z_{1n}\right)$ for different $Z_{1n}=0.1(n+1), n=0,1,...,9$ (the points on the Fig. 3).

Parameters identification in the gas phase

The obtained the values of the function $\bar{C}_{1n}\left(Z_{1n}\right), Z_{1n}=0.1(n+1), n=0,1,...,9$ (using the solution of (19) and (7)), for the concrete process ($\omega=\mathrm{Da}=0$) and "theoretical" value of $K_1=1$, permit to be obtained the concentration values $\bar{C}_1(1)$ and the artificial experimental data:

$$\bar{C}_{1\exp}^m(1)=\left(0.95+0.1B_m\right)\bar{C}_1(1),\quad m=1,...,10, \tag{21}$$

where $0\le B_m\le 1, m=1,...,10$ are obtained by a generator of random numbers.

The obtained artificial experimental data (21) are used for the parameters ($a_{10}, a_{11}, a_{12}, K_1$)

identification in the average concentrations model (20) by the minimization of the least-squares function Q_1 with respect to $a_{10}, a_{11}, a_{12}, K_1$:

$$Q_1\left(a_{10}, a_{11}, a_{12}, K_1\right) = \\ = \sum_{m=1}^{10}\left[\bar{C}_1\left(1, a_{10}, a_{11}, a_{12}, K_1\right) - \bar{C}_{1\exp}^{m}\left(1\right)\right]^2, \quad (22)$$

where the values of $\bar{C}_1(1, a_{10}, a_{11}, a_{12}, K_1)$ are obtained as solutions of (20), using the method in [8]. The obtained after the minimization "experimental" parameter values $a_{10}, a_{11}, a_{12}, K_1$ are compared with the "theoretical" values on the Table 1.

The obtained ("experimental") parameter values $a_{10}, a_{11}, a_{12}, K_1$ are used for the solution of (20) with the help of the method in [8] and the result (the line) is compared on Fig. 3 with the "theoretical" average concentrations $\bar{C}_{1n}\left(Z_{1n}\right)$ for different $Z_{1n} = 0.1\left(n+1\right), n = 0,1,...,9$ (the points).

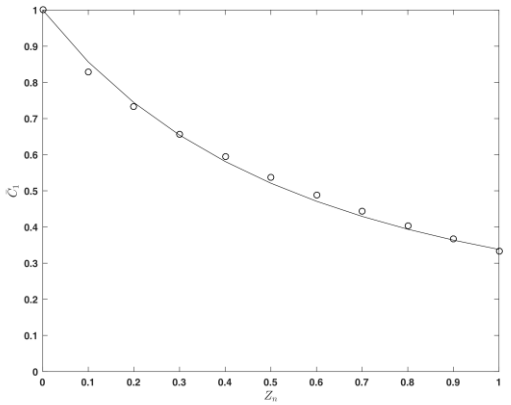

Fig. 3. Average concentration distribution $\bar{C}_1\left(Z\right)$ in the case $\omega = \mathrm{Da} = 0$: "theoretical" values of $\bar{C}_{1n}\left(Z_1\right)$ for different $Z_{1n} = 0.2\left(n+1\right), \quad n = 0,1,...,9$ (points); $\bar{C}_1\left(Z\right)$ as solutions of (20) for "experimental" values of $a_{10}, a_{11}, a_{12}, K_1$ (line).

Physical absorption of lightly soluble gas
($\omega^{-1} = 0, \mathrm{Da} = 0$)

The models (16, 18) is possible to be presented as:

$$U_{1n}\frac{dC_{1n}}{dZ_{1n}} = -\omega^{-1}K_2\left(C_{1n} - C_{2n}\right), \\ 0.1n \le Z_{1n} \le 0.1\left(n+1\right); \\ U_{2n}\frac{dC_{2n}}{dZ_{2n}} = K_2\left(C_{1n} - C_{2n}\right) - \mathrm{Da}\, C_{2n}, \\ 0.1n \le Z_{2n} \le 0.1\left(n+1\right); \quad (23) \\ Z_{jn} = 0.1n, \quad \mathrm{C}_{jn}\left(R, Z_n\right) = C_{j(n-1)}\left(R, Z_{jn}\right); \\ n = 0,1,...,9; \quad j = 1,2; \\ Z_{10} = 0, \quad \mathrm{C}_{10}\left(R, Z_{10}\right) \equiv 1; \\ Z_{20} = 0, \quad C_{20}\left(R, Z_0\right) = 0.$$

$$\left(a_{10} + a_{11}Z + a_{12}Z^2\right)\frac{d\bar{C}_1}{dZ_1} + \left(a_{11} + 2a_{12}Z\right)\bar{C}_1 = \\ = -\omega^{-1}K_2\left(\bar{C}_1 - \bar{C}_2\right); \\ \left(a_{20} + a_{21}Z + a_{22}Z^2\right)\frac{d\bar{C}_2}{dZ_2} + \left(a_{21} + 2a_{22}Z\right)\bar{C}_2 = \quad (24) \\ = K_2\left(\bar{C}_1 - \bar{C}_2\right) - \mathrm{Da}\,\bar{C}_2; \\ Z_1 = 0, \quad \bar{C}_1 = 1; \quad Z_2 = 0, \quad \bar{C}_2 = 0.$$

In (23, 24) $K_2 = \omega K_1$.

In the case of physical absorption of lightly soluble gas ($\omega^{-1} = 0, \mathrm{Da} = 0$), from (23, 24) follows $C_{1n} \equiv 1, n = 0,1,...,9$ and as a result from (23, 24) is possible to be obtained:

$$U_{2n}\frac{dC_{2n}}{dZ_{2n}} = K_2\left(1 - C_{2n}\right); \quad 0.1n \le Z_{2n} \le 0.1\left(n+1\right); \\ Z_{2n} = 0.1n, \quad \mathrm{C}_{2n}\left(R, Z_{2n}\right) = C_{2(n-1)}\left(R, Z_{2n}\right); \\ n = 0,1,...,9; \quad Z_{20} = 0, \quad C_{20}\left(R, Z_{20}\right) = 0. \\ (25)$$

$$\left(a_{20} + a_{21}Z_2 + a_{22}Z_2^2\right)\frac{d\bar{C}_2}{dZ_2} + \left(a_{21} + 2a_{22}Z_2\right)\bar{C}_2 = \\ = K_2\left(1 - \bar{C}_2\right); \quad (26)$$

$$Z_2 = 0, \quad \bar{C}_2 = 0.$$

The solution of (25) for "theoretical" value of $K_2 = 1$ (dimensionless interphase mass transfer coefficient in the liquid phase) permits to be obtained the "theoretical" concentration distributions $C_{2n}\left(R, Z_{2n}\right)$ for different $Z_{2n} = 0.1\left(n+1\right), n = 0,1,...,9$. This solution of (25) and (7) permit to be obtained the "theoretical" average concentration values $\bar{C}_{2n}\left(Z_{2n}\right)$ for different $Z_{2n} = 0.1\left(n+1\right), \quad n = 0,1,...,9$ (the points on the Fig. 4).

Parameters identification in the liquid phase

The obtained the values of the function $\bar{C}_{2n}\left(Z_{2n}\right), Z_{2n}=0.1\left(n+1\right), n=0,1,...,9$ (using the solution of (25) and (7)), for the concrete process ($\omega^{-1}=0, \mathrm{Da}=0$) and "theoretical" value of $K_2=1$, permit to be obtained the concentration values $\bar{C}_2\left(1\right)$ and the artificial experimental data:

$$\bar{C}^m_{2\exp}\left(1\right)=\left(0.95+0.1B_m\right)\bar{C}_2\left(1\right), \quad m=1,...,10, \quad (27)$$

where $0\le B_m\le 1, m=1,...,10$ are obtained by a generator of random numbers.

The obtained artificial experimental data (27) are used for the parameters $(a_{20}, a_{21}, a_{22}, K_2)$ identification in the average concentrations model (26) by the minimization of the least-squares function Q_2 with respect to $a_{20}, a_{21}, a_{22}, K_2$:

$$Q_2\left(a_{20}, a_{21}, a_{22}, K_2\right)= \\ =\sum_{m=1}^{10}\left[\bar{C}_2\left(1, a_{20}, a_{21}, a_{22}, K_2\right)-\bar{C}^m_{2\exp}\left(1\right)\right]^2, \quad (28)$$

where the values of $\bar{C}_2(1, a_{20}, a_{21}, a_{22}, K_2)$ are obtained as solutions of (26), using the method in [8]. The obtained after the minimization "experimental" parameter values $a_{20}, a_{21}, a_{22}, K_2$ are compared with the "theoretical" values on the Table 1.

The obtained ("experimental") parameter values $a_{20}, a_{21}, a_{22}, K_2$ are used for the solution of (26) with the help of the method in [8] and the result (the line) is compared on Fig. 4 with the "theoretical" average concentrations $\bar{C}_{2n}\left(Z_{2n}\right)$ for different $Z_{2n}=0.1\left(n+1\right), n=0,1,...,9$ (the points).

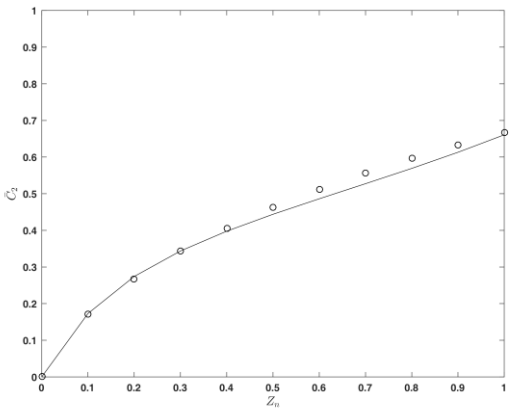

Fig. 4. Average concentration distribution $\bar{C}_2\left(Z\right)$ in the case $\omega^{-1}=0, \mathrm{Da}=0$: "theoretical" values of $\bar{C}_{2n}\left(Z_2\right)$ for different $Z_{2n}=0.2\left(n+1\right), \ n=0,1,...,9$ (points); $\bar{C}_2\left(Z\right)$ as solutions of (26) for "experimental" values of $a_{20}, a_{21}, a_{22}, K_2$ in the Table 1 (line).

Model parameters in the cases of average soluble gases

The parameters $a_{j0}, a_{j1}, a_{j2}, j=1,2,$ in the model (18) are related with the velocity nonuniformity in the column, only. Their "experimental" values are obtained in the cases of absorption of highly and lightly gases (Table 1). The parameter K_1 in (18) must be obtained from the experimental values of K_1 and K_2 in the Table 1 as $K_1=\dfrac{K_1+K_2}{2}=1.05$. The solution of (18), using the experimental parameter values in Table 1 and $K_1=1.05$, leads to the average concentrations in the Fig. 1 (lines).

Effect of the gas solubility

The procedure for determining the concentrations in (18) is repeated for different values of the Henry's number ($\chi=0.5, 1.5$) and the results are presented on the Figs. 5, 6.

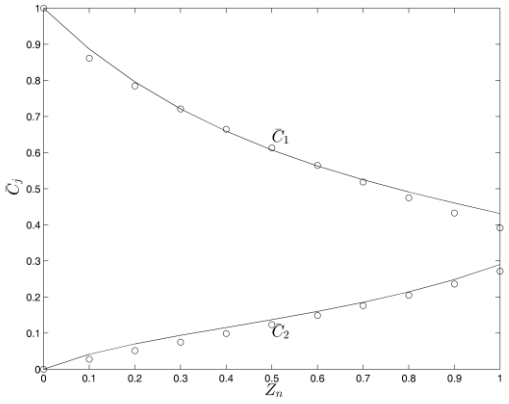

Fig. 5. Average concentration $\bar{C}_j\left(Z_j\right), j=1,2$ in the cases $\omega=0.5, K_1=1$: "theoretical" values $\bar{C}_j\left(Z_j\right)=\bar{C}_{jn}\left(Z_{jn}\right), j=1,2$ as solutions of (11) and (7) for different $Z_{jn}, n=0,1,...,9$ (points); $\bar{C}_j\left(Z_j\right), j=1,2$ as solutions of (16) for "experimental" values of $a_{j0}, a_{j1}, a_{j2}, j=1,2, K_1=1.05$ in the Table 1 (lines).

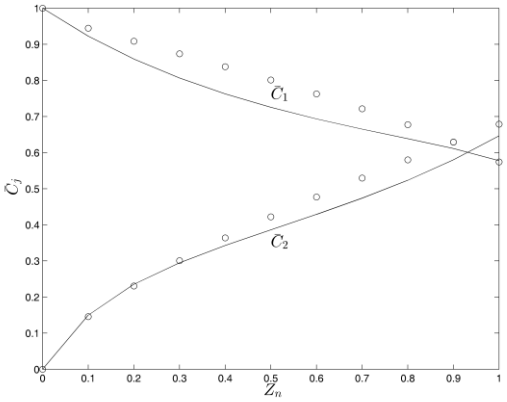

Fig. 6. Average concentration $\bar{C}_j\left(Z_j\right),\ j=1,2$ in the cases $\omega=1.5, K_1=1$: "theoretical" values $\bar{C}_j\left(Z_j\right)=\bar{C}_{jn}\left(Z_{jn}\right),\ j=1,2$ as solutions of (11) and (7) for different $Z_{jn}, n=0,1,...,9$ (points); $\bar{C}_j\left(Z_j\right),\ j=1,2$ as solutions of (16) for "experimental" values of $a_{j0}, a_{j1}, a_{j2},\ j=1,2, K_1=1.05$ in the Table 1 (lines).

Table 1. Parameters $a_{j0}, a_{j1}, a_{j2}, K_j,\ j=1,2,$ (physical absorption).

Parameters	"Theoretical" values	"Experimental" values
a_{10}	0.919	0.567
a_{11}	0.420	0.443
a_{12}	−0.427	−0.420
a_{20}	0.433	0.414
a_{21}	1.105	0.910
a_{22}	−0.632	−0.766
K_1	1	1.077
K_2	1	1.029

Chemical absorption

In the case of chemical absorption, from (9, 10, 16, 18) follow the models:

$$
\begin{aligned}
&U_{1n}\frac{dC_{1n}}{dZ_{1n}}=-K_1\left(C_{1n}-C_{2n}\right),\\
&0.1n\le Z_{1n}\le 0.1\left(n+1\right);\\
&U_{2n}\frac{dC_{2n}}{dZ_{2n}}=\omega K_1\left(C_{1n}-C_{2n}\right)-\mathrm{Da}\,C_{2n},\\
&0.1n\le Z_{2n}\le 0.1\left(n+1\right);\\
&Z_{jn}=0.1n,\quad \mathrm{C}_{jn}\left(R,Z_n\right)=C_{j(n-1)}\left(R,Z_{jn}\right);\\
&n=0,1,...,9;\quad j=1,2;\\
&Z_{10}=0,\quad \mathrm{C}_{10}\left(R,Z_{10}\right)\equiv 1;\\
&Z_{20}=0,\quad C_{20}\left(R,Z_0\right)=0.
\end{aligned}
\tag{28}
$$

$$
\begin{aligned}
&\left(a_{10}+a_{11}Z+a_{12}Z^2\right)\frac{d\bar{C}_1}{dZ_1}+\left(a_{11}+2a_{12}Z\right)\bar{C}_1=\\
&\qquad=-K_1\left(\bar{C}_1-\bar{C}_2\right);\\
&\left(a_{20}+a_{21}Z+a_{22}Z^2\right)\frac{d\bar{C}_2}{dZ_2}+\left(a_{21}+2a_{22}Z\right)\bar{C}_2=\\
&\qquad=\omega K_1\left(\bar{C}_1-\bar{C}_2\right)-\mathrm{Da}\,\bar{C}_2;\\
&Z_1=0,\quad \bar{C}_1=1;\quad Z_2=0,\quad \bar{C}_2=0.
\end{aligned}
\tag{29}
$$

The solution of (28) for a concrete processes ($\omega=1, \mathrm{Da}=1,2$) and a "theoretical" value of $K_1=1$ permits to be obtained the concentration distributions $C_{jn}\left(R,Z_{jn}\right),\ j=1,2$ for different $Z_{jn}=0.1\left(n+1\right),\ j=1,2, n=0,1,...,9$. This solution of (28) and (7) permit to be obtained the "theoretical" average concentration $\bar{C}_{jn}\left(Z_{jn}\right), Z_{jn}=0.1\left(n+1\right),\ j=1,2, n=0,1,...,9$ (the points in the Figs. 7, 8).

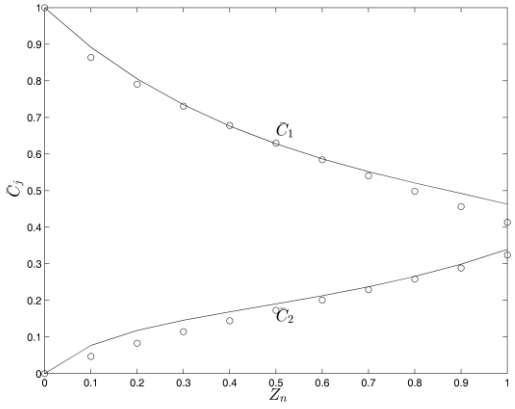

Fig. 7. Average concentration $\bar{C}_j\left(Z_j\right),\ j=1,2$ in the cases $\omega=1, \mathrm{Da}=1$: "theoretical" values $\bar{C}_j\left(Z_j\right)=\bar{C}_{jn}\left(Z_{jn}\right),\ j=1,2$ as solutions of (28) and (7) for different $Z_{jn}=0.1\left(n+1\right),\ j=1,2, n=0,1,...,9$

(points); $\bar{C}_j\left(Z_j\right),\ j=1,2$ as a solution of (29), using the "experimental" parameter values $a_{j0}, a_{j1}, a_{j2},\ j=1,2$ in the Table 1 (lines) and the "experimental" value of $K_1=1.05$.

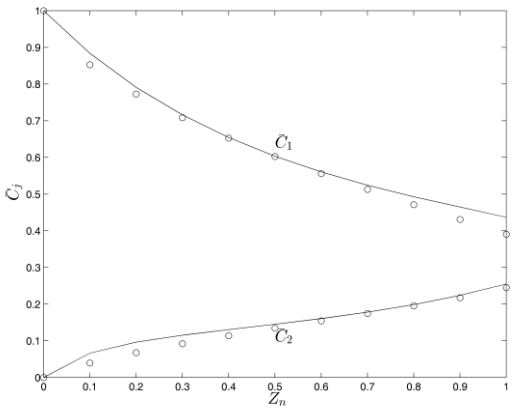

Fig. 8. Average concentration $\bar{C}_j\left(Z_j\right),\ j=1,2$ in the cases $\omega=1, \mathrm{Da}=2$: "theoretical" values $\bar{C}_j\left(Z_j\right)=\bar{C}_{jn}\left(Z_{jn}\right),\ j=1,2$ as solutions of (28) and (7) for different $Z_{jn}=0.1(n+1),\ j=1,2,\ n=0,1,...,9$ (points); $\bar{C}_j\left(Z_j\right),\ j=1,2$ as a solution of (29), using the "experimental" parameter values $a_{j0}, a_{j1}, a_{j2},\ j=1,2$ in the Table 1 (lines) and the "experimental" value of $K_1=1.05$.

CONCLUSIONS

The modeling of the counter-current processes in column apparatuses is complicated because the hydrodynamic models has to be presented in two-coordinate system (in a one-coordinate system one of the equations has no solution due to the negative Laplacian value). The presented numerical analysis of a counter-current absorption process in column apparatus shows, that the average concentration model, where the radial velocity components in the phases are equal to zero (in the cases of constant velocity radial non-uniformities along the column height), is possible to be used in the cases of an axial modification of the radial non-uniformities of the axial velocity components.

The use of experimental data, for the average concentrations in the gas and liquid phases at the column end in the cases of highly and lightly soluble gases, permits to be obtained the gas and liquid phases model parameters, related with the radial non-uniformity of the velocities. These parameter values permit to be used the average concentration models for different absorption processes modeling in counter-current columns (different values of the parameters ω, Da, i.e. different values of the column height, average velocities, chemical reaction rate constant and gas solubility).

REFERENCES

1. B. Boyadjiev, Chr. Boyadjiev, New models of industrial column chemical reactors. *Bulg. Chem. Communications*, **49**(3), 2017 (in press).).
2. B. Boyadjiev, Chr. Boyadjiev, A new approach for modeling of industrial absorption columns. 1.Co-current absorption processes. *Bulg. Chem. Communications*, **49**(3), 2017 (in press).
3. Chr. Boyadjiev, M. Doichinova, B. Boyadjiev, P. Popova-Krumova, "Modeling of Column Apparatus Processes", Springer-Verlag, Berlin Heidelberg, 2016, p. 313.
4. Chr. Boyadjiev, *Int. J. Heat Mass Transfer*, **49,** 796 (2006).
5. Chr. Boyadjiev, Theoretical Chemical Engineering, Modeling and simulation, Springer-Verlag, Berlin Heidelberg, 2010, p. 594.
6. M. Doichinova, Chr. Boyadjiev, *Int. J. Heat Mass Transfer*, **55,** 6705 (2012).
7. Chr. Boyadjiev, *J. Pure Appl. Mathematics: Advances and Applications*, **10** (2), 131 (2013).
8. B. Boyadjiev, M. Doichinova, Chr. Boyadjiev, *J. Eng. Thermophysics*, **24**(3), 247 (2015).

НОВИ МОДЕЛИ НА ИНДУСТРИАЛНИ КОЛОННИ АБСОРБЕРИ. 2. ПРОТИВОТОЧНИ АБСОРБЦИОННИ ПРОЦЕСИ

Б. Бояджиев, Хр. Бояджиев

Институт по инженерна химия, Българска академия на науките, ул. „Акад. Г. Бончев“, бл. 103, 1113, София България

Получена на 13 юли, 2017 г.; приета на 21 юли, 2017 г.

(Резюме)

Представен е теоретичен анализ на ефекта на радиалната неравномерност на скоростта при противоточни абсорбционни процеси в колонни апарати. Моделът на средните концентрации, където радиалната компонента на скоростта е нула (в случаите на постоянна радиална неравномерност на скоростта по височината на колоната), е използван в случаите на аксиално изменение на радиалната неравномерност на аксиалните компоненти на скоростите в газовата и течната фази. Проблемът на моделирането при противоточните потоци е усложнен, защото моделните уравнения трябва да се представят в две координатни системи (в една координатна система уравненията нямат решение поради отрицателната стойност на Лапласиана).

Използването на експериментални данни за средните концентрации в газовата и течната фази на изхода им от колоната, в случаите на силно и слабо разтворими газове, позволява да се намерят моделните параметри, свързани с радиалната неравномерност на скоростите. Стойностите на тези параметри са използвани за намиране на моделите на средните концентрации за моделиране на различни адсорбционни процеси в противоочни колони.

Bulgarian Chemical Communications, Volume 49, Number 3, (pp. 729 – 734) 2017

Application of modified carbon paste electrode with multiwall carbon nanotube as a simple and an effective catalyst for determination of cefixime in real samples

B. Norouzi*, S. Tajjedin

Department of chemistry, Qaemshahr Branch, Islamic Azad University, Qaemshahr, Iran

Received September 1, 2016; Revised March 2, 2017

In this research, a modified electrode has been produced by mixing of graphite and multiwall carbon nanotube (MWCNT-CPE). This modified electrode has a very good activity toward the cefixime electrooxidation in a phosphate buffer solution (pH=5). Under optimal experimental conditions, the peak current response increased linearly with cefixime concentration over the range of 3-12×10^3μM. The detection limit (3δ) of the method was 2.5μM. Therefore, this modified electrode was a simple, rapid and effective electrode to determine cefixime in pharmaceutical preparations.

Keywords: Cefixime, modified electrode, electrooxidation, real sample.

INTRODUCTION

Cefixime [6R-[6a,7b(Z)]]-7-[[(2-amino-4-thiazoyl) [(carboxymethoxy) imino]acetyl]amino] 3-ethenyl -8-oxo -5- thia-1-azabicyclo[4.2.0]oct-2-ne-2-carboxylic acid (Scheme 1)is a third generation cephalosporin. It is a useful antibiotic for the treatment of a number of bacterial infections such asotitis, sinusitis, tonsillitis and bronchitis. It is also used to treat typhoid fever. It is also a primary candidate for switch therapy owing to its very good efficacy and safety profile [1].

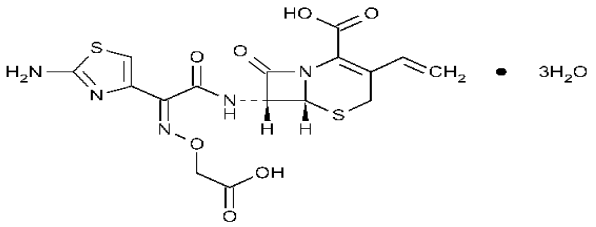

Scheme 1. Chemical structure of cefixime

Up to now, several analytical methods have been reported for the determination of cefixime including High-performance liquid chromatography (HPLC) [2,3], high-performance capillary electrophoresis [4], high-performance thin-layer chromatography (TLC) [5],liquid chromatography (LC)–tandem mass spectrometric [6] and various spectrophotometry methods [7]. In most of the reported methods, the selectivity and sensivity have been improved, but they are time-consuming, involving a large number of complicated pretreatment steps for analysis, and they require sophisticated and expensive instrumentation. In comparison with above methods, using of voltammetric methods has advantages such as simplicity, cheapness and increasing in sensitivity and selectivity by modifying electrodes.

On the other hand, carbon nanotubes (CNTs) are considered as a novel nanosized material playing a main role in the field of nanotechnology. They are widely used in materials sciences, physical and electronic fields for various applications [8-12]. Several unique properties of CNTs such as good electrical conductivity, extremely high mechanical strength and high chemical stability [13, 14] have been caused numerous investigations were focused on the studies of their properties and applications. In addition, the subtle electronic behavior of CNTs reveals that they have the ability to promote electron transfer reaction and have a high electrocatalytic effect when used as electrode materials [15, 16]. All these fa scinating properties make CNTs as a suitable candidate for the modification of electrodes [17, 18].

The goal of this study was to development of new, fully validated and rapid for the simple and direct determination of cefixime in drug dosage forms without any time-consuming extraction or separation steps prior to drug assay.

Our literature survey indicates that, there is no report about using of modified carbon paste electrode with MWCNT-CPE for determination of cefixime. In this work, we decided to use of this modified electrode for the aim of electrocatalytic oxidation of cefixime. Also, the study aimed at examining the applicability of this modified electrode to determine cefixime in some real samples.

EXPERIMENTAL

Reagents and materials

The solvent used in this work was twice distilled water. The electrolyte solutions were 0.1 M

* To whom all correspondence should be sent:
E-mail: norouz2020@yahoo.com

phosphate buffer in pHs of 2, 5, 7, 9,11and 13 respectively. Cefixime was prepared from Sari Pharmaceutical (Sari, Iran) and used without further purification. High viscosity paraffin (density = 0.88 g cm^{-3}) from Fluka (Sydney, Australia) was used as the pasting liquid for CPE. Graphite powder (particle diameter = 0.10 mm) from Merck and MWCNT (New Jersey, US) (with purity >95%, outer diameter 5-20 nm, inner diameter 2-6 nm, length 1-10 mm, number of walls 3-15, apparent density 0.15-0.35 g cm^{-3} from Nanostar Tech. Co., Tehran, Iran) were used as the working electrode substrates. To activate MWCNTs and remove any residual metals in the nano-structure, 0.5 g of MWCNTs plus 20 mL of concentrated acids (H_2SO_4/HNO_3: 3/1) were mixed in a 25-mL flux and then the mixture was refluxed for 8 h. Then, the MWCNTs were separated from the mixture and washed with 50 mL doubly distilled water, centrifuged (3500 rpm) and dried at room temperature. All other reagents were analytical grade.

Apparatus

Electrochemical experiments were performed with potentiostat/galvanostat μ-Auto lab type system (Eco Chemie BV, Netherlands), general purpose electrochemical system (GPES). The voltammetric measurements were performed in a three-electrode cell using the modified CPE as working electrode, a Ag | AgCl | KCl (3 M) from Azar electrode (Urmia, Iran) as reference electrode and a platinum rod from Azar electrode (Urmia, Iran) as counter-electrode. All experiments were carried out at room temperature. No action was taken to remove oxygen from solutions.

The electrode modification

A mixture of graphite powder (0.99 g) plus MWCNT (0.01 g) were blended by hand mixing with a mortar and pestle. Using a syringe, the amount of paraffin was added to the mixture and mixed well until a uniformly wetted paste was obtained. The resulting paste was then inserted in thebottom of a glass tube (internal radius: 1.7 mm). The electrical connection was implemented by a copper wire lead fitted into the glass tube. A fresh electrode surface was generated rapidly by extruding a small plug of the paste out of the tube and smoothing the resulting surface on white paper until a smooth shiny surface was observed.

RESULTS AND DISCUSSION

Oxidation of cefixime at MWCNT-CPE

Preliminary experiments were carried out to compare electrochemical behavior of cefixime in phosphate buffer of pH=5 at CPE and MWCNT-CPE by cyclic voltammetry. Fig. 1 shows cyclic voltammograms recorded at CPE and MWCNT-CPE in the absence and the present of cefixime. No cathodic and anodic peaks were observed in the investigated potential range (0.2 to +1.2 V) on CPE but at the surface of MWCNT-CPE, only an anodic peak was observed at about 0.82 V (more than 380 mV negative shift compared to the observed solvent oxidation wall at CPE).As it is obvious, the cefixime signal is sensitive and occurs at a much lower over potential than on CPE. These results show that MWCNT-CPE reduces the over potential of cefixime oxidation and in fact imparts electrocatalytic activity for cefixime determination.

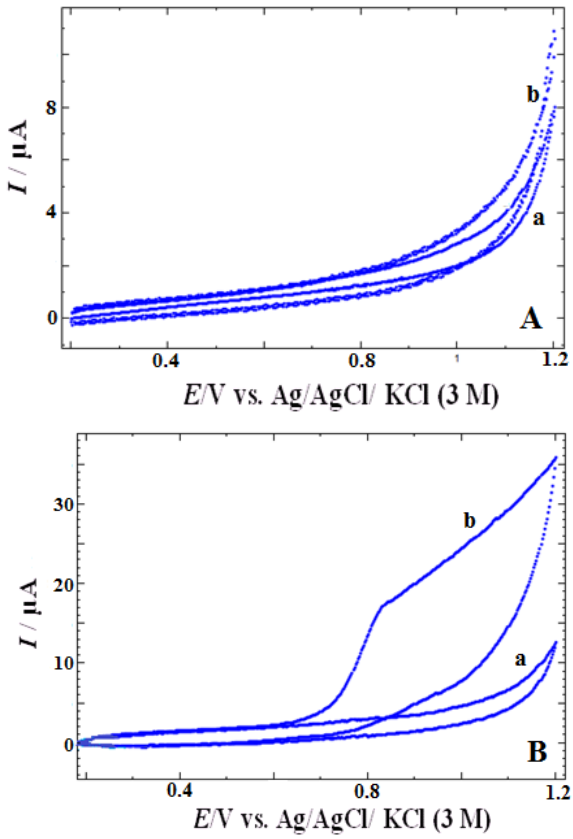

Fig. 1. Cyclic voltammograms of (A) CPE and (B) MWCNT-CPE in 0.1 M phosphate buffer solution (pH=5), in the absence (*a*) and presence of 1 mM cefixime (*b*), Scan rate = 20 mV s^{-1}.

Optimization of electrode variables for efficient performance of MWCNT-CPE towards cefixime oxidation

Effect of different percents of MWCNT to graphite

Figure 2 shows the effect of the paste composition on the resulting voltammetric response. MWCNT-CPE with different percents of MWCNT to graphite (0.5, 1, 5, 10, 15 and 25%) was studied in the absence and the presence of cefixime. There is an increase in the oxidation current peak density with increasing of percents of MWCNT to graphite through a maximum at 1%. Based on Figure 2, as the amount of MWCNT is increased more than 1%, the current value decreases. However, large surface areas can cause increments in background current, which might decrease the resulting current values as in the case of our work in agreement with previous works [19-21]. As a result, further studies were conducted using a 1% MWCNT to graphite.

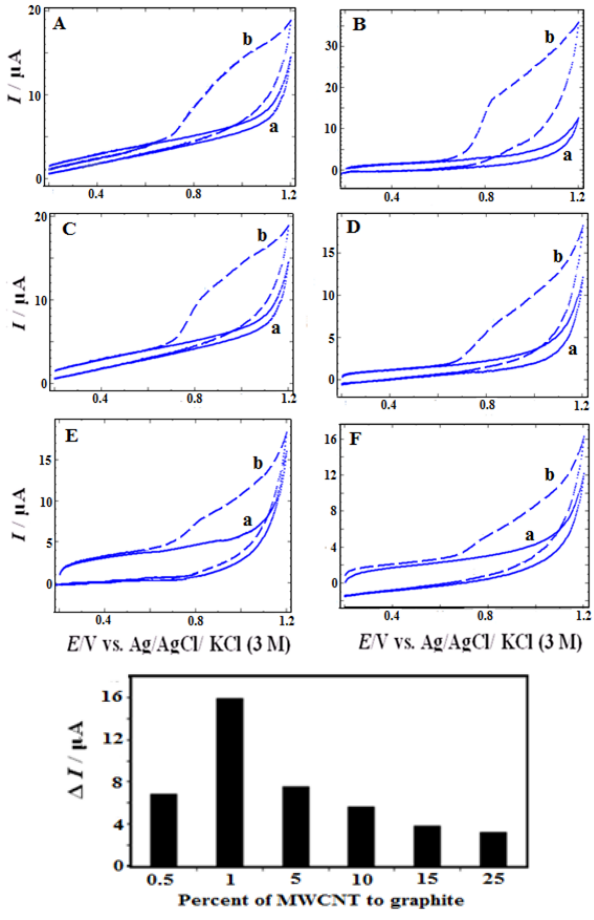

Fig. 2. Cyclic voltammograms of different percents of MWCNT to graphite (A) 0.5%, (B) 1%, (C) 5%, (D) 10%, (E) 15% and (F) 25% at the MWCNT-CPE in (a) absence and (b) in presence of 1 mM cefixime and in 0.1 M phosphate buffer solution (pH=5) at a scan of 20 mV s^{-1}, Inset: Comparison of electrocatalytic currents for the oxidation of cefixime observed on MWCNT-CPE.

Effect of pH

We have tested the electrocatalytic activity of MWCNT deposited on CPE against cefixime electrooxidation in the buffered solutions with various pHs in the range of 2–13 (Fig. 3).For all of them, the modified electrode shows electrocatalytic activity. However, higher electrocatalysis peak currents are observed at pH=5 (the value of Δ*I* is the most of others).Based on such investigations, a buffered solution of pH=5 was chosen as an optimum condition in order to obtain the best sensitivity in all voltammetric measurements.

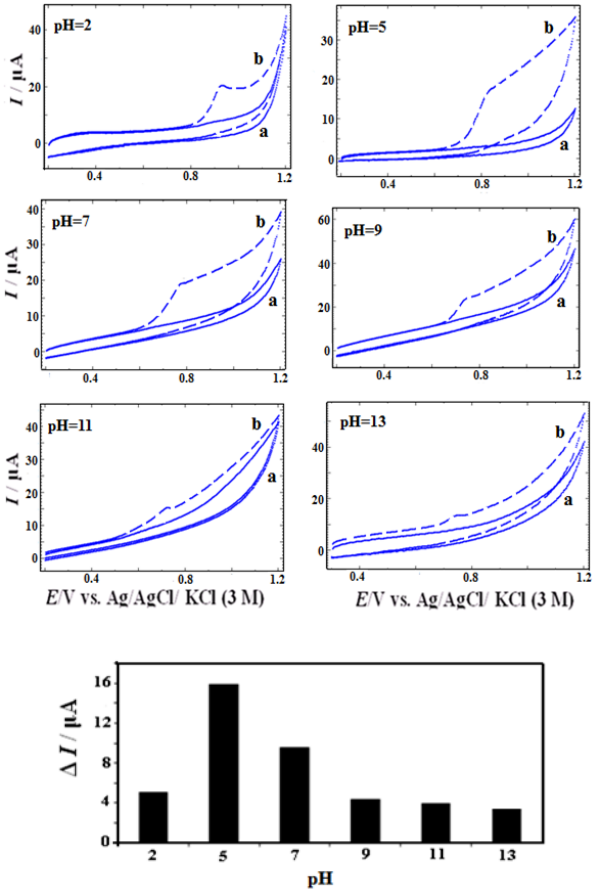

Fig. 3. Cyclic voltammograms of MWCNT-CPE in different pH solutions, in the absence (a) and the presence of 1 mM of cefixime (b) at scan rate of 20 mVs^{-1}.

Effect of cefixime Concentration

Figure 4 shows the effect of cefixime concentration on the cyclic voltammograms of the MWCNT-CPE. As can be seen from this figure, the height of the anodic peak increases with increasing in cefixime concentration. The characteristic shape of CV in this potential region indicates that the signal is due to the oxidation of cefixime. The catalytic peak current is proportional to the concentration of cefixime in the range of 0.003 to 12mM. The linear regression equation is I (µA) = 5.939C_{cefixime} (mM) + 11.68 (R^2 = 0.99). The detection limit calculated

from the calibration graph was 0.0025mM when the signal to noise ratio was 3.

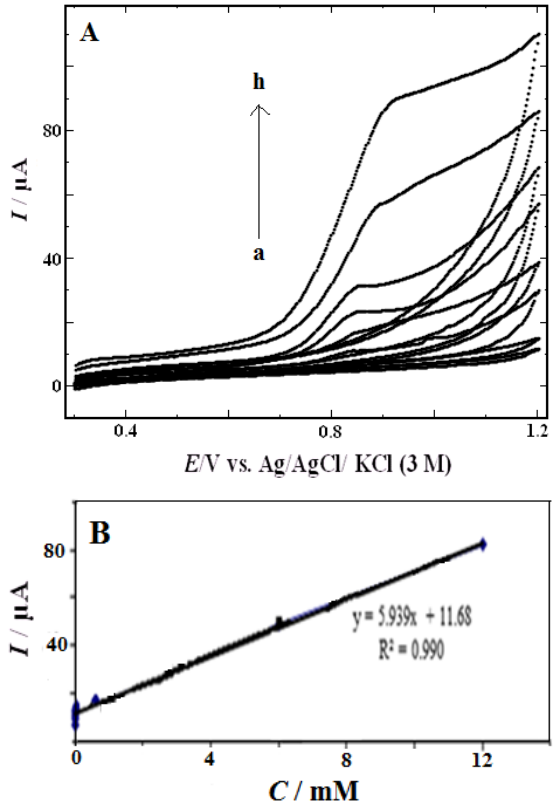

Fig. 4. (A) Cyclic voltammograms of MWCNT-CPE in 0.1 M phosphate buffer solution (pH=5) containing 0.003, 0.008, 0.01, 0.02, 0.04, 0.6, 6 and 12 mM of cefixime from a to h at 20 mV s^{-1} (B) Plot of catalytic current *vs* cefixime concentration.

Real sample analysis

In order to examine the applicability of the proposed method, we tested the determination of cefixime in commercial tablet sample using the standard addition method for preventation of any matrix effect under the optimized conditions. All samples were diluted with phosphate buffer solution (pH=5) and then appropriate amounts of cefixime standard samples were transferred to the electrochemical cell for the determination of it. There is a linear relationship between the I_{pa} versus cefixime concentration. It was found that the drug concentrations determined using this method is in good agreement with the reported values. The value of experimentally determined drug and the declared value in tablet are tabulated in Table 1.

Effect of scan rate

The dependence of the anodic peak current response on the potential scan rate during the electrocatalytic oxidation of cefixime was examined employing CV by varying the scan rate from 10 to 1000 mV s^{-1} (not shown). Results indicated that there is a linear relationship between the anodic peak current (I_{pa}) and the square root of the scan rate ($v^{1/2}$) in the scan rates of 10–1000 mV s^{-1} for cefixime (I_{pa}=1.033 $v^{1/2}$–0.019). This indicates that the oxidation of cefixime at MWCNT-CPE is a diffusion-controlled process.

Chronoamperometric studies

We employed chronoamperometric method for the investigation of electrochemical processes at MWCNT-CPE. Fig. 5 represents the current–time profiles obtained by setting the working electrode potential at 850 mV for various concentrations of cefixime. Plotting of the net current as a function of the inverse square root of time, gives a linear relationship (Fig. 5B), resulting in a diffusion controlled process. The diffusion coefficient of cefixime can be obtained by using the slope of this straight line, according to Cottrell equation [22]:

$$I = nFAD^{1/2}C^{*}\pi^{-1/2}t^{-1/2} \qquad (1)$$

Table 1. Determination of cefixime in pharmaceutical preparation using MWCNT-CPE

Sample	Amount Labeled / g	Amount Founded / g	Recovery %	RSD %, n=5
Cefixime tablet	0.4	0.422	105.5	2.5

Table 2. Comparison of performances of some electrodes in determination of cefixime

Electrode	Modifier	pH	LDR /µM	LOD/ µM	Reference
CPE	Gold nanopartcle	3	1.2-200	1	[23]
GC	MWCNT/$NiFe_2O_4$	8	1.8-600	1.74	[24]
SPGE[a]	Gold nanopartcle	2.6	10-1000	———	[25]
HMDE[b]	———	2.6	9.85-50.4	9.62	[26]
CPE	MWCNT	5	3-12000	2.5	This work

[a]Screen printed gold electrode
[b]Hanging mercury dropping electrode

Where D is diffusion coefficient and C^* is the bulk concentration of cefixime. The value of diffusion coefficient of cefixime was found to be 2.48×10^{-5} $cm^2\ s^{-1}$.

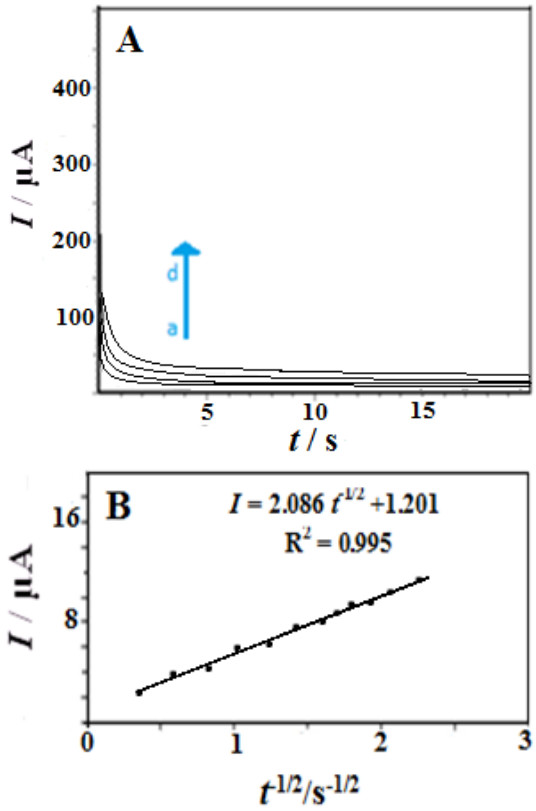

Fig. 5.(A) Chronoamperograms of MWCNT-CPE in 0.1 M phosphate buffer solution (pH=5) with different concentrations of cefixime: (a) 0, (b) 0.1, (c) 0.6 and 6 mM (B) Plot of I *vs.* $t^{-1/2}$

Stability of the modified electrode

The long-term stability of MWCNT-CPE was also studied by storing the electrode for 2 weeks at room temperature. The current response was only decreased by 0.5% after two weeks. It confirms the stability of modified electrode.

CONCLUSION

The study has described successfully the modification of CPE with MWCNT. This modified electrode acts as an active suitable catalyst for the oxidation of cefixime. At the surface of this electrode, the operating potential can be reduced more than 380 mV compared to CPE. The oxidation currents are directly proportional to cefixime concentration in a wide range, which illustrates the potential applications of this type of electrode for the anodic determination of cefixime. Table 2 compared the proposed electrode for cefixime determination with electrodes reported in literatures. As shown, the proposed electrode is comparable with other electrodes. Also, the proposed method provides a fast, sensitive and simple approach to the determination of cefixime in real samples.

REFERENCES

1. J. Hamilton-Miller, *Chemotherapy*, **44**, 24 (1998).
2. L.O. White, D.S. Reeves, A.M. Lovering, A.P. MacGowan, *J. Antimicrob. Chemother.*, **31**, 450 (1993).
3. G.H. Rolando, N.P. Lauro, S.M. Laritza, L.L. Miguel, H. Joseph, *J. Liq. Chromatogr.*, **24**, 2315 (2001).
4. S. Honda, A. Taga, K. Kakehi, S. Koda, Y. Okamoto, *J.Chromatogr.*, **590**, 364 (1992).
5. S. Eric-Jovanovic, D. Agbada, D. Zivanov-Stakic, S. Viadimirov, *J. Pharm. Biomed. Anal.*, **18**, 893 (1998).
6. F. Meng, X. Chen, Y. Zeng, D. Zhong, *J. Chromatogr. B*, **277**, 819 (2005).
7. I.F. Al-Momani, *J. Pharm. Biomed. Anal.*, **25**, 751 (2001).
8. P.M. Ajayan, *Chem. Rev.*, **99**, 1787 (1999).
9. S.S. Wong, E. Joselevich, A. Woolley, C. Cheung, C. Leiber, *Nature*, **394**, 52 (1998).
10. W.A. De Heer, A. Chatelain, D.A. Ugarte, *Science*, **270**, 1179 (1995).
11. S. Tans, A. Verschueren, C. Dekker, *Nature*, **393**, 49 (1998).
12. G.L. Che, B.B. Lakschmi, E.R. Fisher, C. R. Martin, *Nature*, **393**, 346 (1998).
13. J. Wang, *Electroanalysis*, **17**, 7 (2005).
14. G.G. Wildgoose, C.E. Banks, H.C. Leventis, R.G. Compton, *Microchim. Acta*, **152**, 187 (2006).
15. G. Guo, F. Zhao, F. Xiao1, B. Zeng, *Int. J. Electrochem. Sci.*, 4, 1365 (2009).
16. J. Chen, Z. Lin, G. Chen, *Anal. Bioanal. Chem.*, **388**, 399 (2007).
17. A.B. Moghaddam, M. Kazemzad, M.R. Nabid, H.H. Dabaghi, *Int. J. Electrochem. Sci.*, **3**, 291 (2008).
18. G. Hu, Y. Ma, Y. Guo, S. Shao, *Electrochim. Acta*, **53**, 6610 (2008).
19. B. Perez,M. Pumera,A. Merkoci,S. Alegret. *J. Nanosci. Nanotech.*, **5**, 1694 (2005).
20. M. Zhang, A. Smith, W. Gorski., *Anal. Chem.*, **76**, 5045 (2004).
21. U. Anik, M. Cubukcu, *Turk. J. Chem.*, **32**, 711 (2008).
22. A.J. Bard, L.R. Faulkner, *Electrochemical Methods*, John Wiley and Sons, NewYork, 2001.
23. A. Afkhami, F. Soltani-Felehgari, T. Madrakian, *Electrochim Acta*, **34**, 618 (2013).
24. A.A. Ensafi, A.R. Allafchian, *Colloids Biointerfaces*, **102**, 687 (2013).
25. M. Asadollahi-Baboli, A. Mani-Varnosfaderani, *Measurement*, **47**, 145 (2014).
26. R. Jain, V.K. Gupta, N. Jadon, K. Radhapyari, *Anal. Biochem.*, **407**, 79 (2010).

ПРИЛОЖЕНИЕ НА ЕЛЕКТРОД С ВЪГЛЕРОДНА ПАСТА, МОДИФИЦИРАН С МНОГОСТЕННИ ВЪГЛЕРОДНИ НАНОТРЪБИ КАТО ПРОСТ И ЕФЕКТИВЕН КАТАЛИЗАТОР ЗА ОПРЕДЕЛЯНЕТО НА ЦЕФИКСИМ В РЕАЛНИ ПРОБИ

В. Нороузи *, С. Таджедин

Департамент по химия, Клон Каемшахр, Ислямски университет „Азад“, Каемшахр, Иран

Получена на 1 септември, 2016 г.; коригирана на 2 март, 2017 г.

(Резюме)

В това изследване е приготвен модифициран електрод чрез смесването на графит с многостенни въглеродни нанотръби (MWCNT-CPE). Този модифициран електрод има много добра активност спрямо окислението на цефиксим в разтвор на фосфатен буфер (pH = 5). При оптимални експериментални условия максималният ток нараства линейно с концентрацията на цефиксим в интервала 3-12×10^3 μM. Границата на чувствителност (3δ) на метода е 2.5 μM. Затова използването на този електрод позволява просто, бързо и ефективно определяне на цефиксим във фармацевтични препарати.

Bulgarian Chemical Communications, Volume 49, Number 3, (pp. 735 – 741) 2017

Improvement of biodegradability of explosives using anaerobic- intrinsic bioaugmentation approach

M.M. Amin[1], H. Khanahmad[2], F. Teimouri[3]*, M. Sadani[4], M.A. Karami[5], I. Rahimmanesh[2]

[1]*Environment Research Center, Research Institute for Primordial Prevention of Non- communicable disease, Isfahan University of Medical Sciences, Isfahan, Iran, and Department of Environmental Health Engineering, School of Health, Isfahan University of Medical Sciences, Isfahan, Iran*
[2]*Department of Genetics, School of Medicine, Isfahan University of Medical Sciences, Isfahan, Iran*
[3] *Isfahan University of Medical Sciences, Isfahan, Iran. Health Faculty, Yazd University of Medical Sciences, Yazd, Iran.*
[4]*Shahid Beheshti University of Medical Sciences, Tehran, Iran.*
[5]*Lorestan University of Medical Sciences, Khoramabad, Iran.*

Received June 28, 2016; Revised April 12, 2017

A successful anaerobic intrinsic bioremediation (bioaugmentation) was carried out on 2,4,6-trinitrotoluene (TNT) and Pentaerhytritol tetranitrate (PETN) contaminated soil, using indigenous bacteria. Two soil pans were enriched by sewage sludge and one pan was mixed by monorhamnolipid biosurfactant both of which are economically suitable substrates for anaerobic in situ explosive bioremediation. Preliminary concentrations of TNT and PETN were 1000 and 200 mg/kg. The results of this study showed that in order to increase the explosives degradation with more resistant to biodegradation such as PETN, the usage of biosurfactant could be effective. Inoculation of indigenous bacteria had a significant effect on TNT and PETN remediation efficiency and increased them to 99.1% and 91% in the presence of biosurfactant. Seven indigenous strains were identified as *Planomicrobacterium flavidum, Pseudomonas auroginosa, Entrobactor asburiae, Azospirillium, Rhizobium, Methylobacterium and Pseudomonas denitrificant* strains. It is logical that these isolates may have potential for TNT and PETN degradation. Monorhamnolipid might be effective in the improvement of explosives degradation due to impact on the cell membrane of bacteria. The results of this study have shown that intrinsic bioremediation has the potential to reduce the time and costs for in situ explosive bioremediation.

Keywords: Bioaugmentation - intrinsic bioremediation - 2,4,6-trinitrotoluene - Pentaerhytritol tetranitrate

INTRODUCTION

The large scale manufacturing and use of a variety of synthetic chemicals continuously pollutes soil, water, and air which have direct or indirect adverse impacts on our and animals' health[1]. They have significant concerns such as carcinogenicity and potential for bioaccumulation in living systems [2]. According to the estimated annual production of 108 tones, nitro-aromatics are considered as important industrial chemicals [3]. Environmental pollution by explosive residues from TNT and NG is widespread and causes long term health problems. Average contaminated sites may contain more than 10 g of TNT per kg in soil and 100 mg/l in water. TNT and metabolites have high potential for toxicity and mutation on prokaryotes and eukaryotes. It has been estimated that 3200 sites in Germany require environmental management [1]. Toxicity of Explosives is exhibited by symptoms such as irritation, methemoglobinaemia, disturbed heart function, kidney trouble and malfunction of vascular system [2]. Exposure to TNT is known to cause rashes, mucus and blood disorders. Toxic effects such as liver damage and anemia have been reported by workers who worked in manufacturing and handling of TNT [4]. The harmless concentration of TNT in the soil is <30mg/kg [5]. PETN is widely used as a powerful explosive and is classified as a great concern by DoD in the U.S.A. Short term exposure to PETN may affect the cardiovascular system, resulting in a decrease in blood pressure. PETN is known to be "toxic to aquatic organisms" by U.S DoD because of its wide spread use and the potential environmental impact [6]. Several physico-chemical methods [7-11] are available for explosive remediations from aqueous solutions. Some methods such as incineration are currently used, but are expensive and may lead to the formation of by-products that are more toxic than the primary compounds. Biological methods are more cost-effective and reduce toxicity of the soil due to the enzymes produced by specific bacteria [12]. Bioremediation has been considered as a valuable option for remediation of explosive-contaminated soil. Natural bacteria are present in the environment [13] and have an exceptional ability to exploit various compounds for their growth. Most organisms contain redox enzymes, which are able to transform nitro-aromatics to amines. Several enzymes have roles in biodegradation of explosives, but nitro-reductase enzymes are very important since they help with the detoxification of nitro-aromatic

* To whom all correspondence should be sent:
E-mail: f_teimouri@hlth.mui.ac.ir

compounds [14]. However, enzymes for complete breakdown of nitro-compounds are rare [3]. It seems that anaerobic metabolism of nitro-aromatics may provide a treatment for contamination with nitro-compounds, while most of the aerobic studies showed only the modification of these compounds [15]. The biodegradation of TNT under anaerobic conditions occurs by reduction of the nitro group to form the corresponding mononitroso, monohydroxylamino and monoamino derivatives. These monoamino derivatives were further transformed into diamino and triamino derivatives through a reductive mechanism [16-19]. Also, other studies have shown that denitrifying bacteria are able to reduce PETN to precursor derivates [20]. Overall, the general goals for bioremediation are to enhance indigenous bacteria activities by the addition of nutrients or aeration (biostimulation) or the addition of microorganisms (bioaugmentation). Bioaugmentation has proven for remediation of PAHs in sediments with poor intrinsic degradation potential [21]. Hence, for efficient and complete biodegradation, solubilization of hydrocarbons with biosurfactants prior to bioaugmentation is advantageous [22]. Many studies related to bioaugmentation have been based on the use of certain species which were isolated from contaminated soils [23]. Although isolated bacteria can degrade explosives, most authors accept the importance of the growth of natural consortia rather than select specific strains. The latter may survive under laboratory conditions, but usually could not survive or grow in full scale conditions [8]. Nowadays, more than 10000 km^2 of land area in the border provinces of southern-southwest and west of the country of Iran are affected by pollution caused by Iran-Iraq war. Despite the fact that we are over three decades past the war, large areas are not suitable for human applications. Khuzestan is one of the provinces which were repeatedly invaded by Iraqi army and in which soil contamination is higher than other cities. Geographic and climatic characteristics show that most of these areas are located in the wet zone, low rainfall and high humidity [24].

In this study, the natural explosive degrading bacteria in the soil were isolated and inoculated into the soil. The advantages of this method may be that the natural bacterial species in the soil do not change. Considering that a large area of the country is contaminated with explosives, another main purpose of this study was to perform the least expensive and most efficient way so that it can be offered on a large-scale as in situ bioremediation. Characterization of explosives degradation bacterial community, isolation and the influence of dominant indigenous bacteria inoculation on degradation rates (bioaugmentation effect), were the other objectives that were evaluated in this study.

EXPERIMENTAL

Biosurfactant

Monorhamnolipid biosurfactant was purchased from the National Institute for Genetic Engineering and Biotechnology, Institute of Chemistry and Chemical Engineering, which was produced through fermentation by P. aeruginusa strains. The concentration of used rhamnolipid in this study was 120 mg/l [25].

Chemical analysis

TNT and PETN were analyzed using an HPLC system, a Model 486 UV detector and a Nova pak C_{18} guard column. The analytical column was an ODS_2 optimal column (25cm × 4.6 mm id, 5μm) from capital HPLC. The sample was injected into the HPLC system with the following condition: Acetonitrile- water mixture (75:25 v/v) as the mobile phase at a flow rate of 1.0 ml/min. Injection volume for all samples was 20 μl and the wavelength for the UV detector was 210 nm and 230 nm for PETN and TNT detections, respectively. All trace analysis quality or gradient grade solvents were purchased from Merck Company.

Soil sampling, preparation and extraction

After screening, the soil was manually contaminated with explosives. TNT concentrations in the soil were 1000 mg/kg and PETN concentration was 200 mg/kg. The soil had a pH of 6.4. Sampling of the soil was taken periodically during the experiment. Grab sampling was taken from top 3 cm of soil and dried before analyses. Sample preparation was performed according to EPA method 8330. Total extractable explosives were determined by drying 10 g of the homogenized soil pan in ambient air and transferring it to an Erlenmeyer. Acetonitrile (20 ml) was added and vial was placed in a shaker for 18 hr. Then 5 ml of supernatant was filtered through PTFE filter and ultimately explosives were quantified by the HPLC system [26].

Preparation of anaerobic soil pans

Three soil pans were used in this experiment. A pan set consisted of a plastic pan (30cm × 20 cm × 15cm in height) that was placed in a slightly larger pan. The bottom of smaller pans was perforated with 2-mm- diameter holes spaced 8 cm apart to allow for the drainage of fluids. Fluid drainage was recycled

to each pan again. Each small pan contained 4 kg of contaminated soil. In order for soil amendment to occur, screened saw dust was used (soil/saw dust ratio was 1:1). Water was added not only for supplementing the moisture but also for creating and keeping the anaerobic condition, once a week (to maintain a free water surface 2 cm above the surface of the soil).

Three treatments that were investigated in this study include:

1- A pan consisted of contaminated soil + activated sludge as an enrichment for the soil (soil/sludge ratio was 1:0.25) which was only added at the startup of the pan operation.

2- A pan consisted of contaminated soil + activated sludge as an enrichment for the soil (soil/sludge ratio was 1:0.25) + monorhamnolipid biosurfactant in which the two latter (sludge and biosurfactant) were only added at the beginning of pan operations.

3- A pan served as the control in which no substrate was added and explosives were used as the main substrates.

Total DNA extraction

In this study, the boiling method for extraction of DNA was used, because a number of studies show that by performance of this method, good quality of DNA could be obtained. Isolated colonies were grown on nutrient agar plated, mixed with sterile 100 µl Milli – Q water and boiled for 15 min. Then, the solution was centrifuged at 13000 rpm for 10 min and its supernatant was used as the DNA template for PCR analyses [12].

Amplification of DNA

After extraction of total DNA from the soil, bacterial 16srDNA was amplified with universal eubacterial primers that consist of F27 (5′-AGAGTTTGATCMTGGCTCAG-3′) and R1492 (5′- TACGGYTACCTTGTTACGACT-3′), which are targeted to universally conserved regions and permit the amplification of an approximately 1,500-bp fragment [27]. PCR reactions were carried out in 25 µl of microtubes consisting of 1µl of each primer, 2.5 µl 10 × buffer, 1µl $MgCl_2$, 0.5 µl dNTPs, 17.5 µl distilled sterile H_2O, 0.5 µl Taq DNA polymerase and 1 µl of extracted DNA. Thermocycling conditions were as follows: samples were heated at 95ºC for 5 min (1 cycle), 94ºC for 30 sec, 58ºC for 30 sec, 72ºC for 1 min (30 cycles) and 72ºC for 5 min. PCR products were visualized on a 1% agarose gel and quantified with an appropriate molecular weight marker.

Bioaugmentation experiments

In this stage of experiment, natural floras (dominant indigenous degrading bacterial population), which have already been isolated and identified by the PCR method were used. These microorganisms were multiplied under sterile conditions by nutrient broth and incubated (37ºC for 24 hr). Then, optical density was measured by spectrophotometer and inoculated to the anaerobic pans. In order to maintain anaerobic conditions, water was added to each pan once a week.

RESULTS AND DISCUSSION

Effect of Intrinsic Bioaugmentation on TNT and PETN transformation rates

First, microorganism adaptation was performed about three months (TNT and PETN concentrations were 200 and 50 mg/kg respectively). After the degradation rate became constant, the operation of the pans was performed by increasing the TNT and PETN concentrations to 1000 and 200 mg/kg of soil. Figure 1 and 2 shows the effect of bioaugmentation of indigenous bacteria on TNT and PETN degradation rates.

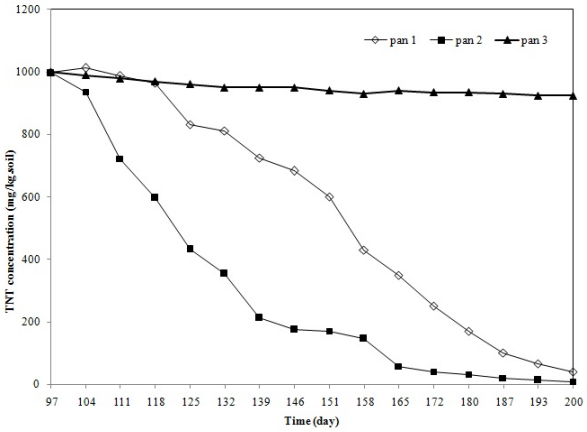

Fig. 1. Effect of intrinstic bioaugmentation on TNT degradation rate

As shown in Figure 1, with the passage of time, TNT degradation rate was decreased and became almost constant. The maximum degradation efficiency was about 40% and 83% in pans 1 and 2, respectively. On the other hand, TNT concentration decreased to 543 and 162 mg/kg in pans 1 and 2. Also, PETN concentration decreased to 142 and 63 mg/kg in pans 1 and 2, respectively (Fig.2).

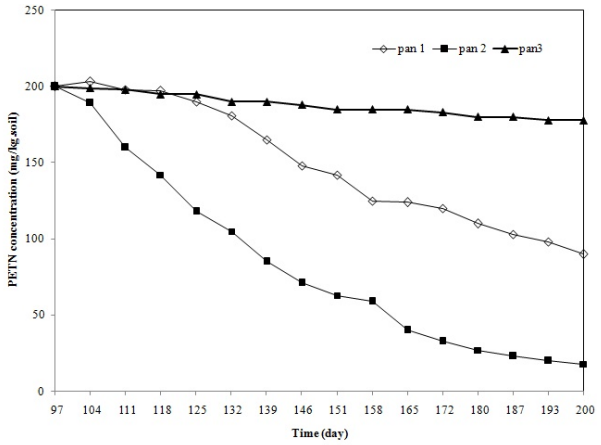

Fig. 2. Effect of intrinstic bioaugmentation on PETN degradation rate

However, as Figure 2 shows, according to the chemical structure, PETN has shown greater biological resistance and its decomposition rate was lower than TNT decomposition rate. After two months of pan operations, degradation rates were relatively constant. Then, bioaugmentation effect was investigated by the inoculation of dominant degrading bacteria that have already been identified by the PCR method. After bioaugmentation, TNT concentration decreased to 40 and 9 mg/kg with the removal percentage equivalent to 96% and 99.1% in pans 1 and 2, respectively (Fig.1). Also, bioaugmentation had a positive effect on PETN degradation rate, as PETN concentration decreased to 90 and 18 mg per kg, the equivalent of 55 and 91 percent in pans 1 and 2, respectively (Fig.2) . In general, the results show that PETN degradation rate is less than TNT degradation. However, inoculation had a positive effect on two explosive degradation, especially in the second pan. It can be interpreted that more degradation rate in pan 2 is related to the presence of monorhamnolipid biosurfactant, since it would be able to increase bioavailability of microorganisms to pollutants and also could be able to change cell membrane permeability of bacteria. This results is confirmed by Muter et al. [23] who reported that bioaugmentation has a significant effect on soil samples with high initial concentrations of TNT (500 mg/kg), in particular for soil samples amended with 50% and 100% nutrient solutions. Also, Elis et al. [28] demonstrated the value of bioaugmentation when evidence indicates the absence of organisms which are capable of complete conversion of cis-DCE to ethene. Also, Zhang and Miller [29] reported that 300 mg/l rhamnolipid increased the mineralization of octadecane about 4 times more than initial value. The results obtained by Manickam et al. [30] confirmed that the halogenated compounds biodegradation efficiencies were increased by 30-50% in 2 days compared to degradation in the absence of biosurfactant. In the control pan (pan 3), the TNT and PETN concentrations remained around 1000 and 200 mg/kg throughout the study indicating the removal of TNT in the soil was biological and was not a chemical or physical process.

Nitrite release from TNT and PETN transformations

Nitrite measurement was performed to detect the release of nitro-group from TNT and PETN during demineralization. The results of nitrite assays are presented in Figure 3. As can be seen, before the microbial inoculation, native soil bacteria were able to use TNT and PETN as the only sources of nitrogen that have been responsible for the disappearance of explosives in the soil.

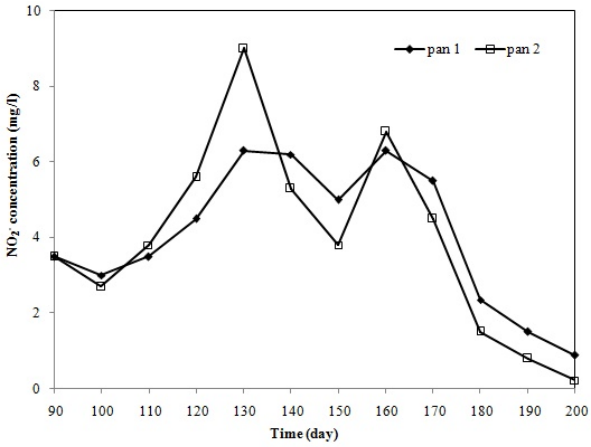

Fig. 3. Nitrite concentrations released during TNT and PETN demineralization

The first step in anaerobic metabolism of nitro-aromatics is reduction. Then, deamination occurs, which removes all nitro groups linked to the ring. Finally, toluene and ammonia form as end products. Of course, toluene could be degraded by denitrifiers or other microorganisms [15]. After inoculation of dominant bacterial populatioin, nitrite concentrations increased and then decreased to 0.89 and 0.22 mg/l in pans 1 and 2, respectively. Nitro-explosives are typically biodegraded by one or more known mechanisms. One or more nitro groups can be reduced to hydroxylamino groups and then N-N bond may be cleaved, releasing a nitro group to nitrite ion as a final product [1]. Nitrite ion is an unstable form of nitrogen and may quickly be converted into ammonium ion and ammonia. This result also confirmed the role of biosurfactant in the improvement of the degradation process due to the higher nitrite concentration in pan 2 than in pan 1. Also, the inoculated bacterial population had a major responsibility for mineralization of these

compounds. This result is in accordance with those obtained by Boopathy and Kulpa [19] that demonstrated certain Pseudomonas sp. can use TNT as a nitrogen source through the removal of nitrogen nitrite from TNT and the further reduction of the released nitrite to ammonium which is incorporated into carbon skeleton. Wittch et al. [see 4] 333noted that unstable reduced derivatives of TNT produced by microorganisms have been found to release nitrite by rearomatization and/or condensation.

Identification of Isolates

PCR analysis has become one of the most popular technologies for the biodiversity assessments. In this study, PCR technology was used to identify the bacterial community structure in the system after 150 days of adaptation and operation. Visualized gel picture of a 16 S rDNA picture for TNT and PETN degrading isolates have been shown in Figure 4.

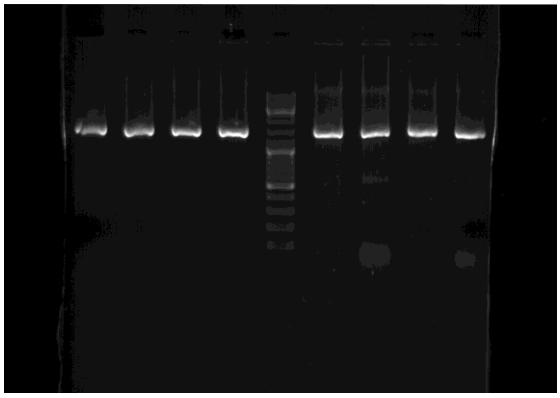

Fig. 4. Visualized gel picture of a 16 S rDNA picture for TNT and PETN degrading isolates

As seen in Figure 4, all targeted DNA had amplification of an approximately 1,500-bp fragment. Seven bacterial strains were isolated from anaerobic pans. In pan 1, two bacterial isolates were capable of growing and were identified as Planomicrobacterium flavidum strain and Pseudomonas auroginosa sp.JB2. Differential experiments show that anaerobic pan 2 had the highest number of bacterial strains. In pan 2, five bacterial isolates were identified as Entrobactor asburiae, Azospirillium, Rhizobium, Methylobacterium and Pseudomonas denitrificant strains**.** Bacteria isolated in this study show that indigenous bacteria are capable of using TNT and PETN as sole sources of nitrogen and energy. Previous studies show that degrading strains are often species of Pseudomonas and rhodococcus that are able to degrade herbicides, phenols, polyaromatic hydrocarbons etc [31]. These results are in agreement with those of Hoffsommer et al (1978) in Naval Surface Weapons Center who reported that TNT in the laboratory under control condition could be biologically transformed into amin isommers with the pure bacterial strains such as Ps. denitrificans [32] and those of Zhang et al [33] who isolated Azospirillium zeae and Rhizobium to treat TNT in red water. He found that Azospirillium might play a key role in reducing the concentration of ammonium. The latter had the ability of nitrogen fixation in the bioreactor [33]. The biotransformation processes ultimately depend on enzyme action. Identification of the enzymes capable of transforming explosives is necessary for bioremediation. Glenn et al. [34] reported that Ps. auroginosa JB2 could degrade 2,4- Dinitrotoluene and aromatics via deoxygenase enzyme and Aken et al. [35] found that Methylobacterium strain have the capacity to metabolize TNT, RDX and HMX explosives. Previously, Bink et al. [36] have reported that Entrobactor Cloacae PB2 isolated from explosive contaminated soil containing only PETN as a nitrogen source. In this study, this is the first report of Entrobactor asburiae and Planomicrobacterium flavidum strains with the ability to degrade TNT and PETN as sole nitrogen and energy sources and therefore it is logical that these isolates may have the potential for TNT and PETN degradation by enzymes potential production (such as nitroreductase, deoxygenase,..). The other isolates have been described to be able to degrade explosives. The results suggest that the indigenous bacteria can effectively degrade explosives in anaerobic conditions.

CONCLUSION

The results of the study demonstrate that TNT and PETN are biodegradable under anaerobic conditions by indigenous bacteria in the presence of sewage sludge as enrichment source, but monorhamnolipid biosurfactant can rapidly increase TNT and PETN degradation rates so that TNT and PETN degradation rates increased to 83% and 68.5% in comparison with 40% and 29% in the absence of biosurfactant. Inoculation of indigenous bacteria have a significantly positive effect on the efficiency of the remediation process, to the extent that TNT removal efficiencies increased to 96% and 99.1% (TNT concentration was less than 30 mg/kg) and PETN removal efficiencies increased to 55% and 91% in pans 1 and 2, respectively. TNT removed significantly higher than PETN in anaerobic conditions. Seven indigenous strains were more potent for explosives degradation which was identified as *Planomicrobacterium flavidum, Pseudomonas auroginosa, Entrobactor asburiae, Azospirillium, Rhizobium*, *Methylobacterium* and *Pseudomonas denitrificant* strains.

Monorhamnolipid biosurfactant might be effective in the improvement of degradation due to the impact on the cell membrane of bacteria. However, knowledge of the metabolic pathways and enzymes is needed so that the microorganisms can degrade explosive compounds more efficiently and effectively.

Acknowledgements: *This study is a PhD approved research project (No. 393924) performed at Isfahan University of Medical Sciences (IUMS), Iran. The authors are thankful for the funding provided by the Department of Environmental Health Engineering and Environment Research Center, IUMS.*

REFERENCES

1. S.N. Singh, Biological remediation of explosive residues. Springer, Switzerland, pp.179-180, 2014.
2. A. Singh, R.C. Kuhad, O.P. Ward, Advances in applied bioremediation. Springer, Switzerland, pp. 38-43, 2009.
3. M. Kulkarni, A. Chaudhari, *J. Environ. Manage.*, **85,** 496 (2007).
4. A.G. Rahal, L.A. Moussa, *Aust. J. Basic Appl. Sci.*, **5,** 8 (2011).
5. N. Čėnas, A. Nemeikaitė-Čėnienė, A. Marozienė, J. Šarlauskas, V. Vilutienė, J. Baublys, EUExcert (Certifying Expertise in European Explosives Sector), 2001, p. 1.
6. L. Zhuang, Ph.D Thesis, University of Waterloo, 2007.
7. R.J. Spanggord, C.D. Yao, T. Mill, *Environ. Sci. Technol*., **34,** 497 (2000).
8. J.D. Rodgers, N.J. Bunce, *Water Res*., **35,** 2101 (2001).
9. P. Kanekar,P. Dautpure, S. Sarnaik, *Indian J Exp Biol.*, **41,** 991 (2003).
10. S.M. King, Dessertation, University of Orlean, 2012.
11. G.El Diwani, S. El Rafie, S. Hawash, *Intl J Environ. Sci. Technol* , **6,** 619(2009).
12. N.E. Georgie, Ph.D Thesis, RMIT University, 2011.
13. P. Innemanová, R. Velebová, A. Filipová, M. Čvančarová, P. Pokorný, J. Němeček, New biotechnology, **32**, 6, 702 (2015).
14. M. Erkelens, E. M.Adetutu, M. Taha, L. Tudararo-Aherobo, J. Antiabong , A. Provatas, *J. Environ. Manage*, **110,** 69 (2012).
15. R. Boopathy, C.F. Kulpa, J. Manning, *Bioresour. Technol.*, **63,** 81 (1998).
16. T. Borch, W. P. Inskeep, J. A. Harwood, R. Gerlach, *Environ. Sci. Tech*., **39,** 7126 (2005).
17. S.S.-B. Moshe, Z. Ronen, O. Dahan, N. Weisbrod, L. Groisman, E. Adar, *Environ. Pollut*., **157,** 2231 (2009).
18. H.-Y. Kim, G.N. Bennett, H.-G. Song, *Biotechnology Letters.*, **24,** 2023 (2002).
19. R. Boopathy, C.F. Kulpa, *Can.J. Microbiol.*, **40,** 273 (1994).
20. L. Zhuang, L. Gui, R.W. Gillham, *Chemosphere*., **89,** 810 (2012).
21. A.L. Juhasz, R. Naidu, *Int. Biodeterior. Biodegrad.*, **45,** 57 (2000).
22. S.N. Singh, and R.D. Tripathi, Environmental bioremediation technologies: Springer Science & Business Media, 2007.
23. O. Muter, K. Potapova, B. Limane, K. Sproge, I. Jakobsone, G. Cepurnieks, *J. Environ. Manage*., **98,** 51(2012).
24. M.M. Amin,, M. Giahi, M. Mansourian, *Int. J. Environ. Health Eng*., **4,** 16 (2015).
25. E. Kaczorek, S. Moszyńska, A. Olszanowski, *Biodegradation*, **22,** 359 (2011).
26. A.A.C. Numbera. Method 8330B Nitroaromatics and Nitramines Esters by High Performance Liquid Chromatoghraphy (HPLC), 2006.
27. L. Muckian, R. Grant, E. Doyle, N. Clipson, *Chemosphere.*, **68,** 1535 (2007).
28. D.E. Ellis, E. J. Lutz, J. M. Odom, R. J. Buchanan, C. L. Bartlett, M. D. Lee, *Environ. Sci. Technol.*, **34,** 2254 (2000).
29. Y. Zhang, R.M. Miller, *Applied and Environmental Microbiology*., **58,** 3276 (1992).
30. N. Manickam, A. Bajaj, H.S. Saini, R. Shanker, *Biodegradation*, **23,** 673 (2012).
31. R. Behki, E.Topp, W. Dick, P. Germon, *Appli. Environ. Microbiol*., **59,** 1955 (1993).
32. J. Hoffsommer, J. Kaplan, D. Glover, D. Kubose, C. Dickinson , Biodegradability of TNT: a three-year pilot plant study, DTIC Document, NAVAL SURFACE WEAPONS CENTER. Dahlgren,Virginia, 22448, 1978,
33. M. Zhang, G.-h. Liu , K. Song, Z. Wang, Q. Zhao, S. Li, *Chem. Eng. J*., **259,** 876 (2015).
34. G.R. Johnson, R.K. Jain, J.C. Spain, *J. Bacteriol*., **184,** 4219 (2002).
35. B. Van Aken, J.M. Yoon, and J.L. Schnoor, *Appli. Environ. Microbiol.*, **70,** 508 (2004).
36. P.R. Binks, C.E. French, S. Nicklin, N.C. Bruce, *Appli. Environ. Microbiol*., **62,** 1214 (1996).

ПОДОБРЕНА БИОДЕГРАДАЦИЯ НА ЕКСПЛОЗИВИ ЧРЕЗ АНАЕРОБНО БИОУСКОРЯВАНЕ

М.М. Амин[1], Х. Канахмад[2], Ф. Теймури[3]*, М. Садами[4], М.А. Карами[5], И. Рахимманеш[2]

[1]*Изследователски център по околна среда, Изследователски институт за предпазване от незаразни болести; Департамент по екологично здраве, Медицински университет в Исфахан, Иран*
[2]*Департамент по генетика, Училище по медицина, Медицински университет в Исфахан, Иран*
[3] *Исфахански университет по медицински науки, Исфахан, Иран. Факултет по здравеопазване, Университет по медицински науки "Язд", Язд, Иран.*
[4] *Университет по медицински науки Шахид Бехещи, Техеран, Иран*
[5] *Университет по медицински науки Лорестан, Хорамабод, Иран*

Постъпила на 28 юни, 2016 г.; Приета на 12 април, 2017 г.

(Резюме)

Извършена е успешна анаеробна биоремедиация на 2,4,6-тринитротолуен (TNT) и на пентаеритритол тетранитрат (PETN), заразени с нативни бактерии. Две почвени проби са обогатени с активна утайка, като едната от тях се смесва с биосърфактанта моно-рамнолипид. И двата субстрата са подходящи за *in situ* биоремедиация на експлозиви. Началните концентрации на TNT и PETN бяха1000 и 200 mg/kg. Резултатите от това изследване показват използването на биосърфактанта води до повишаване биодеградацията на резистентен експлозив, като PETN. Инокулирането с нативни бактерии има значителен ефект за биодеградацията на TNT и PETN, която достига 99,1 и 91 % в присъствие на биосърфактант. Седем микробни щама са идентифицирани като *Planomicrobacterium flavidum, Pseudomonas auroginosa, Entrobactor asburiae, Azospirillium, Rhizobium, Methylobacterium u Pseudomonas denitrificans*. Монорамнолипидът е ефективен за подобряване деградацията на експлозивите поради въздействието му въз клетъчните мембрани. Резултатите от това изследване показаха, че присъщата биоремедиация има потенциал за намаляване на времето и разходите при *in situ* обезвреждането на експлозиви.

Bulgarian Chemical Communications, Volume 49, Number 3, (pp. 742 – 749) 2017

Surface characterization of thiazolidinone derivatives by inverse gas chromatography

Ismail Fidan[1], Dolunay Sakar Dasdan[2]*, Ferdane Karaman[2] and Seniz Kaban[2]

[1]*Gebze Technical University, Faculty of Science, Department of Chemistry, 41400 Gebze Kocaeli, Turkey*
[2]*Yildiz Technical University, Faculty of Arts and Sciences, Department of Chemistry, 34220 İstanbul, Turkey*

Received February 25, 2016; Revised September 9, 2016

Inverse gas chromatography at infinite dilution was used for the first time to determine the adsorption properties and acid-base contributions to the surface energy of thiazoldin-4-ones bearing heteroaryl substituents. *3-(6-Methyl-2-pyridyl)-2-(2-thienyl)-1,3-thiazolidin-4-one* (MPTT) and *3-(6-Methyl-2-pyridyl)-2-(3-methyl-2-thienyl)-1,3-thiazolidin-4-one* (MPMTT) were freshly synthesized via one-pot three component condensation reaction. The retentions of nonpolar solvents such as n-hexane, n-heptane, n-octane, n-nonane, n-decane and other acidic, basic and amphoteric probes such as tetrahydrofurane, dichloromethane, chloroform, acetone and ethyl acetate used without further purification on MPTT and MPMTT were measured in the temperature ranges from 303 to 333 K by inverse gas chromatography (IGC). The dispersive component of the surface energy , γ_S^D of studied adsorbent surface was estimated using retention times of different nonpolar organics in the infinite dilution region. Dispersive components of the surface energies, γ_S^D according to Fowkes and Dorris-Gray approaches and the acid, K_A and base, K_D constants for the *3-(6-Methyl-2-pyridyl)-2-(2-thienyl)-1,3-thiazolidin-4-one* and *3-(6-Methyl-2-pyridyl)-2-(3-methyl-2-thienyl)-1,3-thiazolidin-4-one* were calculated.

Keywords: Inverse gas chromatography; Thiazolidinone derivatives; Surface and adsorption properties; Surface free energies; Lewis acid-base constants.

INTRODUCTION

Thiazolidinone derivatives have growing interest because of their broad spectrum of activities such as antimicrobial [1], anti-HIV [2], cancer treatment agent [3], essence in cosmetics [4], electron releasing layer in solar cell [5], non linear optical property [6] and so on. Recently reported Quantitative Structure-Activity Relationship (QSAR) [7] and docking studies [8,9] were aimed to understand the pharmacological observations of various thiazolidinones. Docking analysis is good tool to elucidate the potential bindings sites of compounds to the active center of targeted enzyme. Even syntheses and biological activities of thiazolidinones are intensely studied, physical properties of them are known little. Surface characterization and acid-base characteristics of thiazolidinione derivatives will contribute to understanding the binding mechanism.

For this reason, in the present study, the surface free energy and acid-base characteristics of compoundS, MPTT and MPMTT were investigated through measurements of net retention volumes of several probe molecules and by use of adsorption on principle in inverse gas chromatography, IGC. The IGC being simple, rapid, low cost, with good accuracy, and available equipment provides valuable thermodynamic information for the physico-chemical and surface characterization of organic materials such as Schiff bases [10,11], liquid crystal [12].

In this work, the possibility of surface characterization by IGC is illustrated with a study of the sorption properties of MPTT and MPMTT. The stationary phase in IGC was prepared thiazolidinione derivatives covered on chromosorb.

EXPERIMENTAL

Probes and Instrumentation

The used solvents were high purity grade nonpolar solvents such as n-hexane (Hx), n-heptane (Hp), n-octane (O), n-nonane (N), n-Decane (D) and polar solvents such as dichloromethane (DCM, acidic), chloroform (TCM, acidic), acetone (Ac, amphoteric), ethyl acetate (EA, amphoteric) and tetrahydrofurane (THF, basic). The all studied solvents and support materials being Chromosorb-W(AW-DMCS-treated, 80/100 mesh) were supplied from Merck AG. Inc. Silane treated glass wool used to plug the ends of the column was obtained from Alltech Associates, Inc.,

The sorption properties of the MPTT and MPMTT were determined using a Hewlett-Packard 6890 Series II gas chromatograph, with a thermal conductivity detector (TCD). High purity helium was used as the carrier gas (flow rate in the range 25–28 cm^3 min^{-1}). A stainless steel columns (0.5 m

* To whom all correspondence should be sent:
E-mail: dolunaykar@yahoo.com

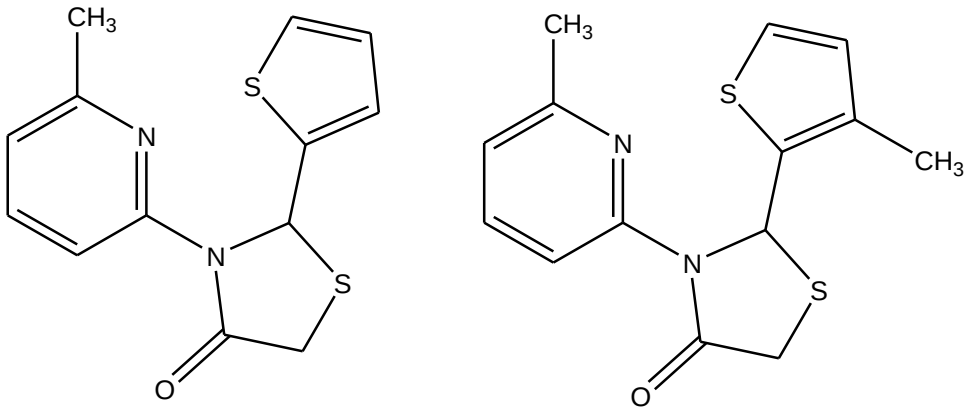

1 **2**

Fig. 1. Chemical Structure of 3-(6-Methyl-2-pyridyl)-2-(2-thienyl)-1,3-thiazolidin-4-one (MPTT) (**1**) and 3-(6-Methyl-2-pyridyl)-2-(3-methyl-2-thienyl)-1,3-thiazolidin-4-one (MPMTT) (**2**)

long, 3.2 mm o.d.) were packed with MPTT and MPMTT covered on chromosorb. After packing, the columns were conditioned overnight at 373 K. Retentions of non polar and polar solvents on MPTT and MPMTT were measured in the temperature range 303–333 K.

Synthesis of 3-(6-Methyl-2-pyridyl)-2-(2-thienyl)-1,3-thiazolidin-4-one (MPTT) and 3-(6-Methyl-2-pyridyl)-2-(3-methyl-2-thienyl)-1,3-thiazolidin-4-one (MPMTT)

3-(6-Methyl-2-pyridyl)-2-(2-thienyl)-1,3-thiazolidin-4-one (**MPTT**) and 3-(6-Methyl-2-pyridyl)-2-(3-methyl-2-thienyl)-1,3-thiazolidin-4-one (**MPMTT**) were prepared according to already known procedure with slight modifications and spectroscopic data are in full agreement with literature [13]. (Figure 1)

INVERSE GAS CHROMATOGRAPHY

The sample under investigation is the stationary phase in inverse gas chromatography while a known substance in the mobile phase acts as a probe molecule. IGC is given information about various adsorption properties, including surface energy, free energy of adsorption and acid–base characteristics. Surface energy is used to describe the energetic situation of a solid surface, being therefore directly related to the adhesion characteristics of a particular material.

In this study, Dorris-Gray and Fowkes methods were applied to determine dispersion component of the surface free energy, γ_S^D of MPTT and MPMTT.

According to Dorris and Gray, corresponding to the adsorption energy of a methylene group, $\Delta G_{A[CH_2]}$ is given by following equation [14]:

$$\Delta G_{A[CH_2]} = -RT \ln(\frac{V_{N,n}}{V_{N,n+1}}) \quad (1)$$

where $V_{N,n}$ and $V_{N,n+1}$ are the retention volumes of two n-alkanes having n and n+1 carbon atoms in their chain and the adsorbate net retention volumes, V_N were calculated from the expression:

$$V_N = Q * J * (t_R - t_A) * T / (T_f) \quad (2)$$

where t_R is the adsorbate retention time, t_A is the retention time of air, Q is volumetric flow rate measured at column outlet and at ambient temperature T_f (K), T is the column temperature (K) and J is James-Martin gas compressibility correction factor [15]. The interactions experienced between an adsorbate and an adsorbent can consist of two components-specific and dispersion forces [16]. Dispersion forces, also known as London forces, are present between all molecules, regardless of their identity. Specific forces generally rely on some compatibility between the structures of the interacting molecules, either physically or electronically.

The adsorption energy for the n-alkanes increases with the number of carbon atoms in the chain.This parameter is independent of the chosen state of the adsorbed molecule. Thus at constant temperature, for a series of alkane probes, a plot $RT\ln V_N$ versus the number of carbon atoms should give a straight line from which $\Delta G_{A[CH_2]}$ can be found.

The methylene adsorption energy can also be defined as [14]

$$\Delta G_{A[CH_2]} = 2N_A a_{[CH_2]}\sqrt{\gamma_S^D \gamma_{L[CH_2]}} \qquad (3)$$

where N_A is Avagadro's number, $a_{[CH_2]}$ is the surface area covered by one methylene group (0.06 nm^2) and $\gamma_L[CH_2]$ is the surface free energy of a surface consisting of methylene groups, i.e. polyethylene, given by

$$\gamma_L[CH_2] = 35.6 + 0.058(293 - T) \qquad (4)$$

Thus using Eqs.(1)-(4) and the experimentally determined values of $V_{N,n}$ and $V_{N,n+1}$, the dispersion component of the surface free energy, γ_S^D may be calculated according to Dorris-Gray approach.

The retention time of a series of homologous n-alkanes is used to determine the dispersive surface energy of the MPTT and MPMTT from following equation: [17]

$$\Delta G_A^S = RT\ln(V_n) = 2N_A(\gamma_S^D)^{0.5} a(\gamma_L^D)^{0.5} + K'' \qquad (5)$$

where ΔG_A^S is the dispersive free energy of adsorption, γ_S^D is the dispersive componenets of the surface tension of the adsorbent such as MPTT and MPMTT, γ_L^D is the dispersive componenets of the surface tension of the adsorbate such as non-polar and polar solvents. ΔG_A^S is the dispersive free energy of adsorption is calculated from following equation:

$$-\Delta G_A^S = RT\ln\left(\frac{V_{N,n}}{V_{N,ref}}\right) \qquad (6)$$

where $V_{N,n}$ and $V_{N,ref}$ are the retention volume for the polar probe and the retention volume for the n-alkanes' reference line, respectively.

ΔH_A^S is the adsorption enthalpy by Lewis acid-base interactions, ΔS_A^S is the adsorption entropy Lewis acid-base interactions and for each polar probe, ΔH_A^S and ΔS_A^S can be determined from belove equation;

$$\Delta G_A^S = \Delta H_A^S - T\Delta S_A^S \qquad (7)$$

The surface Lewis acidity and basicity constants, K_A and K_D, may be calculated from the equation, [18-20]

$$-\Delta H_A^S = K_A DN + K_D AN^* \qquad (8)$$

The constants K_A and K_D describe the acidity and basicity of MPTT and MPMTT surfaces, respectively.

K_A and K_D are obtained from a plot of $-\Delta H_A^S / AN^*$ versus DN/AN^* with K_A as the slope and K_D as the intercept. Parameters K_A and K_D reflect the ability of the examined surface to act as an electron acceptor and electron donor, respectively [21,22].

Values of $a(\gamma_L^D)^{0.5}$ and boiling point, $T_b(^oC)$ of apolar solvents are found in the literature [21,22]. The values of $a(\gamma_L^D)^{0.5}$ used in this study are presented in Table 1. Values of a, $(\gamma_l^d)^{0.5}$, boiling point, $T_b(^oC)$, the Gutmann's modified acceptor number, AN^* and donor number, DN of the polar probes used in this study are presented in Table 2 [23,24].

Table 1. Values of $a(\gamma_L^D)^{0.5}$ for the selected n-alkane solvents

Probe	$a(x10^{-10}m^2)$	$\gamma_L^D(mJ/m^2)$	$a(\gamma_L^D)^{0.5}(m^2(mJ/m^2)^{0.5})$	$T_b(^oC)$
n-Hexane	51.0	18.4	2.19x10^{-18}	68.7
n-Heptane	57.0	20.3	2.57x10^{-18}	98.4
n-Octane	62.8	21.3	2.90x10^{-18}	125.7
n-Nonane	69.0	22.7	3.28x10^{-18}	150.8
n-Decane	75.0	23.4	3.63x10^{-18}	174.1

Table 2. Values of $a(\gamma_l^d)^{0.5}$, DN and AN^* for the selected polar solvents

Probe	$a(x10^{-10}m^2)$	$\gamma_l^d(mJ/m^2)$	$a(\gamma_l^d)^{0.5}(m^2(mJ/m^2)^{0.5})$	$AN^*(kJ/mol)$	$DN(kJ/mol)$	$T_b(^oC)$
THF	45.0	22.5	$2.13x10^{-18}$	2.1	84.0	66.0
Ac	42.5	16.5	$1.73x10^{-1}$	10.5	71.4	56.0
DCM	31.5	27.6	$1.65x10^{-18}$	16.4	0.0	40.0
TCM	44.0	25.9	$2.24x10^{-18}$	22.7	0.0	61.2
EA	48.0	19.6	$2.13x10^{-18}$	6.3	71.8	77.1

RESULTS AND DISCUSSION

The net retention volumes, V_N of the nonpolar and polar solvents on MPTT and MPMTT compounds were obtained from IGC measurements between 303 and 333 K at infinite dilution region using Eq.(2) and retention diagrams of nonpolar and polar solvents were given in Fig.1a and Fig.1b, respectively for MPTT as an example.

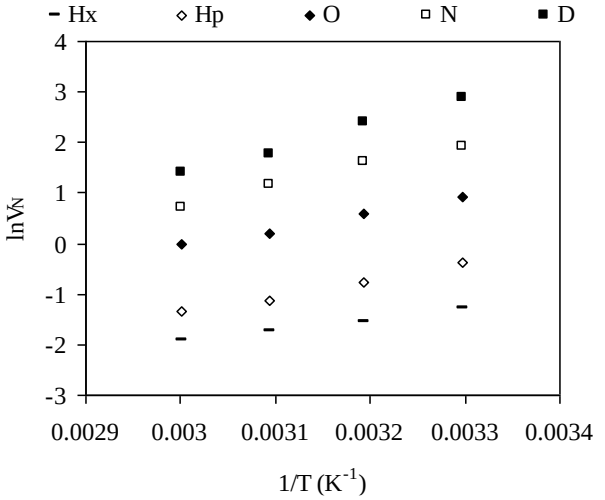

Fig. 1(a). The retention diagram of non-polar solvents adsorbed onto MPTT

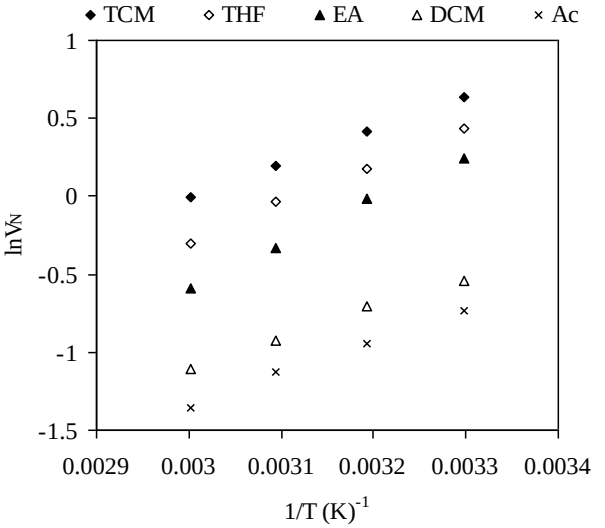

Fig. 1(b). The retention diagram of polar solvents adsorbed onto MPTT

According to Dorris-Gray approaches, Eq.(1), $\Delta G_{A[CH_2]}$ is independent of the chosen reference state of adsorbed molecule. The $RT\ln V_N$ versus carbon number of non-polar solvents were plotted in Fig.(2) for MPTT and Fig.(3) for MPMTT.

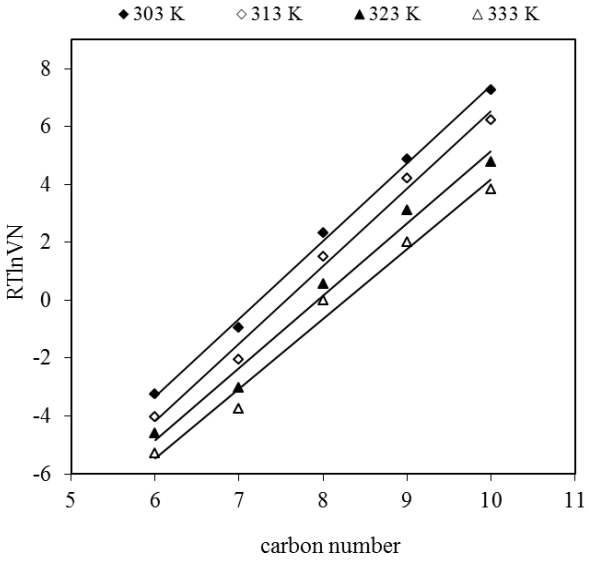

Fig. 2. The plot of $RT\ln V_N$ versus carbon number of non-polar solvents for MPTT

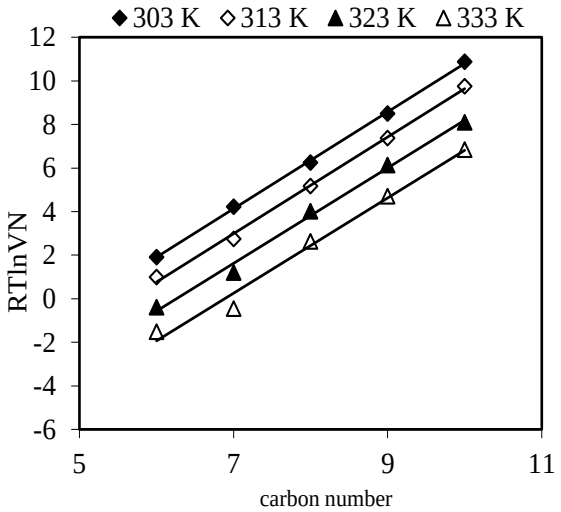

Fig. 3. The plot of versus carbon number of non-polar solvents for MPMTT

The slope of the fitted line is equal to $\Delta G_{A[CH_2]}$. The variation of γ_S^D and $\gamma_L[CH_2]$ with temperature were calculated from Eq.(3) and (4),

respectively. The results of $\Delta G_{A[CH_2]}$, $\gamma_L[CH_2]$ and γ_S^D of MPTT and MPMTT were given in Table 3 and Table 4, respectively .

Table 3 The adsorption energy of a methylene group, $\Delta G_{A[CH_2]}$, the surface free energy of a surface consisting of methylene groups, $\gamma_L[CH_2]$ and dispersion component of surface free energy, γ_S^D values calculated by Doris-Gray approach for MPTT determined at studied temperatures

T(K)	$\gamma_L[CH_2]$ (mJ/m^2)	$\Delta G_{A[CH_2]}$ (10^6 mJ/mol)	γ_S^D (mJ/m^2)
303	35.02	2.68	39.45
313	34.44	2.68	39.96
323	33.86	2.49	35.17
333	33.28	2.41	33.33

Table 4 The adsorption energy of a methylene group, $\gamma_L[CH_2]$ the surface free energy of a surface consisting of methylene groups, $\Delta G_{A[CH_2]}$ and dispersion component of surface free energy, γ_S^D values calculated by Doris-Gray approach for MPMTT determined at studied temperatures

T(K)	$\gamma_L[CH_2]$ (mJ/m^2)	$\Delta G_{A[CH_2]}$ (10^6 mJ/mol)	γ_S^D (mJ/m^2)
303	35.02	2.22	27.02
313	34.44	2.21	27.32
323	33.86	2.19	27.12
333	33.28	2.18	27.54

Table 3 and 4 report that the variation of γ_S^D as a function of temperature was limited and the γ_S^D values of MPTT and MPMTT do not change significantly between 303 and 333 K. In comparison, methyl group was decreased the surface energy of thiazolidinone derivative. The methyl group reduced the dispersive surface energy due to the interaction with lower energetic sites in the surface.

The Fowkes equation (Eq. 5, referred to as Schultz and Lavielle approach by some authors) [17] was used to determine the dispersive component of the surface free energy, γ_S^D over a range of studied temperatures and calculated values of $RT\ln V_N$ were plotted against $a(\gamma_L^D)^{0.5}$. An example of the pattern of results obtained was given in Fig. 4 (MPTT) and Fig.5 (MPMTT) for the isotherm at 303 K.

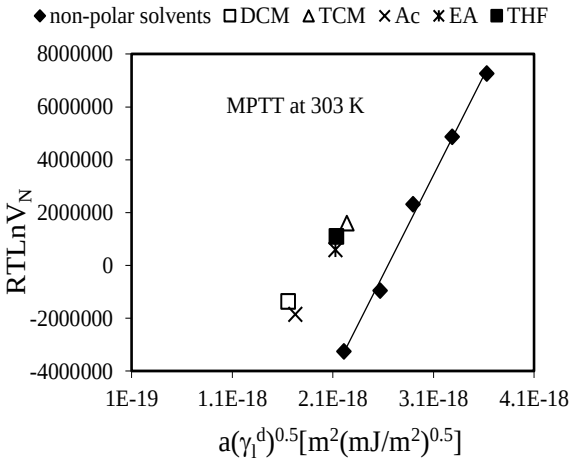

Fig. 4. A plot of $RT\ln V_N$ vs. $a(\gamma_L^D)^{0.5}$ for non-polar and polar probes on MPTT at 303 K

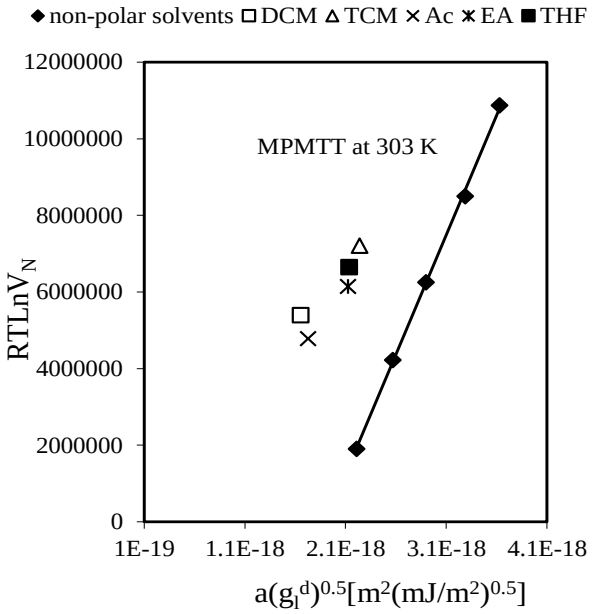

Fig. 5. A plot of $RT\ln V_N$ vs. $a(\gamma_L^D)^{0.5}$ for non-polar and polar probes on MPMTT at 303 K

The linearity was obtained by the non-polar solvents at the studied temperature ranges. The slope ($2N\sqrt{\gamma_S^D}$) of the linear fit, obtained for each n-alkane plot, gives the dispersive component of the surface free energy, γ_S^D at that temperature. The values of γ_S^D at studied temperature ranges were given in Table 5 for MPTT and Table 6 for MPMTT.

Table 5 γ_S^D values calculated by Fowkes approach and slope at studied temperatures for MPTT

T(K)	Slope (x10^{24})	γ_S^D (mJ/m^2)
303	7.5334	39.15
313	7.5195	39.00
323	6.9938	33.74
333	6.7422	31.36

Table 6. γ_S^D values calculated by Fowkes approach and slope at studied temperatures for MPMTT

T(K)	Slope (x10^{24})	γ_S^D (mJ/m^2)
303	6.2370	26.83
313	6.2186	26.68
323	6.1402	26.01
333	6.1348	25.96

The values of γ_S^D of MPTT and MPMTT calculated according to Dorris-Gray and Fowkes approaches are very close each other at the studied temperature ranges. There is no data in the literature to compare these values. Methyl group is decreased the γ_S^D of MPMTT according to MPTT values.

The specific component of the surface free energy, ΔG_A^S, is calculated using the difference between the calculated value of $RT\ln V_N$ and that which was derived using the equation of the linear fit of the n-alkane reference line (Eq.6).

The variation of free energy of specific interactions, ΔG_A^S between MPTT and MPMTT and polar solvents for studied temperatures is given Table 7 and Table 8, respectively.

Table 7. The variation of free energy of specific interactions, $-\Delta G_A^S$ (kJ/mol) between MPTT and polar solvents for studied temperatures

T(K)	*THF*	*Ac*	*DCM*	*TCM*	*EA*
303	*4.9*	*5.1*	*6.1*	*4.7*	*4.5*
313	*5.2*	*5.3*	*6.5*	*5.0*	*4.8*
323	*5.2*	*5.1*	*6.2*	*5.1*	*4.5*
333	*5.1*	*4.9*	*6.1*	*5.2*	*4.4*

Table 8. The variation of free energy of specific interactions, $-\Delta G_A^S$ (kJ/mol) between MPMTT and polar solvents for studied temperatures

T(K)	THF	Ac	DCM	TCM	EA
303	9.1	9.5	10.0	9.5	7.9
313	9.5	9.2	9.7	9.3	7.9
323	9.2	8.9	9.4	9.2	7.6
333	8.9	8.6	9.3	8.9	7.1

The $-\Delta G_A^S$ values of MPMTT were higher than MPTT values. Temperature increasing did not affect significantly the $-\Delta G_A^S$ values of MPTT and MPMTT. ΔH_A^S and ΔS_A^S can be determined from a plot of $-\Delta G_A^S / T$ against $1/T$. (Eq.7)

The values of K_A and K_D were calculated using Eq.(8). The plotting $-\Delta H_A^S / AN^*$ versus DN / AN^* with K_A as the slope and K_D as the intercept. (Fig.6 for MPTT and Fig.7 for MPMTT).

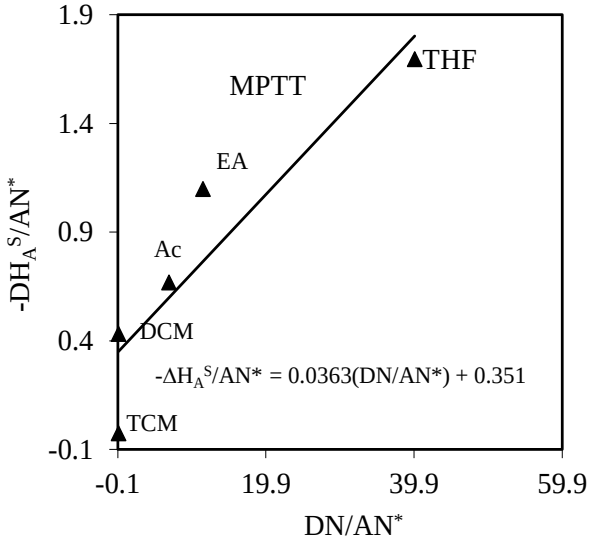

Fig. 6. The plot of $-\Delta H_A^S / AN^*$ versus DN / AN^* for MPTT

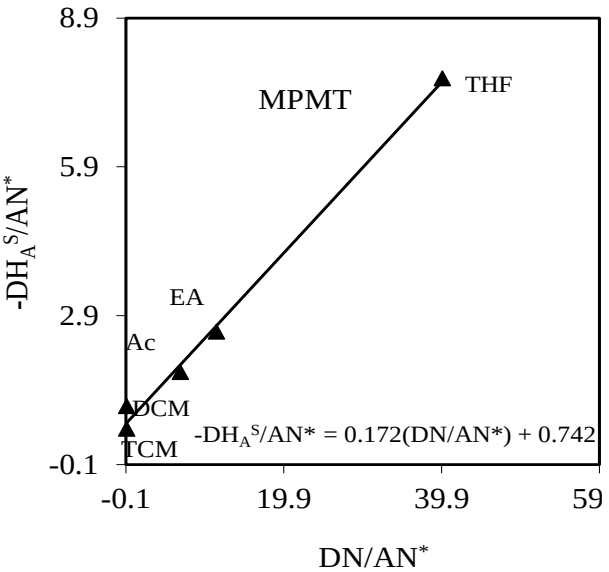

Fig. 7. The plot of $-\Delta H_A^S / AN^*$ versus DN / AN^* for MPMTT

The values of K_A and K_D are found to be 0.04 and 0.4 for MPTT and the values of K_A and

K_D are found to be 0.2 and 0.7 for MPMTT. If the ratio of K_D to K_A is greater than 1, solid surface is basic nature and below 1, it implies that the solid surface is acidic nature [25]. According to the K_D/K_A ratios of MPTT and MPMTT, MPTT surface has more basic nature than MPMTT surface. It can be said that methyl group is decreased the basic nature of thiazolidinone derivatives.

CONCLUSION

Adsorption properties, surface and Lewis acid-base characteristics of MPTT and MPMTT have been examined by means of inverse gas chromatography at infinite dilution, in the temperature range from 303 to 333 K. The γ_S^D values of MPTT change ranges from 39.5 to 33.3 mJ/m^2 and (Dorris-Gray approach) from 39.2 to 31.4 mJ/m^2 (Fowkes approach) with decreasing temperature while the γ_S^D values of MPMTT change ranges from 27.0 to 27.5 mJ/m^2 and (Dorris-Gray approach) from 26.8 to 26.0 mJ/m^2 (Fowkes approach) with decreasing temperature. The values of K_A and K_D parameters indicated that MPTT and MPMTT surfaces are basic nature. IGC is a convenient method for the characterization of the surface and adsorption properties and the acid-base characteristics of thiazolidinone derivatives.

Acknowledgements: *This research has been supported by Yildiz Technical University Scientific Research Projects Coordination Department.*

REFERENCES

1. P. Vicini, A. Geronikaki, K. Anastasia, M. Incerti, F. Zani, *Bioorganic & Medicinal Chemistry*, **14**, 3859 (2006).
2. V. Murugesan, S.V. Tiwari, R. Saxena, R. Tripathi, R. Paranjape, S. Kulkarni, N. Makwana, R. Suryawanashi, S.B. Katti, *Bioorganic & Medicinal Chemistry*, **19**, 6919 (2011).
3. V. Gududuru, E. Hurh, J.T. Dalton, D.D. Miller, *Journal of Medicinal Chemistry*, **48**, 2584 (2005).
4. A. Pawelczyk, L. Zaprutko, *European Journal of Medicinal Chemistry*, **41**, 586 (2006).
5. K. Takahashi, N. Kuraya, T. Yamaguchi, T. Komura, K. Murata, *Solar Energy Materials & Solar Cells*, **61**, 403 (2000).
6. V. Smokal , B. Derkowska, O. Krupka, O. Kolendo, B. Sahraoui, *Optical Materials*, **31**, 554 (2009).
7. R.F. George, *European Journal of Medicinal Chemistry*, doi:10.1016/j.ejmech.2011.11.006, (2011).
8. P. Eleftheriou, et al., *European Journal of Medicinal Chemistry*, doi:10.1016/j.ejmech.2011.10.029 (2011).
9. R. Ottana, et al., *European Journal of Medicinal Chemistry*, **46**, 2797 (2011).
10. G. Karaoglan-Keser, D. Sakar, *Chromatographia*, **73**(1-2), 93 (2012).
11. G. Gumrukcu, S. Garikyan, G. Keser-Karaoglan, D. Sakar, *Journal of Chemistry*, Volume **2013**, Article ID 298205, 6 pages (2013).
12. F. Sesigür, D. Sakar, O. Yasa-Sahin, H. Ocak, O. Cankurtaran, B. Bilgin-Eran, F.Karaman *Liquid Crystals*, **39(1)**, 87 (2012).
13. I. Fidan, C. Kazaz, E. Sahin, S. Kaban, *Journal of Chemical Research*, **2010(5),** 296 (2010).
14. G.M. Dorris and D.G. Gray, *J. Colloid Interf. Sci.*, **77**, 353 (1980).
15. J.R. Conder C.L., Young, Physicochemical Measurement by Gas Chromatography. Wiley-Interscience, New York, 1979.
16. A.V. Kiselev, *Discuss. Faraday Soc.*, **40**, 205 (1965).
17. J. Schultz, L. Lavielle, C. Martin, *Journal of Adhesion*, **23**, 45–60 (1987).
18. D. Gavara, R. Lagarón, A. Voelkel, Journal of Chromatography A, **1148**, 86 (2007).
19. A. Voelkel, *Critical Reviews in Analytical Chemistry*, **22**,411 (1991).
20. V. Gutmann, The donor–acceptor approach to molecular interactions, New York: Plenum Press, 1978.
21. F.L. Riddle and F.M. FowkeS, *J. Am. Chem. Soc.*, **112**, 3259 (1990).
22. D.P. Kamdem , S.K. Bose, P. Luner, *Langmuir*, **9**, 3039 (1993).
23. J.M.R.C.A. Santos and J.T. Guthrie, *Mat. Sci. Eng. R.* , **50**, 79 (2005).
24. J.M.R.C.A. Santos and J.T. Guthrie, *J. Chromatogr. A*, **1070**, 147 (2005).
25. O. Yazici, H. Ocak, O. Yasa-Sahin, D. Sakar, O. Cankurtaran, F. Karaman, B. Bilgin- Eran, *Liquid Crystals*, **39(12),** 1421 (2012).

ПОВЪРХНОСТНО ОХАРАКТЕРИЗИРАНЕ НА ТИАЗОЛИДИНОНОВИ ПРОИЗВОДНИ С ОБРАТНА ГАЗОВА ХРОМАТОГРАФИЯ

И. Фидан[1], Д. Сакар Дасдан[2*], Ф. Караман[2], Ш. Кабан[2]

[1]Технически университет Гебзе, Научен факултет, Департамент по химия, 41400 Гебзе Коджаели, Турция
[2]Технически университет „Йилдиз“, Факултет за изкуство и наука, Департамент по химия, 34220 Истанбул, Турция

Постъпила на 25 февруари, 2016 г.; приета на 9 септември, 2016 г.

(Резюме)

За пръв път е използвана обратната газова хроматография при безкрайно разреждане за определянето на адсорбционните свойства и киселинните отнасяния за повърхностната енергия на тиазолидин-4-они с хетероарилови заместители. *3-(6-метил-2-пиридил)-2-(2-тиенил)-1,3-тиазолидин-4-он* (MPTT) и *3-(6-метил-2-пиридил-2-(3-метил-2-тиенил)-1,3-тиазолидин-4-он* (MPMTT) са прясно синтезирани чрез едно степенна три-компонентна кондензационна реакция. Измервано е задържането на не-полярни разтворители като n-хексан, n-хептан, n-октан, n-нонан, n-декан и други киселинни, базични и амфотерни проби, като тетрахидрофуран, дихлорметан, хлороформ, ацетон и етилацетат без пречистваане на MPTT на MPMTT в температурния интервал от 303 до 333 K чрез обратна газова хроматография (IGC). Дисперсионната компонента на повърхностната енергия γ_S^D на изследваните адсорбционни повърхности е оценена използвайки времената на задържане на различни неполярни органични съединения в областта на безкрайно разреждане. Дисперсионните компоненти на повърхностните енергии γ_S^D по Fowkes и Dorris-Gray са близки и са пресметнати киселинните K_A and базичните константи K_D за съединенията *3-(6-метил-2-пиридил)-2-(2-тиенил)-1,3-тиазолидин-4-он* и *3-(6-метил-2-пиридил-2-(3-метил-2-тиенил)-1,3-тиазолидин-4-он.*

BULGARIAN CHEMICAL COMMUNICATIONS

Instructions about Preparation of Manuscripts

General remarks: Manuscripts are submitted in English by e-mail or by mail (in duplicate). The text must be typed double-spaced, on A4 format paper using Times New Roman font size 12, normal character spacing. The manuscript should not exceed 15 pages (about 3500 words), including photographs, tables, drawings, formulae, etc. Authors are requested to use margins of 3 cm on all sides. For mail submission hard copies, made by a clearly legible duplication process, are requested. Manuscripts should be subdivided into labelled sections, e.g. **Introduction, Experimental, Results and Discussion**, *etc*.

The title page comprises headline, author's names and affiliations, abstract and key words.

Attention is drawn to the following:

a) **The title** of the manuscript should reflect concisely the purpose and findings of the work. Abbreviations, symbols, chemical formulas, references and footnotes should be avoided. If indispensable, abbreviations and formulas should be given in parentheses immediately after the respective full form.

b) **The author**'s first and middle name initials, and family name in full should be given, followed by the address (or addresses) of the contributing laboratory (laboratories). **The affiliation** of the author(s) should be listed in detail (no abbreviations!). The author to whom correspondence and/or inquiries should be sent should be indicated by asterisk (*).

The abstract should be self-explanatory and intelligible without any references to the text and containing not more than 250 words. It should be followed by key words (not more than six).

References should be numbered sequentially in the order, in which they are cited in the text. The numbers in the text should be enclosed in brackets [2], [5, 6], [9–12], etc., set on the text line. References, typed with double spacing, are to be listed in numerical order on a separate sheet. All references are to be given in Latin letters. The names of the authors are given without inversion. Titles of journals must be abbreviated according to Chemical Abstracts and given in italics, the volume is typed in bold, the initial page is given and the year in parentheses. Attention is drawn to the following conventions:

a) The names of all authors of a certain publications should be given. The use of "*et al*." in the list of references is not acceptable.

b) Only the initials of the first and middle names should be given.

In the manuscripts, the reference to author(s) of cited works should be made without giving initials, e.g. "Bush and Smith [7] pioneered...". If the reference carries the names of three or more authors it should be quoted as "Bush *et al*. [7]", if Bush is the first author, or as "Bush and co-workers [7]", if Bush is the senior author.

Footnotes should be reduced to a minimum. Each footnote should be typed double-spaced at the bottom of the page, on which its subject is first mentioned.

Tables are numbered with Arabic numerals on the left-hand top. Each table should be referred to in the text. Column headings should be as short as possible but they must define units unambiguously. The units are to be separated from the preceding symbols by a comma or brackets.

Note: The following format should be used when figures, equations, *etc*. are referred to the text (followed by the respective numbers): Fig., Eqns., Table, Scheme.

Schemes and figures. Each manuscript (hard copy) should contain or be accompanied by the respective illustrative material as well as by the respective figure captions in a separate file (sheet). As far as presentation of units is concerned, SI units are to be used. However, some non-SI units are also acceptable, such as °C, ml, l, etc.

The author(s) name(s), the title of the manuscript, the number of drawings, photographs, diagrams, etc., should be written in black pencil on the back of the illustrative material (hard copies) in accordance with the list enclosed. Avoid using more than 6 (12 for reviews, respectively) figures in the manuscript. Since most of the illustrative materials are to be presented as 8-cm wide pictures, attention should be paid that all axis titles, numerals, legend(s) and texts are legible.

The authors are asked to submit **the final text** (after the manuscript has been accepted for publication) in electronic form either by e-mail or mail on a 3.5'' diskette (CD) using a PC Word-processor. The main text, list of references, tables and figure captions should be saved in separate files (as *.rtf or *.doc) with clearly identifiable file names. It is essential that the name and version of

the word-processing program and the format of the text files is clearly indicated. It is recommended that the pictures are presented in *.tif, *.jpg, *.cdr or *.bmp format, the equations are written using "Equation Editor" and chemical reaction schemes are written using ISIS Draw or ChemDraw programme.

The authors are required to submit the final text with a list of three individuals and their e-mail addresses that can be considered by the Editors as potential reviewers. Please, note that the reviewers should be outside the authors' own institution or organization. The Editorial Board of the journal is not obliged to accept these proposals.

EXAMPLES FOR PRESENTATION OF REFERENCES

REFERENCES

1. D. S. Newsome, *Catal. Rev.–Sci. Eng*., **21**, 275 (1980).
2. C.-H. Lin, C.-Y. Hsu, *J. Chem. Soc. Chem. Commun*., 1479 (1992).
3. R. G. Parr, W. Yang, Density Functional Theory of Atoms and Molecules, Oxford Univ. Press, New York, 1989.
4. V. Ponec, G. C. Bond, Catalysis by Metals and Alloys (Stud. Surf. Sci. Catal., vol. 95), Elsevier, Amsterdam, 1995.
5. G. Kadinov, S. Todorova, A. Palazov, in: New Frontiers in Catalysis (Proc. 10th Int. Congr. Catal., Budapest, 1992), L. Guczi, F. Solymosi, P. Tetenyi (eds.), Akademiai Kiado, Budapest, 1993, Part C, p. 2817.
6. G. L. C. Maire, F. Garin, in: Catalysis. Science and Technology, J. R. Anderson, M. Boudart (eds), vol. 6, Springer-Verlag, Berlin, 1984, p. 161.
7. D. Pocknell, *GB Patent* 2 207 355 (1949).
8. G. Angelov, PhD Thesis, UCTM, Sofia, 2001.
9. JCPDS International Center for Diffraction Data, Power Diffraction File, Swarthmore, PA, 1991.
10. CA **127**, 184 762q (1998).
11. P. Hou, H. Wise, *J. Catal.*, in press.
12. M. Sinev, private communication.
13. http://www.chemweb.com/alchem/articles/1051611477211.html.

CONTENTS

СЪДЪРЖАНИЕ